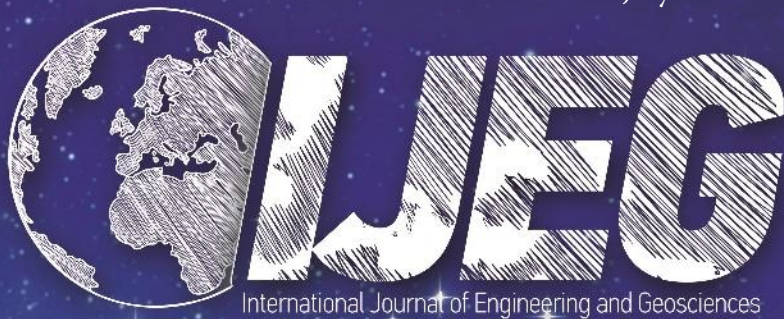


Volume 9 Issue 2 July 2024



IJEG

International Journal of Engineering and Geosciences



e-ISSN 2548-0960

EDITOR IN CHIEF

Prof. Dr. Murat YAKAR
Mersin University Engineering Faculty
Turkey

CO-EDITORS

Prof. Dr. Ekrem TUŞAT
Konya Technical University
Faculty of Engineering and Natural Sciences
Turkey

Prof. Dr. Songnian Li,
Ryerson University
Faculty of Engineering and Architectural Science,
Canada

Assoc. Prof. Dr. Ali ULVI
Mersin University Engineering Faculty
Turkey

ADVISORY BOARD

Prof. Dr. Orhan ALTAN
Honorary Member of ISPRS, ICSU EB Member
Turkey

Prof. Dr. Naser El SHAMY
The University of Calgary Department of Geomatics Engineering,
Canada

Prof. Dr. Armin GRUEN
ETH Zurich University
Switzerland

Prof. Dr. Ferruh YILDIZ
Selcuk University Engineering Faculty
Turkey

Prof. Dr. Artu ELLMANN
Tallinn University of Technology Faculty of Civil Engineering
Estonia

EDITORIAL BOARD

Prof. Dr. Alper YILMAZ
Environmental and Geodetic Engineering, The Ohio State University,
USA

Prof. Dr. Chryssy Potsiou
National Technical University of Athens-Rural and Surveying Engineering,
Greece

Prof. Dr. Cengiz ALYILMAZ
Ataturk University Kazim Karabekir Faculty of Education
Turkey

Prof. Dr. Dieter FRITSCH
University of Stuttgart Institute for Photogrammetry
Germany

Prof. Dr. Edward H. WAITHAKA
Jomo Kenyatta University of Agriculture & Technology
Kenya

Prof.Dr. Halil SEZEN
Environmental and Geodetic Engineering, The Ohio State University
USA

Prof.Dr. Huiming TANG
China University of Geoscience..., Faculty of Engineering,
China

Prof.Dr. Laramie Vance POTTS
New Jersey Institute of Technology, Department of Engineering Technology
USA

Prof.Dr. Lia MATCHAVARIANI
Iv. Javakishvili Tbilisi State University Faculty of Geography
Georgia

Prof.Dr. Məqsəd Hüseyn QOCAMANOV
Baku State University Faculty of Geography
Azerbaijan

Prof.Dr. Muzaffer KAHVECI
Selcuk University Faculty of Engineering
Turkey

Prof.Dr. Nikolai PATYKA
National University of Life and Environmental Sciences of Ukraine
Ukraine

Prof.Dr. Petros PATIAS
The Aristotle University of Thessaloniki, Faculty of Rural & Surveying Engineering
Greece

Prof.Dr. Pierre GRUSSENMEYER
National Institute of Applied Science, Department of Civil Engineering and Surveying
France

Prof.Dr. Rey-Jer You
National Cheng Kung University, Tainan · Department of Geomatics
China

Prof.Dr. Xiaoli DING
The Hong Kong Polytechnic University, Faculty of Construction and Environment
Hong Kong

Assoc.Prof.Dr. Elena SUKHACHEVA
Saint Petersburg State University Institute of Earth Sciences
Russia

Assoc.Prof.Dr. Semra ALYILMAZ
Ataturk University Kazim Karabekir Faculty of Education
Turkey

Assoc.Prof.Dr. Fariz MIKAILSOY
Igdir University Faculty of Agriculture
Turkey

Assoc.Prof.Dr. Lena HALOUNOVA
Czech Technical University Faculty of Civil Engineering
Czech Republic

Assoc.Prof.Dr. Medzida MULIC
University of Sarajevo Faculty of Civil Engineering
Bosnia and Herzegovina

Assoc.Prof.Dr. Michael Ajide OYINLOYE
Federal University of Technology, Akure (FUTA)
Nigeria

Assoc.Prof.Dr. Mohd Zulkifli bin MOHD YUNUS
Universiti Teknologi Malaysia, Faculty of Civil Engineering
Malaysia

Assoc.Prof.Dr. Syed Amer MAHMOOD
University of the Punjab, Department of Space Science
Pakistan

Assist. Prof. Dr. Yelda TURKAN
Oregon State University,
USA

Dr. G. Sanka N. PERERA
Sabaragamuwa University Faculty of Geomatics
Sri Lanka

Dr. Hsiu-Wen CHANG
National Cheng Kung University, Department of Geomatics
Taiwan

The International Journal of Engineering and Geosciences (IJEG)

The International Journal of Engineering and Geosciences (IJEG) is a tri-annually published journal. The journal includes a wide scope of information on scientific and technical advances in the geomatics sciences. The International Journal of Engineering and Geosciences aims to publish pure and applied research in geomatics engineering and technologies. IJEG is a double peer-reviewed (blind) OPEN ACCESS JOURNAL that publishes professional level research articles and subject reviews exclusively in English. It allows authors to submit articles online and track his or her progress via its web interface. All manuscripts will undergo a refereeing process; acceptance for publication is based on at least two positive reviews. The journal publishes research and review papers, professional communication, and technical notes. IJEG does not charge for any article submissions or for processing.

CONTENTS



Volume 9 - Issue 2

RESEARCH ARTICLES

A comparative spectral assessment approach of SEBAL and SEBS for actual evaporation estimation in Ardabil Province	
Khalil Valizadeh Kamran, Mahmoud Sourghali, Samaneh Bagheri	131-146
Determination of alternative forest road routes using produced landslide susceptibility maps: A case study of Tonya (Trabzon), Türkiye	
Fatih Kadı, Osman Salih Yılmaz	147-164
Accuracy assessment of UAS photogrammetry and structure from motion in surveying and mapping	
Sayed Ishaq Deliry, Uğur Avdan	165-190
A practical software package for estimating the periodicities in time series by least-squares spectral analysis	
Ramazan Alpay Abbak	191-198
GIS-based determination of potential snow avalanche areas: A case study of Rize Province of Türkiye	
Ebru Colak, Gamze Bediroglu, Tugba Memisoglu Baykal	199-210
Human micro-doppler detection and classification studies at Mersin University using real outdoor experiments via C-band FMCW radar	
Onur Tekir, Caner Özdemir	211-220
Changes in water surface area of the Middle Atlas-Morocco lakes: A response to climate and human effects	
Abdelaziz El-Bouhali, Mhamed Amyay, Khadija El Ouazani Ech-Chahdi	221-232
Machine learning assisted prediction of land surface temperature (LST) based on major air pollutants over the Annamayya District of India	
Jagadish Kumar Mogaraju	233-246
Detection of upwelling events in the Caspian Sea using thermal satellite image processing	
Said Safarov, Khalil Valizadeh Kamran, Vusal Ismayilov, Elnur Safarov	247-255
Introduction of the Runge-Kutta method in GPS orbit computation	
Sid Ahmed Medjahed	256-263
Mapping the structural vulnerability to drought in Morocco	
Noureddine Bijaber, Atmane Rochdi, Mohammed Yessef, Houda El Yacoubi	264-280
An unmanned aerial vehicle based investigation of roof patch suitability for solar panel installation	
Nizar Polat, Abdulkadir Memduhoğlu	281-291
Registration of interferometric DEM by deep artificial neural networks using GPS control points coordinates as network target	
Ahmed Serwa, Abdul Baser Qasimi, Vahid Isazade	292-301
Comparative analysis of non-invasive measurement methods for optimizing architectural documentation	
Serhan Tuncer, Uğur Avdan	302-313



A comparative spectral assessment approach of SEBAL and SEBS for actual evaporation estimation in Ardabil Province

Khalil Valizadeh Kamran ^{*1}, Mahmoud Sourghali ¹, Samaneh Bagheri ¹

¹ University of Tabriz, Department of Remote Sensing and GIS, Iran, valizadeh@tabrizu.ac.ir, m.sourghali@gmail.com, samanehbagheri99@gmail.com

Cite this study:

Valizadeh Kamran, K., Sourghali, M., & Bagheri, S. (2024). A comparative spectral assessment approach of SEBAL and SEBS for actual evaporation estimation in Ardabil Province. *International Journal of Engineering and Geosciences*, 9 (2), 131-146

<https://doi.org/10.26833/ijeg.1344679>

Keywords

Evapotranspiration
Mughan plain
OLI and TIRS sensors
SEBAL
SEBS

Research Article

Received: 17.08.2023
Revised: 03.12.2023
Accepted: 09.12.2023
Published: 23.07.2024



Abstract

Evapotranspiration is a crucial process in the Earth's water and climate cycle, responsible for transforming water from liquid to water vapor. This transformation plays a vital role in the global water cycle and has a significant impact on the climate, weather patterns, and precipitation in various regions. In this study, actual evapotranspiration in the Mughan plain of Ardabil province has been estimated using spectral data from the OLI and TIRS sensors of the Landsat 8 satellite. The SEBAL (Surface Energy Balance Algorithm for Land) and SEBS (Surface Energy Balance System) methods have been employed to calculate these phenomena. SEBAL is an energy balance algorithm designed for land surfaces, utilizing satellite data to estimate actual evapotranspiration accurately. Similarly, SEBS is a surface energy balance system that provides a more precise estimation of evapotranspiration and transpiration rates. Data from the OLI and TIRS sensors of Landsat 8 were collected from the study area for this research. By applying the SEBAL and SEBS methods to these data, actual evapotranspiration values in the Mughan plain were obtained. The results indicated that SEBAL showed a broader range of actual evapotranspiration values (0.74 to 5.8 mm) compared to SEBS (1.25 to 8.85 mm), highlighting its ability to distinguish different regions with varying evapotranspiration rates. However, SEBAL's implementation is more computationally demanding than SEBS, making the calculation process time-consuming. Overall, both algorithms demonstrated relatively high capabilities in calculating instantaneous evapotranspiration using spectral data. The findings of this study can be valuable for water resources and agricultural management in the research area, as well as for water resource planning and environmental studies.

1. Introduction

In recent years, with the development of remote sensing technologies, many mapping techniques and analyzes have been developed [1]. Remote sensing has long been an important and effective tool for monitoring land cover, with its ability to quickly provide broad, precise, unbiased and easily accessible information regarding the spatial variability of the land surface.

Problems such as global warming and climate change have increased their negative impact in the world in recent years [2]. On the one hand, the use of water resources has been limited, and on the other hand, water consumption in the agricultural sector has increased. While water consumption in the agricultural sector has increased. On the other hand, changes in land use and land cover are also influential factors [3]. Therefore,

efficient use of available water resources, especially in agricultural uses, which constitute a significant portion of a country's water consumption, is essential. The agricultural sector consumes the largest volume of freshwater in the world, making an efficient method for managing freshwater resources crucial in each country. In this regard, the first step is to calculate the water requirements of plants. Evapotranspiration is a good indicator for assessing irrigation efficiency and overall water consumption of plants. Land surface evapotranspiration (ET) is of prime interest for environmental applications, such as optimizing irrigation water use, irrigation system performance, crop water deficit, drought mitigation strategies, and accurate initialization of climate prediction models especially in arid and semiarid catchments where water shortage is a critical problem [4].

Evaporation is a process through which water from the Earth's surface and water bodies returns to the atmosphere. This process involves the transfer of energy, where water molecules acquire 600 calories of heat, reach the state of vaporization, and are consequently released into the air. The amount of evaporation is influenced by various factors, including solar radiation, air dryness, water temperature, water concentration and color, wind speed, surface type, absolute humidity of the air, and atmospheric pressure.

Evapotranspiration potential, or simply potential evapotranspiration, refers to the amount of evaporation and transpiration that would occur under conditions where sufficient moisture is available throughout the entire period, or in other words, the water level that would be evaporated if moisture resources were present. On the other hand, actual evapotranspiration is the amount that occurs under the natural conditions of a specific region, and its value increases with more available water. However, the actual evapotranspiration will never exceed the potential evapotranspiration.

Asadi and Valizadeh Kamran [5] conducted a study comparing the algorithms SEBAL, METRIC, and ALARM for estimating actual evapotranspiration of wheat crops in the Parsabad-Moghan region in northwest Iran, which is one of the main agricultural areas in the country. The research utilized the Surface Energy Balance Algorithm for Land (SEBAL), Mapping Evapotranspiration at High Resolution with Internal Calibration (METRIC), and Analytical Land-Atmosphere Radiative Transfer Model (ALARM) as the research tools. Twelve satellite images from Landsat 7 and 8 were used, covering the crop development period from 2016 to 2019, and the results were compared with lysimeter data.

Yang et al. [6] conducted a study to estimate evapotranspiration (ET) by combining Bayesian Model Averaging (BMA) with machine learning algorithms. The objective of this study was to reduce errors and uncertainties among multiple ET models to improve daily ET estimation. The results indicated that the BMA method outperformed the eight individual models. Four significant models obtained through the BMA method were ranked based on Random Forest, SVM, SEBS, and SEBAL. The combination of BMA with machine learning can significantly improve the accuracy of daily ET estimation, reduce uncertainties among models, and leverage the distinct advantages of empirical and physical-based models to obtain more reliable ET estimates.

Wei et al. [7] conducted a study on rice growth stage identification and evapotranspiration (ET) estimation in paddy fields using an improved SEBAL model with the consideration of the practical application of the surface resistance equation. Comparison between the estimation results and covariance data showed that SEBALR can provide more accurate ET estimates compared to the original surface energy balance algorithm for land, with a root mean square error (RMSE) of 1.02 mm-d⁻¹, mean relative error (MRE) of 22.97%, and Pearson correlation (R²) of 0.790.

Ma et al. [8] conducted a study on estimating regional actual evapotranspiration (ET) using an improved SEBAL model. In this study, a Surface Energy Balance model based on SEBAL and improved sensible heat flux computations (Y-SEBAL) was proposed and used for simulating actual ET at a large scale. The results showed that the Y-SEBAL model's simulation performance was highly consistent with covariance measurement data, with an R value of 0.82, agreement index of 0.90, and root mean square error of 0.81 mm/d. The performance validation indices were better than those of the SEBAL, MOD16, and SSEBop models. The Y-SEBAL model demonstrated the highest sensitivity to wind speed, reaching 0.714.

Therefore, our goal of this research is to estimate plant water needs and optimal management of water resources. For this purpose, SEBAL and SEBS spectra were compared to estimate actual evaporation and transpiration in the study area and the efficiency of these two algorithms was compared. In this regard, we continued to introduce these two algorithms, using each of these two algorithms, we calculated the rate of evaporation and transpiration and compared their results.

2. Material, methods and case studies

In this study, in order to estimate real evaporation and transpiration based on SEBAL and SEBS methods, we will use satellite images and meteorological data. The satellite image used is the spectral data of OLI and TIRS sensors of Landsat 8 satellite. Meteorological data was also prepared from Iran Meteorological Organization.

2.1. Case studies

The study area is located in the northwest of Iran, specifically in Ardabil province, between the cities of Parsabad and Bilasuvar (Moghan Plain), (Figure 1). The area has an average elevation of 100 meters above sea level. The dominant crop in the study area at the time of image acquisition and actual evapotranspiration estimation is wheat.

2.2. Material and dataset

The main data required for implementing the SEBAL (Surface Energy Balance Algorithm for Land) model are satellite images and weather data. Analysis of the climate data series collected can provide insights about the changes in climatic conditions in the region [9].

2.2.1. Satellite data

The used images must be cloud-free. In this research, the OLI sensor images from Landsat 8 satellite were utilized. The Digital Image used corresponds to the date of 04/04/2021, and the local time is approximately 11:00 AM. To calculate evapotranspiration, bands 1 to 7, and also band 10 (thermal band) were utilized.

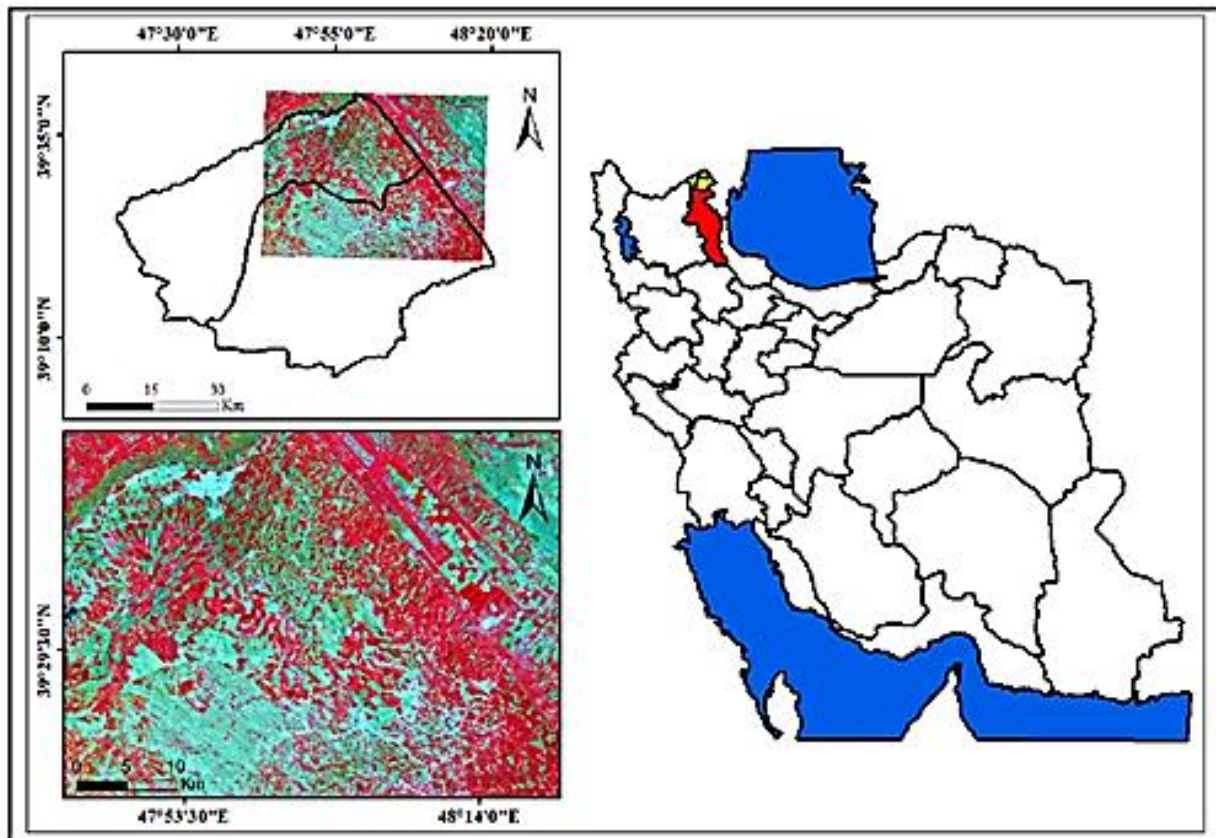


Figure 1. Study area.

2.2.2. Climate data

The climate data used in the model and for calculating the reference evapotranspiration (E_{Tr}) are presented in Table 1. In this research, data from two synoptic stations, Parsabad and Pileh Savar, were utilized, and the final values were obtained by averaging the corresponding measurements from these two stations. E_{Tr} represents the evapotranspiration of well-irrigated crops, which is used to calculate the sensible heat in the cold pixel area and E_{TrF}. E_{TrF} is similar to the crop coefficient (K_c), representing the ratio of instantaneous ET (ET_{inst}) calculated for each pixel to the E_{Tr} calculated from climate data for the image time. E_{TrF} is used for extrapolating ET from the image time to the 24-hour period (ET₂₄) or longer. Its value ranges between zero and one ET₂₄: Generally, daily ET values are more commonly used than instantaneous ET values. SEBAL calculates ET₂₄ assuming that E_{TrF} is constant over the 24-hour period (i.e., relatively constant throughout 24 hours). ET₂₄ can be calculated (Equation 1) as follows [10]:

Table 1. Climate data used in the research.

Data used (unit)	value
Satellite overpass temperature (°C)	19
minimum daily temperature(°C)	6.5
Maximum daily temperature(°C)	21.5
Sunshine duration	10.7
Relative humidity (%)	37.5
Wind speed(M/S)	4
Station height(M)	100

$$ET_{24}=ET_i F \times ET_{i-24} \quad (1)$$

ET₂₄: ET₂₄ is the total accumulated evapotranspiration over a 24-hour period for the satellite passing day. It is calculated by summing up the hourly E_{Tr} values during the satellite passing day.

2.3. Methods

2.3.1. The SEBAL method

According to the definition, the total evaporation and transpiration from all surfaces of vegetation are referred to as evapotranspiration (ET). Regardless of the partial amount of water used in metabolic activities of plants, evapotranspiration can be considered as equivalent to the water consumed by the plant. Evapotranspiration is a process resulting from the turbulent transfer of energy. The complete energy balance equation can be expressed as Equation (2), where (R_n) represents the net incoming radiation to the surface, (G) is the soil heat flux, (H) is the sensible heat flux, and ETλ denotes the latent heat flux. In this equation, the term (R_n) corresponds to the net radiation received by the surface, while (G) and (H) represent the soil heat flux and sensible heat flux, respectively. Most plants use less than one percent of the received solar radiation during the day for photosynthesis. The heat storage in plants during the day is negligible, and thus, both photosynthesis and heat storage in plants can be disregarded in the energy balance equation. Satellite data provide continuous and temporally diverse information about spectral reflectance and surface radiation. To calculate surface heat fluxes (sensible and latent heat), a multi-stage energy balance algorithm based on physical principles

(SEBAL) has been designed. SEBAL uses surface temperature, surface reflectance, and the normalized difference vegetation index (NDVI) as inputs to estimate surface heat fluxes for various land surface covers. By relying on satellite data and a limited amount of meteorological data, the SEBAL model is capable of estimating evapotranspiration. This model calculates the net incoming radiation (Rn), soil heat flux (G), and sensible heat flux (H) (Equation 2), and then subtracts the soil heat flux and sensible heat from the net incoming radiation to obtain the remaining energy, which is equivalent to the energy used for evaporation and transpiration (ET), representing the energy spent on converting water from liquid to vapor (Equation 2 and 3).

$$Rn = G + H + ET\lambda + \text{Heat storage in plants} + \text{Photosynthesis} \quad (2)$$

ETλ: Latent heat flux (W/m²)
 Rn: Net radiation (W/m²)
 G: Soil heat flux (W/m²)
 H: Sensible heat flux (W/m²)

$$Rn = (1 - \alpha) Rs\downarrow + RL\uparrow - RL\downarrow - (1 - \epsilon^\circ) RL\downarrow \quad (3)$$

α: Surface albedo
 RL↓: Incoming longwave radiation (W/m²)
 Rs↓: Incoming shortwave radiation (W/m²)
 ↑RL: Outgoing longwave radiation (W/m²)
 ε°: Broadband surface emissivity

2.3.1.1. Calculation of net radiation

Net radiation (Rn) at the surface is obtained by considering all incoming and outgoing radiation fluxes [10]. The value of net radiation should fall within the range of 100 to 700 W/m².

To generate the net radiation raster layer, the input parameters of surface albedo, outgoing longwave radiation, and incoming shortwave and longwave radiation were calculated as 0.895, 314.714, 6584.314, and 714.314 respectively. Raster layers of vegetation index, emissivity, and surface temperature were used as inputs to calculate the outgoing longwave radiation at the longwave band. Finally, the net incoming radiation (Rn) was computed.

2.3.1.2. Calculation of surface albedo (α):

Surface albedo is defined as the ratio of electromagnetic energy reflected from the soil and vegetation surface to the incoming energy at that surface.

To calculate surface albedo, satellite images were first loaded using the metadata file in ENVI 5.6 software. The Radiometric Calibration command was then used to calculate radiance and spectral reflectance for each band. Subsequently, αtoa (atmospherically-corrected albedo) was computed using the Equation 4 and 5:

$$\alpha_{toa} = \sum(\omega\lambda \times \rho\lambda) \quad (4)$$

$$\omega\lambda = \frac{ESUN\lambda}{\sum ESUN\lambda} \quad (5)$$

αtoa: Atmospherically-corrected albedo
 ρi: Spectral reflectance for each band
 ωi: Weighting coefficient for each band
 λi: Wavelength of the band
 λmin and λmax: Minimum and maximum wavelengths, respectively

The weighting coefficients (ω) for each band of Landsat 8 are shown in Table 2.

Table 2. Weighting coefficients (ω) for each band of Landsat 8.

Band number	1	2	3	4	5	6	7
Weighting coefficients	0.19	0.2	0.2	0.17	0.11	0.09	0.008

Surface albedo is the ratio of the reflected solar radiation from the soil and vegetation surface to the incoming solar radiation [11]. Albedo is influenced by the surface characteristics such as vegetation, soil, and other cover types. The calculation of albedo is performed by correcting Equation (4) for atmospheric transparency effects (Equation 6).

$$\alpha = \frac{\alpha_{toa} - \alpha_{path} - \text{radiance}}{\tau_{sw}2} \quad (6)$$

Γsw: Atmospheric transparency.

path_radianceα: Path radiance-induced albedo, with a value between 0.25 and 0.40. In the SEBAL model, a value of 0.30 is recommended [12], and in this study, a value of 0.30 was selected (Equation 7).

$$\Gamma_{sw} = 0.75 + 2 \times 10^{-5} \times Z \quad (7)$$

Z: Elevation above sea level in meters. This elevation should represent the elevation of the study area, and it is often recommended to use the elevation of the nearest weather station. In this study, an elevation of 100 meters was considered.

2.3.1.3. Calculation of incoming short wave radiation (Rs↓)

The shortwave incoming radiation (Rs↓) is the actual solar radiation that reaches the Earth's surface under clear atmospheric conditions. It can be calculated using Equation (8):

$$Rs\downarrow = G_{sc} \times \text{Cos}\theta \times dr \times \Gamma_{sw} \quad (8)$$

Gsc: Solar constant (1367 W/m²)
 Cosθ: Cosine of the solar zenith angle
 dr: Inverse square of the relative distance between the Earth and the Sun
 Γsw: Solar radiation atmospheric transmission factor

The calculated values for dr and θ for the studied region are 0.96 and 23.772°, respectively.

2.3.1.4. Long wave output radiation (↑) RL

The outgoing longwave radiation (RL↑) is a type of thermal radiation with a wavelength longer than 8

micrometers that is emitted from the Earth's surface into the atmosphere. Its magnitude varies based on the spatial and temporal location and ranges between 200 to 700 watts per square meter.

Equation (9) can be used to calculate $RL\uparrow$:

$$RL\uparrow = \varepsilon^{\circ} \times \sigma \times Ts^4 \quad (9)$$

ε° : Surface emissivity, which is the ratio of emitted thermal radiation to that of a perfect blackbody ($0 \leq \varepsilon^{\circ} \leq 1$)

σ : Stefan-Boltzmann constant ($5.67 \times 10^{-8} \text{ W/m}^2/\text{K}^4$)

Ts : Surface temperature in Kelvin

Please note that the value of $RL\uparrow$ is influenced by the surface temperature and emissivity of the area at the time of imaging.

2.3.1.5. Long wave input radiation ($RL\downarrow$)

The input longwave radiation ($RL\downarrow$) is the thermal radiation from the atmosphere towards the Earth's surface, measured in watts per square meter (W/m^2). It can be calculated using equation (11) and its value varies depending on the spatial and temporal location of the imaging, typically ranging between 200 to 500 W/m^2 .

Equation (10) describes the calculation of $RL\downarrow$:

$$RL\downarrow = \varepsilon a \times \sigma \times Ta^4 \quad (10)$$

where:

εa : Atmospheric emissivity, which is the ratio of emitted thermal radiation from the atmosphere to that of a perfect blackbody ($0 \leq \varepsilon a \leq 1$)

σ : Stefan-Boltzmann constant ($5.67 \times 10^{-8} \text{ W/m}^2/\text{K}^4$)

Ta : Air temperature near the surface in Kelvin

Please note that the value of $RL\downarrow$ depends on the atmospheric emissivity and the air temperature near the Earth's surface at the time of imaging.

2.3.1.6. Vegetation indicators

The SEBAL (Surface Energy Balance Algorithm for Land) model accepts vegetation indices as input data to calculate surface emissivity, surface temperature, and outgoing longwave radiation in the energy balance equation. Therefore, two important vegetation indices used in this model are presented below:

2.3.1.6.1. Normalized difference vegetation index (NDVI)

NDVI is a vegetation index that is sensitive to vegetation cover but cannot eliminate the effects of background soil. Its values range between 1+ to 1- where positive values indicate healthy vegetation. NDVI is calculated using the following formula, by placing near-

infrared (NIR) and red bands in the Equation 11 and executing it (Figure 2):

$$NDVI = (NIR - R) / (NIR + R) \quad (11)$$

2.3.1.6.2. Leaf area index (LAI):

LAI is a vegetation index that represents the ratio of the area covered by the vegetation canopy to the ground area beneath it. It is commonly calculated using the relationship between LAI and NDVI (Equation 12):

$$LAI = 4.04 * \ln(NDVI) + 7.04 \quad (12)$$

In this study, after performing radiometric and atmospheric corrections on the input imagery, the vegetation indices NDVI and LAI were generated (Figure 3).

2.3.1.7. Surface temperature

In order to generate the surface temperature layer, thermal band number 10 of Landsat 8 was utilized. After performing radiometric and atmospheric corrections on band 10, radiance and brightness temperature were calculated using Equations 13 and 14, respectively.

$$\text{Radiance } (\lambda) = 0.0370588 * (DN) + 3.2 \quad (13)$$

$$\text{Brightness Temperature } (Tb) = (K2 / (\ln(K1 / \lambda + 1))) \quad (14)$$

K1: 774.89

K2: 1321.08

Subsequently, surface emissivity was calculated and corrected using Equation 15, and finally, surface temperature in Kelvin was computed using Equation 16.

$$\varepsilon (\text{Emissivity}) = 1.009 + 0.047 * \ln(NDVI) \quad (15)$$

$$\text{Surface Temperature } (Ts) = Tb / (1 + (\lambda * Tb / \gamma) * \ln \varepsilon) \quad (16)$$

Tb: Brightness temperature

λ : Radiance

γ : 14380

ε : Corrected emissivity

These calculations were performed to derive the surface temperature layer in Kelvin using the available thermal band data from Landsat 8 after radiometric and atmospheric corrections (Figure 4).

2.3.1.8. Surface emissivity

Surface emissivity is the ratio of the thermal radiation emitted by the Earth's surface to that emitted by a blackbody at a specific temperature. In the SEBAL model, two emissivity are defined: the narrowband emissivity (ε_{NB}) that represents the behavior of surface emission in the narrow thermal band (with a small bandwidth), and the broad emissivity (ε_0) that represents the behavior of surface emission in the broad thermal band (ranging from 6 to 14 micrometers).

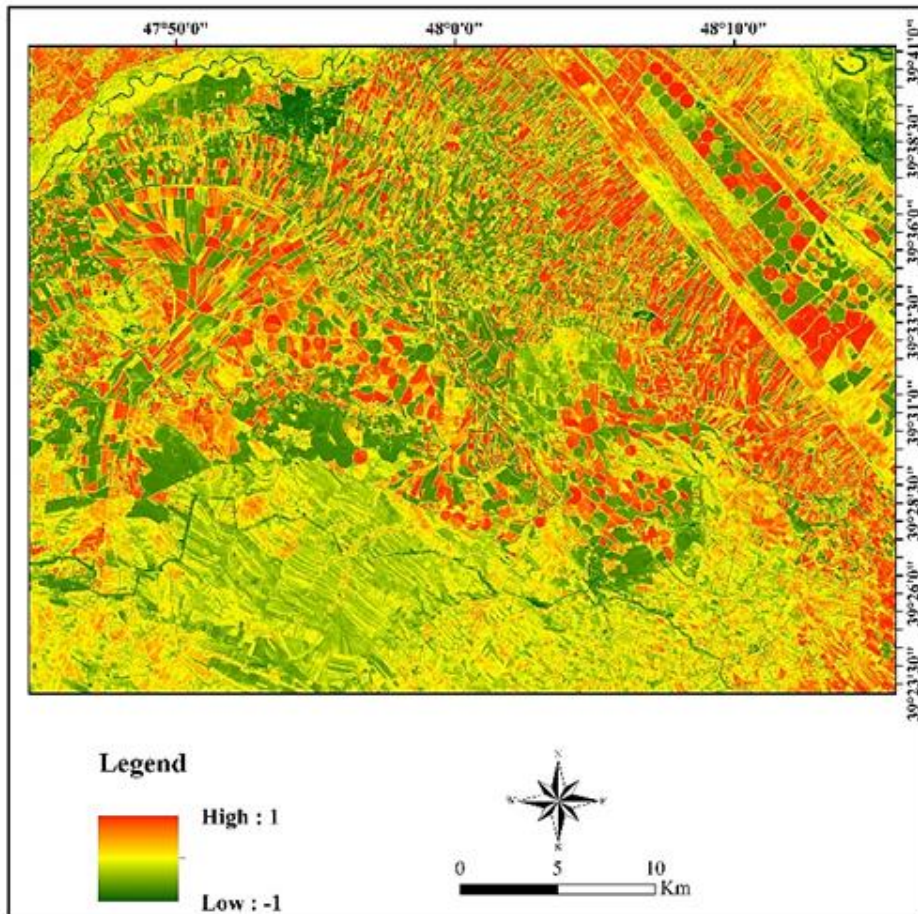


Figure 2. Normalized difference vegetation index (NDVI).

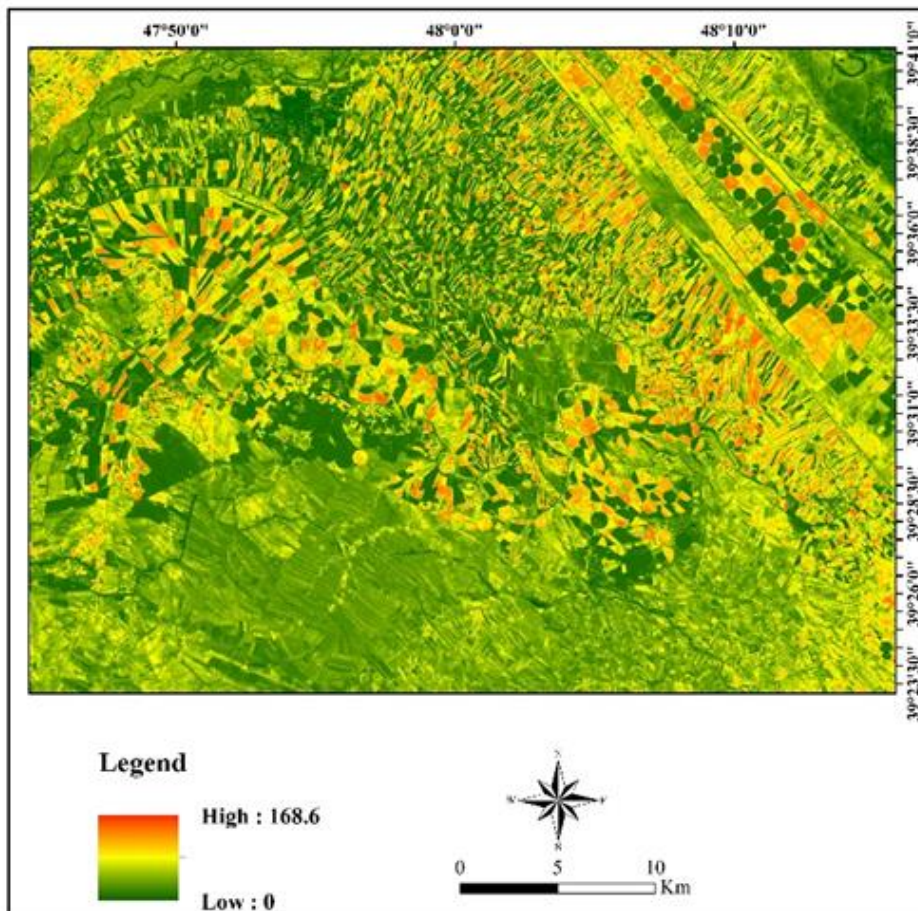


Figure 3. Leaf area index (LAI).

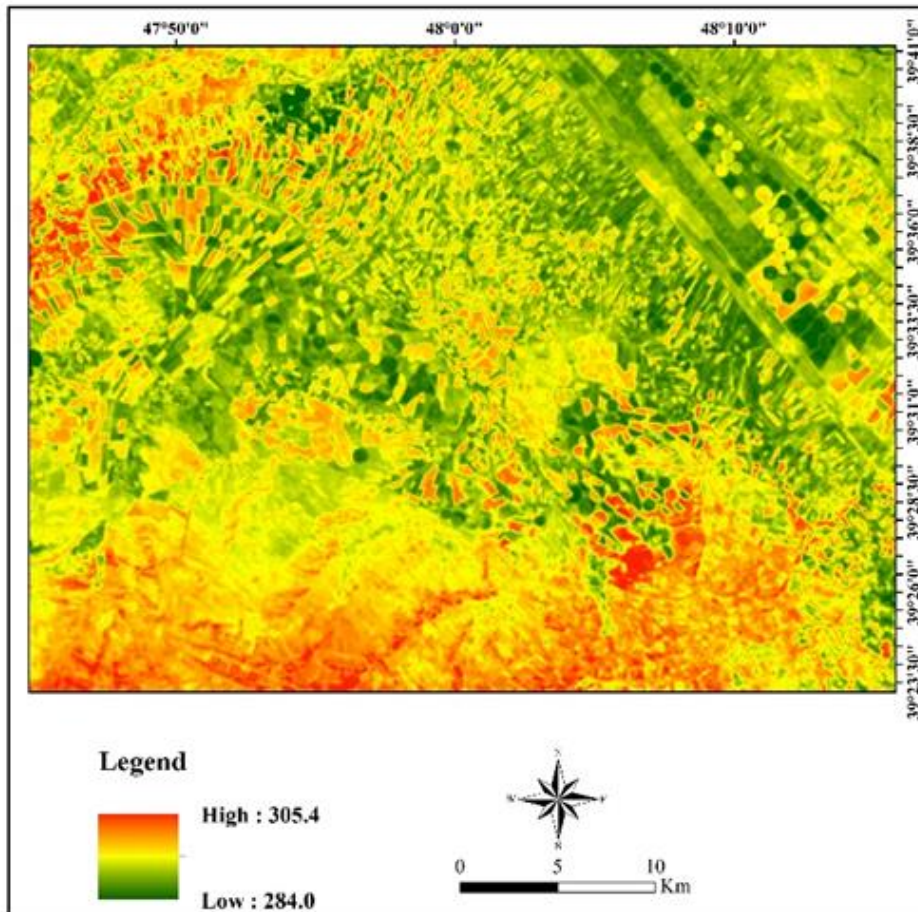


Figure 4. Land surface temperature.

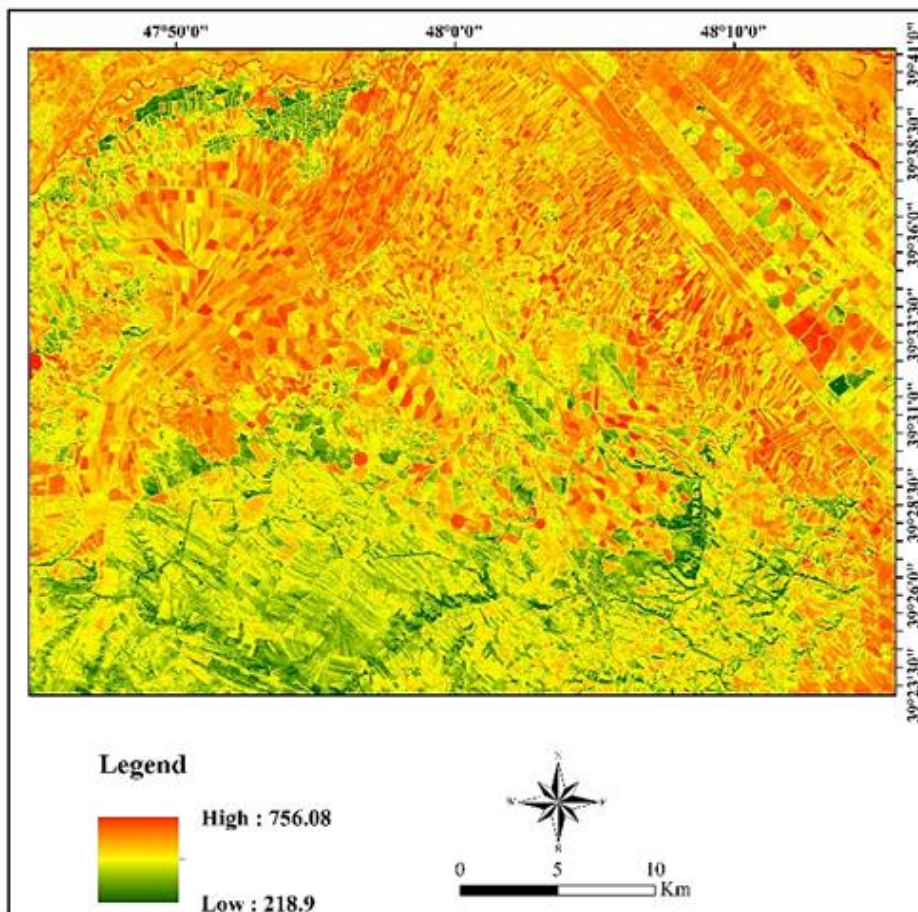


Figure 5. Net radiation (Rn).

The values of these emissivities are calculated using empirical Equation 17 and 18.

$$\text{For LAI} < 3: \epsilon_{NB} = 0.97 + 0.0033 \times \text{LAI} \quad (17)$$

$$\text{For LAI} \geq 3: \epsilon_0 = 0.95 + 0.01 \times \text{LAI} \quad (18)$$

If LAI ≥ 3 , the values of both emissivities are set to 0.98.

For water with $\alpha < 0.47$ and NDVI < 0 , and for snow with $\alpha > 0.47$ and NDVI < 0 , the values of both emissivities are set to 0.985 for ϵ_0 and 0.99 for ϵ_{NB} .

After calculating the required parameters, the net surface radiation (Rn) is computed as the final output in the SEBAL model (Figure 5).

2.3.1.9. Soil heat flux (G)

Soil heat flux is the amount of heat stored in the soil and vegetation cover on the Earth's surface due to molecular conduction processes. In the SEBAL model, the ratio of G/Rn is calculated using an empirical equation (Equation 19) presented by Allen (2000). In Equation 19, the temperature is in degrees Celsius (Figure 6).

$$G/Rn = (Ts / \alpha) * (0.0032\alpha + 0.007\alpha^2) * (1 - 0.98 * NDVI^4) \quad (19)$$

For clear and deep water and for snow, the ratio is set to 0.5. The values of this ratio for other land cover types are provided in Table 3.

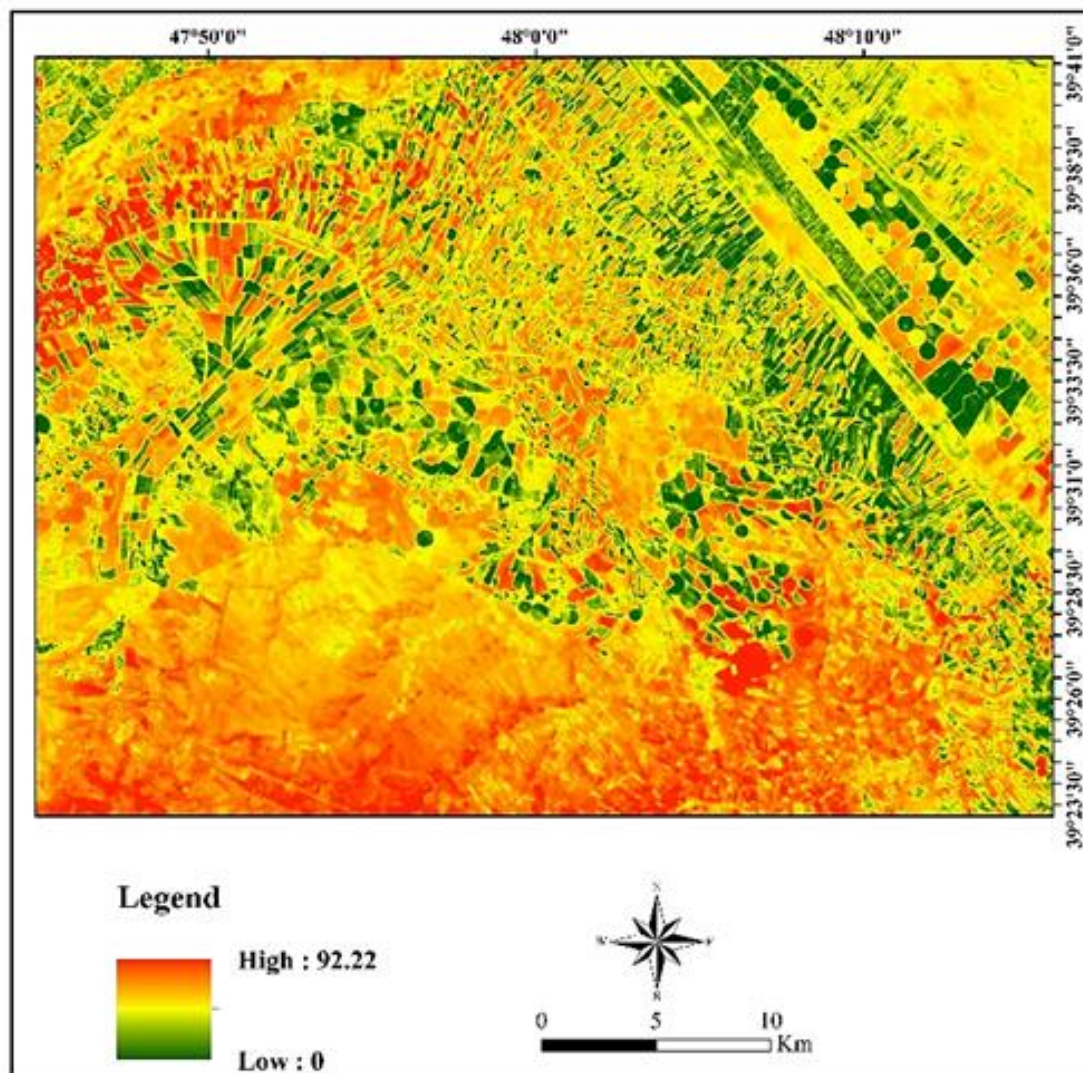


Figure 6. Soil Heat Flux (G).

Table 3. Values of G/Rn for some land cover types.

Surface type	G/Rn
Deep, Clear water	0.5
Snow	0.5
Desert	0.2 - 0.4
Agriculture	0.05 - 0.15
Bare Soil	0.2 - 0.4
Full Cover Alfalfa	0.04
Rock	0.2 - 0.6

2.3.1.10. Sensible heat flux (H)

Sensible heat flux represents the amount of heat loss from the surface to the air through processes of convection and molecular conduction due to temperature differences. Sensible heat flux is calculated using Equation (20) for heat transfer (Figure 7).

$$H = (\rho \times Cp \times dT) / rah \quad (20)$$

In Equation (20), ρ is the air density (kg/m^3), C_p is the specific heat of air (1004 J/kg/K), dT is the temperature difference (T_1-T_2) between two heights (Z_1 and Z_2), and rah is the aerodynamic resistance for heat transfer (s/m).

Initially, using data from synoptic weather stations, the wind speed at a distance of 200 meters above the ground (U_{200}) is calculated. Then, the friction velocity (U^*) is estimated for each separate pixel. Finally, the aerodynamic resistance parameter (rah) is calculated for each pixel. After determining the aerodynamic resistance

and air density, the coldest and warmest pixels are selected, and based on those, H_{cold} and H_{hot} are calculated. Subsequently, dt_{cold} and dt_{hot} are determined, leading to the final calculation of dt_{total} .

After obtaining the initial H , the aerodynamic resistance is corrected, and the sensible heat flux is recalculated. This cycle continues until the average values of aerodynamic resistances converge. In this study, the convergence of rah values were achieved after repeating this cycle five times (Figure 8).

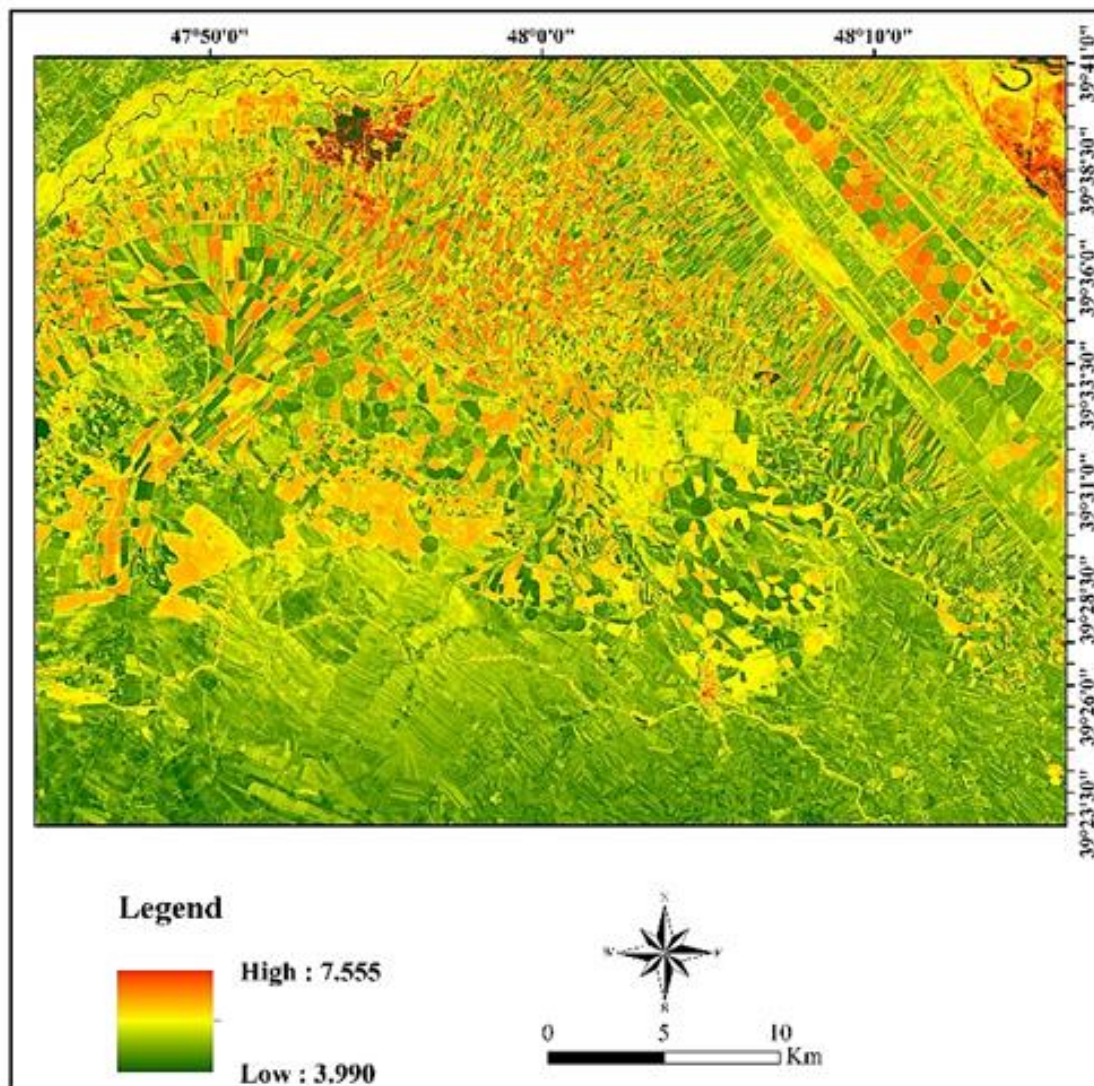


Figure 7. Corrected aerodynamic resistance.

2.3.1.11. Aerodynamic resistance to heat transport (rah)

Aerodynamic resistance is calculated using Equation (21).

$$rah = \ln(Z_2 / Z_1) / (U^* \times K) \quad (21)$$

- Z2: 2 meters (height above the surface)
- Z1: 1/0 meters (reference height, typically at the surface)
- U*: Friction velocity
- K: Karman constant (0.41)

Parameters u^* , Z_0m , and u_{200} were calculated using Equations (22, 23, and 24), respectively.

$$u^* = \frac{k u_x}{\ln \frac{z_x}{z_0m}} \quad (22)$$

$$Z_0m = 0.018 * LAI \quad (23)$$

$$u_{200} = \mu^* \frac{\ln \left(\frac{200}{z_0m} \right)}{k} \quad (24)$$

- K: Karman constant (0.41)
- Ux: Wind speed at height x
- ZX: Height x
- Z0m: Momentum roughness length (in meters)

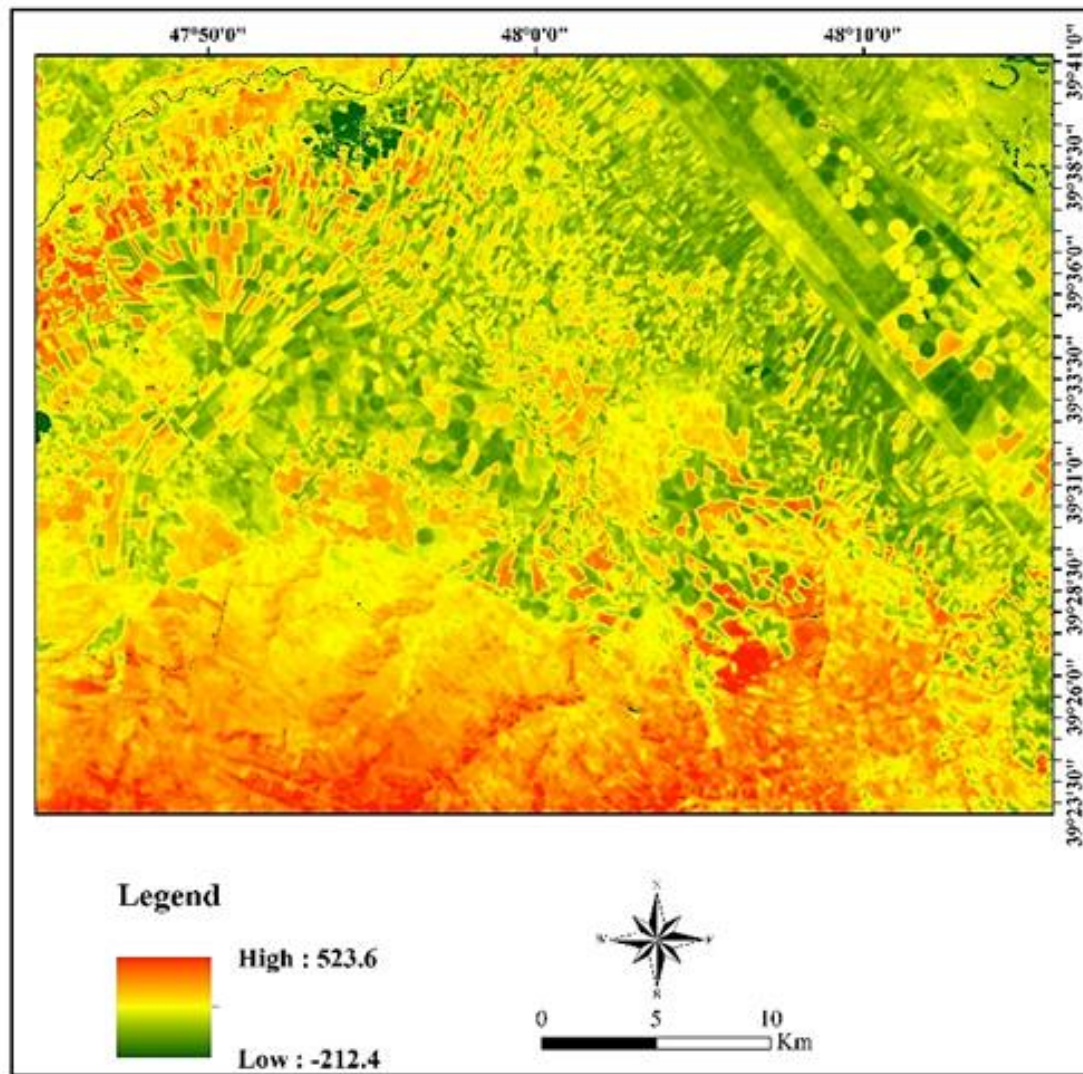


Figure 8. Sensible heat flux (H).

2.3.1.2. Cold and warm pixels

Sabal uses two reference pixels to determine the boundary conditions in the energy balance equation, which are called cold and warm pixels. Cold pixels are selected from fully irrigated fields and are free from moisture stress, appearing green and vibrant within the study area. In these pixels, the surface temperature and near-surface air temperature are assumed to be equal. Warm pixels are chosen from drylands with no vegetation cover [13]. To select these two pixels, a complete understanding of the study area, familiarity with the spectral behavior of phenomena, and proficiency in interpreting images are necessary. The accuracy of calculating evapotranspiration in Sabal relies on the precise selection of these two reference pixels."

2.3.1.2.1. Calculation of H_{cold} and H_{hot}

H_{cold} and H_{hot} are calculated using Equation 25 and 26 respectively.

$$H_{cold} = R_n - G - \lambda ETr \quad (25)$$

λ : Latent heat of evaporation

ETr: Reference evapotranspiration for the cold pixel

In Equation (26), the reference evapotranspiration for the reservoir pixel is calculated using the FAO Penman-Monteith method and estimated to be 1743.0.

$$H_{hot} = R_n - G \quad (26)$$

The value of H_{hot} for the selected warm pixel is estimated to be 262.499. It is important to note that the value of H_{hot} should not be less than the value of H_{cold} .

2.3.1.2.2. Calculation of "dt_{cold}" and "dt_{hot}"

In the context of the original Equations 27 and 28, "dt_{cold}" and "dt_{hot}" are likely terms used in a specific scientific or engineering domain to represent temperature differences or changes. Without further context or specific information about the equations, it's challenging to provide a more precise translation. If you can provide more details or the full equations, I would be glad to assist further.

$$dT_{cold} = H_{cold} \times rah / (\rho \times Cp) \quad (27)$$

$$dT_{hot} = H_{hot} \times rah / (\rho \times Cp) \quad (28)$$

2.3.1.2.3. Modification of aerodynamic resistance

In order to correct the aerodynamic resistance, the length of the Monin-Obukhov length (L) needs to be calculated (Equation 29). If the value of L is negative, it indicates atmospheric instability, and if L is zero or positive, it signifies atmospheric stability.

$$L = -(\rho C_p \mu^3 T_s) / kgH \quad (29)$$

ρ : Air density (kg/m³)

C_p : Specific heat of air (1004 J/kg/K)

U^* : Friction velocity

T_s : Surface temperature

K : 41/0

g : 81/9

H : Sensible heat flux

In order to converge the aerodynamic resistance, the correction cycle was repeated 5 times. which is shown in Figure 9.

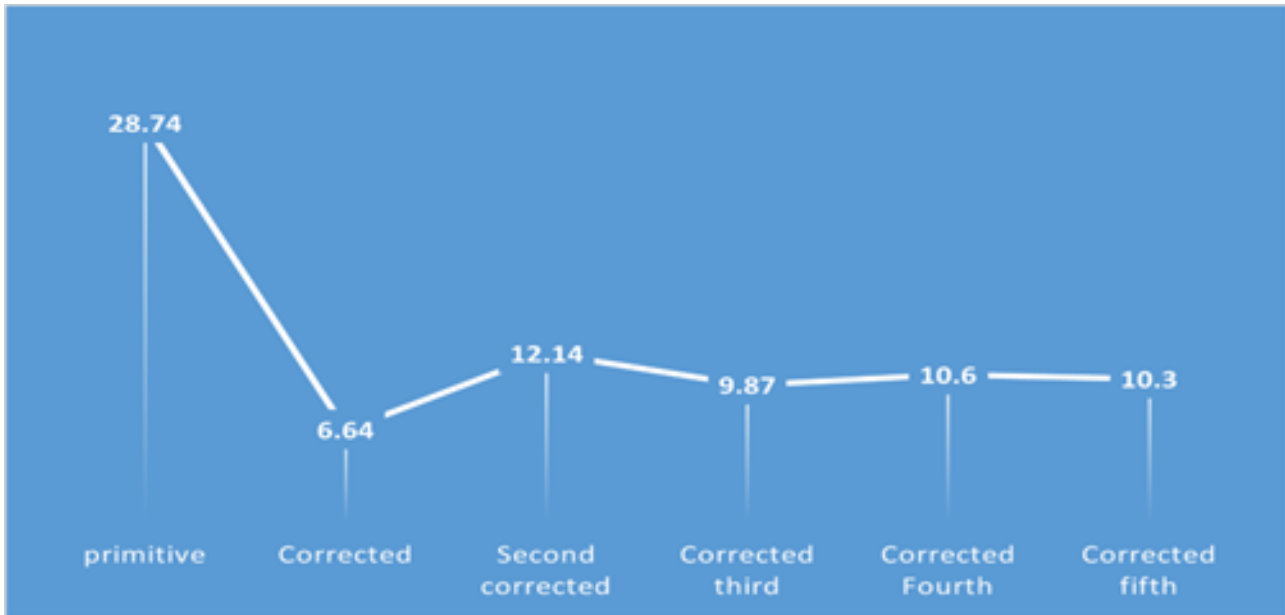


Figure 9. Aerodynamic resistance correction process

2.4. Instantaneous and daily evapotranspiration (ET)

To calculate instantaneous and daily evapotranspiration (ET) after estimating the parameters R_n , G , and H , you can use the Equation 30:

$$ET\lambda = R_n - G - H \quad (30)$$

$ET\lambda$: Latent heat flux (J/m²/s)

R_n : Net radiation (J/m²/s)

G : Soil heat flux (J/m²/s)

H : Sensible heat flux (J/m²/s)

The instantaneous evapotranspiration (ET_{inst}) can be calculated as (Equation 31):

$$ET_{inst} = 3600 * (\lambda ET / \lambda) \quad (31)$$

ET_{inst} : Instantaneous evapotranspiration (mm/hr)

λ : Latent heat of evaporation of water or the amount of heat needed to evaporate one kilogram of water (J/kg)

3600: Conversion factor from seconds to hours

The value of λET can be obtained from Equation (32). To calculate the daily evapotranspiration (ET_{24}), which has more practical significance compared to instantaneous evapotranspiration, the following steps are taken:

$$ETrF = ET_{inst} / ETr \quad (32)$$

$ETrF$: Fraction of daily reference evapotranspiration

ET_{inst} : Instantaneous evapotranspiration (mm/hr)

ETr : Reference evapotranspiration, which is the average 24-hour evapotranspiration

Daily evapotranspiration was calculated using Equation 33.

$$ET_{24} = ETrF * ETr-24 \quad (33)$$

ET_{24} : Daily evapotranspiration (mm/day)

$ETrF$: Fraction of daily reference evapotranspiration (dimensionless)

$ETr-24$: Total sum of reference evapotranspiration over 24 hours (mm/day)

$ETr-24$ is obtained by summing up the hourly values of ETr during the day of interest, which can be derived from satellite data. $ETr-24$ is estimated using CROPWAT software with synoptic data at 5.4 mm per day for the study area.

After calculating R_n , G , and H , the latent heat flux ($ET\lambda$) is determined, and then the instantaneous actual evapotranspiration (ET_{inst}) is estimated (Figure 10). Finally, the daily actual evapotranspiration is calculated in millimeters per day (Figure 11).

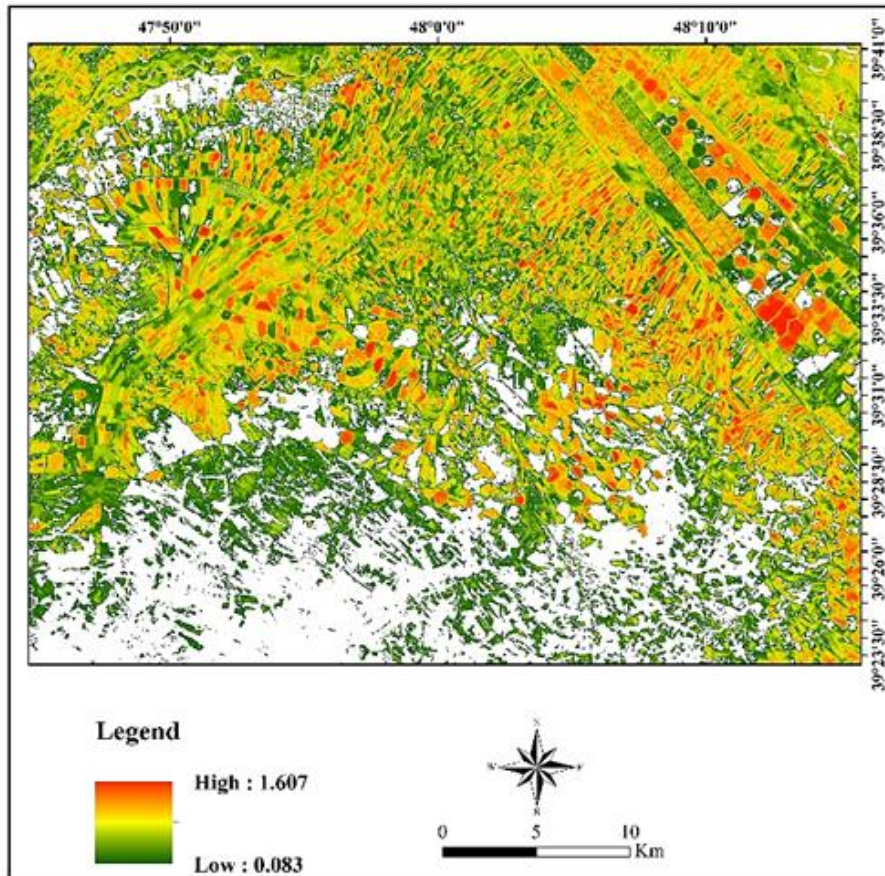


Figure 10. instantaneous actual evapotranspiration (ET_{inst}) (mm/hr) (SEBAL).

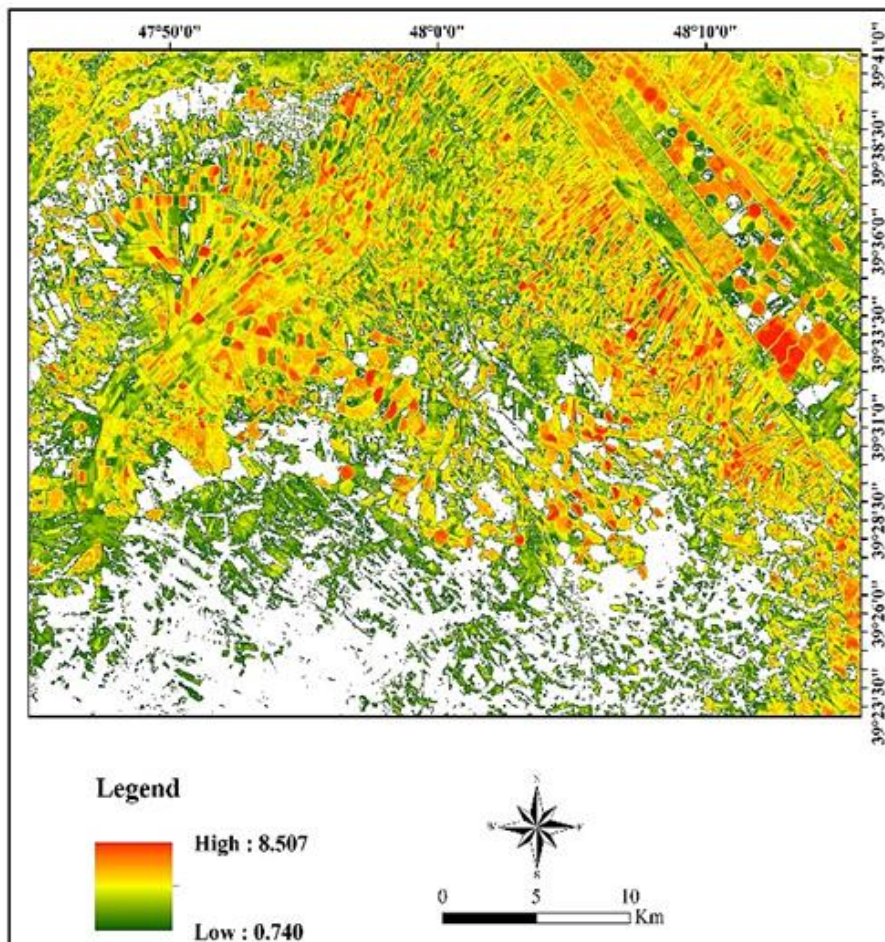


Figure 11. Daily actual evapotranspiration (SEBAL).

2.3.2. The SEBS method

SEBS is based on the Crop Water Stress Index (CWSI; [14]), idea in which the surface meteorological scaling of CWSI is replaced with planetary boundary layer (PBL) scaling. It uses the contrast between wet and dry areas appearing within a remotely sensed scene to derive ET from the relative evaporative fraction.

The basis of this method is to use the energy balance equation and calculate the latent heat flux as the residual of this equation for each pixel. This approach follows similar theoretical principles as the SEBAL algorithm.

The required input data include layers generated from satellite images and data obtained from weather stations. The output of the SEBS algorithm, unlike the SEBAL algorithm, provides daily actual evapotranspiration.

2.3.2.1. Evapotranspiration

The surface energy balance is commonly written as (Equation 34):

$$Rn = G_0 + H + \lambda E \quad (34)$$

where R_n is the net radiation flux, G_0 is the soil surface heat flux, H is the sensible heat flux, and λE is the latent heat flux. The unit of energy balance terms is watts per square meter.

To estimate the evaporative fraction, SEBS makes use of energy balance at limiting cases at dry limit and wet limit, such that the relative evaporation (ratio of the actual evaporation to the evaporation at wet limit) can be derived as (Equation 35):

$$Ar = 1 - \frac{H - H_{wet}}{H_{dry} - H_{wet}} \quad (35)$$

where the H_{wet} is sensible heat flux at the wet limit and H_{dry} is sensible heat flux at the dry limit. The estimations of H_{wet} and H_{dry} were detailed by Su [15]. The evaporative fraction (ratio of latent heat flux to available energy) is estimated by (Equation 36 and 37):

$$\frac{Rn - G}{Rn - G} \quad (36)$$

$$\Lambda = \frac{\lambda E}{Rn - G} = \frac{Ar \cdot \lambda E_{wet}}{Rn - G} \quad (37)$$

where λE_{wet} is the latent heat flux at the wet limit (i.e., the evaporation is only limited by the available energy under the given surface and atmospheric conditions). The latent heat flux (λE) can then be calculated by (Equation 38):

$$\lambda E = \Lambda(Rn - G_0) \quad (38)$$

Finally, the daily actual ET can be written (Equation 39):

$$ET = 8.64 \times 10^7 \times \Lambda_{24} \times \frac{Rn - G_0}{\lambda \rho_w} \quad (39)$$

where ρ_w is the density of water ($1,000 \text{ kgm}^{-3}$) and R_n is the average daily net radiation in this equation. Moreover, the soil heat flux G_0 for 24 h is normally assumed negligible (G average).

2.3.2.2. Daily actual evapotranspiration

The results of the daily evapotranspiration calculated by the SEBS algorithm are presented in Figure 12.

3. Results

The results obtained from the SEBAL and SEBS algorithms indicate that the SEBAL algorithm exhibits a broader range of actual evapotranspiration values (0.74 to 5.8 millimeters) compared to the SEBS algorithm (1.25 to 8.85 millimeters), demonstrating its greater capability in distinguishing areas with different evapotranspiration rates. On the other hand, the implementation of the SEBAL algorithm is more complex and time-consuming compared to SEBS. The results showed that both algorithms have relatively high capabilities in calculating instantaneous evapotranspiration using spectral data. Estimating plant water consumption on a pixel-by-pixel (spatial) basis is a unique advantage of spectral methods, as other empirical methods provide a single value estimation for all farms and different varieties of a crop. Generally, satellite data has the potential to estimate evapotranspiration for different plant species. Additionally, due to the pixel-based nature of satellite data, it allows for estimating surface properties such as temperature, emissivity, and actual evapotranspiration within a specific region instead of point-based estimation (at a stationary location). This capability is perhaps one of the most important characteristics of satellite data, as it enables the investigation and analysis of spatially distributed environmental characteristics. Therefore, it is recommended that when investigating spatial and temporal changes in environmental variables, the use of raster data, or satellite data, is highly advantageous as it can significantly aid in such investigations with minimal time and cost. The valuable results obtained from such analyses can be crucial for resource management. Additionally, considering the scarcity and inadequate distribution of weather stations and the subsequent unavailability of synoptic data in the country, employing methods based on digital data is highly suitable.

4. Discussion

The study aimed to estimate actual evapotranspiration using the SEBAL and SEBS algorithms and spectral data from the OLI and TIRS sensors of the Landsat 8 satellite in the Mughan plain of Ardabil province. The results of the analysis revealed valuable insights into the performance of these algorithms and their applicability in the specific study area.

Firstly, the comparison between the SEBAL and SEBS algorithms demonstrated distinct differences in their estimated values of actual evapotranspiration. The SEBAL algorithm showed a wider range of values, indicating its ability to discern variations in

evapotranspiration rates across different areas in the Mughan plain. On the other hand, the SEBS algorithm provided a more limited range of values, suggesting a

somewhat less nuanced representation of the spatial distribution of evapotranspiration.

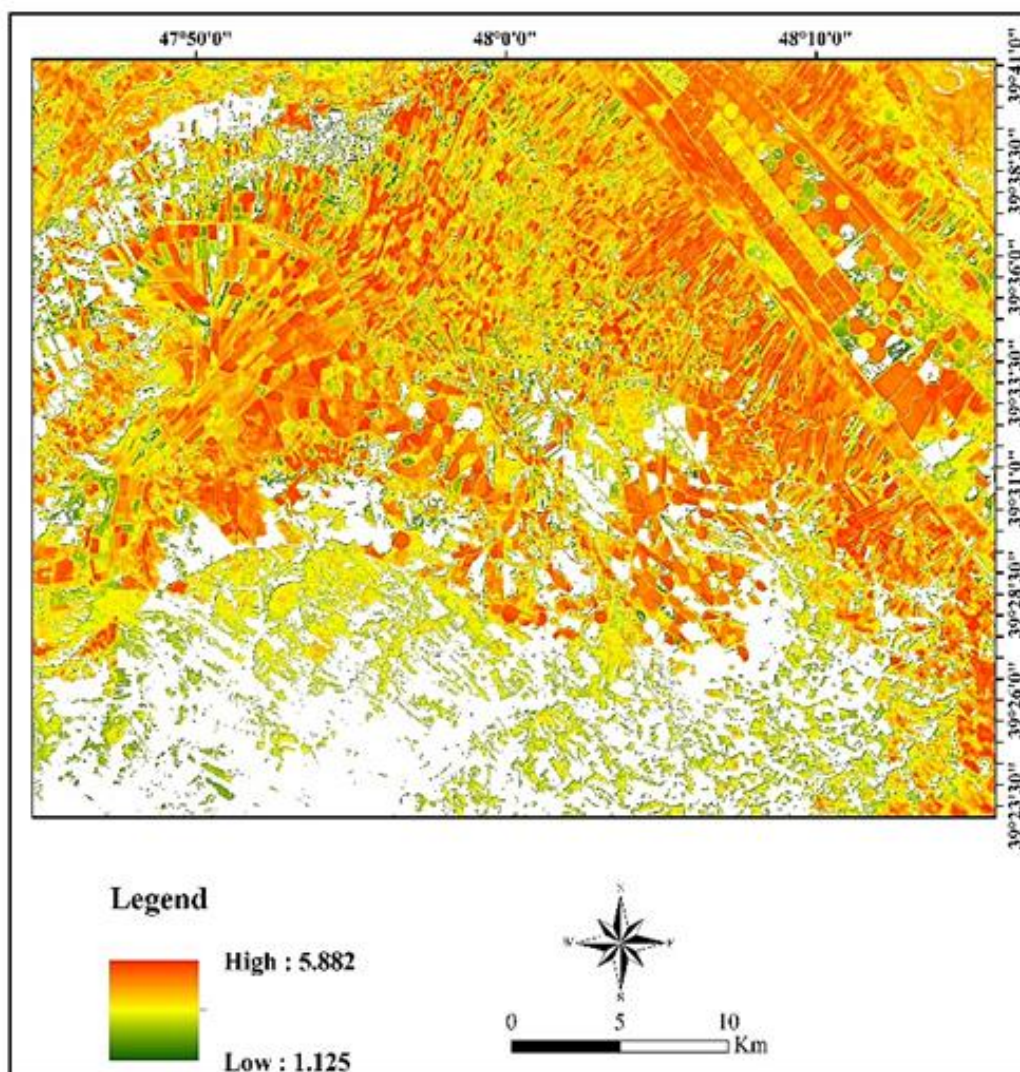


Figure 12. Daily actual evapotranspiration (SEBS).

Secondly, while the SEBAL algorithm exhibited superior capabilities in distinguishing areas with different evapotranspiration rates, it also presented challenges in terms of computational complexity and time consumption. This issue needs to be considered when implementing SEBAL for large-scale or time-sensitive applications.

Furthermore, the utilization of spectral data from the OLI and TIRS sensors of Landsat 8 enabled a pixel-based approach to estimate evapotranspiration. This pixel-level estimation offers a significant advantage over point-based methods since it allows for a more comprehensive analysis of surface properties, such as temperature, emissivity, and actual evapotranspiration, within specific regions. This spatially distributed information provides valuable insights into the environmental characteristics of the study area.

Overall, the results indicated that both SEBAL and SEBS algorithms have relatively high capabilities in estimating instantaneous evapotranspiration using spectral data. This finding highlights the potential of

satellite data for accurately estimating evapotranspiration for various plant species. However, it is essential to consider the trade-off between the finer spatial resolution and computational complexity when choosing the most suitable algorithm for a particular study.

The results of this research, in comparison with the findings of previous studies such as the calculation of actual evapotranspiration using the SEBAL algorithm by Asadi and Valizadeh Kamran [5], Wei et al [7], and Ma et al [8], as well as the estimation of actual evapotranspiration using the SEBS algorithm by Yang and colleagues [6] and Matinfar & Soorghali [4], are consistent.

5. Conclusion and suggestions

In conclusion, the study successfully demonstrated the application of SEBAL and SEBS algorithms in estimating actual evapotranspiration in the Mughan plain. The findings contribute valuable information to water resource management, agricultural planning, and

environmental studies in the region. Additionally, the use of spectral data from satellite sensors opens up possibilities for further investigations into the spatial distribution of environmental variables, enhancing our understanding of the local climate and water balance. The application of the SEBAL and SEBS algorithms, along with spectral data from the OLI and TIRS sensors of the Landsat 8 satellite, proved to be a successful approach in estimating actual evapotranspiration in the Mughan plain of Ardabil province. The study provided valuable insights into the spatial distribution of evapotranspiration rates, shedding light on the water balance dynamics and environmental characteristics of the region.

The findings of this research lead to several key conclusions and offer valuable suggestions for future studies:

Algorithm Performance: Both SEBAL and SEBS algorithms demonstrated the capability to estimate actual evapotranspiration using satellite data. However, further comparative analysis and validation against ground-based measurements are recommended to identify the strengths and weaknesses of each algorithm for specific study areas and environmental conditions. **Spatial and Temporal Variability:** The observed wide range of evapotranspiration values highlights the spatial variability in water use and transpiration rates across the Mughan plain. It is essential to consider this variability in water resource management and agricultural planning to optimize irrigation practices and ensure sustainable water use.

Data Integration and Validation: Integrating data from multiple satellite sensors and ground-based measurements can enhance the accuracy of evapotranspiration estimates. Validation of remote sensing-derived results through field measurements is critical to ensuring reliable and precise evapotranspiration calculations. **Long-Term Monitoring:** Continuous monitoring of evapotranspiration over time can provide valuable insights into climate trends and changes in water availability. Establishing long-term monitoring networks and using historical satellite data can contribute to a better understanding of the region's hydrological dynamics.

Application in Water Resource Management: The estimated evapotranspiration data can be instrumental in water resource management and decision-making processes. Utilizing this information can aid in the sustainable use of water resources and improve irrigation practices in the Mughan plain and other similar regions. **Climate Change Implications:** Considering the potential impact of climate change on evapotranspiration patterns is essential for anticipating future water availability and planning for adaptation measures. Future studies should explore the correlation between evapotranspiration and climate change indicators.

Capacity Building: Promoting capacity building initiatives among researchers and practitioners in remote sensing and hydrological modeling can enhance the application of these techniques in water resource management and environmental studies. **Data Accessibility:** Ensuring open access to remote sensing

data and making relevant datasets publicly available can foster collaboration and enable more researchers to contribute to advancing the understanding of evapotranspiration dynamics.

In conclusion, this study lays the groundwork for further investigations into evapotranspiration dynamics in the Mughan plain and serves as a valuable resource for water resource management and agricultural planning. The implementation of the suggested improvements can lead to more accurate and comprehensive assessments of evapotranspiration in the region and contribute to sustainable water management strategies.

Author contributions

Khalil Valizadeh Kamran: Conceptualization, Methodology, Data collecting. **Mahmoud Sourghali:** Analysis, Visualization, Writing-Reviewing. **Samaneh Bagheri:** Investigation, Editing, Writing-Reviewing

Conflicts of interest

The authors declare no conflicts of interest.

References

1. Erdoğan, A., Görken, M., Kabadayı, A., & Temizel, S. (2022). Evaluation of green areas with remote sensing and GIS: A case study of Yozgat city center. *Advanced Remote Sensing*, 2(2), 58-65.
2. Kotan, B., Tatmaz, A., Kılıç, S., & Erener, A. (2021). LST change for 16-year period for different land use classes. *Advanced Remote Sensing*, 1(1), 38-45.
3. Çelik, M. Ö., & Yakar, M. (2023). Arazi kullanımını ve arazi örtüsü değişikliklerinin uzaktan algılama ve cbs yöntemi ile izlenmesi: Mersin, Türkiye örneği. *Türkiye Coğrafi Bilgi Sistemleri Dergisi*, 5(1), 43-51. <https://doi.org/10.56130/tucbis.1300704>
4. Matinfar, H. R., & Soorghali, M. (2014). Estimate evapotranspiration (ET) using SEBS model based on Landsat 5 (TM) thermal data and GIS. *Indian Journal of Fundamental and Applied Life Sciences*, 4(3), 30-34.
5. Asadi, M., & Kamran, K. V. (2022). Comparison of SEBAL, METRIC, and ALARM algorithms for estimating actual evapotranspiration of wheat crop. *Theoretical and Applied Climatology*, 149(1), 327-337. <https://doi.org/10.1007/s00704-022-04026-3>
6. Yang, Y., Sun, H., Xue, J., Liu, Y., Liu, L., Yan, D., & Gui, D. (2021). Estimating evapotranspiration by coupling Bayesian model averaging methods with machine learning algorithms. *Environmental Monitoring and Assessment*, 193, 1-15. <https://doi.org/10.1007/s10661-021-08934-1>
7. Wei, J., Cui, Y., & Luo, Y. (2023). Rice growth period detection and paddy field evapotranspiration estimation based on an improved SEBAL model: Considering the applicable conditions of the advection equation. *Agricultural Water Management*, 278, 108141. <https://doi.org/10.1016/j.agwat.2023.108141>

8. Ma, Y., Sun, S., Li, C., Zhao, J., Li, Z., & Jia, C. (2023). Estimation of regional actual evapotranspiration based on the improved SEBAL model. *Journal of Hydrology*, 619, 129283. <https://doi.org/10.1016/j.jhydrol.2023.129283>
9. Orhan, O., Dadaser-Celik, F., & Ekercin, S. (2019). Investigating land surface temperature changes using Landsat-5 data and real-time infrared thermometer measurements at Konya closed basin in Turkey. *International Journal of Engineering and Geosciences*, 4(1), 16-27. <https://doi.org/10.26833/ijeg.417151>
10. Waters, R., Allen, R., Tasumi, M., Trezza, R., & Bastiaanssen, W. (2002). Surface energy balance algorithms for land. *Advanced Training and User's Manual*.
11. Jensen, M. E., Burman, R. D., & Allen, R. G. (1990). *Evapotranspiration and irrigation water requirements: a manual*. ASCE manuals and reports on engineering practice (USA), 70.
12. Bastiaanssen, W. G. M. (2000). SEBAL-based sensible and latent heat fluxes in the irrigated Gediz Basin, Turkey. *Journal of hydrology*, 229(1-2), 87-100. [https://doi.org/10.1016/S0022-1694\(99\)00202-4](https://doi.org/10.1016/S0022-1694(99)00202-4)
13. Jackson, R. D., Idso, S. B., Reginato, R. J., & Pinter Jr, P. J. (1981). Canopy temperature as a crop water stress indicator. *Water Resources Research*, 17(4), 1133-1138. <https://doi.org/10.1029/WR017i004p01133>
14. Jackson, R. D., Idso, S. B., Reginato, R. J., & Pinter Jr, P. J. (1981). Canopy temperature as a crop water stress indicator. *Water resources research*, 17(4), 1133-1138. <https://doi.org/10.1029/WR017i004p01133>
15. Su, Z. (2002). The Surface Energy Balance System (SEBS) for estimation of turbulent heat fluxes. *Hydrology and Earth System Sciences*, 6(1), 85-100. <https://doi.org/10.5194/hess-6-85-2002>



© Author(s) 2024. This work is distributed under <https://creativecommons.org/licenses/by-sa/4.0/>



Determination of alternative forest road routes using produced landslide susceptibility maps: A case study of Tonya (Trabzon), Türkiye

Fatih Kadı¹ , Osman Salih Yılmaz² 

¹ Karadeniz Technical University, Department of Geomatics Engineering, Türkiye, fatihkadı@ktu.edu.tr

² Manisa Celal Bayar University, Demirci Vocational School, Türkiye, osmansalih.yilmaz@cbu.edu.tr

Cite this study:

Kadı, F., & Yılmaz, O. S. (2024). Determination of alternative forest road routes using produced landslide susceptibility maps: A case study of Tonya (Trabzon), Türkiye. *International Journal of Engineering and Geosciences*, 9 (2), 147-164

<https://doi.org/10.26833/ijeg.1355615>

Keywords

Frequency ratio
Modified information value
Landslide susceptibility map
Forest roads
Costpath analysis

Abstract

Firstly, Landslide Susceptibility Maps of the study area were produced using Frequency Ratio and Modified Information Value models. Nine factors were defined and the Landslide Inventory Map was used to produce these maps. In the Landslide Susceptibility Maps obtained from the Frequency Ratio and Modified Information Value models, the total percentages of high and very high-risk areas were calculated as 10% and 15%, respectively. To determine the accuracy of the produced Landslide Susceptibility Maps, the success and the prediction rates were calculated using the receiver operating curve. The success rates of the Frequency Ratio and Modified Information Value models were 82.1% and 83.4%, respectively, and the prediction rates were 79.7% and 80.9%. In the second part of the study, the risk situations of 125 km of forest roads were examined on the map obtained by combining the Landslide Susceptibility Maps. As a result of these investigations, it was found that 4.28% (5.4 km) of the forest roads are in very high areas and 4.27% (5.3 km) in areas with high landslide risk areas. In the last part of the study, as an alternative to forest roads with high and very high landslide risk, 9 new forest road routes with a total length of 5.77 km were produced by performing costpath analysis in with geographic information systems.

Research Article

Received: 05.09.2023
Revised: 02.01.2024
Accepted: 15.01.2024
Published: 23.07.2024



1. Introduction

Disasters are essentially different types of events, whether natural, technological, or human-induced, that have adverse consequences in terms of physical, economic, and social losses. These events have a significant impact on societies by disrupting normal life and are beyond the capability of local interventions to prevent [1]. There are many disasters that affect life in the world, and landslides are one of these types of disaster. Landslide: commonly defined as the movement or sliding of material, typically consisting of soil, rock, or their mixture, on the surface, often leading to human casualties and property loss, is a prevalent type of natural disaster [2, 3].

According to data from the Emergency Events Database (EM-DAT), it was reported that 765 individuals lost their lives due to landslides in Türkiye from 1923 to 2023, with a total of 14,740 people being affected by this calamity. Furthermore, an observation indicates that over half of the natural disasters occurring in Türkiye during the same period were geophysical in nature,

incorporating landslides [4]. In addition, it was also found that Trabzon province, which includes the study area, was the first province in Türkiye in terms of the number of landslides with 38 fatalities and 336 fatalities in terms of the number of incidents and fatalities [5]. To reduce the devastation caused by landslides, it is crucial to identify the areas at risk of potential landslides [6, 7].

One of the map types commonly used to identify potential landslide areas is the landslide susceptibility map (LSM) [8-22]. A LSM is a type of map that generally defines the relative susceptibility of areas within a region to landslide hazards [23-26]. The use of this type of map by local governments and practitioners in activities for various purposes (route and appropriate site selection, etc.) will make it possible to reduce the destructive power of landslide disasters.

Numerous scientific studies have investigated different methods for generation of LSMs. In [27] the models used to generate LSM were categorized into three different classes: based on physical, heuristics, and statistics. Physically depended on models employ mechanical rules to control slope stability. The most

important advantage of this model is that it can be used more efficiently than other models in cases where the data used to generate the LSM are missing or insufficient [27, 28]. In heuristic-based models, the factors used to produce the LSM are first identified. Each factor is then scored by experts by comparing it with other factors [28]. There are heuristic-based models such as the fuzzy logic approach [29-33] and the analytical hierarchy process [16, 30, 34-37]. Conversely, statistical models, intend to predict future landslide disasters by correlating previous landslides and the factors that triggered them. Logistic regression [38-44] frequency ratio (FR) method [16, 45-49], information value (IV) model [7, 26, 36, 50, 51] and the modified information value (MIV) [32, 52] are among the statistical models employed during the generation of LSM. FR and MIV models, which are statistical-based methods, ensure that the accuracy of the produced map is more reliable and understandable compared to other methods [53]. Therefore, FR and MIV methods have been used in many studies [54-59,52,60].

In forested areas affected by landslides, another at-risk element is forest roads [61-64]. Forest roads, which are the subject of the aim of the research, are the roads located in the forest area and allow the forests to be put into operation in a rational way by systematically penetrating every part of the forest. Forest roads are an important physical element for the implementation of forestry policies. In addition, these roads should be constructed in such a way as to cause the least damage to the stand, land and natural nature, and the maintenance, construction and transportation works of the roads should be investigated in a sensitive and detailed way to carry out the works at minimum cost [65]. The destruction of forest roads because of unplanned and disorganized design causes forestry activities to not be carried out in a healthy way and causes many environmental problems that affect social life and nature. Landslide disaster, which has a significantly more destructive effect in the region compared to other disaster types, has become one of the most important factors to be considered during the design and building of forest roads. Therefore, considering the LSMs of the region to produce forest road routes makes it possible for the forest roads to be healthy and long-lasting.

The objective of this study is to determine alternative forest roads using the produced LSMs. To achieve this goal, firstly, LSMs of Tonya district were produced using FR and MIV methods and the performances of these methods were compared. In addition, unlike the previous scientific studies focused on developing LSM, this work investigated the landslide risk associated with the forest roads currently under the responsibility of the forest regional directorate. Lastly, this research is to create new routes for the forest road using costpath analysis. These routes will then be compared with the existing roads. This study offers an exemplary approach to developing optimal alternative routes for forest road in landslide-prone areas. By designing forest road routes while considering LSM, it will be possible to prevention potential natural disasters caused by landslides in the future and support the successful implementation of forestry policies in a sustainable manner.

2. Method

2.1. Study area

Based on the report compiled from extensive research conducted by the Provincial Disaster and Emergency Directorate, Trabzon province in Türkiye has experienced the highest number of landslides among all other provinces, with a total of 1673 occurring between 1950 and 2019. In addition, considering the count of landslides that occurred in 2019, Trabzon ranks first with 102 landslides [66]. The most recent statistical data regarding landslide disasters at the provincial level is based on the year 2019.

In this study, the town of Tonya in the Trabzon province was selected as the study area (Figure 1). The Tonya district, located within Trabzon, stands out as one of the prominent districts in terms of the frequency of landslide incidents and the number of people affected by these disasters. The study area contains very steep regions in terms of topography. Additionally, since the annual average precipitation value in the region is approximately 2200 mm, it has been observed that the region has a very high tendency towards landslide and rockfall disasters. When examining the lithological structure of the research area, it has been noted that the region mostly consists of volcanic and volcano-clastic units [67].

The altitude values of Tonya district, characterized by its steep terrain, range between 250 and 2350 m, with slope values varying between 0° to 80°.

According to the 2020 data for Tonya district, which covers an area of 264 km², the population density is 13914. The region experiences a transitional climate, combining the characteristics of the Black Sea climate and continental climate. During the summer months, the temperature in the area reaches around 20°C, while in the winter months; it drops to approximately 6-7°C [68].

2.2. Workflow

The process steps applied in this study were converted into a workflow chart as depicted in (Figure 2).

Figure 2 summarizes the methodology in the article. The geological and geomorphological factors used in the production of the landslide susceptibility map and the landslide inventory map of the study area constitute the data production part of this study. The landslide inventory map is randomly divided into training (70%) and validation (30%) data. The production of landslide susceptibility maps of the study area using two different models constitutes the second stage of the study. Then, the verification phase of the landslide susceptibility maps produced was started. At this stage, the verification of the maps was carried out with the help of verification data randomly derived from the landslide inventory map. Then, the risk status of existing forest roads was examined using validated landslide susceptibility maps. Finally, alternative forest road routes were produced on the base map created by combining landslide susceptibility maps.

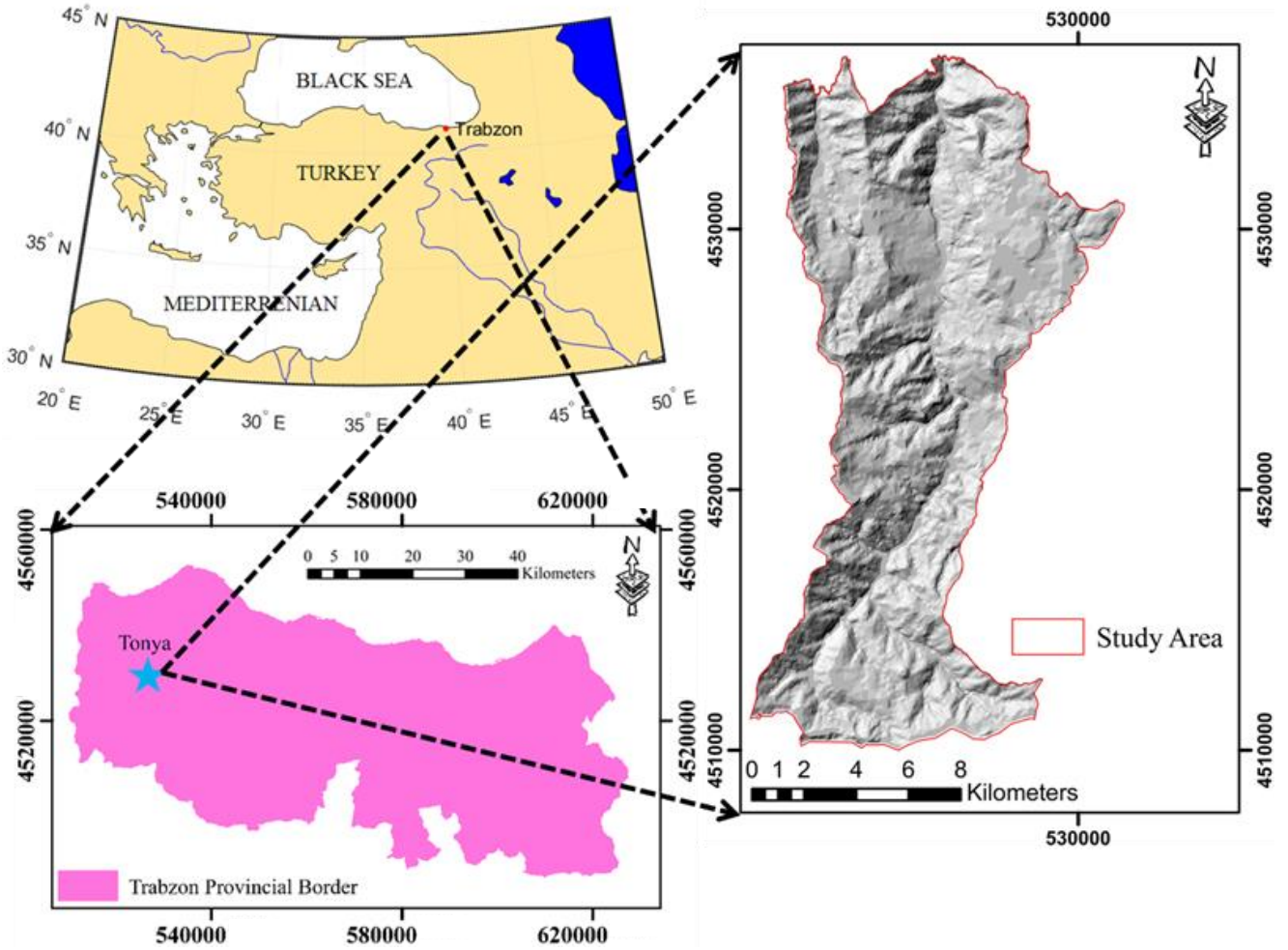


Figure 1. Study area.

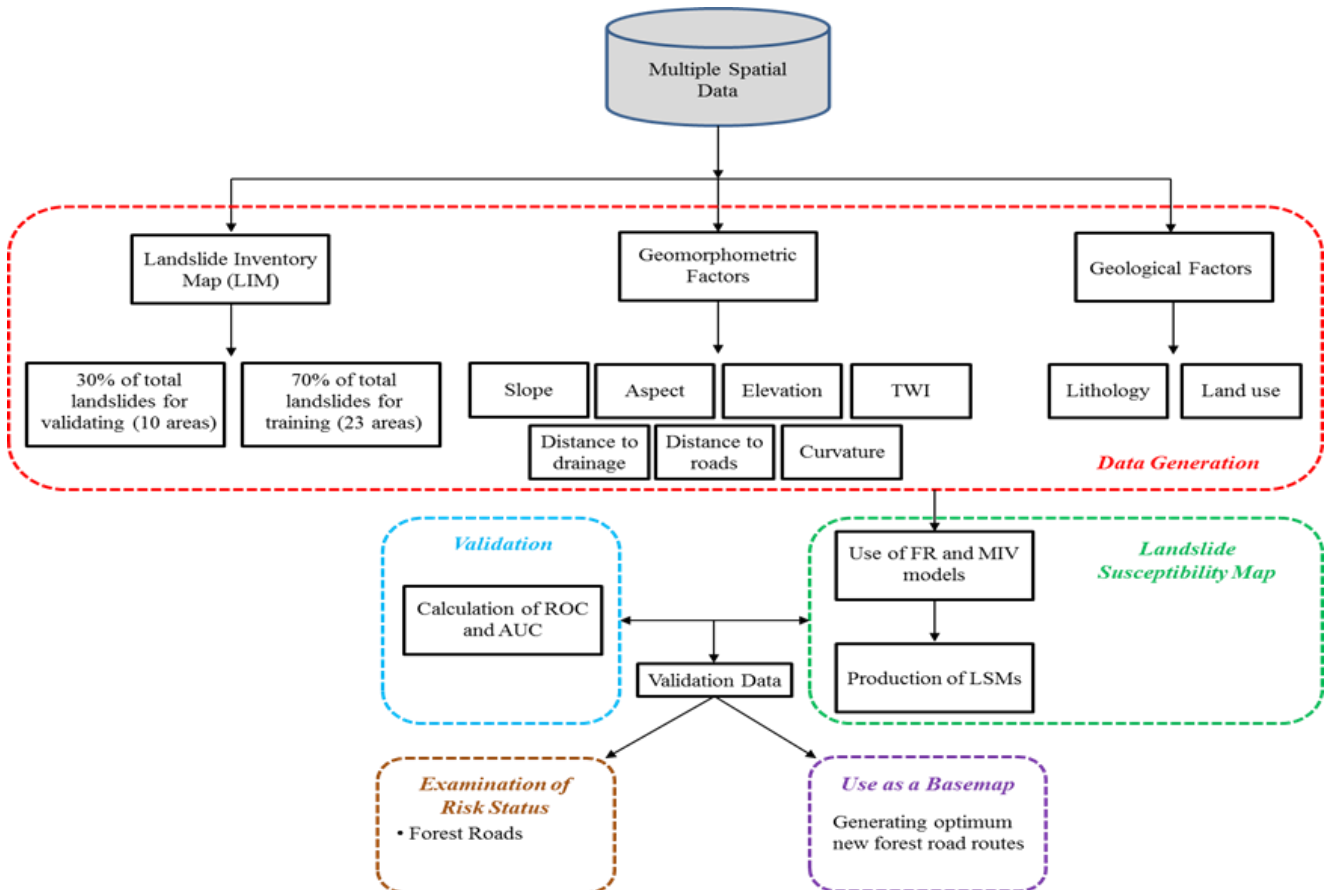


Figure 2. Workflow.

2.3. Factors used in the production of LSM

LSM is a type of map that illustrates the tendency of areas in a region for landslide disaster, divided into various classes. Type of map is generated based on the correlations between the landslide inventory map (LIM) and the factors that trigger the landslide [28, 35].

The production of a LSM is primarily based on the availability of a LIM. An LIM serves as a foundational map created for a specific region and at a particular scale. This map encompasses spatial data related to landslide disasters that have occurred in a region from the past to the present. The spatial information in the map includes details about the position and magnitude of the landslide events [16]. The precise and reliable generation of an LIM significantly influences the accuracy of all derived

products from it. Therefore, it is crucial to establish a well-designed LIM specifically tailored for the area to achieve high level of correctness in the LSM.

In this study, the utilized LIM was created through the digitization of reports obtained from comprehensive area surveys conducted by the General Directorate of Mineral Research and Exploration. As a result, the produced LIM for the study area encompasses 33 distinct landslide zones, covering a total surface area of 15.68 km² (Figure 3).

Within the context of this application, the generated LIM is categorized into two distinct groups: training data and validation data. In this context, 23 landslide areas were arbitrarily determined as training data (70%) and 10 landslide areas as validation data (30%) (Figure 3).

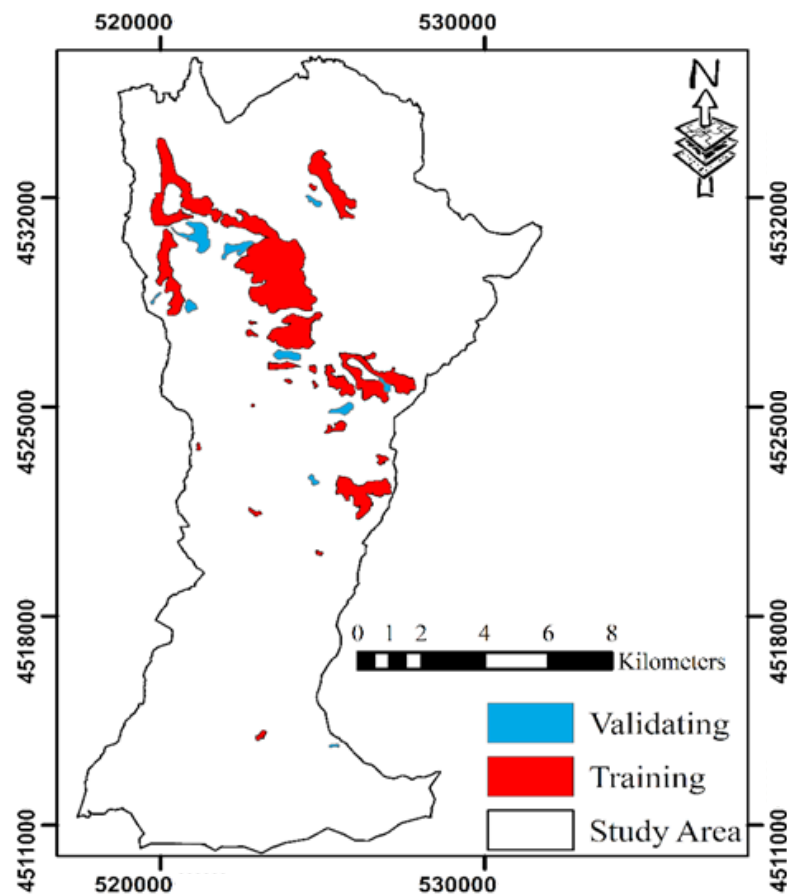


Figure 3. LIM for the study area.

The selection of the factors used in the production of the LSM is a significant research topic that directly affects the applicability and realism of the LSM. Since the parameters that trigger the landslide vary from region to region, the morphological, physical, geological, and meteorological characteristics of that region should be considered in the production of a LSM for a region [7].

In this study, nine main factors triggering landslide have been identified. These factors include slope, aspect, elevation, lithology, land use, distance to road, distance to drainage, curvature, and topographic wetness index (TWI).

It is expected that the factors used in the LSM produced with the help of statistical-based models are

independent of each other and therefore the correlations between them are weak [36]. Two main indices used in the determining this correlation are, Tolerance (TOL) and variance inflation factor (VIF), which are frequently employed in the scientific researches. If the TOL value exceeds 0.1 or the VIF value is below 10, it signifies that the factors employed in generation the LSM are mutually independent, indicating a lack of significant correlation among them [69, 70]. The TOL and VIF values of the factors employed in this research were obtained with the help of the R software, which is one of the statistical-based software (Table 1). When the calculated TOL and VIF values of all factors were considered, it was observed that there was no strong relationship among the factors.

Table 1. Indicative values of factors.

Factors	VIF	TOL
Slope	1.5406	0.6491
Aspect	1.0527	0.9499
Elevation	1.4720	0.6793
Land Use	1.1828	0.8455
Lithology	1.0206	0.9798
TWI	1.3261	0.7541
Curvature	1.1203	0.8926
Distance to drainage	1.1105	0.9005
Distance to roads	1.4928	0.6699

In this research, the factors employed in generating the LSM were prepared by utilizing a map with a scale of 1: 25,000 and a contour interval 10 meters. This process was carried out through Topo to Raster analysis in the ArcGIS program and a high-resolution digital elevation model (DEM) with a resolution of 10 m x 10 m was created. Consequently, slope, aspect, elevation, TWI, and distance to drainage, which are utilized in the generation of the LSM, were created employing the DEM data through the utilization of ArcGIS software.

Slope is considered one of the most important factors that can affect landslide disaster. Many scientific articles in the literature support the view that increasing the slope angle increases the susceptibility to landslide [71, 72]. Slope, which is frequently used in the production of susceptibility maps, has been preferred as the main factor in many scientific studies produced today [29, 36, 73, 74]. The slope factor produced for this study is divided into a total of 10 subclasses at 5° intervals (Figure 4c). Aspect is another important factor used in the production of LSMs. This type of disaster occurs on slopes with a certain orientation. Sunlight, drainage, and climatic effects of the regions facing different aspects of the land include differences. Therefore, the tendency levels towards landslide disasters of regions with different aspect values are also different [75]. The aspect produced for the research area is separated into 9 different groups in total (Figure 4a). Elevation is another important factor used in the production of a LSM. The elevation value of a region is an important criterion that directly affects the gravitational potential energy in that region [76]. In this study, the elevation factor used in the production of the LSM was divided into a total of 10 subclasses (Figure 4b). Lithology is another factor used in this study. The types of materials in the existing layers under the ground have different properties and types of movement from each other. Since the sliding movements and water permeability resistances of each material structure are different from each other, their effects on slope stability are also different [77]. The lithology map used was created using ArcGIS software, utilizing the geological map created at a scale of 1:25000 (Figure 4d). In the lithology map generated for the study area, there are 9 different soil types (Kru1, Kru2, Kru3, Kru4b, Kru5b, Kru5a, Gama2, Jlh, Ev). The outcropping units of the study area mostly consist of volcanic and volcanoclastic units. The age of these units follows a sequence from the Jurassic to the Late Cretaceous and ends with the Eocene. There are Eocene aged, units expressed as Ev consisting of basalt, andesite and pyroclasts and containing partly sandy limestone, and Gama2 units with

granite, granodiorite, quartz diorite and dolerite structures. While Kru1, Kru2, Kru3, Kru4b, Kru5a, basalt, andesite, dacite, rhyodacite and pyroclasts from Late Cretaceous units, Kru5b has sandy reef limestone content. When the spatial dispersion of these units in the research area is analyzed, it becomes apparent that the Ev units have the highest frequency, comprising approximately 35% of the total. Curvature is another basic terrain factor used in the production of a LSM. This type of factor, defined as the slope angle or the amount of change in aspect, is divided into 3 classes: concave, flat and convex [77]. The factor in question was created using ArcGIS software with the DEM (Figure 4g). Land use is another factor commonly utilized in LSMs. Land use is a type of map in which land and soil are classified according to their capabilities, taking into account climatic characteristics. In this type of map, based on basic soil surveys, the soil is divided into eight classes. The first four classes include lands with land structure suitable for agriculture. On the other hand, the last four classes include the classes where there are pastures, forests and lands suitable for natural life, which are not suitable for agriculture. The first four and the last four classes are ordered according to their profile shape and slope level. Within the study area, four classes (I, IV, VI, and VII) have been identified (Figure 4f). The topographic wetness index (TWI) is an additional factor that measures the influence of water movement and accumulation on the terrain across the basin [78]. The TWI is commonly employed to assess the influence on hydrological processes. Calculation of this index is achieved through Equation 1.

$$TWI = \ln \frac{a}{\tan\beta} \quad (1)$$

Where a value represents the upward slope area at the unit point, and the $\tan\beta$ value represents the slope angle at the point. This factor, which was produced using ArcGIS software with the help of DEM, was divided into 5 subclasses in total in this study (Figure 4e). Another factor generated from the DEM is the distance to the drainage. This factor was generated using the hydrological analysis module, which is one of the spatial research tools provided in the ArcGIS software. The factor to drainage network was computed for the research area and separated into 10 subclasses. The maximum distance to the drainage network was determined as 2260 m (Figure 4h). The distance to the road factor is another important aspect considered in this study. The road network, often characterized by unplanned and haphazard construction, significantly influences the slope stability in the region. The road network was obtained from Open Street Map data and 1:25,000 scale maps. Once the road network was established, the process of creating the distance map to the road network commenced. The ArcGIS software was employed to determine the distance from every pixel to the road network. The distance to the road factor was separated into 10 subclasses (Figure 4i). Using the ArcGIS software, all factors employed in the production phases of the LSM were converted into raster, ensuring a spatial resolution of 10 m.

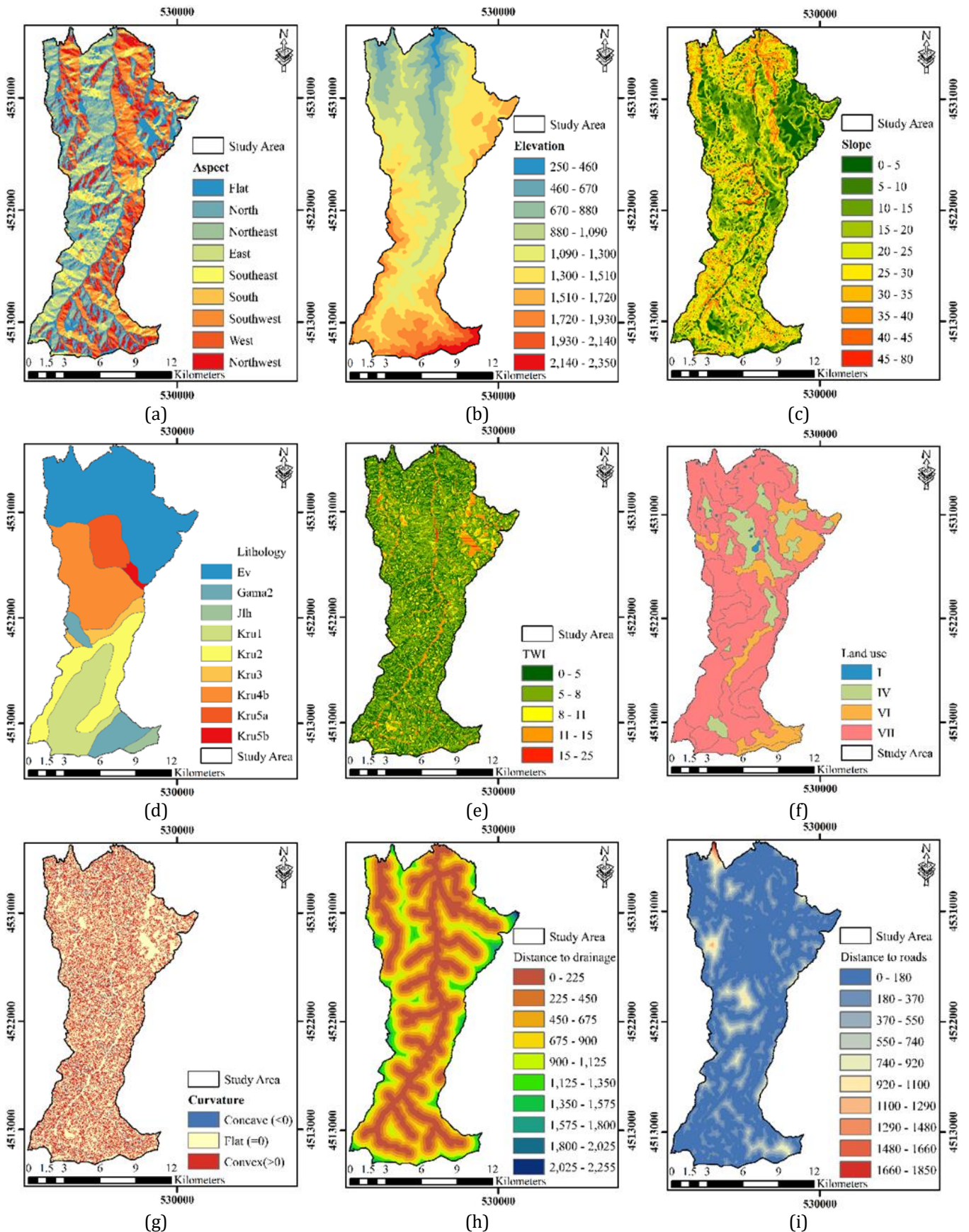


Figure 4. Factors used in LSM (a: aspect, b: elevation, c: slope, d: lithology, e: TWI, f: land use, g: curvature, h: distance to drainage, i: distance to road).

2.4. Models used in the production of LSM

Two different models, FR and MIV, were used in the production of LSMs of the study area.

2.4.1. FR model

Various approaches exist for predicting future landslides. The FR model employs a methodology that

seeks to establish a correlation between the factors influencing past landslides and those that may take place in times to come. The primary objective of the FR model is to estimate potential landslides by analyzing the factors that have triggered previous occurrences of landslides. By employing this approach, it becomes possible to gain a comprehensive understanding of the relationship among old landslide data and the probability of future landslide occurrences [28, 54, 55]. The FR model, which is one of the statistical-based approaches, has a simpler and more understandable structure compared to others. Moreover, the FR model is a reliable model type that is frequently used in the production of LSMs that require high accuracy and precision. For this reason, the FR model has been used in numerous scientific researches to produce LSMs. In this study, each of the factors affecting the landslide is divided into various subclasses. FR model values of each class were calculated with Equation 2.

$$F_r = \frac{\frac{N_{pix}(L_{ij})}{N_{pix}(L)}}{\frac{N_{pix}(S_{ij})}{N_{pix}(S_a)}} \quad (2)$$

In this context, $N_{pix}(L_{ij})$ signifies the count of pixels located within the landslide area belonging to the j th subclass of factor i , $N_{pix}(L)$ the all count of pixels within all landslide areas in the study area, and $N_{pix}(S_{ij})$ denotes the corresponding count of pixels. And finally, $N_{pix}(S_a)$ represents the all count of pixels.

Factors with FR values higher than 1 are known to have better correlations with landslide areas than factors with FR values lower than 1 [28]. The sum of the FR values of each subclass is equal to the landslide susceptibility index (LSI). Equation 3 is used to calculate this index value.

$$LSI = \sum_{i=1}^n Fr_i = Fr_1 + Fr_2 + Fr_3 + \dots + Fr_n \quad (3)$$

A high index value means that the region has a high tendency to landslide disaster. The LSI values calculated for the study area change among 3.00 and 14.11 (Table 2).

The FR model was utilized to create the LSM. The map was separated into 5 groups in total, considering the risk situation (Figure 5).

2.4.2. MIV model

One of the other statistical-based models frequently used in the literature is the MIV model. The MIV model is a type of model that is depend on information theory and works in accordance with a statistical data analysis method [79].

This model has an approach that considers the information values of the factors used in the production of the LSM. In this context, the information values of the

subclasses of whole the factors used in the production of the sensitivity map were calculated with Equation 4.

$$I(H, x_j) = \ln \frac{\frac{N_{pix}(S_j)}{N_{pix}(N_j)}}{\frac{\sum N_{pix}(S_j)}{\sum N_{pix}(N_j)}} \quad (4)$$

Where, $N_{pix}(S_j)$ value symbolizes the total count of pixels falling on landslide areas in subclass j of all factors, and $N_{pix}(N_j)$ value represents the all count of pixels in subclass i of factors. In addition, the $\sum N_{pix}(S_j)$ value symbolizes the whole number of pixels falling on the landslide areas, and the $\sum N_{pix}(N_j)$ value symbolizes the all pixel area in the study area.

The $I(H, x_j)$ value calculated because of the equation numbered 3 symbolizes the information value in the j subclass of the factors.

The cumulative sum of the information values computed for the subclasses of all factors, as determined by Equation 4, equals the LSI . The specific formula is provided in Equation 5.

$$LSI = \sum_{j=1}^n I(H, x_j) \quad (5)$$

A negative value of LSI means that likelihood of a landslide disaster to occur in the relevant region is low. A LSI value of zero indicates that the likelihood of a landslide disaster happening is average or moderate. Finally, a positive value of LSI means that the probability of a landslide disaster is above medium.

The MIV for each subclass of the nine factors was determined by utilizing the landslide data from the training set and referring to the LIM (Table 2). The results obtained from the MIV model revealed a range of LSI values between 2.91 and 9.67.

The LSM produced using MIV was separated into 5 different groups in total, considering the risk situation (Figure 6).

3. Results

In line with the data obtained in Table 2, LSMs were generated employing both the FR and the MIV (Figure 5-6). Each of the LSMs produced on different models is separated into 5 groups.

The spatial and percentile distributions of the LSM produced using FR are 804.52 ha (4%), 1206.78 ha (6%), 1206.78 ha (6%), 6637.29 ha (33%), and 10,257.63 ha (51%) (very high, high, medium, low and very low). The areal and percentage distributions of the LSM produced using MIV were calculated as 1206.78 ha (6%), 1810.17 ha (9%), 4223.73 ha (21%), 6033.90 ha (30%) and 6838.42 ha (34%). In light of these results, the areal and percentage distribution of high and very high classes in the LSMs created from the FR and MIV models are seen as 2011.30 ha (10%) and 3016.95 ha (15%), respectively (Figure 7).

Table 2. The FR and MIV values were calculated for the various factors.

Factors	Subclasses	No. of pixels in domain	Percentage of domain	No. of landslide pixels	Percentage of landslide	FR	MIV
Elevation	250-460	15,931	0.7958	381	0.2430	0.3054	0.3487
	460-670	69,396	3.4666	8702	5.5510	1.6013	1.6421
	670-880	202,706	10.1260	50,971	32.5143	3.2110	2.7893
	880-1090	352,580	17.6129	60,449	38.5603	2.1893	1.9431
	1090-1300	433,825	21.6714	27,395	17.4752	0.8064	0.9677
	1300-1510	459,035	22.9308	8211	5.2378	0.2284	0.3185
	1510-1720	297,923	14.8825	656	0.4185	0.0281	0.0590
	1720-1930	103,898	5.1902	0	0.0000	0.0000	0.0000
	1930-2140	40,919	2.0441	0	0.0000	0.0000	0.0000
	2140-2350	25,617	1.2797	0	0.0000	0.0000	0.0000
Slope	0-5	335,526	16.7610	22,208	14.1664	0.8452	0.9674
	5-10	104,899	5.2402	24,963	15.9238	3.0388	2.4013
	10-15	242,180	12.0979	54,410	34.7080	2.8689	1.9788
	15-20	301,487	15.0606	29,424	18.7695	1.2463	1.0370
	20-25	328,485	16.4092	13,262	8.4598	0.5156	0.7055
	25-30	305,965	15.2843	6219	3.9671	0.2596	0.4021
	30-35	213,039	10.6422	3668	2.3398	0.2199	0.2711
	35-40	110,780	5.5339	1709	1.0902	0.1970	0.3164
	40-45	41,041	2.0502	533	0.3400	0.1658	0.2253
	45-80	18,428	0.9206	369	0.2354	0.2557	0.2984
Aspect	Flat	390,321	19.4982	29,351	18.7229	0.9602	1.3092
	North	225,785	11.2789	33,997	21.6866	1.9228	1.5017
	Northeast	230,546	11.5168	30,017	19.1478	1.6626	1.2963
	East	176,522	8.8180	6232	3.9754	0.4508	0.8721
	Southeast	123,494	6.1691	1678	1.0704	0.1735	0.2673
	South	159,427	7.9641	1494	0.9530	0.1197	0.1933
	Southwest	240,937	12.0358	10,537	6.7215	0.5585	0.7042
	West	230,714	11.5252	20,146	12.8511	1.1150	1.0853
Northwest	224,084	11.1940	23,313	14.8713	1.3285	1.1928	
Curvature	<0	723,592	36.1465	57,730	36.8258	1.0188	0.9239
	0	542,316	27.0910	43,149	27.5246	1.0160	0.9410
	>0	735,922	36.7625	55,886	35.6495	0.9697	1.0498
TWI	0-5	579,624	28.9547	26,271	16.7582	0.5788	0.6214
	5-8	1,023,829	51.1447	96,262	61.4053	1.2006	1.0986
	8-11	214,909	10.7356	20,985	13.3863	1.2469	1.1849
	11-15	163,126	8.1488	11,280	7.1955	0.8830	0.9321
	15-25	20,342	1.0162	1967	1.2547	1.2348	1.1244
Lithology	Ev	729,115	36.4323	59,097	37.6978	1.0347	0.9572
	Gama2	120,665	6.0294	273	0.1741	0.0289	0.0897
	Jlh	27,885	1.3934	0	0.0000	0.0000	0.0000
	Kru1	284,953	14.2385	0	0.0000	0.0000	0.0000
	Kru2	272,579	13.6202	9175	5.8527	0.4297	0.5034
	Kru3	54,295	2.7130	3794	2.4202	0.8921	0.9593
	Kru4b	370,184	18.4973	20,575	13.1247	0.7095	0.7682
	Kru5a	124,283	6.2102	56,822	36.2466	5.8367	3.2799
Kru5b	17,327	0.8658	7029	4.4838	5.1788	3.1080	
Distance to Drainage (m)	0-225	494,398	24.5745	43,222	27.5712	1.1219	1.0672
	225-450	432,259	21.4859	32,462	20.7074	0.9638	1.1230
	450-675	393,813	19.5749	29,953	19.1069	0.9761	1.0566
	675-900	320,570	15.9342	24,903	15.8856	0.9969	1.0834
	900-1125	216,948	10.7836	17,905	11.4216	1.0592	0.8937
	1125-1350	105,726	5.2552	6952	4.4347	0.8439	1.1028
	1350-1575	35,604	1.7697	1349	0.8605	0.4862	0.6217
	1575-1800	9789	0.4866	19	0.0121	0.0249	0.1470
	1800-2025	1741	0.0865	0	0.0000	0.0000	0.0000
	2025-2265	982	0.0488	0	0.0000	0.0000	0.0000
Distance to Roads (m)	0-180	1,314,001	65.3137	13,2982	84.8289	1.2988	1.1834
	180-360	406,420	20.2015	14,669	9.3573	0.4632	0.6217
	360-530	169,054	8.4030	4500	2.8705	0.3416	0.3922
	530-710	75,094	3.7326	1704	1.0870	0.2912	0.3758
	710-880	30,522	1.5171	1534	0.9785	0.6450	0.7004
	880-1060	10,250	0.5095	792	0.5052	0.9916	1.1028
	1060-1240	3167	0.1574	584	0.3725	2.3665	2.0793
	1240-1410	1457	0.0724	0	0.0000	0.0000	0.0000
	1410-1590	1311	0.0652	0	0.0000	0.0000	0.0000
	1590-1770	554	0.0275	0	0.0000	0.0000	0.0000
Land Use	I	9938	0.4940	3214	2.0502	4.1504	2.7814
	IV	235,784	11.7199	126,479	80.6806	6.8841	3.1447
	VI	276,189	13.7282	12,197	7.7804	0.5667	0.6879
	VII	1,489,919	74.0579	14,875	9.4887	0.1281	0.2019

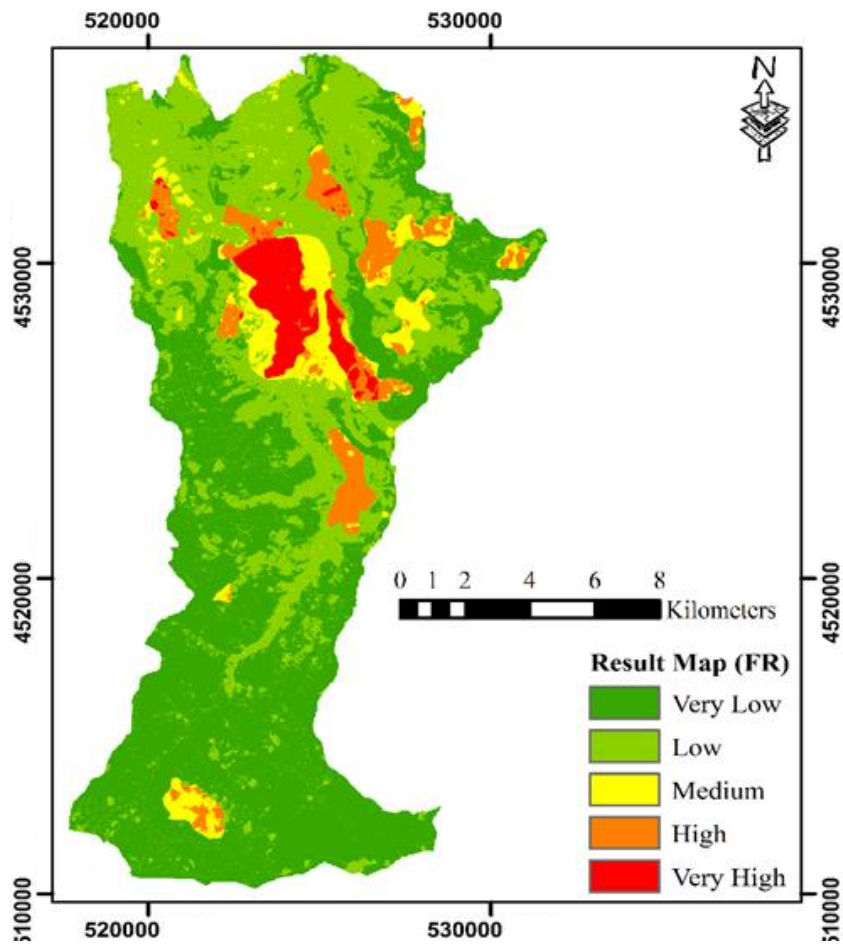


Figure 5. LSM generated by the FR model.

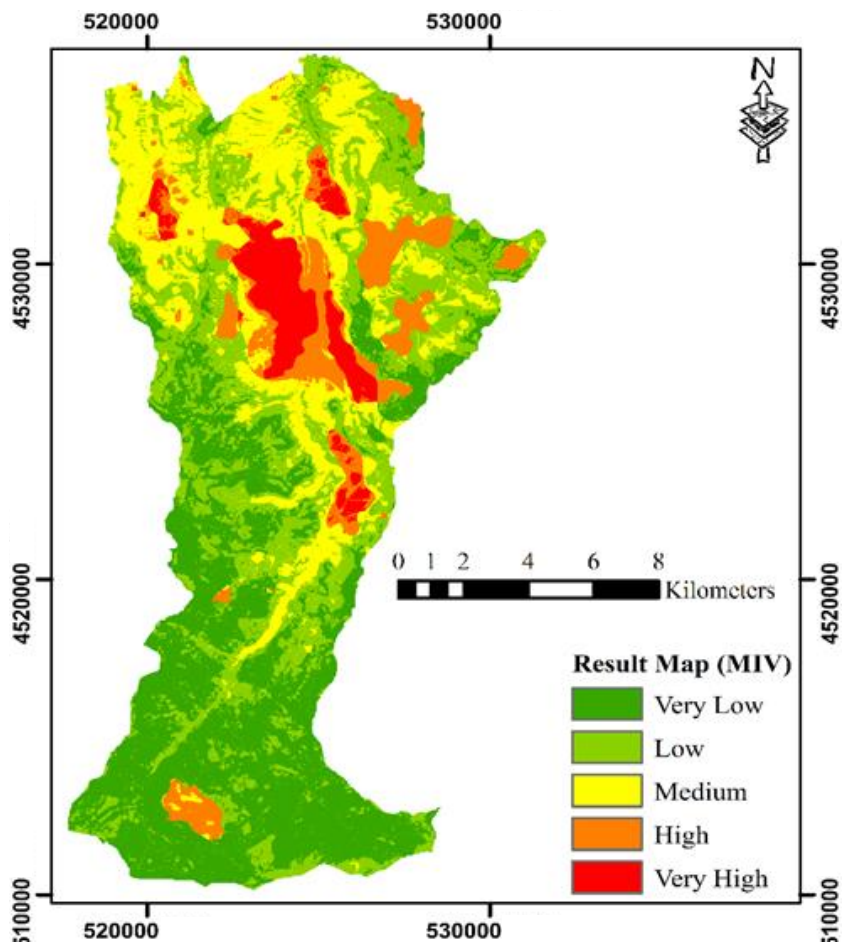


Figure 6. LSM generated by the MIV model.

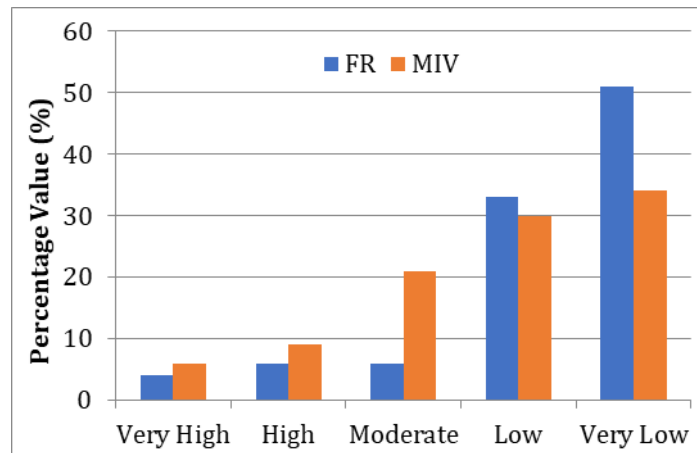


Figure 7. Percentage distributions of classes in the LSM for FR and MIV models.

3.1. Validation of LSMs

The accuracy of the generated LSM is a very important criterion in terms of the applicability and realism of the map. Therefore, testing the correctness of the generated LSM is a clear indication of how reliable the product produced is.

There are many methods to check the accuracy of the LSM produced today. The receiver operating characteristic (ROC) curve and the area under the ROC curve (AUC) are widely employed and highly reliable techniques in the researches [18, 35, 80, 81]. In this context, the precision of the generated LSM was evaluated employing the ROC and AUC methods. The ROC curve consists of two axes (horizontal and vertical). The X-axis is the false positive rate, while the Y-axis is the true positive rate. The most basic criterion used in the analysis of the correctness of the LSM produced in this curve is the AUC value. A model with values between 0.5 and 1 AUC is defined as a model type that is adequate in terms of accuracy [18].

The accuracy of the LSMs generated employing the FR and MIV models was evaluated employing the success rate and prediction rate methods. The AUC values of the

FR and MIV models were computed employing the training data from the LIM, as part of the success rate analysis.

The LSMs obtained from both models were overlapped with the training data and the degree of overlap of the layers was checked. Thus, the success rate percentages of both models were calculated. In this study, the success rates of the FR and MIV models were computed as 82.1% and 83.4%, respectively (Figure 8). Prediction rate method, on the other hand, is a type of method that is frequently used in estimating areas that are prone to landslide according to the success rate method. This type of method aims to test how accurately the produced LSMs identifies areas prone to landslides [28, 82]. The validation dataset, which constitutes 30% of the LIM and includes ten randomly determined landslide areas, was used to estimate the areas prone to landslides. In this context, the AUC values for the FR and MIV models are 79.7% and 80.9%, respectively (Figure 9). As a result, although the MIV model was more successful than the FR model in detecting areas prone to landslides, it was observed that both models gave very good results in this study.

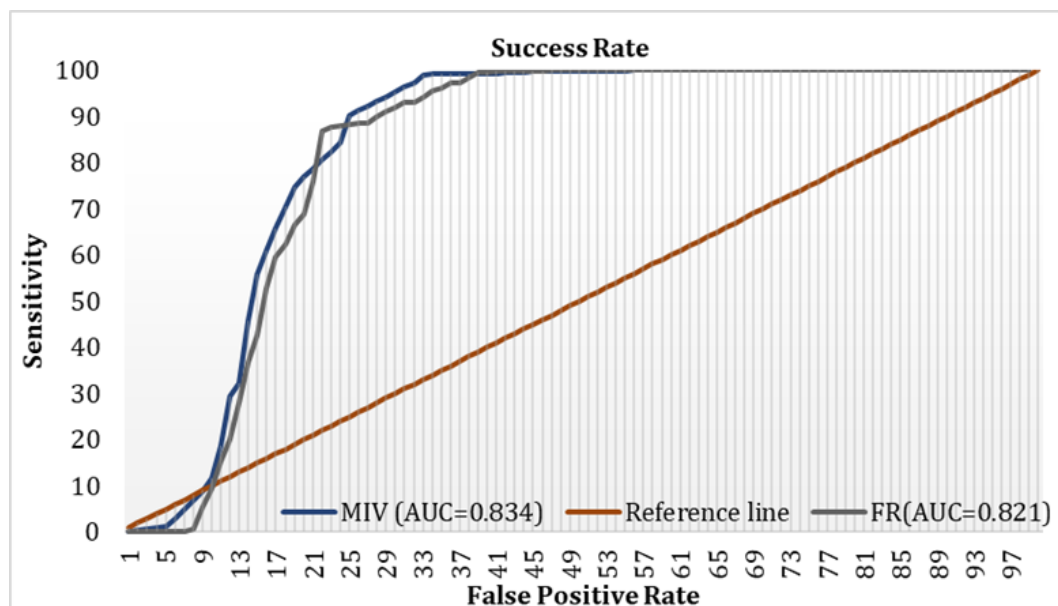


Figure 8. Success rate curves for FR and MIV models.

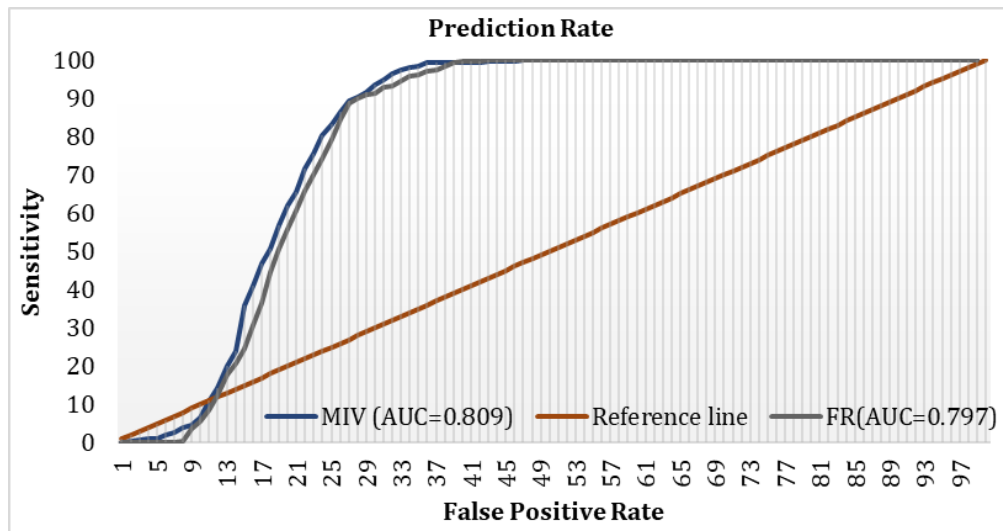


Figure 9. Curves displaying the prediction rates for the FR and MIV models.

3.2. Risk situations of forest roads and determination of new routes

This section investigates the risk conditions of forest roads in the study area by employing LSMs generated through the utilization of FR and MIV models. Within the study area, there are approximately 125 km of forest roads present (Figure 10).

In this context, forest roads overlapped with LSMs produced on two different models (Figure 11). The risk situations on the LSMs of forest roads were evaluated by dividing them into 4 classes. Considering the LSM produced on the FR model, it was determined that 9.5 km (7.6%) of the 125 km forest road is on high and very high-risk areas. In the LSM created using the MIV model, this value is 11.85 km (9.5%).

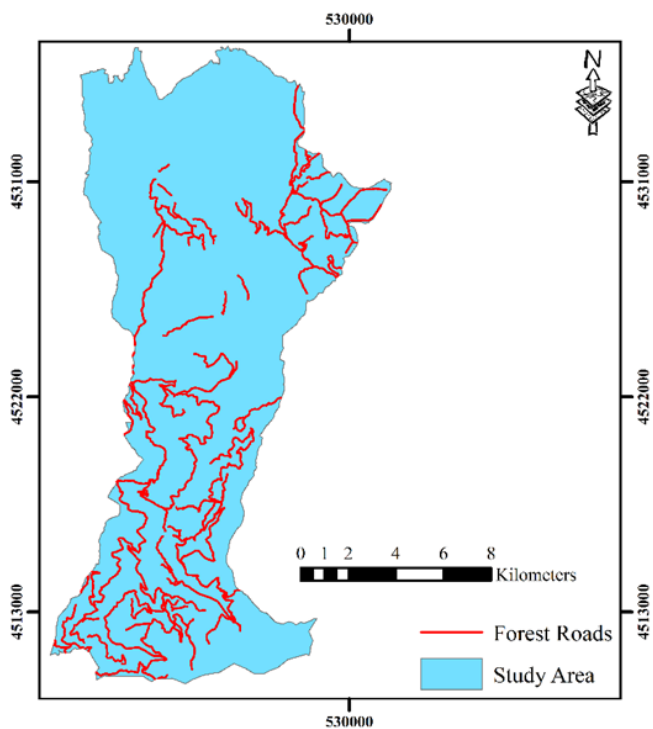


Figure 10. Available forest roads in the study area.

The forest roads, which are in the risky classes in the

LSMs produced through both models, pose a risk in terms of the healthy execution of the forestry policies implemented by the forest enterprises in that region. Therefore, it is significant for the continuity of forestry activities to be able to produce alternative forest road routes instead of the risky forest roads. In the process of generating alternative forest road routes, a single map derived from the combination of 2 different LSMs produced with the help of different models in this study was used as a base map. A single map derivation from two different LSMs produced on different models for the same region was performed with the overlap analysis in ArcGIS software (Figure 12).

The risk situations of the available forest roads area were determined by considering the high and very high classes in the combined LSM shown in Figure 12. The lengths of the existing forest roads in both classes are given in Table 3. In addition, in the light of the evaluations made on the combined LSM, it has been determined that 5.4 km of the 125 km forest roads are in the very high (4.28%) class and 5.3 km in the high (4.27%) class. Therefore, it has been observed that forest roads with a length of 10.68 km in regions with high and very high landslide risk carry a high risk in terms of landslides.

It is necessary to produce new alternative forest road routes in order not to interrupt the forestry activities in the region, instead of the canceled forest road routes in regions with high and very high landslide risk. To achieve this objective, costpath analysis was performed utilizing the ArcGIS software. Costpath analysis is a type of analysis that aims to determine the most suitable route in terms of cost, considering criteria such as slope, mandatory point, restricted area. In this study, the base map produced because of overlaying the LSM combined with the slope map was used as an input for costpath analysis. The new forest road routes obtained because of the costpath analysis are presented in Figure 13. In addition, the quantity information regarding the new forest road routes in question are given in Table 4. In this study, 10.68 km of forest roads in the study area were canceled due to being on risky landslide areas, while new forest road routes of 5.77 km were produced with the help of costpath analysis in the GIS.

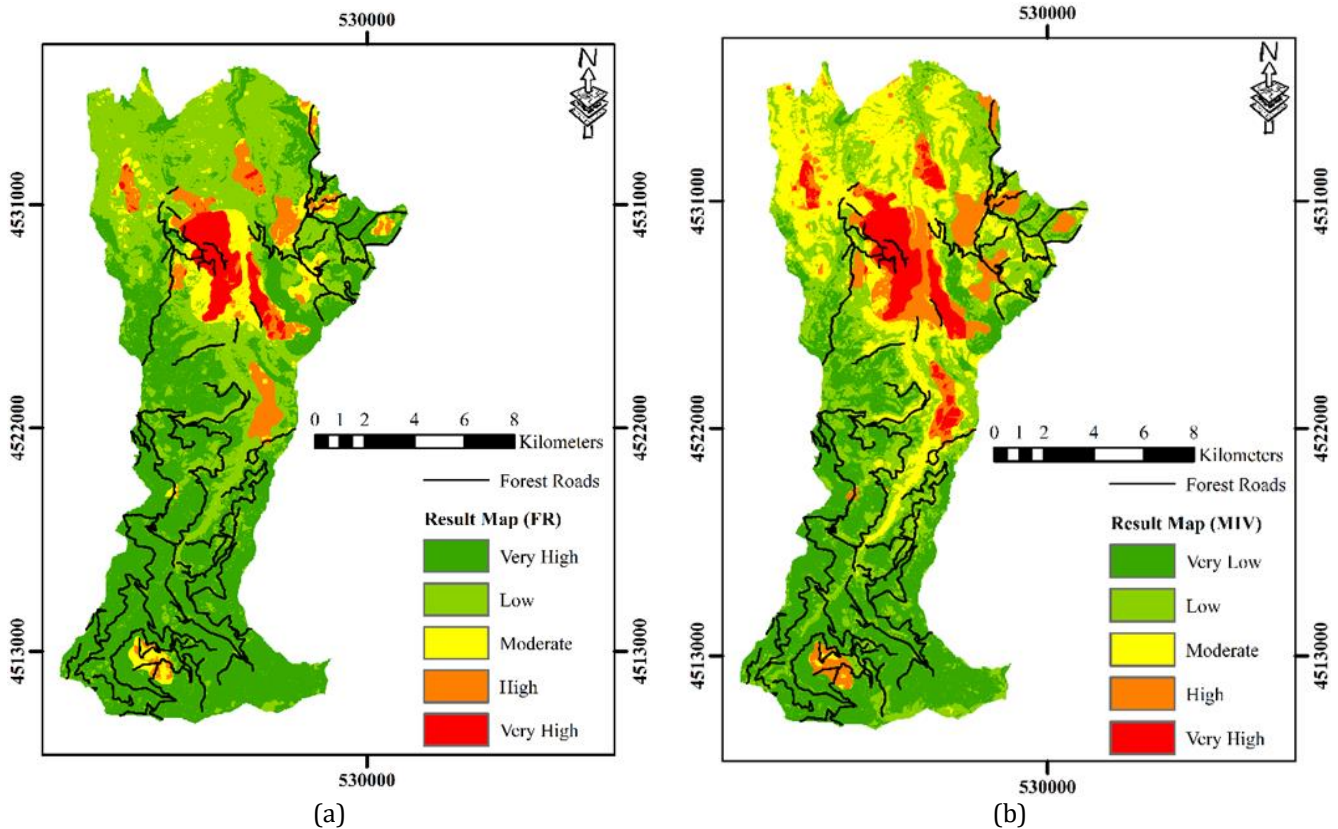


Figure 11. Representation of forest roads on produced LSMs (a: FR model, b: MIV model).

Table 3. Forest roads in high and very high classes, canceled routes.

Forest road number	Forest road intersection with risk classes (m)		Canceled route (m)
	Very High	High	
1	-	344.35	344.35
2	-	1128.34	1128.34
3	-	176.56	176.56
4	-	111.80	111.80
5	-	415.15	415.15
6	-	322.92	322.92
7	187.78	22.91	210.69
8	1590.82	-	1590.82
9	150.64	-	150.64
10	595.98	-	595.98
11	964.14	-	964.14
12	442.24	-	442.24
13	438.12	-	438.12
14	981.72	-	981.72
15	-	159.16	159.16
16	-	227.7	227.7
17	-	185.56	185.56
18	-	595.01	595.01
19	-	241.82	241.82
20	-	608.23	608.23
21	-	794.63	794.63
Total	5351.44	5334.14	10685.58

4. Discussion

The LSM for the study area was initially produced by [67]. The author aimed to create an LSM for the region using a method falling within the cluster classifier category known as fuzzy adaptive resonance theory (FuzzyART-BURT). The production of the LSM involved lithology, elevation, slope, aspect, stream power index and TWI data. The accuracy of the LSM resulting from the

study was assessed with the area under the curve (ROC-EAA) method. Following the validation analysis, the AUC value was calculated as 0.72, indicating the success of the generated LSM.

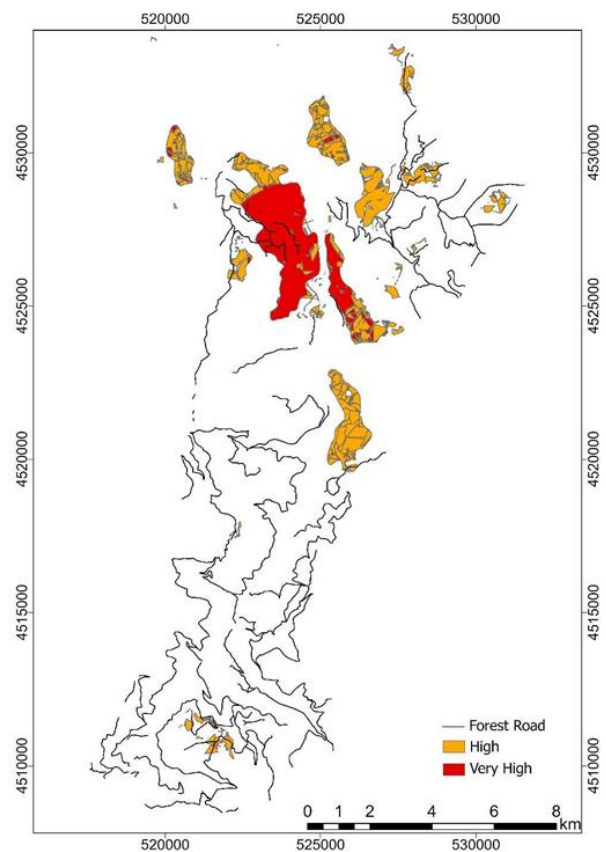


Figure 12. Base map obtained by overlaying the LSMs produced on the FR and MIV models.

To validate the produced LSMs, ROC and AUC parameters were employed, comparing the performance of the FR and MIV models using ROC curves and AUC analysis. According to many scientific studies, a model with AUC values between 0.5 and 1 is considered adequate in terms of accuracy [18]. The computed AUC values for the success rate of the FR and MIV models were 82.1% and 83.4%, respectively. Additionally, the AUC values for the predicted rate were determined as 79.7% and 80.9% for the FR and MIV models, respectively. As a result, although the MIV model outperformed the FR model in detecting areas prone to landslides, both models yielded excellent results.

Table 4. New forest road routes generated with costpath analysis.

New route name	New route distance (m)
A-B	673.84
A-C	797.69
D-E	375.16
F-G	319.79
I-J	648.36
P-R	254.80
K-L	614.65
M-N	819.08
O-Q	1262.99
Total	5766.36

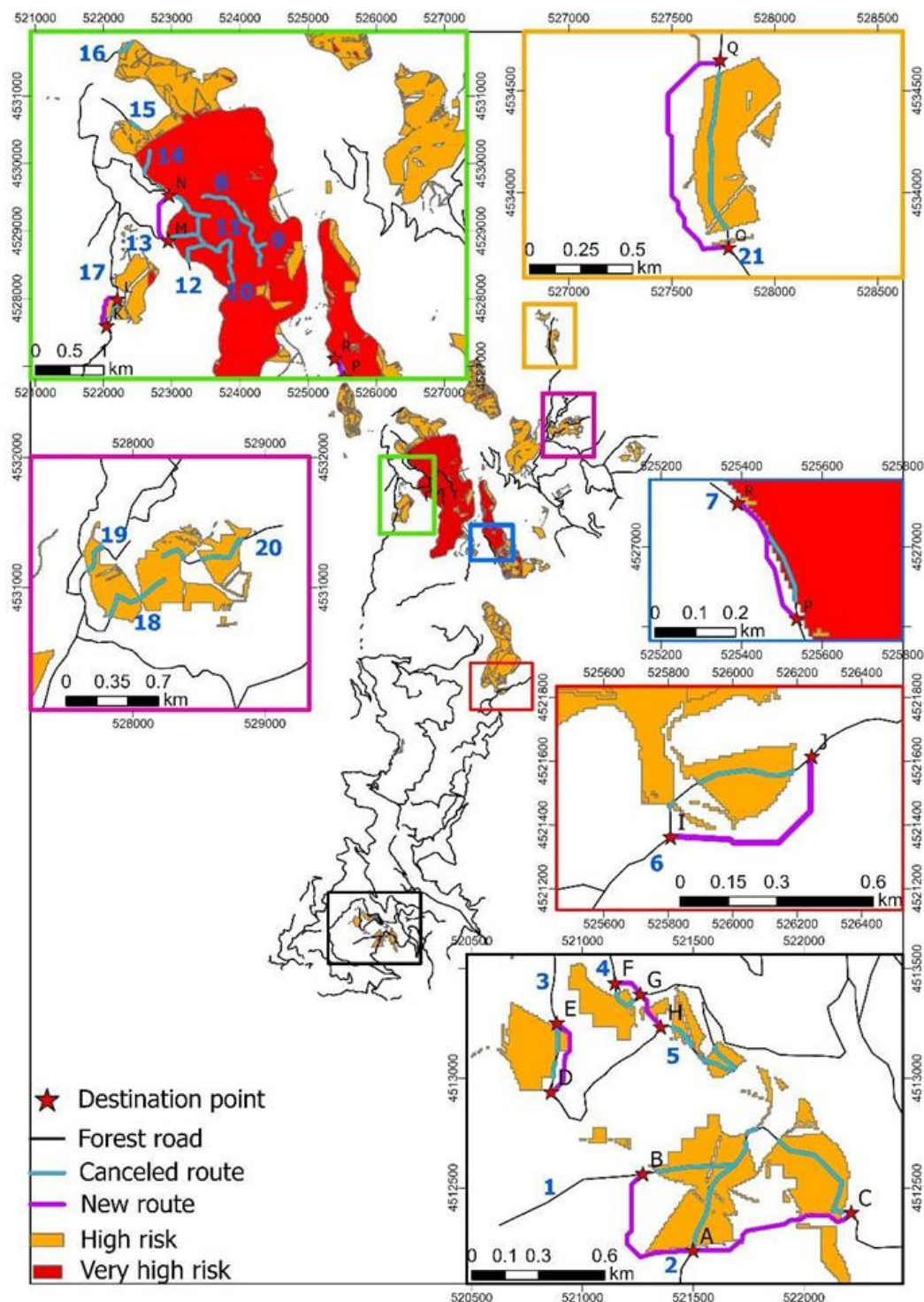


Figure 13. New forest road routes map.

5. Conclusion

LSMs of the research were generated for the research area using two different models, namely FR and MIV (Figure 5-6). Given the both models are statistically based, it has been frequently emphasized in the literature that the maps created from these models are more understandable [32, 52]. The LSMs were generated using nine factors (Figure 4) with the LIM serving as another input. There are 33 landslide areas recorded and processed on the LIM in study area (Figure 3). During the production of LSMs with the FR and MIV models, 70% of the landslide areas (23 landslide areas) were utilized for training the models, while the remaining 30% (10 landslide areas) were employed for model validation purposes. The random division of landslide areas into training and verification classes, was performed based on percentages referenced in the previous sentence using existing literature for both the distribution type and the percentages [83-87]. The second phase of the study involved assessing the risk conditions of existing forest roads based on the LSMs. In the LSMs generated with the help of FR and MIV models, it was determined that 7.6% and 9.5% of the existing forest roads are situated on areas with high and very high landslide risk. Producing new alternative forest road routes instead of existing forest roads in high and very high risk areas will facilitate forestry activities in that region. In the final stage of the study, a total of 9 alternative forest road routes were produced instead of existing routes affected by landslide (Figure 13) (Table 4). Costpath analysis in ArcGIS software was applied in the process of generating these alternative optimum forest road routes. This type of analysis frequently used in the literature, determines the optimum route between the start and end points [88-91]. As a result of the analysis, 10.68 km of existing forest roads in the study area were canceled due to their location in high risk landslide areas, while new forest road routes of 5.77 km were proposed. The newly determined routes play an important role in the healthy and systematic execution of forestry activities. For all that, the LSMs created with the two different models can serve as a base map for practitioners when the generating of new forest road routes or proposing alternative route solutions.

Author contributions

Fatih Kadi: Conceptualization, Methodology, Investigation, Data curation, Writing-Original draft preparation. **Osman Salih Yilmaz:** Writing-Original draft preparation, Software, Validation, Visualization, Reviewing and Editing.

Conflicts of interest

The authors declare no conflicts of interest.

References

- Şentürk, E., & Erener, A. (2017). Determination of temporary shelter areas in natural disasters by GIS: A case study, Gölcük/Turkey. *International Journal of Engineering and Geosciences*, 2(3), 84-90. <https://doi.org/10.26833/ijeg.317314>
- Kaya, H., & Gazioglu, C. (2015). Real estate development at landslides. *International Journal of Environment and Geoinformatics*, 2(1), 62-71. <https://doi.org/10.30897/ijegeo.302433>
- Stanley, T., & Kirschbaum, D. B. (2017). A heuristic approach to global landslide susceptibility mapping. *Natural Hazards*, 87, 145-164. <https://doi.org/10.1007/s11069-017-2757-y>
- EM-DAT. (2023). The International Disaster Database. Inventorying hazards & disasters worldwide since 1988. <https://www.emdat.be>
- Görüm, T., & Fidan, S. (2021). Spatiotemporal variations of fatal landslides in Turkey. *Landslides*, 18(5), 1691-1705. <https://doi.org/10.1007/s10346-020-01580-7>
- Dahal, R. K., Hasegawa, S., Nonomura, A., Yamanaka, M., Masuda, T., & Nishino, K. (2008). GIS-based weights-of-evidence modelling of rainfall-induced landslides in small catchments for landslide susceptibility mapping. *Environmental Geology*, 54, 311-324. <https://doi.org/10.1007/s00254-007-0818-3>
- Chen, W., Li, W., Hou, E., Zhao, Z., Deng, N., Bai, H., & Wang, D. (2014). Landslide susceptibility mapping based on GIS and information value model for the Chencang District of Baoji, China. *Arabian Journal of Geosciences*, 7(11), 4499-4511. <https://doi.org/10.1007/s12517-014-1369-z>
- Ercanoglu, M., & Gokceoglu, C. (2004). Use of fuzzy relations to produce landslide susceptibility map of a landslide prone area (West Black Sea Region, Turkey). *Engineering Geology*, 75(3-4), 229-250. <https://doi.org/10.1016/j.enggeo.2004.06.001>
- Komac, M., & Ribičić, M. (2006). Landslide susceptibility map of Slovenia at scale 1: 250,000. *Geologija*, 49(2), 295-309. <https://doi.org/10.5474/geologija.2006.022>
- Petschko, H., Brenning, A., Bell, R., Goetz, J., & Glade, T. (2014). Assessing the quality of landslide susceptibility maps—case study Lower Austria. *Natural Hazards and Earth System Sciences*, 14(1), 95-118. <https://doi.org/10.5194/nhess-14-95-2014>
- Chawla, A., Chawla, S., Pasupuleti, S., Rao, A. C. S., Sarkar, K., & Dwivedi, R. (2018). Landslide susceptibility mapping in darjeeling Himalayas, India. *Advances in Civil Engineering*, 2018(1), 6416492. <https://doi.org/10.1155/2018/6416492>
- Silalahi, F. E. S., Pamela, Arifianti, Y., & Hidayat, F. (2019). Landslide susceptibility assessment using frequency ratio model in Bogor, West Java, Indonesia. *Geoscience Letters*, 6(1), 10. <https://doi.org/10.1186/s40562-019-0140-4>
- Ram, P., Gupta, V., Devi, M., & Vishwakarma, N. (2020). Landslide susceptibility mapping using bivariate statistical method for the hilly township of Mussoorie

- and its surrounding areas, Uttarakhand Himalaya. *Journal of Earth System Science*, 129, 1-18. <https://doi.org/10.1007/s12040-020-01428-7>
14. Sangeeta, Maheshwari, B. K., & Kanungo, D. P. (2020). GIS-based pre-and post-earthquake landslide susceptibility zonation with reference to 1999 Chamoli earthquake. *Journal of Earth System Science*, 129, 1-20. <https://doi.org/10.1007/s12040-019-1319-y>
 15. Bahrami, Y., Hassani, H., & Maghsoudi, A. (2021). Landslide susceptibility mapping using AHP and fuzzy methods in the Gilan province, Iran. *GeoJournal*, 86, 1797-1816. <https://doi.org/10.1007/s10708-020-10162-y>
 16. Kadi, F., Yildirim, F., & Saralioglu, E. (2021). Risk analysis of forest roads using landslide susceptibility maps and generation of the optimum forest road route: a case study in Macka, Turkey. *Geocarto International*, 36(14), 1612-1629. <https://doi.org/10.1080/10106049.2019.1659424>
 17. Roccati, A., Paliaga, G., Luino, F., Faccini, F., & Turconi, L. (2021). GIS-based landslide susceptibility mapping for land use planning and risk assessment. *Land*, 10(2), 162. <https://doi.org/10.3390/land10020162>
 18. Kincal, C., & Kayhan, H. (2022). A combined method for preparation of landslide susceptibility map in Izmir (Türkiye). *Applied Sciences*, 12(18), 9029. <https://doi.org/10.3390/app12189029>
 19. Roy, P., Ghosal, K., & Paul, P. K. (2022). Landslide susceptibility mapping of Kalimpong in Eastern Himalayan Region using a Rprop ANN approach. *Journal of Earth System Science*, 131(2), 130. <https://doi.org/10.1007/s12040-022-01877-2>
 20. Sweta, K., Goswami, A., Nath, R. R., & Bahuguna, I. M. (2022). Performance assessment for three statistical models of landslide susceptibility zonation mapping: A case study for Dharamshala Region, Himachal Pradesh, India. *Journal of Earth System Science*, 131(3), 143. <https://doi.org/10.1007/s12040-022-01881-6>
 21. Khusulio, K., & Kumar, R. (2023). Feasibility assessment of multi-criteria decision making and quantitative landslide susceptibility methods: A case study of Mao-Maram Manipur. *Journal of Earth System Science*, 132(2), 56. <https://doi.org/10.1007/s12040-023-02062-9>
 22. Som, S. K., Ghosh, S., Dasgupta, S., Kumar, N. T., Hindayar, J. N., Mohan, M., ... & Bhattacharya, S. (2023). Utility of common variance of equally-weighted variables for GIS-based landslide susceptibility mapping at the eastern Himalaya. *Journal of Earth System Science*, 132(1), 16. <https://doi.org/10.1007/s12040-022-02017-6>
 23. Guzzetti, F., Galli, M., Reichenbach, P., Ardizzone, F., & Cardinali, M. J. N. H. (2006). Landslide hazard assessment in the Collazzone area, Umbria, Central Italy. *Natural Hazards and Earth System Sciences*, 6(1), 115-131. <https://doi.org/10.5194/nhess-6-115-2006>
 24. Erener, A., Mutlu, A., & Düzgün, H. S. (2016). A comparative study for landslide susceptibility mapping using GIS-based multi-criteria decision analysis (MCDA), logistic regression (LR) and association rule mining (ARM). *Engineering Geology*, 203, 45-55. <https://doi.org/10.1016/j.enggeo.2015.09.007>
 25. Loche, M., Alvioli, M., Marchesini, I., Bakka, H., & Lombardo, L. (2022). Landslide susceptibility maps of Italy: Lesson learnt from dealing with multiple landslide types and the uneven spatial distribution of the national inventory. *Earth-Science Reviews*, 232, 104125. <https://doi.org/10.1016/j.earscirev.2022.104125>
 26. Liu, S., Wang, L., Zhang, W., Sun, W., Fu, J., Xiao, T., & Dai, Z. (2023). A physics-informed data-driven model for landslide susceptibility assessment in the Three Gorges Reservoir Area. *Geoscience Frontiers*, 14(5), 101621. <https://doi.org/10.1016/j.gsf.2023.101621>
 27. Luo, W., & Liu, C. C. (2018). Innovative landslide susceptibility mapping supported by geomorphon and geographical detector methods. *Landslides*, 15, 465-474. <https://doi.org/10.1007/s10346-017-0893-9>
 28. Akinci, H., & Yavuz Ozalp, A. (2021). Landslide susceptibility mapping and hazard assessment in Artvin (Turkey) using frequency ratio and modified information value model. *Acta Geophysica*, 69(3), 725-745. <https://doi.org/10.1007/s11600-021-00577-7>
 29. Pradhan, B. (2011). Use of GIS-based fuzzy logic relations and its cross application to produce landslide susceptibility maps in three test areas in Malaysia. *Environmental Earth Sciences*, 63(2), 329-349. <https://doi.org/10.1007/s12665-010-0705-1>
 30. Kumar, R., & Anbalagan, R. (2016). Landslide susceptibility mapping using analytical hierarchy process (AHP) in Tehri reservoir rim region, Uttarakhand. *Journal of the Geological Society of India*, 87, 271-286. <https://doi.org/10.1007/s12594-016-0395-8>
 31. Fatemi Aghda, S. M., Bagheri, V., & Razifard, M. (2018). Landslide susceptibility mapping using fuzzy logic system and its influences on mainlines in lashgarak region, Tehran, Iran. *Geotechnical and Geological Engineering*, 36, 915-937. <https://doi.org/10.1007/s10706-017-0365-y>
 32. Mandal, S., Mondal, S., Mandal, S., & Mondal, S. (2019). Frequency ratio (FR) model and modified information value (MIV) model in landslide susceptibility assessment and prediction. *Statistical Approaches for Landslide Susceptibility Assessment and Prediction*, 77-105. https://doi.org/10.1007/978-3-319-93897-4_3
 33. Okoli, J., Nahazanan, H., Nahas, F., Kalantar, B., Shafri, H. Z. M., & Khuzaimah, Z. (2023). High-Resolution lidar-derived DEM for landslide susceptibility assessment using AHP and fuzzy logic in Serdang, Malaysia. *Geosciences*, 13(2), 34. <https://doi.org/10.3390/geosciences13020034>
 34. Ünel, F. B., Kuşak, L., Yakar, M., & Doğan, H. (2023). Coğrafi bilgi sistemleri ve analitik hiyerarşi prosesi kullanarak Mersin ilinde otomatik meteoroloji

- gözlem istasyonu yer seçimi. *Geomatik*, 8(2), 107-123. <https://doi.org/10.29128/geomatik.1136951>
35. Pourghasemi, H. R., Mohammady, M., & Pradhan, B. (2012). Landslide susceptibility mapping using index of entropy and conditional probability models in GIS: Safarood Basin, Iran. *Catena*, 97, 71-84. <https://doi.org/10.1016/j.catena.2012.05.005>
 36. Achour, Y., Boumezbeur, A., Hadji, R., Chouabbi, A., Cavaleiro, V., & Bendaoud, E. A. (2017). Landslide susceptibility mapping using analytic hierarchy process and information value methods along a highway road section in Constantine, Algeria. *Arabian Journal of Geosciences*, 10, 194. <https://doi.org/10.1007/s12517-017-2980-6>
 37. Kohno, M., & Higuchi, Y. (2023). Landslide susceptibility assessment in the Japanese archipelago based on a landslide distribution map. *ISPRS International Journal of Geo-Information*, 12(2), 37. <https://doi.org/10.3390/ijgi12020037>
 38. Zhu, L., & Huang, J. F. (2006). GIS-based logistic regression method for landslide susceptibility mapping in regional scale. *Journal of Zhejiang University-Science A*, 7(12), 2007-2017. <https://doi.org/10.1631/jzus.2006.A2007>
 39. Akgun, A. (2012). A comparison of landslide susceptibility maps produced by logistic regression, multi-criteria decision, and likelihood ratio methods: a case study at İzmir, Turkey. *Landslides*, 9(1), 93-106. <https://doi.org/10.1007/s10346-011-0283-7>
 40. Rasyid, A. R., Bhandary, N. P., & Yatabe, R. (2016). Performance of frequency ratio and logistic regression model in creating GIS based landslides susceptibility map at Lompobattang Mountain, Indonesia. *Geoenvironmental Disasters*, 3, 1-16. <https://doi.org/10.1186/s40677-016-0053-x>
 41. Polykretis, C., & Chalkias, C. (2018). Comparison and evaluation of landslide susceptibility maps obtained from weight of evidence, logistic regression, and artificial neural network models. *Natural Hazards*, 93, 249-274. <https://doi.org/10.1007/s11069-018-3299-7>
 42. Wubalem, A., & Meten, M. (2020). Landslide susceptibility mapping using information value and logistic regression models in Goncha Siso Eneses area, northwestern Ethiopia. *SN Applied Sciences*, 2, 1-19. <https://doi.org/10.1007/s42452-020-2563-0>
 43. Sekarlangit, N., Fathani, T. F., & Wilopo, W. (2022). Landslide susceptibility mapping of Menoreh Mountain using logistic regression. *Journal of Applied Geology*, 7(1), 51-63. <https://doi.org/10.22146/jag.72067>
 44. Yadav, M., Pal, S. K., Singh, P. K., & Gupta, N. (2023). Landslide susceptibility zonation mapping using frequency ratio, information value model, and logistic regression model: a case study of Kohima district in Nagaland, India. In *Landslides: Detection, Prediction and Monitoring: Technological Developments*, 333-363. https://doi.org/10.1007/978-3-031-23859-8_17
 45. Lee, S., & Sambath, T. (2006). Landslide susceptibility mapping in the Damrei Romel area, Cambodia using frequency ratio and logistic regression models. *Environmental Geology*, 50, 847-855. <https://doi.org/10.1007/s00254-006-0256-7>
 46. Yilmaz, I. (2009). Landslide susceptibility mapping using frequency ratio, logistic regression, artificial neural networks and their comparison: a case study from Kat landslides (Tokat—Turkey). *Computers & Geosciences*, 35(6), 1125-1138. <https://doi.org/10.1016/j.cageo.2008.08.007>
 47. Akinci, H., Doğan, S., Kiliçoğlu, C., & Temiz, M. S. (2011). Production of landslide susceptibility map of Samsun (Turkey) City Center by using frequency ratio method. *International Journal of the Physical Sciences*, 6(5), 1015-1025. <https://doi.org/10.5897/IJPS11.133>
 48. Karaman, M. O., Çabuk, S. N., & Pekkan, E. (2022). Utilization of frequency ratio method for the production of landslide susceptibility maps: Karaburun Peninsula case, Turkey. *Environmental Science and Pollution Research*, 29(60), 91285-91305. <https://doi.org/10.1007/s11356-022-21931-2>
 49. Addis, A. (2023). GIS-Based landslide susceptibility mapping using frequency ratio and Shannon Entropy Models in Dejen District, Northwestern Ethiopia. *Journal of Engineering*, 2023(1), 1062388. <https://doi.org/10.1155/2023/1062388>
 50. Ba, Q., Chen, Y., Deng, S., Wu, Q., Yang, J., & Zhang, J. (2017). An improved information value model based on gray clustering for landslide susceptibility mapping. *ISPRS International Journal of Geo-Information*, 6(1), 18. <https://doi.org/10.3390/ijgi6010018>
 51. Du, G. L., Zhang, Y. S., Iqbal, J., Yang, Z. H., & Yao, X. (2017). Landslide susceptibility mapping using an integrated model of information value method and logistic regression in the Bailongjiang watershed, Gansu Province, China. *Journal of Mountain Science*, 14, 249-268. <https://doi.org/10.1007/s11629-016-4126-9>
 52. Mandal, B., & Mandal, S. (2017). Landslide susceptibility mapping using modified information value model in the Lish river basin of Darjiling Himalaya. *Spatial Information Research*, 25, 205-218. <https://doi.org/10.1007/s41324-017-0096-4>
 53. Khan, H., Shafique, M., Khan, M. A., Bacha, M. A., Shah, S. U., & Calligaris, C. (2019). Landslide susceptibility assessment using Frequency Ratio, a case study of northern Pakistan. *The Egyptian Journal of Remote Sensing and Space Science*, 22(1), 11-24. <https://doi.org/10.1016/j.ejrs.2018.03.004>
 54. Jadda, M., Shafri, H. Z., Mansor, S. B., Sharifikia, M., & Pirasteh, S. (2009). Landslide susceptibility evaluation and factor effect analysis using probabilistic-frequency ratio model. *European Journal of Scientific Research*, 33(4), 654-668.
 55. Jaafari, A., Najafi, A., Pourghasemi, H. R., Rezaeian, J., & Sattarian, A. (2014). GIS-based frequency ratio and index of entropy models for landslide susceptibility assessment in the Caspian forest, northern Iran. *International Journal of Environmental Science and Technology*, 11, 909-926.

- <https://doi.org/10.1007/s13762-013-0464-0>
56. Liu, L. L., Zhang, Y. L., Xiao, T., & Yang, C. (2022). A frequency ratio-based sampling strategy for landslide susceptibility assessment. *Bulletin of Engineering Geology and the Environment*, 81(9), 360. <https://doi.org/10.1007/s10064-022-02836-3>
57. Alam, A., Ahmed, B., Sammonds, P., & Kamal, A. M. (2023). Applying rainfall threshold estimates and frequency ratio model for landslide hazard assessment in the coastal mountain setting of South Asia. *Natural Hazards Research*, 3(3), 531-545. <https://doi.org/10.1016/j.nhres.2023.08.002>
58. Singh, P., Sur, U., Rai, P. K., & Singh, S. K. (2023). Landslide susceptibility prediction using frequency ratio model: a case study of Uttarakhand, Himalaya (India). *Proceedings of the Indian National Science Academy*, 89(3), 600-612. <https://doi.org/10.1007/s43538-023-00171-z>
59. Thambidurai, P., Veerappan, R., Beigh, I. H., & Luitel, K. K. (2023). Landslide susceptibility assessment using frequency ratio model in Turung Mamring, south district of Sikkim, India. In *Landslides: Detection, Prediction and Monitoring: Technological Developments*, 285-305. https://doi.org/10.1007/978-3-031-23859-8_14
60. Kadi, F. (2024). Statistical-based models for the production of landslide susceptibility maps and general risk analyses: a case study in Maçka, Turkey. *Acta Geophysica*, 1-26. <https://doi.org/10.1007/s11600-024-01380-w>
61. Tampekis, S., Sakellariou, S., Samara, F., Sfougaris, A., Jaeger, D., & Christopoulou, O. (2015). Mapping the optimal forest road network based on the multicriteria evaluation technique: the case study of Mediterranean Island of Thassos in Greece. *Environmental Monitoring and Assessment*, 187, 1-17. <https://doi.org/10.1007/s10661-015-4876-9>
62. Picchio, R., Pignatti, G., Marchi, E., Latterini, F., Benanchi, M., Foderi, C., ... & Verani, S. (2018). The application of two approaches using GIS technology implementation in forest road network planning in an Italian mountain setting. *Forests*, 9(5), 277. <https://doi.org/10.3390/f9050277>
63. Çölkuşu, T., & Buğday, E. (2022). Planning optimal forest road network using unmanned aerial vehicle (Eldivan Sample). 1st International Karatekin Science and Technology Conference, 199-204.
64. Taş, İ., Kaska, M. S., & Akay, A. E. (2023). Assessment of using UAV photogrammetry based DEM and ground-measurement based DEM in computer-assisted forest road design. *European Journal of Forest Engineering*, 9(1), 1-9. <https://doi.org/10.33904/ejfe.1312514>
65. Boston, K. (2016). The potential effects of forest roads on the environment and mitigating their impacts. *Current Forestry Reports*, 2, 215-222. <https://doi.org/10.1007/s40725-016-0044-x>
66. AFAD, (2019). Overview of Disaster Management and Natural Disaster Statistics. https://en.afad.gov.tr/kurumlar/en.afad/Afet_Ististikleri_2020_eng_1.pdf
67. Akgün, A. (2018). Bulanık uyarlanabilir rezonans teorisi (FuzzyART) yöntemi kullanılarak heyelan duyarlılık analizi: Tonya (Trabzon) Örneği. *Gümüşhane Üniversitesi Fen Bilimleri Dergisi*, 8(1), 135-146. <https://doi.org/10.17714/gumusfenbil.346532>
68. <http://www.tonya.gov.tr/ilcemizin-cografi-durumu>
69. Abeyasiriwardana, H. D., & Gomes, P. I. (2022). Integrating vegetation indices and geo-environmental factors in GIS-based landslide-susceptibility mapping: using logistic regression. *Journal of Mountain Science*, 19(2), 477-492. <https://doi.org/10.1007/s11629-021-6988-8>
70. Wang, X., Huang, F., Fan, X., Shahabi, H., Shirzadi, A., Bian, H., ... & Chen, W. (2022). Landslide susceptibility modeling based on remote sensing data and data mining techniques. *Environmental Earth Sciences*, 81(2), 50. <https://doi.org/10.1007/s12665-022-10195-1>
71. Kanwal, S., Atif, S., & Shafiq, M. (2017). GIS based landslide susceptibility mapping of northern areas of Pakistan, a case study of Shigar and Shyok Basins. *Geomatics, Natural Hazards and Risk*, 8(2), 348-366. <https://doi.org/10.1080/19475705.2016.1220023>
72. Ali, S. A., Parvin, F., Vojteková, J., Costache, R., Linh, N. T. T., Pham, Q. B., ... & Ghorbani, M. A. (2021). GIS-based landslide susceptibility modeling: A comparison between fuzzy multi-criteria and machine learning algorithms. *Geoscience Frontiers*, 12(2), 857-876. <https://doi.org/10.1016/j.gsf.2020.09.004>
73. Melese, T., Belay, T., & Andemo, A. (2022). Application of analytical hierarchical process, frequency ratio, and Shannon entropy approaches for landslide susceptibility mapping using geospatial technology: The case of Dejen district, Ethiopia. *Arabian Journal of Geosciences*, 15(5), 424. <https://doi.org/10.1007/s12517-022-09672-5>
74. Rabby, Y. W., Li, Y., & Hilafu, H. (2023). An objective absence data sampling method for landslide susceptibility mapping. *Scientific Reports*, 13(1), 1740. <https://doi.org/10.1038/s41598-023-28991-5>
75. Yılmaz, O. S. (2023). Frekans oranı yöntemiyle coğrafi bilgi sistemi ortamında heyelan duyarlılık haritasının üretilmesi: Manisa, Demirci, Tekeler Köyü örneği. *Geomatik*, 8(1), 42-54. <https://doi.org/10.29128/geomatik.1108735>
76. Yalcin, A., & Bulut, F. (2007). Landslide susceptibility mapping using GIS and digital photogrammetric techniques: a case study from Ardesen (NE-Turkey). *Natural Hazards*, 41(1), 201-226. <https://doi.org/10.1007/s11069-006-9030-0>
77. Yılmaz, O. S. (2022). Flood hazard susceptibility areas mapping using Analytical Hierarchical Process (AHP), Frequency Ratio (FR) and AHP-FR ensemble based on Geographic Information Systems (GIS): A case study for Kastamonu, Türkiye. *Acta Geophysica*, 70(6), 2747-2769. <https://doi.org/10.1007/s11600-022-00882-9>

78. Moore, I. D., Grayson, R. B., & Ladson, A. R. (1991). Digital terrain modelling: a review of hydrological, geomorphological, and biological applications. *Hydrological Processes*, 5(1), 3-30. <https://doi.org/10.1002/hyp.3360050103>
79. Wang, L. J., Guo, M., Sawada, K., Lin, J., & Zhang, J. (2016). A comparative study of landslide susceptibility maps using logistic regression, frequency ratio, decision tree, weights of evidence and artificial neural network. *Geosciences Journal*, 20, 117-136. <https://doi.org/10.1007/s12303-015-0026-1>
80. Sun, X., Chen, J., Han, X., Bao, Y., Zhou, X., & Peng, W. (2020). Landslide susceptibility mapping along the upper Jinsha River, south-western China: a comparison of hydrological and curvature watershed methods for slope unit classification. *Bulletin of Engineering Geology and the Environment*, 79, 4657-4670. <https://doi.org/10.1007/s10064-020-01849-0>
81. Yılmaz, Ç. Ş. (2022). Improving the land cover mapping accuracy of the Sentinel-2 imagery on Google Earth Engine. *Türk Uzaktan Algılama ve CBS Dergisi*, 3(2), 150-159. <https://doi.org/10.48123/rsgis.1119572>
82. Althuwaynee, O. F., Pradhan, B., Park, H. J., & Lee, J. H. (2014). A novel ensemble bivariate statistical evidential belief function with knowledge-based analytical hierarchy process and multivariate statistical logistic regression for landslide susceptibility mapping. *Catena*, 114, 21-36. <https://doi.org/10.1016/j.catena.2013.10.011>
83. Gudiyangada Nachappa, T., Kienberger, S., Meena, S. R., Hölbling, D., & Blaschke, T. (2020). Comparison and validation of per-pixel and object-based approaches for landslide susceptibility mapping. *Geomatics, Natural Hazards and Risk*, 11(1), 572-600. <https://doi.org/10.1080/19475705.2020.1736190>
84. Hussain, S., Mubeen, M., Akram, W., Ahmad, A., Habibur-Rahman, M., Ghaffar, A., ... & Nasim, W. (2020). Study of land cover/land use changes using RS and GIS: a case study of Multan district, Pakistan. *Environmental Monitoring and Assessment*, 192, 1-15. <https://doi.org/10.1007/s10661-019-7959-1>
85. Chen, X., & Chen, W. (2021). GIS-based landslide susceptibility assessment using optimized hybrid machine learning methods. *Catena*, 196, 104833. <https://doi.org/10.1016/j.catena.2020.104833>
86. Hakim, W. L., Rezaie, F., Nur, A. S., Panahi, M., Khosravi, K., Lee, C. W., & Lee, S. (2022). Convolutional neural network (CNN) with metaheuristic optimization algorithms for landslide susceptibility mapping in Icheon, South Korea. *Journal of Environmental Management*, 305, 114367. <https://doi.org/10.1016/j.jenvman.2021.114367>
87. Chen, W., & Yang, Z. (2023). Landslide susceptibility modeling using bivariate statistical-based logistic regression, naïve Bayes, and alternating decision tree models. *Bulletin of Engineering Geology and the Environment*, 82(5), 190. <https://doi.org/10.1007/s10064-023-03216-1>
88. Yu, C., Lee, J. A. Y., & Munro-Stasiuk, M. J. (2003). Extensions to least-cost path algorithms for roadway planning. *International Journal of Geographical Information Science*, 17(4), 361-376. <https://doi.org/10.1080/1365881031000072645>
89. Effat, H. A., & Hassan, O. A. (2013). Designing and evaluation of three alternatives highway routes using the Analytical Hierarchy Process and the least-cost path analysis, application in Sinai Peninsula, Egypt. *The Egyptian Journal of Remote Sensing and Space Science*, 16(2), 141-151. <https://doi.org/10.1016/j.ejrs.2013.08.001>
90. McDonald, M. D., & Kessler, F. C. (2022). Least-Cost path and accessibility analysis of a high speed railway corridor: Victorville, CA to Las Vegas, NV. *Journal of Geographic Information System*, 14(1), 40-60. <https://doi.org/10.4236/jgis.2022.141003>
91. Sawant, S., & Sawant, S. (2023). Finding optimal path for gas pipeline using GIS and RS. *Proceedings of the International Conference on Cognitive and Intelligent Computing: ICCIC 2021*, 2, 321-333. https://doi.org/10.1007/978-981-19-2358-6_31





Accuracy assessment of UAS photogrammetry and structure from motion in surveying and mapping

Sayed Ishaq Deliry¹, Uğur Avdan^{*2}

¹ Eskisehir Technical University, Department of Remote Sensing and Geographical Information Systems, Türkiye, deliry.ishaq@gmail.com

² Eskisehir Technical University, Institute of Earth and Space Sciences, Türkiye, uavdan@eskisehir.edu.tr

Cite this study:

Deliry, S. I., & Avdan, U. (2024). Accuracy assessment of UAS photogrammetry and structure from motion in surveying and mapping. *International Journal of Engineering and Geosciences*, 9 (2), 165-190

<https://doi.org/10.26833/ijeg.1366146>

Keywords

Structure from motion
Unmanned aerial systems
Unmanned aerial vehicle
SfM photogrammetry
Rapid surveying

Research Article

Received: 25.09.2023
Revised: 21.11.2023
Accepted: 26.11.2023
Published: 23.07.2024



Abstract

Rapid and accurate surveying has always attracted great interest in all scientific and industrial activities that require high-resolution topographic data. The latest automation and advancement in geomatics engineering are remote sensing solutions using Unmanned Aerial Systems (UAS) and Structure from Motion (SfM) with Multi-View Stereo (MVS) photogrammetry. This research aimed to find the influence of flight height, Ground Control Point (GCP), and software on the geometric accuracy of UAS-SfM-derived Digital Surface Models (DSMs) and orthoimages, as well as to analyze and evaluate the accuracy of UAS-SfM as a rapid and low-cost alternative to conventional survey methods. To achieve the aim of the study, aerial surveys using a fixed-wing UAS and field surveys using RTK GNSS and total station were conducted. A total of 16 photogrammetric projects were processed using different GCP configurations, and detailed statistical analysis was performed on the results. Moreover, the contribution of cross flight on bundle adjustment was investigated empirically by conducting a combined photogrammetric image processing. The analysis revealed that flight height, GCP number and distribution, and the processing software significantly affect products' quality and accuracy. Evaluation of the achieved accuracies was made based on the American Society for Photogrammetry and Remote Sensing (ASPRS) positional accuracy standard for digital geospatial data. The findings of this study revealed that using the optimal flight height and GCP configuration, 3D models, orthomosaics and DSMs can be rapidly reconstructed from 2D images with the quality and accuracy sufficient for most terrain analysis applications, including civil engineering projects.

1. Introduction

Digital elevation models (DEMs) are the primary database for topography-related analysis such as engineering planning, infrastructure design, and earth observations [1, 2]. Very high-resolution 3D models and associated orthoimages derived from Unmanned Aerial Systems (UAS) images are of great importance in scientific fields involving mapping subtle topographic variations and surface analysis, for instance, in structural monitoring and studies of earth surface dynamics [3-5]. Unmanned aerial systems, also known as drones, commonly termed as Unmanned Aerial Vehicles (UAVs), are aircraft systems that operate without a pilot on board. With the development of technology, the application of UAS as a remote sensing platform and SfM-MVS as a photogrammetric and computer vision technique to produce high-resolution topographic maps is increasing [3, 6, 7]. The application of UAS and SfM-

MVS is gaining increasing interest in most disciplines, particularly in engineering and earth sciences [5-10]. Photogrammetric applications of UAS are pervasive and in high demand in engineering and geosciences. Recently, UAS-based photogrammetry, commonly known as UAV photogrammetry, is widely used in surveying and 3D modeling applications.

Surveying is a rapidly developing engineering field that has changed dramatically over the past decades and benefited from a wide range of technological advances such as ground-based, water-based, airborne, and spaceborne [11-21]. Engineering surveying includes planning, designing, and conducting surveys of different accuracy classes for development, designing, construction, quality control, inspection, and operation and maintenance of civil and other engineering projects [21-23]. Surveying has a wide engineering professional practice, which provides high-accuracy topographic maps as one of the main activities. Technological

advances related to surveying and mapping have been rapid over the past decades, especially in digital terrain modeling. However, cost and time-consumption are common limitations in conventional methods [11, 24, 25]. In physical surveying using the conventional methods, each individual point is surveyed in a subjective manner in which professional engineering surveyors with sufficient geomorphological knowledge determine where to be measured to get accurate interpolation. The decision on the number and location of points for an accurate representation of topography using traditional methods highly depends on the surveyor's skill. Although highly detailed topographical surveys using physical surveying techniques are possible, these methods are subjective, costly, and extremely time-consuming.

Structure from motion is one of the most recent and important developments in digital surveying [5, 6, 26, 27]. With the advances in computer vision, the combination of digital technology and SfM has revolutionized the photogrammetry field. Motion-based reconstruction was first introduced by Ullman [28] in the late 1970s. SfM became more popular with the development of computer vision algorithms in the 2000s [29–33]. These techniques are used to reconstruct high-quality 3D structures from a range of 2D photogrammetric images. The SfM-MVS algorithms produce true color 3D dense point clouds, which are quite comparable to those of laser scanning surveys. Unlike classic aerial stereophotogrammetry, which requires careful flight planning and camera pre-calibration [34], UAS-based SfM (UAS-SfM) provides simplicity in data acquisition and image processing without the need for comprehensive planning or camera calibration [2]. Today, photogrammetric software packages with high computational power are available that can process hundreds of images simultaneously and extract 3D surface information using feature detection and matching algorithms. With these developments, using a lightweight UAV and a digital non-metric camera, unprecedented high-resolution 3D elevation models can be generated, which are comparable in scale and accuracy to that of terrestrial laser scanner (TLS), airborne laser scanner, and conventional photogrammetric approaches [3, 5]. In addition to achieving more detailed 3D models than traditional photogrammetry methods, SfM-MVS can reduce processing efforts by about 3-6 times [35]. However, in UAS-based surveys, some influential parameters such as the number and distribution of GCPs, flight height, and image overlap can significantly affect the mapping accuracy.

To overcome the limitation of traditional surveying techniques, and to obtain rapid and cost-effective data, the application of UAS-SfM has been the subject of many studies in recent years [10, 11, 36–45]. Very high spatial and temporal resolution images can be provided by combining UAS data and remote sensing techniques. UAVs have distinguished advantages over satellites and human-crewed aircraft, such as higher spatial and temporal resolution, lower cost, availability, rapid data acquisition, and operational flexibility [3, 7, 46–48].

Furthermore, accessibility is a challenging issue in terrestrial surveys where neither TLS nor ground photogrammetry is a practical option. Terrestrial surveys for generating 3D models are quite challenging in many situations, for example, in hazardous areas, steep and narrow valleys, and buildings with slanted roofs. UAS photogrammetry is the solution for such problems; therefore, UAS-SfM can be considered as an effective alternative to traditional photogrammetry.

In engineering works, data accuracy is the most important concern that should be within acceptable limits; hence, accuracy assessment is crucial. Recently, many studies have been conducted to assess the ability of UAS-SfM as an alternative to conventional survey methods. However, each quantitative validation study is different from another due to variations in method, platform, camera, survey scale, terrain, comparison method, and software used for processing. Although many studies have focused on the influence of GCP number and distribution on the accuracy of UAS-SfM products, only a few studies have analyzed the relationship between errors and their distance from the nearest GCP. For example, Ruzgienė et al. [49] examined the accuracy of UAS-SfM-derived DSM; they indicated that the accuracy and quality of DSM mainly depend on sensor resolution, flight height, image overlap, and GCP number and accuracy. The authors reported that by adding 5 more GCPs to a cluster of 5 GCPs, the DSM vertical accuracy improved by 1.5 cm. Long et al. [50] stated that a correlation exists between the number of GCPs and the vertical accuracy; the higher the number of GCPs, the higher the accuracy. Gerke and Przybilla [51] studied direct and indirect georeferencing in the UAS-based survey. As a result of their analysis, the RTK based UAS survey achieved a vertical accuracy of up to 10 cm, while by adding the cross flight data, the accuracy improved to 5 cm, and adding GCPs greatly contributed to the accuracy. Agüera-Vega et al. [11] conducted a study on 60 photogrammetric projects by utilizing a rotary-wing UAS and a non-metric camera. In their analyses, the most accurate results were achieved from 5 to 10 GCPs, which from 50 m flight height, they obtained vertical accuracy of 5 cm. Unlike other studies, Tonkin and Midgley [52] obtained high DSM accuracy using just 4 GCPs. The researchers produced DSMs from UAV images applying a varying number of GCPs (3-101) to study the relation between the number and placement of GCPs. The authors stated that for all DSMs, the vertical error was less than 20 cm. Their results revealed improvements in DSM quality where four and more number of GCPs were used; however, the difference in vertical error between the DSM produced using 4 GCPs (6.4 cm) and the DSM generated by applying 101 GCPs (5.9 cm) was 0.5 cm. The results indicated that the distribution of GCPs is important because vertical error increased as the study points moved away from the GCP cluster. Coveney and Roberts [38] used a fixed-wing UAS with a camera on-board to generate a DEM of an urban area, including a river. The authors investigated the influence of 0 to 61 GCPs in various projects, and as a result, they concluded that using 1 GCP per every 2 ha is sufficient for UAS-based mapping, and no significant

improvements were observed using more than 15 GCPs. Oniga et al. [53] reported that from the images obtained from lower heights (~ 30 m), using 1 GCP per 200 square meters, 3D data can be produced at the level of 1 to 2 cm. Sanz-Ablanedo et al. [44] analyzed the role of the number and location of GCPs on the geometrical accuracy of DSM. They found that accuracy was greatly improved using 4 GCPs per hundred photos, which made it possible to achieve horizontal accuracy of the same as ground sampling distance (GSD) and vertical accuracy of $\pm 1.5 \times$ GSD. Using fewer GCPs (1 GCP per hundred photos) degraded both horizontal and vertical accuracies to $\pm 4 \times$ GSD and $\pm 5 \times$ GSD, respectively. Martinez-Carricondo et al. [2] evaluated the accuracy of UAS-based mapping by focusing on the variation of GCPs. They concluded that GCPs should be placed at the edge of the study area to achieve optimal planimetric results. However, this configuration did not increase the vertical accuracy. The best results were obtained by stratified and dense distribution of GCPs within the study area, which resulted in horizontal and vertical accuracy of 3.5 and 4.8 cm. In the literature, the GCP and accuracy correlation has not been investigated conclusively; thus, it requires a thorough statistical analysis. Given the sensitivity of the information obtained from UAS-based mapping, and the variation in the accuracy achieved in the literature, in-depth studies are needed to find the influential parameters and evaluate the accuracy of UAS-SfM in surveying applications.

The main objective of this study was to analyze the influence of flight height and GCP distribution on the geometric accuracy of UAS-SfM-derived DSMs and

orthoimages, and to evaluate the accuracy of UAS-based surveying by conducting field surveys using a fixed-wing UAS, RTK GNSS, and total station. Analyses were conducted to find the impact of distance from GCPs on planimetric and vertical accuracy. Evaluation of the achieved accuracies was made based on the American Society for Photogrammetry and Remote Sensing (ASPRS) positional accuracy standard for digital geospatial data. In addition, the contribution of cross flight on bundle adjustment was investigated empirically by performing a combined photogrammetric image processing. The research also presents a comparison of the accuracy and performance of three SfM software packages, namely Agisoft PhotoScan, Pix4Dmapper, and 3Dsury in the DSM reconstruction from the same sets of UAV images with optimal image processing parameters.

2. Materials and method

2.1. Study area and data acquisition

Eskisehir Technical University Iki Eylul campus was selected as the study area (Figure 1). The campus is located at $39^\circ 48' 57.4''$ latitude and $30^\circ 31' 55.4''$ longitude in the Tepebasi district of Eskisehir, Türkiye. The study area covers approximately 35 hectares of the campus, which comprises roads, parking lots, and vegetation. The purpose of adopting the campus as the study area was the presence of vegetated and non-vegetated land cover as well as the ease of obtaining licenses for conducting several close-range flights.

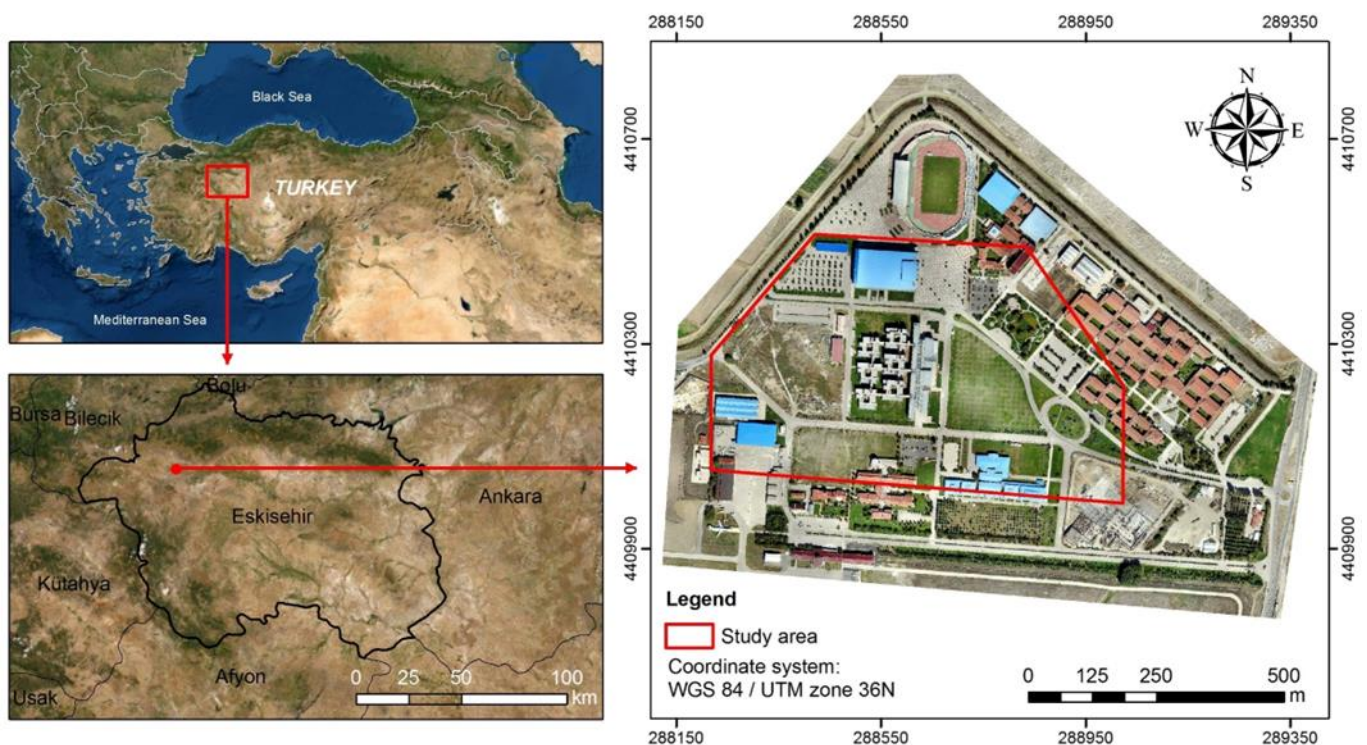


Figure 1. Study area: Eskisehir Technical University Campus.

Project planning is the first and most important step in photogrammetric projects to be carried out extensively. In a particular photogrammetric project,

various products can be developed, the final decision on the selection of products, scale, and accuracy is made according to the project requirements. To achieve the

aim of the study, two nadir image acquisition plans were designed to be surveyed using senseFly fixed-wing UAS at average flight heights of 100 and 170 m Above Ground Level (AGL), and 80% and 70%, frontal and 70% and 65% side overlaps to achieve 2.5 and 4.0 cm GSDs, respectively.

According to the new ASPRS standard [54], the GSD of the source imagery should be two times higher or at least equal to the required accuracy. Based on ASPRS Root Mean Square Error (RMSE) accuracy metric, for planimetric works, an accuracy of $1 \times$ GSD is recommended that can be used in the highest accuracy works, $2 \times$ GSD is suitable for standard mapping and GIS tasks, and $3 \times$ GSD and greater is not recommended for measurements, yet can be used for visualization and less accurate estimations. As per ASPRS, the vertical accuracy (non-vegetated) for Class 1 is 1 cm, for Class 2 is 2.5 cm, and for Classes 3 and 4 are 5 and 10 cm, respectively. A fixed-wing UAS covers larger areas by flying at higher altitudes, which considerably reduces the processing time; thus, it is more suitable for surveys of larger areas. Considering this, 2.5 cm and 4 cm GSDs were selected for vertical aerial surveys, which accordingly, the flight altitudes were determined (100 m and 170 m, respectively). Figure 2 illustrates the overall workflow of the methods adopted in this study.

SenseFly eBee Plus fixed-wing UAS was used for photogrammetric image acquisition. The UAS has an onboard GNSS receiver with optional RTK/PPK functionality that is used for navigation and image geotagging. The supplied payload sensor used in this study is a compact 20-megapixel high-resolution SODA RGB camera. The SODA camera is specially developed for UAS photogrammetric works. This camera has a 13.2 x 8.8 mm sensor size, 10.6 mm focal length, and 5472 x 3648-pixel RGB resolution. The area of interest was defined, and flight paths were designed on an aerial map in eMotion 3 flight and data management software. By defining the survey area, ground sampling distance, and image longitudinal and side overlaps, the flight speed was set, and flights were carried out according to the flight path in automatic navigation mode. In the image acquisition process, an operator was responsible for monitoring the take-off and landing, the battery status, the connection between the UAV and ground control system (via a computer stationed at the operating station) for ensuring that the drone is on its designed pathway. Photogrammetric flights at two flight heights were conducted to determine the influence of flight height on the accuracy of products as well as to assess the accuracy of cross flight data in a combined image processing. The photogrammetric characteristics of both flights are shown in the following Table 1.

JAVAD TRIUMPH-1 dual-frequency GNSS receiver was used for the RTK measurements of GCPs and checkpoints. This geodetic instrument has ± 1 cm +1 ppm horizontal and ± 1.5 cm +1 ppm vertical accuracy, as stated in the manufacturer's specifications. RTK DGNS technique usually provides high positioning, and the best results can be achieved if the distance to the nearest base station is within 10 km. Since the distance from the study area to the base station is about 9 km, using RTCM (Radio

Technical Commission for Maritime Services) and FKP (Flaechen-Korrektur-Parameter) standards, it is possible to achieve vertical and horizontal accuracy within 2 cm. Trimble M3 total station was used for validating GNSS RTK measurement and GCP network adjustment. Trimble M3 has angle measurement accuracy of 2" and 2 mm ± 2 ppm distance measurement accuracy. This instrument has the ability of reflectorless measurements of inaccessible points. Figure 3 illustrates the equipment used in this study.

Table 1. Flight and data acquisition parameters

Parameter	Value	
Height above ground level	100 m	170 m
Average flight speed	12.32 m·s ⁻¹	11.53 m·s ⁻¹
Flight GNSS mode	Standalone	Standalone
Number of strips	13	9
Distance between strips	39 m	66 m
Distance between images (Base)	17 m	51 m
Ground resolution	2.5 cm·px ⁻¹	4 cm·px ⁻¹
Single image ground coverage	129 x 86 m	219 x 146 m
Number of images	548	155
Forward overlap	80%	70%
Side overlap	70%	65%

GCPs and CPs were marked on the ground and measured accurately using GNSS with differential corrections in real-time kinematic (RTK) mode by connecting to the nearest Continuous Operating Reference Station (CORS). The GCP network was then adjusted using TS measurements. Accurate measurement of the 3D coordinates of GCPs and marking them during the image processing is a time-consuming task, and in challenging terrain, it is difficult to measure a large number of GCPs. According to the literature, in small areas, 5-15 number of GCPs can provide optimum results [11, 55]. Hence, in this study, two GCP clusters (5 and 10) were used to analyze their influence on the accuracy of DSM and orthomosaic. To examine the influence of GCP distribution on the accuracy, and to find the relationship between the vertical accuracy and the distance to the nearest GCP, the positions of 5 GCPs were selected in a way that some checkpoints were outside the GCP polygon. To minimize the distance between the checkpoints and the nearest GCPs, a set of 10 GCPs were formed by adding 5 additional GCPs to the cluster. Figure 4 shows ground control points and checkpoints on vegetated and non-vegetated test areas. GCPs 1-5 were used for the 5 GCP scheme, and for the 10 GCP layout, GCPs from 1-10 were used.

Ground control points are points with known spatial coordinates marked on the ground. These points are measured precisely by terrestrial survey methods such as Differential Global Navigation Satellite System (DGNS) or total station (TS). GCPs are used for image georeferencing, which includes scale calculation, orientation, and transforming positions to a desired coordinate system [56, 57]. Ground control points can serve as adjustment points or checkpoints (CPs) for accuracy validation of the final product. GCPs are usually marked on a flat surface and evenly distributed within the study area to be visible in at least two images. The number and location of GCPs used to scale a photogrammetric model have a significant impact on the mean error and error distribution within the model [11].

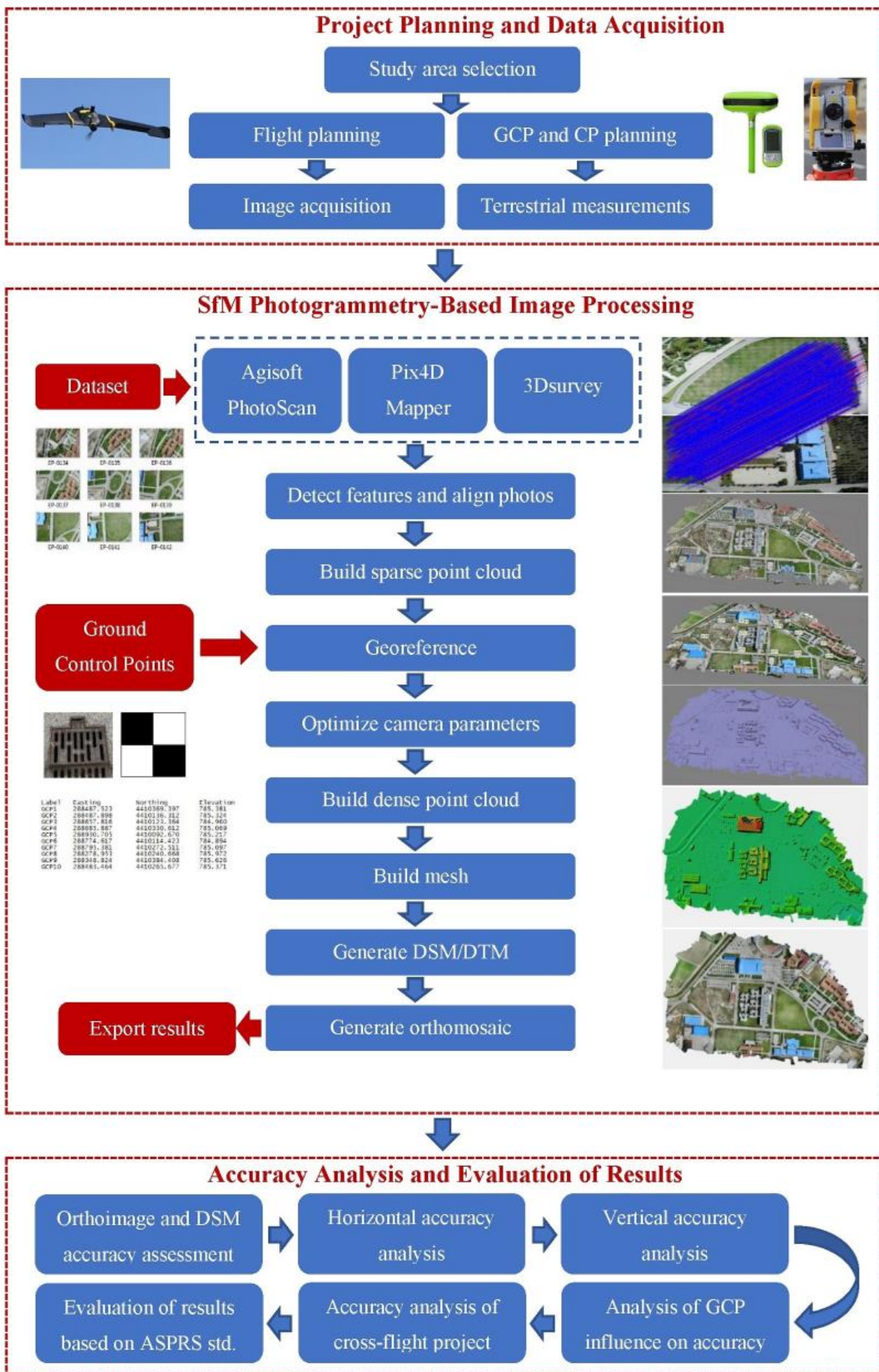


Figure 2. Overall workflow of the methods used in this research. In the SfM image processing section, the left side of the diagram illustrates input data, and the right side shows the generated models, from top to bottom: sparse point cloud, dense point cloud, mesh, DSM, and orthomosaic.

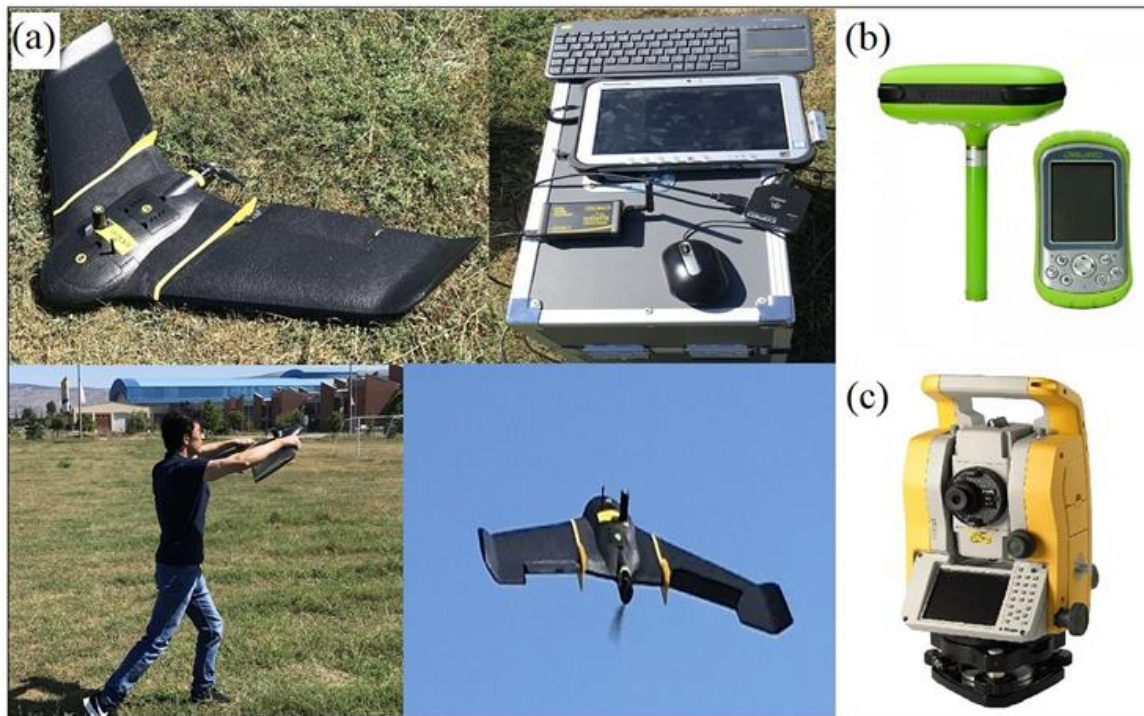


Figure 3. Equipment used in the study: (a) SenseFly eBee Plus with its ground control system used as the photogrammetric platform, and (b and c) GNSS, and TS used as terrestrial measurement instruments, respectively.

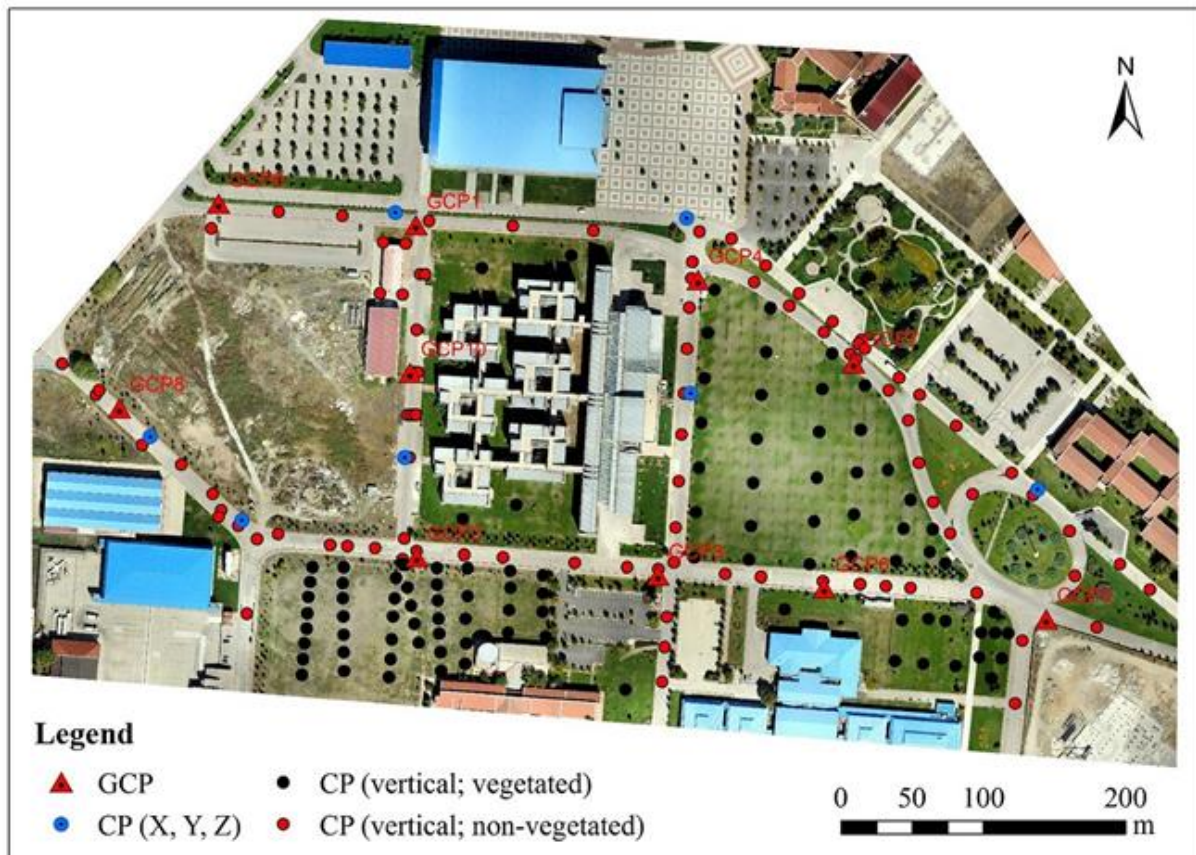


Figure 4. Ground control points and checkpoint.

The number of GCPs depends on the area extent and terrain height difference; the greater the variation, the higher the number of GCPs are required to increase the absolute accuracy [50, 57]. However, using a higher

number of GCPs (i.e., more than 10) in small areas does not significantly contribute to higher accuracy; practically, 5 to 10 GCPs are sufficient [51, 52, 57].

Acquired images can be georeferenced directly during the flight or during data processing. If a UAV is equipped with an RTK (Real-Time Kinematic) GPS receiver, this allows images to be directly georeferenced. However, if the data-link connection with the base station is interrupted, the real-time corrections for camera positions will also be affected. The signal interruption will lead to uncertainties that can be improved by using GCPs. Even if the UAV is equipped with a non-RTK ordinary GPS receiver, this will capture georeferenced images with enough metric accuracy to adjust the image bundles and produce maps for emergency response [7]. In the bundle adjustment process based on non-linear least-squares minimization, at least three GCPs are required, which are treated as weighted observations in the least-square minimization [7, 34]. The least-square minimization approach reduces possible deformations and systematic errors of the image block, which leads to the correct estimation of 3D structures [7]. For validating the processing accuracy, checkpoints with known 3D coordinates are used in the process of defining GCPs. When GCPs are defined as CPs, they are not included in the computation of bundle block adjustments, but the software uses these points to find the difference between the interpolated surface coordinates and the actual points to determine the accuracy of the adjustment.

All measurements were performed in Universal Transverse Mercator (UTM) coordinate system, where the World Geodetic System 1984 (WGS 84) reference ellipsoid is the horizontal datum, and as the vertical datum, the Earth Gravitational Model 1996 (EGM96) was selected. A minimum of 6 GPS and 5 GLONASS satellites above 15 degrees in elevation were maintained in all measurements. During the fieldwork, by maintaining a higher number of satellites, PDOP (Position Dilution of Precision) values were in the range of 2.0 to 4.0, indicating the appropriate satellite geometry.

2.2. SfM photogrammetry-based image processing

To generate photogrammetric products from UAS images, image processing was carried out in photogrammetric software packages, which are developed based on computer vision and structure from motion algorithms. The process of image matching, aligning, and bundle block adjustment was performed in SfM software. Exterior orientation parameters were determined by software in the process of aerial triangulation, which is based on least square accurate mathematical models. As a result, three-dimensional structures were obtained from two-dimensional image sequences using the SfM-MVS method. By performing computations in software packages, the following products were generated from images of UAS: 3D dense point clouds, triangulated mesh surfaces, orthomosaics, and digital elevation models (DSMs and DTMs).

A total of 16 photogrammetric projects (with different flight heights and GCP configuration) were processed using three different commercial photogrammetric 3D reconstruction software packages, namely Agisoft PhotoScan Professional version 1.4.3 [56], Pix4Dmapper version 4.3.31 [57], and 3Dsury

version 2.7.0 [58]. The purpose of processing in different software packages was to analyze, compare, and evaluate the influence of computer applications on the accuracy of products. In order to obtain similar products, in the workflow of all the three software packages, full keypoint extraction and optimal processing options were adopted. Although extremely high processing options are available, they are not recommended for mapping purposes of large data. The SfM-MVS workflow implemented in Agisoft PhotoScan is summarized in the following paragraphs. The specifics of this workflow slightly vary in the three software packages, but a clear commonality exists. Image processing was performed in the following steps.

In the first step, the project was created, the reference coordinate system was chosen, and the images along with their EXIF metadata, including intrinsic camera parameters, were imported in the project workspace. In the next step, the images were aligned by identifying and matching features between overlapping images. The alignment step in PhotoScan comprises three phases. First, features (keypoints) are detected by applying a feature detection algorithm. After locating keypoints in neighboring images, matching keypoints are identified, and inconsistent matches are removed. In the third stage, 3D geometry of the scene and camera parameters (focal length, radial lens distortions, and positions of the principal point) are solved simultaneously using a bundle-adjustment algorithm. In the alignment step, the accuracy was set to "high", and limits were not specified for the key point and tie point parameters because defining an upper limit for these parameters may cause missing in some parts of the point cloud model and affect the comparison with the other software. At this stage, which is the crucial step in the SfM workflow, the camera position and orientation corresponding to each photo were estimated, and a sparse point cloud model was generated.

After generating the sparse point cloud, the points with the highest reprojection error were removed using the gradual selection option. For generating accurately georeferenced products, 3D coordinates of GCPs were imported, and each was marked manually on visible photos. Subsequently, the camera alignment was optimized using the GCPs. To achieve higher accuracy, an optimization process must be performed; this process calculates camera external and internal parameters and corrects the probable image distortions like the bowl effect [56]. The RMSE of bundle adjustment was under 2.5 cm.

Once the camera parameters and the geometry of the output sparse point cloud were optimized, a dense point cloud was generated by applying MVS image matching algorithms, which are based on the estimated camera positions and the calculated depth information [56]. The depth filtering algorithm was used to filter out the erroneous points in the process of dense point cloud generation. This stage, which requires a longer time for processing (depends on the computer processor and RAM), resulted in a highly detailed 3D point cloud. The dense point cloud can be modified and classified prior to exporting or proceeding to the next step.

Following the above step, a 3D polygonal mesh model was generated based on the dense point cloud data and interpolation between points. Subsequently, the texture was built and applied to the mesh model. Polygonal mesh models can be exported in many formats with significantly less data size compared to point clouds. However, generating mesh models are optional and can be skipped, and the digital surface model (DSM) can be produced directly following dense cloud generation.

Subsequently, the DSM was generated from the dense point clouds. DSM can be generated and rasterized from a sparse point cloud, dense point cloud, or mesh model in geographic or planar projection. Since the dense point cloud yields more accurate results, the digital surface model was generated based on the whole dense point cloud data. The three utilized software packages use noise filtering algorithms for the DSM generation. To generate the DTM of the study area, the dense point cloud was first classified into ground and non-ground classes using the automatic and semi-automatic classification algorithms.

For generating high-resolution orthorectified images of the study area, orthomosaics were generated based on the input photos and constructed DSM at 4.0 and 2.5 cm resolutions. Orthorectification can be done based on the DSM or mesh model. The orthorectification process removes the image perspective effects (i.e., tilt, terrain distortions) and creates orthomosaic, which is planimetrically correct. The abovementioned photogrammetric products generated using PhotoScan are illustrated in Figure 2. Additionally, a combined image processing was performed using the images of both flights to study the contribution of integrated image processing on the accuracy of models. Finally, the generated orthomosaics and elevation models were exported to raster format for further analysis.

The processing was performed using a workstation computer with Windows 10 Professional 64-bit operating system, 3.4 GHz Intel processor, and 128 GB RAM. The total processing time for one project was about 2 hours for PhotoScan and Pix4Dmapper, and approximately 10 hours for 3Dsurvey. For comparing the processing time, the same number of images were processed using a PC with a 3.6 GHz processor and 32 GB RAM. With this system, the processing time for PhotoScan as well as Pix4Dmapper was about 6 hours, and for 3Dsurvey, it took about 20 hours.

2.3. Accuracy assessment

To achieve the aim of the research, comparative absolute and relative accuracy assessment between the derived data and the accurate field measurements was performed. The absolute accuracy assessment in this research is based on CPs that had been accurately measured using ground-based survey methods and had not been involved in the least-squares bundle adjustment and orientation calculation process. The relative accuracy assessment deals with the inter-relational performance of different methods.

Accuracy evaluation was performed based on RMSE because this is the most common metric used in

geospatial accuracy analysis, and the new ASPRS standard was also presented in this metric. The errors in RMSE are squared before averaging; therefore, it gives relatively higher weights to large errors. With this in mind, it is better to use the RMSE rather than the mean absolute error (MAE) in such studies. In surveying, RMSE is often preferred to avoid undesirable large errors [2, 11, 59].

Since errors in UAS-SfM-based surveying usually occur in elevations and vertical uncertainty is the primary concern in the literature, this research mainly focuses on vertical accuracy. For vertical accuracy assessment, two sets of CPs (vegetated and non-vegetated) were measured directly on the ground without marking them. A total of 200 CPs (located within and outside of GCP polygons) were surveyed, 100 of which are located in vegetated and 100 in non-vegetated terrain. From the 100 CPs located on the bare surface, 7 of them were marked on the ground and used for horizontal and vertical accuracy assessment, and the rest (unmarked) were used for only vertical accuracy assessment. Accuracy analysis was performed separately on the bare surface and vegetated landcover. Although photogrammetric software packages calculate and provide the horizontal and vertical accuracy assessment report based on the identified GCPs and CPs, the reports cannot satisfy the user. Therefore, the accuracy analysis and evaluation of the products were performed from the end user's point of view.

Linear RMSE of each coordinate, Easting (X), Northing (Y), and elevation (Z), as well as the horizontal (XY), was calculated for each marked checkpoint. Horizontal accuracy assessment was performed on orthomosaics, and then by comparing the coordinates to the actual surveyed (GNSS) coordinates, RMS errors (RMSEX, RMSEY, and RMSEXY) were calculated using the Equation 1 and 2 [2, 11, 54]:

$$RMSE_X = \sqrt{\frac{\sum_{i=1}^n (X_{Oi} - X_{GNSSi})^2}{n}} \quad (1)$$

$$RMSE_Y = \sqrt{\frac{\sum_{i=1}^n (Y_{Oi} - Y_{GNSSi})^2}{n}} \quad (2)$$

where n is the number of tested CPs; X_{Oi} and Y_{Oi} are X and Y coordinates measured in the orthomosaic for the i th CP; X_{GNSSi} and Y_{GNSSi} are X and Y coordinates measured with the use of RTK GNSS for the i th CP (Equation 3).

$$RMSE_{XY} = \sqrt{RMSE_X^2 + RMSE_Y^2} \quad (3)$$

For the seven check points, vertical accuracy was calculated in two methods. In the first method, the horizontal positions of CPs were considered from the orthomosaic, and the height value was derived from the grid DSM, and by comparing to the GNSS measurements, $RMSE_{Z0}$ was calculated (Equation 4).

$$RMSE_{ZO} = \sqrt{\frac{\sum_{i=1}^n (Z_{O_i} - Z_{GNSSi})^2}{n}} \quad (4)$$

where Z_{O_i} is the elevation in the i th CP obtained from the DSM, considering its X and Y coordinates measured on the orthomosaic; Z_{GNSSi} is the Z coordinate of the i th CP measured with the GNSS.

This approach was adopted as it would be the process that a user would determine the elevation of a point identified on the orthomosaic. However, to some extent, the above method mitigates the effect of horizontal errors. Therefore, the second method used to assess the vertical accuracy was to calculate the elevation difference between DSM and GNSS measurements, while the horizontal positions of CPs were considered directly from the GNSS measurements. In the second method, the RMSE_{ZD} was calculated as using Equation 5, which the errors of all vegetated and non-vegetated unmarked CPs were also calculated using this method.

$$RMSE_{ZD} = \sqrt{\frac{\sum_{i=1}^n (Z_{D_i} - Z_{GNSSi})^2}{n}} \quad (5)$$

where Z_{D_i} is the elevation in the i th CP, derived from the DSM, while its X and Y coordinates, measured with the GNSS; and Z_{GNSSi} is the Z coordinate of the i th CP surveyed with the GNSS.

The vertical RMS errors of all vegetated and non-vegetated 200 unmarked CPs were calculated using the second method. Following the calculations, accuracy tables were prepared, and relative frequency histograms of error distribution and scatter plots of elevations were plotted to analyze the correlation and linear association

between different survey methods. The R programming language was used to analyze and plot not only the histograms and linear regression models, but also the correlation matrices, including distribution histograms along with the fitted normal density curves, bivariate scatter plots containing a fitted regression model, correlation ellipses, and correlation coefficient values to provide a statistical presentation of data. The charts plotted in R, significantly facilitate the pairwise comparisons. Finally, the obtained accuracies were compared with the ASPRS [54] positional accuracy standard for digital geospatial data.

3. Results and discussion

3.1. Absolute accuracy analysis and evaluation of results

Several factors influence the accuracy of a DSM derived from UAS images, such as flight height, distance to the nearest GCP, image overlap, topography, surface structure, and varying contrast in images [11, 52, 60–66]. In this study, the first two factors were investigated. The following sections present the results of horizontal and vertical accuracy assessment of CPs calculated based on RMSE equations discussed in Section 2.3.

3.1.1. Horizontal and vertical accuracy assessment based on marked CPs

Horizontal errors of orthomosaics in the X direction, Y direction, and radial direction (XY) were calculated for all projects based on 7 marked CPs. The error statistics of one project are given as an example in Table 2. Complete tables are given in the Table 3-6.

Table 2. Horizontal and vertical error statistics of orthomosaics and DSMs derived from 170 m AGL nadir images, processed with 10 GCPs and assessed with 7 GNSS CPs. All values are in meters.

	PhotoScan				Pix4Dmapper				3Dsurvey			
	X	Y	Z ₀	Z _D	X	Y	Z ₀	Z _D	X	Y	Z ₀	Z _D
Min	-0.007	-0.029	-0.016	-0.016	-0.043	-0.014	-0.033	-0.034	-0.029	-0.015	-0.134	-0.134
Max	0.053	0.021	0.108	0.108	0.048	0.068	0.068	0.068	0.018	0.074	0.107	0.107
Mean	0.010	-0.005	0.040	0.040	0.011	0.014	0.027	0.026	0.004	0.025	-0.055	-0.055
MAE	0.014	0.018	0.045	0.044	0.027	0.020	0.036	0.036	0.012	0.032	0.086	0.085
RMSE	0.022	0.020	0.054	0.053	0.031	0.030	0.040	0.040	0.015	0.042	0.092	0.092
RMSE _{XY}	0.029				0.044				0.045			
RMSE _{XYZ}	0.061				0.059				0.102			

Table 3. Horizontal and vertical error statistics of orthomosaics and DSMs derived from 100 m AGL nadir images, processed with 5 GCPs and assessed with 7 GNSS CPs. All values are in meters.

	PhotoScan				Pix4Dmapper				3Dsurvey			
	X	Y	Z ₀	Z _D	X	Y	Z ₀	Z _D	X	Y	Z ₀	Z _D
Min	-0.018	0.006	-0.216	-0.222	-0.018	0.009	-0.151	-0.151	-0.053	0.023	-0.088	-0.108
Max	0.030	0.052	0.157	0.157	0.037	0.051	0.100	0.099	0.052	0.166	0.123	0.123
Mean	0.005	0.018	-0.023	-0.024	0.004	0.024	-0.003	-0.004	0.012	0.078	-0.014	-0.025
MAE	0.017	0.018	0.098	0.097	0.014	0.024	0.083	0.081	0.040	0.078	0.075	0.070
RMSE	0.018	0.023	0.125	0.125	0.018	0.028	0.096	0.095	0.042	0.093	0.079	0.076
RMSE _{XY}	0.029				0.033				0.102			
RMSE _{XYZ}	0.128				0.101				0.129			

Table 4. Horizontal and vertical error statistics of orthomosaics and DSMs derived from 100 m AGL nadir images, processed with 10 GCPs and assessed with 7 GNSS CPs. All values are in meters.

	PhotoScan				Pix4Dmapper				3Dsurvey			
	X	Y	Z ₀	Z _D	X	Y	Z ₀	Z _D	X	Y	Z ₀	Z _D
Min	-0.008	-0.015	-0.151	-0.146	-0.013	-0.029	-0.024	-0.024	-0.038	-0.027	-0.139	-0.139
Max	0.038	0.087	0.008	0.003	0.034	0.056	0.076	0.075	0.016	0.060	0.190	0.190
Mean	0.007	0.022	-0.053	-0.056	0.006	0.016	0.020	0.019	-0.005	0.025	-0.018	-0.018
MAE	0.011	0.027	0.055	0.056	0.012	0.032	0.038	0.037	0.014	0.033	0.086	0.086
RMSE	0.016	0.036	0.073	0.073	0.016	0.036	0.046	0.045	0.019	0.040	0.104	0.104
RMSEXY	0.040				0.039				0.044			
RMSEXYZ	0.083				0.060				0.113			

Table 5. Horizontal and vertical error statistics of orthomosaics and DSMs derived from 170 m AGL nadir images, processed with 5 GCPs and assessed with 7 GNSS CPs. All values are in meters.

	PhotoScan				Pix4Dmapper				3Dsurvey			
	X	Y	Z ₀	Z _D	X	Y	Z ₀	Z _D	X	Y	Z ₀	Z _D
Min	-0.020	-0.014	-0.138	-0.138	-0.036	-0.017	-0.172	-0.175	-0.036	0.003	-0.268	-0.268
Max	0.030	0.013	0.027	0.027	0.070	0.093	0.071	0.071	0.137	0.099	0.055	0.055
Mean	0.005	0.002	-0.055	-0.055	0.008	0.035	-0.017	-0.019	0.017	0.052	-0.083	-0.081
MAE	0.015	0.011	0.063	0.063	0.021	0.040	0.070	0.071	0.047	0.052	0.105	0.102
RMSE	0.017	0.011	0.074	0.075	0.032	0.048	0.085	0.087	0.062	0.064	0.139	0.138
RMSEXY	0.020				0.058				0.089			
RMSEXYZ	0.077				0.103				0.165			

Table 6. Horizontal and vertical error statistics of orthomosaics and DSMs derived from the merged process of 100 and 170 m AGL nadir images and assessed with 7 GNSS CPs in Photoscan. All values are in meters.

	X	Y	Z ₀	Z _D
Min	-0.013	-0.006	-0.086	-0.086
Max	0.037	0.054	0.029	0.029
Mean	0.002	0.019	-0.025	-0.025
MAE	0.013	0.021	0.037	0.036
RMSE	0.016	0.027	0.047	0.047
RMSEXY	0.032			
RMSEXYZ	0.057			

The results showed that horizontal accuracy was not affected by flight height; however, it was significantly affected by the number and distribution of GCPs. The results of Pix4Dmapper and 3Dsurvey showed that accuracy was improved by increasing the number of GCPs. Nevertheless, by increasing the number of GCPs, no improvement was observed in the horizontal accuracy of the results processed by PhotoScan. The maximum horizontal and vertical errors indicate the error of points outside of GCP polygon. Since the results show that the horizontal errors are in the level of 1-1.5 × GSD, the values of Z₀ and Z_D in the above table demonstrate that vertical accuracy was not affected by the horizontal error.

To summarize the horizontal accuracy of PhotoScan, from both flight heights, orthomosaics were produced with RMSEX and RMSEY of ~2 cm, and horizontal accuracy (RMSEXY) of ~3 cm. According to the American Society for Photogrammetry and Remote Sensing (ASPRS) positional accuracy standards for digital geospatial data [54], the horizontal accuracy obtained from the images of 100 m AGL with 2.5 cm GSD meets the ASPRS 2014 standard horizontal accuracy class RMSEX and RMSEY of 2.5 cm and RMSEr (the horizontal linear RMSE) of 3.5 cm for normal error distribution. The

RMSEXY matches 6.1 cm accuracy at 95% confidence level. According to Class 1 of the legacy ASPRS map standard 1990 [67], the equivalent map scale for the achieved horizontal accuracy is 1:100. Similarly, the horizontal accuracy achieved from the images of 170 m AGL with 4.0 cm GSD meets the ASPRS 2014 standard horizontal accuracy class RMSEX and RMSEY of 5.0 cm and RMSEr of 7.1 cm for normal error distribution, and the horizontal accuracy at 95% confidence level is 12.2 cm. Referring to Class 1 of ASPRS 1990, the corresponding map scale for the achieved horizontal accuracy is 1:200.

The achieved horizontal accuracies in this study agree with the findings of Agüera-Vega et al. [11]; Bennassi et al. [68]; Cryderman et al. [69]; Fernández et al. [40]; Gerke & Przybilla [51]; Gindraux [62]; Gonçalves & Henriques [47]; Jaud et al. [59]; Martínez-Carricondo et al. [2]; Rehak & Skaloud [70]; Reshetyuk & Mårtensson [55]; Whitehead & Hugenholtz, [71]; and Wierzbicki et al. [72]. However, some studies achieved lower accuracy from closer ranges. For instance, from a flight height of about 50 m AGL, Pérez et al. [73] and Lucieer et al. [41] obtained RMSEXY of 7.2 and 7.0 cm, respectively. Similarly, Coveney and Roberts [38] obtained RMSEXY of 7.6 cm from 90 m height AGL. Sanz-Ablanedo et al. [44]

and Hill [74] achieved horizontal accuracy of 8.6 and 10 cm, respectively. Hastaoğlu et al. [75, 76] achieved horizontal accuracy of $1-2 \times$ GSD in their studies.

The double block combined processing of the images taken from the cross flights (100 and 170 m heights AGL processed with 5 GCP) showed remarkable 3D accuracy improvement (~ 2 cm). Nevertheless, horizontal accuracy was not improved significantly. PhotoScan outperformed both Pix4Dmapper and 3Dsurvey in horizontal accuracy. It is worth to mention that vertical accuracy evaluation based on the 7 CPs were performed not only to assess the horizontal accuracy but also to find the effect of the horizontal error on the vertical accuracy. Vertical accuracy (RMSEZD) was evaluated comprehensively based on 200 CPs, which is given in the following section.

3.1.2. Vertical accuracy assessment based on 200 unmarked CPs

As discussed in previous sections, according to literature, horizontal accuracy is not the main concern in UAS-SfM-based surveying. In UAS-SfM-derived DSMs, the major errors usually occur in Z values. With this in mind, horizontal accuracy was assessed based on 7 CPs, and given the importance of elevation in topographic mapping, vertical accuracy assessment was performed based on 200 CPs in vegetated and non-vegetated areas. The vertical accuracy of non-vegetated and vegetated land cover was evaluated separately. The results of the accuracy assessment and statistical analysis are presented in the following sections. The vertical error statistics are given in Table 7 and Table 8.

Table 7. Vertical error statistics of DSMs derived from 100 m AGL nadir images, processed with 5 & 10 GCPs, and assessed with 100 GNSS CPs. All values are in meters.

	PhotoScan		Pix4Dmapper		3Dsurvey	
	5 GCP	10 GCP	5 GCP	10 GCP	5 GCP	10 GCP
Min	-0.344	-0.165	-0.245	-0.104	-0.190	-0.270
Max	0.163	0.030	0.123	0.101	0.123	0.222
Mean	-0.004	-0.051	0.011	0.002	-0.059	-0.059
MAE	0.075	0.053	0.068	0.031	0.076	0.118
RMSE	0.102	0.066	0.085	0.039	0.091	0.137

Table 8. Vertical error statistics of DSMs derived from 170 m AGL nadir images, processed with 5, 10, and without GCPs, and assessed with 100 GNSS CPs. All values are in meters.

	PhotoScan			Pix4Dmapper			3Dsurvey		
	5 GCP	10 GCP	without GCP	5 GCP	10 GCP	without GCP	5 GCP	10 GCP	without GCP
Min	-0.324	-0.080	-1.633	-0.375	-0.302	-1.264	-0.481	-0.190	-1.034
Max	0.091	0.203	-0.577	0.394	0.330	0.320	0.266	0.107	0.463
Mean	-0.044	0.031	-0.974	0.016	0.031	-0.320	-0.080	-0.042	-0.008
MAE	0.055	0.048	0.974	0.077	0.050	0.398	0.100	0.071	0.293
RMSE	0.076	0.059	1.015	0.103	0.071	0.514	0.133	0.084	0.356

Table 7 compares the elevation error statistics of DSMs derived from 100 m AGL nadir images processed with 5 and 10 GCPs using the three software. The results of PhotoScan and Pix4Dmapper clearly showed the impact of GCP on the accuracy, where the highest elevation accuracy was achieved by Pix4Dmapper (3.9 cm) and PhotoScan (6.6 cm) using 10 GCPs. Georeferencing using 10 GCPs resulted in 3.6 and 4.6 cm improvement in accuracy comparing to 5 GCPs. On the contrary, in 3Dsurvey, the RMS error increased by increasing the number of GCPs.

As Table 4 demonstrates, the errors in DSMs derived from images of 170 m show the same trend for PhotoScan and Pix4Dmapper, where vertical accuracy increased by doubling the GCP numbers. However, PhotoScan shows higher accuracy than Pix4Dmapper. Contrary to 3Dsurvey's results at 100 m AGL, accuracy was increased in the 10 GCP schemes of 170 m AGL; however, it is still lower than PhotoScan and Pix4Dmapper. The vertical accuracy ranged from 0.356 m to 1.015 m when processed without GCP.

For the ease of interpretation, comparison, and correlation analysis, relative frequency histograms of errors were plotted in classes of 2 cm interval to compare each class to the total number of errors. To measure the linear dependence between SfM DSM elevations and the validation data of DGNSS, correlation analysis was performed based on the Pearson correlation method, which is the most common technique for measuring the strength of the association between two variables. Pairwise matrices were prepared, and correlation coefficients were computed. Figure 5 shows relative frequency histograms of elevation difference between UAS-SfM and DGNSS elevations along with the fitted linear regression models for the projects processed with 5 GCPs.

For relative accuracy analysis of SfM DSMs generated using three different software packages, correlation matrices were plotted using the R programming language to investigate the relationship between multiple variables (DGNSS validation elevations, Agisoft PhotoScan DSM elevations, Pix4Dmapper DSM

elevations, and 3Dsurvey DSM elevations) simultaneously. A chart of the correlation matrix was plotted for each project. In the correlation matrix diagram, the distribution histogram of each variable (elevation) along with a fitted normal density curve is shown on the diagonal. The bivariate scatter plots, including a fitted line and correlation ellipses, are displayed at the bottom of the diagonal. Correlation coefficient values are given above the diagonal. The chart

combines the statistical presentation of data, which facilitates pairwise comparison and measuring the linear association between two variables as well as the visual test for bivariate normality. Pairwise elevation correlation matrix for projects processed with 5 GCPs are given in Figure 6. Figure 7 shows relative frequency histograms of elevation difference between UAS-SfM and DGNSS elevations with the fitted linear regression models for the projects processed with 10 GCPs.

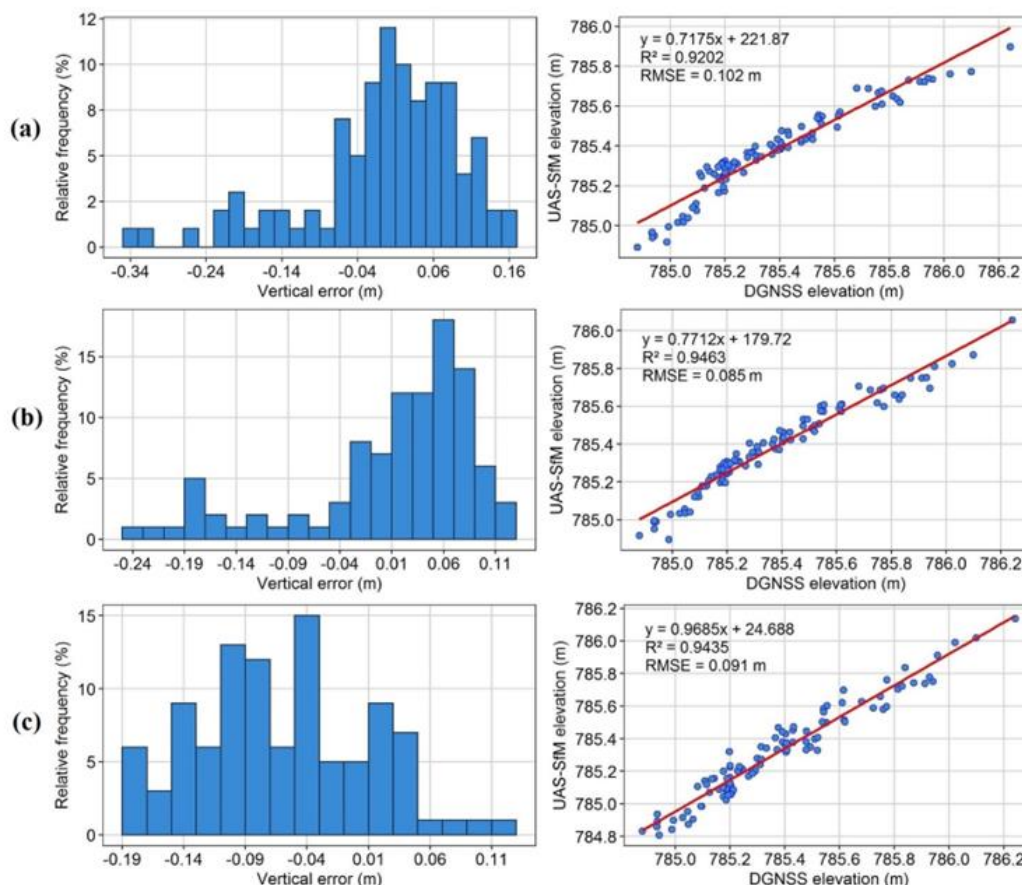


Figure 5. Relative frequency histogram of non-vegetated vertical errors and scatter plot of correlation between UAS-SfM and DGNSS elevations. UAS-SfM DSM derived from 100 m AGL nadir images, processed with 5 GCPs using (a) PhotoScan, (b) Pix4Dmapper, and (c) 3Dsurvey.

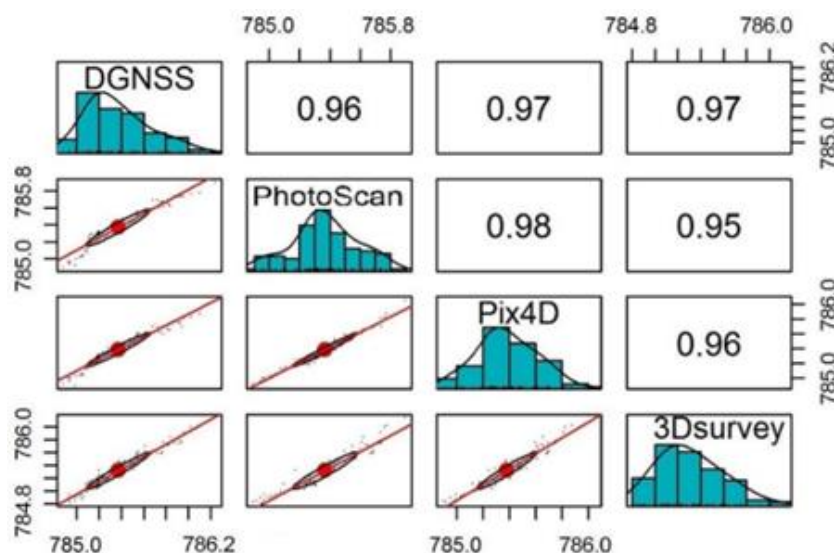


Figure 6. Correlation matrix plot with bivariate scatter plots, distributions, and correlation ellipses of DGNSS non-vegetated elevations and UAS-SfM DSM elevations derived from 100 m AGL nadir images, processed with 5 GCPs.

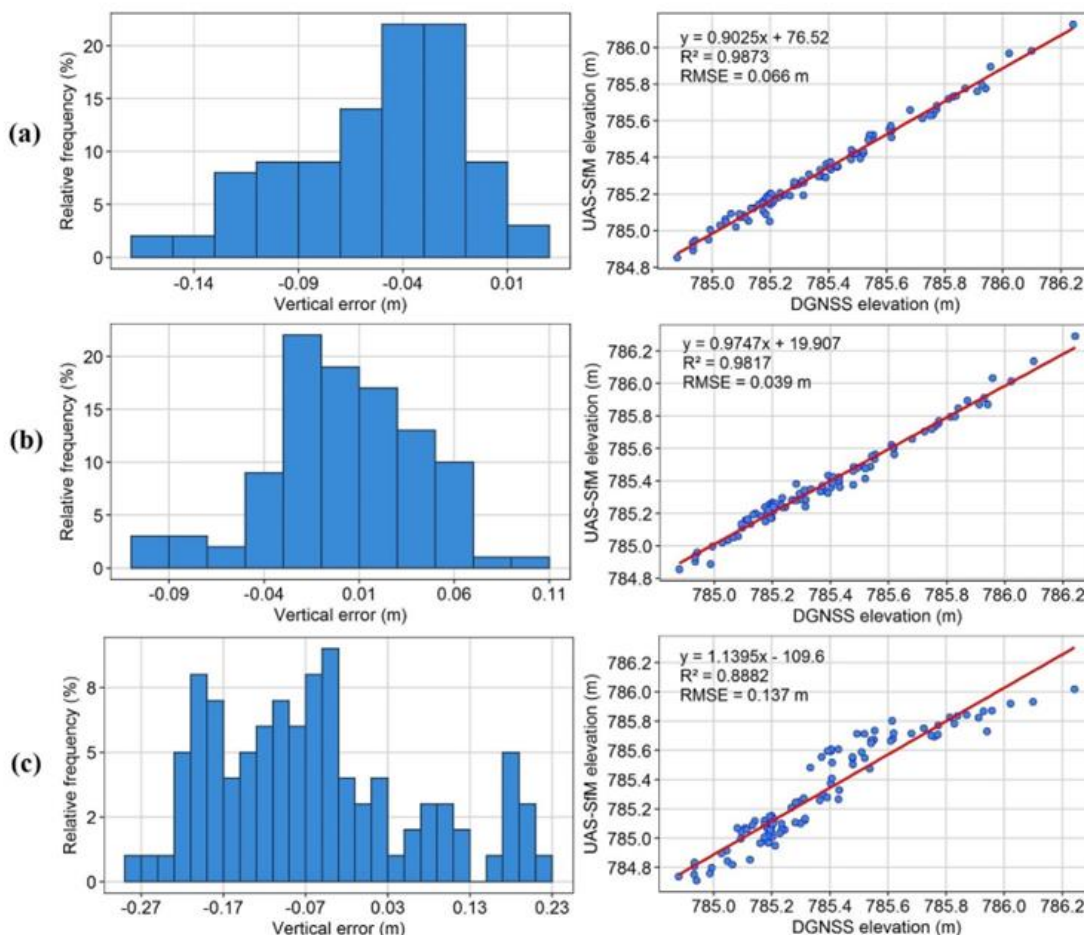


Figure 7. Relative frequency histogram of non-vegetated vertical errors and scatter plot of correlation between UAS-SfM and DGNSS elevations. UAS-SfM DSM derived from 100 m AGL nadir images, processed with 10 GCPs using (a) PhotoScan, (b) Pix4Dmapper, and (c) 3Dsuryey.

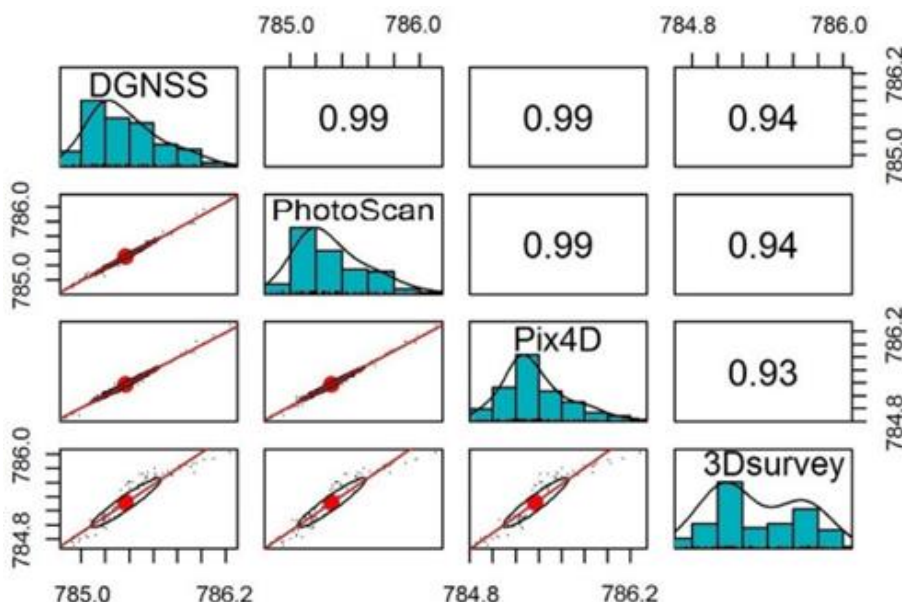


Figure 8. Correlation matrix plot with bivariate scatter plots, distributions, and correlation ellipses of DGNSS non-vegetated elevations and UAS-SfM DSM elevations derived from 100 m AGL images, processed with 10 GCPs.

Figure 7 shows pairwise elevation correlation matrix for the projects processed with 10 GCPs. Figures 5 to 8 illustrate the relative frequency histograms of vertical error and pairwise correlation of elevations for the DSMs derived from images collected at 100 m height (Figure 9-

12 for the DSMs derived from 170 m AGL images). The figures indicate that there is a high positive linear correlation between DGNSS and SfM DSM elevations. For the 5 GCP scheme, as RMSE values for PhotoScan, Pix4Dmapper, and 3Dsuryey are very close (10.2, 8.5, and

9.1 cm, respectively), they show almost the same trend, and there is no significant difference in correlation. However, histograms show high similarities in error distribution between PhotoScan and Pix4Dmapper. On the other hand, 3Dsurvey shows quite different error distribution and fewer outliers. The results of the 10 GCP scheme showed that vertical accuracy remarkably

increased in Pix4Dmapper and PhotoScan. R-squared values in scatter plots also showed a high correlation between the elevations of PhotoScan, Pix4Dmapper, and DGNS. The minimum and maximum error values decreased, and outliers were significantly reduced in the 10 GCP scheme. However, the result of 3Dsurvey showed higher error values and a relatively weak correlation.

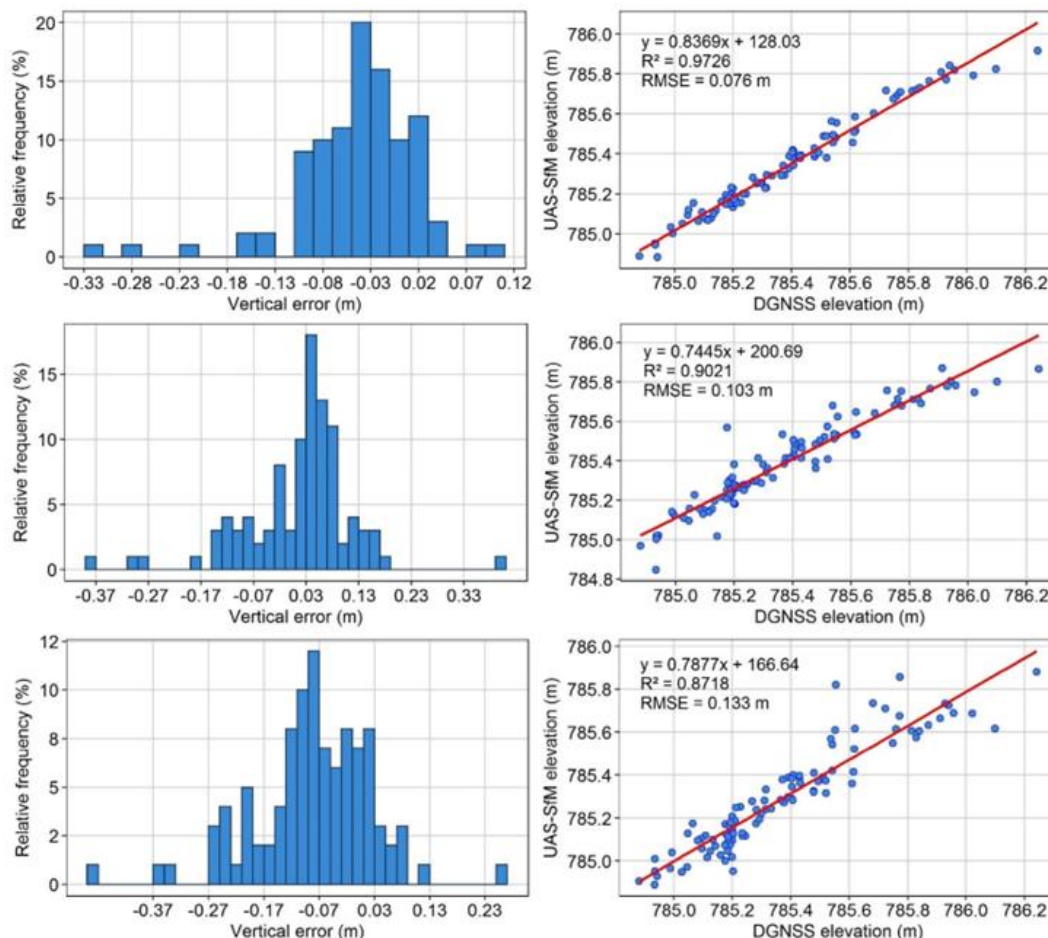


Figure 9. Relative frequency histogram of non-vegetated vertical errors and scatter plot of correlation between UAS-SfM and DGNS elevations. UAS-SfM DSM derived from 170 m AGL nadir images, processed with 5 GCPs using PhotoScan (top), Pix4Dmapper (middle), and 3Dsurvey (bottom).

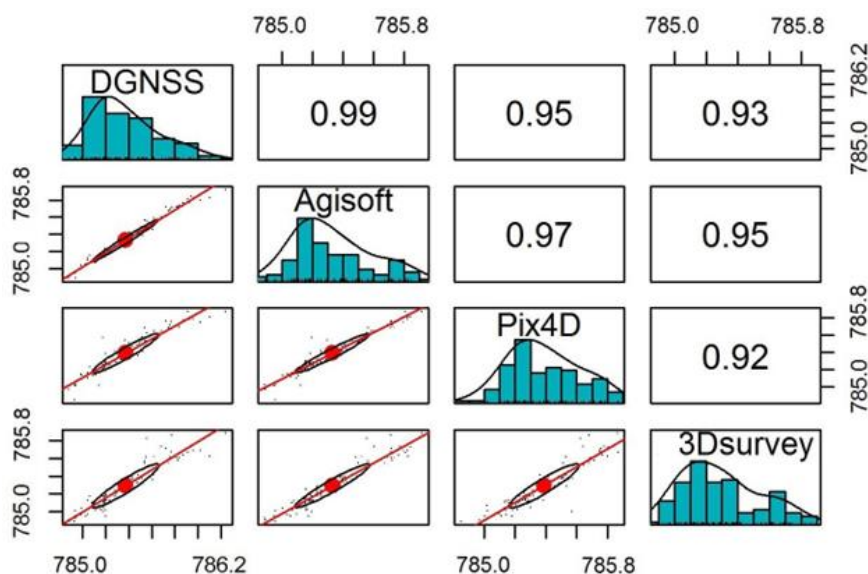


Figure 10. Correlation scatter plot matrix of DGNS non-vegetated elevations and UAS-SfM DSM elevations derived from 170 m AGL nadir images, processed with 5 GCPs.

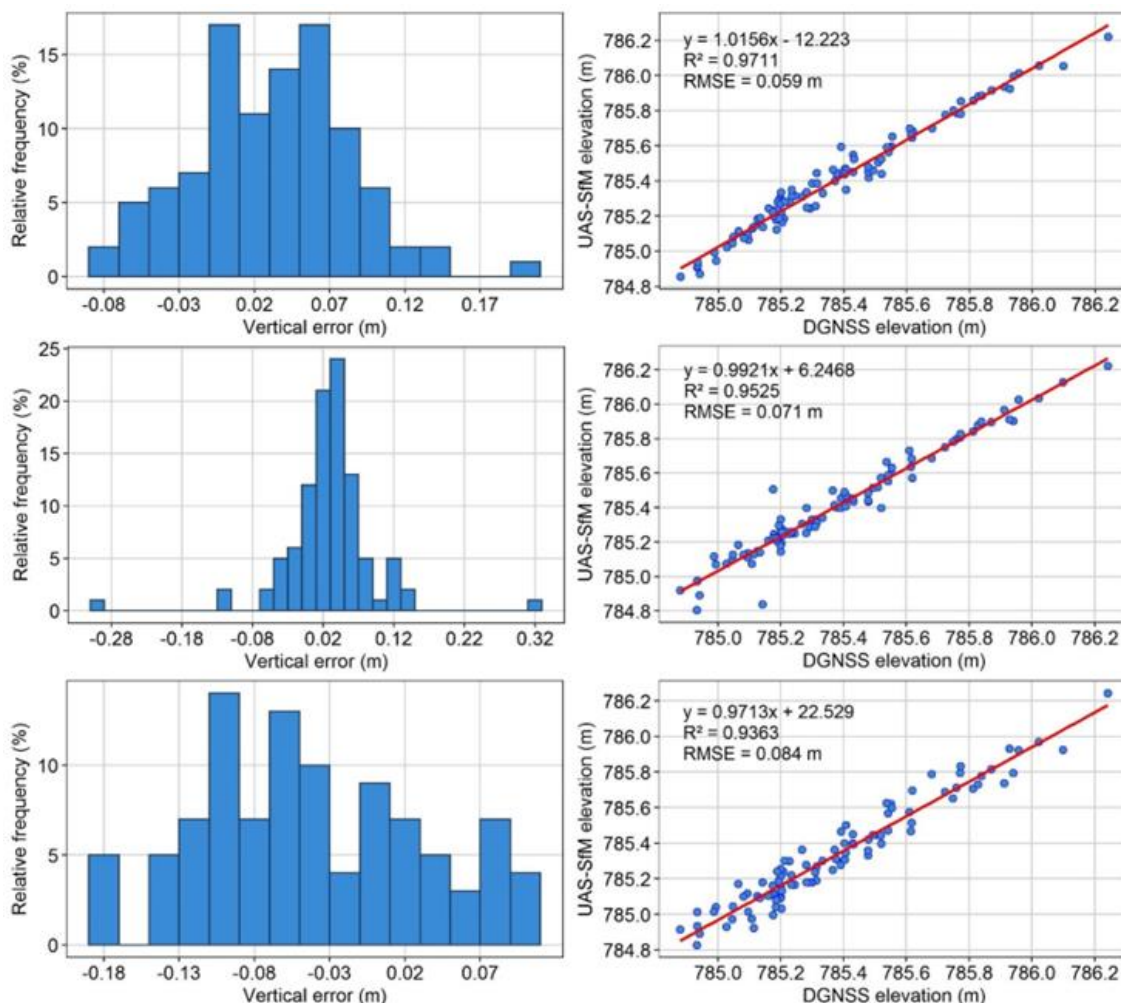


Figure 11. Relative frequency histogram of non-vegetated vertical errors and scatter plot of correlation between UAS-SfM and DGNSS elevations. UAS-SfM DSM derived from 170 m AGL nadir images, processed with 10 GCPs using PhotoScan (top), Pix4Dmapper (middle), and 3Ds survey (bottom).

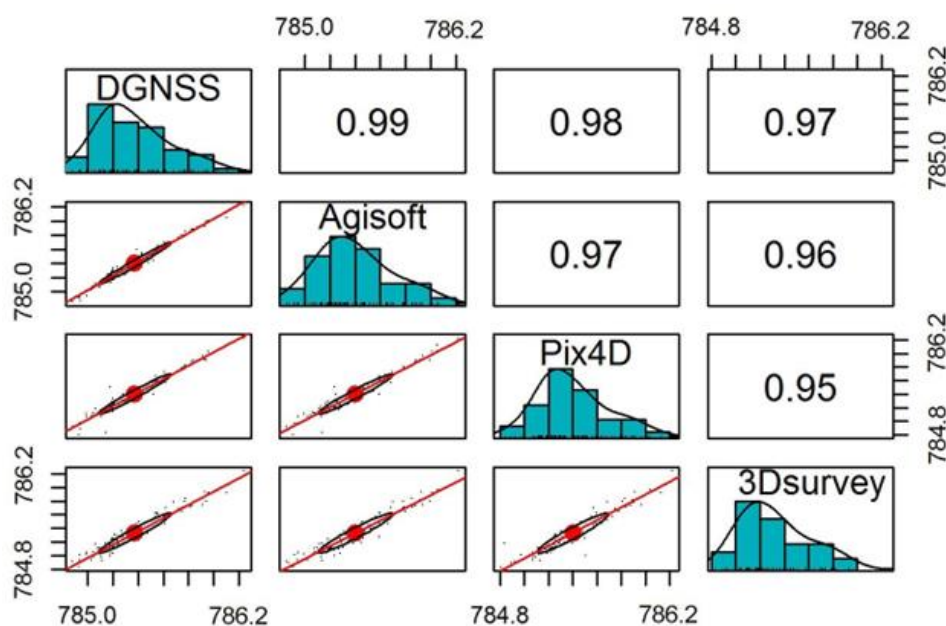


Figure 12. Correlation scatter plot matrix of DGNSS non-vegetated elevations and UAS-SfM DSM elevations derived from 170 m AGL nadir images, processed with 10 GCPs.

The results of statistical analysis illustrate that in 5 GCP scheme, the vertical correlation is weaker, and the number of outliers is higher than the 10 GCP scheme for

both projects. For the project 170 m AGL, in the 10 GCP scheme, the error distribution for PhotoScan was almost normal, ranging from -8.0 cm to 20.3 cm with only one

outlier; this is because lightweight drones with fixed wings can maintain overlap at higher altitudes. Similarly, Pix4Dmapper showed a nearly normal distribution ranging from -30.2 cm to 33.0 cm with three outliers. The error distribution in 3Dsuryey ranges from -19.0 to 10.7 cm. PhotoScan and Pix4Dmapper showed higher accuracy and correlation in both GCP schemes; however, 3Dsuryey yielded lower accuracy with a relatively weak correlation.

To sum up, in the non-vegetated area, the highest vertical accuracy of 3.9 cm was achieved from the images of 100 m AGL using 10 GCPs by Pix4Dmapper. This accuracy meets Class 3 (RMSE 5 cm) of ASPRS 2014 absolute accuracy, which the equivalent Class 1 contour interval as per ASPRS 1990 is 15 cm. Since PhotoScan achieved 6.6 cm accuracy, based on the ASPRS standard, this is equivalent to 9.8 cm absolute accuracy at 95% confidence level. From the images of 170 m AGL, the highest achieved accuracy was 5.9 cm by PhotoScan, which agrees with Class 4 (RMSE 10 cm) of ASPRS 2014; accordingly, 95% confidence level is 19.6 cm. The equivalent Class 1 contour interval as per ASPRS 1990 is 30 cm. The achieved vertical results are also consistent with the literature mentioned in the above section. Although the number of GCPs used in the literature varies, the synthesis of results from the literature used in

this study indicates that the average vertical accuracy reliability is at the level of 10 cm, which this accuracy agrees with Class 4 of ASPRS 2014.

Using a passive sensor in remote sensing, terrain modeling under densely vegetated areas is difficult and practically not recommended for topographic mapping. However, in sparsely vegetated areas using filtering algorithms or by integrating with terrestrial measurements, topographic data can be provided. Bearing this in mind, the accuracy assessment of the DTMs was carried out on areas covered with grasses and sparse trees. The vertical error distribution histograms, scatter plot of correlations, and matrices are given in the supplementary document (Figure 13-20). According to the ASPRS 2014, vegetated vertical accuracy is an estimate of the vertical accuracy based on the 95% confidence level in vegetated terrain, where vertical errors do not necessarily approximate a normal distribution. The results showed a vertical accuracy of 7 to 11 cm in areas with sparse and low-height vegetation. The results revealed that by increasing the GCP numbers, the vegetated accuracy also increased to some extent. The correlation was also improved using 10 GCPs; nevertheless, some outliers remained, which is normal for vegetated areas.

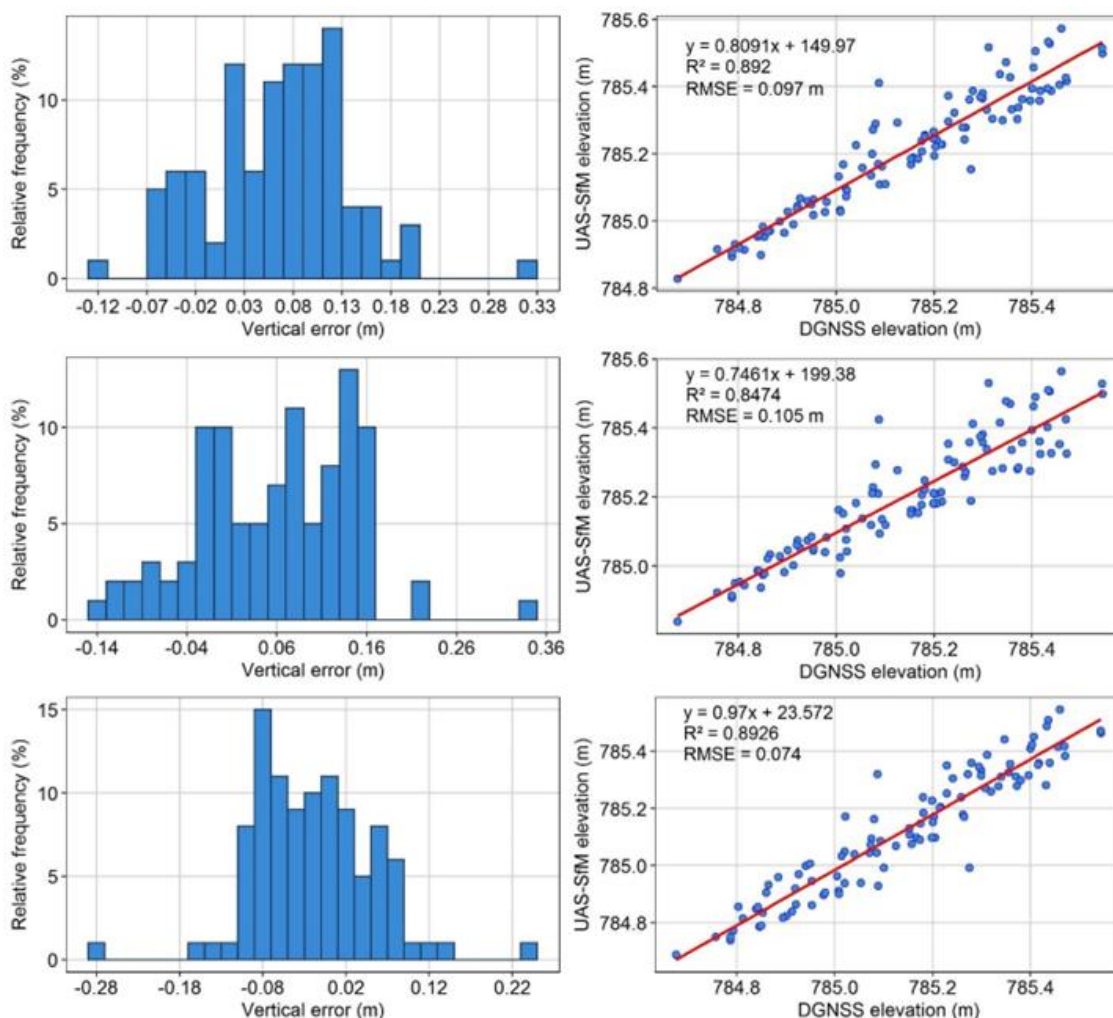


Figure 13. Relative frequency histogram of vegetated vertical errors and scatter plot of correlation between UAS-SfM and DGNSS elevations. UAS-SfM DTM derived from 100 m AGL nadir images, processed with 5 GCPs using PhotoScan (top), Pix4D (middle), and 3Dsuryey (bottom).

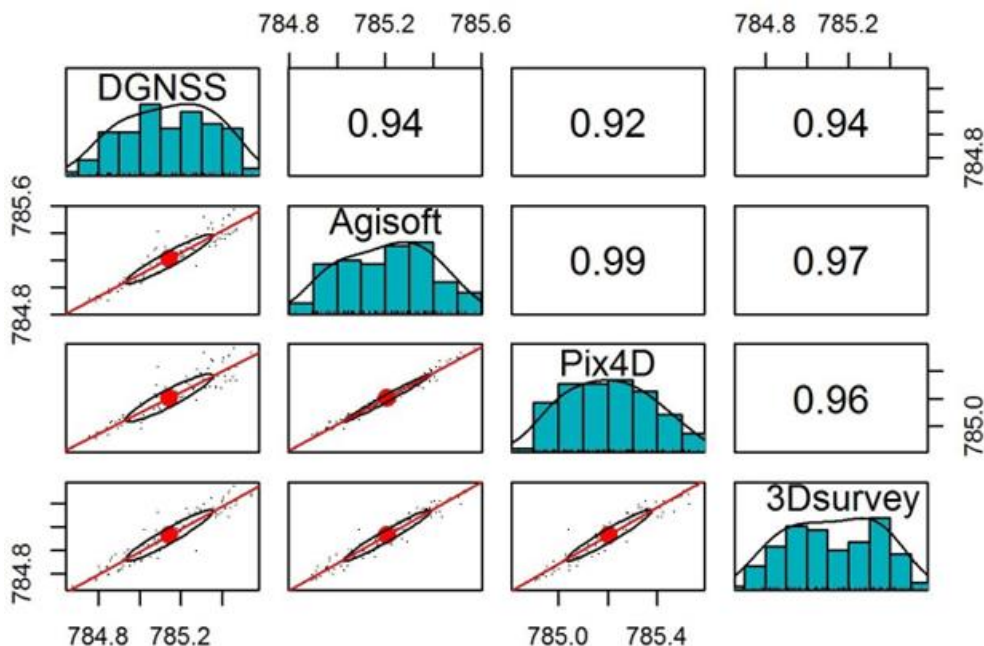


Figure 14. Correlation scatter plot matrix of DGNSS vegetated elevations and UAS-SfM DTM elevations derived from 100 m AGL nadir images, processed with 5 GCPs.

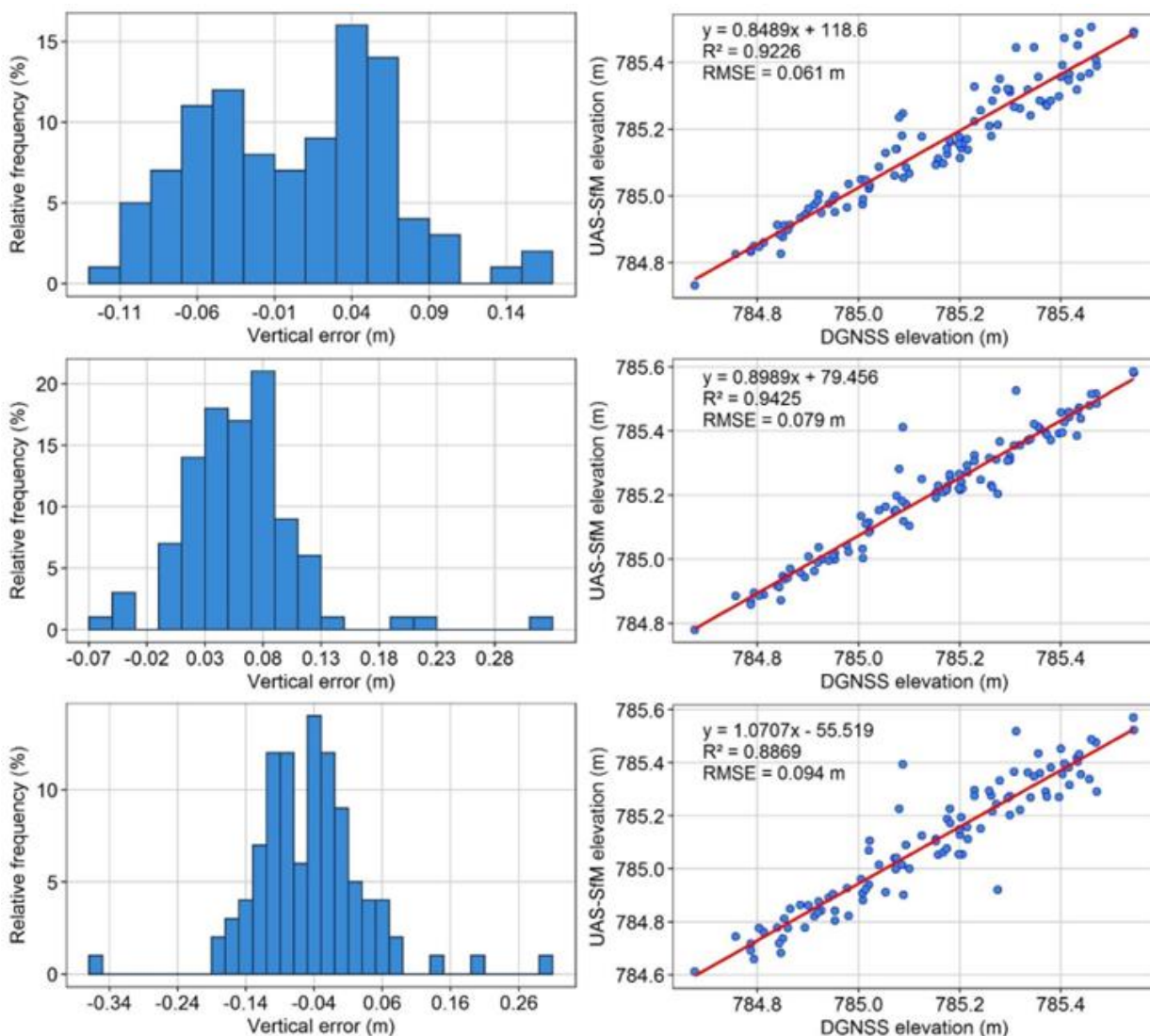


Figure 15. Relative frequency histogram of vegetated vertical errors and scatter plot of correlation between UAS-SfM and DGNSS elevations. UAS-SfM DTM derived from 100 m AGL nadir images, processed with 10 GCPs using PhotoScan (top), Pix4D (middle), and 3Dsurvey (bottom).

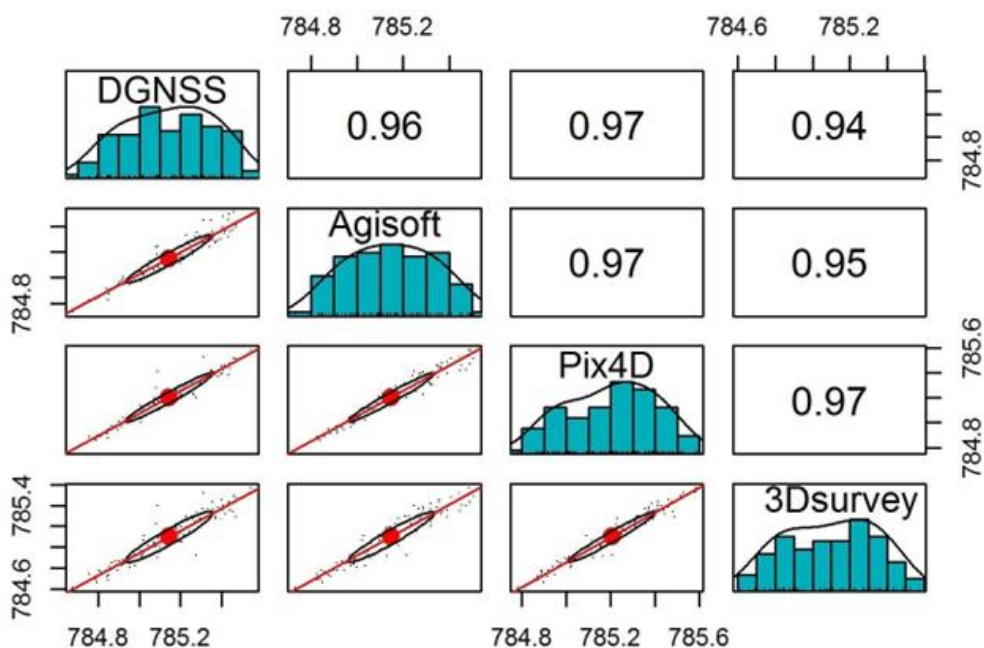


Figure 16. Correlation scatter plot matrix of DGNSS vegetated elevations and UAS-SfM DTM elevations derived from 100 m AGL nadir images, processed with 10 GCPs.

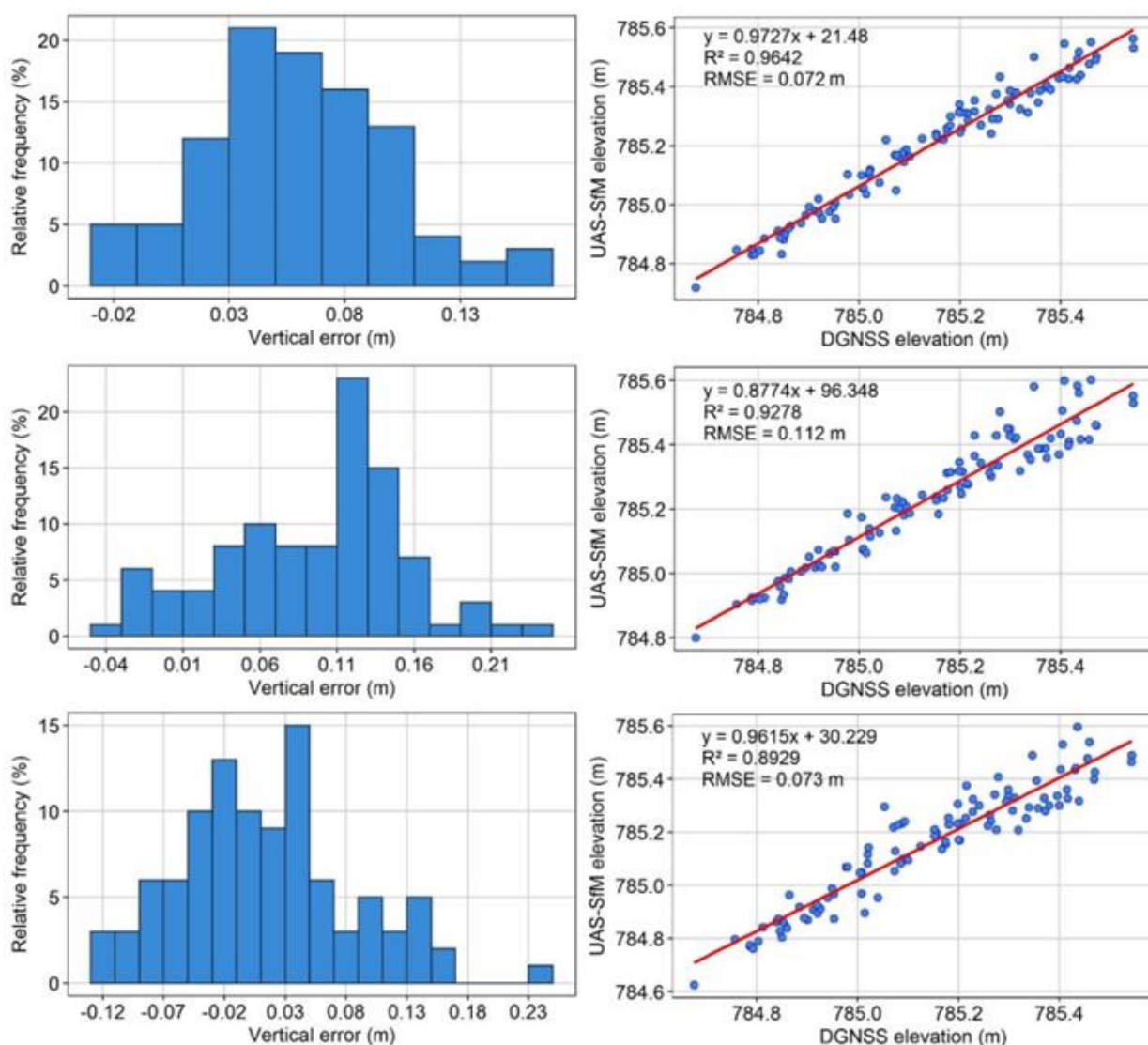


Figure 17. Relative frequency histogram of vegetated vertical errors and scatter plot of correlation between UAS-SfM and DGNSS elevations. UAS-SfM DTM derived from 170 m AGL nadir images, processed with 5 GCPs using PhotoScan (top), Pix4D (middle), and 3Dsurvey (bottom).

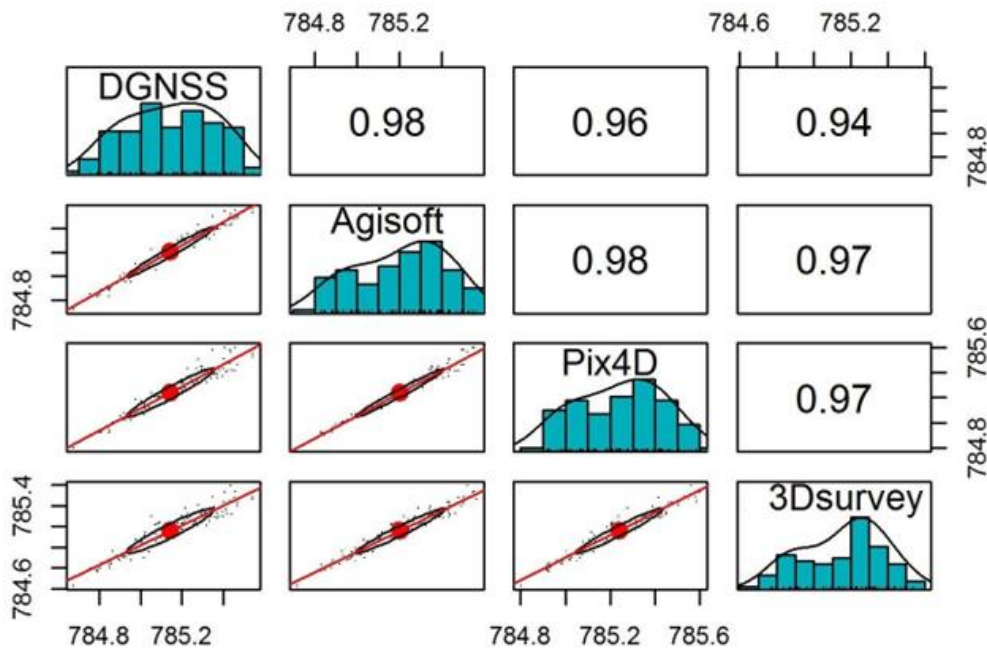


Figure 18. Correlation scatter plot matrix of DGNSS vegetated elevations and UAS-SfM DTM elevations derived from 170 m AGL nadir images, processed with 5 GCPs.

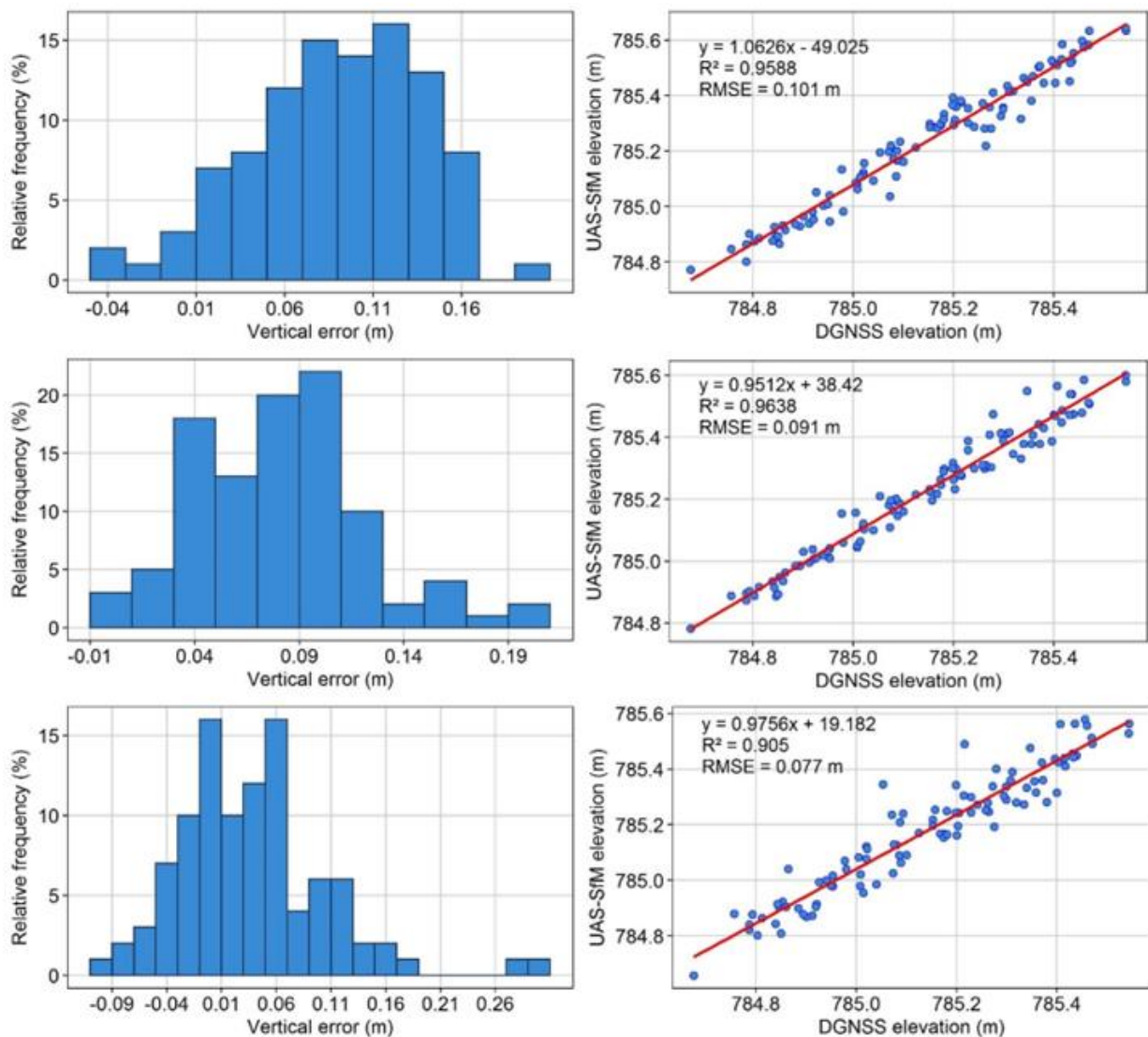


Figure 19. Relative frequency histogram of vegetated vertical errors and scatter plot of correlation between UAS-SfM and DGNSS elevations. UAS-SfM DTM derived from 170 m AGL nadir images, processed with 10 GCPs using PhotoScan (top), Pix4D (middle), and 3Dsurvey (bottom).

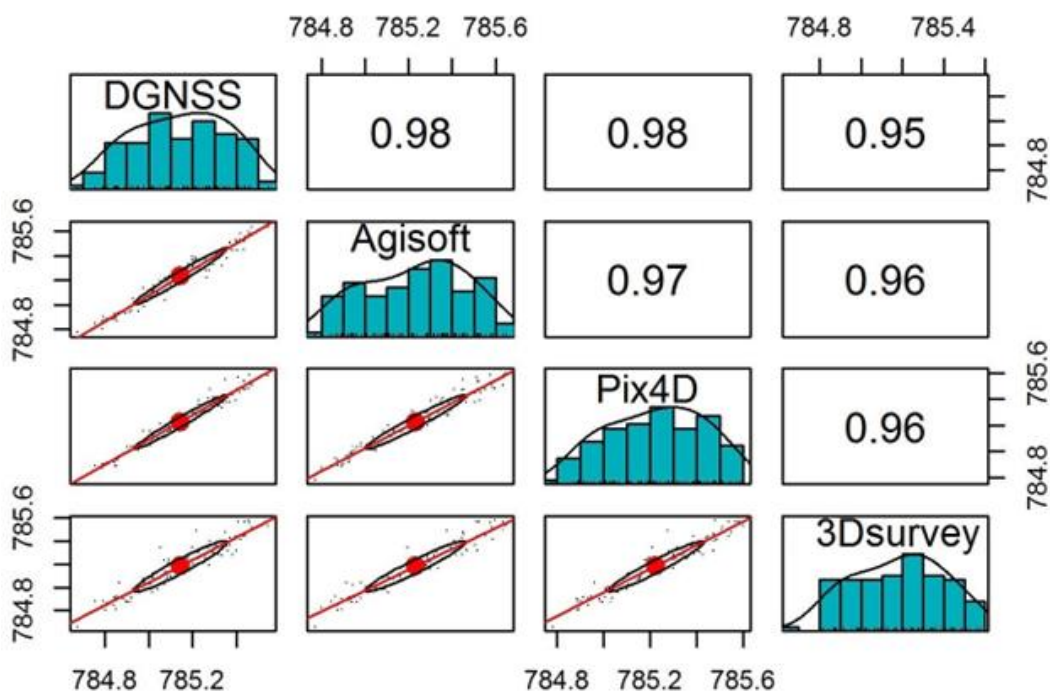


Figure 20. Correlation scatter plot matrix of DGNSS vegetated elevations and UAS-SfM DTM elevations derived from 170 m AGL nadir images, processed with 10 GCPs.

3.1.3. Vertical accuracy of the combined project

To assess the accuracy of the project combined from different flight heights, an integrated image processing was performed by combining images of cross flights. Blocks of 100 m and 170 m AGL nadir images were processed using PhotoScan with 5 GCPs. Figure 21 and Figure 22 demonstrate the histogram and correlation matrix of accuracy analysis for the combined project. By comparing the DSM accuracy of this project with that of projects that were processed individually with 5 GCPs, we can see that in flight 1 (170 m AGL), the error range is from -34 to 16 cm, in flight 2 (100 m AGL) with the same GCP number, errors range from -32 to 9 cm, while in the combined project, the error range is from -15 to 7 cm.

The error histogram of the DSM derived from the combined project (Figure 21) shows a significant

improvement in the elevation accuracy. Although the scatter plots of both separately processed projects show high correlation coefficient values, the error distribution histograms show large outliers in both projects. The relative frequency histogram of errors in the combined project shows that outliers were removed, and errors have a nearly normal distribution. Moreover, considering the correlation coefficient and the confidence ellipses (Figure 22), the correlation of the combined project processed with 5 GCPs is comparable with that of projects that were separately processed using 10 GCPs. Figure 22 shows that a high correlation exists between the elevations of the DSM derived from the integrated process and other DSMs that were generated from single flight blocks. The integrated project not only improved accuracy but also resulted in more detail and better 3D models.

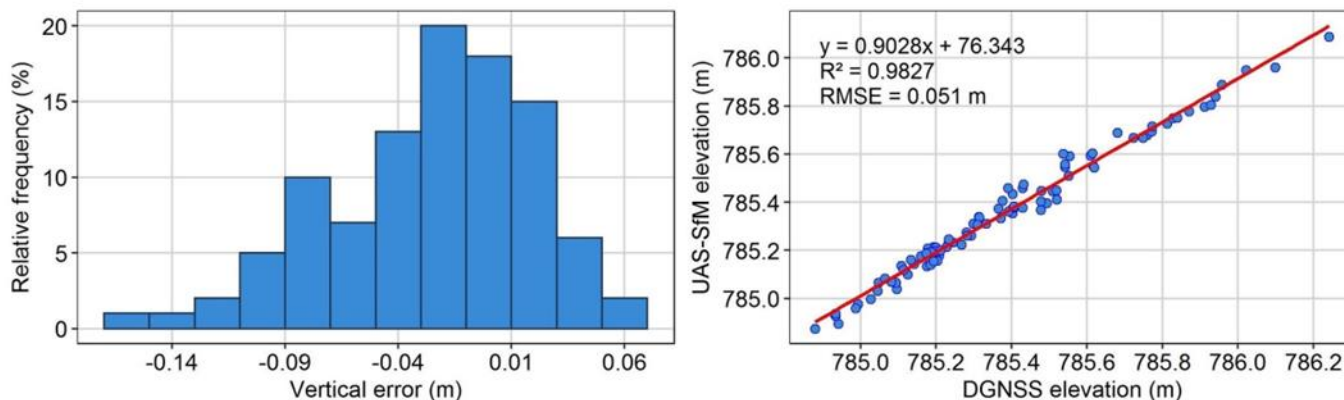


Figure 21. Relative frequency histogram of vertical errors and scatter plot of correlation between UAS-SfM and DGNSS non-vegetated elevations. UAS-SfM DSM derived from the combined process of cross flight nadir images, processed with 5 GCPs using PhotoScan.

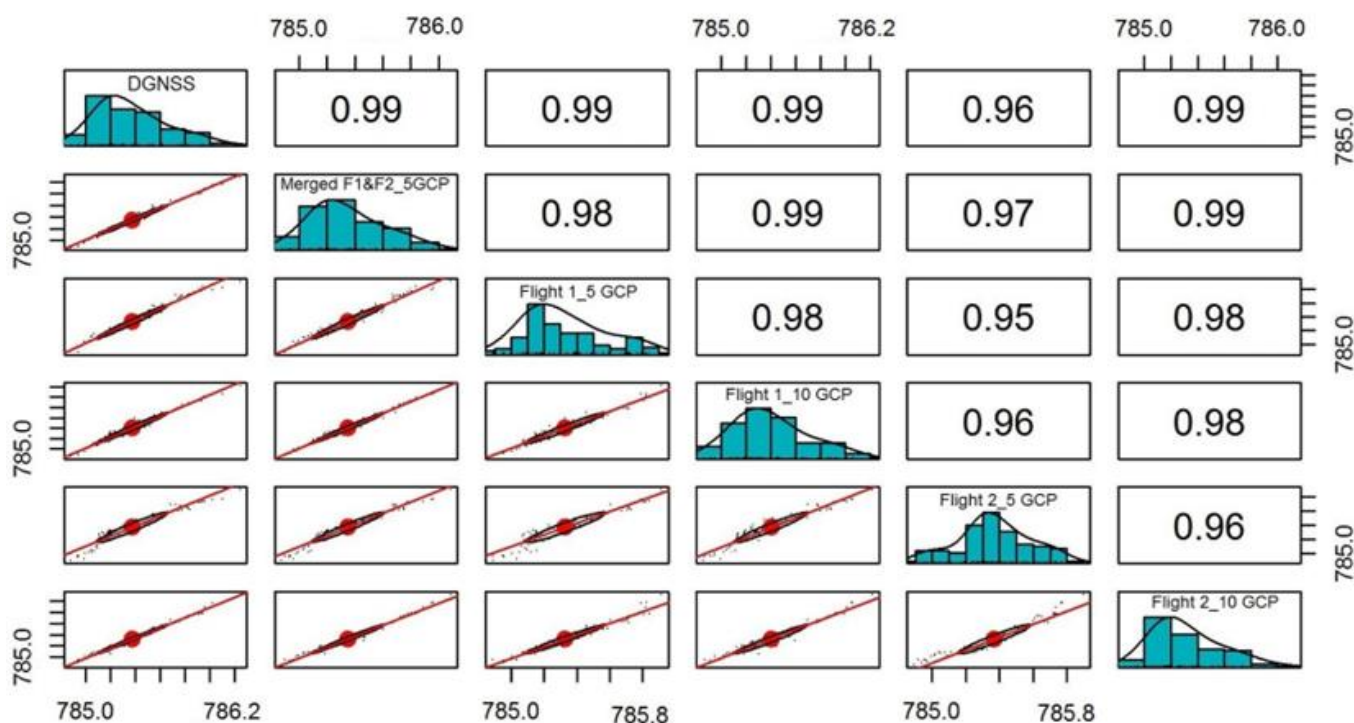


Figure 22. Correlation matrix plot with bivariate scatter plots, distributions, and correlation ellipses of DGNSs non-vegetated elevations and UAS-SfM DSM elevations derived from the combined process of 170 m (Flight 1) and 100 m (Flight 2) AGL nadir images, processed with 5 GCPs using PhotoScan.

3.1.4. Influence of GCP distribution on vertical accuracy

Images of both flights were georeferenced using 5 and 10 GCPs in PhotoScan. The location of 5 GCPs was intentionally selected in the middle of the study area to leave some areas outside of the GCP polygon to analyze the relationship between errors and their distance to the nearest GCP. In Figures 23a and 23b (georeferenced using 5 GCP scheme), the farthest point from the nearest GCP is 267 m; it shows that error increases with distance from GCP. Polynomial regression of 100 samples of difference between SfM DSM elevations and DGNSs in non-vegetated terrain highlights the influence of GCP distribution on vertical error. The figure illustrates that up to a distance of 170 m, almost all of the errors are under 20 cm. As the distance increases, the error also increases gradually, where after 170 m, a 100 m increase in the distance indicates about 1 dm increase in error (in both 100 and 170 m AGL).

For an in-depth investigation of the relationship, images of both flights were georeferenced using 10 GCPs and distributed in a way that most of the validation points fall within the GCP polygon, and the maximum distance of validation points from the GCP cluster is 125 m. Figure 23c and Figure 23d indicate that using 10 GCPs, the correlation between the distance to GCP and the error is weakened, where up to a distance of 100 m, the majority of errors are below 15 cm, most of which range from 0 to 10 cm.

From Figure 23, we conclude that up to 100 m, the correlation between distance to the nearest GCP and

vertical error is almost zero in both flights, and positive correlation starts from 100 m, where after 150 m, the vertical error increases dramatically. The results of Pix4Dmapper showed the same trend, which distances greater than 150 m greatly affected the vertical accuracy.

Images of 170 m AGL were processed using the three software without using GCP to evaluate the relative accuracy. The images were aligned and georeferenced using the EXIF geotags. As shown in Table 8, when the images processed without using GCPs, the vertical error ranged from decimeters to meters, which shows the importance of GCPs on accuracy. Figure 24 illustrates the correlation scatter plot matrix of DGNSs elevations and SfM elevation processed without using GCPs.

As the diagram shows, it is not possible to get a strong correlation between the SfM elevation and the DGNSs elevation without GCP because the UAS internal GPS in non-RTK mode cannot yield vertical accuracy comparable with the DGNSs. Nevertheless, the matrix shows a strong elevation correlation between PhotoScan and Pix4D DSMs. 3Dsurvey also shows a positive correlation with both PhotoScan and Pix4D, but the correlation is weak. However, 3D survey produced DSM with less error compared to the other two software (Table 8). Considering the relative accuracy, if the images are scaled with simple measurements instead of georeferencing with GCPs, the DSMs produced using these software packages can be used for many applications such as visualization or in emergency response. However, for obtaining high-accuracy 3D models, georeferencing using GCPs is inevitable.

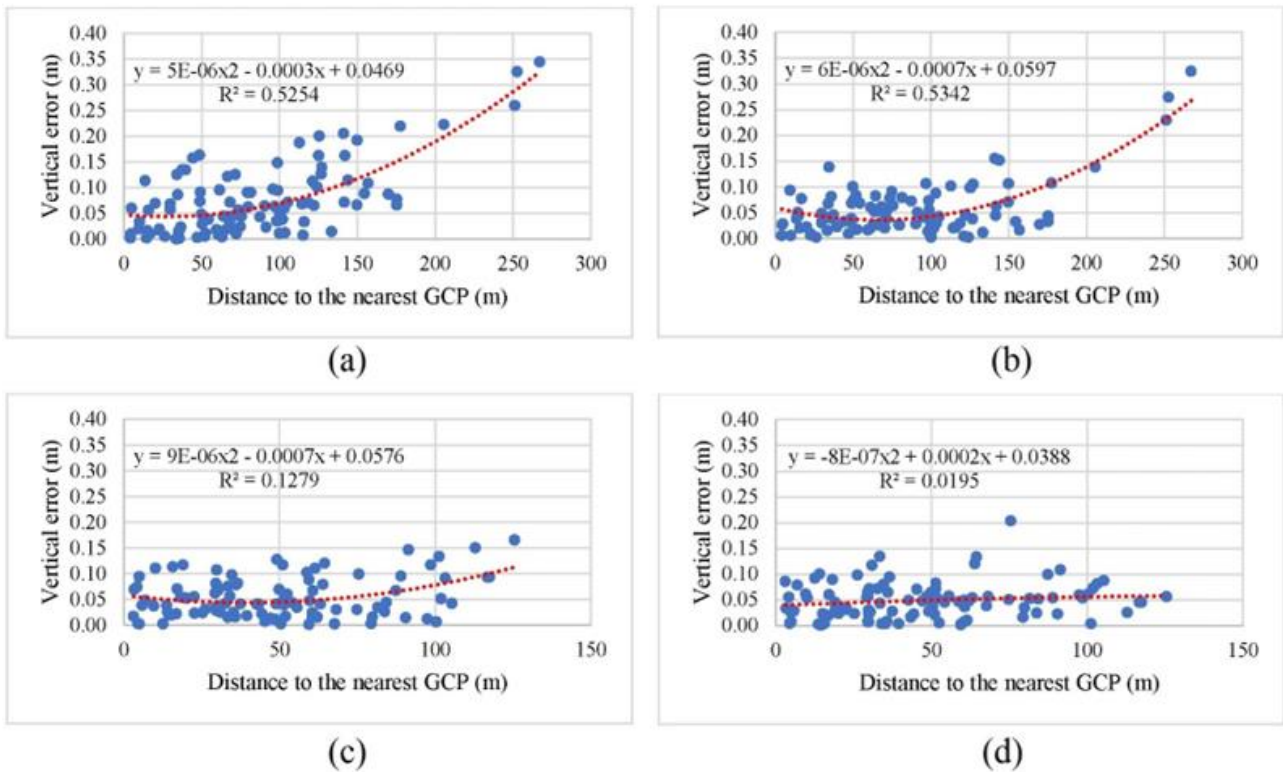


Figure 23. Scatter plot of correlation between distance to the nearest GCP and vertical error. (a) derived from DSM of 100 m AGL nadir images georeferenced with 5 GCPs; (b) derived from DSM of 170 m AGL nadir images georeferenced with 5 GCPs; (c) derived from DSM of 100 m AGL nadir images georeferenced with 10 GCPs (d) derived from DSM of 170 m AGL nadir images georeferenced with 10 GCPs.

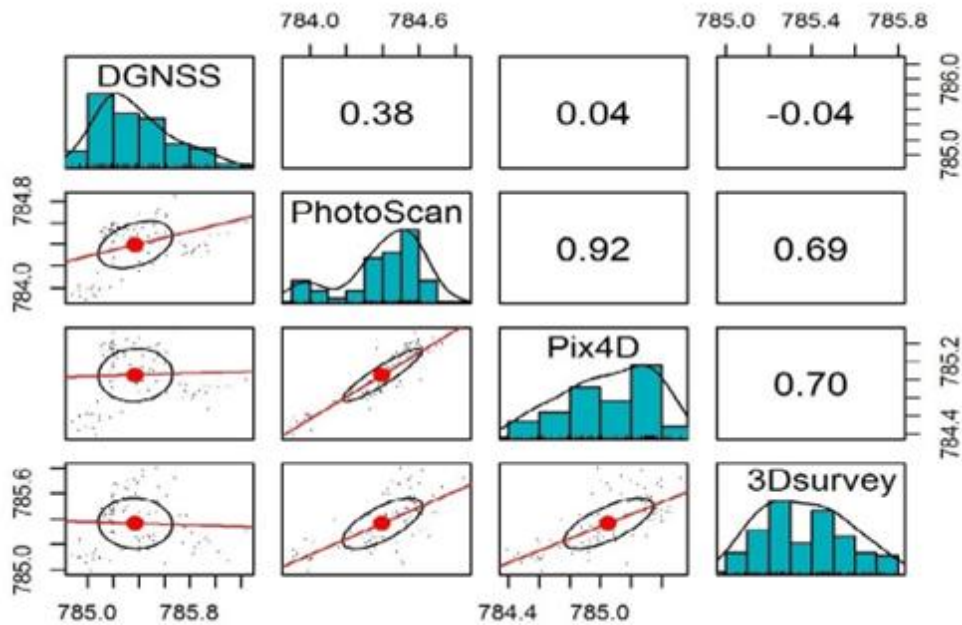


Figure 24. Correlation scatter plot matrix of DGNSS non-vegetated elevations and UAS-SfM DSM elevations derived from 170 m AGL nadir images, processed using the three software without GCP.

4. Conclusion

The aim of this study was to evaluate the accuracy of UAS photogrammetry and structure from motion as a low-cost alternative to terrestrial surveys for geomatics engineering applications. The absolute accuracy assessment showed that the best horizontal and vertical

accuracy achieved from the images of 100 m AGL, in which the horizontal RMSE for the orthomosaic was 3 cm, and the vertical RMSE for the DSM was 4 cm. Similarly, orthomosaic with 3 cm horizontal accuracy and DSM with 6 cm vertical accuracy were obtained from the images of 170 m AGL. According to the ASPRS positional accuracy standards for digital geospatial data,

the achieved horizontal accuracies of orthomosaics derived from 100 m and 170 m AGL images meet the ASPRS 2014 horizontal accuracy classes RMSE 2.5 and RMSE 5.0 cm, respectively. These accuracies are equivalent to map scales of 1:100 and 1:200 of ASPRS 1990. In the same way, the obtained vertical accuracies of DSMs derived from 100 and 170 m AGL images in non-vegetated areas are in accordance with Class 3 (RMSE 5 cm) and Class 4 (RMSE 10 cm) of the ASPRS 2014 absolute accuracy, respectively. The equivalent Class 1 contour interval as per ASPRS 1990 is 15 and 30 cm, respectively. The achieved results meet the ASPRS 2014 95% confidence level vertical accuracy of 9.8 and 19 cm, respectively. The analysis results confirm that orthomosaics and DSMs reconstructed from 100 m AGL images can be used for most terrain analysis applications, including civil engineering projects.

This study's findings showed that horizontal accuracy was not affected by flight height; however, flight height greatly affected the vertical accuracy, where a 70 m increase in flight height caused a 3 cm decrease in vertical accuracy. This demonstrated the strong influence of flight height on vertical accuracy. Vertical accuracy was significantly improved by increasing the number of GCPs. The number and distribution of GCPs are crucial in horizontal and vertical accuracy. The vertical accuracy of the DSM processed without GCP is not reliable because the results which were processed without GCPs showed vertical discrepancies in decimeters. Moreover, the results showed that combining two photogrammetric blocks of cross flight images significantly contributes to vertical accuracy and the production of a denser point cloud. The study highlighted that by integrating the images of two different flight heights, outlier values were substantially reduced, and errors showed a normal distribution. Both PhotoScan and Pix4Dmapper generated satisfactory models; however, PhotoScan produced more accurate and high-quality 3D models from images with higher overlap.

Acknowledgement

This paper was extracted from an MSc thesis entitled "Accuracy Analysis and Evaluation of UAS Photogrammetry and Structure from Motion in Engineering Surveying," conducted by Sayed Ishaq Deliry [77] at Eskisehir Technical University under the supervision of Professor Dr. Uğur Avdan.

Author contributions

Sayed Ishaq Deliry: Conceptualization, Methodology, Data Collection, Analysis, Investigation, Writing - Original Draft, Writing - Review & Editing

Uğur Avdan: Supervision, Validation, Writing - Review & Editing

Conflicts of interest

The authors declare no conflicts of interest.

References

1. Li, Z., Zhu, C., & Gold, C. (2004). Digital terrain modeling: principles and methodology. CRC press.
2. Martínez-Carricondo, P., Agüera-Vega, F., Carvajal-Ramírez, F., Mesas-Carrascosa, F. J., García-Ferrer, A., & Pérez-Porras, F. J. (2018). Assessment of UAV-photogrammetric mapping accuracy based on variation of ground control points. *International Journal of Applied Earth Observation and Geoinformation*, 72, 1-10. <https://doi.org/10.1016/j.jag.2018.05.015>
3. Agüera-Vega, F., Carvajal-Ramírez, F., Martínez-Carricondo, P., López, J. S. H., Mesas-Carrascosa, F. J., García-Ferrer, A., & Pérez-Porras, F. J. (2018). Reconstruction of extreme topography from UAV structure from motion photogrammetry. *Measurement*, 121, 127-138. <https://doi.org/10.1016/j.measurement.2018.02.062>
4. Ajayi, O. G., Salubi, A. A., Angbas, A. F., & Odigure, M. G. (2017). Generation of accurate digital elevation models from UAV acquired low percentage overlapping images. *International Journal of Remote Sensing*, 38(8-10), 3113-3134. <https://doi.org/10.1080/01431161.2017.1285085>
5. Carrivick, J. L., Smith, M. W., & Quincey, D. J. (2016). Structure from motion in the geosciences. John Wiley & Sons.
6. Greenwood, W. W., Lynch, J. P., & Zekkos, D. (2019). Applications of UAVs in civil infrastructure. *Journal of Infrastructure Systems*, 25(2), 04019002. [https://doi.org/10.1061/\(ASCE\)IS.1943-555X.0000464](https://doi.org/10.1061/(ASCE)IS.1943-555X.0000464)
7. Nex, F., & Remondino, F. (2014). UAV for 3D mapping applications: a review. *Applied Geomatics*, 6, 1-15. <https://doi.org/10.1007/s12518-013-0120-x>
8. International Civil Aviation Organization (2011). Unmanned Aircraft Systems (UAS).
9. Liu, P., Chen, A. Y., Huang, Y. N., Han, J. Y., Lai, J. S., Kang, S. C., ... & Tsai, M. H. (2014). A review of rotorcraft unmanned aerial vehicle (UAV) developments and applications in civil engineering. *Smart Structures and Systems*, 13(6), 1065-1094. <http://dx.doi.org/10.12989/sss.2014.13.6.1065>
10. Pajares, G. (2015). Overview and current status of remote sensing applications based on unmanned aerial vehicles (UAVs). *Photogrammetric Engineering & Remote Sensing*, 81(4), 281-330. <https://doi.org/10.14358/PERS.81.4.281>
11. Agüera-Vega, F., Carvajal-Ramírez, F., & Martínez-Carricondo, P. (2017). Accuracy of digital surface models and orthophotos derived from unmanned aerial vehicle photogrammetry. *Journal of Surveying Engineering*, 143(2), 04016025. [https://doi.org/10.1061/\(ASCE\)SU.1943-5428.0000206](https://doi.org/10.1061/(ASCE)SU.1943-5428.0000206)
12. Awange, J. L. (2012). Environmental monitoring using GNSS: Global navigation satellite systems. Berlin: Springer. <https://doi.org/10.1007/978-3-211-73017-1>
13. Dai, F., & Lu, M. (2010). Assessing the accuracy of applying photogrammetry to take geometric

- measurements on building products. *Journal of Construction Engineering and Management*, 136(2), 242-250. [https://doi.org/10.1061/\(ASCE\)CO.1943-7862.0000114](https://doi.org/10.1061/(ASCE)CO.1943-7862.0000114)
14. Ehrhart, M., & Lienhart, W. (2017). Accurate measurements with image-assisted total stations and their prerequisites. *Journal of Surveying Engineering*, 143(2), 04016024. [https://doi.org/10.1061/\(ASCE\)SU.1943-5428.0000208](https://doi.org/10.1061/(ASCE)SU.1943-5428.0000208)
 15. Holland, D. A., Boyd, D. S., & Marshall, P. (2006). Updating topographic mapping in Great Britain using imagery from high-resolution satellite sensors. *ISPRS Journal of Photogrammetry and Remote Sensing*, 60(3), 212-223. <https://doi.org/10.1016/j.isprsjprs.2006.02.002>
 16. Honkavaara, E., Arbiol, R., Markelin, L., Martinez, L., Cramer, M., Bovet, S., ... & Veje, N. (2009). Digital airborne photogrammetry—A new tool for quantitative remote sensing?—A state-of-the-art review on radiometric aspects of digital photogrammetric images. *Remote Sensing*, 1(3), 577-605. <https://doi.org/10.3390/rs1030577>
 17. Kizil, U., & Tisor, L. (2011). Evaluation of RTK-GPS and total station for applications in land surveying. *Journal of Earth System Science*, 120, 215-221. <https://doi.org/10.1007/s12040-011-0044-y>
 18. Patino, J. E., & Duque, J. C. (2013). A review of regional science applications of satellite remote sensing in urban settings. *Computers, Environment and Urban Systems*, 37, 1-17. <https://doi.org/10.1016/j.compenvurbsys.2012.06.003>
 19. Slattery, K. T., & Slattery, D. K. (2013). Modeling earth surfaces for highway earthwork computation using terrestrial laser scanning. *International Journal of Construction Education and Research*, 9(2), 132-146. <https://doi.org/10.1080/15578771.2012.700298>
 20. Telling, J., Lyda, A., Hartzell, P., & Glennie, C. (2017). Review of Earth science research using terrestrial laser scanning. *Earth-Science Reviews*, 169, 35-68. <https://doi.org/10.1016/j.earscirev.2017.04.007>
 21. Wolf, P. R. (2002). Surveying and mapping: History, current status, and future projections. *Journal of Surveying Engineering*, 128(3), 79-107. [https://doi.org/10.1061/\(ASCE\)0733-9453\(2002\)128:3\(79\)](https://doi.org/10.1061/(ASCE)0733-9453(2002)128:3(79))
 22. ASCE. (2018). Policy Statement 333 - Engineering surveying definition. <https://www.asce.org/advocacy/policy-statements/ps333---engineering-surveying-definition>
 23. Kreisle, W. E. (1988). History of engineering surveying. *Journal of Surveying Engineering*, 114(3), 102-124. [https://doi.org/10.1061/\(ASCE\)0733-9453\(1988\)114:3\(102\)](https://doi.org/10.1061/(ASCE)0733-9453(1988)114:3(102))
 24. Bangen, S. G., Wheaton, J. M., Bouwes, N., Bouwes, B., & Jordan, C. (2014). A methodological intercomparison of topographic survey techniques for characterizing Wadeable streams and rivers. *Geomorphology*, 206, 343-361. <https://doi.org/10.1016/j.geomorph.2013.10.010>
 25. Mancini, F., Dubbini, M., Gattelli, M., Stecchi, F., Fabbri, S., & Gabbianelli, G. (2013). Using unmanned aerial vehicles (UAV) for high-resolution reconstruction of topography: The structure from motion approach on coastal environments. *Remote Sensing*, 5(12), 6880-6898. <https://doi.org/10.3390/rs5126880>
 26. Michelletti, N., Chandler, J. H., & Lane, S. N. (2015). Structure from motion (SfM) photogrammetry. *Geomorphological Techniques*, 1-12.
 27. Deliry, S. I., & Avdan, U. (2021). Accuracy of unmanned aerial systems photogrammetry and structure from motion in surveying and mapping: a review. *Journal of the Indian Society of Remote Sensing*, 49(8), 1997-2017. <https://doi.org/10.1007/s12524-021-01366-x>
 28. Ullman, S. (1979). The interpretation of visual motion. Massachusetts Inst of Technology Pr.
 29. Furukawa, Y., & Ponce, J. (2009). Accurate, dense, and robust multiview stereopsis. *IEEE Transactions on Pattern Analysis and Machine Intelligence*, 32(8), 1362-1376. <https://doi.org/10.1109/TPAMI.2009.161>
 30. Lowe, D. G. (1999). Object recognition from local scale-invariant features. *Proceedings of the Seventh IEEE International Conference on Computer Vision*, 2, 1150-1157. <https://doi.org/10.1109/ICCV.1999.790410>
 31. Lowe, D. G. (2004). Distinctive image features from scale-invariant keypoints. *International Journal of Computer Vision*, 60, 91-110. <https://doi.org/10.1023/B:VISI.0000029664.99615.94>
 32. Snavely, N., Seitz, S. M., & Szeliski, R. (2006). Photo tourism: exploring photo collections in 3D. *ACM siggraph 2006 papers*, 835-846. <https://doi.org/10.1145/1179352.1141964>
 33. Snavely, N., Seitz, S. M., & Szeliski, R. (2008). Modeling the world from internet photo collections. *International Journal of Computer Vision*, 80, 189-210. <https://doi.org/10.1007/s11263-007-0107-3>
 34. DeWitt, B. A., & Wolf, P. R. (2000). *Elements of Photogrammetry (with Applications in GIS)*. McGraw-Hill Higher Education.
 35. Mölg, N., & Bolch, T. (2017). Structure-from-motion using historical aerial images to analyse changes in glacier surface elevation. *Remote Sensing*, 9(10), 1021. <https://doi.org/10.3390/rs9101021>
 36. Alptekin, A., & Yakar, M. (2020). Determination of pond volume with using an unmanned aerial vehicle. *Mersin Photogrammetry Journal*, 2(2), 59-63.
 37. Çelik, M. Ö., Alptekin, A., Ünel, F. B., Kuşak, L., & Kanun, E. (2020). The effect of different flight heights on generated digital products: DSM and Orthophoto. *Mersin Photogrammetry Journal*, 2(1), 1-9.
 38. Coveney, S., & Roberts, K. (2017). Lightweight UAV digital elevation models and orthoimagery for environmental applications: data accuracy evaluation and potential for river flood risk modelling. *International Journal of Remote Sensing*, 38(8-10), 3159-3180. <https://doi.org/10.1080/01431161.2017.1292074>

39. Deliry, S. I., & Avdan, U. (2023). Accuracy evaluation of UAS photogrammetry and structure from motion in 3D modeling and volumetric calculations. *Journal of Applied Remote Sensing*, 17(2), 024515. <https://doi.org/10.1117/1.JRS.17.024515>
40. Fernández, T., Pérez, J. L., Cardenal, J., Gómez, J. M., Colomo, C., & Delgado, J. (2016). Analysis of landslide evolution affecting olive groves using UAV and photogrammetric techniques. *Remote Sensing*, 8(10), 837. <https://doi.org/10.3390/rs8100837>
41. Lucieer, A., Jong, S. M. D., & Turner, D. (2014). Mapping landslide displacements using Structure from Motion (SfM) and image correlation of multi-temporal UAV photography. *Progress in Physical Geography*, 38(1), 97-116. <https://doi.org/10.1177/0309133313515293>
42. Mesas-Carrascosa, F. J., Notario García, M. D., Meroño de Larriva, J. E., & García-Ferrer, A. (2016). An analysis of the influence of flight parameters in the generation of unmanned aerial vehicle (UAV) orthomosaics to survey archaeological areas. *Sensors*, 16(11), 1838. <https://doi.org/10.3390/s16111838>
43. Öztürk, O., Bilgilioğlu, B. B., Çelik, M. F., Bilgilioğlu, S. S., & Uluğ, R. (2017). İnsanız hava aracı (İHA) görüntüleri ile ortofoto üretiminde yükseklik ve kamera açısının doğruluğa etkisinin araştırılması. *Geomatik*, 2(3), 135-142. <https://doi.org/10.29128/geomatik.327049>
44. Sanz-Ablanedo, E., Chandler, J. H., Rodríguez-Pérez, J. R., & Ordóñez, C. (2018). Accuracy of unmanned aerial vehicle (UAV) and SfM photogrammetry survey as a function of the number and location of ground control points used. *Remote Sensing*, 10(10), 1606. <https://doi.org/10.3390/rs10101606>
45. Kanun, E., Alptekin, A., Karataş, L., & Yakar, M. (2022). The use of UAV photogrammetry in modeling ancient structures: A case study of "Kanytellis". *Advanced UAV*, 2(2), 41-50.
46. Colomina, I., & Molina, P. (2014). Unmanned aerial systems for photogrammetry and remote sensing: A review. *ISPRS Journal of Photogrammetry and Remote Sensing*, 92, 79-97. <https://doi.org/10.1016/j.isprsjprs.2014.02.013>
47. Goncalves, J. A., & Henriques, R. (2015). UAV photogrammetry for topographic monitoring of coastal areas. *ISPRS Journal of Photogrammetry and Remote Sensing*, 104, 101-111. <https://doi.org/10.1016/j.isprsjprs.2015.02.009>
48. Stöcker, C., Bennett, R., Nex, F., Gerke, M., & Zevenbergen, J. (2017). Review of the current state of UAV regulations. *Remote Sensing*, 9(5), 459. <https://doi.org/10.3390/rs9050459>
49. Ruzgienė, B., Berteška, T., Gečyte, S., Jakubauskienė, E., & Aksamitauskas, V. Č. (2015). The surface modelling based on UAV Photogrammetry and qualitative estimation. *Measurement*, 73, 619-627. <https://doi.org/10.1016/j.measurement.2015.04.018>
50. Long, N., Millescamp, B., Pouget, F., Dumon, A., Lachaussee, N., & Bertin, X. (2016). Accuracy assessment of coastal topography derived from UAV images. In *Xxiii Isprs Congress, Commission I*, 41, B1, 1127-1134. <https://doi.org/10.5194/isprsarchives-XLI-B1-1127-2016>
51. Gerke, M., & Przybilla, H. J. (2016). Accuracy analysis of photogrammetric UAV image blocks: Influence of onboard RTK-GNSS and cross flight patterns. *Photogrammetrie, Fernerkundung, Geoinformation*, 2016(1), 17-30. <https://doi.org/10.1127/pfg/2016/0284>
52. Tonkin, T. N., & Midgley, N. G. (2016). Ground-control networks for image based surface reconstruction: An investigation of optimum survey designs using UAV derived imagery and structure-from-motion photogrammetry. *Remote Sensing*, 8(9), 786. <https://doi.org/10.3390/rs8090786>
53. Oniga, V. E., Breaban, A. I., & Statescu, F. (2018). Determining the optimum number of ground control points for obtaining high precision results based on UAS images. *Proceedings*, 2(7), 352. <https://doi.org/10.3390/ecrs-2-05165>
54. American Society for Photogrammetry and Remote Sensing. (2014). ASPRS positional accuracy standards for digital geospatial data. <https://doi.org/10.14358/PERS.81.3.A1-A26>
55. Reshetyuk, Y., & Mårtensson, S. G. (2016). Generation of highly accurate digital elevation models with unmanned aerial vehicles. *The Photogrammetric Record*, 31(154), 143-165. <https://doi.org/10.1111/phor.12143>
56. Agisoft, L. L. C. (2018). Agisoft PhotoScan User Manual: Professional Edition, Version 1.4. Petersburg, Russia: Agisoft LLC.
57. Pix4D, S. A. (2017). Pix4Dmapper 4.1 user manual. Pix4D SA: Lausanne, Switzerland.
58. 3Dsurvey. (2018). 3Dsurvey User Manual: Version 2.7.
59. Jaud, M., Passot, S., Le Bivic, R., Delacourt, C., Grandjean, P., & Le Dantec, N. (2016). Assessing the accuracy of high resolution digital surface models computed by PhotoScan® and MicMac® in sub-optimal survey conditions. *Remote Sensing*, 8(6), 465. <https://doi.org/10.3390/rs8060465>
60. Avanzi, F., Bianchi, A., Cina, A., De Michele, C., Maschio, P., Pagliari, D., ... & Rossi, L. (2018). Centimetric accuracy in snow depth using unmanned aerial system photogrammetry and a multistation. *Remote Sensing*, 10(5), 765. <https://doi.org/10.3390/rs10050765>
61. Duran, Z., & Atik, M. E. (2021). Accuracy comparison of interior orientation parameters from different photogrammetric software and direct linear transformation method. *International Journal of Engineering and Geosciences*, 6(2), 74-80. <https://doi.org/10.26833/ijeg.691696>
62. Gindraux, S., Boesch, R., & Farinotti, D. (2017). Accuracy assessment of digital surface models from unmanned aerial vehicles' imagery on glaciers. *Remote Sensing*, 9(2), 186. <https://doi.org/10.3390/rs9020186>
63. Maraş, E. E., & Nasery, N. (2023). Investigating the length, area and volume measurement accuracy of UAV-Based oblique photogrammetry models

- produced with and without ground control points. *International Journal of Engineering and Geosciences*, 8(1), 32-51.
<https://doi.org/10.26833/ijeg.1017176>
64. Nesbit, P. R., & Hugenholtz, C. H. (2019). Enhancing UAV-SFM 3D model accuracy in high-relief landscapes by incorporating oblique images. *Remote Sensing*, 11(3), 239.
<https://doi.org/10.3390/rs11030239>
65. Ruiz, J. J., Diaz-Mas, L., Perez, F., & Viguria, A. (2013). Evaluating the accuracy of DEM generation algorithms from UAV imagery. *The International Archives of the Photogrammetry, Remote Sensing and Spatial Information Sciences*, 40, 333-337.
<https://doi.org/10.5194/isprsarchives-XL-1-W2-333-2013>
66. Senkal, E., Kaplan, G., & Avdan, U. (2021). Accuracy assessment of digital surface models from unmanned aerial vehicles' imagery on archaeological sites. *International Journal of Engineering and Geosciences*, 6(2), 81-89. <https://doi.org/10.26833/ijeg.696001>
67. American Society for Photogrammetry and Remote Sensing. (1990). ASPRS accuracy standards for large-scale maps, 1068–1070.
68. Benassi, F., Dall'Asta, E., Diotri, F., Forlani, G., Morra di Cella, U., Roncella, R., & Santise, M. (2017). Testing accuracy and repeatability of UAV blocks oriented with GNSS-supported aerial triangulation. *Remote Sensing*, 9(2), 172.
<https://doi.org/10.3390/rs9020172>
69. Cryderman, C., Mah, S. B., & Shufletoski, A. (2014). Evaluation of UAV photogrammetric accuracy for mapping and earthworks computations. *Geomatica*, 68(4), 309-317. <https://doi.org/10.5623/cig2014-405>
70. Rehak, M., & Skaloud, J. (2015). Fixed-wing micro aerial vehicle for accurate corridor mapping. *ISPRS Annals of the Photogrammetry, Remote Sensing and Spatial Information Sciences*, 2, 23-31.
<https://doi.org/10.5194/isprsannals-II-1-W1-23-2015>
71. Whitehead, K., & Hugenholtz, C. H. (2015). Applying ASPRS accuracy standards to surveys from small unmanned aircraft systems (UAS). *Photogrammetric Engineering & Remote Sensing*, 81(10), 787-793.
<https://doi.org/10.14358/PERS.81.10.787>
72. Wierzbicki, D., Kedzierski, M., & Fryskowska, A. (2015). Assessment of the influence of UAV image quality on the orthophoto production. *The International Archives of the Photogrammetry, Remote Sensing and Spatial Information Sciences*, 40, 1-8. <https://doi.org/10.5194/isprsarchives-XL-1-W4-1-2015>
73. Pérez, M., Agüera, F., & Carvajal, F. (2013). Low cost surveying using an unmanned aerial vehicle. *The International Archives of the Photogrammetry, Remote Sensing and Spatial Information Sciences*, 40, 311-315. <https://doi.org/10.5194/isprsarchives-XL-1-W2-311-2013>
74. Hill, A. C. (2019). Economical drone mapping for archaeology: Comparisons of efficiency and accuracy. *Journal of Archaeological Science: Reports*, 24, 80-91.
<https://doi.org/10.1016/j.jasrep.2018.12.011>
75. Hastaoğlu, K. Ö., Gül, Y., Poyraz, F., & Kara, B. C. (2019). Monitoring 3D areal displacements by a new methodology and software using UAV photogrammetry. *International Journal of Applied Earth Observation and Geoinformation*, 83, 101916.
<https://doi.org/10.1016/j.jag.2019.101916>
76. Hastaoglu, K. O., Kapicioglu, H. S., Gül, Y., & Poyraz, F. (2023). Investigation of the effect of height difference and geometry of GCP on position accuracy of point cloud in UAV photogrammetry. *Survey Review*, 55(391), 325-337.
<https://doi.org/10.1080/00396265.2022.2097998>
77. Deliry, S. I. (2020). Accuracy analysis and evaluation of UAS photogrammetry and structure from motion in engineering surveying. [Master's thesis, Anadolu University].



© Author(s) 2024. This work is distributed under <https://creativecommons.org/licenses/by-sa/4.0/>



A practical software package for estimating the periodicities in time series by least-squares spectral analysis

Ramazan Alpay Abbak*¹ 

¹ Konya Technical University, Department of Geomatics Engineering, Türkiye, raabbak@ktun.edu.tr

Cite this study:

Abbak, R. A. (2024). A practical software package for estimating the periodicities in time series by least-squares spectral analysis. *International Journal of Engineering and Geosciences*, 9 (2), 191-198

<https://doi.org/10.26833/ijeg.1366950>

Keywords

Least-squares principle
Periodicity
Spectral analysis
Tide-gauge data

Research Article

Received: 26.09.2023
Revised: 03.12.2023
Accepted: 09.12.2023
Published: 23.07.2024



Abstract

The researchers investigate some phenomena by continuously observing physical variables, i.e., time series. Nowadays, the Least-Squares Spectral Analysis (LSSA) technique has been preferred for the analysis of time series to conduct more reliable analysis. This technique uses the least-squares principle to estimate the hidden periodicities in the time series. Based on the previous investigations, LSSA gives more reasonable results in the experimental time series that have disturbing effects such as the datum shifts, linear trend, unequally spaced data and etc. The LSSA method is a unique method that can overcome these problems without pre-processing the original series. However, a practical and user-friendly software package in C programming language is not available for scientific purposes to implement the LSSA method. In this paper, we review the computational scheme of the LSSA method, then a software (LSSASOFT) package in the C programming language is developed in the view of the simplicity of the method and compatibility of all types of data. Finally, LSSASOFT is applied in two sample studies for the determining hidden periods in the synthetic data and sea level observations. Consequently, the numerical results indicate that LSSASOFT is a useful tool that can efficiently predicting hidden periodicity for the experimental time series that have disturbing effects.

1. Introduction

It is customary to analyse the successive observations which are ordered chronologically, i. e., time series. There are two main aims of the time series analysis: (i) understanding the nature of the phenomena represented by the sequence of observations, and (ii) predicting the future from the observed time series variables [1-3].

The spectral analysis of any time series means that the hidden periodicities are determined in the data, particularly, the researchers investigate some phenomena in order to identify the physical processes that cause periodic behaviours. For this purpose, a variety of methods have been recently developed and inter-compared in the literature such as Fourier, singular spectrum, wavelet, and least-squares spectral analysis [3-5].

Occasionally, the time series originating from certain experiments (experimental measurements) have many disturbances that directly affect the analysis. Some disturbing effects are the presence of datum shift, trend, short gap, unequally spaced data, and weighted data in the time series. In practice, several temporary solutions

are performed to overcome these difficulties. For instance, (i) the trend (linear) is removed before the analysis; (ii) if the data includes two or more datum shifts, every datum is analysed separately, which means the disorder of complete analysis; (iii) when the time series have short gaps or unequally spaced data, the gaps or certain values are predicted and filled by using the harmonic analysis or any interpolation technique [5]. The whole solutions discussed above change the spectral content of the time series. Thus, an alternative technique is developed without the corruption of data originality, which is called "Least Squares Spectral Analysis (LSSA)". The previous investigations indicate that the LSSA method gives more reasonable results in the experimental time series, compared with other spectral analysis methods [5-8].

The LSSA method was first invented and published by Petr Vanicek who is one of the most famous geodesists [9,10]. Therefore, this method was also so-called "Vanicek Spectral Analysis" in geodetic literature [11].

Later, Vanicek and his colleagues released an improved version of the method furnished with a primitive FORTRAN codes [12]. Many researchers

successfully applied this technique in some fields, especially, in geodesy and related disciplines such as electronic distance measurement, tidal data, superconducting gravimeter data, star positioning, earth-quake, temperature estimating, and seismic data [4, 13-18]. However, a practical and user-friendly software package in the C programming language is still not publicly available for the scientific communities, although a MATLAB code can be found in the literature [17]. As is known, FORTRAN programming is an old fashion language which is not easily understandable for new generation programmers. Hence, as an alternative, an open-source scientific program is developed in the C platform and presented to global users by adding a new algorithm and some elective options as well as considering the former FORTRAN codes written by [12].

The manuscript begins with a brief review of the computational scheme of the LSSA method in section 2. Then, the software which employs the LSSA approach with the new algorithm is presented and discussed in section 3. Afterwards, the paper is followed by two numerical applications based on the simulated and real data, respectively, in section 4. Finally, a short summary concludes the paper in section 5.

2. Least-squares spectral analysis

This section shortly discusses the general structure of any time series, then, briefly reviews the computational scheme of the LSSA method which is used in the software.

2.1. Basic approach

The LSSA method is an application of the least-squares approach in the spectral analysis of time series. This method utilises the least squares approximation to minimize the norm of the residual vector of the time series by estimating the periodic components as well as non-periodic ones [19].

The empirical time series consist of signal and noise. The noise which is the disturbing effect on the observation is divided into two components: random (white) and systematic (coloured). An ideal noise called "white noise" is uncorrelated with any dependent variable. Nevertheless, in practice, a systematic noise called "coloured noise" occurs and is correlated with one or more variables. Systematic noise can be defined by mathematical functions, but their magnitudes are not known in the time series. It is categorized into two types: periodic and non-periodic. The main aim of the LSSA method is to be able to determine these systematic noises (both periodic and non-periodic) simultaneously [19].

2.2. Mathematical theory

The mathematical background of the spectral analysis can be described as follows;

1. vector of observation time: $t_i, i = 1, 2, \dots, n$
2. vector of observables: $f(t_i)$
3. vector of frequencies for which spectral values are desired: $\omega_j, j = 1, 2, \dots, m$

The $s(\omega_j)$ vector which is the spectral value of the ω_j frequency, is sought by the spectral analysis. There are a wide range of ways of calculating a spectrum from the time series. Here, we simply state the problem in the Least Squares Approximation (LSA). Thus, the time series can be modelled by Equation 1.

$$g = Ax \tag{1}$$

where A is the coefficients matrix designing the mathematical relationship between the vectors of observations and unknown parameters. The elements of the design matrix are summarized by Equation 2:

$$A = \begin{bmatrix} \cos \omega_j t_1 & \sin \omega_j t_1 \\ \cos \omega_j t_2 & \sin \omega_j t_2 \\ \vdots & \vdots \\ \cos \omega_j t_n & \sin \omega_j t_n \end{bmatrix} \tag{2}$$

where n represents maximum number of elements.

For computing these parameters by the least-squares approximation, the square root of differences between f and g functions should be minimum. Using the standard least-squares notation [20], we can write it as (Equation 3).

$$\hat{r} = f - \hat{g} = f - A(A^T P A)^{-1} A^T P f \tag{3}$$

where \hat{r} is the residual vector, \hat{g} is the best approximation of f by the least squares method. A spectral value can be calculated by the ratio (Equation 4),

$$s = \frac{f^T \hat{g}}{f^T f} \tag{4}$$

where T denotes transpose of the matrix.

In the case where the spectral value is desired to compute for a frequency ω_j , the result is calculated by (Equation 5).

$$s(\omega_j) = \frac{f^T \hat{g}(\omega_j)}{f^T f} \tag{5}$$

In the parameter estimation methodology through the least-squares approximation, it is essential important to evaluate the results, statistically. Therefore, another great advantage of the LSSA method is that the significance of peaks in the spectrum can be tested statistically in a rigorous manner, which is called confidence level.

Pagiatakis [21] introduces a test as follows: a statistical test of null hypothesis $H_0 : s(\omega_j) = 0$ can be tested with a decision function by Equation 6.

$$s(\omega_j) \begin{cases} < (1 + (\alpha^{-2m/v} - 1)^{-1})^{-1} ; \text{accept } H_0 \\ > (1 + (\alpha^{-2m/v} - 1)^{-1})^{-1} ; \text{reject } H_0 \end{cases} \tag{6}$$

where α is the significance level (usually 5%), m is the number of frequencies participated in simultaneously estimation of the LSSA, v is the degree of freedom.

2.3 LSSA with the known constituents

For some applications, it is known that there are some constituents (e. g. datum shift) in the time series. In this case, we should know something about constituents to deal with them more efficiently. In other words, we know the type of base functions $\phi_i(t)$, but do not need to know the magnitudes of the constituents in the experimental time series. Hence, it is given by Equation 7.

$$f(t) = \sum_i^{NK} c_i \phi_i(t) \quad (7)$$

where NK is the number of known constituents, c_i are the unknown parameters. We know all the $\phi_i(t)$, but not the coefficients c_i in any time series. Thus, the design (coefficients) matrix can be divided into the known constituents and spectral functions ($\cos \omega_j$, $\sin \omega_j$). The design matrix A can be extended as follows (Equation 8).

$$A = \begin{bmatrix} \phi_1 & \phi_2 & \dots & \phi_{NK} & \cos \omega_j t_1 & \sin \omega_j t_1 \\ \phi_1 & \phi_2 & \dots & \phi_{NK} & \cos \omega_j t_2 & \sin \omega_j t_2 \\ \vdots & \vdots & \ddots & \vdots & \vdots & \vdots \\ \phi_1 & \phi_2 & \dots & \phi_{NK} & \cos \omega_j t_n & \sin \omega_j t_n \end{bmatrix} \quad (8)$$

Thereby, the known constituents are not necessary to be removed from f before the evaluation of the spectrum [10].

Accordingly, three types of known constituents are inserted into the software. [12] explains their base functions in detail. They are concisely reviewed as follows:

- datum bias ($\phi(t) = 1$): For example, a tide gauge is moved to other places a few times during the sea level observations. The dates of the movement are well-documented, but the vertical relationship of the movement is not reported properly.
- linear trend ($\phi(t) = t$): For example, the dock where a tide gauge is located, is slowly sinking into the seabed. Another reason may be that the mean sea level is rising due to global warming.
- forced period ($\phi_1(t) = \cos \mu t$ and $\phi_2(t) = \sin \mu t$). For example, it is known that the time series consists of some frequencies, so we desire to remove these frequencies from the series and to analyse what is remained.

The known constituents mentioned above can be modelled and removed from the given time series simultaneously, then, the residual time series is examined by the LSSA method.

3. LSSASOFT: Software for Estimating Periodicities in Time Series

This section is dedicated to providing a comprehensive explanation of the structure of the software, named 'Least Squares Spectral Analysis SOFTWARE (LSSASOFT),' which is encoded in the C++ platform. Furthermore, the author has rigorously

integrated a new approach into the software to accelerate the LSSA procedures.

3.1 Functions of the software

The LSSASOFT comprises a main function and four sub-functions (subroutines): SPEC, BASE, CHLS, and HELP. Below are brief descriptions of these functions:

- MAIN function: At first, it takes the data file name and all options from the command line (i.e. console user interfaces). In the data file, every record should include the time and variable, respectively. The program enables the evaluation of the weighted data in the case that the third column should be the weight of the observation. In this case, user do not need to revise the software namely, it directly reads the third column. Afterwards, considering the options and the other parameters, all periodic components obtained from the time series are reflected to the screen sequentially.
- SPEC function: It computes the spectral values of the frequencies determined at the beginning of the MAIN function. Wells et al. [12] introduces two algorithms that estimate the spectral values: the first is for equally spaced data and the other is for unequally spaced data. The algorithm for unequally spaced data covers that for equally spaced data. Nevertheless, the algorithm for equally spaced data is faster than the other with respect to the computation time [12]. In the current software, the algorithm for unequally spaced data was preferred by considering the advances in today's computer technology, because the time differences between two algorithms can be comfortably neglected.
- BASE function: It calculates the functional values of the known constituents stated in the user's options. This function concerns three types of known constituents, i. e., the datum bias, linear trend, and forced period. Indeed, the type of known constituent in the time series may be more than three, in this case, the interested users can easily adopt a new constituent (e. g. an exponential trend) according to their experiences.
- CHLS function: It computes the inversion of the normal equation matrix through the use of Cholesky decomposition. Cholesky decomposition is integrated into LSSASOFT due to its compatibility with symmetric and positive-definite matrices. Interested readers can replace the function with a more efficient algorithm such as the LU (Lower-Upper) decomposition.
- HELP function: It offers an overview of the software. When you input the '-h' option or unexpected options, the HELP function becomes active. It elaborates on how LSSASOFT functions alongside different options and outlines the necessary parameters for each option.

3.2 New algorithm

In order to expedite the computational procedures of the LSSA method, a new algorithm designed by the

author is adapted to the LSSASOFT. This algorithm automatically enables the determination of the periods in the time series.

The normal procedure of the LSSA method is following: firstly, the time series and its constituents (linear trend, datum shifts, and forced periods) are read from the data and options files, then the spectral values of the whole frequencies determined by the user are computed, finally, the peaks over the confidence level are manually determined as indicators of the periodicities. Every periodicity determined in the previous step is sequentially suppressed by adding it to a forced period for the purpose of detecting other un-catched periodicities manually [22]. Moreover, the user should know the approximate spectral band to determine the periodicities very well, which means that analyst should be expert on the subject. These procedures are time consuming and laborious tasks for the analysts to get reliable results.

Considering all these limitations, a new algorithm was developed in this study as:

1. start,
2. get the parameters from the command line (LT: linear trend, NDAT: number of datum bias, DAT: times of datum bias, NPER: number of forced periods, PER: forced periods), and read the data file (f(t)),
3. produce all periods (P) ranging from 0.5 (corresponding to the nyquistik frequency) and N/2 (the half-length of the data),
4. compute the spectral value of every period (S(P)) increased by δt ,
5. determine the period (p) corresponding to the highest spectral value (S_{max}),
6. if this spectral value is lower than the confidence level (CL), exit to the program successfully.
7. otherwise, zoom this period (p) by giving ± 1 to the interval, i. e., the new spectral band is ranging from $p - 1$ to $p + 1$ in order to determine the period more precisely,
8. compute the spectral values of all periods in the new interval,
9. promote the period whose spectral value is the highest in all, to the forced period, and print to screen,
10. return to item 3.

The flow chart of the algorithm is pictured in Figure 1. In order to assess the performance of this algorithm, two example applications are done in the next section. The data files are provided together with the program in the case that the user re-simulates the results and checks the implementations.

4. Numerical applications

In order to exemplify the capabilities of the LSSASOFT and the usefulness of the new algorithm in the studies, two representative sample data were analysed separately. In the first example, we used synthetic data which comprises 300 records. In the second example, we utilized the hourly sea level observations obtained from the Antalya tide-gauge in 1990, Türkiye. Hence, it was

shown whether the periods estimated by the software are reliable or not.

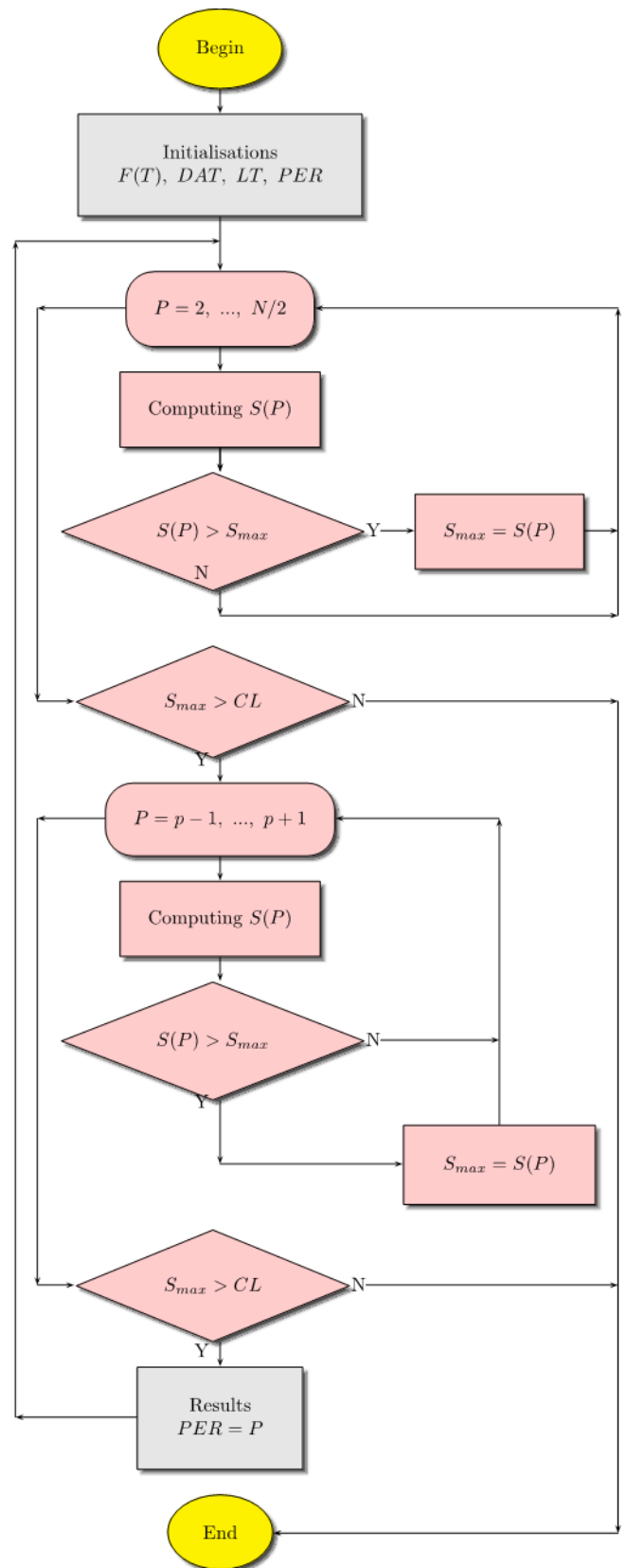


Figure 1. The flow chart of new algorithm added to the software.

4.1 Testing the software on synthetic data

In this example, synthetic data representing a typical

coloured time series, was generated from Equation (9) which is partly used by [12]. This series was equally spaced and equally weighted with no covariance information, subsequently, it was chosen to perform the statistical testing at the 99% confidence level, which is the most rigorous option in geodetic literature.

The mathematical illustration of the test time series is given as:

$$f(t) = c_i + 0.01t + \sum_{j=1}^4 (a_j \cos \mu_j t + b_j \cos \mu_j t) \quad (9)$$

where t is the time (unit: year), c_i is the datum bias, μ_j is the periodic component, a_j and b_j are the coefficients of the periodic components.

Three hundred values of f , which spans 50 years were calculated and grouped into four sub-intervals consisting of equally spaced data, that is

$$t \in D_k, k = 1, 2, 3, 4,$$

where

- $D_1 \equiv [0.1, 0.2, \dots, 10.0]$ years (100 values)
- $D_2 \equiv [20.1, 20.2, \dots, 25.0]$ years (50 values)
- $D_3 \equiv [28.1, 28.2, \dots, 40.0]$ years (120 values).
- $D_4 \equiv [47.1, 47.2, \dots, 50.0]$ years (30 values)

The datum biases are $c_1 = 1.0, t \in D_1; c_2 = -1.0, t \in D_2; c_3 = 3.0, t \in D_3, D_4$. The coefficients of the trigonometric terms are $a_j = 0.5, 1.0, 0.0, -0.25; b_j = 1.0, 0.5, 1.0, 0.0$, respectively. The periods are $p_j = 2\pi/\mu_j = 2.759, 3.636, 5.714, 18.0$ years. Figure 2 displays the behaviour of test series under investigation.

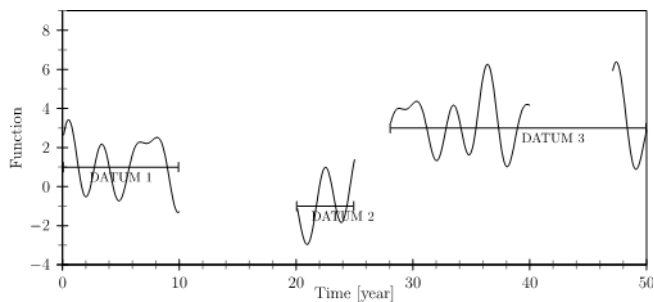


Figure 2. Graph of the test time series.

According to these parameters, the software run with the following options:

```
./LSSASOFT test.dat -d3/0.1/20.1/28.1 -l
```

where the “test.dat” file contains the test time series made of time and value which are available along with the software package; the “d” option denotes the number of datum bias and times of datum biases in sequence; the “l” option means that the time series posses the linear trend. The numerical results from the analysis are listed in Table 1.

According to Table 1, the periodicities in the test series were successfully determined by the LSSASOFT. The differences between the real and estimated values are very small, which is negligible in the numerical analysis.

Table 1. The numerical results from running the LSSASOFT by the first test time series.

Number	Real period	Estimated period	Spectral value	Differences
1	2.759	2.758	94.81	0.001
2	3.636	3.629	44.13	0.007
3	5.714	5.726	43.09	0.012
4	18.00	17.671	52.69	0.329

4.2 Sea level observations

In the second example, we utilized the real sea level observations supplied from the Antalya tide-gauge in 1990 in Türkiye. These observations were selected as test data because they inherently involved all kinds of disturbances due to the fact that the tide-gauge had a classical instrument.

Before the analysis, the general structure of the sea level data should be considered more closely. Accordingly, the sea level observations are decomposed to three components (Equation 10) [23]:

$$\text{Observation} = \text{mean sea level} + \text{tides} + \text{atmospheric residuals} \quad (10)$$

where all components are related with the different physical process and uncorrelated with each other. The mean sea level is determined by averaging hourly data at least 20 years long since the longest period of tidal components is 18.6 years. Accordingly, the tides are the periodic sea level changes that are consistent with some geophysical effects, and are of the certain amplitude and phase [24]. Atmospheric residuals are irregular variations related with weather conditions, which is the so-called “surge effect”.

The tides mentioned above are simply explained by Newton’s gravity force. This force (F) is summarized by (Equation 11).

$$F = -G \frac{m_1 m_2}{r^2} \quad (11)$$

where G denotes the Newtonian gravitation constant, r represents the distance between m_1 and m_2 . Provided that the masses of the Earth and the Moon, and also the distance between the planets are inserted to the equation, the result is the gravitational force between them. The gravitation between the Earth and Sun can be achieved similarly. Both gravitations affect the sea level changes in the same periods with the movements of the Sun and the Moon [25]. Accordingly, tidal components are demonstrated in Table 2.

Table 2. The primary short tidal components [26].

Tidal components	Real Period	Description	Explanation
M2	12.4206	Principal lunar	Semi-diurnal
S2	12.0000	Principal solar	Semi-diurnal
N2	12.6584	Larger Lunar elliptic	Semi-diurnal
K2	11.9673	Luni-solar	Semi-diurnal
K1	23.9344	Luni-solar diurnal	Diurnal
Q1	25.8194	Principal lunar diurnal	Diurnal
P1	24.0659	Principal solar diurnal	Diurnal
Q1	26.8684	Larger Lunar elliptic	Diurnal

Before the numerical analysis of our sea level observation, the observations were plotted month by month. While the observations are examined carefully, it is clear that there is a variety of difficulties (e. g. gappy data, linear trend) in the time series (Figure 3).

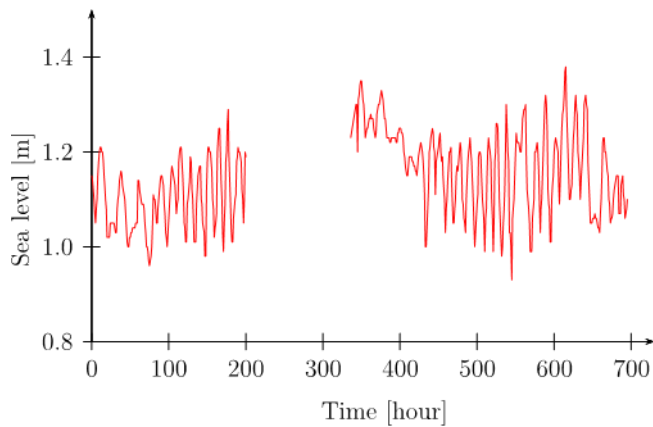


Figure 3. A sample data from the Antalya tide gauge (April 1990).

The hourly sea level data obtained from every month was analysed in a sequence. As a result of this analysis, two dominant periods were successfully estimated in the sea level observations (Table 3). Unfortunately, others are not determined due to the data length (i. e. one month long).

Table 3. The numerical results from the running the LSSASOFT by the sea level series.

Month	Period 1	Period 2
January	11.998	12.416
February	12.009	12.437
March	11.957	12.393
May	11.860	12.337
June	12.325	12.386
July	11.987	12.405
August	11.987	12.418
September	11.971	12.393
October	11.982	12.405
November	12.048	12.447
December		12.418
Average	12.013	12.412
Std.	0.11	0.037

In order to check whether the results are compatible with astronomical counterparts, a test was carried out by using the student distribution (t test). A statistical test of null hypothesis $H_0: \bar{x} = \mu_0$ can be tested through a decision function by Equation 12.

$$t_{test} = \frac{|\bar{x} - \mu_0|}{\sigma_x / \sqrt{n}} \begin{cases} \leq t_{\alpha, f} & ; \text{accept } H_0 \\ > t_{\alpha, f} & ; \text{reject } H_0 \end{cases} \quad (12)$$

where α is the significance level (5%), f is the degree of freedom, σ_x is the standard deviation of the periodicity, \bar{x} denotes the average value of the periodicity, μ_0 represents the astronomical value of the periodicity.

As a result of the test, all periods derived from the analysis are well-consistent with the astronomical

counterparts at a confidence level of 95%. This result indicates that the software is successful on the determination of the hidden periodicity in the time series induced by the disturbing effects.

Although there are totally eight diurnal and semi-diurnal tidal components, two of them could be determined by using the program in the current study, which are compatible with a previous study done by FORTRAN codes [27]. The reasons of incomplete frequencies are evaluated that the other components might have low amplitudes, or that the dock structure and geographical position of the tide gauge might be unsuitable to sense the other tidal components.

On the other hand, nowadays the least squares principle has been frequently employed in some geodetic problems such as gravimetric geoid determination [28,29].

4. Conclusion

The present contribution has reviewed the fundamental theory of the LSSA approach to spectral analysis of time series. The LSSA is an efficient method to determine the periodicities in the empirical time series that have difficulties. Then, an open-source software package developed according to the mentioned theory of the LSSA approach is presented by adding a new algorithm with a range of elective options. Lastly, the present paper is continued by two numerical applications based on the synthetic and real data, respectively. The numerical analyses point out that the LSSASOFT produces considerably reasonable results in both time series.

The current contribution focuses on the significant computational aspects of the LSSA approach. To determine the best solution for estimating periodicities using LSSASOFT, we strongly encourage interested users to run the software with their data, experiment with various modifications, compare the results, and draw conclusions based on their test results.

From another perspective, the software is intentionally designed to consist of a range of different sub-routines. This structure enables end users to replace their specific sub-routines (e.g., adding an alternative base function and inverse function for normal equation matrix etc.) without adversely affecting the remaining components of LSSASOFT.

As a result, the software is highly structured and user-friendly, making it suitable for academic purposes. We hope that the availability of LSSASOFT will encourage researchers in various scientific fields to apply the LSSA method to their data, including disciplines such as GNSS (Global Navigation Satellite Systems) coordinate time series, which mostly exhibit discontinuities (offsets) and linear trends due to tectonic phenomena.

As a future work, it is noteworthy mentioned here that the extended version of LSSA, such as Least Squares Wavelet Analysis [30] can be also developed in the C programming language. Hence, a rich C/C++ library about spectral analysis may be created for the scientific communities.

Acknowledgement

The author cordially thanks to eng. Habibe Saraçoğlu for assistance with typesetting the manuscript and fruitful discussions during the compilation of the manuscript. The author is grateful to General Directorate of Mapping for providing the sea level data.

Computer code availability

The current software, developed in the C programming language, is freely available under the GNU General Public License. Interested readers can access the software, along with synthetic and experimental data, on GitHub at www.github.com/aabbak/LSSASOFT. The author welcomes inquiries and bug reports related to the software.

Conflicts of interest

The authors declare no conflicts of interest.

References

- Zeray Öztürk, E., & Abbak, R. A. (2020). PHCSOFT: A Software package for computing physical height changes from GRACE based global geopotential models. *Earth Science Informatics*, 13(4), 1499-1505. <https://doi.org/10.1007/s12145-020-00490-5>
- Zeray Öztürk, E., Godah, W., & Abbak, R. A. (2020). Estimation of physical height changes from GRACE satellite mission data and WGHM over Turkey. *Acta Geodaetica et Geophysica*, 55(2), 301-317. <https://doi.org/10.1007/s40328-020-00294-5>
- Beşel, C., & Kayıkçı, E. T. (2020). Investigation of Black Sea mean sea level variability by singular spectrum analysis. *International Journal of Engineering and Geosciences*, 5(1), 33-41. <https://doi.org/10.26833/ijeg.580510>
- Erol, S. (2011). Time-frequency analyses of tide-gauge sensor data. *Sensors*, 11(4), 3939-3961. <https://doi.org/10.3390/s110403939>
- Abbasi, M. (1999). Comparison of Fourier, least-squares and wavelet spectral analysis methods, tested on Persian Gulf tidal data. [Master's Thesis, KN Toosi University of Technology].
- Craymer, M. R. (1998). The least squares spectrum, its inverse transform and autocorrelation function: theory and some applications in geodesy. [Doctoral Dissertation, University of Toronto].
- Abbak, R. A., & Yerci, M. (2012). En küçük karelerle spektral analiz ve fourier tekniğinin karşılaştırılması. *Selcuk University Journal of Engineering Sciences*, 11(1), 32-47.
- Ghaderpour, E., Ince, E. S., & Pagiatakis, S. D. (2018). Least-squares cross-wavelet analysis and its applications in geophysical time series. *Journal of Geodesy*, 92(10), 1223-1236. <https://doi.org/10.1007/s00190-018-1156-9>
- Vaniček, P. (1969). Approximate spectral analysis by least-squares fit: Successive spectral analysis. *Astrophysics and Space Science*, 4, 387-391. <https://doi.org/10.1007/BF00651344>
- Vaniček, P. (1971). Further development and properties of the spectral analysis by least-squares. *Astrophysics and Space Science*, 12, 10-33. <https://doi.org/10.1007/BF00656134>
- Taylor, J., & Hamilton, S. (1972). Some tests of the Vaniček method of spectral analysis. *Astrophysics and Space Science*, 17, 357-367. <https://doi.org/10.1007/BF00642907>
- Wells, D. E., Vaniček, P., & Pagiatakis, S. D. (1985). Least squares spectral analysis revisited. Technical Report 84, Geodesy and Geomatics Engineering, University of New Brunswick, Canada.
- Espy, P. J., & Witt, G. (1996). Observation of a quasi 16-day oscillation in the polar summer mesospheric temperature. *Geophysical Research Letters*, 23(10), 1071-1074. <https://doi.org/10.1029/96GL01068>
- Mantegazza, L. (1997). High azimuthal number pulsation modes in fast rotating delta Scuti stars: the case of HD 101158= V837 Gen. *Astronomy and Astrophysics*, 323, 844-852.
- Abd El-Gelil, M., Pagiatakis, S., & El-Rabbany, A. (2010). Normal mode detection and splitting after Sumatra-Andaman earthquake. *Journal of Geodynamics*, 50(2), 49-56. <https://doi.org/10.1016/j.jog.2010.02.003>
- Abbasi, M., & Mashhadizadeh Maleki, S. (2017). Iranian surface air temperature periodicities and correlations with the North Atlantic and Indian Ocean Sea surface temperature variations. *Meteorological Applications*, 24(2), 268-275. <https://doi.org/10.1002/met.1625>
- Ghaderpour, E., Liao, W., & Lamoureaux, M. P. (2018). Antileakage least-squares spectral analysis for seismic data regularization and random noise attenuation. *Geophysics*, 83(3), V157-V170. <https://doi.org/10.1190/geo2017-0284.1>
- Omerbashich, M. (2003). Earth-Model Discrimination Method. [Doctoral Dissertation, University of New Brunswick].
- Amerian, Y., & Voosoghi, B. (2011). Least squares spectral analysis for detection of systematic behaviour of digital level compensator. *Journal of Geodetic Science*, 1(1), 35-40. <https://doi.org/10.2478/v10156-010-0005-4>
- Vanicek, P. & Krakiwsky, E. (1987). *Geodesy: The Concepts*, 2. Elsevier Science Publishers B.V.
- Pagiatakis, S. D. (1999). Stochastic significance of peaks in the least-squares spectrum. *Journal of Geodesy*, 73, 67-78. <https://doi.org/10.1007/s001900050220>
- Abd El-Gelil, M., Pagiatakis, S., & El-Rabbany, A. (2008). Frequency-dependent atmospheric pressure admittance of superconducting gravimeter records using least squares response method. *Physics of the Earth and Planetary Interiors*, 170(1-2), 24-33. <https://doi.org/10.1016/j.pepi.2008.06.031>
- Ainscow, B., Blackman, D., Kerridge, J., Pugh, D., & Shaw, S. (1985). *Manual on sea level measurement and interpretation*, I.
- Abbak, R. A. (2005). Deniz düzeyi gözlemlerinin en küçük kareler yöntemiyle spektral analizi. [Master's Thesis, Selcuk University].

25. Maul, G. A., & Yanaway, A. (1978). Deep sea tides determination from GEOS-3. Collected Reprints, 78.
26. Stewart, R. H. (2004). Introduction to physical oceanography. Texas A&M University, USA.
27. Abbak, R. A. (2023). Least-Squares Spectral Analysis of Hourly Tide Gauge Data–A Case Study: LSSA of Hourly Tide-Gauge Data. *Advanced Geomatics*, 3(1), 23-27.
28. İl, H. T. A., Abbak, R. A., Bildirici, İ. Ö., & Demir, S. (2018). SRTM1 ve ASTER sayısal yükseklik modellerinin gravimetrik jeoit belirlemeye katkısı. *Geomatik*, 3(3), 203-212. <https://doi.org/10.29128/geomatik.402331>
29. Demir, S., Abbak, R. A., & İl, H. T. A. (2018). Global yerpotansiyel modellerin gravimetrik jeoit belirlemeye katkısı. *Geomatik*, 3(3), 213-224. <https://doi.org/10.29128/geomatik.403776>
30. Ghaderpour, E., & Pagiatakis, S. D. (2017). Least-squares wavelet analysis of unequally spaced and non-stationary time series and its applications. *Mathematical Geosciences*, 49, 819-844. <https://doi.org/10.1007/s11004-017-9691-0>



© Author(s) 2024. This work is distributed under <https://creativecommons.org/licenses/by-sa/4.0/>



GIS-based determination of potential snow avalanche areas: A case study of Rize Province of Türkiye

Ebru Colak ¹, Gamze Bediroglu ², Tugba Memisoglu Baykal ^{*3}

¹ Karadeniz Technical University, Department of Geomatics Engineering, Türkiye, ecolak@ktu.edu.tr

² Kilis 7 Aralık University, Vocational School of Technical Sciences, Türkiye, gamze.bediroglu@kilis.edu.tr

³ Ankara Hacı Bayram Veli University, School of Land Registry and Cadastre, Türkiye, tugbamemisoglu@gmail.com, tugba.memisoglubaykal@hbv.edu.tr

Cite this study:

Colak, E., Bediroğlu, G., & Baykal, T. M. (2024). GIS-based determination of potential snow avalanche areas: A case study of Rize Province of Türkiye. *International Journal of Engineering and Geosciences*, 9 (2), 199-210

<https://doi.org/10.26833/ijeg.1367334>

Keywords

Snow avalanche
Potential avalanche areas
GIS
Spatial analysis
Rize

Abstract

Natural hazards are a part of critical issues affecting people and the environment. One of these natural hazards is snow avalanches. With the increase in the world population, it has emerged that decision-makers should take precautions against such natural hazards for population movements, construction, transportation, and tourism. Essential solution parts of this problem lay behind surveying, GIS, and spatial analysis-planning. This situation will be primarily due to the snow conditions, but certain terrain areas are susceptible. Snow avalanches' release mechanism depends on many factors, such as terrain, meteorological reports, snowpack, and other triggering parameters. Areas with certain topographical features that allow the deposition of snow masses are called avalanche-release areas. GIS helps to make decisions concerning spatial planning within avalanche release areas and finding risky zones. This study aimed to determine the potential avalanche release areas in the GIS environment in Rize, Türkiye, which was chosen as the pilot region. In the study, the detection of these avalanche areas was estimated using a mathematical equation model proposed by Hreško (1998) and determined with the help of GIS. Factors such as elevation, curvature, aspect, slope, and land cover type were used to estimate avalanche risk areas. A Model Builder workflow has also been created to automate the process stages. As a result of the study, avalanche risk areas were determined and mapped for the Rize mountainous region.

Research Article

Received: 27.09.2023
Revised: 25.03.2024
Accepted: 05.04.2024
Published: 23.07.2024



1. Introduction

Natural disasters are among the critical problems that the world faces and affect people and the environment. One of the most important of these is snow avalanches, one of the natural disasters of meteorological character. Avalanches begin when weak layers of snow release the weight of the more stable snowpack above them, and then the snowpack continues to move downhill, accelerating and collecting more snow [1]. These appear as rapid mass movements controlled by weather conditions, snow cover, and topography of the land [2-4]. Avalanches usually occur in mountainous areas, affecting transportation corridors, ski areas, and buildings, disrupting infrastructure, and causing loss of lives. Today, it is experiencing precarious environmental conditions condemning deterioration and causing great harm to people and human-made features, leading to different adverse effects [5]. As a result of these worsening effects, hazard and risk assessment studies

have become necessary to take preventive measures against avalanche events.

Determination of the potential avalanche release area is the first step in avalanche hazard and risk assessment and mapping. The formation of snow avalanches depends on many different parameters. These parameters can be classified into three groups: terrain parameters such as slope, curvature, roughness, and vegetation; meteorological parameters like wind, temperature, amount of snow, and air humidity; snowpack parameters such as weak layers and gain forms [6-8]. In addition, there is the triggering of the avalanche, which can be initiated by additional loading caused by humans naturally by fresh snow or by abrupt warming [6, 7].

GIS has been widely adopted in many fields with the advance of computers, geoinformatics, and their applications [9,10] within natural hazards zoning [11-14]. One of them is the studies in which snow avalanches are detected. GIS helps to make decisions concerning spatial planning within avalanche release areas and

finding risky zones. Terrain models [15] and GIS have been used to estimate the probable avalanche release zones [16-17], model avalanche run-outs [18-19], or assess the protective function of the forest against avalanches [20-22].

Information about snow avalanches, predictions, and mapping of the danger they pose is very important from a scientific point of view [23-24]. Currently, avalanche, snowmelt, and landslide studies are addressed in many studies around the world; Many methods and techniques have been proposed and tried to be put into practice, especially for landslide hazard and risk mapping. Apart from these, there are also studies in which snow avalanche risk zones are detected and integrated with GIS, which is one of the favorites of information systems. In addition, there are analyses in which snow avalanche risk areas are determined using GIS and Multi-criteria decision analysis together. There are also analyses in which snow avalanche risk areas are detected using remote sensing. Potential snow avalanches are determined using machine learning methods that have become popular recently. The literature summary is shown in Table 1.

Modeling is one of the main tools for assessing natural hazards [55]. Modeling techniques are divided into two groups: deterministic and stochastic models. Physical or mathematical models are deterministic models, while models that include an analytic hierarchy process, such as fuzzy logic, are stochastic. In this study, a mathematical model was used to assess snow avalanches. In the literature, different mathematical algorithms are used to model potential snow avalanches and generate risk maps with GIS. Some of these methods were developed by Hreško [16], Barbolini [47], Bühler [7], and Marana [5] at different times. Hreško's [16] model approach was based on terrain factors. This model is developed to identify potential snow avalanche areas. Marana [5] has developed and suggested an avalanche risk model for determining risky areas. His model

included height, slope, aspect, and land use data, and his model (Equation 1):

Table 1. Literature summary.

Reference	Study Region	Analysis method
[25]	-	
[26]	Croatia	
[27]	Western United States	
[28]	Canada	landslide hazard and risk mapping
[29]	-	
[30]	Global	
[31]	Austria	
[32]	-	
[33]	Kazakhstan	
[7]	India	
[14]	Western Himalaya	
[17]	Switzerland	
[34]	Italy	
[35]	-	
[36]	Iran	
[37]	Switzerland	
[38]	Switzerland	
[39]	Switzerland	snow avalanche risk zone mapping with GIS
[40]	Slovakia	
[41]	Türkiye	
[42]	Switzerland	
[43]	USA	
[44]	USA	
[45]	Slovakia	
[46]	Türkiye	
[47]	Between Italy and Switzerland	
[48]	Italy	
[49]	Türkiye	risk analysis using GIS and Multi-criteria decision
[50]	Colorado	
[51]	Serbia	
[52]	India	potential snow avalanche risk analysis using remote sensing
[53]	India	
[54]	Türkiye	Risk analysis using machine learning methods

$$\text{Avalanche Risk} = \text{Risk Height} \times (\text{Risk Slope} + \text{Risk Aspect} + \text{Risk Land - Use}) \quad (1)$$

Based on digital elevation models, Bühler's [7] model was about the automated identification of potential snow avalanche release areas. This model is partly based on the work of Maggioni [56] but has been improved so it can be used on DEM datasets with higher resolutions. The terrain parameters must be defined to identify the potential snow avalanche release areas with this model. Barbolini's [47] model was about avalanche hazard mapping over large undocumented areas [8].

In this investigation, Hreško's equation model was implemented and used to automate avalanche release area mapping in GIS [16]. The reason for this is that it is the most appropriate method to detect snow avalanche areas in the region and also because no study based on this method has been carried out before in our country. The study focused on land parameters; because they can be obtained from digital elevation models (DEMs) and do not change as rapidly as meteorological and snow cover parameters [7]. Terrain can affect areas that are more or less susceptible to avalanches, while terrain parameters

such as slope surface cover and profile curvature will affect the strength of the snowpack. In turn, factors such as aspect will determine the amount of sunlight an area receives and influence temperature direction [1].

Therefore, based on all this information, this study aims to develop a method to estimate potential avalanche release areas in a GIS environment. Rize province of Türkiye, which has high mountain zones named Kackar Mountains, was selected. The land cover layer and Digital Elevation Model (DEM) were this model's main data inputs. Factors such as aspect, slope, plan, and profile curvature were produced from DEM. Each factor and land cover were classified, and the final grid layer was calculated. A model builder was created in these process stages, and the calculation process was automated. As a result, avalanche release areas were estimated and mapped for Rize. This study is important because there is no similar study representing snow avalanches in our country and it will serve as an example for future studies on this subject. A regional study will provide a basis and

guidance for the provinces suffering from snow avalanches.

2. Method

2.1. Methodology

The study consists of 9 stages.

- Selecting the study area
- Determining criteria and obtaining data
- Editing the data and associating it with the coordinates. Conversion of data to WGS 1984 Lambert Conformal Conic projection system.
- Adding the edited data to the geographic database in ArcGIS 10.8.
- Determination of the criteria scores to be used in the avalanche release area determination model
- Application of the avalanche release area determination model to the data

- Detection of potential snow avalanche risky areas as a result of the analysis performed with the model and identification of alternative points
- Presenting visual maps.

2.2. Study area

This study was performed in the Rize province of Türkiye. Rize is located in the northeastern parts of Türkiye and located between 40°21' - 41°25' east longitude and 40°33' - 41°20' north latitude (Figure 1). Rize covers an area of 3,920 km², and 78% of this area is mountains, 21% is plateaus, and 1% is plains. 25% of Türkiye's forest areas are located in the Black Sea region where Rize province is located. The population of Rize in 2018 was 346.608 [57]. Total rainfall values for Rize province are 238 mm for December, 234 mm for January, and 185 mm for February; these months are the coldest periods in Rize [58]. Weather is generally -10°C or colder at high altitude areas.

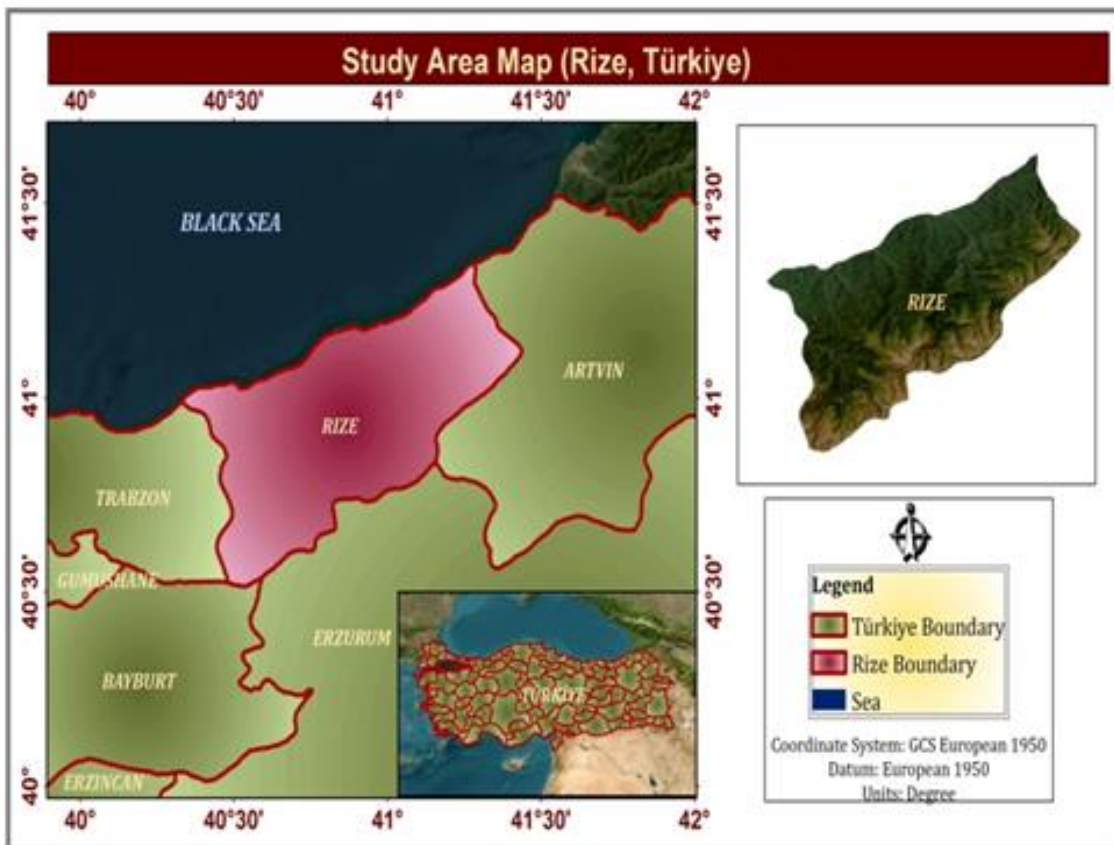


Figure 1. Study area.

The most important reason for choosing Rize is the fact that many avalanche disasters have occurred in this region in the past years has been deemed important in terms of examining the avalanche risk points of the region. The other reason is; that this province is surrounded by high and rugged mountains that extend parallel to the Black Sea. Kackar mountain range is within the boundaries of the province area, one of Türkiye's most important mountains. With a total height of 3,932 meters, the Kackar mountain range is also the highest mountain in the Black Sea Region. The highest peaks of

the Kackar mountain range are Altinparmak (3,480 m), Kavrun (3,932 m), and Vercenik (3,710 m) mountain [59].

2.3. Determining criteria

At this stage, two leading data inputs are needed to identify potential avalanche release areas. These are the land cover and the DEM layer. Apart from these, slope, aspect, plan curvature, and profile curvature are other criteria that should be used in the analysis, but these data

are produced from DEM data. The reason for choosing these data is that they were selected from the criteria considered in the detection studies of potential snow avalanches and that they are criteria that can be provided in the analysis to be carried out in the region. To briefly explain the data used in the analysis;

Land cover: The type of terrain and the land cover influence the strength of a snowpack. A dense enough forest inhibits large avalanche formation because it influences the amount of deposited snow and the stability of the snow cover itself [60-61]. The regions covered by forest are thus excluded from the potential release areas [47]. The falling snow slowly accumulates between the trees and forms an irregular snow cover. In addition, tree trunks can support fixing snow cover to the ground, preventing avalanches from occurring [62]. Open, extensive hollow forests cannot fix the snow mass and prevent avalanche formation [63]. Areas covered with trees, large shrubs, and rocks will provide attachment points where snow can hold. This will increase the strength of the snow mass and become an important trigger by requiring more weight. Barren areas with permanent ice and snow or grassland will increase the likelihood of an avalanche occurring as there will be less friction to stop the avalanche [8].

Elevation: In snow avalanche risk assessment, elevation is an essential parameter because factors such as snowfall, wind, and temperature change depend on the elevation. In higher areas, more snowfall occurs, and more cooling occurs at air temperatures. In addition, as the elevation increases, vegetation can be diluted, exposure to solar radiation is higher, and stronger winds are observed [64].

Slope angle: The priority in the slope parameter is to determine the steepness limit of the slopes. Avalanches are typically released on slopes with inclinations between 30° and 50°, but depending on snow conditions, the range can be; between 25° and 60° [2, 6, 8]. Below 28, the gravitational force is too weak to initiate an avalanche, whereas on slopes steeper than 50, releases are limited to persistent small avalanches [47]. Delparte [19] states that deep snow masses, which cause the formation of large avalanches, cannot accumulate on such slopes if the slope exceeds 60°.

Aspect: It is an essential topographic parameter, but that does not have a direct effect on avalanche formation. It is the direction of the slope. The aspect depends on local circumstances. In the Northern Hemisphere, northern slopes receive less sun than southern slopes. Therefore, a cold snowdrift forms in this area. Eastern slopes will develop a colder snowpack than western slopes due to the difference between morning and afternoon sunlight [1]. The situation in the Southern Hemisphere is the opposite of the Northern Hemisphere.

Curvature: Curvature is examined in two parts: profile and plan curvature. Profile curvature is the curvature in the direction of the maximum slope and is in the vertical direction. Plan curvature is perpendicular to the profile curvature and is in the horizontal orientation. Positive values donate concave slopes, negative values donate convex slopes, and 0 means almost no curvature.

The frequency of formation of avalanches is higher in concave profile global lands [65]. Plan curvature is also defined as several fractures in the avalanche flow path, with a change in inclination of at least 5 ° [66]. The stress areas occurring in the snow cover and the fractures just below it is caused by convexity. Another important factor is land curvature. This factor is used effectively in determining the spatial limitation of avalanche release areas. Those paths that have a concave plan curvature, such as bowls or cirques, can trap blowing snow from several directions about the wind direction [67], while paths that have convex plan curvature have a thinner snowpack because the snow is often blown away [47]. The plan curvature separates open areas from flat and convex areas to define the snow avalanche potential release areas. Open areas differ from convex areas by the following rule [17]:

- Concave zones: plan curvature $\leq - 0.002 \text{ m}^{-1}$
- Flat zones: $- 0.002 \text{ m}^{-1} < \text{plan curvature} < + 0.002 \text{ m}^{-1}$
- Convex zones: plan curvature $\geq + 0.002 \text{ m}^{-1}$

2.4. Obtaining data and data processing

At this stage, the data belonging to the determined criteria were obtained and arranged for use in the analyses. A 10 m interval contours were used for creating DEM, obtained by Karadeniz Technical University (KTU) GISLab. Land cover layer and topography (for DEM) obtained topographical geodatabase provided by the General Directorate of Mapping / Türkiye. The other terrain factors, such as slope, aspect, plan curvature, and profile curvature raster layers, were derived from DEM. The obtained data were converted to the WGS 1984 Lambert Conformal Conic projection system, and all data were made ready for analysis by integrating the geodatabase to be used in the ArcGIS 10.8 program. The provided data is shown in Figure 2.

2.5. Mathematical model of determination potential avalanche area

The mathematical model used to identify potential snow avalanche risk areas has been created in this part of the study. While establishing the mathematical model, the criteria mentioned in the previous paragraphs affecting the avalanche formation were considered.

Hreško (1998) [16] proposed a mathematical equation model to estimate potential avalanche areas [16, 68]. In this study, we used Hreško's model to estimate potential avalanche areas in Rize Province of Türkiye (Equation 2).

$$A_v = (A_l + E_x + F_x + F_y) * S * R_g \quad (2)$$

Here, A_v is the value estimating potential avalanche trigger zones; A_l is the elevation factor; E_x is the aspect factor; F_x is the profile curvature factor; F_y is the plan curvature factor; S is the slope inclination factor, R_g is the land cover factor.

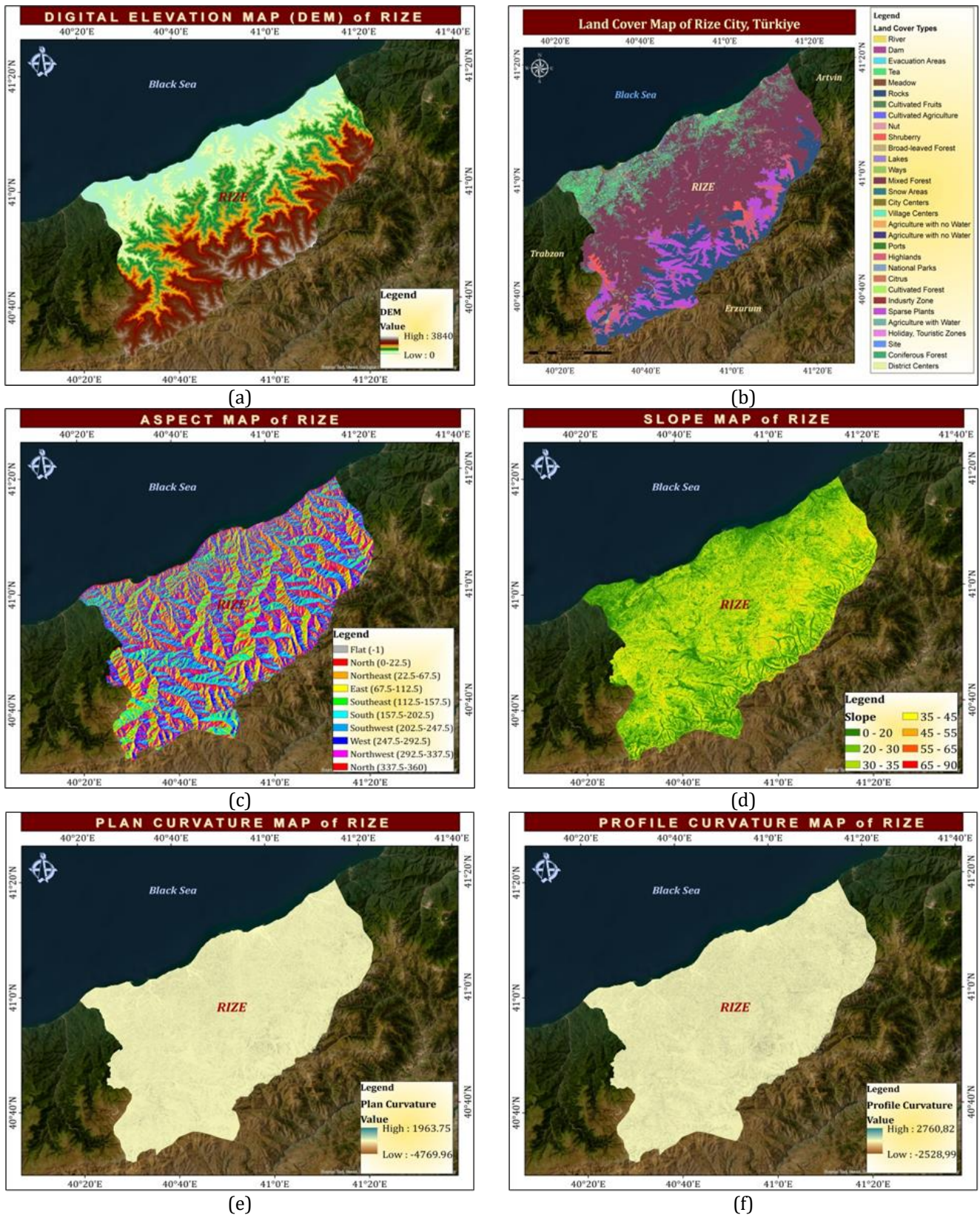


Figure 2. Input geographic data used in the study. Elevation map (a), Land cover map (b), Aspect map (c), Slope map (d), Plan curvature map (e), Profile curvature map (f).

2.6. Reclassifying criteria

The sub-criteria of the criteria required for detecting potential snow avalanche risky areas were determined, and the importance levels of the sub-criteria in determining snow avalanche areas were tried to be determined. At this point, the studies in the literature

were used, and the sub-criteria were classified [5, 6, 7, 22, 40, 63, 69].

North or South Hemisphere directly changes aspect values. Marana [5] has aimed to detect avalanche-risky areas in a North Hemisphere Country, Italy. Türkiye is also located in the North Hemisphere. We have derived aspect classification and score from Marana's study.

Slope score is used widely in most avalanche studies, and the score is similar in different literature studies. In this study, the slope score was derived from McClung and Schaerer [6], Biskupič and Barka [40] and Maers [63]. Plan-profile curvature classification and score were derived from the study by Bühler et al. [7]. The elevation score was derived from Türkiye’s National Avalanche Risk Activation Plan Report [64]. The land cover types score was derived from Marana [5], Biskupič and Barka [22] and Richnavský et al. [70]. Finally, classification and scoring of land cover type factors were done by commenting on related sub-factors of land cover types. With a small example, if a zone is filled with rocks, it means this is a risky area and gets a high score, but if a zone is filled with dense forest, it brings a barrier for avalanches catching snow and getting a low score.

The determined sub-criteria were scored on a scale of 0-10, and their values, which were important in detecting potential snow avalanches, were determined. In this range, 0 indicates the lowest value, while a value of 10 indicates the regions with the highest potential avalanche risk. Table 2 and 3 show the factors, sub-factors, and their scores (points) used in the study. The classification row matches with sub-factors. We have applied all the analysis due to the score calculations shown in the tables.

Table 2. Factor, sub-factors, and their score calculations used in the study.

	Classification	Elevation Score
Elevation	0-750	0
	750-1600	2
	1600-1900	6
	1900-2200	8
	2200-2700	10
	2700-3850	2
Slope	0-20°	2
	20° - 30	4
	30° - 35°	6
	35° - 45°	10
	45° - 55°	8
	55° - 65°	5
Aspect	65° - 90°	0
	Flat areas (-1)	0
	N (0° - 22.5°)	10
	NE (22.5° - 67.5°)	10
	E (67.5° - 112.5°)	8
	SE (112.5° - 157.5°)	5
	S (157.5° - 202.5°)	4
	SW (202.5° - 247.5°)	2
W (247.5° - 292.5°)	5	
Plan Curvature	NW (292.5°- 360°)	7
	-4769,96 - (-4)	0
	(-4) - (-0,2)	0
	(-0,2) - 0,2	5
	0,2 - 0,5	3
Profile Curvature	0,5 - 4	1
	4 - 1963,75	0
	2760,82 - 4	0
	4 - 0,2	2
	0,2 - (-0,2)	2
Profile Curvature	(-0,2) - (-0,5)	2
	(-0,5) - (-4)	2

Table 2 is related to topology and its post-processed layers. Table 3 is related to the classification of the land cover layer. Table 4 shows the final classification of the calculated accumulated cost surface for determining risky areas.

The final classification of analysis results is directly related to our score points. The lowest score is 0, and the highest point is 2700. This scale was separated into five evaluation intervals, as seen in Table 4.

Table 3. The classified land cover factor and score.

Land Cover Type	Land Cover Score
Rocks	10
Sparse Plants	8
Snow Areas	7
Agriculture with no Water	
Agriculture with no Water Highlands	
Citrus	
Agriculture with Water	
Cultivated Agriculture	6
Cultivated Fruits	
Tea	5
Meadow	
Nut	
Shrubbery	
Cultivated Forest	
Site	
Mixed Forest	3
National Parks	
Coniferous Forest	2
River	0
Dam	
Evacuation Areas	
Broad-leaved Forest	
Lakes	
District Centers	
Ways	
City Centers	
Village Centers	
Ports	
Industry Zone	
Holiday, Touristic Zones	

Table 4. Final reclassification.

Equation result	Potential avalanche risky areas
0 - 225	Low
225 - 468	Moderate
468 - 850	Considerable
850 - 1440	High
1440 - 2700	Very High

3. Results and discussion

At this stage, the data belonging to the criteria for detecting potential snow avalanche risky areas were classified by considering the sub-criteria scores determined in the ArcGIS 10.8 program and converted to a raster format. Thus, the model developed for detecting potential snow avalanches is ready for analysis. Then the classified raster maps were used in the avalanche release area determination model. As a result of the analysis carried out with the model, the potential snow avalanche risk areas were determined and presented with maps. Alternative potential snow avalanche risk areas were

determined with the outputs obtained and presented with maps.

3.1. Classification of criteria by points

The determined criteria are classified according to sub-criteria in this section. First of all, DEM data was classified according to its subclasses. The subclasses of the criteria were reclassified according to the scores and converted to raster format. Then, slope, aspect, land cover, plan curvature, and profile curvature data of all layers were classified and made ready for analysis in raster format, respectively. The resulting raster maps are shown [Figure 3](#). In the study, 10 * 10 pixels were chosen as the raster pixel size, and this value was considered when converting all spatial data to raster formats.

3.2. Determining harmonized model for avalanche risky area detection

The model analysis developed for detecting potential snow avalanche risky areas was carried out at this stage. This model was implemented by harmonizing recent models and formulas. Each factor was classified according to the following tables, and then the equation was performed with ArcGIS. A Model Builder workflow has been created to automate the process steps. In this way, the analysis hierarchy has been re-applicable. GRID layer was provided with a 10 m* 10 m resolution. The final layer was reclassified into five classes. A model builder is developed to enable the re-applicable analysis process for different areas. The model builder brings time reduction. On the other hand, it is possible to convert the model to Python codes and use it in an add-in or interface development process. One other benefit of the model builder is enabling users to see all the process hierarchy and operations in one figure and replace and remove any operation if not necessary or wrong.

3.3. Detection of potential avalanche risk areas and identification of alternative areas

Specific determination of risky areas has been done after the general determination. [Figure 4](#) shows areas that have high avalanche possibilities. Application steps of this stage have been done by reclassifying raster data getting the highest scores. Then these areas were converted to vector (shape) files. We can estimate avalanche risky areas by understanding the mathematical formula proposed by Hreško of nature and topography. The second essential factors are land cover and land use because they directly affect avalanche accidents. For example, intensive forest areas avoid avalanches because of becoming natural barriers. When visiting the land at some points, it has been determined that there are snow-melting lines to prevent avalanches. These are artificial settings to guide snow movements. There were also metal barriers at some points. However, the areas with the highest avalanche risk were determined from the identified areas, and most were open to accident risk.

According to the classification range in [Table 3](#), the resulting product map was classified as low, moderate, considerable, high, and very high, respectively, and it was determined where the risky areas of snow avalanches were more intensified. This classification as low, moderate, considerable, high, and very high was made according to the European 5 danger levels reference scale [71]. According to the results obtained, it has been determined that the low suitable area was % 43.04 of the whole area, the moderate suitable area was % 32.20, the considerable suitable area was % 15.30, and the high suitable area was % 6.82, the exceptionally high suitable area was % 2.64 ([Table 5](#)), ([Figure 5](#)).

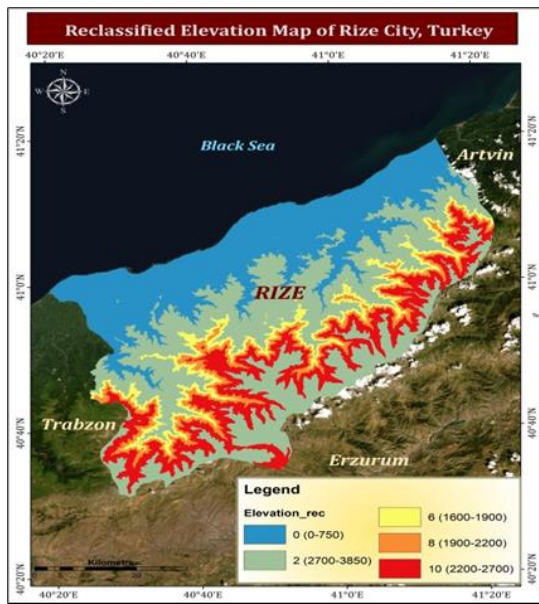
Looking at the map, it can be observed that the riskiest areas in the selected pilot region are generally in the regions where the slope is quite intense in Rize Province. In addition, the areas close to the sea have been identified as areas where the potential snow avalanche risk is quite low, with the effect of decreasing slope. It is seen that the potential snow avalanche risk is intense, especially in many parts of the mountainous regions of Rize province, and these areas coincide with 149,985 points. Among these risky areas, the most dangerous areas in terms of risk were determined as alternative areas (alternative 1, alternative 2, alternative 3) and shown on the map ([Figure 6](#)).

In [Figure 6](#), the Alternative 1 area corresponds to the Yaylaköy village region of Rize province and covers an area of approximately 3,411.53 square meters. It is the first area that is highly risky in terms of snow avalanches. Since the determined area is very close to the Kaçkar Mountains National Park, it coincides with an important point of the province. In addition, the region is close to many tourist plateaus such as the Amlakit, Palovit, and Trovit plateaus.

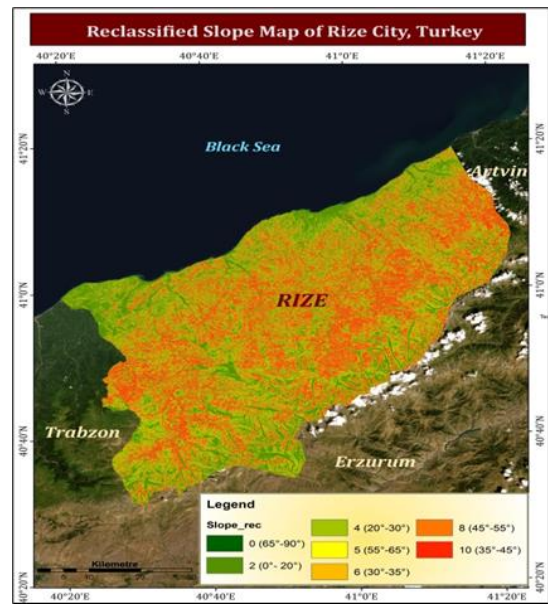
Alternative 2 area corresponds to Yukarışimşirli village region and covers an area of approximately 3,169.27 square meters. The determined area is important because it has an important location in terms of its proximity to the Ayder plateau, which is one of the most important tourist points of the province.

Alternative 3 coincides with the Başköy village region of Rize province and covers an area of approximately 2,104.46 square meters. These three regions determined as alternatives and the regions determined as high risk as a result of the analysis appear as important points with potential snow avalanche risk. Therefore, great attention should be paid to the risk of snow avalanches in this region, which is presented as an alternative, measures should be taken against a possible snow avalanche that will occur at these identified points, and if necessary, prevention policies should be developed by planning.

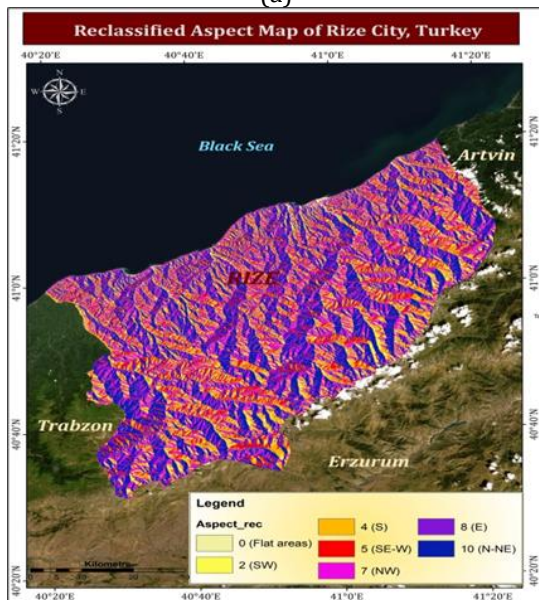
When these most dangerous alternative areas in terms of risk were examined, it was observed that there was no forest in these areas and there were sparse plant settlements. In fact, it can be seen from the figure that the alternative 3 area consists of rocks. This makes these regions attractive for avalanches [60-63]. On the other hand, the elevation value in these areas is between 2000-3000. As the elevation increases, vegetation can be diluted and more cooling occurs at air temperatures [63].



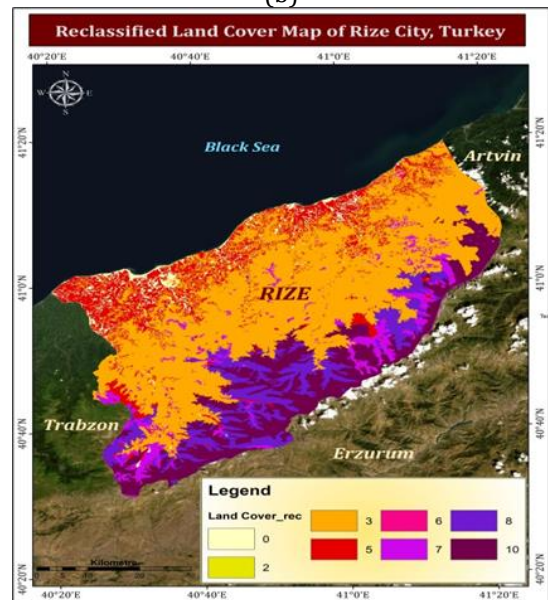
(a)



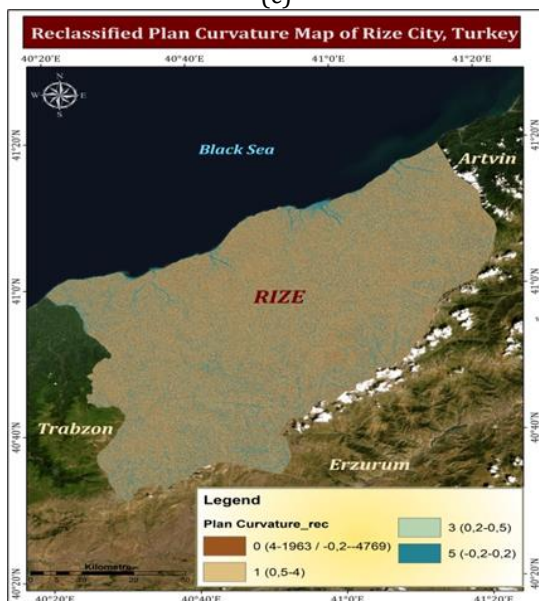
(b)



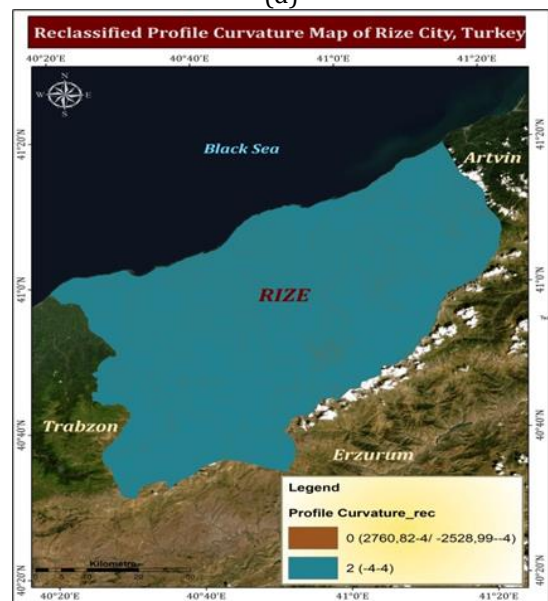
(c)



(d)



(e)



(f)

Figure 3. Raster classification map of criteria according to scores. Elevation (a), Slope (b), Aspect (c), Land cover (d), Plan curvature (e-f).

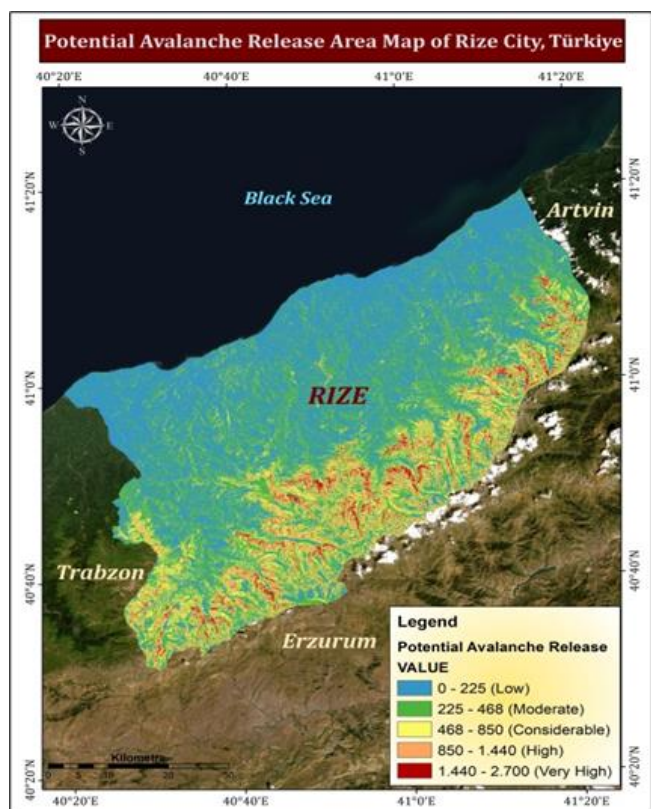


Figure 4. Determined avalanche risky areas.

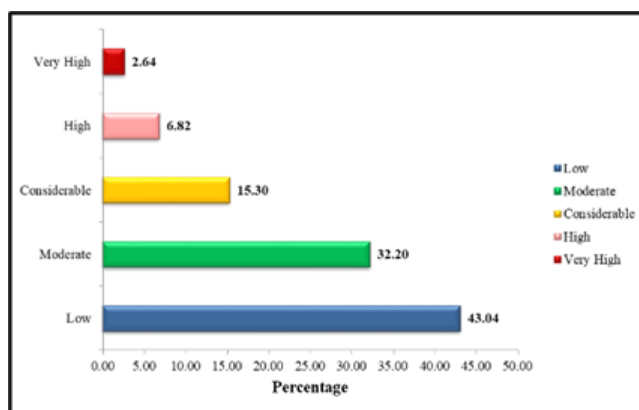


Figure 5. Percentage results of potential avalanche zones in the study area.

Table 5. Analysis results.

Equation Result	Total Area (m ²)	Total Area (km ²)	Percentage%
Low	1,651,607,516.10	1,651.61	43.04
Moderate	1,235,930,624.41	1,235.93	32.20
Considerable	587,186,885.00	587.19	15.30
High	261,821,601.36	261.82	6.82
Very High	101,151,372.36	101.15	2.64

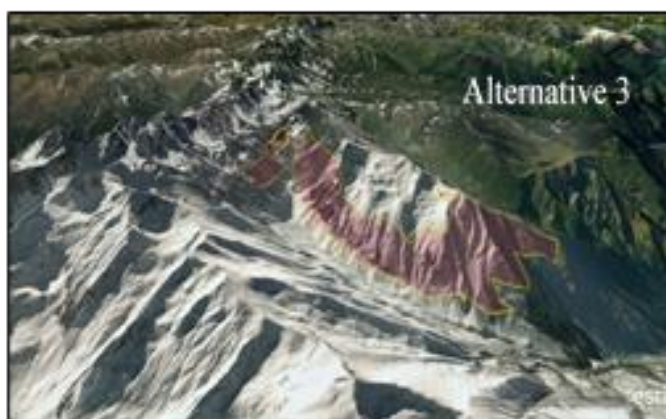
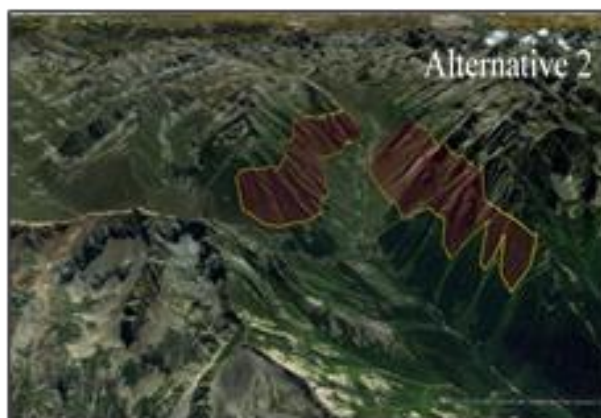


Figure 6. Determined avalanche risky alternative areas.

This situation may trigger an avalanche. In addition, when the slope value of these regions is examined, the region generally has slope values varying between 35°-50°. According to literature, these values are considered

to be the most suitable values for avalanche formation [2, 6, 8]. The combination of all these different impacts has made these regions the most dangerous alternative regions for avalanches.

4. Conclusion

Potential risk areas should be identified before natural hazards occur. Risk analysis studies should be conducted in this context, and risk regions should be defined with maps. Risk maps are essential for the development of emergency action plans. For snow avalanches, one of the natural hazards of meteorological origin, it is necessary to determine the potential risk zones regarding hazard-related studies.

In this study, we have determined possible avalanche areas with the help of GIS methods. The first analysis group included all areas of Rize province, which was the general determination of risky areas. In the second stage, we examined risky areas in detail and detected exact avalanche risky areas. Results have shown that GIS technology is essential for determining risky areas. The relevant data and analysis model for this study is raster-based methods. In this way, all the areas can be analyzed in pixels.

In this study, the area with the highest total value was accepted as the riskiest in terms of potential snow avalanches. As a result of the analysis, the area of 10115.14 hectares was determined to be risky in terms of potential snow avalanches. Three different alternative areas were selected from this area, and these areas were determined as the points with the highest risk in terms of risk. Therefore, minimizing the snow avalanche risks that will occur in risky areas, including these selected alternative areas, or carrying out necessary precautions is essential. Thus, snow avalanche risks can be minimized.

This study shows that recent risky avalanche area determination studies are valuable in applicability and accuracy. However, every practical study for developing risky area determination algorithms supports and enriches GIS studies. Soon, we will focus on determining risky avalanche areas with the help of machine learning. Using technology and newly developed GIS systems will decrease labor loss and budgets for risk planning. Moreover, more human and animal life and nature will be protected.

Acknowledgement

The authors thank Karadeniz Technical University GISLab for providing the data.

Author contributions

Ebru Colak: Conceptualization, Data Collection, Reviewing and Editing **Gamze Bediroğlu:** Conceptualization, Data Collection, Methodology, Software, Visualization, Investigation, Writing-Reviewing and Editing **Tugba Memişoğlu Baykal:** Conceptualization, Data Collection, Methodology, Software, Visualization, Investigation, Writing, Reviewing and Editing

Conflicts of interest

The authors declare no conflicts of interest.

References

- Renner K. (2015). Avalanche risk terrain susceptibility. <http://hydrology.usu.edu/giswr/Archive15/Renner/Termproject.pdf>
- Schweizer, J., Bruce Jamieson, J., & Schneebeli, M. (2003). Snow avalanche formation. *Reviews of Geophysics*, 41(4). <https://doi.org/10.1029/2002RG000123>
- Castebrunet, H., Eckert, N., & Giraud, G. (2012). Snow and weather climatic control on snow avalanche occurrence fluctuations over 50 yr in the French Alps. *Climate of the Past*, 8(2), 855-875. <https://doi.org/10.5194/cp-8-855-2012>
- Korzeniowska, K., Bühler, Y., Marty, M., & Korup, O. (2017). Regional snow-avalanche detection using object-based image analysis of near-infrared aerial imagery. *Natural Hazards and Earth System Sciences*, 17(10), 1823-1836. <https://doi.org/10.5194/nhess-17-1823-2017>
- Marana, B. (2017). An ArcGIS geo-morphological approach for snow avalanche zoning and risk estimation in the Province of Bergamo. *Journal of Geographic Information System*, 9(2), 83-97. <https://doi.org/10.4236/jgis.2017.92006>
- McClung, D., & Schaerer, P. A. (2006). *The avalanche handbook*. The Mountaineers Books.
- Bühler, Y., Kumar, S., Veitinger, J., Christen, M., Stoffel, A., & Snehmani. (2013). Automated identification of potential snow avalanche release areas based on digital elevation models. *Natural Hazards and Earth System Sciences*, 13(5), 1321-1335. <https://doi.org/10.5194/nhess-13-1321-2013>
- Waldenström B. (2016). Identifying potential snow avalanche release areas in Sweden: An analysis of GIS methods and data resolutions. [Doctoral Dissertation, Stockholm University].
- Çolak, E., & Memişoğlu, T. (2021). Thornthwaite iklim sınıflandırma yöntemine göre Karadeniz Bölgesi iklim sınır haritasının CBS ile üretilmesi. *Geomatik*, 6(1), 31-43. <https://doi.org/10.29128/geomatik.651702>
- Doğan, A., Başgeçmez, M., & Aydın, C. C. (2023). Geniş çalışma alanlarında jeofizik ve jeoteknik ölçümlerin yerine geçebilecek vekil özelliklerin CBS ile belirlenmesi. *Geomatik*, 8(3), 293-305. <https://doi.org/10.29128/geomatik.1161434>
- Uyan, M. (2017). Güneş enerjisi santrali kurulabilecek alanların AHP yöntemi kullanılarak CBS destekli haritalanması. *Pamukkale Üniversitesi Mühendislik Bilimleri Dergisi*, 23(4), 343-351. <https://doi.org/10.5505/pajes.2016.59489>
- Geymen, A. (2017). Coğrafi bilgi sistemlerinde kullanılan konumsal analizlerin animasyon tabanlı öğrenimi. *Pamukkale Üniversitesi Mühendislik Bilimleri Dergisi*, 23(2), 165-170. <https://doi.org/10.5505/pajes.2016.02703>
- Eşsiz, M., & Acar, Z. (2023). Synoptic analysis of the January 2004 snowstorm: Example of Çanakkale. *International Journal of Engineering and Geosciences*, 8(1), 11-18. <https://doi.org/10.26833/ijeg.988115>

14. Siddique, F., & Rahman, A. U. (2023). Genesis and spatio-temporal analysis of glacial lakes in the periglacial environment of Western Himalayas. *International Journal of Engineering and Geosciences, Geosciences*, 8(2), 154-164.
<https://doi.org/10.26833/ijeg.1097912>
15. Toppe, R. (1987). Terrain models: a tool for natural hazard mapping. *International Association of Hydrological Sciences (IAHS)*, 629-638.
16. Hreško, J. (1998). Avalanche hazard of the Tatra high mountain landscape. *Folia Geographica*, 2, 348-352.
17. Maggioni, M., & Gruber, U. (2003). The influence of topographic parameters on avalanche release dimension and frequency. *Cold Regions Science and Technology*, 37(3), 407-419.
[https://doi.org/10.1016/S0165-232X\(03\)00080-6](https://doi.org/10.1016/S0165-232X(03)00080-6)
18. Barka, I. (2003). Identification of snow avalanche trigger areas and avalanche paths by the GIS. *Geomorphologia Slovaca*, 3(2), 60-63.
19. Delparte D. (2008). *Avalanche Terrain Modeling in Glacier National Park, Canada*. [Doctoral Dissertation, University of Calgary].
20. Sitko R. (2008). Identification, classification, and assessment of forest function with the use of geoinformatics. [Doctoral Dissertation, Technical University in Zvolen].
21. Bebi, P., Kienast, F., & Schönenberger, W. (2001). Assessing structures in mountain forests as a basis for investigating the forests' dynamics and protective function. *Forest Ecology and Management*, 145(1-2), 3-14.
[https://doi.org/10.1016/S0378-1127\(00\)00570-3](https://doi.org/10.1016/S0378-1127(00)00570-3)
22. Biskupič, M., & Barka, I. (2009). Statistical avalanche run-out modelling using GIS on selected slopes of Western Tatras National park, Slovakia. *International snow Science Workshop, Davos*, 482-487.
23. McClung, D. M. (2002). The elements of applied avalanche forecasting, Part I: The human issues. *Natural Hazards*, 26, 111-129.
<https://doi.org/10.1023/A:1015665432221>
24. AS Mohammed, A. A., Naqvi, H. R., & Firdouse, Z. (2015). An assessment and identification of avalanche hazard sites in Uri sector and its surroundings on Himalayan Mountain. *Journal of Mountain Science*, 12, 1499-1510.
<https://doi.org/10.1007/s11629-014-3274-z>
25. Leroi, E. (1996). Landslide hazard-risk maps at different scales: objectives, tools and developments. In *Landslides*, 35-51.
26. Mihalić, S. (1998). Recommendations for landslide hazard and risk mapping in Croatia. *Geologia Croatica*, 51(2), 195-204.
27. Birkeland, K. W., & Mock, C. J. (2001). The major snow avalanche cycle of February 1986 in the western United States. *Natural Hazards*, 24, 75-95.
<https://doi.org/10.1023/A:1011192619039>
28. Jamieson, B., & Stethem, C. (2002). Snow avalanche hazards and management in Canada: challenges and progress. *Natural Hazards*, 26, 35-53.
<https://doi.org/10.1023/A:1015212626232>
29. Glade, T., Anderson, M. G., & Crozier, M. J. (2005). *Landslide hazard and risk*, 807. Chichester: Wiley.
30. Nadim, F., Kjekstad, O., Peduzzi, P., Herold, C., & Jaedicke, C. (2006). Global landslide and avalanche hotspots. *Landslides*, 3, 159-173.
<https://doi.org/10.1007/s10346-006-0036-1>
31. Höller, P. (2007). Avalanche hazards and mitigation in Austria: a review. *Natural Hazards*, 43(1), 81-101.
<https://doi.org/10.1007/s11069-007-9109-2>
32. Maggioni, M., Gruber, U., Purves, R. S., & Freppaz, M. (2006). Potential release areas and return period of avalanches: is there a relation?. *International Snow Science Workshop*, 566-571.
33. Omirzhanova, Z. T., Urazaliev, A. S., & Aimenov, A. T. (2015). GIS for predicting the avalanche zones in the mountain regions of Kazakhstan. *The International Archives of the Photogrammetry, Remote Sensing and Spatial Information Sciences*, 40, 39-44.
<https://doi.org/10.5194/isprsarchives-XL-2-W4-39-2015>
34. Cappabianca, F., Barbolini, M., & Natale, L. (2008). Snow avalanche risk assessment and mapping: A new method based on a combination of statistical analysis, avalanche dynamics simulation and empirically-based vulnerability relations integrated in a GIS platform. *Cold Regions Science and Technology*, 54(3), 193-205.
<https://doi.org/10.1016/j.coldregions.2008.06.005>
35. Peitzsch, E. H., Hendriks, J., & Fagre, D. B. (2015). Terrain parameters of glide snow avalanches and a simple spatial glide snow avalanche model. *Cold Regions Science and Technology*, 120, 237-250.
<https://doi.org/10.1016/j.coldregions.2015.08.002>
36. Yariyan, P., Avand, M., Abbaspour, R. A., Karami, M., & Tiefenbacher, J. P. (2020). GIS-based spatial modeling of snow avalanches using four novel ensemble models. *Science of The Total Environment*, 745, 141008.
<https://doi.org/10.1016/j.scitotenv.2020.141008>
37. Teich, M., & Bebi, P. (2009). Evaluating the benefit of avalanche protection forest with GIS-based risk analyses—A case study in Switzerland. *Forest Ecology and Management*, 257(9), 1910-1919.
<https://doi.org/10.1016/j.foreco.2009.01.046>
38. Gruber, U., & Bartelt, P. (2007). Snow avalanche hazard modelling of large areas using shallow water numerical methods and GIS. *Environmental Modelling & Software*, 22(10), 1472-1481.
<https://doi.org/10.1016/j.envsoft.2007.01.001>
39. Maggioni, M., Gruber, U., & Stoffel, A. (2002). Definition and characterisation of potential avalanche release areas. *Proceedings of the ESRI Conference, San Diego*.
40. Marek, B., & Ivan, B. (2010). Spatial modelling of snow avalanche run-outs using GIS. *Proceedings from Symposium GIS, Ostrava*.
41. Aydin, A., Bühler, Y., Christen, M., & Gürer, I. (2014). Avalanche situation in Turkey and back calculation of selected events. *Natural Hazards and Earth System Sciences*, 14(5), 1145-1154.
<https://doi.org/10.5194/nhess-14-1145-2014>

42. Harvey, S., Schmudlach, G., Bühler, Y., Dürr, L., Stoffel, A., & Christen, M. (2018). Avalanche terrain maps for backcountry skiing in Switzerland. *International Snow Science Workshop*, Innsbruck, Austria, 1625-1631.
43. Peitzsch, E. H., Hendrikx, J., & Fagre, D. B. (2014). Assessing the importance of terrain parameters on glide avalanche release. *International Snow Science Workshop*, 708-716.
44. Bolognesi, R., Denuelle, M., & Dexter, L. (1996). Avalanche forecasting with GIS. *International Snow Science Workshop (ISSW)*, Banff, Canada, 11-13.
45. Košová, V., Molokáč, M., Čech, V., & Jesenský, M. (2022). Avalanche hazard modelling within the kráľova hoľa area in the low tatra mountains in Slovakia. *Land*, 11(6), 766.
<https://doi.org/10.3390/land11060766>
46. Aydın, A., & Eker, R. (2017). GIS-Based snow avalanche hazard mapping: Bayburt-Aşağı Dere catchment case. *Journal of Environmental Biology*, 38, 937-943.
[https://doi.org/10.22438/jeb/38/5\(si\)/gm-10](https://doi.org/10.22438/jeb/38/5(si)/gm-10)
47. Barbolini, M., Pagliardi, M., Ferro, F., & Corradeghini, P. (2011). Avalanche hazard mapping over large undocumented areas. *Natural Hazards*, 56(2), 451-464. <https://doi.org/10.1007/s11069-009-9434-8>
48. Pistocchi, A., & Notarnicola, C. (2013). Data-driven mapping of avalanche release areas: a case study in South Tyrol, Italy. *Natural Hazards*, 65, 1313-1330. <https://doi.org/10.1007/s11069-012-0410-3>
49. Selcuk, L. (2013). An avalanche hazard model for Bitlis Province, Turkey, using GIS based multicriteria decision analysis. *Turkish Journal of Earth Sciences*, 22(4), 523-535.
<https://doi.org/10.3906/yer-1201-10>
50. Yılmaz B. (2016). CBS tabanlı bulanık mantık ve analitik hiyerarşi sürecinin (AHP) kar çığı duyarlılık haritalamasına uygulanması, Kuzey San Juan, Colorado. [Master's Thesis, Karadeniz Technical University].
51. Durlević, U., Valjarević, A., Novković, I., Ćurčić, N. B., Smiljić, M., Morar, C., ... & Lukić, T. (2022). GIS-based spatial modeling of snow avalanches using analytic Hierarchy process. a case study of the Šar Mountains, Serbia. *Atmosphere*, 13(8), 1229.
<https://doi.org/10.3390/atmos13081229>
52. Bhardwaj, A. S., Pandit, A., & Ganju, A. (2014). Demarcation of potential avalanche sites using remote sensing and ground observations: a case study of Gangotri glacier. *Geocarto International*, 29(5), 520-535.
<https://doi.org/10.1080/10106049.2013.807304>
53. Kumar, S., Srivastava, P. K., & Snehmani. (2018). Geospatial modelling and mapping of snow avalanche susceptibility. *Journal of the Indian Society of Remote Sensing*, 46, 109-119.
<https://doi.org/10.1007/s12524-017-0672-z>
54. Akay, H. (2021). Spatial modeling of snow avalanche susceptibility using hybrid and ensemble machine learning techniques. *Catena*, 206, 105524.
<https://doi.org/10.1016/j.catena.2021.105524>
55. Nefeslioglu, H. A., Sezer, E. A., Gokceoglu, C., & Ayas, Z. (2013). A modified analytical hierarchy process (M-AHP) approach for decision support systems in natural hazard assessments. *Computers & Geosciences*, 59, 1-8.
<https://doi.org/10.1016/j.cageo.2013.05.010>
56. Maggioni, M. (2004). Avalanche release areas and their influence on uncertainty in avalanche hazard mapping. [Doctoral Dissertation, University of Zurich].
57. Turkish Statistical Institute. (2022). Address Based Population Registration System Database Online. <https://biruni.tuik.gov.tr/medas/?kn=95&locale=tr>
58. State Meteorological Service (2022). Rize sıcaklık istatistikleri. <https://www.mgm.gov.tr/veridegerlendirme/il-ve-ilceler-istatistik.aspx?m=RIZE>
59. T.C. Culture and Tourism Ministry (2022). Rize-Kaçkar Dağları. <https://yigm.ktb.gov.tr/TR-9905/rize-kackar-siradaglari.html>
60. Gubler, H., & Rychetnik, J. (1991). Effects of forests near timberline on avalanche formation.
61. Weir, P. (2002). Snow avalanche management in forested terrain. *British Columbia, Forest Science Program*.
62. Aydın, A., & Eker, R. (2014). Topografik Parametreler Kullanılarak Potansiyel Çığ Başlama Bölgelerinin CBS Tabanlı Olarak Belirlenmesi. II. Ulusal Akdeniz Orman Ve Çevre Sempozyumu, 426-435.
63. Mears, A. I. (1992). Snow-avalanche hazard analysis for land-use planning and engineering. *Colorado Geological Survey, Department of Natural Resources*.
64. Fredston, J. A., & Fesler, D. (1994). Snow sense: A guide to evaluating snow avalanche hazard. *Alaska Mountain Safety Center, Incorporated*.
65. McClung, D. M. (2001). Characteristics of terrain, snow supply and forest cover for avalanche initiation caused by logging. *Annals of Glaciology*, 32, 223-229.
<https://doi.org/10.3189/172756401781819391>
66. Schaerer, P. A. (1977). Analysis of snow avalanche terrain. *Canadian Geotechnical Journal*, 14(3), 281-287. <https://doi.org/10.1139/t77-034>
67. Armstrong, B., & Williams, K. (1986). *The Avalanche book: Golden. Colorado, Fulcrum Inc*, 240.
68. Boltížiar, M., Biskupič, M., & Barka, I. (2016). Spatial avalanche modelling by application of GIS on the selected slopes of Western Tatra Mts. and Belianske Tatra Mts., Slovakia. *Geographia Polonica*, 89(1), 79-90.
69. T. C. Ministry of Forestry and Water Management (2016). *National Avalanche Risk Activation Plan Report*. Ankara, Turkey.
70. Richnavský, J., Biskupič, M., Mudroň, I., Devečka, B., Unucka, J., Chrustek, P., ... & Matějček, L. (2011). Using modern GIS tools to reconstruct the avalanche: A case study of Magurka 1970. *Proceedings of the 8th International Symposium GIS Ostrava*, 175-185.
71. <http://mintsnowboarding.com/blog/avalanche-facts-and-tips/>





Human micro-doppler detection and classification studies at Mersin University using real outdoor experiments via C-band FMCW radar

Onur Tekir ^{*1} , Caner Özdemir ¹ 

¹ Mersin University, Department of Electrical-Electronics Engineering, Türkiye, onur_tek@hotmail.com, cozdemir@mersin.edu.tr

Cite this study:

Tekir, O., & Özdemir, C. (2024). Human micro-doppler detection and classification studies at Mersin University using real outdoor experiments via C-band FMCW radar. *International Journal of Engineering and Geosciences*, 9 (2), 211-220

<https://doi.org/10.26833/ijeg.1380658>

Keywords

Micro-doppler radar
Radar imaging
Spectrogram
Human detection and classification

Research Article

Received: 24.10.2023
Revised: 21.01.2024
Accepted: 24.01.2024
Published: 23.07.2024

Abstract

In this work, a unique radar hardware is introduced for human-gait micro-Doppler studies. The developed radar sensor operates in C-band microwave frequencies. We share several outdoor experiments at Mersin University facilities to detect and characterize human walking and running movements. In these experiments, various walking and running movements were performed with different people. To examine the Doppler properties of human motion, raw data gathered is transformed onto 2D joint-time-frequency plane. The generation of micro-Doppler signatures in the transformed data is the first step in the extraction of features of the walking/running human motion. It is shown that the directions, durations, range distances as well as torso and limb velocities of walking and running human movements in each experiment are successfully obtained from these micro-Doppler signatures.



1. Introduction

Human detection and motion classification offer many advantages for applications such as search and rescue, intelligent environments, and security. Infrared, lidar [1-3], acoustic, vibration/seismic, and visual sensors have long been used in human recognition and detection systems. Radar technology, on the other hand, offers advantages in human detection applications because it can detect at longer distances, is more comprehensive and can operate in all weather conditions [4-7].

With today's developments, the need for long-range radar systems that can detect targets with low radar cross-sectional area [8] such as humans is increasing significantly. In the last ten years, many studies have been published on the automatic classification of various human movements and different targets from radar signals [9]. In human classification studies, the radar signature of a human being is usually very different from the radar signature of other targets.

If the signal sent by the radar hits a target that is moving relative to the radar, the frequency of the return signal from the target is slightly different from the

frequency of the transmitted signal. This phenomenon is called "Doppler shift" [10]. The amplitude of the Doppler shift depends on the speed of the target relative to the radar and the frequency of the transmitted signal. If the target has parts that oscillate, vibrate, and rotate in addition to the translational motion, additional modulations due to these parts are observed in the return signal in addition to the basic Doppler shift. This phenomenon is called the micro-Doppler effect and the signal returned from the target is called the micro-Doppler signature of the target [11].

Micro-Doppler has been utilized for target recognition in many studies, especially in applications such as pedestrian safety with automotive radar networks [12-13]. In 2010, Van Dorp and Groen conducted a basic classification study on human arm swing using Frequency-Modulated Continuous-Wave (FMCW) radar networks with micro-Doppler analysis [14].

In any surveillance application, real-time estimation and visualization of human posture is critical for threat analysis. Human movement and gait characteristics (hand, arm and leg movements) can be detected by applying detailed radar signal techniques on micro-

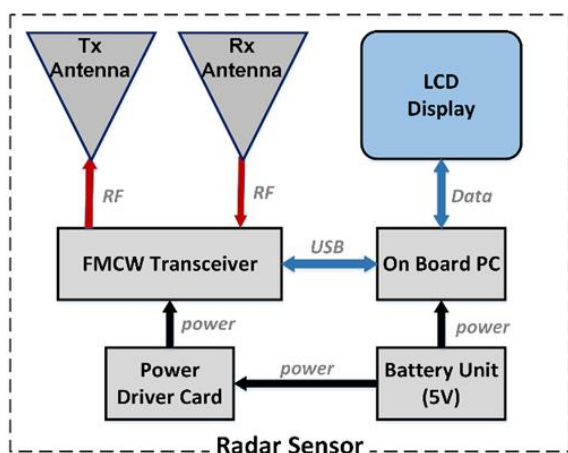
Doppler echoes. In addition to the radar image of holistic human body motion, micro-Doppler features contain unique spectral information about gait characteristics. Mainly because the legs, arms and wrists do not move at constant speed, the micro-Doppler effect exhibits a periodic characteristic. Time-varying micro-Doppler features due to different parts of the body are deduced by combined time-frequency analyses [15]. Time-frequency micro-Doppler images describe the motion characteristics. The characteristics of human gait have been studied in detail by researchers in the fields of biomechanics and computer vision [16-18]. However, the use of radar signals in this field is quite recent [19]. Geisheimer experimentally demonstrated that a human spectrogram can be obtained from signals reflected from different parts of the body [20]. In this paper, we present recent experiments that we have conducted at Mersin University in characterization and analysis of the human movements including basic walking and running activities.

Organization of paper is as follows: In the second section, the micro-Doppler radar sensor that we have developed and the data gathering arrangement are introduced. In the third next section, various experiments the micro-Doppler experiments and corresponding micro-Doppler images based on spectrogram are presented together with numerical analysis after the evaluation of the constructed micro-Doppler images. The final section summarizes and concludes the work presented in this paper.

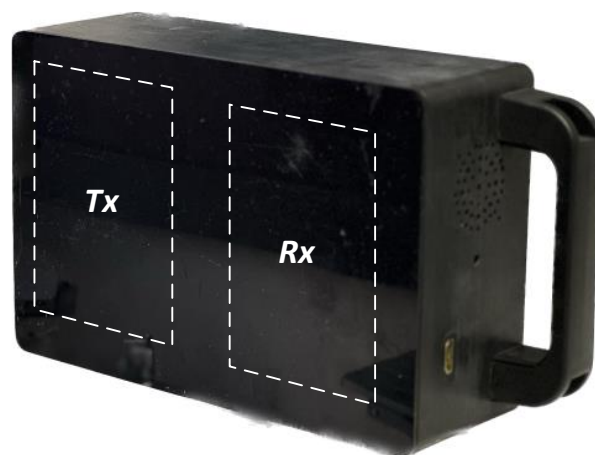
2. Method

2.1. Radar sensor

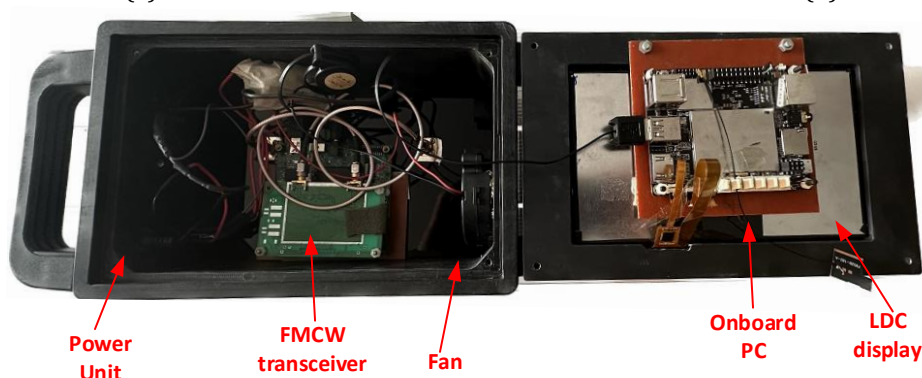
A micro-Doppler radar hardware has been developed which is based on a frequency modulated continuous wave (FMCW) transceiver [Ancortek's SDR-KIT-580AD]. Figure 1a shows the block diagram of our radar sensor. Two two-by-three microstrip patch antenna array with an antenna gain of more than 12 dBi for the whole frequency bandwidth of 400 MHz at the center frequency of 5800 MHz. Figure 1b depicts the perspective view of the developed radar device in which the locations of the transmitting and receiving antennas are labelled. For the experiments, the chirp time interval is chosen to be 1 ms such that it can cover the extremum values of full human micro-Doppler signatures for indoor and outdoor activities. More precisely, the radar can measure Doppler frequencies from -500 Hz to + 500 Hz. Radar device has the power output of approximately 0.08 watts. The FMCW transceiver equipment is controlled by the on-board PC board. The Matlab script, including the implementation of all signal processing routines, was used together with the on-board PC hardware. A 7-inch LCD touchscreen display is integrated for the easy use of the operator. A power board was used to provide +5V to all the hardware of the micro-Doppler radar sensor module [21]. The front and back photos of this radar sensor are shown in Figure 1c, where all electronic components can be viewed.



(a)



(b)



(c)

Figure 1. Prototyped micro-Doppler radar sensor: (a) block diagram, (b) Perspective view, (c) inner hardware.

2.2. Experimental set-up

This radar sensor was used for experimental research to detect human movement and possibly classify human body parts. In the experimental setup, the radar sensor was placed on a tripod at a height of 1m above the ground level and various people walked, walked away and/or ran towards the radar sensor. Figure 2a, 3a, 4a, 5a and 6a show some photos from the experimental scenes.

3. Results and discussion

Five different experiments were accomplished for several types of human movements: In the first experiment, the human walked towards and then moved from the radar at approximately 26 m range distance with swinging both arms as shown in Figure 2a, maintaining a relatively stationary velocity during the data collection period of 35 s. The micro-Doppler signature was then generated by applying a short-time Fourier transform (STFT) process, i.e. spectrogram, to the FMCW-based time-domain scattered electric field data; $E^s(t)$ obtained the micro-Doppler signature as (Equation 1).

$$E^s(\tau, f) = \int_{-\infty}^{\infty} E^s(t) \cdot w(t - \tau) \exp(-j2\pi ft) dt \quad (1)$$

Here $w(t)$ is a 200-point Hamming-type sliding window corresponding to 0.2 seconds with 95% overlap [10]. A notch filter [22] was also applied to minimize the effect of static clutter around the DC frequencies and to highlight the true signature. After these operations, obtained micro-Doppler signature image was extracted as shown in Figure 2b. As can be seen from the image, both the main motion of the torso and the swinging arm signatures can be easily recognized. The Doppler frequency of the torso starts from $f_D = 0$ Hz (for a fixed human target) at $t = 0$ and reaches a maximum value of about 65 Hz (corresponding to a speed of 6.05 km/h) just after $t = 7$ s as seen from the time-Doppler image in Figure 2b. Figure 2c shows the time-velocity image, which allows the velocity information to be detected more easily during the movement time.

In the second experiment, the man walked towards and then moved away from the radar with still arms at about 28 m along the range distance, keeping a relatively stable speed during the 35 s data collection period as shown in Figure 3a. The Doppler frequency of the torso starts at $f_D = 0$ Hz (for a fixed human target) at $t = 0$ and reaches a maximum value of about 63 Hz (corresponding to a torso speed of 5.86 km/h) just after $t = 7$ s, as seen from the time-Doppler image in Figure 3b. Figure 3c shows the time-velocity image, which allows the velocity information to be detected more easily during the movement time.

In the third experiment the man walked towards to the radar from approximately 8.5 m at range distance again for a time duration of 8 s as pictured in Figure 4a. After using the identical spectrogram examination described above, a micro-Doppler spectrogram image was extracted as shown in Figure 4b. If this image is

carefully examined, one can undoubtedly observe that the man has no movement at $t = 0$ and moves away from the radar as time progresses, reaching an average body Doppler frequency of about 38 Hz (equivalent to torso speed of 3.58 km/s). Once more, the signatures of the swinging arms and the responses of other body pieces are distinctly noticeable in Figure 4b. Figure 4c shows the time-velocity image, which allows the velocity information to be detected more easily during the movement time.

In the fourth experiment, the human first ran towards the radar, then away from the radar and finally towards the radar, sustaining a reasonably stable velocity during the 18 s data acquisition period. Each running lap has approximately 21 m. An image from the experiment and the Doppler spectrogram are shown in Figure 5a and Figure 5b, respectively. From the spectrogram in Figure 5b, it is clearly read that the Doppler frequency can reach a highest value of about 210 Hz, equivalent to a running velocity of 19.55 km/h. This amount, evidently, includes the sum of both torso and arm/hand velocities. When computing the speed of the torso, the average Doppler frequency of the torso was measured to be 135 Hz when the man was running towards the radar at a uniform speed. Hence, this Doppler frequency amount specifies a nominal torso velocity measurement of 12.57 km/h. Figure 5c shows the time-velocity image, which allows the velocity information to be detected more easily during the movement time.

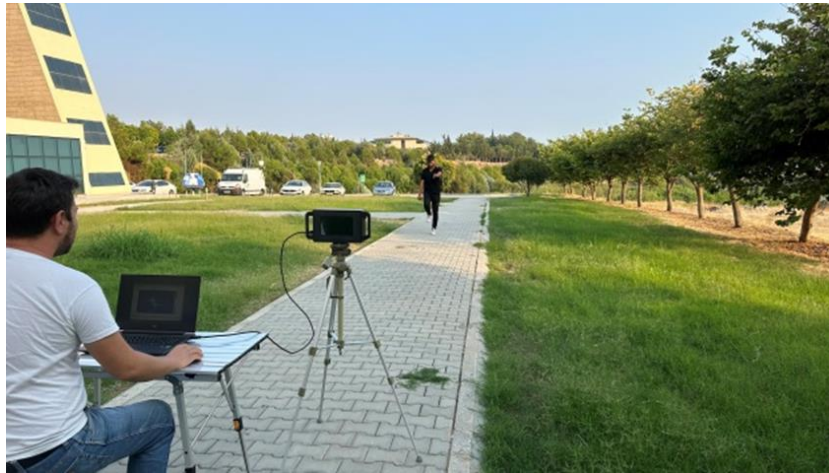
For the fifth experimentation, two men have run in an outdoor field as portrayed in Figure 6a. First, one man run towards to radar at the same time other man run away from the radar by preserving a uniform velocity during the data gathering interval of 7 s. Each man has run up to a maximum distance of around 22 m along the range. It is obviously interpreted from the spectrogram in Figure 6b that the first running man's Doppler frequency can attain a highest value of approximately 226 Hz which matches to a running velocity of 21.04 km/h. The second running man's Doppler frequency can achieve a largest amount of around 261 Hz which resembles a running speed of 24.3 km/h. These values; obviously, contain the sum of the speeds of torso, arms, and hands. The torso average Doppler frequencies of running men were measured to be 150 Hz and 155 Hz, respectively during men were running towards the radar with a uniform velocity. So, these men's Doppler frequency values provide a nominal torso speed measurement of 13.96 km/h and 14.43 km/h, respectively. Figure 6c shows the time-velocity image, which allows the velocity information to be detected more easily during the movement time. The flow diagram in Figure 7 shows how to obtain the characteristics of the movement by using the information on the spectrogram obtained by using the short-time Fourier transform.

4. Conclusion

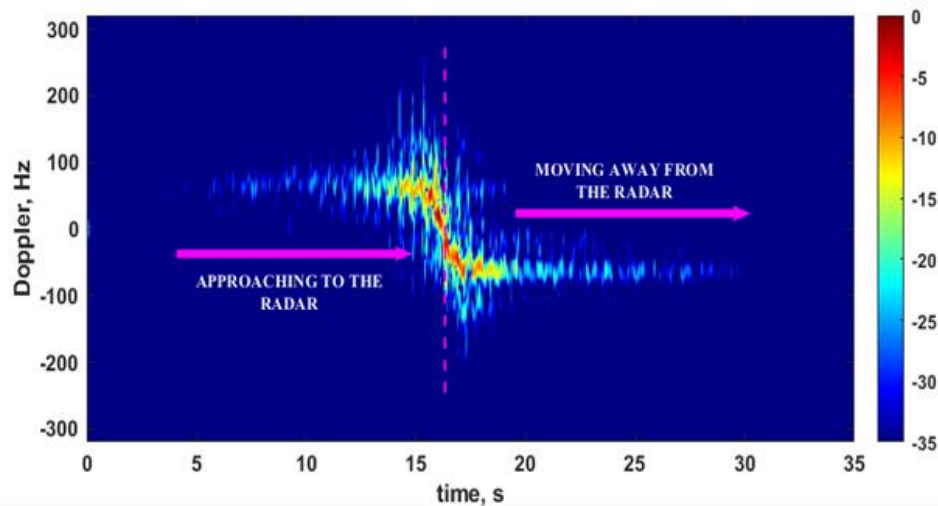
In this paper, we have presented a radar sensor that we have specially developed for the detection and classification of human micro-Doppler characteristics. As shared in the second and third sections, several

experiments were conducted outdoors using. We have demonstrated throughout experiments that the radar sensor has the capability of detecting human motions such as walking and running with good fidelity. By utilizing the time-frequency tool of spectrogram [23], it is possible to further analyze the micro-Doppler features of these motions including, characterization such as

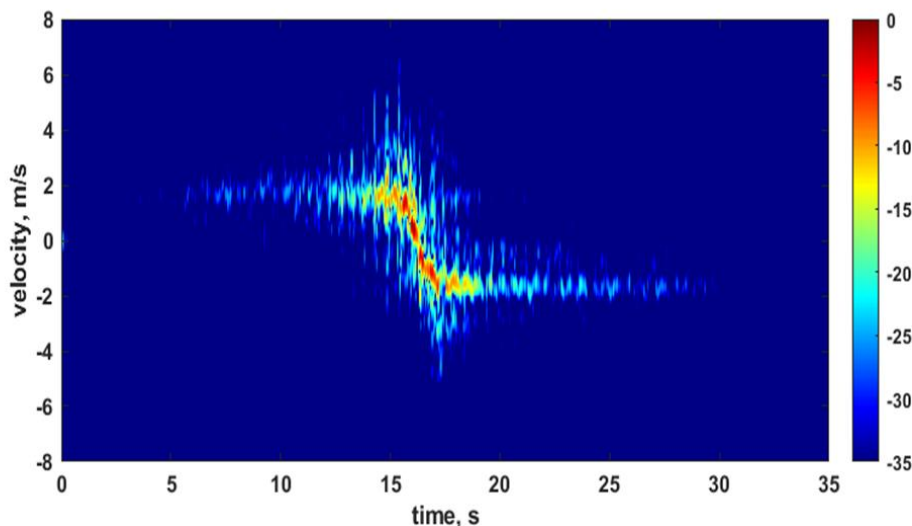
walking with still arms or running and calculation of other distinct features such as velocity information of human motion and range distance of the man, etc. Such extracted features are very crucial and thus, can be used for many useful applications in detecting and classifying men, women, children, and possibly different animals.



(a)

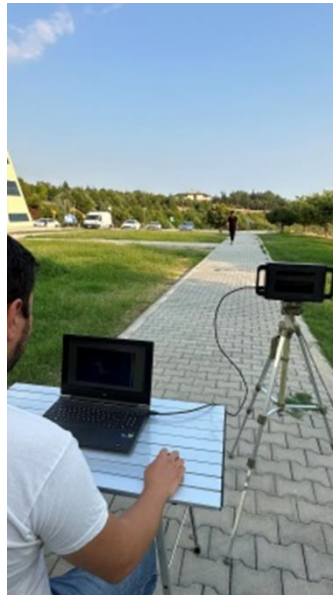


(b)

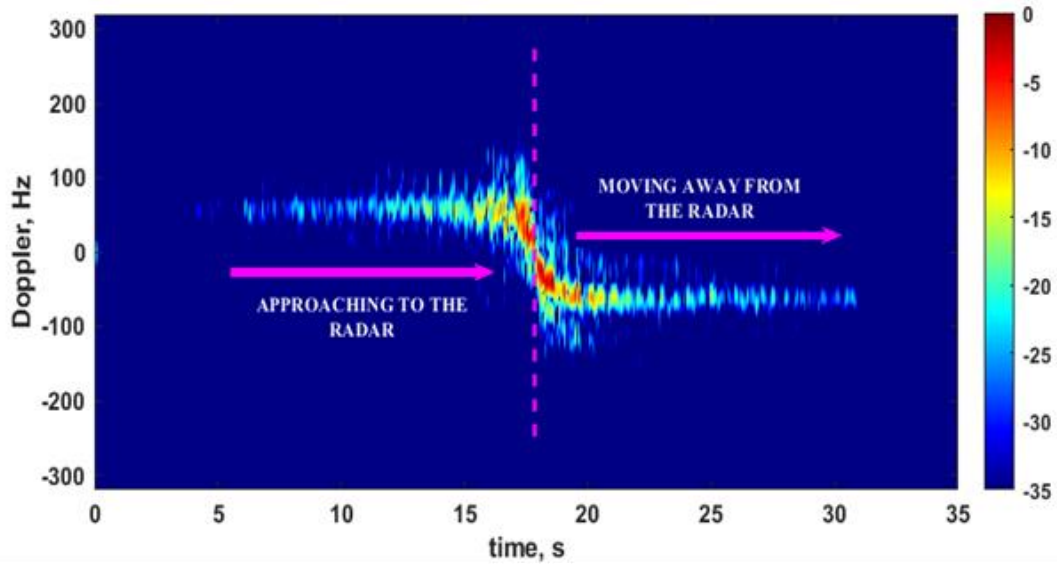


(c)

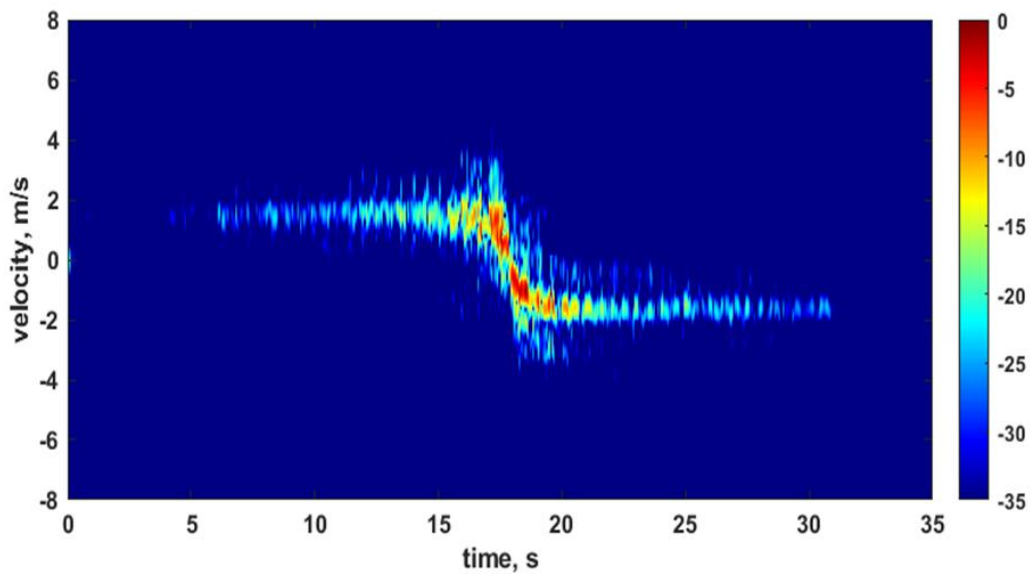
Figure 2. (a) The man first approached the radar and then moved away radar while walking with swinging arms, (b) corresponding spectrogram image (c) spectrogram image with velocity information.



(a)

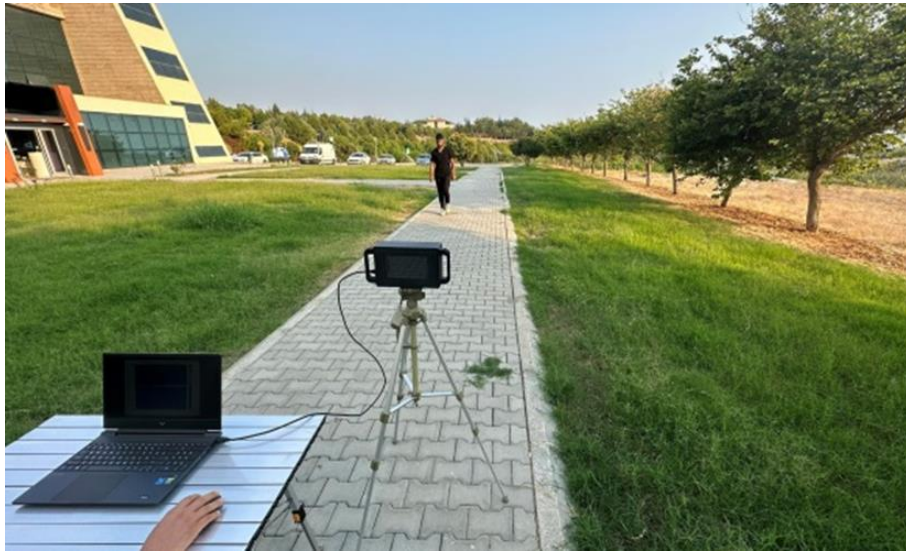


(b)

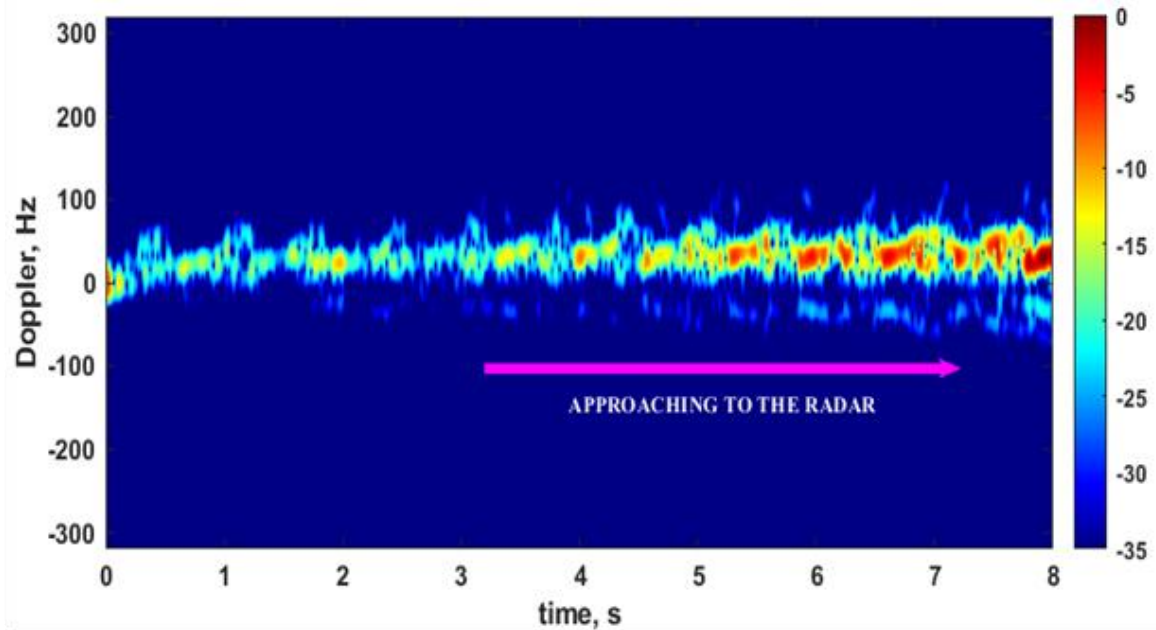


(c)

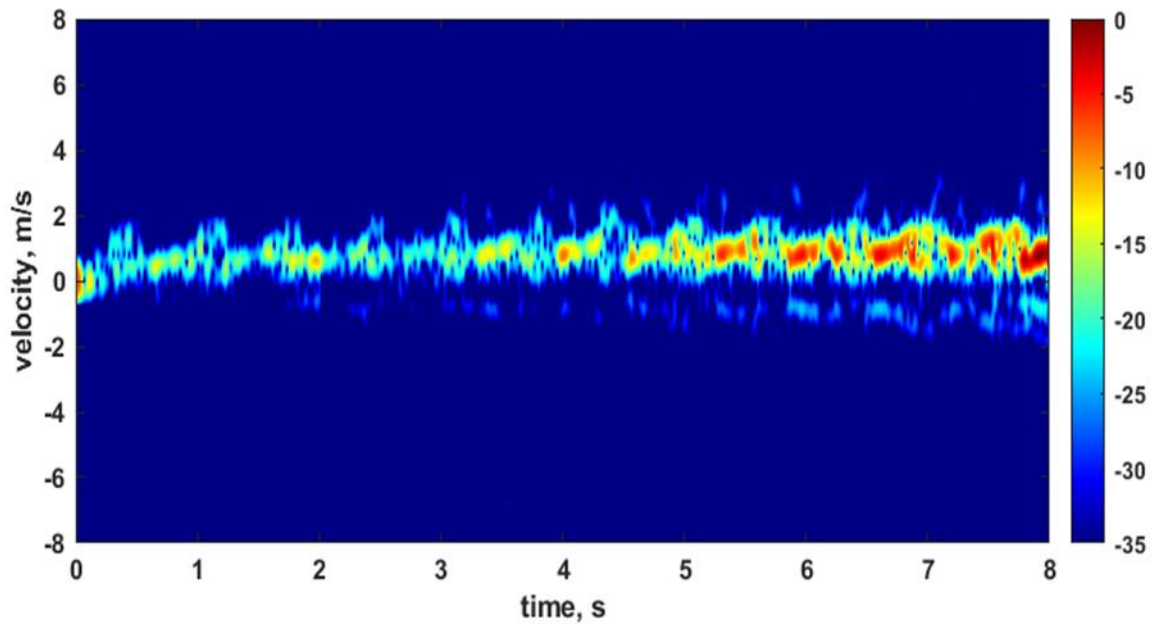
Figure 3. (a) The man approached the radar and then moved away from the radar while walking with still arms, (b) corresponding spectrogram image (c) radar image on time-velocity plane.



(a)

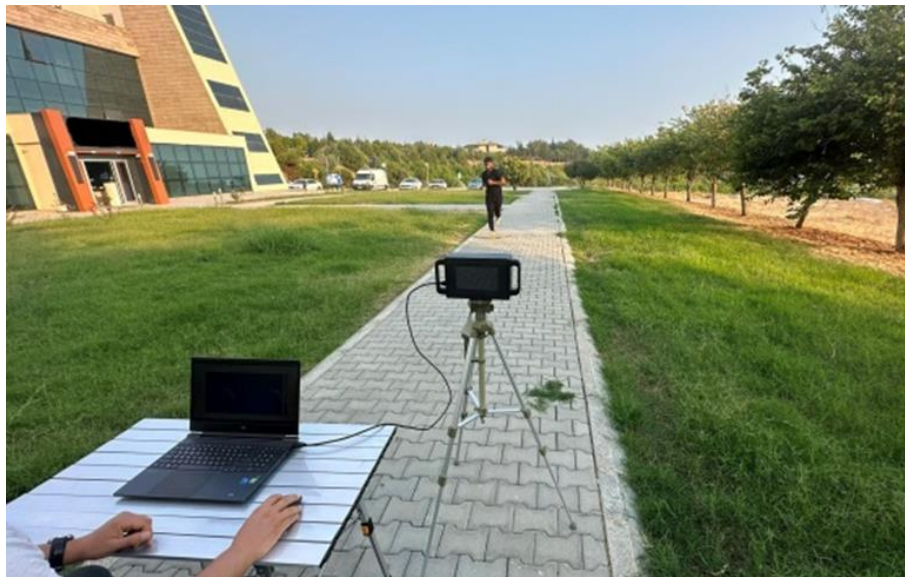


(b)

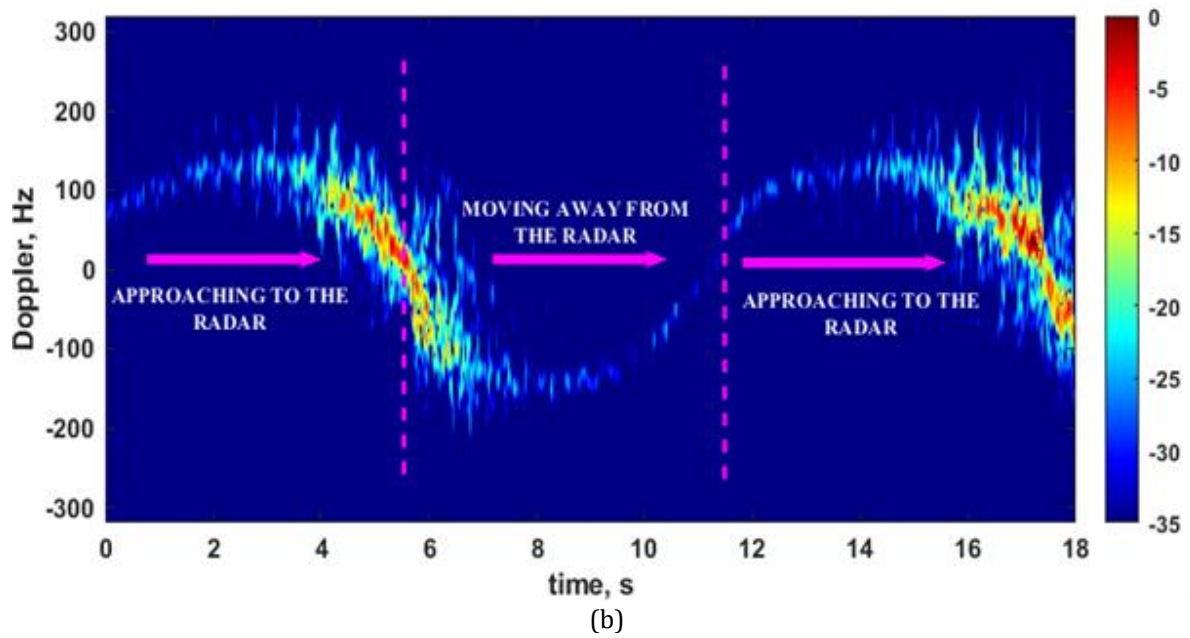


(c)

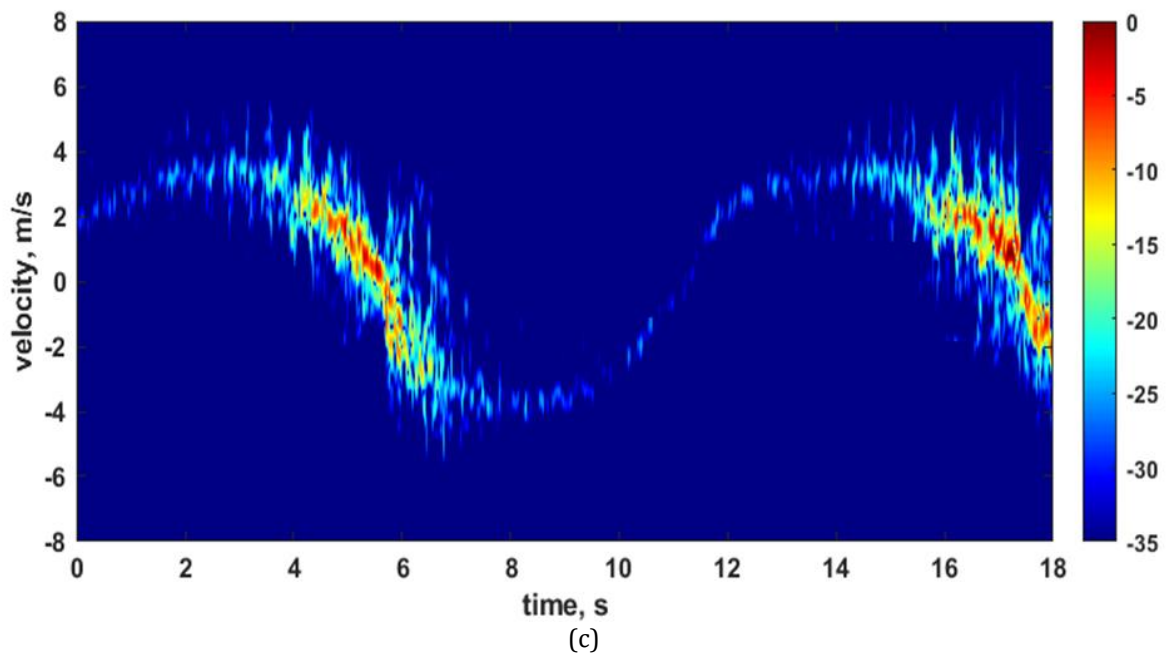
Figure 4. (a) The man approached the radar while walking with still arms, (b) corresponding spectrogram image (c) radar image on time-velocity plane.



(a)



(b)

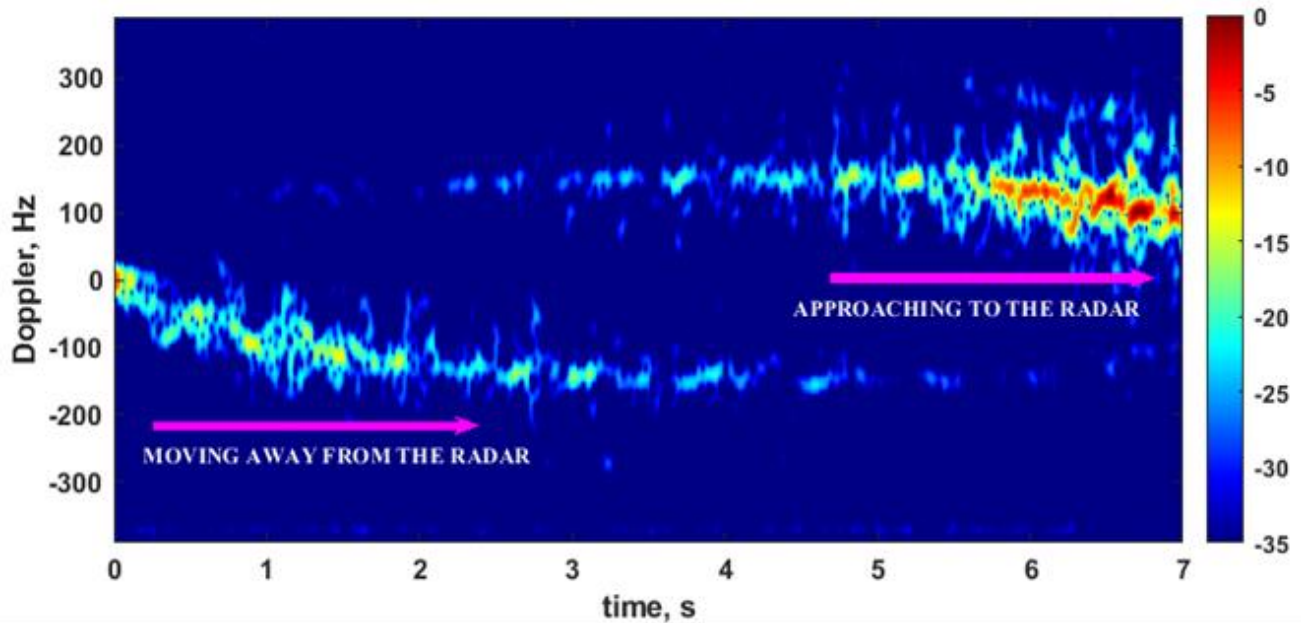


(c)

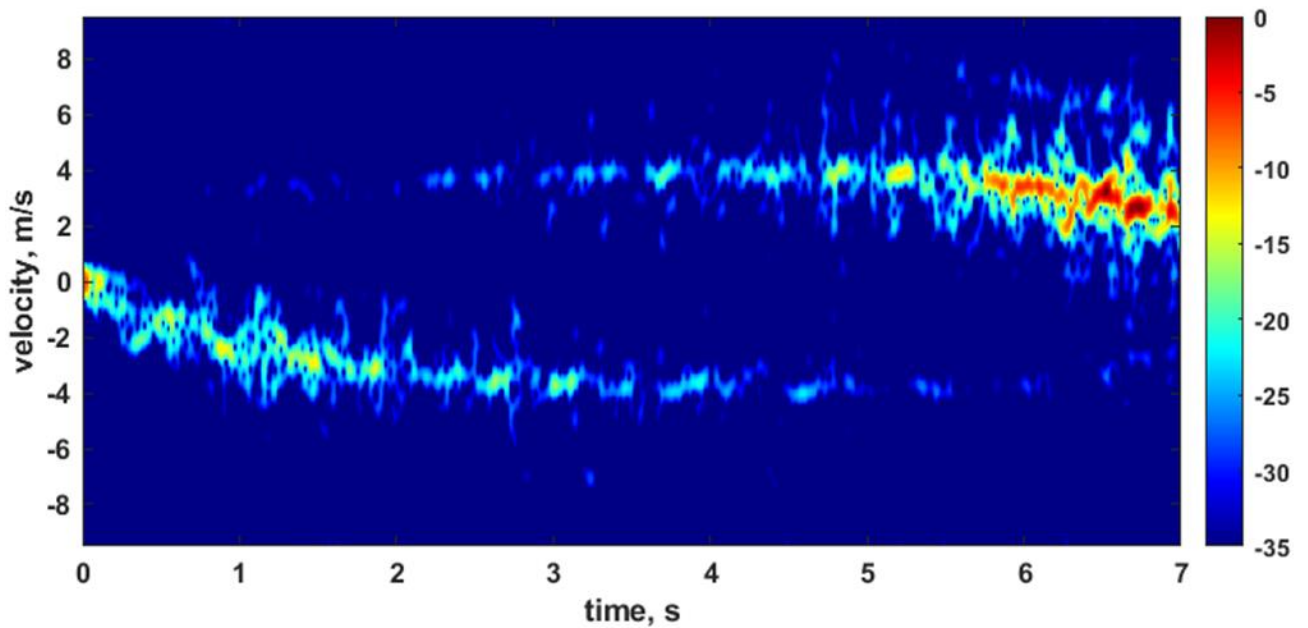
Figure 5. Running experiment: (a) The man first approached to the radar, then moved away from the radar, and finally approached the radar again, (b) corresponding spectrogram image (c) radar image on time-velocity plane.



(a)



(b)



(c)

Figure 6. Two running men experiment (a) The men run opposite directions, (b) corresponding spectrogram image (c) spectrogram image with velocity information.

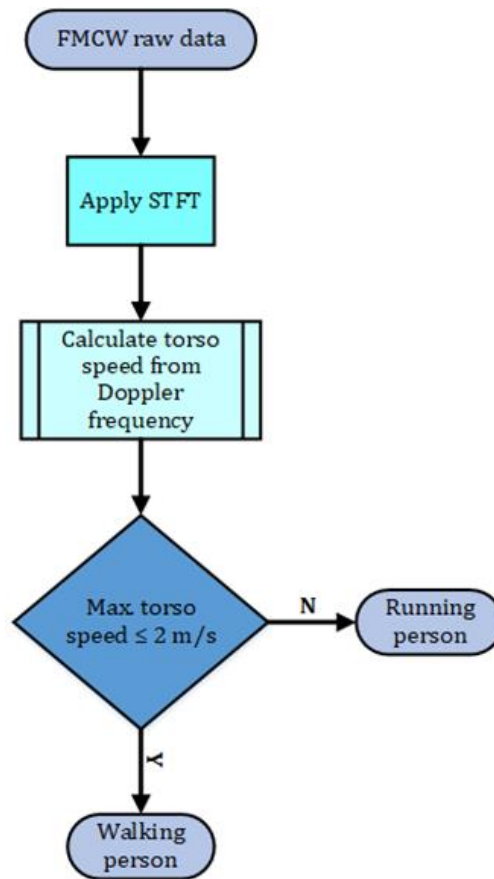


Figure 7. Classification of the movements according to the Doppler frequency with a flow diagram.

Acknowledgement

This work is supported by Mersin University Scientific Research Unit under Project No. 2018-2-TP3-2924. Authors would like to thank Mr. Gökhan Karabacak, Mr. Ahmet Özbek and Mrs. Yurdağül Olgun for their help during experiments.

Author contributions

Onur Tekir: Investigation, data curation, methodology, software, field study, writing-original draft preparation

Caner Özdemir: Conceptualization, validation, writing, reviewing, and editing.

Conflicts of interest

The authors declare no conflicts of interest.

References

1. Ağca, M. (2020). PALS, ICESat/GLAS ve ICESat-2 lazer sistemleri ve kullanım alanları. *Geomatik*, 5(1), 27-35. <https://doi.org/10.29128/geomatik.560344>
2. Navruz, M. (2017). Airborne LIDAR Ve Dted2 verilerinde yükseklik (H) karşılaştırması. *Geomatik*, 2(3), 112-117. <https://doi.org/10.29128/geomatik.319270>
3. Sevgen, S. C., & Karsli, F. (2020). Automatic ground extraction for urban areas from airborne lidar data. *Turkish Journal of Engineering*, 4(3), 113-122. <https://doi.org/10.31127/tuje.641501>
4. Yılmaz, B., & Özdemir, C. (2017). Design and prototype of a compact, ultra wide band double ridged horn antenna for behind obstacle radar applications. *Turkish Journal of Engineering*, 1(2), 76-81. <https://doi.org/10.31127/tuje.316696>
5. Demirci, Ş., & Özdemir, C. (2021). An investigation of the performances of polarimetric target decompositions using GB-SAR imaging. *International Journal of Engineering and Geosciences*, 6(1), 9-19. <https://doi.org/10.26833/ijeg.665175>
6. Demirci, Ş., & Özdemir, C. (2020). Anechoic chamber measurements for circular isar imaging at Mersin University's Meatrç Lab. *International Journal of Engineering and Geosciences*, 5(3), 150-159. <https://doi.org/10.26833/ijeg.649961>
7. Akgül, M. A. (2018). Sentetik açıklıklı radar verilerinin taşkın çalışmalarında kullanılması: Berdan Ovası Taşkını. *Geomatik*, 3(2), 154-162. <https://doi.org/10.29128/geomatik.378123>
8. Özdemir, C. (2020). Radar cross section analysis of unmanned aerial vehicles using predics. *International Journal of Engineering and Geosciences*, 5(3), 144-149. <https://doi.org/10.26833/ijeg.648847>
9. Gurbuz, S. Z., Melvin, W. L., & Williams, D. B. (2011). A nonlinear-phase model-based human detector for radar. *IEEE Transactions on Aerospace and Electronic Systems*, 47(4), 2502-2513. <https://doi.org/10.1109/TAES.2011.6034647>
10. Ozdemir, C. (2021). Inverse synthetic aperture radar imaging with MATLAB algorithms. John Wiley & Sons.
11. Chen, V. C. (2019). The micro-Doppler effect in radar. Artech house.

12. Kim, Y., & Ling, H. (2009). Human activity classification based on micro-Doppler signatures using a support vector machine. *IEEE Transactions on Geoscience and Remote Sensing*, 47(5), 1328-1337. <https://doi.org/10.1109/TGRS.2009.2012849>
13. Heuel, S., & Rohling, H. (2012, May). Pedestrian classification in automotive radar systems. 13th International Radar Symposium, 39-44. <https://doi.org/10.1109/IRS.2012.6233285>
14. van Dorp, P., & Groen, F. C. (2010). Human motion estimation with multiple frequency modulated continuous wave radars. *IET Radar, Sonar & Navigation*, 4(3), 348-361. <https://doi.org/10.1049/iet-rsn.2009.0015>
15. Chen, V. C., & Ling, H. (2002). Time-frequency transforms for radar imaging and signal analysis. Artech house.
16. Hurmuzlu, Y., Basdogan, C., & Carollo, J. J. (1994). Presenting joint kinematics of human locomotion using phase plane portraits and Poincaré maps. *Journal of Biomechanics*, 27(12), 1495-1499. [https://doi.org/10.1016/0021-9290\(94\)90199-6](https://doi.org/10.1016/0021-9290(94)90199-6)
17. Boulic, R., Thalmann, N. M., & Thalmann, D. (1990). A global human walking model with real-time kinematic personification. *The Visual Computer*, 6, 344-358. <https://doi.org/10.1007/BF01901021>
18. Boulic, R., Ulicny, B., & Thalmann, D. (2004). Versatile walk engine. *Journal of Game Development*, 1(1), 29-50.
19. Chen, V. C. (2000). Analysis of radar micro-Doppler with time-frequency transform. In *Proceedings of the Tenth IEEE Workshop on Statistical Signal and Array Processing (Cat. No. 00TH8496)*, 463-466. <https://doi.org/10.1109/SSAP.2000.870167>
20. Geisheimer, J. L., Grenaker III, E. F., & Marshall, W. S. (2002). High-resolution Doppler model of the human gait. In *Radar Sensor Technology and Data Visualization*, 4744, 8-18. <https://doi.org/10.1117/12.488286>
21. Tekir, O., Yilmaz, B., & Özdemir, C. (2023). Signal preprocessing routines for the detection and classification of human micro-Doppler radar signatures. *Microwave and Optical Technology Letters*, 65(8), 2132-2149. <https://doi.org/10.1002/mop.33684>
22. Persico, A. R., Clemente, C., Gaglione, D., Ilioudis, C. V., Cao, J., Pallotta, L., ... & Soraghan, J. J. (2017). On model, algorithms, and experiment for micro-Doppler-based recognition of ballistic targets. *IEEE Transactions on Aerospace and Electronic Systems*, 53(3), 1088-1108. <https://doi.org/10.1109/TAES.2017.2665258>
23. Ozdemir, C., & Ling, H. (1997). Joint time-frequency interpretation of scattering phenomenology in dielectric-coated wires. *IEEE Transactions on Antennas and Propagation*, 45(8), 1259-1264. <https://doi.org/10.1109/8.611245>



© Author(s) 2024. This work is distributed under <https://creativecommons.org/licenses/by-sa/4.0/>



Changes in water surface area of the Middle Atlas-Morocco lakes: A response to climate and human effects

Abdelaziz El-Bouhali ¹, Mhamed Amyay ¹, Khadija El Ouazani Ech-Chahdi ¹

¹ Sidi Mohamed Ben Abdellah University, Natural Environments, Planning, and Socio-Spatial Dynamics, Fez, Morocco, abdelaziz.elbouhali@usmba.ac.ma, mhamedamyay@hotmail.com, khadija.elouazaniechachahdi@usmba.ac.ma

Cite this study:

El-Bouhali, A., Amyay, M., & El Ouazani Ech-Chahdi, K. (2024). Changes in water surface area of the Middle Atlas-Morocco lakes: A response to climate and human effects. *International Journal of Engineering and Geosciences*, 9 (2), 221-232

<https://doi.org/10.26833/ijeg.1391957>

Keywords

Lakes
Changes in water area
Drought periods
Land use
Middle Atlas

Abstract

The lakes represent crucial surface water resources and an integral part of wetlands. The most concerning aspect of the degradation of these areas is the complete drying up of the lakes. In the Mediterranean region, successive changes in land use practices in the context of climate change have strongly influenced wetland areas. In this study, we used Landsat TM, OLI, and OLI-2 satellite images to monitor the water surface area in two representative lakes (Aoua and Ifrah) of the Tabular Middle Atlas and to map land use across the entire study area. To extract information related to lakes and land use, we employed the Support Vector Machine machine learning algorithm, widely used in remote sensing studies. However, we identified drought periods from precipitation data using the Standardized Precipitation Index (SPI) recommended by the World Meteorological Organization (WMO). The results obtained from the processing of Landsat satellite images indicate a significant reduction in the surface area of the lakes, with periods of drying for Aoua lake, endangering their fragile ecosystems and biodiversity. The critical situation of the two lakes is attributed to a combination of natural and anthropogenic factors. The analysis of climatic data shows a significant climate change from the 1980s, with long periods of drought. In parallel, the study area has undergone remarkable modifications in land use patterns, mainly characterized by a significant extension of irrigated agricultural surfaces to the detriment of grazing and rainfed lands. In three decades, the area of irrigated crops has increased from approximately 1300 hectares in 1985 to 7070 hectares in 2022, representing an increase of 542%. The findings presented in this study reveal the extent of lake degradation in the TMA and reflect the alarming decline in groundwater levels. This situation indicates the necessity of formulating a strategy to protect water resources and wetlands in the Middle Atlas.

Research Article

Received: 16.11.2023
Revised: 16.01.2024
Accepted: 28.01.2024
Published: 23.07.2024



1. Introduction

Managing water resources in the 21st century is increasingly challenging [1]. In many regions of the world, water scarcity has appeared as a principal risk affecting sustainable development [2]. The United Nations report on Sustainable Development goals has shown an increase in water scarcity in most countries [3]. Also, this report indicates that «worldwide, 32 countries are experiencing water stress of between 25 and 70 per cent; 22 countries experience it above 70 per cent and are considered to be seriously stressed. This concerning situation is linked to climate change and anthropogenic pressure [4,5]. Increasing water withdrawals for agriculture and urban areas in the context of climate change will exacerbate water stress by 2050 [6].

Generally, aspects of water resource degradation manifest as declining groundwater levels, reduced flows from springs and rivers, and the drying up of lakes. Indeed, the lakes represent precise indicators to measure the effects of factors affecting the hydrological system, such as land-use alterations, changes in precipitation patterns, and increasing water extraction for agricultural and urban purposes.

The lakes represent crucial surface water resources and an integral part of wetlands [7]. The most concerning aspect of the degradation in these areas is the complete drying of the lakes. In the Mediterranean region, successive changes in land use (LU) practices in the context of climate change (CC) have strongly influenced wetland areas. According to [8], they have lost 50% of their surface area during the 20th century. The processes

of modifications in wetland areas in general, and lakes in particular, stem from complex interactions between climate and LU practices. Over the past few decades, lakes have experienced concerning variations in different countries. Several works recently focused on the study of lakes in various locations show that the variation in their surface areas, such as extension or shrinkage, is explained by CC [9-13]. Therefore, lakes are considered sensitive and reliable indicators of CC [14]. Others have indicated that changes in LU have influenced hydrological processes [15-16], imposing impacts on available water resources and watershed runoff patterns worldwide [16].

In Morocco, the lakes located in the Middle Atlas have faced significant pressure due to changes in climate and LU, essentially marked by the intensification of agricultural practices based on irrigation [17-19]. The pressure exerted on the lakes in this strategic sector of the Moroccan mountains is manifested locally by a significant reduction in the water surface area (WSA). Studies conducted on the lakes of the Middle Atlas [19] highlight their responses to CC and anthropogenic pressure. These studies relied on analysis of hydrological and climatic data obtained from the Sebou Hydraulic Basin Agency (ABHS) and sometimes the interpretation of aerial photographs. However, this data is not always available and does not cover all lakes. To address the data issue, we used remote sensing data (Landsat data) to monitor the dynamics of water areas in two representative lakes of the Tabular Middle Atlas (TMA).

The mapping of lake water surface areas (LWA) and their change detection using remote sensing have garnered notable interest across diverse research domains [20]. Remote sensing technology is widely accepted as an effective and suitable means to extract the evolution of water bodies in various areas and temporal scales [15,21-27]. For this reason, significant efforts have been made to develop robust techniques for lake monitoring using available satellite images, such as Landsat (TM, OLI, OLI-2) and Sentinel-2 [28]. Remote sensing data can significantly contribute to addressing the issue of data availability concerning lakes [10]. In recent years, time series of satellite images, notably from missions Landsat, have been extensively used to monitor water areas in lakes, as they provide accurate information with high spatial and temporal resolution. [29] have indicated that this data will be a valuable source for assessing water levels and their changes over the coming decades.

At the global scale, several studies have shown the capacity and precision of remote sensing in studying lakes. This study relies on multi-sensor Landsat satellite images (TM, OLI and OLI-2) to monitor recent variations in the water area of Aoua and Ifrah lakes in the TMA. The objective is to understand how they respond to environmental changes, including climate and LU alterations. Therefore, this study proposes remote sensing data to detect water areas in the TMA lakes over more than three decades (1984 to 2022). It also emphasizes the analysis of existing climate data and the quantification of irrigated surfaces as driving factors in the degradation of lakes. Indeed, understanding the

hydrological impacts of climate and LU changes is imperative for water resource planning and management [30] and for preserving the ecosystem and meeting the increasing water needs of local populations.

2. Materials and method

2.1. Study area

The study area (Figure 1) is located in the TMA, considered among the strategic sectors of Morocco, often referred to as the "water tower of Morocco. It covers an area of 805 km² and is administratively part of the Sefrou and Ifrane provinces. The elevations in this area range from 870 m in low depressions (Sahb Achar) to over 1800 m in the mountains (Jebel Medouar). The geometry of tectonic faults has facilitated the formation of an alternation of depressions and more or less extensive mounds in the area. These depressions, rich in soil and water resources, are today highly converted for agricultural practices. The dominance of faulted lithological formations, characterized by a high permeability coefficient [31] and substantial precipitation (averaging 985 mm annually at the Ifrane station), contributes to abundant water resources. The abundance of water has resulted in a notable extension of irrigated areas in the valleys and intramountain depressions.

Similar to other mountainous regions in Morocco, this area has undergone significant landscape changes in recent decades [32]. The main aspects of these major modifications include the expansion of irrigated crops to the detriment of grazing lands and rainfed agricultural areas. This dynamism results from the interplay of natural factors, encompassing precipitation and water resources, and anthropogenic factors, including population growth and government interventions. According to [33], the transformations occurring in the Middle Atlas reflect the desire to better capitalize on the richness of this region. Thus, the processes leading to this evolution are generated by the intentions of both indigenous and non-indigenous actors and the state through the different programs and incentive plans for the development of agriculture [32]. Thus, the study area is marked by a remarkable urban extension, particularly in the center of Imouizzer-kandar, reflecting a significant increase in population. Information on population changes in this region is available in the general population and housing census. The observed changes in the landscape within the study area may generate adverse effects on the environment. We selected this region for its significant biological, geological, landscape, and socio-economic importance, strongly threatened by inappropriate anthropogenic interventions in the climate change context.

2.2. Satellite data processing

In this study, we utilized Landsat satellite images to map LU and track changes in the water area of Aoua and Ifrah lakes from August 1984 to August 2022. For the years 2002 and 2011, we used the September and July images, respectively (Table 1). All the data were obtained

from the freely accessible archives of the U.S. Geological Survey (USGS). Satellite images from Landsat are widely used in the remote sensing field [34] due to their significant temporal resolution, making them valuable for studying the Earth's surface. This data has become essential for monitoring ecosystems at different spatial and temporal scales [35]. Remote sensing data provided by USGS require radiometric pre-processing to facilitate

classification and interpretation. The pre-processing was performed using the Semi-Automated Classification (SCP) extension installed in the QGIS software. The SCP plugin was used to apply the radiometric correction algorithm to convert the raw pixel values (DN) to TOA reflectance. This powerful package [36] is widely used for satellite image pre-processing [37-40].

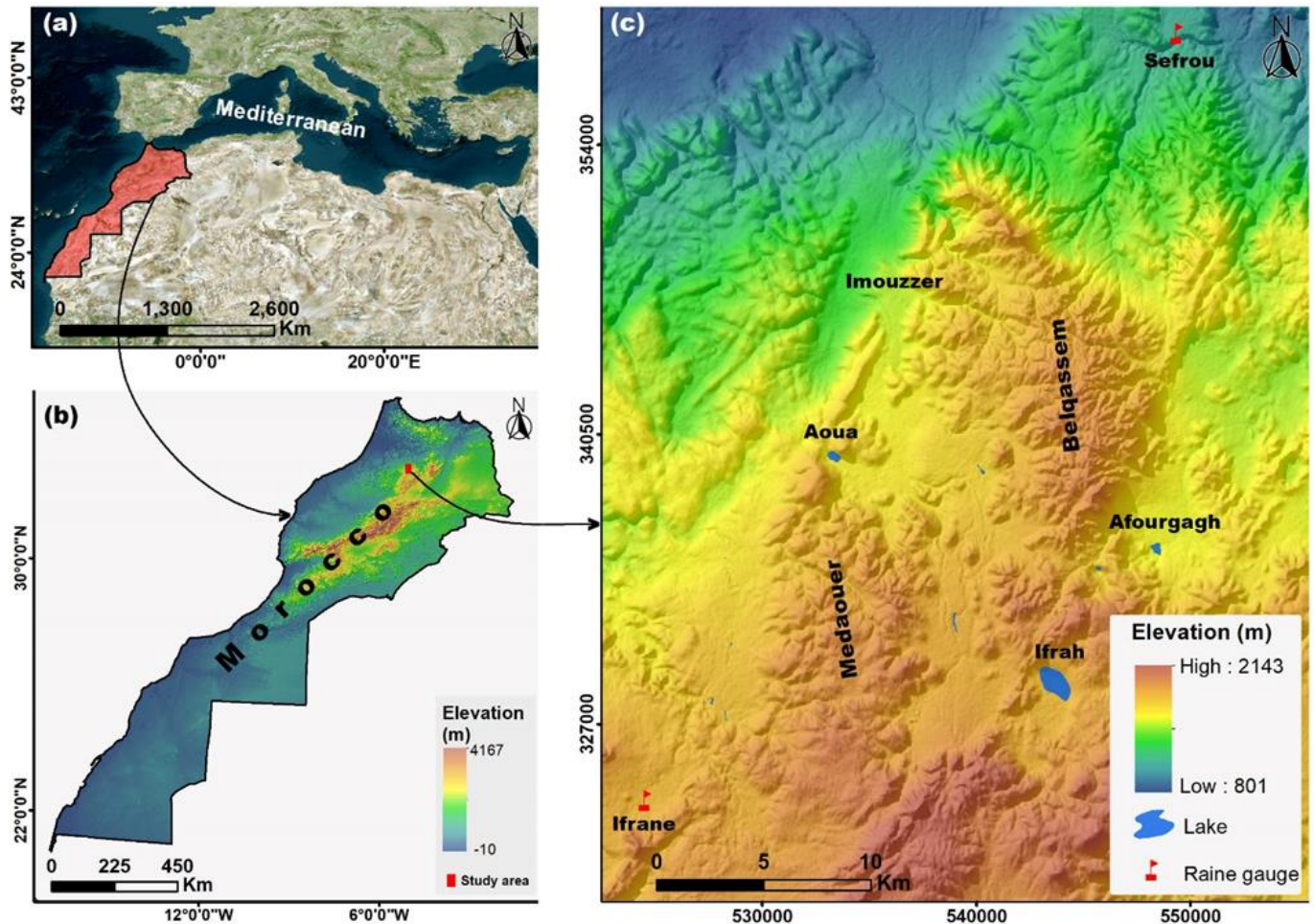


Figure 1. Geographical location of the study area: a) Morocco within the Mediterranean Basin; b) location of the study area in Morocco; c) Study area.

Table 1. Landsat satellite images used in this study [41].

Acquisition date	Sensor	Acquisition date	Sensor	Source	Spatial resolution
August 18, 1984	TM	September 16, 2002	TM	USGS	30 m
August 14, 1985	TM	August 23, 2003	TM	USGS	30 m
August 17, 1986	TM	August 18, 2004	TM	USGS	30 m
August 20, 1987	TM	August 12, 2005	TM	USGS	30 m
August 06, 1988	TM	August 08, 2006	TM	USGS	30 m
August 09, 1989	TM	August 11, 2007	TM	USGS	30 m
August 03, 1990	TM	August 20, 2008	TM	USGS	30 m
August 22, 1991	TM	August 07, 2009	TM	USGS	30 m
August 17, 1992	TM	August 03, 2010	TM	USGS	30 m
August 11, 1993	TM	July 28, 2011	TM	USGS	30 m
August 07, 1994	TM	August 01, 2015	OLI	USGS	30 m
August 01, 1995	TM	August 19, 2016	OLI	USGS	30 m
August 12, 1996	TM	August 22, 2017	OLI	USGS	30 m
August 15, 1997	TM	August 09, 2018	OLI	USGS	30 m
August 09, 1998	TM	August 12, 2019	OLI	USGS	30 m
August 21, 1999	TM	August 05, 2020	OLI	USGS	30 m
August 14, 2000	TM	August 08, 2021	OLI	USGS	30 m
August 17, 2001	TM	August 03, 2022	OLI-2	USGS	30 m

Satellite image pre-processing is followed by classification to extract LU classes and LWA. The extraction of information from the raw images is performed using several supervised classification algorithms (ML, RF and SVM), unsupervised algorithms (K-means, ISO Cluster) and spectral index calculations (NDVI, EVI and NDWI). In this study, we used the Support Vector Machine (SVM) supervised classification algorithm, which is widely used by researchers [34,42]. Due to its high accuracy in classification results [42-45], this non-parametric algorithm has been used extensively in recent years. The results obtained in the study area also demonstrate the power of SVM in extracting the

LWA (Figure 2). Figure 3 illustrates the statistical evaluation performance of the satellite image classification on August 14, 1985, using the SVM algorithm. In this example, overall accuracy and the Kappa coefficient perfectly illustrate the quality of the classification, with values of 0.98 (98%) and 0.99 (99%) respectively. The distinction of the water area of the lakes from other LU classes in a satellite image is relatively easy due to the separability of spectral reflectance. Water always exhibits very low reflectance in the near-infrared (NIR) compared to other classes, such as vegetation and bare lands.

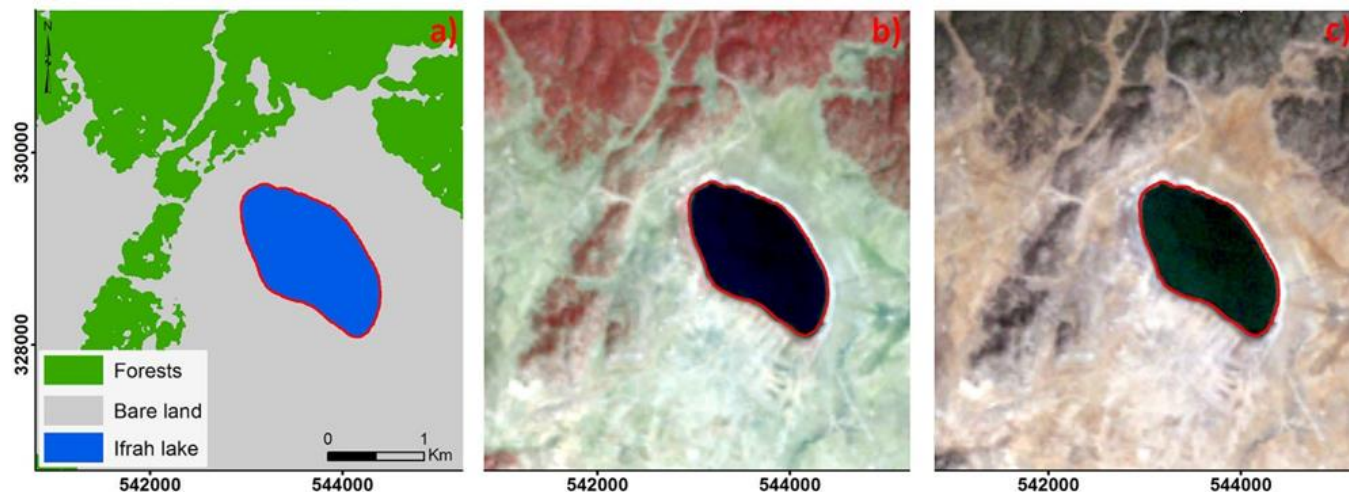


Figure 2. The comparison between a classified satellite image and a raw image, dated August 14, 1985. a) Classified image; b) Raw image in false color; c) Raw image in true color.

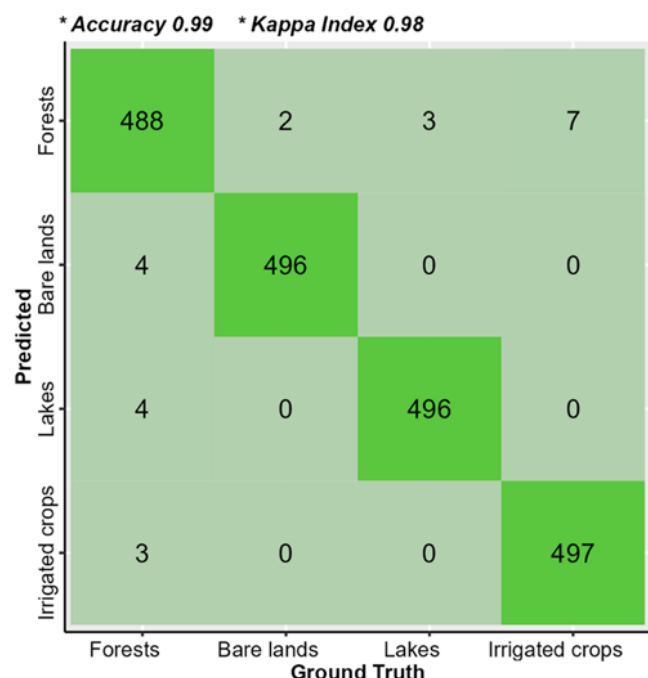


Figure 3. Classification accuracy of land use classes: example of Landsat TM satellite image: August 14, 1985.

The selection of satellite images is based on ground observations and spectral reflectance monitoring. These two sources of information have allowed us to choose the most suitable month for studying irrigated surfaces and extracting the water area of the lakes. The agricultural

calendars conducted in the field and the analysis of remote sensing data throughout the year have revealed that August is the most suitable for achieving this type of study. In August, the area of irrigated lands experienced a remarkable increase, which puts significant pressure on groundwater resources. The tracking of lake water areas from August 1984 to August 2022 is very interesting to assess the impact of irrigation on water resources in the TMA. However, we used ground samples in the classification process (training data) and in validating the results. The methodology employed to map land use and the water surface area of the lakes is depicted in Figure 4.

2.3. Climate data processing

We used the SPEI package in R-statistical software to calculate the Normalized Precipitation Index (Equation 1) from the precipitation time series for the Ifrane and Sefrou stations. The Standardized Precipitation Index (SPI) [46] is recommended by the World Meteorological Organization (WMO). This index has been used in over 70 countries [47] to identify wet and dry periods based on long-term precipitation data. Drought intensity varies depending on the SPI values, as presented in Table 2. Negative anomalies (starting from -1.0) indicate periods of drought, and they end when the SPI values become positive. SPI allows measuring the intensity and severity of drought. The selection of the period for calculating the SPI is precisely defined by [48]; short-term durations can

be important for agronomic studies, while long-term durations are suitable for hydrological issues.

$$SPI = (X_i - X_m) / \sigma \quad (1)$$

Where:

SPI: is the drought index;

X_i: annual, seasonal and monthly precipitation;

X_m: long-term mean;

σ: standard deviation.

Table 2. SPI values [46].

SPI value	Class
More than 2	Extremely wet
1.5 to 1.99	Very wet
1.0 to 1.49	Moderately wet
0 to 0.99	Mildly wet
-0.99 to 0	Mildly dry
-1.0 to -1.49	Moderately dry
-1.5 to -1.99	Severely dry
-2 and less	Extremely dry

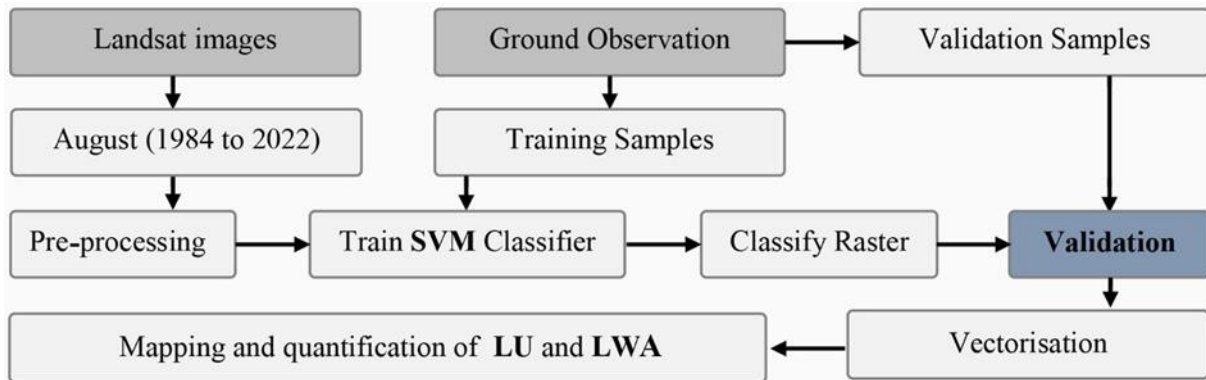


Figure 4. The flowchart of the used methodology for LU and LWA extraction.

3. Results and discussion

3.1. Variation of the water area in Aoua and Ifrah lakes

Monitoring the water area in Aoua and Ifrah lakes (Figure 5) using multi-date satellite images revealed significant changes. However, the rate of increase, shrinkage, and drying up varies from one lake to another depending on the factors influencing this dynamism. The total area of the lakes has significantly decreased between 1984 and 2022, with a reduction of 70 ha for Aoua lake and 136 ha for Ifrah lake (Figure 6 and 7).

Figure 6a illustrates the spatial distribution and quantification of the water area in Aoua lake from August 1984 to August 2022. Between the two dates, the water area has undergone distinct fluctuations. These fluctuations range between 0 ha or complete drying and 116 ha. Over more than three decades, Aoua lake has experienced significant oscillations, with periods of

complete drying (2001-2002; 2008; 2018 to 2022). In recent years, the hydrological deficit of the lake has increased worryingly. Locally, this is manifested by the total drying of the lake for an extended period (2018 to 2022). Before 2000, the lake experienced variations in its area, reaching a minimum value of 11.5 ha in 1995 and a maximum of 96.7 ha in 1992. Since 2000, the water area has significantly decreased (2000-2003; 2005-2008; 2016-2022), with some exceptions of increasing in water area during specific periods, notably in 2004 (85 ha) and from 2009 to 2015. Figure 6b indicates the rapid variations in the surface area of Aoua lake. Over the years, the lake underwent significant changes, especially in 2003-2004, 2008-2009, and 2015-2016. These variations illustrate a rapid increase and decrease in lake water surface area, from 8 ha in 2003 to 85 ha in 2004 and from 0 ha in 2008 to 120 ha in 2009. The transition from complete drying to nearly full filling (116 ha) and vice versa occurs rapidly.

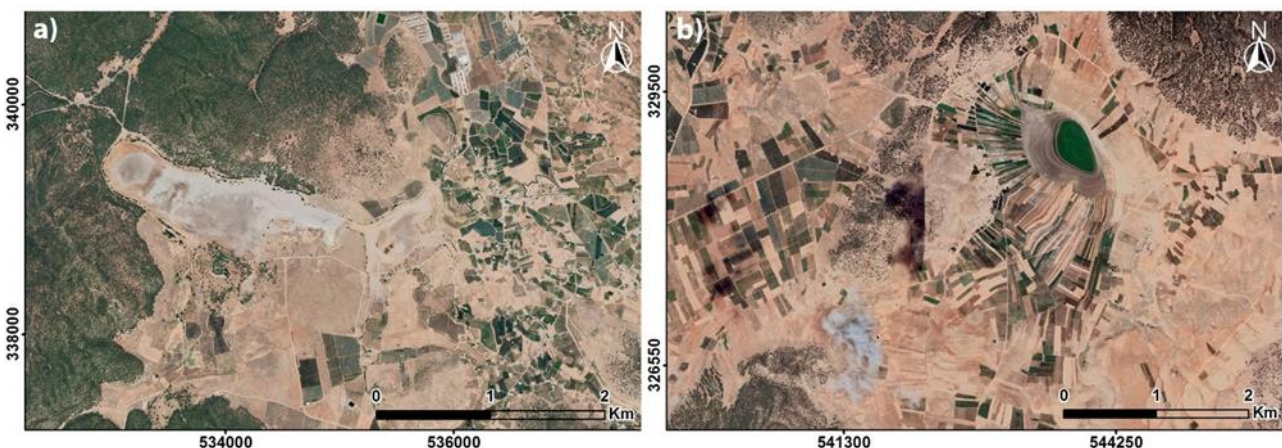


Figure 5. Situation of the lakes in July 2022 (Google Earth images). a) Aoua lake; b) Ifrah lake. The two maps show the alarming reduction of the water surface and the remarkable extension of irrigated areas around the lakes.

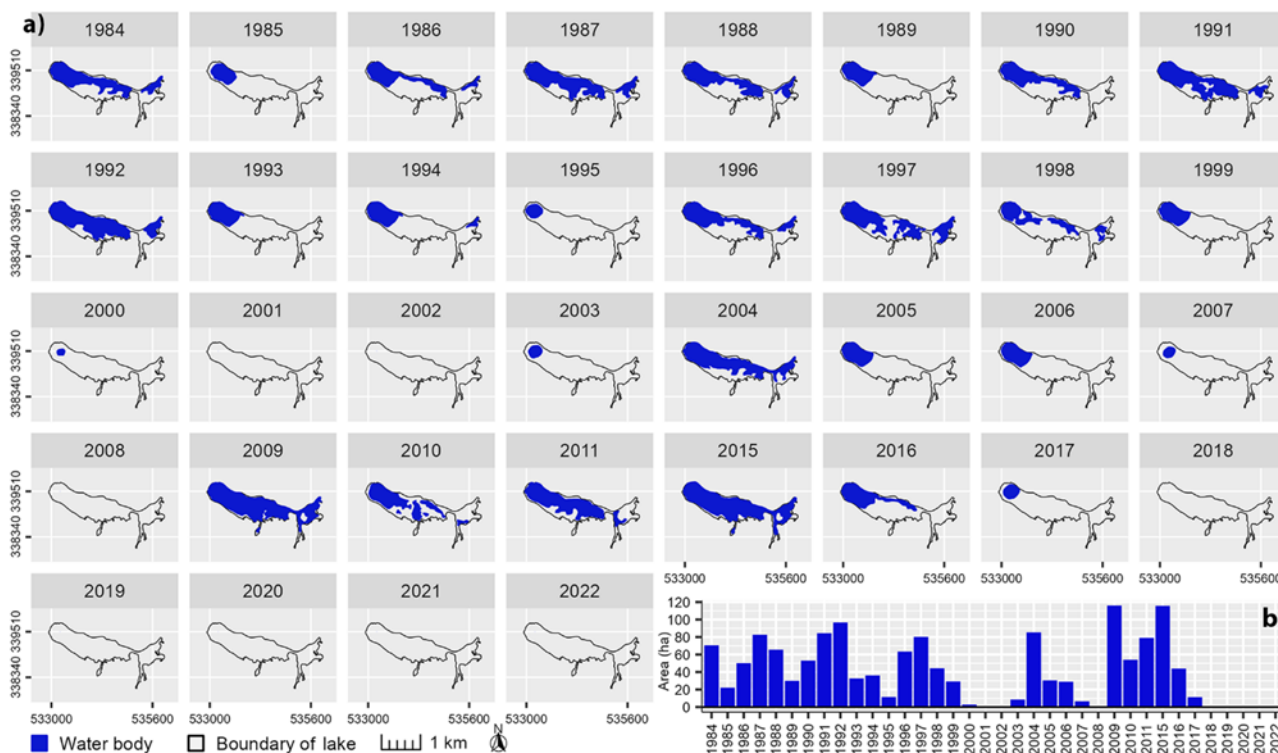


Figure 6. Variation in surface area (ha) of Aoua lake from August 1984 to August 2022 (Landsat satellite images: TM, OLI and OLI-2).

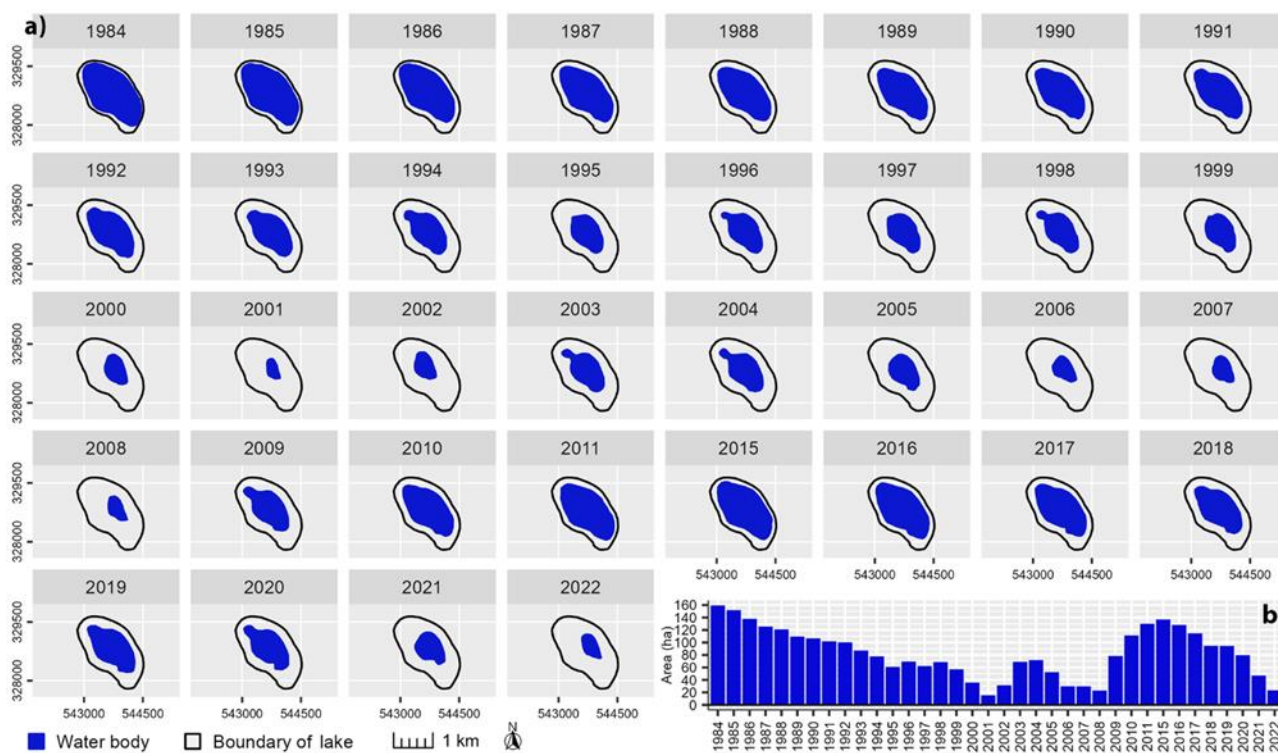


Figure 7. Variation in surface area (ha) of Ifrah lake from August 1984 to August 2022 (Landsat satellite images: TM, OLI and OLI-2).

Figure 7a shows the changes in the water area of Ifrah lake from August 1984 to August 2022. During this period, the lake fluctuated in its area, ranging from 159 ha in 1984 to 15 ha in 2001. Over three decades, Ifrah lake experienced significant variations, with periods of concerning reduction (2000-2008; 2021-2022). We distinguished three periods of variations in the lake water area. The first period extends from August 1984 to

August 2001 and is characterized by a significant shrinking of the water area, with a change of 144 ha over 17 years. The second period, from 2001 to 2008, experienced a slight increase in the water area. In the third period, there was an increase in the water surface until 2015 due to the rise in precipitation between 2009 and 2012. This phase was followed by a new trend of the lake regressing until 2022. The decrease in the area of

Ifrah lake (23 ha in 2022) indicates the very critical situation of the groundwater in recent years. Figure 7b illustrates that the reduction and progression of Ifrah areas occur slowly compared to Aoua lake, which is characterized by a rapid variation pattern.

The results obtained from Landsat satellite images indicate a significant decrease in the water area in both Aoua and Ifrah lakes. The continuous reduction of LWA in the TMA reflects the concerning situation of water resources, influenced by changes in hydrological parameters and radical modifications in traditional LU practices, giving way to modern practices based on irrigation.

3.2. Effect of drought severity and LU on lakes water areas variation

The changes in LWA in the TMA are often considered accurate and sensitive representations of climate parameter changes and profound modifications in LU practices. In three decades, the Imouzzer and Aoua depressions have experienced a progressive development of rosaceous orchards. The spatiotemporal evolution of irrigated areas in the TMA has led to notable transformations in landscape structures. These changes in LU practices have coincided with long periods of severe drought that have affected Morocco since the 1980s [49,50].

3.2.1. Drought severity

The calculation of SPI for Ifrane and Sefrou stations over 24 months shows wet and dry periods. The results presented in Figure 8 and 9 demonstrate that the wet and dry periods are more clearly visible for SPI 24 months (Figure 8) compared to SPI 12 months (Figure 9). For the stations of Ifrane and Sefrou, we distinguished two principal periods, from 1935 to 1979 and 1980 to 2015. The first is characterized by a remarkable dominance of wet to very wet years of long duration, with positive

anomalies exceeding 2. In the second period, we observed a persistent drought characterized by extended periods, indicated by negative anomalies exceeding -2, interspersed with brief wet spells. The frequency and intensity of drought increased significantly after 1980. The increase in the number of long-lasting droughts from the 1980s has strongly influenced the water area of the lakes. During wet periods, the lakes in the TMA show significant extension of their water area. However, an alarming decrease in the LWA, even complete drying, occurs during severe drought periods.

In parallel with this abrupt change in precipitation and the dominance of long periods of drought since the 1980s, temperatures have recorded a significant increase in positive anomalies, as highlighted in the official reports of the Intergovernmental Panel on Climate Change [51,52]. The trend of decreasing precipitation, rising temperatures, and the progressive extension of irrigated areas in the TMA have contributed significantly to the amplification of hydrological deficits. Locally, this is manifested by the decline in groundwater levels and, consequently, the drying up of springs, reduced river flows, and alarming depletion of lakes, especially in recent years.

3.2.2. Land use changes

Studies on the Middle Atlas confirm that this region of Morocco was primarily used for pastoral activities [17, 32,33, 53-55], with a limited area devoted to rainfed and irrigated crops. However, with population growth, increased connectivity to other regions, the desire to exploit natural resources and government subsidies, these areas have witnessed significant rural development, resulting in profound landscape changes. These transformations include the extension of irrigated agriculture and orchards at the expense of grazing lands and rainfed crop areas. The change rates, the processes implemented, and the actors involved in this dynamic have been different throughout this period [32].

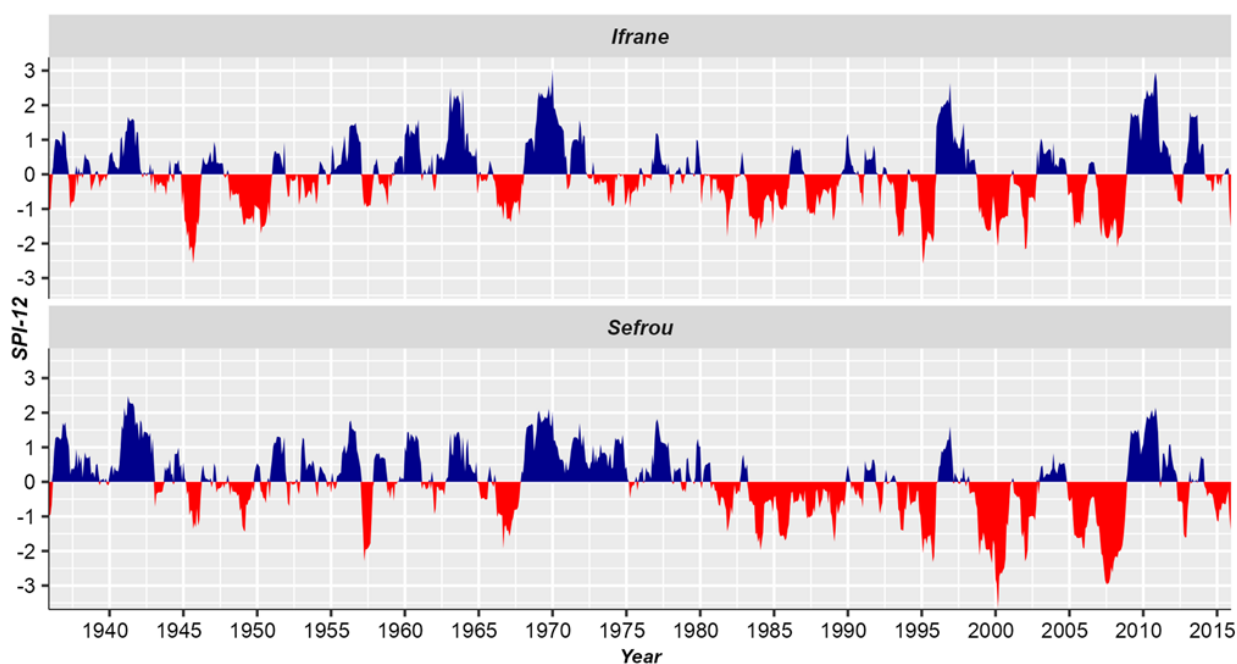


Figure 8. Temporal variation of the SPI at the 12-month scale in Ifrane and Sefrou stations.

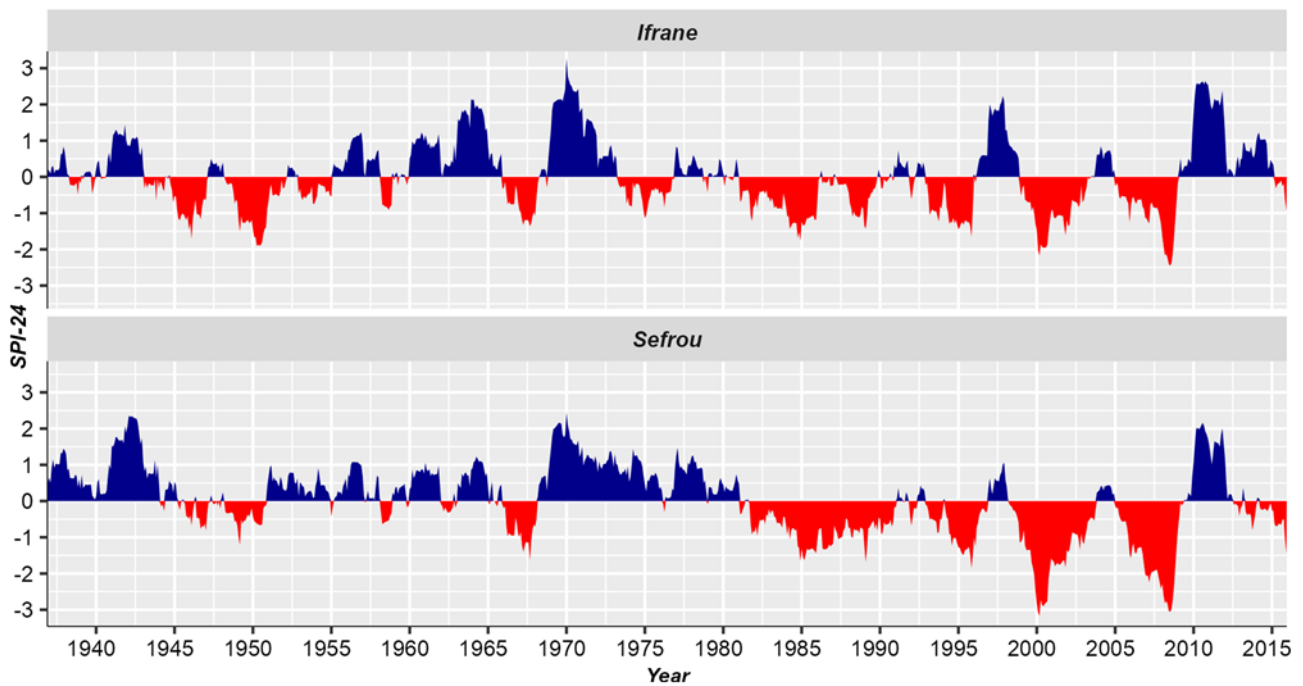


Figure 9. Temporal variation of the SPI at the 24-month scale in Ifrane and Sefrou stations.

Over the past decades, the Imouzzer and Aoua depressions have witnessed a continuous extension of agricultural practices based on irrigation. LU map derived from the Landsat image of August 2022 clearly shows a significant increase in irrigated areas compared to 1985 (Figure 10). The development and arrangement of land for irrigation have expanded in all directions. Irrigated lands are now found on the slopes of depressions, marshlands, grasslands, and even at the edges of forests. The profit generated by irrigated crops, government incentives, and the influx of external capital into the region are the driving forces behind this development. The irrigation of these new farms is provided exclusively by groundwater. The water extraction from the aquifer in these areas withdraws significant volumes of water.

The mapping and quantification of LU in the study area (Figure 10 and Table 3) have highlighted a significant landscape dynamic characterized by a marked increase in irrigated agricultural areas and built-up lands. Between 1985 and 2022, the area of irrigated land increased from 1300 hectares to 7070 hectares (+7.16% of the total area), representing a growth of 542% over 37 years. This extension of irrigated areas often occurred at the expense of uncultivated lands (pasturelands), which decreased from approximately 32,000 hectares to 26,000 hectares, experiencing a reduction of about 6000 hectares (-7.44% of the total area). The entire water surface of the lakes in this area significantly decreased, from approximately 205 hectares in 1985 to only 27 hectares in 2022, resulting in a decrease of 178 hectares. Thus, we observed a notable increase in built-up within the study area, especially in the center of Imouzzer-Kandar. Between the two dates, the built-up area increased from approximately 33 ha to 287 ha, representing a growth of 254 ha. The forest area remains almost stable, with a slight estimated positive change of 0.19%.

Between 1985 and 2022, the study area experienced a significant landscape transformation, primarily characterized by a progressive increase in irrigated agriculture and built-up areas. The shift of population activities towards irrigation and adopting modern water exploitation techniques have led to the decline of traditional society. Alongside the extension of irrigated areas, the demand for irrigation water has increased, exerting significant pressure on the groundwater resources of the TMA. The consequences of modifications in LU, within the context of CC, have had a striking impact on the water resources in the study area. The intensification of irrigation and the continuous increase in water extraction downstream of Aoua lake and in the vicinity of Ifrah lake have widely contributed to the disruption of the hydrological regime. Consequently, the complete drying of Aoua lake for extended periods (2018-2022) reflects the deeply critical condition of the groundwater level, characterized by a significant and widespread decline. Although this decline dates back to the mid-1990s, its magnitude has become alarming today.

4. Conclusion

While lakes are crucial surface water resources and rich ecosystems in biodiversity, they have experienced a significant shrinking over the past decades, endangering their ecological, biological, and landscape diversity. Studies on lakes indicate that this critical situation is primarily linked to the interaction of natural factors such as CC and anthropogenic factors like rapid urbanization, extension of irrigated areas, groundwater extraction, and dam construction. Consequently, changes in LU practices in the context of reduced rainfall and increased temperatures have accelerated the negative variation in lake water surface areas. Monitoring lake surface areas from satellite images in different countries reveals their alarming situation. In this context, Zhang et al. [56]

demonstrated that Ebinur lake has undergone drastic fluctuations, with a significant loss of water surface area. Between 2003 and 2015, the lake's surface area decreased from 817.63 km² to 384.60 km² in 2015, representing a decrease of over 50% of its surface. Davraz et al. [15] indicated that the water level of Burdur lake has consistently decreased. The lake's surface area experienced a remarkable shrinkage between 1975 and

2016, declining from 210 km² to 131 km², presenting a 37% reduction. Xu et al. [57] showed that, since the 1990s, many lakes in Inner Mongolia have significantly decreased with varying rates based on each lake's characteristics. In this study, we mapped the surface area of two lakes in the Tabular Middle Atlas to understand their responses to environmental changes, including climate and LU.

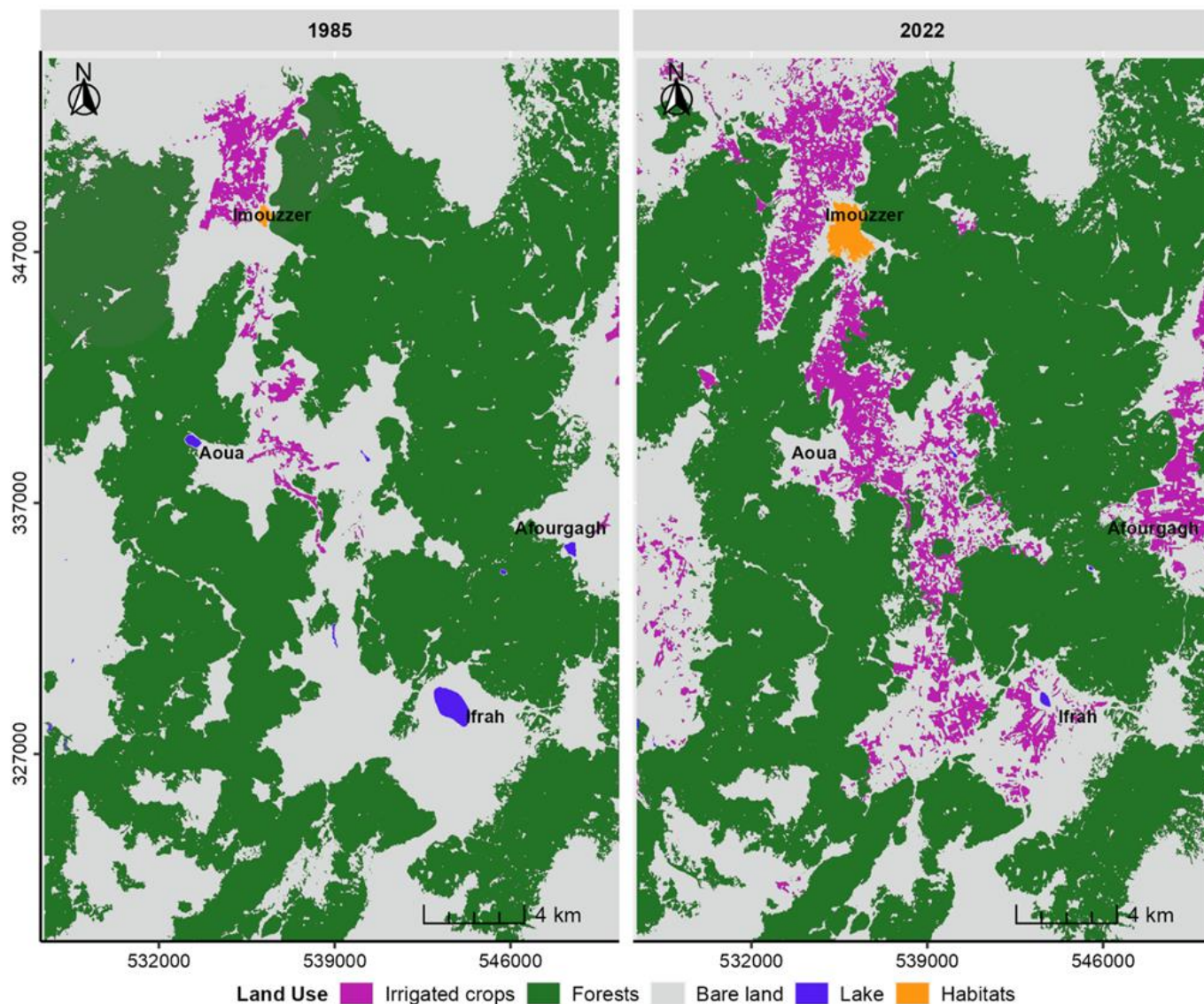


Figure 10. Changes of irrigated areas in Imouizzer and Aoua depressions (Landsat TM and OLI-2 satellite images).

Table 3. Evolution of LU (ha) from 1985 to 2022.

LU classes	1985		2022		1985 - 2022	
	ha	%	ha	%	ha	%
Irrigated crops	1304	1.62	7071	8.78	5767	7.16
Forests	46948	58.29	47100	58.48	152	0.19
Bare lands	32050	39.79	26055	32.35	-5995	-7.44
Lakes	205	0.25	27	0.03	-178	-0.22
Habitats	33	0.04	287	0.36	254	0.32

With multi-sensor Landsat satellite images (TM, OLI, and OLI-2), we studied changes in the LWA in the TMA over 38 years. The results demonstrate the effectiveness of remote sensing data in monitoring variations in the LWA, with an overall accuracy exceeding 0.9. During the studied period, the lakes of Aoua and Ifrah exhibited remarkable variations. Recently, we have observed a

general trend of decreasing lake surface area. Between 1984 and 2022, Aoua lake lost 100% of its area (from 70 ha to complete drying), and Ifrah lake lost 87% of its surface area (from 159 ha to 23 ha). This finding indicates that the pressure exerted on the lakes in the TMA region directly reflects a significant reduction in the

water area, with periods of complete drying, endangering fragile ecosystems and biodiversity.

The highly critical situation of the lakes results from the interplay between natural and anthropogenic factors. The mapping and quantification of LU in the study area indicate significant changes. It is a remarkable extension of irrigated surfaces to the detriment of uncultivated lands. Over three decades, the area of irrigated crops has increased significantly, representing a growth of 542%. The progressive trend of irrigated agricultural areas has coincided with long periods of drought that have affected Morocco since the 1980s (as indicated by the SPI index). The combination of precipitation deficits and intense human pressure on water resources has led to a decline in groundwater levels in the depressions of the TMA. The results presented in this study demonstrate the concerning variations in LWA and reflect the alarming decline in groundwater levels. This situation highlights the need to formulate a strategy to mitigate the impacts of CC and reduce anthropogenic pressure.

Acknowledgement

The authors are grateful to the USGS for providing the Landsat TM, OLI and OLI-2 satellite images. The authors also thank the Sebou Hydraulic Basin Agency (ABHS) for providing precipitation data.

Author contributions

Abdelaziz El-Bouhali: Methodology, Software, Investigation, Data analysis, Writing – original draft. **Mhamed Amyay:** Supervision, Conceptualization, Writing – review & editing, Validation. **Khadija El Ouazani Ech-Chahdi:** Data analysis, Writing - Review & editing.

Conflicts of interest

The authors declare no conflicts of interest.

References

- Raneesh, K. Y. (2014). Impact of climate change on water resources. *Journal of Earth Science & Climatic Change*, 5(3), 1. <http://dx.doi.org/10.4172/2157-7617.1000185>
- Kummu, M., Guillaume, J. H., de Moel, H., Eisner, S., Flörke, M., Porkka, M., ... & Ward, P. J. (2016). The world's road to water scarcity: shortage and stress in the 20th century and pathways towards sustainability. *Scientific Reports*, 6(1), 1-16. <https://doi.org/10.1038/srep38495>
- FAO. (2018). Progress on level of water stress - Global baseline for SDG 6 Indicator 6.4.2.
- Konapala, G., Mishra, A. K., Wada, Y., & Mann, M. E. (2020). Climate change will affect global water availability through compounding changes in seasonal precipitation and evaporation. *Nature Communications*, 11(1), 3044. <https://doi.org/10.1038/s41467-020-16757-w>
- Huang, Z., Yuan, X., & Liu, X. (2021). The key drivers for the changes in global water scarcity: Water withdrawal versus water availability. *Journal of Hydrology*, 601, 126658. <https://doi.org/10.1016/j.jhydrol.2021.126658>
- Connor, R., & Miletto, M. (2023). Rapport mondial des Nations Unies sur la mise en valeur des ressources en eau 2023: partenariats et coopération pour l'eau; résumé.
- Williamson, C. E., Saros, J. E., Vincent, W. F., & Smol, J. P. (2009). Lakes and reservoirs as sentinels, integrators, and regulators of climate change. *Limnology and Oceanography*, 54(6part2), 2273-2282. https://doi.org/10.4319/lo.2009.54.6_part_2.2273
- Beltrame, C., Perennou, C., & Guelmami, A. (2015). Évolution de l'occupation du sol dans les zones humides littorales du Bassin méditerranéen de 1975 à 2005. *Méditerranée. Revue géographique des pays méditerranéens/Journal of Mediterranean geography*, (125), 97-111. <https://doi.org/10.4000/mediterranee.8046>
- Abdelhalim, A., Sefelnasr, A., & Ismail, E. (2020). Response of the interaction between surface water and groundwater to climate change and proposed megastructure. *Journal of African Earth Sciences*, 162, 103723. <https://doi.org/10.1016/j.jafrearsci.2019.103723>
- Emami, H., & Zarei, A. (2021). Modelling lake water's surface changes using environmental and remote sensing data: A case study of lake urmia. *Remote Sensing Applications: Society and Environment*, 23, 100594. <https://doi.org/10.1016/j.rsase.2021.100594>
- Zhang, R., Zhu, L., Ma, Q., Chen, H., Liu, C., & Zubaida, M. (2021). The consecutive lake group water storage variations and their dynamic response to climate change in the central Tibetan Plateau. *Journal of Hydrology*, 601, 126615. <https://doi.org/10.1016/j.jhydrol.2021.126615>
- Kayastha, M. B., Ye, X., Huang, C., & Xue, P. (2022). Future rise of the Great Lakes water levels under climate change. *Journal of Hydrology*, 612, 128205. <https://doi.org/10.1016/j.jhydrol.2022.128205>
- Gbetkom, P. G., Crétaux, J. F., Tchilibou, M., Carret, A., Delhoume, M., Bergé-Nguyen, M., & Sylvestre, F. (2023). Lake Chad vegetation cover and surface water variations in response to rainfall fluctuations under recent climate conditions (2000– 2020). *Science of The Total Environment*, 857, 159302. <https://doi.org/10.1016/j.scitotenv.2022.159302>
- Zhang, Y., An, C. B., Zheng, L. Y., Liu, L. Y., Zhang, W. S., Lu, C., & Zhang, Y. Z. (2023). Assessment of lake area in response to climate change at varying elevations: A case study of Mt. Tianshan, Central Asia. *Science of The Total Environment*, 869, 161665. <https://doi.org/10.1016/j.scitotenv.2023.161665>
- Davraz, A., Sener, E., & Sener, S. (2019). Evaluation of climate and human effects on the hydrology and water quality of Burdur Lake, Turkey. *Journal of African Earth Sciences*, 158, 103569. <https://doi.org/10.1016/j.jafrearsci.2019.103569>
- Liu, Y., Wu, G., Fan, X., Gan, G., Wang, W., & Liu, Y. (2022). Hydrological impacts of land use/cover

- changes in the Lake Victoria basin. *Ecological Indicators*, 145, 109580.
<https://doi.org/10.1016/j.ecolind.2022.109580>
17. Amyay, M., Laaouane, M., & Akdim, B. (2001). La pression anthropique sur les ressources en eau souterraine dans le Moyen Atlas. Exemple de la dépression d' Afourgagh. *Mosella*, 25(3-4), 341-352.
 18. Sayad, A., & Chakiri, S. (2010). Impact of the evolution of the climate on the level of Dayet Aoua in the Moroccan Middle Atlas. *Science et Changements planétaires/Sécheresse*, 21(4), 245-251.
<https://doi.org/10.1684/sec.2010.0252>
 19. Sayad, A., Chakiri, S., Martin, C., Bejjaji, Z., & Echarfaoui, H. (2011). Effet des conditions climatiques sur le niveau du lac Sidi Ali (Moyen Atlas, Maroc). *Physio-Géo. Géographie Physique et Environnement*, 5, 251-268.
<https://doi.org/10.4000/physio-geo.2145>
 20. Wang, J., Ding, J., Li, G., Liang, J., Yu, D., Aishan, T., ... & Liu, J. (2019). Dynamic detection of water surface area of Ebinur Lake using multi-source satellite data (Landsat and Sentinel-1A) and its responses to changing environment. *Catena*, 177, 189-201.
<https://doi.org/10.1016/j.catena.2019.02.020>
 21. Bastawesy, M. A., Khalaf, F. I., & Arafat, S. M. (2008). The use of remote sensing and GIS for the estimation of water loss from Tushka lakes, southwestern desert, Egypt. *Journal of African Earth Sciences*, 52(3), 73-80.
<https://doi.org/10.1016/j.jafrearsci.2008.03.006>
 22. Eid, A. N. M., Olatubara, C. O., Ewemoje, T. A., El-Hennawy, M. T., & Farouk, H. (2020). Inland wetland time-series digital change detection based on SAVI and NDWI indices: Wadi El-Rayan lakes, Egypt. *Remote Sensing Applications: Society and Environment*, 19, 100347.
<https://doi.org/10.1016/j.rsase.2020.100347>
 23. Gu, Z., Zhang, Y., & Fan, H. (2021). Mapping inter-and intra-annual dynamics in water surface area of the Tonle Sap Lake with Landsat time-series and water level data. *Journal of Hydrology*, 601, 126644.
<https://doi.org/10.1016/j.jhydrol.2021.126644>
 24. Jumaah, H. J., Ameen, M. H., Mohamed, G. H., & Ajaj, Q. M. (2022). Monitoring and evaluation Al-Razzaza lake changes in Iraq using GIS and remote sensing technology. *The Egyptian Journal of Remote Sensing and Space Science*, 25(1), 313-321.
<https://doi.org/10.1016/j.ejrs.2022.01.013>
 25. Cazzaniga, I., Zibordi, G., Alikas, K., & Kratzer, S. (2023). Temporal changes in the remote sensing reflectance at Lake Vänern. *Journal of Great Lakes Research*, 49(2), 357-367.
<https://doi.org/10.1016/j.jglr.2023.01.006>
 26. Su, Y., Ran, Y., Zhang, G., & Li, X. (2023). Remotely sensed lake area changes in permafrost regions of the Arctic and the Tibetan Plateau between 1987 and 2017. *Science of the Total Environment*, 880, 163355.
<https://doi.org/10.1016/j.scitotenv.2023.163355>
 27. Wang, C., Xie, W., Li, T., Wu, G., Wu, Y., Wang, Q., ... & Pan, X. (2023). Analysis of Spatial and Temporal Variation in Water Coverage in the Sub-Lakes of Poyang Lake Based on Multi-Source Remote Sensing. *Remote Sensing*, 15(11), 2788.
<https://doi.org/10.3390/rs15112788>
 28. Urbański, J. A. (2022). Monitoring and classification of high Arctic lakes in the Svalbard Islands using remote sensing. *International Journal of Applied Earth Observation and Geoinformation*, 112, 102911.
<https://doi.org/10.1016/j.jag.2022.102911>
 29. Jawak, S. D., Kulkarni, K., & Luis, A. J. (2015). A review on extraction of lakes from remotely sensed optical satellite data with a special focus on cryospheric lakes. *Advances in Remote Sensing*, 4(3), 196-213.
<https://doi.org/10.4236/ars.2015.43016>
 30. Vorosmarty, C. J., Green, P., Salisbury, J., & Lammers, R. B. (2000). Global water resources: vulnerability from climate change and population growth. *Science*, 289(5477), 284-288.
<https://doi.org/10.1126/science.289.5477.284>
 31. Bentayeb, A., & Leclerc, C. (1977). Le Causse moyen atlasique. *Ressources en Eaux du Maroc, Tome3, Domaines Atlasiques et Sud-Atlasiques*, 37-66.
 32. El-Bouhali, A. (2023). L'évolution des surfaces irriguées et leur impact sur les ressources en eau dans le contexte climatique actuel au Moyen Atlas tabulaire. [Thèse de doctorat. Université Sidi Mohamed Ben Abdellah].
 33. Jennan, L. (1986). Mutations récentes des campagnes du Moyen Atlas et de ses bordures. *Méditerranée*, 59(4), 49-62.
 34. Ozdogan, M., Yang, Y., Allez, G., & Cervantes, C. (2010). Remote sensing of irrigated agriculture: Opportunities and challenges. *Remote Sensing*, 2(9), 2274-2304. <https://doi.org/10.3390/rs2092274>
 35. Bian, J., Li, A., Lei, G., Zhang, Z., & Nan, X. (2020). Global high-resolution mountain green cover index mapping based on Landsat images and Google Earth Engine. *ISPRS Journal of Photogrammetry and Remote Sensing*, 162, 63-76.
<https://doi.org/10.1016/j.isprsjprs.2020.02.011>
 36. Correia, R., Duarte, L., Teodoro, A. C., & Monteiro, A. (2018). Processing image to geographical information systems (PI2GIS)—A learning tool for QGIS. *Education Sciences*, 8(2), 83.
<https://doi.org/10.3390/educsci8020083>
 37. Yawson, D. O., Adu, M. O., & Osei, K. N. (2018). Spatial assessment of sugarcane (*Saccharum spp. L.*) production to feed the Komenda Sugar Factory, Ghana. *Heliyon*, 4(11).
<https://doi.org/10.1016/j.heliyon.2018.e00903>
 38. Obodai, J., Adjei, K. A., Odai, S. N., & Lumor, M. (2019). Land use/land cover dynamics using landsat data in a gold mining basin—the Ankobra, Ghana. *Remote Sensing Applications: Society and Environment*, 13, 247-256.
<https://doi.org/10.1016/j.rsase.2018.10.007>
 39. Congedo, L. (2021). Semi-automatic classification plugin: A Python tool for the download and processing of remote sensing images in QGIS. *Journal of Open Source Software*, 6(64), 3172.
<https://doi.org/10.21105/joss.03172>
 40. Belenok, V., Noszczyk, T., Hebryn-Baidy, L., & Kryachok, S. (2021). Investigating anthropogenically transformed landscapes with remote sensing. *Remote Sensing Applications: Society and Environment*, 24,

100635.
<https://doi.org/10.1016/j.rsase.2021.100635>
41. <https://earthexplorer.usgs.gov>
42. Zheng, B., Myint, S. W., Thenkabail, P. S., & Aggarwal, R. M. (2015). A support vector machine to identify irrigated crop types using time-series Landsat NDVI data. *International Journal of Applied Earth Observation and Geoinformation*, 34, 103-112. <https://doi.org/10.1016/j.jag.2014.07.002>
43. Sharma, A. K., Hubert-Moy, L., Buvaneshwari, S., Sekhar, M., Ruiz, L., Bandyopadhyay, S., & Corgne, S. (2018). Irrigation history estimation using multitemporal Landsat satellite images: Application to an intensive groundwater irrigated agricultural watershed in India. *Remote Sensing*, 10(6), 893. <https://doi.org/10.3390/rs10060893>
44. Rana, V. K., & Suryanarayana, T. M. V. (2020). Performance evaluation of MLE, RF and SVM classification algorithms for watershed scale land use/land cover mapping using Sentinel 2 bands. *Remote Sensing Applications: Society and Environment*, 19, 100351. <https://doi.org/10.1016/j.rsase.2020.100351>
45. Avci, C., Budak, M., Yağmur, N., & Balçık, F. (2023). Comparison between random forest and support vector machine algorithms for LULC classification. *International Journal of Engineering and Geosciences*, 8(1), 1-10. <https://doi.org/10.26833/ijeg.987605>
46. McKee, T. B., Doesken, N. J., & Kleist, J. (1993, January). The relationship of drought frequency and duration to time scales. *Proceedings of the 8th Conference on Applied Climatology*, 17(22), 179-183.
47. WMO. (World Meteorological Organization) (2012). *Standardized Precipitation Index User Guide*, 24.
48. Guttman, N. B. (1999). Accepting the standardized precipitation index: a calculation algorithm 1. *JAWRA Journal of the American Water Resources Association*, 35(2), 311-322. <https://doi.org/10.1111/j.1752-1688.1999.tb03592.x>
49. Barakat, F., & Handoufe, A. (1997). La sècheresse agricole au Maroc. *Sustainability of Water Resources Increasing Uncertainty*, 31-41.
50. Stour, L., & Agoumi, A. (2008). Climatic drought in Morocco during the last decades. *Hydroécologie Appliquée*, 16, 215-232.
51. Pachauri, R. K., & Reisinger, A. (2007). *Climate change 2007: Synthesis report. Contribution of working groups I, II and III to the fourth assessment report of the Intergovernmental Panel on Climate Change*. IPCC.
52. Stocker, T. F., Qin, D., Plattner, G-K, Tignor, M. M. B., Allen, S. K., Boschung, J., Nauels, A., Xia, Y., Bex, V., & Midgley, P. M. (2013). *Climate Change 2013: The Physical Science Basis*.
53. Badidi, B. (1995). *La révolution des vergers de rosacées dans le Moyen-Atlas*. [Doctoral dissertation, thèse de doctorat, Faculté des Lettres et Sciences Humaines, Limoges].
54. Jihad, M. D. E. (2016). *Climate change and rural development in the middle Atlas Mountains and fringe areas (Morocco)*. *Journal of Alpine Research| Revue de Géographie Alpine*, (104-4). <https://doi.org/10.4000/rga.3465>
55. Tag, B. (1996). *Les potentialités de développement du Moyen-Atlas oriental et leur appréciation par les acteurs locaux/Development possibilities in the eastern Middle Atlas Mountains and their assessment by local actors*. *Revue de Géographie Alpine*, 84(4), 51-60.
56. Zhang, J., Ding, J., Wu, P., Tan, J., Huang, S., Teng, D., ... & Chen, W. (2020). Assessing arid inland lake watershed area and vegetation response to multiple temporal scales of drought across the Ebinur Lake Watershed. *Scientific Reports*, 10(1), 1354. <https://doi.org/10.1038/s41598-020-57898-8>
57. Xu, Y., Gun, Z., Zhao, J., & Cheng, X. (2022). Variations in lake water storage over Inner Mongolia during recent three decades based on multi-mission satellites. *Journal of Hydrology*, 609, 127719. <https://doi.org/10.1016/j.jhydrol.2022.127719>



© Author(s) 2024. This work is distributed under <https://creativecommons.org/licenses/by-sa/4.0/>



Machine learning assisted prediction of land surface temperature (LST) based on major air pollutants over the Annamayya District of India

Jagadish Kumar Mogaraju *¹ 

¹ International Union for Conservation of Nature Commission on Ecosystem Management, Agroecosystems, India, jagadishmogaraju@gmail.com

Cite this study: Mogaraju, J. K. (2024). Machine learning assisted prediction of land surface temperature (LST) based on major air pollutants over the Annamayya District of India. International Journal of Engineering and Geosciences, 9 (2), 233-246

<https://doi.org/10.26833/ijeg.1394111>

Keywords

Machine learning
Geographic information systems
Sentinel-5-P
MODIS
Land surface temperature

Research Article

Received: 21.11.2023
Revised: 15.05.2024
Accepted: 04.06.2024
Published: 24.07.2024



Abstract

Remote sensing (RS), Geographic information systems (GIS), and Machine learning can be integrated to predict land surface temperatures (LST) based on the data related to carbon monoxide (CO), Formaldehyde (HCHO), Nitrogen dioxide (NO₂), Sulphur dioxide (SO₂), absorbing aerosol index (AAI), and Aerosol optical depth (AOD). In this study, LST was predicted using machine learning classifiers, i.e., Extra trees classifier (ET), Logistic regressors (LR), and Random Forests (RF). The accuracy of the LR classifier (0.89 or 89%) is higher than ET (82%) and RF (82%) classifiers. Evaluation metrics for each classifier are presented in the form of accuracy, Area under the curve (AUC), Recall, Precision, F1 score, Kappa, and MCC (Matthew's correlation coefficient). Based on the relative performance of the ML classifiers, it was concluded that the LR classifier performed better. Geographic information systems and RS tools were used to extract the data across spatial and temporal scales (2019 to 2022). In order to evaluate the model graphically, ROC (Receiver operating characteristic) curve, Confusion matrix, Validation curve, Classification report, Feature importance plot, and t-SNE (t-distributed stochastic neighbour embedding) plot were used. On validation of each ML classifier, it was observed that the RF classifier returned model complexity due to limited data availability and other factors yet to be studied post data availability. Sentinel-5-P and MODIS data are used in this study.

1. Introduction

The land surface temperature (LST) can be considered an essential indicator in assessing the environmental conditions that might exist at a place at any point in time [1]. Satellite-derived products have helped us monitor the LST dynamics on a large scale for three decades, and more data is being added by the day, helping many researchers yield insights [2]. The urban centers are in focus since most of the population ingress is apparent there, causing congestion in the living space inside the regulatory frames of reference [3]. LST can be classified under critical geophysical parameters as it is dynamic across all the land-water interfaces we know [4]. It is a continuous task to monitor LST across spatial and temporal scales, which can assist governments in framing specific rules in extreme heat situations [5]. Aerosols suspended in the lower atmosphere can affect LST fluctuations and may induce a negative feedback mechanism on surface temperature that can influence the inhabitants [6]. The landscape dynamics initiated due to population ingress and unprecedented urban sprawl

can alter local microclimate in terms of LST and Aerosol optical depth (AOD) [7]. The seasonal temperatures were lowered across the Indian subcontinent due to increased AOD levels [8]. Carbon monoxide (CO) emission can be anthropogenic, and its release into the lower atmosphere before an earthquake in 2001 was observed, reflecting that natural CO emission is possible [9]. The combined effect of forest fires and formaldehyde (HCHO) on surface temperature was observed using satellite-derived observations [10]. The fluctuation in HCHO concentrations in the troposphere was associated with the biogenic volatile organic compounds (BVOC) that were released by plants in response to abiotic stress (LST) [11]. The isoprene emissions released by the abiotically stressed plants were tracked using formaldehyde variations, and these emissions can affect radiative forcing on a large scale [12]. The surface temperatures are sensitive to the Nitrogen dioxide (NO₂) levels, and lightning-induced reactions can also favor NO₂ generation [13, 14]. The sulfur dioxide (SO₂) concentrations affect the radiative forcing, surface temperature, and climate change on a global scale [15,

16]. Plants cannot tolerate surface temperatures greater than 35°C with few exceptions and will release compounds that we can interpret as abiotic stress signals [17–23].

Machine learning (ML) algorithms were used in land cover and land use (LULC) dynamics in relation to surface temperature fluctuations assisted by remote sensing instruments. The Artificial Neural Networks (ANN) and Cellular Automata (CA) supported by Support Vector Machine (SVM) [24] were used to understand LST dynamics over urban landscapes [18, 25]. Soil Moisture and Ocean Salinity (SMOS) derived soil moisture, Moderate Resolution Image spectrometer (MODIS) for LST, along with generalized linear models (GLM) of Artificial Intelligence (AI) framework was used in hydrological applications [26]. The urban form metrics, i.e., building density (BD) and floor area ratio (FAR), were associated with LST fluctuations with the aid of machine learning [27]. The LST products of MODIS were successfully downscaled using ML frameworks, enabling high spatial and temporal resolutions for use in diverse applications [28]. Deep learning and neural networks (DL-NN) were used to optimize LST retrieval (MODIS) methods, and other geophysical parameters were also obtained easily [29]. Convolutional neural networks (CNN) of DL were used to get the LST values from Advanced microwave scanning radiometer 2 (AMSR2), and long-term LST disparities were easily studied [30]. XGB (Extra Gradient Boosting) regression and ANN-CA were used to extract urban heat islands using LST and LULC data [31]. Land use/Land cover variations and population can change LST [32]. Changes in indices such as normalized difference vegetation index (NDVI), normalized difference bareness index (NDBaI), normalized difference built-up index (NDBI), and modified normalized difference water index (MNDWI) can influence LST [33]. The effect of seasons in estimating LST was estimated using Landsat 8 data, and the Thermal sharpening (TsHARP) algorithm was also used [34]. The tendency of interrelationships between MNDWI, NDBaI, NDBI, and NDVI was apparent in the winter season than summer [35]. Fallow lands and settlements can enhance LST rate but water bodies, agricultural land and forests can reduce LST rate [36].

This work is done to possibly fill the research gap in predicting LST using major air pollutants, i.e., CO, HCHO, NO₂, SO₂, and other parameters like Aerosol optical depth (AOD) and Aerosol absorption index (AAI) using machine learning algorithms.

2. Method

2.1. Data

The datasets needed for this study are obtained from Earth Explorer (USGS) and Giovanni (NASA) websites [37, 38]. The required data is collected in the .csv and GeoTIFF formats so that the entire procedure involving processing, interpretation, and analysis can be done using in-house equipment. The satellite data is obtained from Sentinel-5- P (TROPOMI) [39] and MODIS platforms [40]. AAI, CO, HCHO, NO₂, and SO₂-related data is obtained from Sentinel-5- P, whereas Land surface

temperature data is obtained from MODIS. AOD (500nm) related datasets are retrieved from MCD19A2.006: Terra & Aqua MAIAC. The spatial distribution maps of pollutants CO, HCHO, NO₂, SO₂, AAI, AOD, and LST were prepared to know the anomalies on a spatial scale. The LST values greater than 35°C are labeled as 'Hot,' and those less than 35°C are labeled as 'Normal.' These two classes were considered essential classes, and the datasets were passed onto the machine learning frameworks. Three ML algorithms, i.e., Extra Trees classifier (ET) [41, 42], Logistic regression (LR) [43, 44], and Random Forest (RF) [43], were used in this study as they performed better than others.

2.2. Study area

The study area selected for this study is Annamayya district, located in the southern part of Andhra Pradesh state, India [37], as shown in Figure 1. After reorganizing the Cuddapah and Chittoor districts of Andhra Pradesh, it is a newly formed district. The study area is about 7951 square kilometers and extends from 78° 18' 55" and 79° 20' 26" E longitude and 13° 19' 55" and 14° 42' 32" of N latitude. Rajampet, Rayachoti, and Madanapalle are the main urban centers of the district, and most of the business activities are witnessed here [45]. The effects of the selected pollutants on the land surface temperature were studied for the years 2019, 2020, 2021, and 2022. The time-averaged maps (annual) are prepared to know the spatial and temporal spread of the effects produced due to selected pollutants, and their effect on time-averaged LST is studied. The detailed methodology is given in Figure 2.

2.3. Interpretation of metrics and outputs

The evaluation metrics used in knowing the performance of the models are Accuracy, AUC (Area under the curve), Recall, Precision, F1 score (F-measure), Kappa, and MCC (Matthews correlation coefficient) values [46, 47]. After scrutinizing the evaluation metrics, accuracy values were given more weightage than other metrics. The results for each ML model are given through ROC (Receiver operating characteristic) curves, Confusion matrix, Validation curve, Classification report, Feature importance plot, and t-SNE (t-distributed stochastic neighbor embedding) manifold plots [48, 49]. The ROC curve illustrates model performance in a binary classification system with varied discrimination threshold or limit. It is generated using TPR or true positive rate and FPR or false positive rate. The primary advantage of an ROC curve is that there is no need for threshold optimization for each label or class. A confusion matrix can be employed to evaluate the classifier product quality. The diagonal values show us the points for which the label predicted = actual label. The off-diagonal values show the classifier's prediction error. If the diagonal values are higher than the off-diagonal values, then we can assume that there are more correct predictions. The F₁ score can be considered a harmonic mean of recall and precision (1-best, 0- worst). The kappa statistic vibrates between -1 (chance agreement) and +1 (complete agreement).

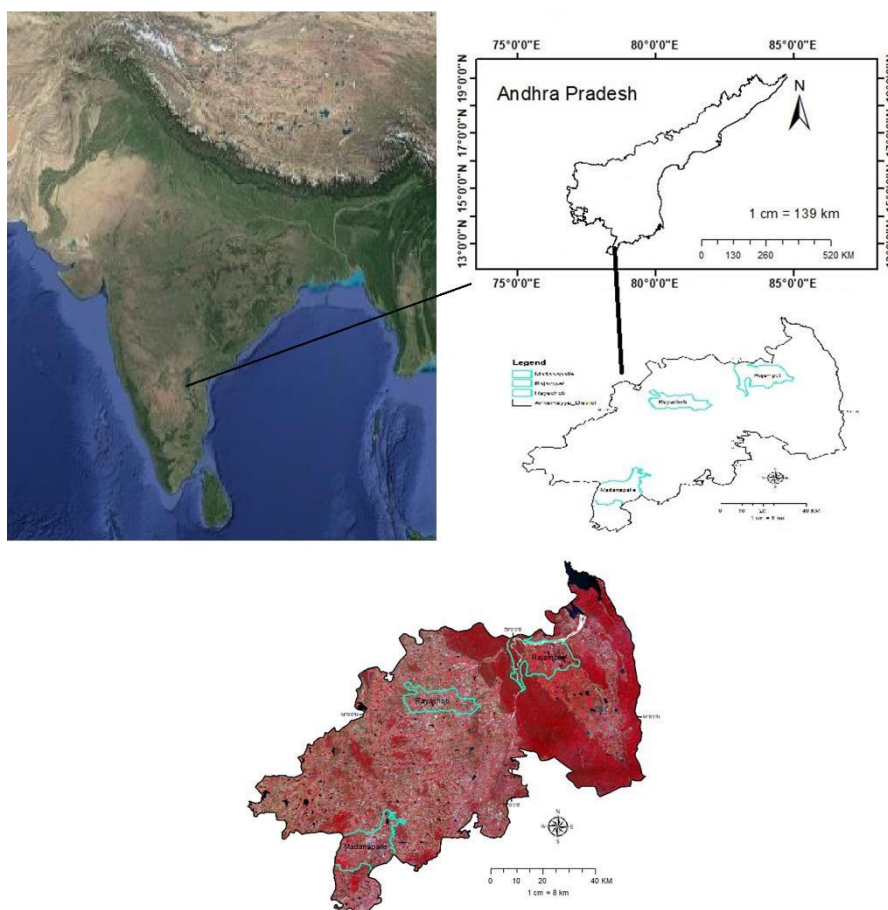


Figure 1. Study area with False colour composite.

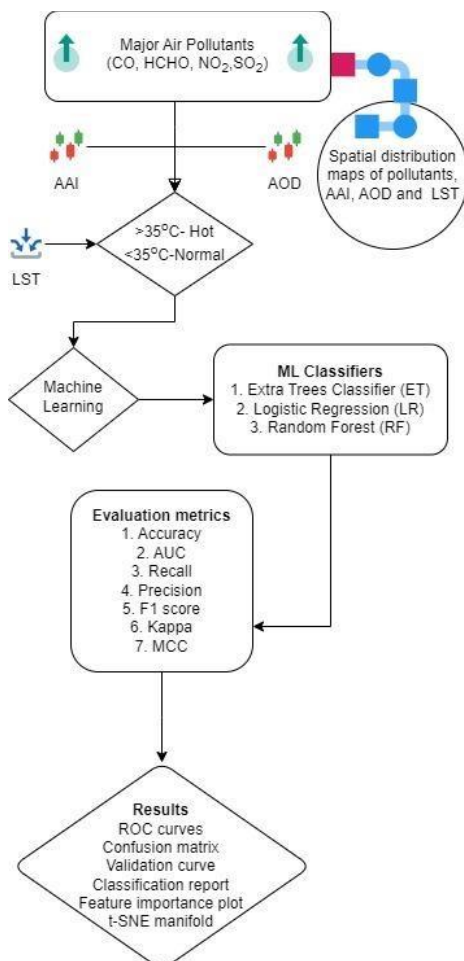


Figure 2. Methodology.

MCC score reflects the quality of the binary classification in this case. The primary advantage of the MCC metric is that it is a balanced measure and can be employed for classes of varied sizes. The MCC (phi coefficient) values fluctuate between -1 (inverse prediction), 0 (random prediction), and +1 (Perfect prediction). The validation and training score can explain the model's performance, i.e., underfitting, overfitting, and fit (well fitted). If the validation and training scores are low, we can assume that the estimator/model will be underfitting and, if high, overfitting or a well-fitted estimator. The classification report shows all the metrics, such as precision, recall, F1, and support (occurrence of each class in test data). The depth or relative rank of a specific feature can be used to evaluate the importance of that feature in relation to the predictability of the desired variable (target), and this can be shown in the form of a feature importance plot. t-SNE can be used to visualize the data (high-dimension) by transforming the similarities between the data points to cumulative probabilities, and it also lowers the Kullback-Leibler divergence.

2.4 Methodology

The data pertaining to the major air pollutants were subjected to preprocessing. Random points were selected for all the variables. In preprocessing, we removed outliers, eliminated perfect collinearity, and applied normalization and transformation. The independent variables are CO, HCHO, NO₂, SO₂, AAI, AOD, and LST alone is a dependent variable. The dataset was

subjected to a machine learning framework. ML classifiers were used to predict LST (at two levels), and three were selected among several classifiers. The evaluation metrics like MCC, Kappa, F_1 score, Precision, Recall, AUC, and accuracy were used to gauge prediction capability. The outputs were for selected ML classifiers. GIS maps were prepared for each variable to express their spatial distribution.

3. Results

3.1. GIS

The spatial distribution of the Absorbing aerosol index (AAI), i.e., the prevalence of aerosols, is given in Figure 3 (a-d). The Aerosol index can be considered as a qualitative index of the presence of aerosols generated from dust and biomass burning (plumes from volcanic ash are ignored as the study area is devoid of volcanic activity) [50]. The wavelength variations of Rayleigh scattering (UV) are minimal due to limited ozone absorption [51]. Top Of atmosphere (TOA) reflectance and Rayleigh scattering reflectance result in residual values where the positive values represent aerosols (UV-absorbing) [52]. The NE corners of the study area showed less aerosol index (-1.33844 in 2019) (-1.6613 in 2020) (-1.40316 in 2021) (-0.705651 in 2022) and high in E and central portions (-0.986181 in 2019) (-1.37002 in 2020) (-1.06346 in 2021) (-0.294711 in 2022). The spatial distribution of Aerosol optical depth (AOD) is given in Figure 4 (a-d). The AOD is low (593.324 in 2019) (508.243 in 2020) (795.5 in 2021) (791.5 in 2022) in the NE, S, and W and high in the N and central portions (68 in 2019) (250.053 in 2020) (183.5 in 2021) (68 in 2022).

The spatial distribution of carbon monoxide is given in Figure 5 (a-d). Except for S and some portions in the NE (0.0328049 in 2019) (0.0333505 in 2020) (0.0317095 in 2021) (0.0310688) of the study area, most of the region exhibited high levels (0.0378867 in 2019) (0.0384048 in 2020) (0.0368594 in 2021) (0.0362371) of CO (mol/m²). The spatial distribution of formaldehyde (HCHO) is given in Figure 6 (a-d). The HCHO (mol/m²) concentration is higher in the NE portions (0.00018135 in 2019) (0.000181125 in 2020) (0.000175397 in 2021) (0.000180444 in 2022) and low in the S and E portions (0.00011805 in 2019) (0.000107572 in 2020) (0.00010903 in 2021) (0.00010737) of the study area. The spatial distribution of nitrogen dioxide NO₂ (mol/m²) is given in Figure 7 (a-d). The N and NE corners exhibited high NO₂ concentrations (2.68345e-005 in 2019) (2.31525 e-005 in 2020) (2.62399 e-005 in 2021) (2.62361 e-005 in 2022) than other regions (2.08934 e-005 in 2019) (1.43907 e-005 in 2020) (1.68165 e-005 in 2021) (1.71763 e-005 in 2022) of the study area. The spatial distribution of sulphur dioxide (SO₂) (mol/m²) is given in Figure 8 (a-d). The SO₂ concentration was high in the NE (0.000151513 in 2019) (0.00134435 in 2020) (0.000171003 in 2021) (0.000177544 in 2022), extending towards S and low in the central and E (-3.01868e-005 in 2019) (-6.71495 e-005 in 2020) (-4.07475e-005 in 2021) (-1.24852e-005 in 2022) portions of the study area. The spatial distribution of land surface temperature (LST) (°C) is given in Figure 9 (a-d). The E and central portions (43.88 °C in 2019) (43.28 °C in 2020) (41.70 °C in 2021) (41.59 °C in 2022) exhibited high temperatures, and NE portions (25.87 °C in 2019) (25.60 °C in 2020) (25.02 °C in 2021) (25.05 °C in 2022) exhibited low LST in the study area.

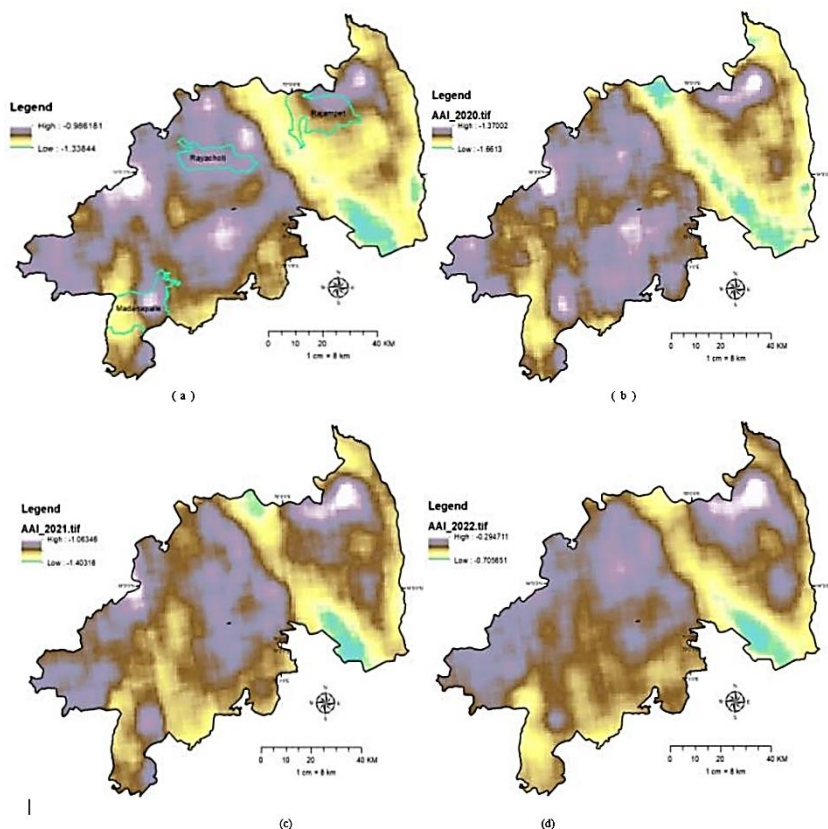


Figure 3. Absorbing Aerosol Index (AAI) (a) 2019, (b) 2020, (c) 2021, (d) 2022.

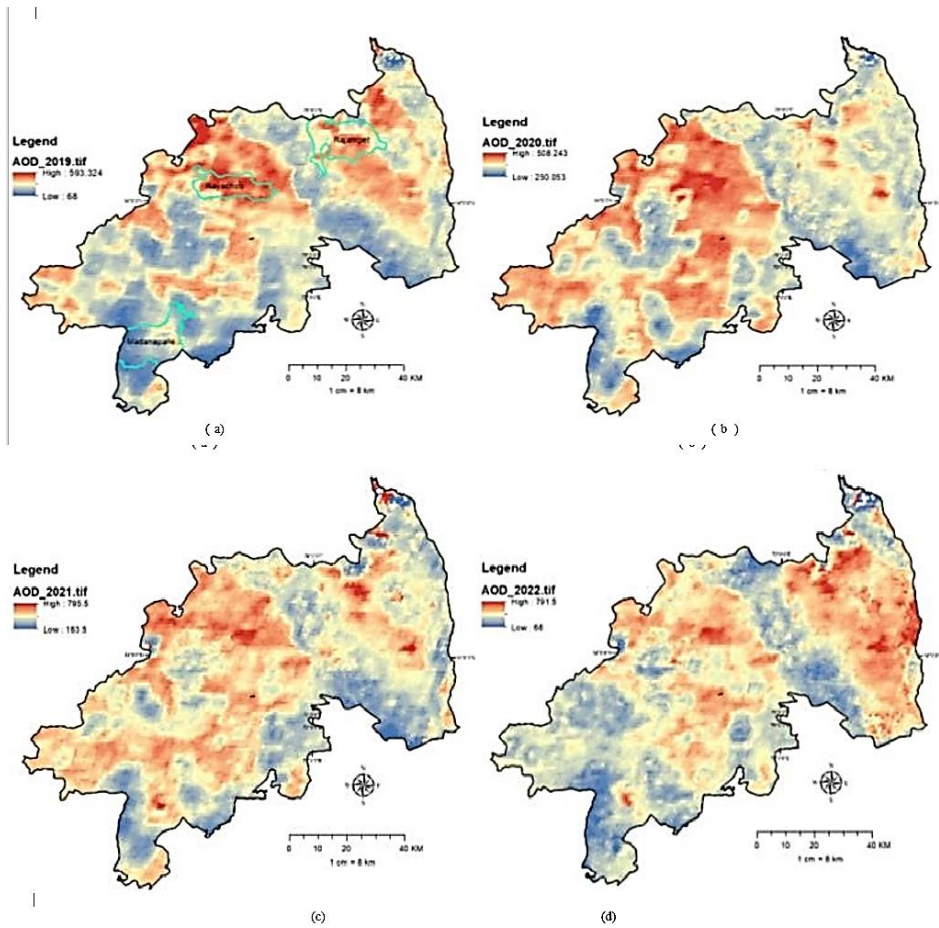


Figure 4. Aerosol optical depth (AOD) (a) 2019, (b) 2020, (c) 2021, (d) 2022.

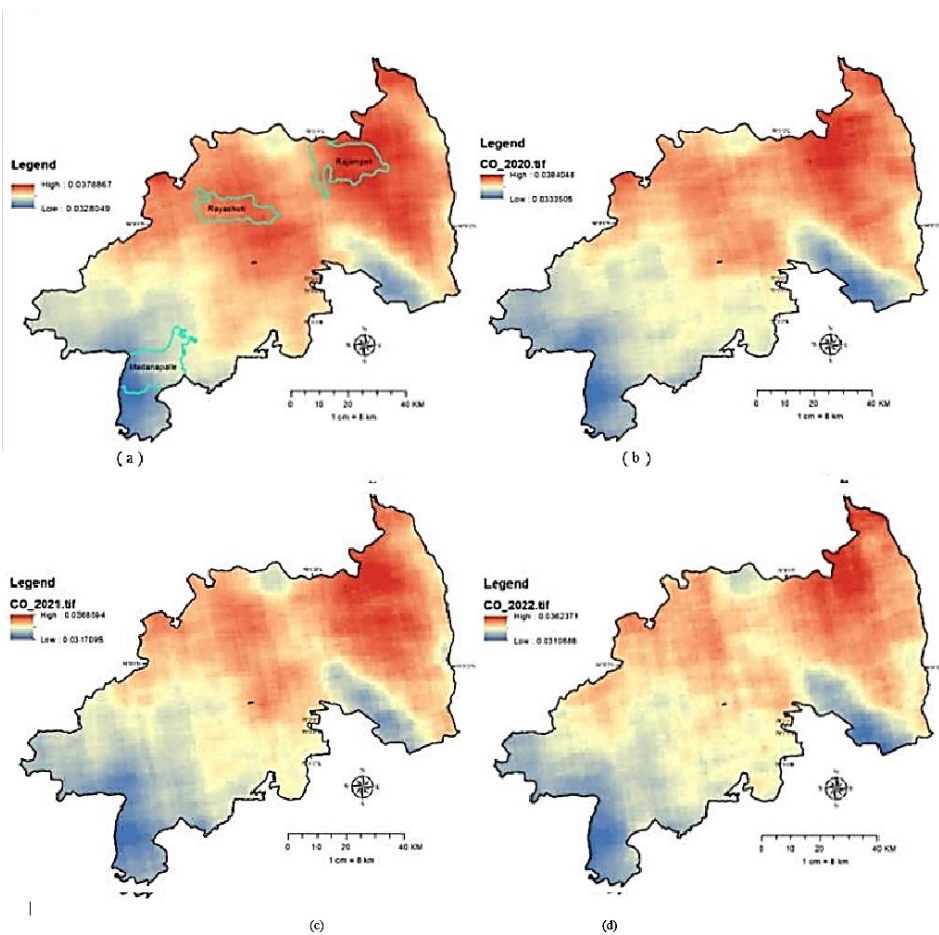


Figure 5. Carbon monoxide (CO) (mol/m²) (a) 2019, (b) 2020, (c) 2021, (d) 2022.

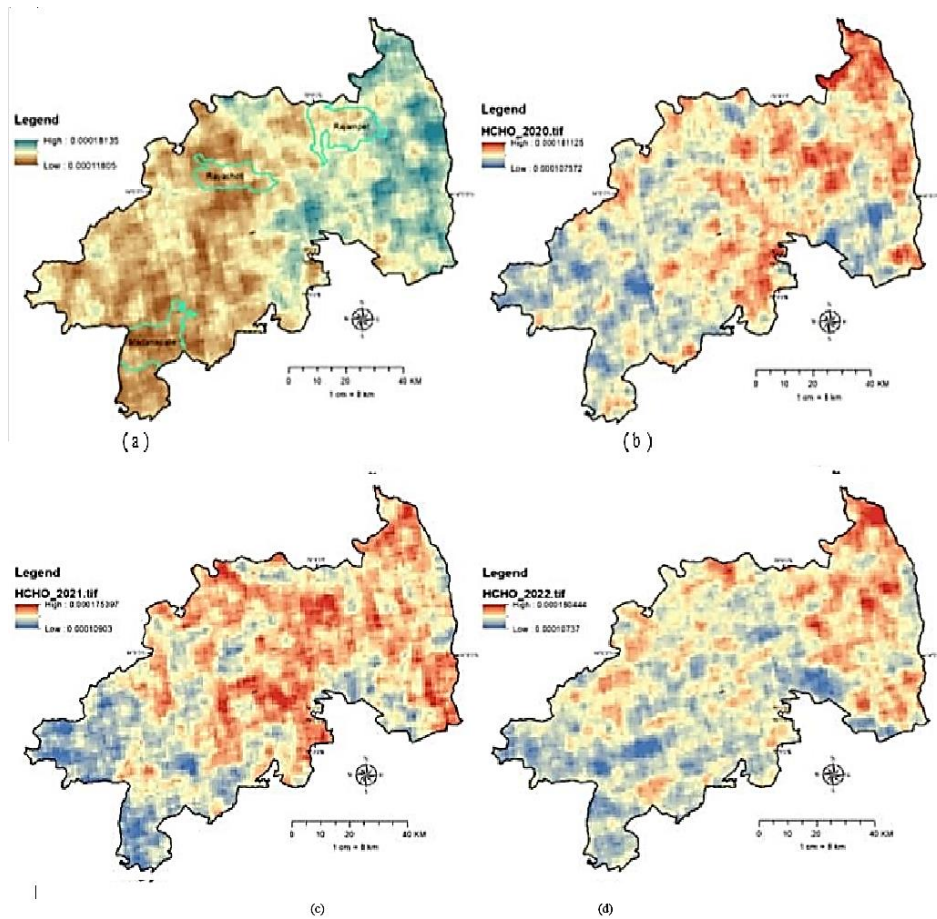


Figure 6. Formaldehyde (HCHO) (mol/m²) (a) 2019, (b) 2020, (c) 2021, (d) 2022.

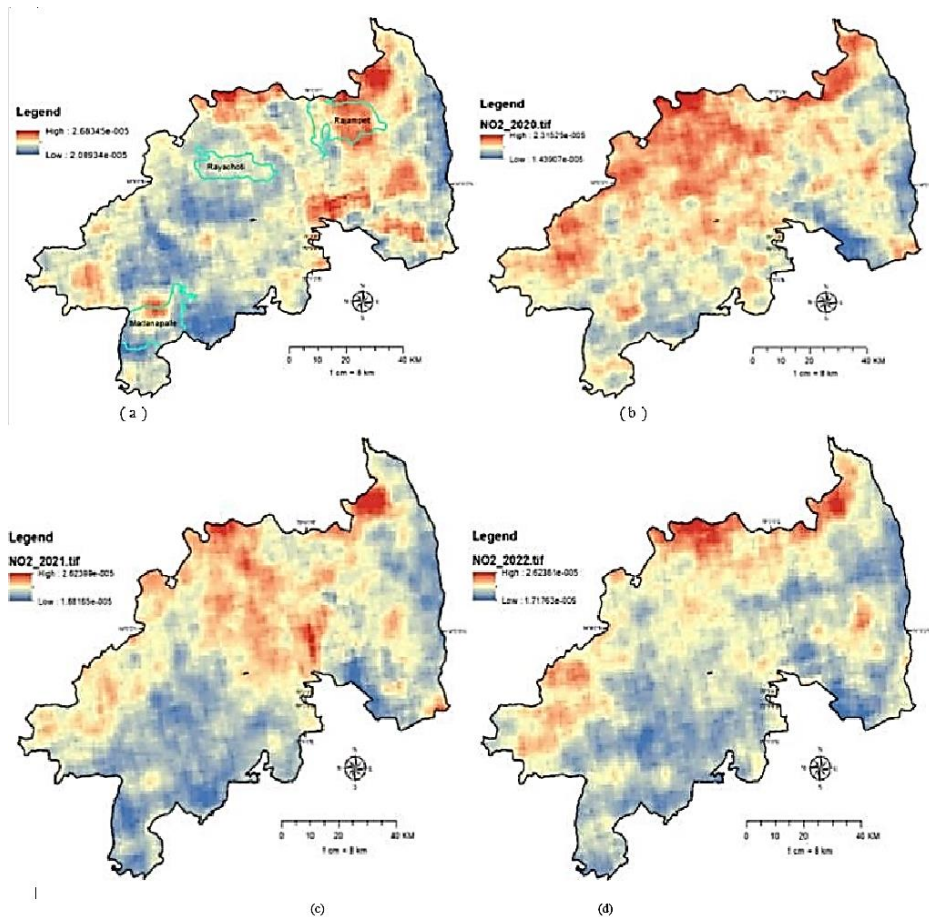


Figure 7. Nitrogen dioxide (NO₂) (mol/m²) (a) 2019, (b) 2020, (c) 2021, (d) 2022.

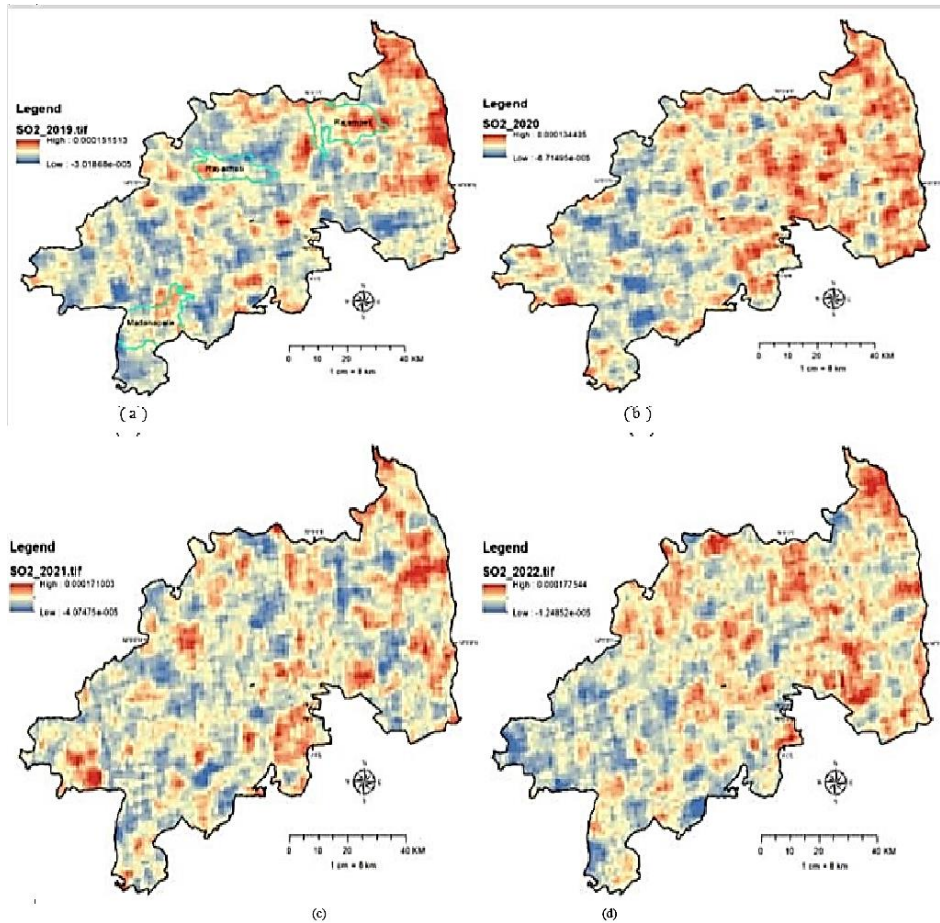


Figure 8. Sulfur dioxide (SO₂) (mol/m²) (a) 2019, (b) 2020, (c) 2021, (d) 2022.

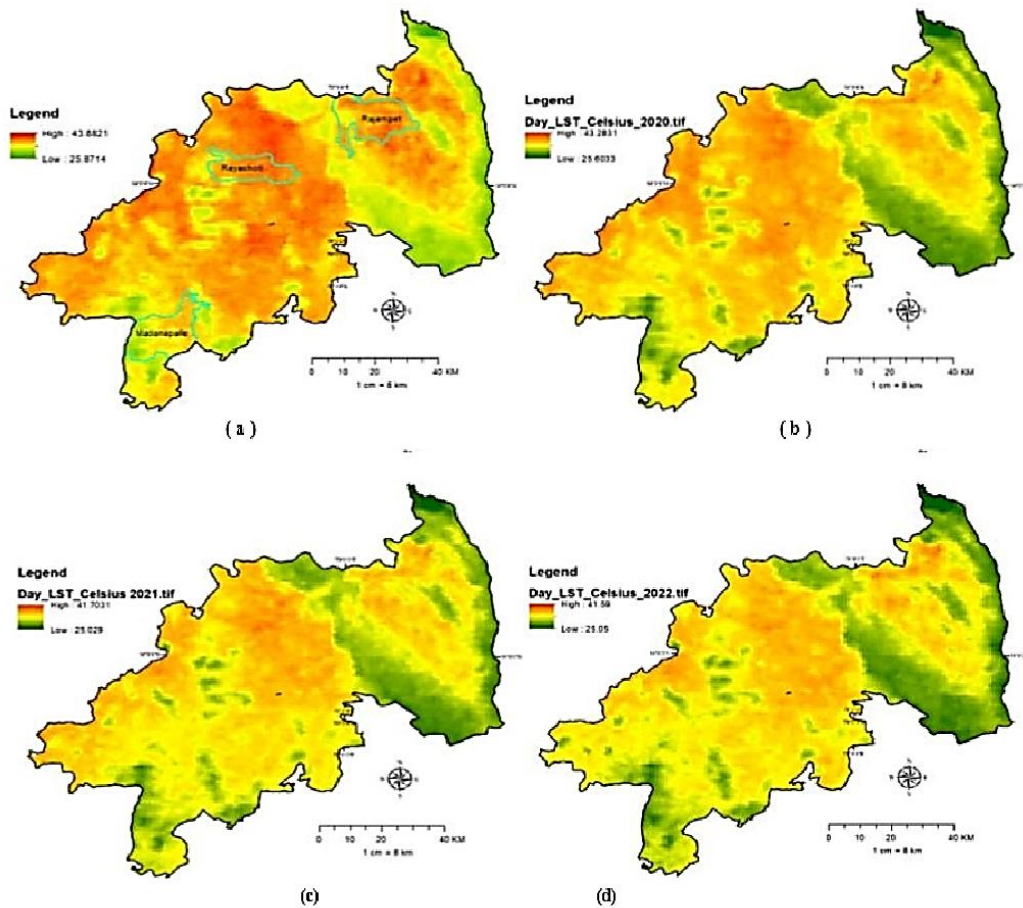


Figure 9. Land surface temperature (LST) (°C) (a) 2019, (b) 2020, (c) 2021, (d) 2022.

3.2. Machine learning

The ROC curve of the Extra Trees classifier (Figure 10a) shows AUC of 0.89 for both the 'Hot' and 'Normal' classes.

The micro-average ROC curve reflects AUC of 0.91, and the macro-average curve shows 0.90. The AUC values show that the classifier predicted the classes well (0.89). The confusion matrix is given in Figure 10b. The training curve reached a high level at maximum depths of 6 to 10, whereas the cross-validation curve reached a high level

at maximum depths of 4, 7, and 8. This shows that neither of the curves reached a high score quickly (relatively), and hence, through the validation curve given in Figure 10c, it is apparent that model performance is appropriate. The classification report containing some of the essential metrics is given in the Figure 10d. The feature importance plot given in Figure 10e shows that AAI and AOD have more influence on LST prediction. The t-SNE manifold plot shows minimal clustering and some negligible overlaps and is given in Figure 10f.

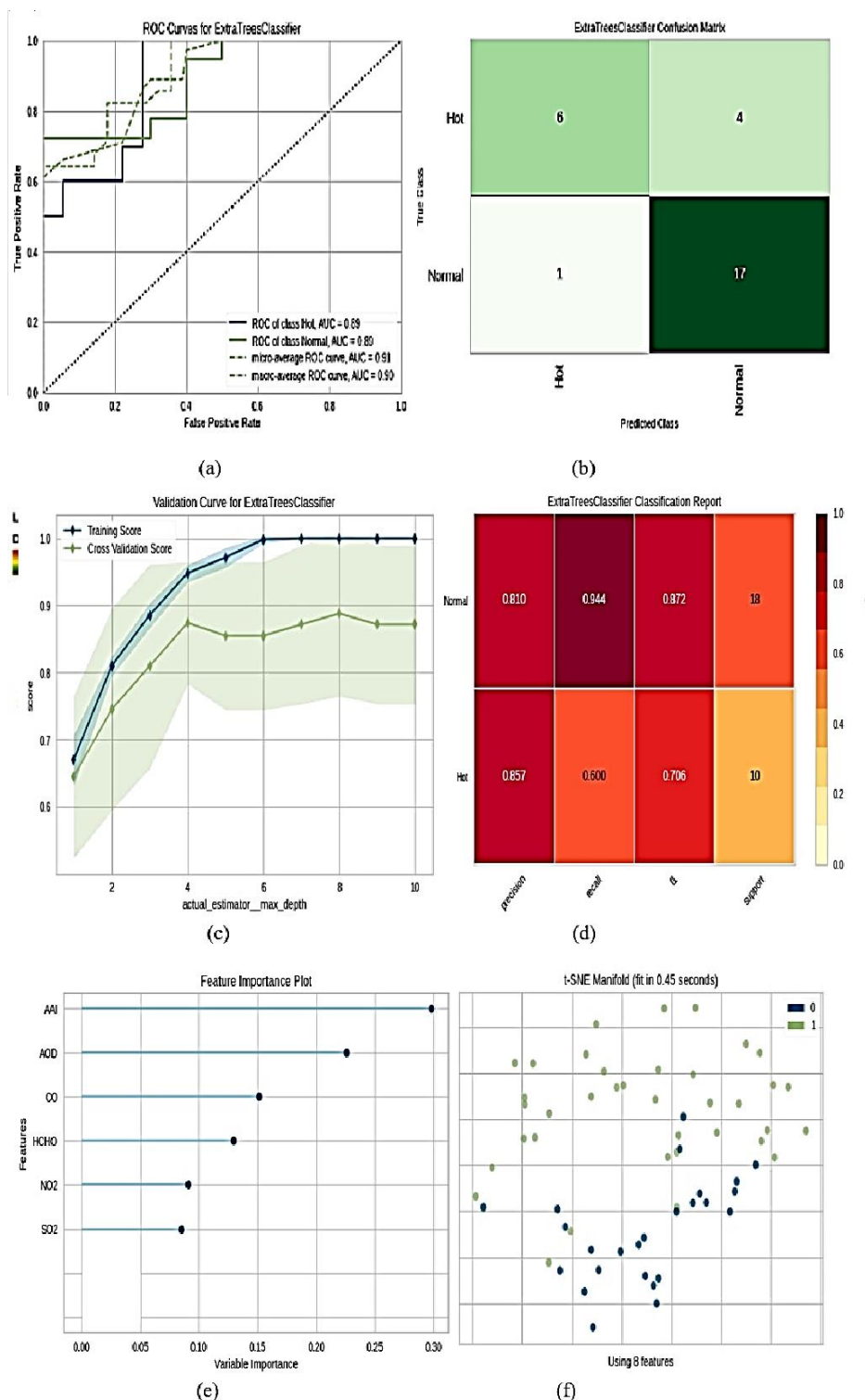


Figure 10. Extra Trees Classifier (ET) (a) ROC curve, (b) Confusion matrix, (c) Validation curve, (d) Classification report, (e) Feature importance plot, (f) t-SNE plot.

The ROC curve of the logistic regression classifier (Figure 11a) shows AUC of 0.96 for both the 'Hot' and 'Normal' classes. The micro-average ROC curve reflects AUC of 0.96, and the macro-average curve shows 0.97. The AUC values obtained show that the classifier performed better (0.96) in predicting the classes. The confusion matrix is given in Figure 11b. The training curve and cross-validation curve travelled steadily all along. This shows that neither of the curves reached a

high score quickly (relatively) nor reached a low score immediately (Figure 11c). It is apparent that model performance is appropriate. The classification report containing some of the essential metrics is given in Figure 11d. The feature importance plot in Figure 11e shows that AAI has more influence on LST prediction. The t-SNE manifold plot shows a minimal clustering and is given in Figure 11f.

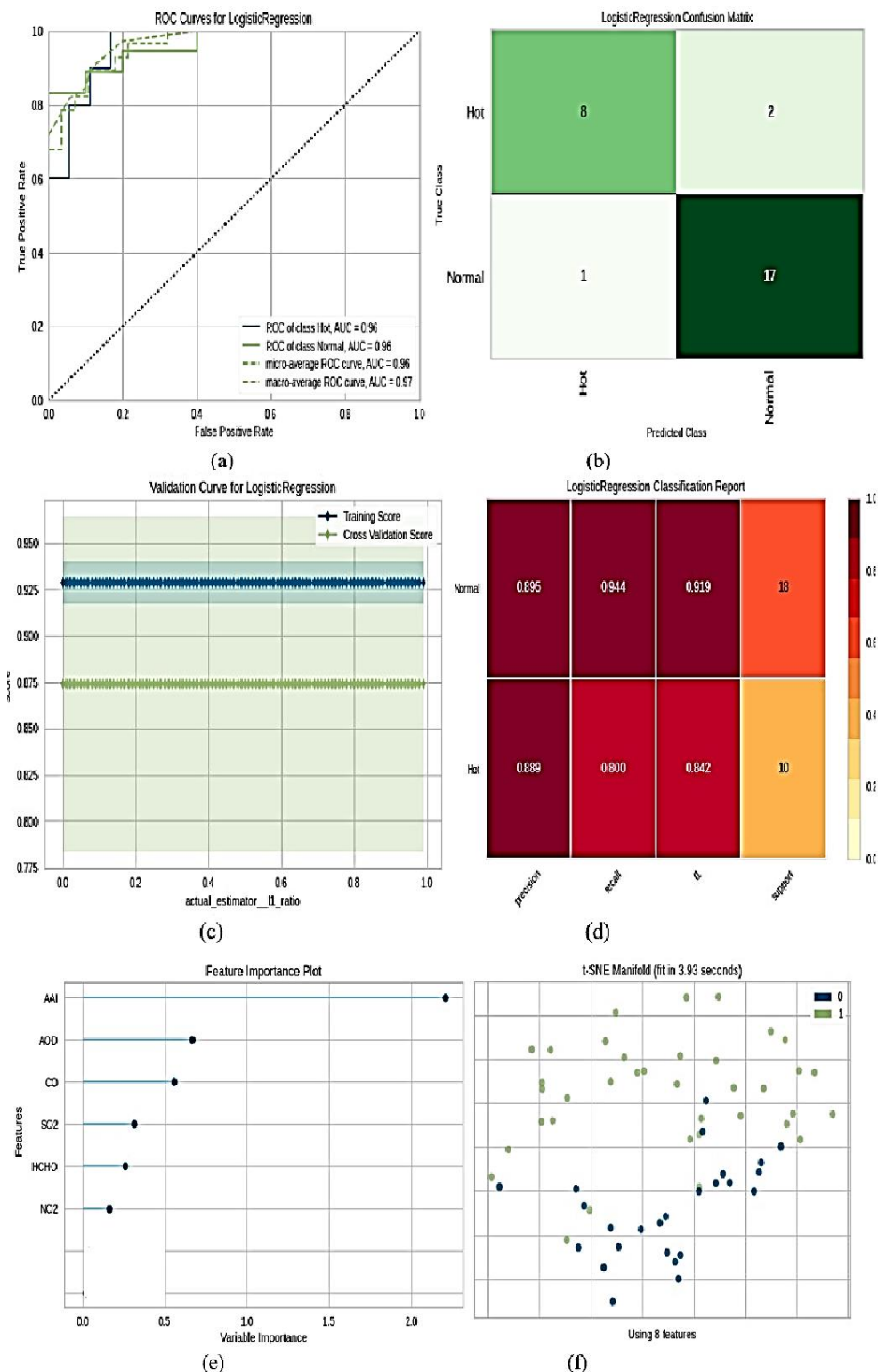


Figure 11. Logistic Regression (LR) (a) ROC curve, (b) Confusion matrix, (c) Validation curve, (d) Classification report, (e) Feature importance plot, (f) t-SNE plot.

The ROC curve of the Random Forest classifier (Figure 12a) shows AUC of 0.94 for both the 'Hot' and 'Normal' classes. The micro-average ROC curve reflects AUC of 0.93, and the macro-average curve shows 0.94. The AUC values obtained show that the classifier performed appropriately (0.94) in predicting the classes. The confusion matrix is given in Figure 12b. The training curve reached a high level at a maximum depth of 5, whereas the cross-validation curve reached a high level at a maximum depth of 2. This shows that the cross-validation curve reached a high score quickly (relatively) (Figure 12c). It is apparent that model complexity is present. This can be due to limited data available for

analysis or other factors. The classification report containing some of the essential metrics is given in Figure 12d. The feature importance plot in Figure 12e shows that AAI and AOD have more influence on LST prediction. The t-SNE manifold plot shows minimal clustering and negligible overlaps and is given in Figure 12f. The comparison of evaluation metrics for each model is given in Figure 13. The logistic regression classifier performed well when accuracy was considered. Even with other evaluation metrics taken into consideration, the logistic regression classifier performed well, i.e., AUC (0.9611), Recall (0.9444), Precision (0.08947), F1 score (0.9189), kappa (0.7614), and MCC score (0.7638).

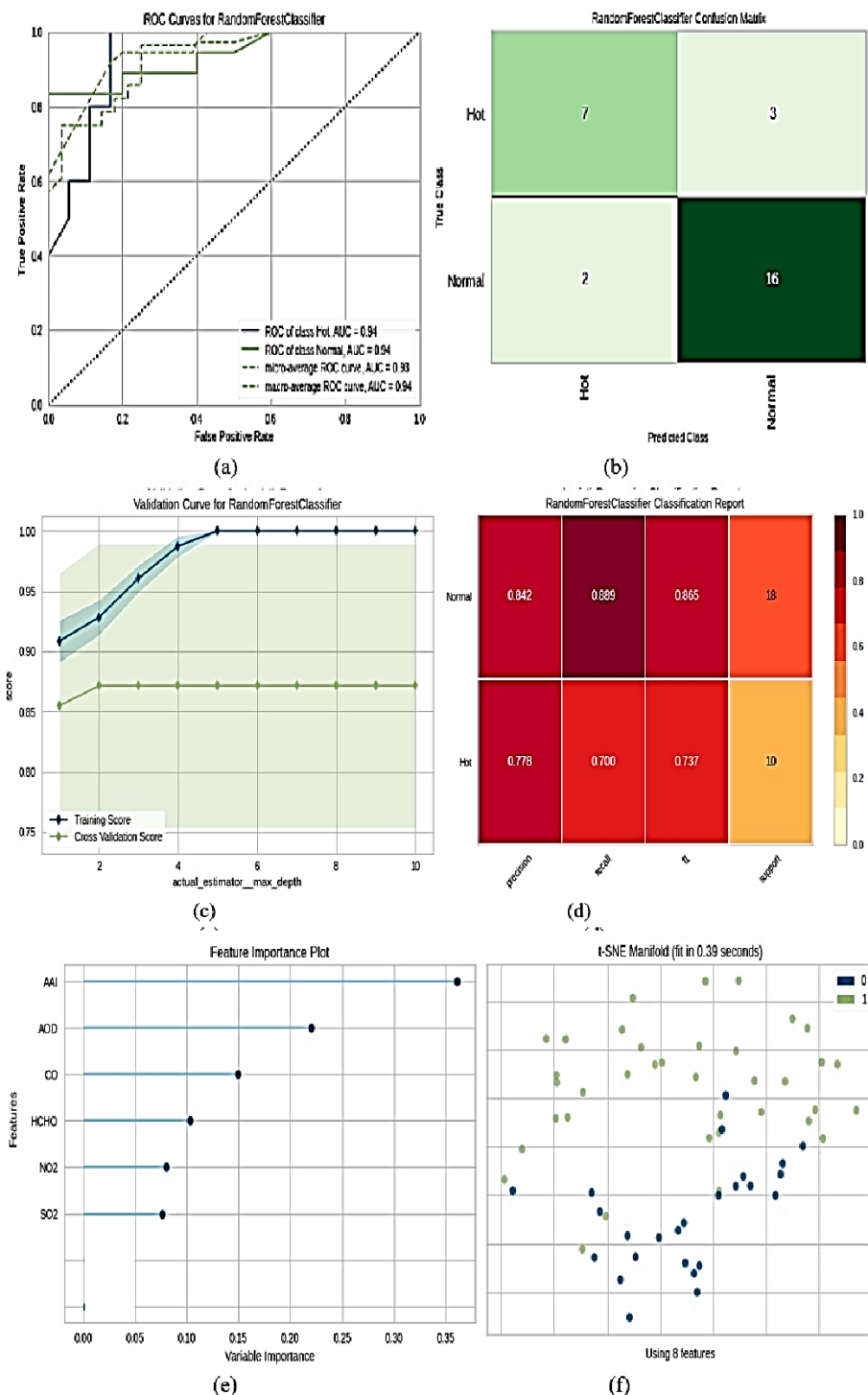


Figure 12. Random Forest Classifier (RF) (a) ROC curve, (b) Confusion matrix, (c) Validation curve, (d) Classification report, (e) Feature importance plot, (f) t-SNE plot.



Figure 13. Model comparison (ET, LR, RF).

4. Discussion

Machine learning tools can be used with ease, and this can be due to their reliability and cost-reducing functionalities [53, 54]. Artificial Intelligence includes machine learning tools that deal with structured and unstructured data and help researchers across various domains achieve appropriate results [55, 56]. This study used AI (ML) tools to predict land surface temperatures based on air quality parameters like CO, HCHO, NO₂, SO₂, AAI, and AOD. Prior to ML treatment, the data is derived from remote sensing and GIS platforms. It was observed that Machine learning tools could predict land surface temperatures effectively and within low-cost frameworks. The main limitations of this study are: 1. Limited availability of ground data, 2. Lack of air pollution sensors in the study area, 3. Excess reliance on satellite-based data, 4. Problems with cross-validation (satellite versus ground data). These problems might be solved by installing air pollution monitoring stations and training the personnel to use mobile monitoring stations.

5. Conclusion

This work aimed at the integration of geographic information systems (GIS) and Machine learning (ML) frameworks to predict land surface temperatures (LST) over the Annamayya district of India (Andhra Pradesh state). After systematic analysis and interpretation in this study, it is concluded that machine learning tools can easily predict land surface temperatures with reliable results. The prediction capabilities can be improved once more data across spatial and temporal scales is available.

Acknowledgement

The authors sincerely thank the Government of India, NASA, USGS, ISRO, Government of Andhra Pradesh, District administration of Annamayya district for helping in this research work through data supply.

Conflicts of interest

The authors declare no conflicts of interest.

References

- Hulley, G. C., Ghent, D., Göttsche, F. M., Guillevic, P. C., Mildrexler, D. J., & Coll, C. (2019). Land surface temperature. Taking the Temperature of the Earth, 57-127. <https://doi.org/10.1016/B978-0-12-814458-9.00003-4>
- Tran, D. X., Pla, F., Latorre-Carmona, P., Myint, S. W., Caetano, M., & Kieu, H. V. (2017). Characterizing the relationship between land use land cover change and land surface temperature. *ISPRS Journal of Photogrammetry and Remote Sensing*, 124, 119-132. <https://doi.org/10.1016/j.isprsjprs.2017.01.001>
- Pal, S., & Ziaul, S. K. (2017). Detection of land use and land cover change and land surface temperature in English Bazar urban centre. *The Egyptian Journal of Remote Sensing and Space Science*, 20(1), 125-145. <https://doi.org/10.1016/j.ejrs.2016.11.003>
- Li, Z. L., Wu, H., Duan, S. B., Zhao, W., Ren, H., Liu, X., ... & Zhou, C. (2023). Satellite remote sensing of global land surface temperature: Definition, methods, products, and applications. *Reviews of Geophysics*, 61(1). <https://doi.org/10.1029/2022RG000777>
- Mumtaz, F., Tao, Y., de Leeuw, G., Zhao, L., Fan, C., Elnashar, A., ... & Wang, D. (2020). Modeling spatio-temporal land transformation and its associated impacts on land surface temperature (LST). *Remote Sensing*, 12(18), 2987. <https://doi.org/10.3390/rs12182987>
- Walker, J. C., Hays, P. B., & Kasting, J. F. (1981). A negative feedback mechanism for the long-term stabilization of Earth's surface temperature. *Journal of Geophysical Research: Oceans*, 86(C10), 9776-9782. <https://doi.org/10.1029/JC086iC10p09776>
- Xiang, Y., Ye, Y., Peng, C., Teng, M., & Zhou, Z. (2022). Seasonal variations for combined effects of landscape

- metrics on land surface temperature (LST) and aerosol optical depth (AOD). *Ecological Indicators*, 138, 108810. <https://doi.org/10.1016/j.ecolind.2022.108810>
8. Roy, S. S. (2008). Impact of aerosol optical depth on seasonal temperatures in India: a spatio-temporal analysis. *International Journal of Remote Sensing*, 29(3), 727-740. <https://doi.org/10.1080/01431160701352121>
 9. Singh, R. P., Kumar, J. S., Zlotnicki, J., & Kafatos, M. (2010). Satellite detection of carbon monoxide emission prior to the Gujarat earthquake of 26 January 2001. *Applied Geochemistry*, 25(4), 580-585. <https://doi.org/10.1016/j.apgeochem.2010.01.014>
 10. Marbach, T., Beirle, S., Liu, C., Platt, U., & Wagner, T. (2008). Biomass burning emissions from satellite observations: synergistic use of formaldehyde (HCHO), fire counts, and surface temperature. In *Remote Sensing of Fire: Science and Application*, 7089, 131-140. <https://doi.org/10.1117/12.793654>
 11. Morfopoulos, C., Müller, J. F., Stavrou, T., Bauwens, M., De Smedt, I., Friedlingstein, P., ... & Regnier, P. (2022). Vegetation responses to climate extremes recorded by remotely sensed atmospheric formaldehyde. *Global Change Biology*, 28(5), 1809-1822. <https://doi.org/10.1111/gcb.15880>
 12. Zheng, Y., Unger, N., Barkley, M. P., & Yue, X. (2015). Relationships between photosynthesis and formaldehyde as a probe of isoprene emission. *Atmospheric Chemistry and Physics*, 15(15), 8559-8576. <https://doi.org/10.5194/acp-15-8559-2015>
 13. Ramanathan, V., Callis, L. B., & Boughner, R. E. (1976). Sensitivity of surface temperature and atmospheric temperature to perturbations in the atmospheric concentration of ozone and nitrogen dioxide. *Journal of the Atmospheric Sciences*, 33(6), 1092-1112. [https://doi.org/10.1175/1520-0469\(1976\)033<1092:SOSTAA>2.0.CO;2](https://doi.org/10.1175/1520-0469(1976)033<1092:SOSTAA>2.0.CO;2)
 14. Schumann, U., & Huntrieser, H. (2007). The global lightning-induced nitrogen oxides source. *Atmospheric Chemistry and Physics*, 7(14), 3823-3907. <https://doi.org/10.5194/acp-7-3823-2007>
 15. Conley, A. J., Westervelt, D. M., Lamarque, J. F., Fiore, A. M., Shindell, D., Correa, G., ... & Horowitz, L. W. (2018). Multimodel surface temperature responses to removal of US sulfur dioxide emissions. *Journal of Geophysical Research: Atmospheres*, 123(5), 2773-2796. <https://doi.org/10.1002/2017JD027411>
 16. Ward, P. L. (2009). Sulfur dioxide initiates global climate change in four ways. *Thin Solid Films*, 517(11), 3188-3203. <https://doi.org/10.1016/j.tsf.2009.01.005>
 17. Abidin, M. R., Nur, R., Mayzarah, E. M., & Umar, R. (2021). Estimating and monitoring the land surface temperature (LST) using Landsat OLI 8 TIRS. *International Journal of Environment, Engineering and Education*, 3(1), 17-24. <https://doi.org/10.55151/ijeedu.v3i1.43>
 18. Kafy, A. A., Shuvo, R. M., Naim, M. N. H., Sikdar, M. S., Chowdhury, R. R., Islam, M. A., ... & Kona, M. A. (2021). Remote sensing approach to simulate the land use/land cover and seasonal land surface temperature change using machine learning algorithms in a fastest-growing megacity of Bangladesh. *Remote Sensing Applications: Society and Environment*, 21, 100463. <https://doi.org/10.1016/j.rsase.2020.100463>
 19. Roberts, D. A., Dennison, P. E., Roth, K. L., Dudley, K., & Hulley, G. (2015). Relationships between dominant plant species, fractional cover and land surface temperature in a Mediterranean ecosystem. *Remote Sensing of Environment*, 167, 152-167. <https://doi.org/10.1016/j.rse.2015.01.026>
 20. Sekertekin, A., Kutoglu, S. H., & Kaya, S. (2016). Evaluation of spatio-temporal variability in Land Surface Temperature: A case study of Zonguldak, Turkey. *Environmental Monitoring and Assessment*, 188, 1-15. <https://doi.org/10.1007/s10661-015-5032-2>
 21. Wan, Z., Zhang, Y., Zhang, Q., & Li, Z. L. (2004). Quality assessment and validation of the MODIS global land surface temperature. *International Journal of Remote Sensing*, 25(1), 261-274. <https://doi.org/10.1080/0143116031000116417>
 22. Zaitunah, A., Silitonga, A. F., & Syaefina, L. (2022). Urban greening effect on land surface temperature. *Sensors*, 22(11), 4168. <https://doi.org/10.3390/s22114168>
 23. Ziaul, S., & Pal, S. (2018). Analyzing control of respiratory particulate matter on Land Surface Temperature in local climatic zones of English Bazar Municipality and Surroundings. *Urban Climate*, 24, 34-50. <https://doi.org/10.1016/j.uclim.2018.01.006>
 24. Mahdavi, M., Ahangar, S. K., Feizizadeh, B., Kamran, K. V., & Karimzadeh, S. (2023). Spatio-temporal monitoring of Qeshm mangrove forests through machine learning classification of SAR and optical images on Google Earth Engine. *International Journal of Engineering and Geosciences*, 8(3), 239-250. <https://doi.org/10.26833/ijeg.1118542>
 25. Ebrahimi, H., & Azadbakht, M. (2019). Downscaling MODIS land surface temperature over a heterogeneous area: An investigation of machine learning techniques, feature selection, and impacts of mixed pixels. *Computers & Geosciences*, 124, 93-102. <https://doi.org/10.1016/j.cageo.2019.01.004>
 26. Srivastava, P. K., Han, D., Ramirez, M. R., & Islam, T. (2013). Machine learning techniques for downscaling SMOS satellite soil moisture using MODIS land surface temperature for hydrological application. *Water Resources Management*, 27, 3127-3144. <https://doi.org/10.1007/s11269-013-0337-9>
 27. Sun, Y., Gao, C., Li, J., Wang, R., & Liu, J. (2019). Quantifying the effects of urban form on land surface temperature in subtropical high-density urban areas using machine learning. *Remote Sensing*, 11(8), 959. <https://doi.org/10.3390/rs11080959>
 28. Li, W., Ni, L., Li, Z. L., Duan, S. B., & Wu, H. (2019). Evaluation of machine learning algorithms in spatial downscaling of MODIS land surface temperature. *IEEE Journal of Selected Topics in Applied Earth Observations and Remote Sensing*, 12(7), 2299-2307. <https://doi.org/10.1109/JSTARS.2019.2896923>

29. Wang, S., Ma, Y., Wang, Z., Wang, L., Chi, X., Ding, A., ... & Zhang, Y. (2021). Mobile monitoring of urban air quality at high spatial resolution by low-cost sensors: impacts of COVID-19 pandemic lockdown. *Atmospheric Chemistry and Physics*, 21(9), 7199-7215. <https://doi.org/10.5194/acp-21-7199-2021>
30. Tan, J., NourEldeen, N., Mao, K., Shi, J., Li, Z., Xu, T., & Yuan, Z. (2019). Deep learning convolutional neural network for the retrieval of land surface temperature from AMSR2 data in China. *Sensors*, 19(13), 2987. <https://doi.org/10.3390/s19132987>
31. Mohammad, P., Goswami, A., Chauhan, S., & Nayak, S. (2022). Machine learning algorithm based prediction of land use land cover and land surface temperature changes to characterize the surface urban heat island phenomena over Ahmedabad city, India. *Urban Climate*, 42, 101116. <https://doi.org/10.1016/j.uclim.2022.101116>
32. Pandey, A., Mondal, A., Guha, S., Singh, D., & Kundu, S. (2023). Analysis of the Variability in Land Surface Temperature Due to Land Use/Land Cover Change for a Sustainable Urban Planning. *Journal of Landscape Ecology*, 16(3), 20-35. <https://doi.org/10.2478/jlecol-2023-0015>
33. Pandey, A., Mondal, A., Guha, S., Upadhyay, P. K., & Singh, D. (2023). A long-term analysis of the dependency of land surface temperature on land surface indexes. *Papers in Applied Geography*, 9(3), 279-294. <https://doi.org/10.1080/23754931.2023.2187314>
34. Pandey, A., Mondal, A., Guha, S., Upadhyay, P. K., Rashmi, & Kundu, S. (2023). Analysis of spectral indices-based downscaled land surface temperature in a humid subtropical city. *International Journal of Image and Data Fusion*, 14(4), 336-358. <https://doi.org/10.1080/19479832.2023.2252818>
35. Pandey, A., Mondal, A., Guha, S., & Upadhyay, P. K. (2022). A seasonal investigation on land surface temperature and spectral indices in Imphal City, India. *Journal of Landscape Ecology*, 15(3), 1-18. <https://doi.org/10.2478/jlecol-2022-0015>
36. Pandey, A., Mondal, A., Guha, S., Upadhyay, P. K., & Singh, D. (2022). Land use status and its impact on land surface temperature in Imphal city, India. *Geology, Ecology, and Landscapes*, 1-15. <https://doi.org/10.1080/24749508.2022.2131962>
37. <https://earthexplorer.usgs.gov/>
38. <https://giovanni.gsfc.nasa.gov/giovanni/>
39. <https://developers.google.com/earth-engine/datasets/catalog/sentinel-5p>
40. <https://developers.google.com/earth-engine/datasets/catalog/modis>
41. Khan, P. W., Byun, Y. C., & Jeong, O. R. (2023). A stacking ensemble classifier-based machine learning model for classifying pollution sources on photovoltaic panels. *Scientific Reports*, 13(1), 10256. <https://doi.org/10.1038/s41598-023-35476-y>
42. Mogaraju, J. K. (2023). Application of machine learning algorithms in the investigation of groundwater quality parameters over YSR district, India. *Turkish Journal of Engineering*, 7(1), 64-72. <https://doi.org/10.31127/tuje.1032314>
43. Gong, X., Huang, Y., Duong, J., Leng, S., Zhan, F. B., Guo, Y., ... & Luo, L. (2023). Industrial air pollution and low birth weight in New Mexico, USA. *Journal of Environmental Management*, 348, 119236. <https://doi.org/10.1016/j.jenvman.2023.119236>
44. Mogaraju, J. K. (2024). Machine learning empowered prediction of geolocation using groundwater quality variables over YSR district of India. *Turkish Journal of Engineering*, 8(1), 31-45. <https://doi.org/10.31127/tuje.1223779>
45. Raju, R. S., Raju, G. S., & Rajasekhar, M. (2023). A study on hydro-geological characterization through Dar-Zarrouk parameters in hard rock terrain of Mandavi River Basin, Andhra Pradesh, India. *Arabian Journal of Geosciences*, 16(8), 453. <https://doi.org/10.1007/s12517-023-11573-0>
46. Naidu, G., Zuva, T., & Sibanda, E. M. (2023, April). A review of evaluation metrics in machine learning algorithms. *Computer Science On-line Conference*, 15-25. https://doi.org/10.1007/978-3-031-35314-7_2
47. Psaros, A. F., Meng, X., Zou, Z., Guo, L., & Karniadakis, G. E. (2023). Uncertainty quantification in scientific machine learning: Methods, metrics, and comparisons. *Journal of Computational Physics*, 477, 111902. <https://doi.org/10.1016/j.jcp.2022.111902>
48. Islam, S. M., & Talukder, K. H. (2023). Exploratory Analysis of Smartphone Sensor Data for Human Activity Recognition. *IEEE Access*, 99481 - 99498. <https://doi.org/10.1109/ACCESS.2023.3314651>
49. Hughes, B. K., Wallis, R., & Bishop, C. L. (2023). Yearning for machine learning: applications for the classification and characterisation of senescence. *Cell and Tissue Research*, 394(1), 1-16. <https://doi.org/10.1007/s00441-023-03768-4>
50. Annapurna, S. M., Anitha, M., & Kumar, L. S. (2024). Composition and source based aerosol classification using machine learning algorithms. *Advances in Space Research*, 73(1), 474-497. <https://doi.org/10.1016/j.asr.2023.09.068>
51. Choi, M., Zhang, J., Zhang, Y., Fan, J., Li, X., & Ying, Q. (2024). Impact of wildfires on regional ozone and PM_{2.5}: Considering the light absorption of Brown carbon. *Atmospheric Environment*, 316, 120196. <https://doi.org/10.1016/j.atmosenv.2023.120196>
52. Zhen, Z., Chen, S., Yin, T., & Gastellu-Etchegorry, J. P. (2023). Globally quantitative analysis of the impact of atmosphere and spectral response function on 2-band enhanced vegetation index (EVI₂) over Sentinel-2 and Landsat-8. *ISPRS Journal of Photogrammetry and Remote Sensing*, 205, 206-226. <https://doi.org/10.1016/j.isprsjprs.2023.09.024>
53. vom Scheidt, F., & Staudt, P. (2024). A data-driven Recommendation Tool for Sustainable Utility Service Bundles. *Applied Energy*, 353, 122137. <https://doi.org/10.1016/j.apenergy.2023.122137>
54. Moghadam, S. M., Yeung, T., & Choisne, J. (2023). A comparison of machine learning models' accuracy in predicting lower-limb joints' kinematics, kinetics, and muscle forces from wearable sensors. *Scientific Reports*, 13(1), 5046. <https://doi.org/10.1038/s41598-023-31906-z>

55. Javed, A. R., Saadia, A., Mughal, H., Gadekallu, T. R., Rizwan, M., Maddikunta, P. K. R., ... & Hussain, A. (2023). Artificial intelligence for cognitive health assessment: state-of-the-art, open challenges and future directions. *Cognitive Computation*, 15(6), 1767-1812. <https://doi.org/10.1007/s12559-023-10153-4>
56. Singh, P. (2023). Systematic review of data-centric approaches in artificial intelligence and machine learning. *Data Science and Management*, 6(3), 144-157. <https://doi.org/10.1016/j.dsm.2023.06.001>



© Author(s) 2024. This work is distributed under <https://creativecommons.org/licenses/by-sa/4.0/>



Detection of upwelling events in the Caspian Sea using thermal satellite image processing

Said Safarov¹, Khalil Valizadeh Kamran^{*2}, Vusal Ismayilov³, Elnur Safarov¹

¹ Institute of Geography of Ministry of Education and Sciences of Azerbaijan Republic, Azerbaijan, safarov53@mail.ru, elnur.safarov@outlook.com

² University of Tabriz, Department of Remote Sensing and GIS, Iran, valizadeh@tabrizu.ac.ir

³ Baku State University of Azerbaijan Republic, Azerbaijan, vusalhakimoglu@gmail.com

Cite this study:

Safarov, S., Kamran, K. V., Ismayilov, V., & Safarov, E. (2024). Detection of upwelling events in the Caspian Sea using thermal satellite image processing. *International Journal of Engineering and Geosciences*, 9 (2), 247-255

<https://doi.org/10.26833/ijeg.1394363>

Keywords

Caspian Sea
MODIS Aqua
Upwelling phenomenon
Sea surface temperature
Advection

Abstract

In this article, we studied the upwelling phenomena observed in the surface waters of the Caspian Sea. Studying upwelling is crucial for understanding and managing the complex interactions between the ocean, climate, and marine life, with implications for both environmental conservation and human well-being. To accomplish this, we utilized data from MODIS-Aqua satellite observations in the infrared range of 11 microns. These observations had a spatial resolution of 4 km and covered the period from 2003 to 2021. The data was accessed through the NASA Giovanni online data system databases. Our findings indicate that upwelling phenomena are primarily observed in the eastern part of the Middle and South Caspian from May to September. The most intense upwelling occurs along the eastern coast of the Middle Caspian in July and August. Based on long-term averaged data, the upwelling phenomenon is typically observed between 40-44° latitude during this period. The width of the upwelling zone increases gradually from north to south, extending approximately 60-70 km towards the Kazakh Gulf before decreasing towards the south. In the upwelling zone, the temperature gradient can at times reach 4.0°C per 100 km. In certain years, the upwelling zone that initially forms along the eastern coasts can extend over long distances and even reach the western coasts. Generally, the upwelling phenomenon occurs alongside the advection of warm waters from the South Caspian towards the Middle Caspian.

Research Article

Received: 22.11.2023
Revised: 19.02.2024
Accepted: 25.02.2024
Published: 24.07.2024



1. Introduction

The phenomenon of upwelling is the transfer of water masses from the deep layers to the surface in the world oceans and seas.

The climate of the earth is extremely complex due to interactions between the atmosphere, hydrosphere, geosphere, biosphere and cryosphere. Moreover, the exchange of energy, of matter and moisture between these environmental spheres are the main mechanisms that govern the climate system. The global atmospheric and oceanic circulations are strongly interdependent and the Sea Surface Temperature (SST) is the link between the two [1] Identifying understanding the causes of sea level change is important in global and regional climate change studies [2].

Remote Sensing (RS) technology enables to generate spatial and temporal data of a number of physical attributes about the watershed surface that can be utilized to map the extent of land and water bodies at

watershed scale, and to monitor their dynamics at regular and frequent time intervals [3].

The physical mechanism leading to coastal upwelling is related to the Coriolis force, which tends to deflect wind currents to the right in the Northern Hemisphere and to the left in the Southern Hemisphere.

On the one hand, they provide mixing of deep and surface waters, which is important from a climatic point of view. On the other hand, upwelling transports nutrient-rich water masses to the upper photic water layer. As a result, zones of increased primary water production and intensive development of plankton communities are formed in upwelling areas, which is of great importance for fisheries [4]. The upwelling phenomenon also occurs near the eastern and western coasts of the Middle and partly South Caspian.

The phenomenon of upwelling in the Caspian Sea and its causes are the subject of many scientific works. A number of researchers showed in their studies that the

rise of deep waters to the surface is due to the water cycle under the influence of wind [5-10].

According to some researchers' easterly winds prevail over the eastern part of the Caspian Sea from mid-July to October [5]. These winds drive relatively warm water from the sea surface into the open sea, and it is replaced by cold water rising to the surface from the deep layers. On the other hand, currents directed from the shore to the open sea create reverse currents of water in the lower layers, i.e., currents of cold water directed towards the shore.

However, it should be noted that according to the results of a number of studies, it has been established that in the eastern part of the Middle Caspian, easterly winds actually prevail in the cold season. However, in the summer-autumn period, when upwelling phenomena are observed, northern and northwestern winds prevail [11-14]. In [6] almost all considered cases with upwelling were observed at the northern wind direction.

There are different explanations for the occurrence of upwelling. So, in the 1960s. it was suggested that groundwater is the cause of temperature anomalies in the eastern part of the Middle Caspian [7]. One of the arguments against this idea is the observed homogeneity of salinity and other hydrochemical properties of the waters of the eastern part of the Middle Caspian.

In 1977 Karimov and Klevtsova put forward a hypothesis about the relationship between temperature anomalies and internal waves [8].

The upwelling phenomenon is observed both on the eastern and western coasts of the Middle and South Caspian. However, it should be noted that if on the east coast in May-September upwelling is systematic, then on the west coast it is relatively episodic. The study of temperature anomalies occurring in the western part of the Middle Caspian showed that they are of a "synoptic" nature [9]. From this point of view, and since the study considered only long-term average monthly, average seasonal and average annual distributions, it is difficult to identify and study the manifestations of upwelling on the west coast based on the corresponding satellite images. Therefore, in this paper, upwelling phenomena observed in the eastern part of the Middle and South Caspian are considered.

2. Method

Until recently between 2002 to 2020, to study upwelling in the Caspian Sea, mainly data from hydrological stations located mainly on the coasts and islands were used [4,5,9,10]. Such contact data make it possible to identify the upwelling phenomenon and its development quite clearly over time, but do not allow us to assess its spatial scales [10].

It is known that data from a number of NOAA series satellites have recently been used to remotely determine hydrometeorological parameters, including land and water basin surface temperatures. Practically all meteorological satellites of this series are equipped with infrared radiometers, which allow estimating land, ocean and sea surface temperatures on a global scale.

A number of scientific articles are devoted to the study of the surface temperature of the Caspian Sea using

satellite data [15-18] which studied various aspects of the problem under consideration. The present study used monthly average sea surface temperature (SST) data (2003-2021) from the NASA Giovanni online information system database based on nighttime measurements of the MODIS radio spectrometer installed on the Aqua satellite. The MODIS spectroradiometer with a wavelength of 11 μm has a horizontal spatial resolution of 4 km, which makes it possible to detect mesoscale anomalies in the distribution of the SST of the Caspian Sea, especially upwelling zones, and their characteristic features.

One of the disadvantages of the MODIS Aqua spectroradiometer is the inability to measure temperature on ice-covered water surfaces in the cold season, but this problem applies only to the North Caspian Sea, since the water surface in other parts of the sea is almost never frozen. On the other hand, upwelling phenomena are observed in warm seasons.

In order to verify the degree of correspondence of the satellite data to the real data, they were compared with the data of contact observations.

Maps of SST distribution over the sea area for every month and season were obtained using the procedures provided at [19].

Remote sensing data of SST by the MODIS Aqua radio spectrometer has a relatively high resolution (4 km). This factor allows comparing the corresponding satellite data with real contact data (calibration) and revealing the statistical relation between them. For individual observation points of the Middle and South Caspian Sea such comparison shows that there is quite a high correlation between them ($R = 0.91-0.98$). Moreover, the degree of coincidence of satellite and actual data was about 0,5 $^{\circ}\text{C}$ (Figure 1), which is close to the results obtained by other researchers (10). A similar pattern is observed when comparing SST for the May-September period (Table 1).

Table 1. Correlation coefficients (r) between the actual SST and the corresponding MODIS Aqua data in different months of the year for the Neft Dashlari (Oil Stones) observation point.

Month	May	June	July	August	September	Year
r	0,91	0,98	0,96	0,94	0,92	0,94

3. Results and discussion

As it was mentioned above in the Caspian Sea water area, the upwelling phenomenon occurs mainly during the period May-September.

The continued increase in air temperature in May creates a peculiar distribution of water surface temperature in the Caspian Sea.

As SST in the North Caspian increases rapidly (due to shallow water), the north-south temperature gradient at the border with the Middle Caspian continues to be high (-2,7 $^{\circ}\text{C}/100$ km). The lowest water surface temperatures in the North Caspian are observed at the boundary with the Middle Caspian (16,0 $^{\circ}\text{C}$) and in the Ural Basin (17,0 $^{\circ}\text{C}$), and the highest - in coastal areas (20,0 $^{\circ}\text{C}$) (Figure 2).

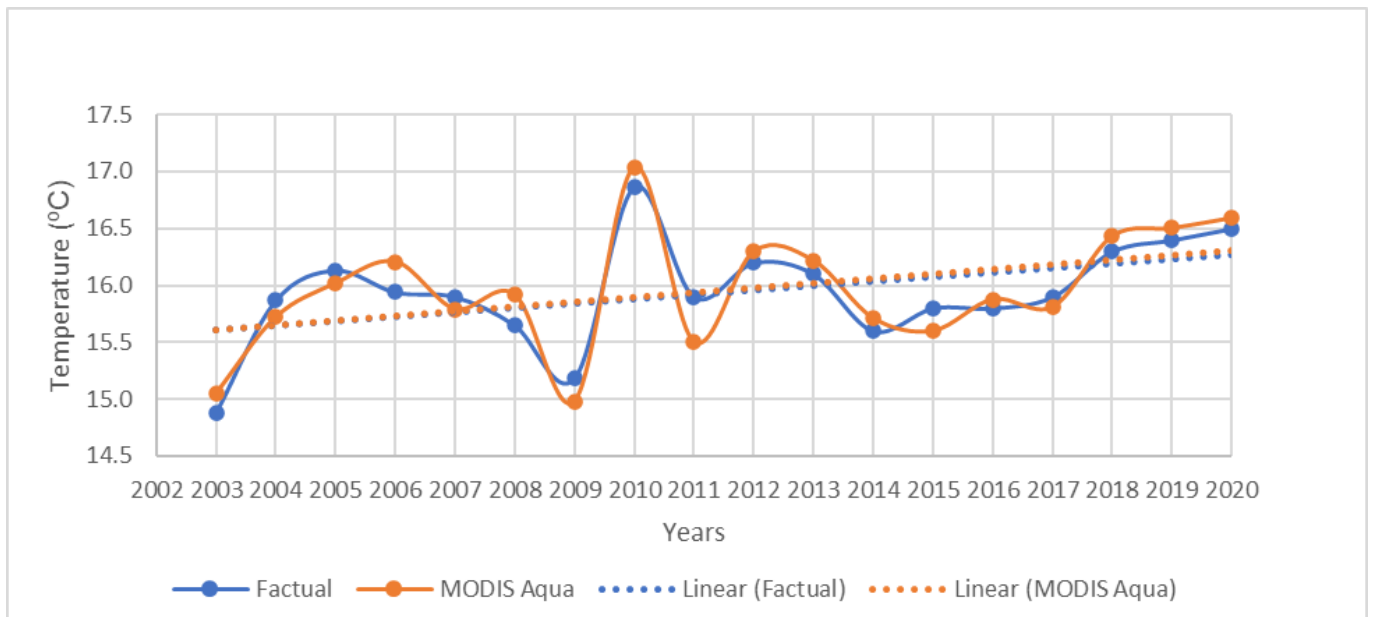


Figure 1. Dynamics of mean annual SST from the observation point data and corresponding MODIS Aqua data.

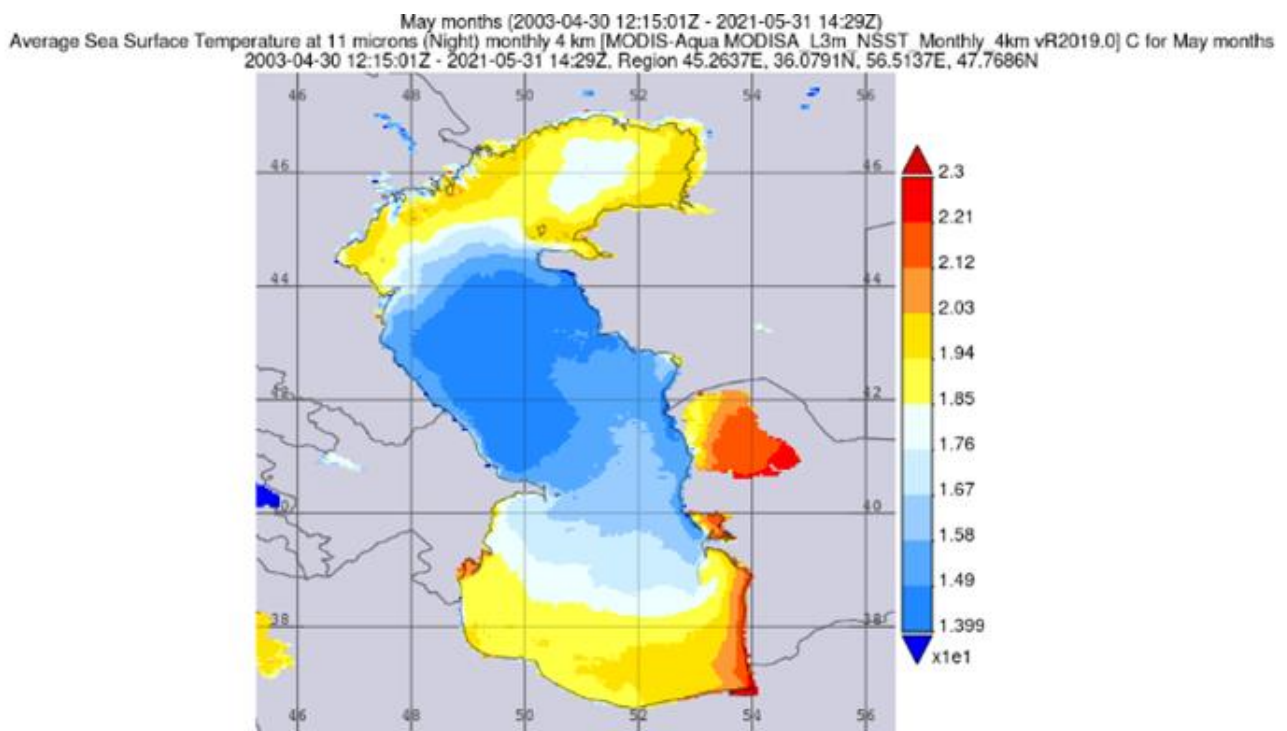


Figure 2. Distribution of SST in the Caspian Sea in May for 2003-2021.

SST of the Middle Caspian Sea varies between 14-17 °C and increases mainly from north to south. The influence of the relatively warm waters of the South Caspian Sea is felt in the southern part of the area (Figure 1). In May, the highest SST is recorded in Kara-Bogaz-Gol Bay (19-22 °C).

SST of the South Caspian Sea in the meridional direction from north to south increases from 15.5 °C to 22 °C. There is a noticeable increase in SST from west to east, especially in the southern part of the area. The highest temperatures are observed in the eastern coastal waters and especially in bays (Figure 2).

As can be seen from Figure 2, the upwelling in May in average is not very intense, but the size and intensity of the upwelling zone in May in different years can be different [20,21]. Upwelling, which began mainly in the

eastern part of the Middle Caspian in May, relatively weakens the advection of warm water mass from the South Caspian to the Middle Caspian.

In June, the air temperature rises even more. This increase, in combination with other meteorological factors, complex geomorphological conditions and sea bathymetry, creates unique features of SST distribution in the Caspian Sea (Figure 3).

As can be seen from Figure 1 and Figure 2, in June compared to May, the increase in surface temperature of the North Caspian is 5,0-6,0 °C, the Middle Caspian 5 °C, the South Caspian 3,0-3,5 °C.

As in May, in June the lowest SST observed in the Middle Caspian Sea, while to the north and south of it there is a gradual increase in temperature (Figure 3).

SST in the North Caspian varies between 22-25 °C. The average SST gradient at the boundary between the Middle Caspian and the North Caspian is -1.6 °C (Figure 3). Except for the eastern coastal areas, SST varies between 20-22 °C throughout the Middle Caspian. In the eastern coastal areas, the surface temperature is close to 19 °C. SST of the South Caspian varies from north to south within the range of 19-25 °C. Higher temperatures are noted in the southeastern regions and bays.

In most parts of the Kara-Bogaz-Gol Bay SST is above 25 °C.

In June, the upwelling phenomenon, which began from the eastern coast of the sea, begins to manifest itself

more clearly (Figure 3). Thus, the upwelling zone extends along the eastern part of the sea along the 20,2 °C isotherm from latitude 44,2^o to 39,5^o and covers large areas to the west. It can spread to the western coast of Ogurchink Island [6]. As can be seen from Figure 2, the minimum SST in the upwelling zone is 18 °C, but in some years it can drop to 14 °C.

In June, the intensification of the upwelling phenomenon in the eastern part of the Middle and partly the South Caspian is accompanied by a noticeable weakening of the advection of warm water masses from the east of the South Caspian and its deviation to the west (Figure 3).

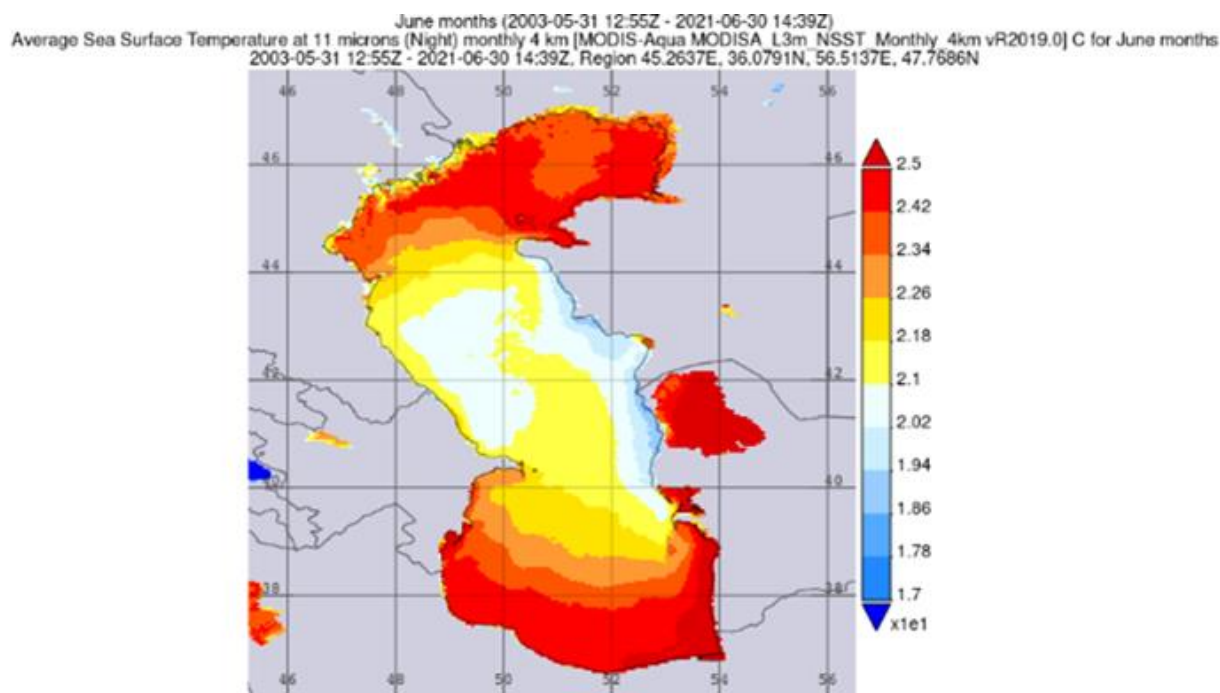


Figure 3. Distribution of SST in the Caspian Sea in June for 2003-2021.

In July, SST distribution in the Caspian Sea area is generally similar to that in June. In addition, as in May and June, the lowest temperatures are observed in the Middle Caspian and gradually increase towards the North and South Caspian. In July, compared to June, the mean multiyear SST increases by 2,0-3,5 °C in the North Caspian, by 2,5-3,5 °C in the Middle Caspian and by 5,0-5,5 °C in the South Caspian (Figure 4).

SST distribution in the North Caspian is rather homogeneous and varies only within 25,5-27 °C. SST gradient at the boundary between the Middle Caspian and the North Caspian is much lower compared to June and amounts to -0,9 °C and is directed from north to south (Figure 4).

SST in the western areas of the Middle Caspian is almost unchanged (24,5-25,5 °C), but sharply decreases to the east, due to the upwelling phenomenon, and approaches 21,5 °C in the coastal zone. SST of the South Caspian Sea varies from north to south within the range of 24,5-28,0 °C. Higher temperatures (30 °C) are observed in the southeastern regions, as well as in the Kara-Bogaz-Gol area and bays located to the south of it (Figure 4).

In July, a pronounced upwelling was recorded on the eastern coast of the Middle and partly Southern Caspian

(Figure 4). As can be seen from the figure, the width of the upwelling zone increases from north to south, and in some places even reaches 60 km. In the east of the Middle Caspian, SST drops from 25 °C to 21 °C from west to east. The temperature gradient is 4,2 °C/100 km.

Figure 4 shows that the upwelling zone extends from the 40th parallel to the 44,5th parallel, expands to the south from Cape Peschany and even penetrates the South Caspian. Intense upwelling partially extinguishes the advection of warm water mass from the South Caspian to the Middle Caspian, and even the reverse process occurs, i.e., advection of the upwelling mass of cold water from the Middle Caspian to the South Caspian.

It should be noted that the distribution of mean SST in July and the shape and size of the upwelling zone may differ in individual years [22,23].

In August, the positive heat balance reaches its maximum in the Caspian Sea [2]. As can be seen from Figure 3 and Figure 5, in most areas of the North Caspian Sea, compared to July, the mean multiyear SST in August is almost unchanged, and even in some places slightly decreases by 0,5 °C. In the Middle Caspian there is an increase in SST by 1,0 °C, and in the South Caspian - by 0-1,5 °C.

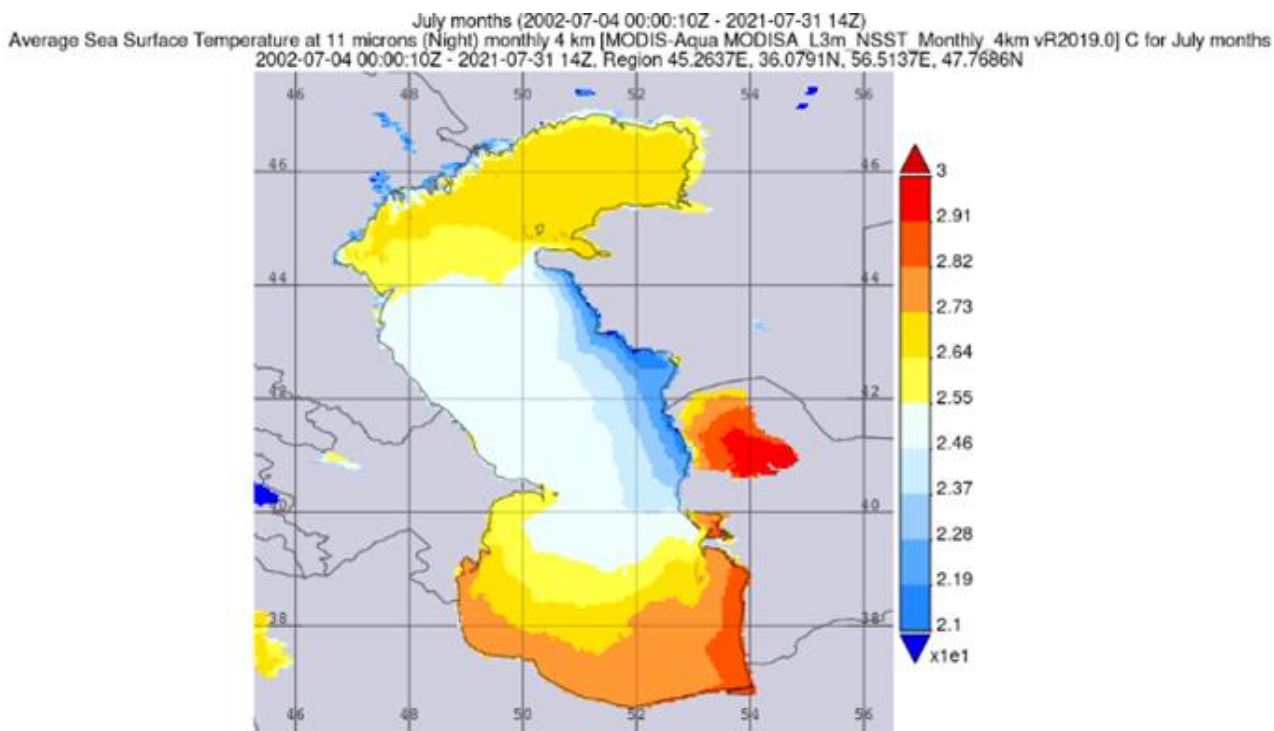


Figure 4. Distribution of SST in the Caspian Sea in July for 2003-2021.

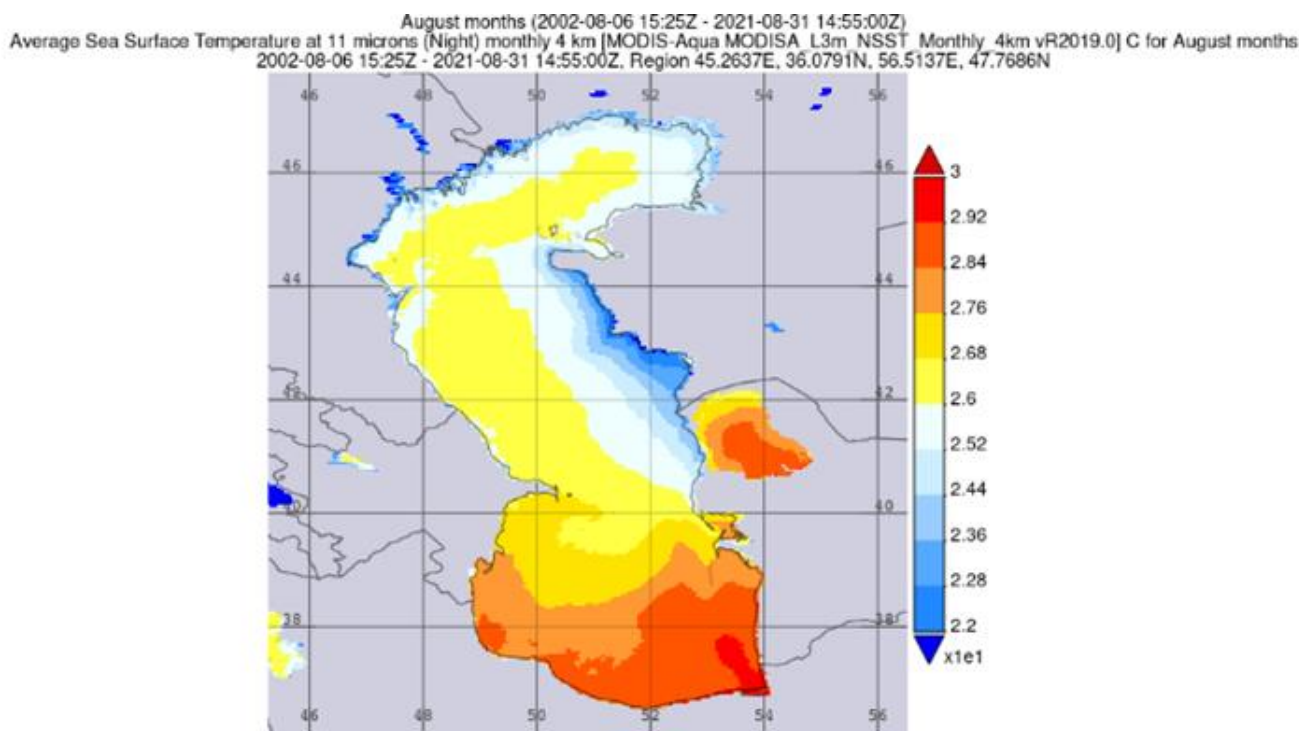


Figure 5. Distribution of average SST in the Caspian Sea in August for 2003-2021.

This month, except for the eastern regions, the surface temperature distribution in the Middle Caspian is almost the same as in the North Caspian (25 -27 °C). In the North Caspian, higher temperatures are noted in the central parts and gradually decrease towards the coasts, which is most likely due to cooler waters brought by the Volga and Ural rivers (Figure 5). On average over the multiyear period, no significant temperature gradient is observed at the boundary between the North Caspian and the Middle Caspian. However, in some years, high gradients may occur at the boundary due to the

intensification of the upwelling phenomenon in the eastern regions (Figure 7).

In the Middle Caspian Sea, SST does not change from north to south. The temperature change is characterized by its decrease from west to east. As can be seen from Figure 4, the zone of warm waters is directed towards the western part of the sea, while towards the east, due to the upwelling process, the SST drops with a large gradient (up to 3,2 °C /100 km). Outside the zones of anomalous upwelling, the SST of the Middle Caspian Sea is 26-27 °C, which is about 1 °C higher than indicated in [9]) and

characterizes the temperature increase over the last 20 years compared to the previous period.

In the northern part of the South Caspian Sea, SST is close to 26 °C and rises to 30 °C towards the southeast. SST in Kara-Bogaz-Gol Bay increases from 26 °C to 29,5 °C from north to southeast.

As can be seen from Figure 5, the upwelling process in August remains intense, but compared to July, its southern border shifts by about 0,5-0,7° to the north, and the process cannot penetrate the South Caspian. As can be seen from Figure 4, the reason for this is the advection of warm waters from the South Caspian to the Middle Caspian more often than in July. In the western part of the South Caspian, on the contrary, advection of relatively cold waters from the Middle Caspian prevails. Lower upwelling temperatures (22 °C) are observed in the area

from the southern coast of Cape Peschanyi to the northern part of the Kazakh Bay.

It should be noted that in some years the nature of the distribution of the average SST in August may undergo certain changes. Figure 6 shows the distribution of the average SST for August 2009 over the sea area. As can be seen, there is a strong advection of warm water masses from the eastern part of the South Caspian to the Middle Caspian, as evidenced by the convexity of the corresponding isotherms to the north. This process prevents the upwelling zone from spreading to the south. Instead, the rising cold-water mass extends to the west in a strip about 200 km long and about 100 km wide from the direction of Cape Peschany, and even individual jets of cold water reach the western coast.

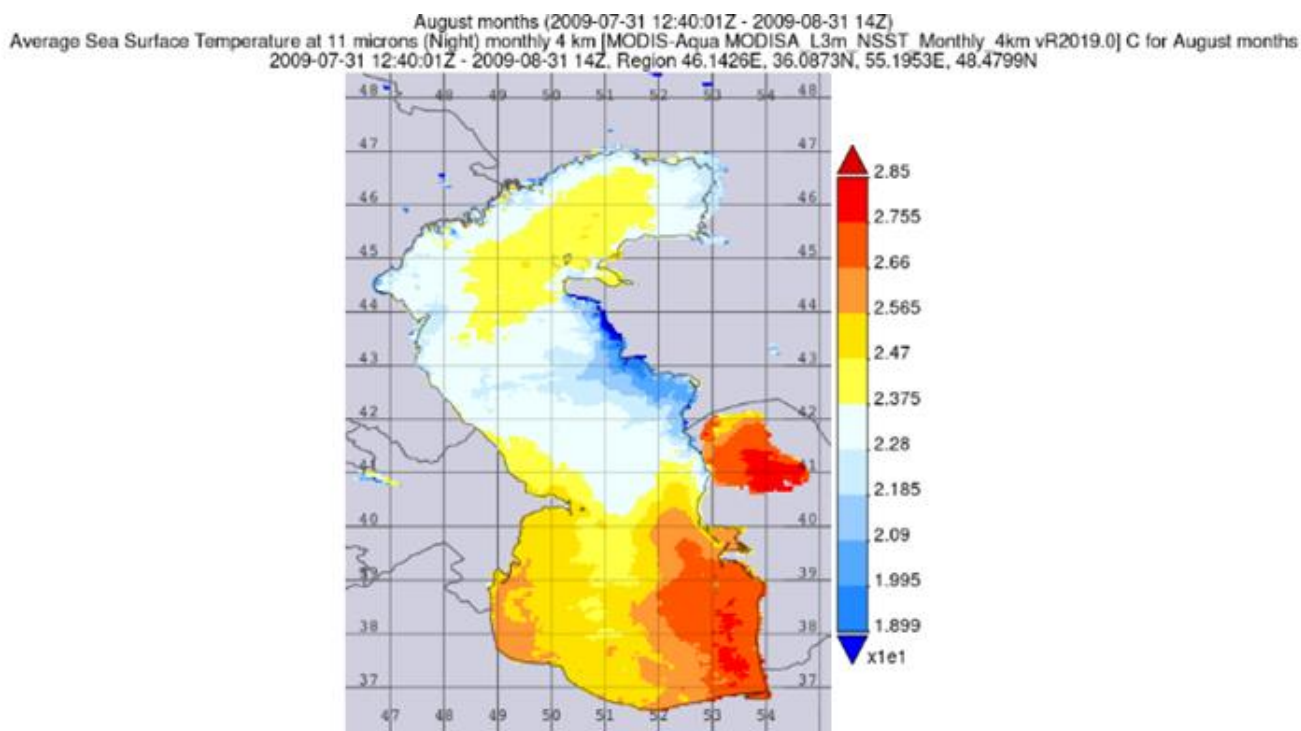


Figure 6. Distribution of the average SST in the Caspian Sea area in August 2009

The upwelling event, which took place in August 2014, is of greater interest due to its uniqueness. The distribution of the average surface temperature for August 2014 is shown in Figure 7. As can be seen from the figure, the upwelling phenomenon here occurs under conditions of strong temperature advection, which originates in the eastern part of the South Caspian and is directed to the north, which prevents upwelling from spreading to the south. Temperature advection from the eastern part of the South Caspian to the north extends along the eastern coast of the Middle Caspian to the Kazakh Gulf, and therefore the southern border of the upwelling zone begins only from the northern coastal waters of this bay. From the north, the upwelling zone is limited by the southern coastal waters of the Tyube-Karagan peninsula.

As can be seen from Figure 6, the upwelling waters, which could not penetrate south from the Kazakh Gulf due to strong temperature advection from the southeast, spread to the west and south, reaching a very significant

part of the Middle Caspian and even the northeastern coastal waters of the South Caspian, or rather the Azerbaijani sector of the sea. From this point of view, this effect can explain the sometimes-sharp cooling of the waters of the western coast of the sea during hot periods of the year. On the other hand, the penetration of upwelling waters into the South Caspian leads to anomalous changes in the distribution of surface waters here (Figure 7).

In September, the character of the average SST distribution over the Caspian Sea area is influenced, especially in the northern areas, by the relative air temperature decrease and continuation of the upwelling process in the eastern coastal waters. As a result, the positive heat balance turns into a negative one. In this connection, the mean multiyear SST in September decreases by 4,5-7,0 °C in the Northern Caspian, by 2,5-3,5 °C in the Middle Caspian and by 1,5-2,0 °C in the Southern Caspian (Figure 5 and Figure 8). As can be seen,

the decrease in the heat balance has the greatest impact on the North Caspian, which is shallower.

The mean annual SST of the North Caspian decreases from 22,5 °C in the south to 18 °C to the north and especially to the east. The temperature gradient at the North Caspian-Middle Caspian boundary is 1,5 °C/100 km (Figure 8). SST of the Middle Caspian Sea increases from 22,5 °C to 24,5 °C from north to south and decreases from 24,0 °C to 19,0 °C from west to east due to the

upwelling phenomenon. A slight decrease in surface temperature in the western coastal zone of the Middle Caspian is associated with the arrival of cyclonic cold surface currents from the north. The surface temperature of the Southern Caspian increases from 24,5 °C to 28,0 °C from north to south. Although the latitudinal distribution of surface temperature in the northern part of the southern water area is relatively homogeneous, a significant temperature gradient is recorded to the south.

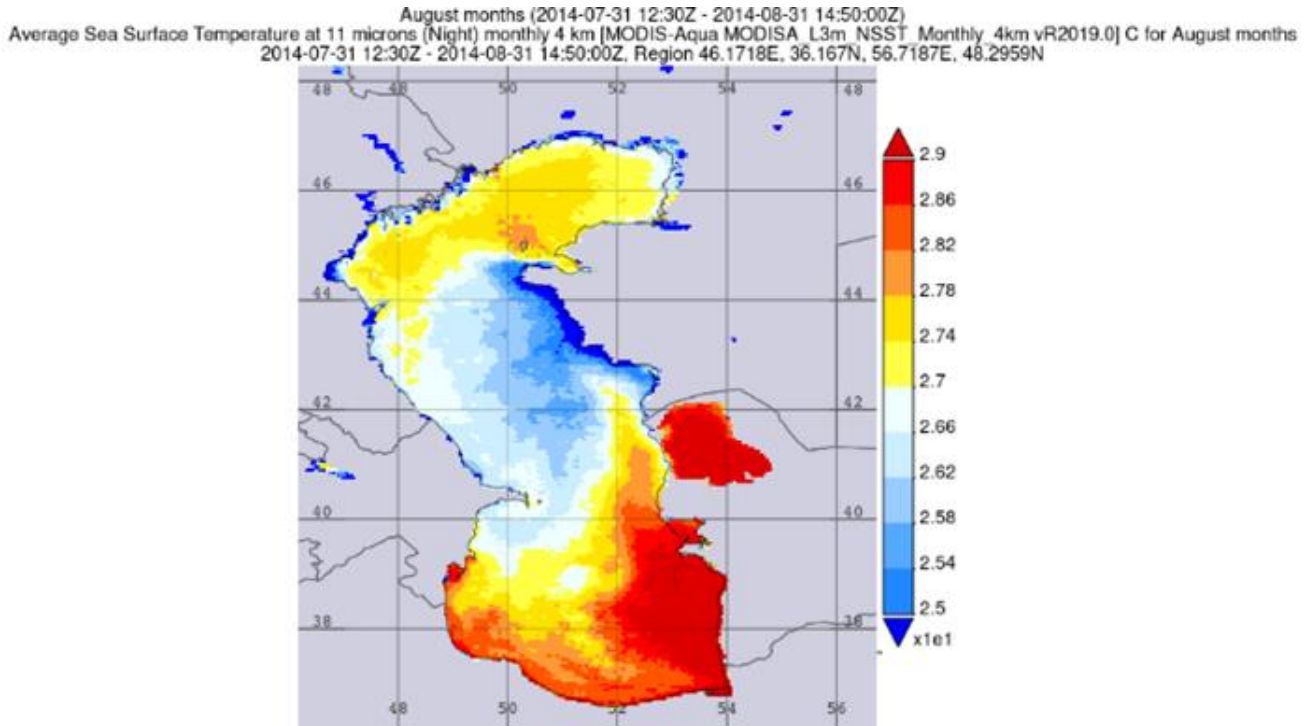


Figure 7. Distribution of the average SST in the Caspian Sea area in August 2014.

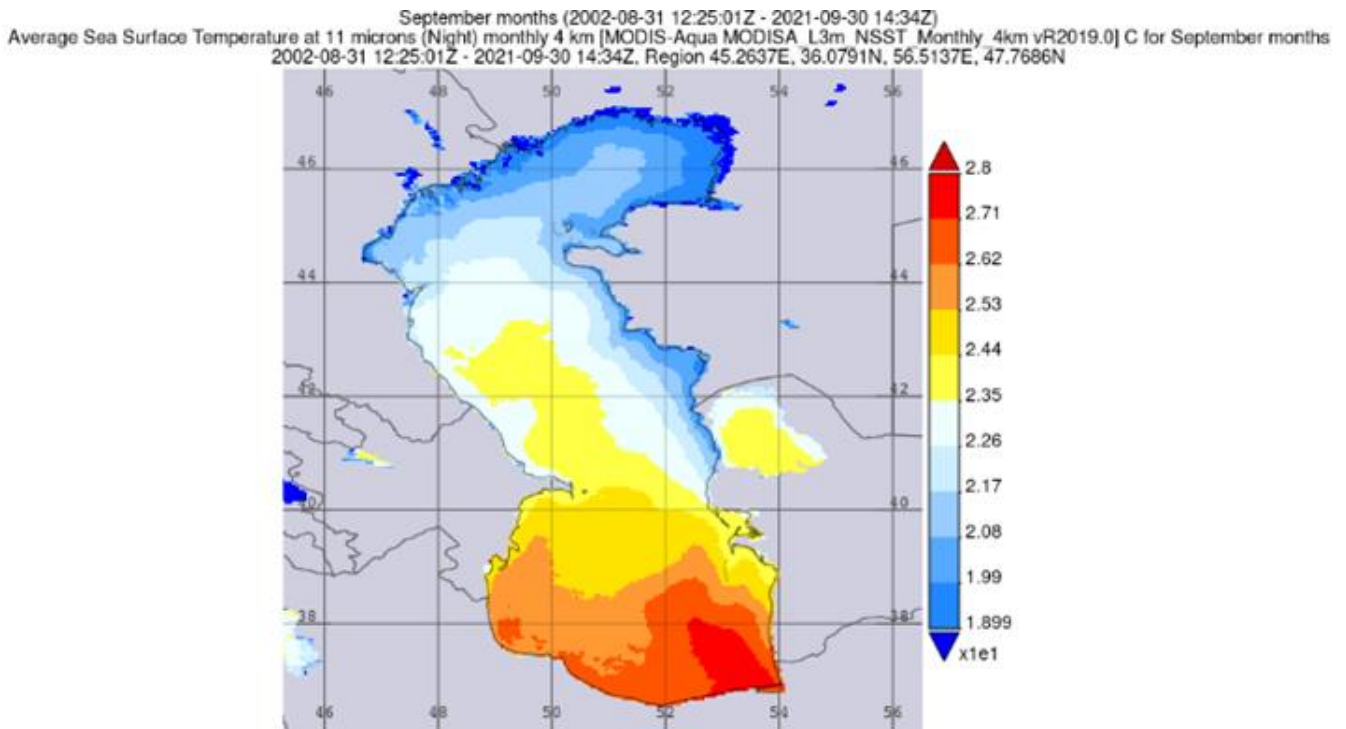


Figure 8. Distribution of SST in the Caspian Sea in September for 2003-2021.

In September, the southern border of the upwelling zone in the east of the Caspian Sea (isotherm 22,6 °C)

passes through the latitude 40,5°, as in August. Since the water temperature in the North Caspian begins to

decrease in September, it becomes difficult to determine the northern boundary of the upwelling zone. The main difference between the upwelling observed in this month and August is that the upwelling zone is narrower, against the background of a relatively lower temperature.

It should be noted that the upwelling processes observed in September of different years can manifest themselves in different ways. During the years of intense advection of warm water mass from the South Caspian to the Middle Caspian, the southern border of upwelling is significantly shifted to the north. For example, in September 2014, warm advective currents moving north along the east coast from the South Caspian extended to about the 42th parallel, preventing the upwelling process from spreading south, and instead, the transformed upwelling waters moved westward from the coastal zone to the direction to the south and reached a latitude of 38,5° in the South Caspian [7]. On the contrary, in years when there is no advection of the waters of the South Caspian into the Middle Caspian, the southern boundary of the upwelling belt can move up to the 40th parallel [24].

According to coastal observations in the area of Fort Shevchenko and Aktau for the period 1961...2018. it was revealed that upwelling near the Kazakh coast is seasonal. Out of 179 cases of upwelling, 87,7% were observed in summer and 6,7% in autumn. Only 18% of the considered cases of upwelling were associated with surge events [25].

This means that in most cases upwellings with Ekman transport mechanism prevail in the eastern part of the Middle Caspian. In other words, in the summer season, long moderate winds blowing along the shores of the eastern part of the Middle Caspian (mainly north and northwest winds) create surface currents, which, in turn, are deflected to the right under the influence of the Coriolis force, creating a corresponding pattern of temperature distribution of upwelling phenomenon (Figure 2, Figure 5, Figure 8). Sometimes strong east and northeast winds can somewhat distort the Ekman transport mechanism of upwelling formation. Since the wind force is proportional to the square of its velocity and the Coriolis force to its first degree, the role of the Coriolis force is significantly reduced at high velocities. In such cases, the upwelling zone can occupy significant areas (Figure 7).

4. Conclusion

Analysis of MODIS Aqua data showed that in the period May-September, upwelling occurs in the eastern and western coastal waters of the Middle Caspian and partly in the South Caspian. It occurs regularly on the east coast, and fragmentarily on the west coast. The most intense upwelling is observed on the eastern coast of the Middle Caspian in July-August. According to averaged long-term data, the upwelling phenomenon during this period is mainly observed between 40-44° latitude, and its width increases from north to south, reaches 60-70 km in the direction of the Kazakh Gulf and decreases to the south. In the upwelling zone, the temperature

gradient sometimes reaches 4,0 °C/100 km. In some years, the upwelling zone that has arisen on the eastern coasts can spread over long distances and even reach the western coasts. In most cases, the upwelling phenomenon occurs against the background of advection of warm waters from the South Caspian to the Middle Caspian.

Author contributions

Said Safarov: Developed the theoretical framework and performed the experiments **Khalil Valizadeh Kamran:** Conceptualization, Methodology, Data collecting. **Vusal Ismayilov:** Analysis, Visualization, Writing-Reviewing. **Elnur Safarov:** Investigation, Editing, Writing-Reviewing

Conflicts of interest

The authors declare no conflicts of interest.

References

- Nacef, L., Bachari, N. E. İ., Bouda, A., & Boubnia, R. (2016). Variability and decadal evolution of temperature and salinity in the mediterranean sea surface. *International Journal of Engineering and Geosciences*, 1(1), 24-33. <https://doi.org/10.26833/ijeg.285222>
- Beşel, C., & Kayıkçı, E. T. (2020). Investigation of Black Sea mean sea level variability by singular spectrum analysis. *International Journal of Engineering and Geosciences*, 5(1), 33-41. <https://doi.org/10.26833/ijeg.580510>
- Shcherbak, S. Ya. (1940). Surface water temperature in the middle and southern parts of the Caspian Sea. *Proceedings on the integrated study of the Caspian Sea*. Publishing House of the Academy of Sciences of the USSR, 66-69 (in Russian).
- Shtokman, V. B. (1947). On the wind-induced circulation in the deep waters of the Caspian Sea. *Meteorology and Hydrology*, 2, 42-50 (in Russian).
- Eltay, A. G., Ivkina, N. I., & Narbayeva, K. T. (2019). Upwelling phenomenon near the Kazakhstani part of the Caspian Sea. *Hydrometeorology and Ecology*, 3, 17-25 (in Russian).
- Ginzburg, A. I., Kostyanoy, A. G., & Sheremet, N. A. (2020). Dynamics of upwelling zone near the eastern coast of the Caspian Sea in the seasonal cycle (May - September) by satellite mean annual temperature data (2003-2019). *Modern Problems of Earth Remote Sensing*, 17(7), 215-226 (in Russian).
- Safarov, S. H., Safarov, E. S., & Ismayilova, N. N. (2023). Study of the wind regime of the oil stones area. *Scientific conference dedicated to the 100th anniversary of H. Aliyev* (in Azerbaijani)
- Lavrova, O. Y., Kostyanoy, A. G., Lebedev, S. A., Mityagina, M. I., Ginzburg, A. I., & Sheremet, N. A. (2011). *Integrated satellite monitoring of the seas of Russia*. Moscow: Space Research Institute of the Russian Academy of Sciences (IKI RAS).

9. Yağmur, N., Tanık, A., Tuzcu, A., Musaoğlu, N., Erten, E., & Bilgilioglu, B. (2020). Opportunities provided by remote sensing data for watershed management: example of Konya Closed Basin. *International Journal of Engineering and Geosciences*, 5(3), 120-129. <https://doi.org/10.26833/ijeg.638669>
10. Jeong, J. Y., Lee, S., Kwon, J. I., Jeong, S. H., & Noh, J. H. (2016). Assessment of MODIS-Aqua Sea surface temperature in the Yellow Sea and East China Seas. *American Geophysical Union*, 2016, P014A-2757.
11. Ivkina, N. I. (2011). Wind conditions in the northern and middle parts of the Caspian Sea. *Hydrometeorology and Ecology*, 4, 27-38 (in Russian).
12. Dyakonov, G. S., & Ibraev, R. A. (2019). Dynamics of the waters of the Caspian Sea over the Apsheron threshold in 2003. *Marine Hydrophysical Journal*, 35 (6), 633-645 (in Russian).
13. Allahverdiyev, Z. S. (2017). Statistical and energetic characteristics of wind speed series in the Caspian Sea. *Water problems: Science and technologies*, 2(10), 20-27 (in Azerbaijani).
14. Ginzburg, A. I., Kostyanoy A. G. G., Solovyev, D. M., & Sheremet, N. A. (2006). Frontal upwelling zone near the eastern coast of the Caspian Sea (satellite observations). *Earth Observations from Space*, 4, 3-12 (in Russian).
15. Serebrennikov, A. N. (2019). The technique of spatial separation of the upwelling by seasonal character. *Modern Problems of Remote Sensing of the Earth from Space*, 16(2), 9-17 (in Russian).
16. Arkhipova, E. G. (1957). Thermal balance of the Caspian Sea. *Tr. GOIN*, 35, 3-102 (in Russian).
17. Goryachkin, Yu. N. (2018). Upwelling nearby the Crimea Western Coast. *Morskoy Gidrofizicheskiy Zhurnal*, [e-journal] 34(5), 399-411. <https://doi.org/10.22449/0233-7584-2018-5-399-411> (in Russian).
18. Monakhova, G. A., & Akhmedova, G. A. (2010) Rise of deep waters near the western coast of the Middle Caspian. *Scientific Journal of KubGAU*, 63(09), 1-12 (in Russian).
19. <https://giovanni.gsfc.nasa.gov/>.
20. Khoshakhlagh, F., Katigari, A. Sh., Saboori, Sh. H., Mojtahedi, N. F., Pour, F. M., & Oskuee, E. A. (2016). Trend of the Caspian Sea surface temperature changes. *Natural Environment Change*, 2(1), 57-66.
21. Mayantsev, G. P., & Osyandin, Yu. A. (1965). On underground runoff from Mangyshlak to the Caspian Sea. *Oceanology*, 5, 854-855 (in Russian).
22. Khoshakhlagh, F., Shakouri Katigari, A., Hadinejad Saboori, S., Farid Mojtahedi, N., Momen Poor, F., & Asadi Oskuee, E. (2016). Trend of the Caspian Sea surface temperature changes. *Natural Environment Change*, 2(1), 57-66.
23. Kerimov, A. A., & Klevtsova, N. T. (1977) Anomaly of water temperature and internal waves in the Middle Caspian. *Proceedings of the TCRIH*, 70, 53-63 (in Russian).
24. Kosarev, A. N. (1980) Water structure and conditions for the formation of biological productivity in the Middle and South Caspian. *Water Resources*, 3, 26-36 (in Russian).
25. Kazmin, A. S. (2021). Multidecadal variability of the hydrometeorological parameters in the Caspian Sea. *Estuarine, Coastal and Shelf Science*, 250, 107150. <https://doi.org/10.1016/j.ecss.2020.107150>



© Author(s) 2024. This work is distributed under <https://creativecommons.org/licenses/by-sa/4.0/>



Introduction of the Runge-Kutta method in GPS orbit computation

Sid Ahmed Medjahed *¹ 

¹ Algerian Space Agency (ASAL), Centre of Space Techniques CTS, Department of Spatial Geodesy. Oran, Algeria, smedjahed@cts.asal.dz

Cite this study: Medjahed, S. A. (2024). Introduction of the Runge-Kutta method in GPS orbit computation. International Journal of Engineering and Geosciences, 9 (2), 256-263

<https://doi.org/10.26833/ijeg.1403435>

Keywords

Broadcast ephemeris
IS-GPS algorithm
Runge-Kutta method
Precise ephemeris
Lagrange interpolation

Research Article

Received: 11.12.2023
Revised: 23.04.2024
Accepted: 25.04.2024
Published: 24.07.2024

Abstract

In all Global Navigation Satellite Systems (GNSS) applications, the determination of the satellite orbits is an important task. In this study, we present the equations given in the Interface Specification Document of GPS and the Runge-Kutta method in the computation of the position P, velocity V, and acceleration A of the GPS satellites using the broadcast ephemeris. The definition of the differential equation describing the GPS satellite's motion has enabled us to introduce the Runge-Kutta method in the GPS orbit computation; this method uses the initial conditions determined in this study from the Keplerian elements provided in the broadcast ephemeris files. The Lagrange interpolation method is used for comparison of the results, where the vectors P, V, and A are estimated using the precise ephemeris. The difference not exceeding 2.4 m was obtained in the X, Y, and Z axes during seven days on the position of the GPS satellite number 9 tested in this study. In velocity and acceleration, the difference is about a few mm/s and mm/s², respectively.



1. Introduction

GNSS stands for Global Navigation Satellite System; it is a general term describing any satellite constellation. The most well-known and widely used GNSS is the Global Positioning System (GPS), developed and operated by the United States. The objectives of GPS are the instantaneous determination of position, velocity, and precise time in the World Geodetic System 84 (WGS84) [1, 2].

GLONASS is the Russian system, which stands for Globalnaya Navigazionnaya Sputnikovaya Sistema, or Global Navigation Satellite System, it is one of the GNSS systems [3]. GLONASS uses the PZ-90 (Parametry Zemli 1990 or Parameters of the Earth 1990) as a reference coordinate system [4].

There are also other global and regional GNSS systems, such as BeiDou China's system, the Galileo system of the European Union, the Navic (Navigation with Indian Constellation) system of India, and the QZSS (Quasi-Zenith Satellite System) system of Japan.

The computation of satellite positions is a fundamental task in all GPS positioning software [5]. The determination of a GPS position begins with the determination of the GPS satellite's coordinates in orbit;

these coordinates are used for a combined use of the GPS and GLONASS observations [6, 7].

In the GPS positioning technique, the data used for the determination of the PVA (Position, Velocity, Acceleration) of satellites can come in the form of a broadcast or a precise ephemeris [5].

In the ICD-GLONASS (Interface Control Document-GLONASS) [4], the authors presented the Runge-Kutta method for the determination of the PVA using the initial conditions provided in the GLONASS broadcast ephemerides file. In [3, 6, 7] the authors used the Runge Kutta method in the computation of the GLONASS satellite orbits. In these papers, several Runge Kutta orders were used.

In the ISD (Interface Specification Documents-GPS) [2], the authors presented the equations of the PVA computation from the GPS broadcast ephemerides file. The ISD-GPS are technical documents that define the specifications for signals, messages, and interfaces within GPS systems [8]. In [5,6], the authors used the equations given in the IS-GPS document in the computation of the position; in Remondi [9], the author presents the derivation of the position equations (velocity); and in Thompson et al. [10], the authors

present the acceleration equation of the satellite's motion.

The main objective of this manuscript is the introduction of the Runge-Kutta method in the computation of the orbits (Position, Velocity, and Acceleration) using the Keplerian elements transmitted in the broadcast files.

The methodology used in the estimation and comparison between the positions (P), velocities (V), and accelerations (A) of the GPS satellites computed from the broadcast and precise ephemeris is as follows:

1-The equations given in the ISD noted IS-GPS Algorithm. This algorithm is applied when the Toe (Time of ephemerides) is equal to Tc (Time of Computation).

2-The Runge-Kutta integration method; this method is used when the Toe and Tc are different. The Runge Kutta method requires the initial conditions to compute the PVA vectors of the GPS satellites in orbit. In this study, these initial conditions (P0; V0; A0) were computed from the Keplerian elements provided in the broadcast ephemeris file using the IS-GPS Algorithm.

3-The Lagrange interpolation method to compute the polynomial of position using the X, Y, and Z coordinates of the GPS satellites provided in the precise ephemerides file. The first and second derivations of the position polynomial give the polynomials of velocity and acceleration, respectively.

The broadcast and precise ephemerides of the GPS satellite number 9, registered between January 8 and 14, 2023, are used to get the PVA of this satellite using the IS-GPS Algorithm, the Runge Kutta integration method, and the Lagrange interpolation method. These ephemerides are produced by the International GNSS Service (IGS) and downloaded from the Crustal Dynamics Data Information System (CDDIS) database. The application date corresponds to the GPS week number 2244.

This paper is organized according to the following sections: Section 2 describes the PVA computation by the IS-GPS Algorithm and the Runge-Kutta method using the Keplerian elements provided in the broadcast ephemerides file. Section 3 describes the PVA estimation by the Lagrange interpolation method using the coordinates of the GPS satellites provided in the precise ephemerides file. In Section 4, a comparison and discussion of the results application are given. Finally, a summary of the conclusions is given.

2. PVA computation from broadcast ephemeris data

2.1. Broadcast ephemeris data

The broadcast ephemeris is the Keplerian elements transmitted by the GPS satellite to the user every two hours and referenced to the time of ephemeris (Toe).

Figure 1 shows an example of the GPS broadcast ephemeris file of GPS SV 9. This figure is taken from the navigation message and has been modified.

According to [11-14], the parameters given in Figure 1 and needed in the computation of PVA are:

- *Toe*: Reference time of ephemeris (sec of GPS week).

- \sqrt{a} : Square root of the semi-major axis (sqrt(m)).
- M_0 : Mean anomaly at the reference time (radians).
- Δn : Mean motion difference from the computed value (radians/sec).
- *e*: Eccentricity.
- w (Omega): Argument of perigee (radians).
- i_0 : Inclination angle at reference time Toe (radians).
- *i* (IDOT): Rate of inclination angle (radians/sec).
- *Cuc*: Amplitude of the cosine harmonic correction term to the argument of latitude (radians).
- *Cus*: Amplitude of the sine harmonic correction term to the argument of latitude (radians).
- *Crc* : Amplitude of the cosine harmonic correction term to the orbit radius (meters).
- *Crs* : Amplitude of the sine harmonic correction term to the orbit radius (meters).
- *Cic* : Amplitude of the cosine harmonic correction term to the angle of inclination (radians).
- *Cis* : Amplitude of the sine harmonic correction term to the angle of inclination (radians).
- Ω_0 OMEGA0: Longitude of the ascension node of the orbit plane at the weekly epoch (radians).
- $\dot{\Omega}$ OMEGA DOT: Rate of right ascension (radians/sec).

G09	2023	01	13	09	59	44
SV	Y	M	D	H	M	S
	4.00E+00		-6.03E+01		4.60E-09	1.80E+00
IODE			Crs		Delta n	M0
	-3.22E-06		2.58E-03		8.26E-06	5.15E+03
Cuc			e		Cus	sqrt(a)
	4.67E+05		-2.60E-08		5.44E-01	-4.84E-08
Toe			Cic		OMEGA0	Cis
	9.55E-01		2.13E+02		1.95E+00	-8.08E-09
i0			Crc		Omega	OMEGA DOT
	-1.75E-10		1.000E+00		2.24E+03	0.00E+00
IDOT			Codes L2		Crs	L2 P data
	2.00E+00		0.00E+00		1.39E-09	4.00E+00
SV accurcy			SV health		TGD	IODC
	4.66E+05		4.00E+00			
Tran time			Fit int			

Figure 1. Broadcast ephemeris data of GPS SV 9.

2.2. IS-GPS algorithm

The position, velocity, and acceleration at time (Tc) are computed as given in the following sections:

2.2.1. Positions of the GPS satellites (P)

The positions are computed by using the equations given in [2, 14-16];

- Compute mean motion (Equation 1):

$$n_0 = \sqrt{\mu/a^3} \tag{1}$$

Where; $\mu = 3.986005 \times 10^{14} m^3/s^2$ is the gravitational constant

-Time from ephemeris reference epoch (Equation 2):

$$t_k = t - T_{oe} \quad (2)$$

-Corrected mean motion (Equation 3):

$$n = n_0 + \Delta n \quad (3)$$

-Mean anomaly (Equation 4):

$$M_k = M_0 + nt_k \quad (4)$$

-Eccentric anomaly: Kepler's equation of eccentric anomaly solved by iteration [13, 16, 17] (Equation 5):

$$E_k = M_k + e \sin E_k \quad (5)$$

-True anomaly (Equation 6):

$$\upsilon_k = \arctan(\sin \upsilon_k / \cos \upsilon_k) \quad (6)$$

$$\text{Where: } \sin \upsilon_k = \frac{(\sqrt{1-e^2} \sin E_k)}{(1-e \cos E_k)} \quad \text{and} \quad \cos \upsilon_k = \frac{(1-e \cos E_k)}{(\cos E_k - e)}$$

-Argument of latitude (Equation 7):

$$\phi_k = \upsilon_k + w \quad (7)$$

-Argument of latitude correction (Equation 8):

$$\delta u_k = C_{us} \sin 2\phi_k + C_{uc} \cos 2\phi_k \quad (8)$$

-Radius correction (Equation 9):

$$\delta r_k = C_{rs} \sin 2\phi_k + C_{rc} \cos 2\phi_k \quad (9)$$

-Inclination correction (Equation 10):

$$\delta i_k = C_{is} \sin 2\phi_k + C_{ic} \cos 2\phi_k \quad (10)$$

-Corrected argument of latitude (Equation 11):

$$u_k = \phi_k + \delta u_k \quad (11)$$

-Corrected radius (Equation 12):

$$r_k = a(1 - e \cos E_k) + \delta r_k \quad (12)$$

-Corrected inclination (Equation 13):

$$i_k = i_0 + \delta i_k + i(IDOT)t_k \quad (13)$$

-Position in the orbital plane (Equation 14):

$$\begin{cases} x'_k = r_k \cos u_k \\ y'_k = r_k \sin u_k \end{cases} \quad (14)$$

-Corrected longitude of the ascending node (Equation 15):

$$\Omega_k = \Omega_0 + (\dot{\Omega} - \dot{\Omega}_e)t_k - \dot{\Omega}_e T_{oe} \quad (15)$$

Where: $\dot{\Omega}_e = 7.2921151467 \times 10^{-5} \text{ rad/s}$ is the Earth's rotation rate.

-Earth-fixed geocentric satellite coordinates (Equation 16):

$$\vec{P} = \begin{cases} X_k = x'_k \cos \Omega_k - y'_k \cos i_k \sin \Omega_k \\ Y_k = x'_k \sin \Omega_k + y'_k \cos i_k \sin \Omega_k \\ Z_k = y'_k \sin i_k \end{cases} \quad (16)$$

2.2.2. Velocities of the GPS satellites (V)

The velocities are computed by taking the time derivative of the position equations [2,9]:

-Eccentric anomaly rate (Equation 17):

$$\dot{E}_k = n / (1 - e \cos E_k) \quad (17)$$

-True anomaly rate (Equation 18):

$$\dot{\upsilon}_k = \dot{E}_k \sqrt{1 - e^2} / (1 - e \cos E_k) \quad (18)$$

-Corrected Inclination angle rate (Equation 19):

$$\left(\frac{di_k}{dt} \right) = i(IDOT) + 2\dot{\upsilon}_k (C_{is} \cos 2\phi_k - C_{ic} \sin 2\phi_k) \quad (19)$$

-Corrected argument of latitude rate (Equation 20):

$$\dot{u}_k = \dot{\upsilon}_k + 2\dot{\upsilon}_k (C_{us} \cos 2\phi_k - C_{uc} \sin 2\phi_k) \quad (20)$$

-Corrected radius rate (Equation 21):

$$\dot{r}_k = e \times a \sin \dot{E}_k + 2\dot{\upsilon}_k (C_{rs} \cos 2\phi_k - C_{rc} \sin 2\phi_k) \quad (21)$$

-Longitude of ascending node rate (Equation 22):

$$\dot{\Omega}_k = \dot{\Omega} - \dot{\Omega}_e \quad (22)$$

-Velocity in the orbital plane (Equation 23):

$$\begin{cases} \dot{x}'_k = \dot{r}_k \cos u_k - r_k \dot{u}_k \sin u_k \\ \dot{y}'_k = \dot{r}_k \sin u_k + r_k \dot{u}_k \cos u_k \end{cases} \quad (23)$$

-Earth's fixed geocentric velocity satellite (Equation 24):

$$\vec{V} = \begin{cases} \dot{X}_k = -x'_k \dot{\Omega}_k \sin \Omega_k + \dot{x}'_k \cos \Omega_k - \dot{y}'_k \sin \Omega_k \cos i_k \\ \quad - y'_k (\dot{\Omega}_k \cos \Omega_k \cos i_k - (di_k/dt) \sin \Omega_k \sin i_k) \\ \dot{Y}_k = x'_k \dot{\Omega}_k \cos \Omega_k + \dot{x}'_k \sin \Omega_k + \dot{y}'_k \cos \Omega_k \cos i_k \\ \quad - y'_k (\dot{\Omega}_k \sin \Omega_k \cos i_k + (di_k/dt) \cos \Omega_k \sin i_k) \\ \dot{Z}_k = \dot{y}'_k \sin i_k + y'_k (di_k/dt) \cos i_k \end{cases} \quad (24)$$

2.2.3. Accelerations of the GPS satellites (A)

The accelerations are computed by taking the time derivative of the velocity [2,10] (Equation 25):

$$\vec{A} = \begin{cases} \ddot{X}_k = -\mu \frac{X_k}{r_k^3} + F \left[\left(1 - 5 \left(\frac{Z_k}{r_k}\right)^2\right) \left(\frac{X_k}{r_k}\right) \right. \\ \quad \left. + 2\dot{Y}_k \dot{\Omega}_e + X_k \dot{\Omega}_e^2 \right] \\ \ddot{Y}_k = -\mu \frac{Y_k}{r_k^3} + F \left[\left(1 - 5 \left(\frac{Z_k}{r_k}\right)^2\right) \left(\frac{Y_k}{r_k}\right) \right. \\ \quad \left. - 2\dot{X}_k \dot{\Omega}_e + Y_k \dot{\Omega}_e^2 \right] \\ \ddot{Z}_k = -\mu \frac{Z_k}{r_k^3} + F \left[\left(3 - 5 \left(\frac{Z_k}{r_k}\right)^2\right) \left(\frac{Z_k}{r_k}\right) \right] \end{cases} \quad (25)$$

Where: $F = (3/2)J_2(\mu/r_k^2)(Re/r_k)^2$;

$J_2 = 0.0010826262$ is the second-order harmonic coefficient; $Re = 6378137.0m$ is the WGS 84 Earth equatorial radius.

2.3. Runge-Kutta (R-K) method

The high accuracy that is nowadays required in the computation of satellite orbits can only be achieved by using numerical methods for the solution of the equation of motion [16]. Among these methods; the Runge-Kutta integration method, originally presented by Carl Runge (1856–1927) in 1895 and Wilhelm Kutta (1867–1944) in 1901 [17]. Runge-Kutta method is particularly easy to use and may be applied to a wide range of different problems [14].

In this section, we present the Runge-Kutta method as an alternative solution for the PVA computation of the GPS satellites using the broadcast ephemerides.

Equation 25 is a second-order differential equation describing the motion of the GPS satellites in orbit. This equation is transformed into a first-order differential Equation (26) and can be resolved numerically by the Runge-Kutta method [3, 4, 16, 18].

$$\begin{cases} \dot{X} = V_x \\ \dot{Y} = V_y \\ \dot{Z} = V_z \\ \dot{V}_x = -\frac{\mu}{r^3} X + F \left(1 - \frac{5Z^2}{r^2}\right) X + \dot{\Omega}_e^2 X + 2\dot{\Omega}_e V_y \\ \dot{V}_y = -\frac{\mu}{r^3} Y + F \left(1 - \frac{5Z^2}{r^2}\right) Y + \dot{\Omega}_e^2 Y - 2\dot{\Omega}_e V_x \\ \dot{V}_z = -\frac{\mu}{r^3} Z + F \left(3 - \frac{5Z^2}{r^2}\right) Z \end{cases} \quad (26)$$

Equation 26 has the general form: $\dot{Y} = F(t, Y)$ and the resolution by the fourth-order R-K method is given in [3, 13, 16] by (Equation 27):

$$Y_{i+1} = Y_i + (K_1 + 2K_2 + 2K_3 + K_4)/6 \quad (27)$$

The coefficients K_i are:

$$\begin{cases} K_1 = f(t_n, Y_n) \\ K_2 = f(t_n + h/2, Y_n + K_1/2) \\ K_3 = f(t_n + h/2, Y_n + K_2/2) \\ K_4 = f(t_n, Y_n) \end{cases} \quad h \text{ is the integration step.}$$

The initial conditions required by the Runge-Kutta method are the position (P_0), the velocity (V_0), and the acceleration (A_0) determined using the IS-GPS Algorithm at time T_{0e} when ($T_{0e} \neq T_c$).

For the computation of the GPS satellite PVA vectors by using the R-K integration method, the Equation 27 becomes (Equation 28):

$$Y = \begin{cases} X_{i+1} = X_i + (K_1 + 2K_2 + 2K_3 + K_4)/6 \\ Y_{i+1} = Y_i + (K_1 + 2K_2 + 2K_3 + K_4)/6 \\ Z_{i+1} = Z_i + (K_1 + 2K_2 + 2K_3 + K_4)/6 \\ Vx_{i+1} = Vx_i + (K_1 + 2K_2 + 2K_3 + K_4)/6 \\ Vy_{i+1} = Vy_i + (K_1 + 2K_2 + 2K_3 + K_4)/6 \\ Vz_{i+1} = Vz_i + (K_1 + 2K_2 + 2K_3 + K_4)/6 \\ Ax_{i+1} = Ax_i = Ax_0 \\ Ay_{i+1} = Ay_i = Ay_0 \\ Az_{i+1} = Az_i = Az_0 \end{cases} \quad (28)$$

More information about the application of this method for GLONASS satellites is given in [3, 4, 18].

3. PVA computation from precise ephemeris data

3.1. Precise Ephemeris Data

The coordinates of all GPS satellites are given in precise ephemeris data (predicted, rapid, and final) produced by various agencies [5, 14, 19].

Figure 2 shows an example of a GPS precise ephemeris file corresponding to the GPS week number 2244. This figure is taken from the precise file and has been modified.

* 2023	1	13	10	0	0.0000000
Year	Month	Day	Hour	Minutes	Seconds
PG09	4741.044216	22896.999356	-12631.801873		
SV	X(km)	Y(km)	Z(km)		

Figure 2. Precise ephemeris data of GPS SV 9.

According to [20], the parameters given in Figure 2 are the X, Y, and Z coordinates of the GPS satellites in. The format of the precise ephemeris is SP3 (Standard Product 3), proposed in 1989 by Remondi [20].

3.2. Lagrange Interpolation

In this section, we present the Lagrange interpolation method used in the PVA estimation of the GPS satellites using precise ephemeris, and thereafter compare our results from the R-K method.

Lagrange interpolation is the most commonly used because of its ease of implementation and accuracy in the interpolation of precise orbits.

The polynomial $P_m(x)$ of order $(n - 1)$ that passes through the (n) points is given by [1, 12, 21]:

$$P_m(x) = \sum_{i=0}^n f(a_i) \cdot L_i(x) \quad \text{where} \quad L_i(x) = \prod_{j=0, j \neq i}^n \left(\frac{x-a_j}{a_i-a_j}\right)$$

To interpolate the X-coordinates of a GPS satellite at a given time (t), the Lagrange polynomial formula becomes (Equation 29):

$$P_m(x) = X_1 \frac{(t - t_2)(t - t_3) \dots (t - t_n)}{(t_1 - t_2)(t_1 - t_3) \dots (t_1 - t_n)} + \dots \quad (29)$$

The $P_m(y)$ and $P_m(z)$ Lagrange polynomials of the Y and Z coordinates are formed in the same way.

The Lagrange polynomials of P, V and A can be written as (Equation 30-32):

3.2.1. Lagrange polynomial of P:

$$P_m(P) = \begin{cases} P_m(X) = A_1 t^{13} + \dots A_{14} \\ P_m(Y) = B_1 t^{13} + \dots B_{14} \\ P_m(Z) = C_1 t^{13} + \dots C_{14} \end{cases} \quad (30)$$

3.2.2. Lagrange polynomial of V (derivation of $P_m(P)$):

$$P_m(V) = \begin{cases} P_m(V_x) = 13A_1 t^{12} + \dots A_{13} \\ P_m(V_y) = 13B_1 t^{12} + \dots B_{13} \\ P_m(V_z) = 13C_1 t^{12} + \dots C_{13} \end{cases} \quad (31)$$

3.2.3. Lagrange polynomial of A (derivation of $P_m(V)$):

$$P_m(A) = \begin{cases} P_m(A_x) = 156A_1 t^{11} + \dots A_{12} \\ P_m(A_y) = 156B_1 t^{11} + \dots B_{12} \\ P_m(A_z) = 156C_1 t^{11} + \dots C_{12} \end{cases} \quad (32)$$

4. Application: Broadcast and precise PVA of GPS satellites computation

4.1. Data sources and PVA estimation steps

In this application, the vectors of positions P, velocities V, and accelerations A of the GPS satellite number 9 are computed and compared using the broadcast and precise files.

The data used are the broadcast and precise ephemerides of the GPS satellite number 9 between January 8 and 14, 2023. This data, produced by IGS and downloaded from (<https://cddis.nasa.gov/>) corresponds to the GPS week number 2244.

In the Figure 3 and 4, we present the broadcast and precise orbits of the GPS satellite number 9 between January 8 and 14, 2023.

The computational steps from the broadcast and precise ephemeris of the P, V, and A are given in the Figure 5.

5. Results and discussion

The positions of the GPS satellite number 9 in the orbital plane (Equation 14) computed by the IS-GPS Algorithm during the GPS week number 2244 are shown in Figure 6.

The Lagrange polynomial functions $P_m(X)$, $P_m(Y)$, $P_m(Z)$ of January 14, 2023, computed between 09:15 and 12:30 are given in Figure 7.

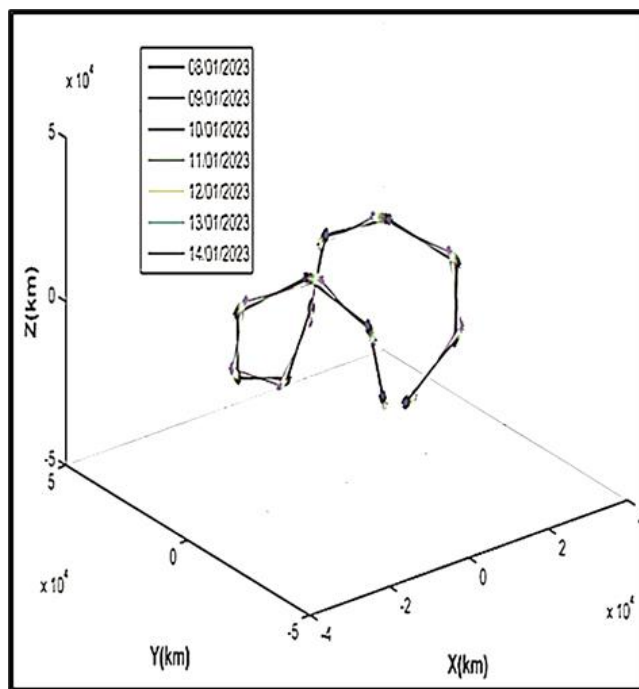


Figure 3. Broadcast orbits of SV 09 (7 days).

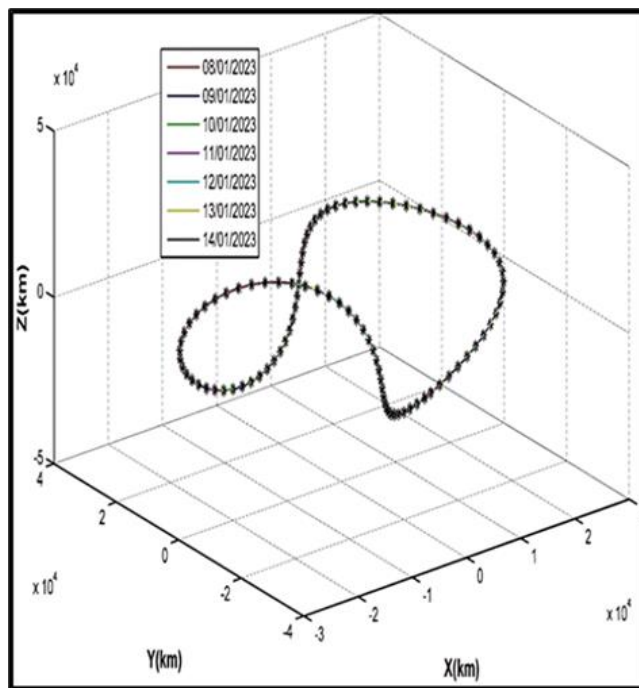


Figure 4. Precises orbits of SV 09 (7 days).

Table 1 gives an example of the differences between the R-K method and the Lagrange interpolation at 10h00m00s on January 13, 2023.

In the Table 1, the computation is carried out at time (Toe = 09h59m44s) using the IS-GPS algorithm and the ephemerides given in Figure 1. The results are used as initial conditions to determine the P, V, and A of the GPS satellite number 9 at time Tc = 10h00m00s by the Runge-Kutta method. The Lagrange interpolation was applied at time (Tc) for the computation of V and A using P given in the precise ephemerides file (Figure 2). In this application, the differences between the Toe and Tc equal 16 sec.

Table 1. 3D Differences (Broadcast vs. Precise).

Tc	P cm	V cm/s	A cm/s ²	Methods of computation
10h00m00s	183	0.016	0.0003	IS-GPS algorithm R-K method Lagrange interpolation

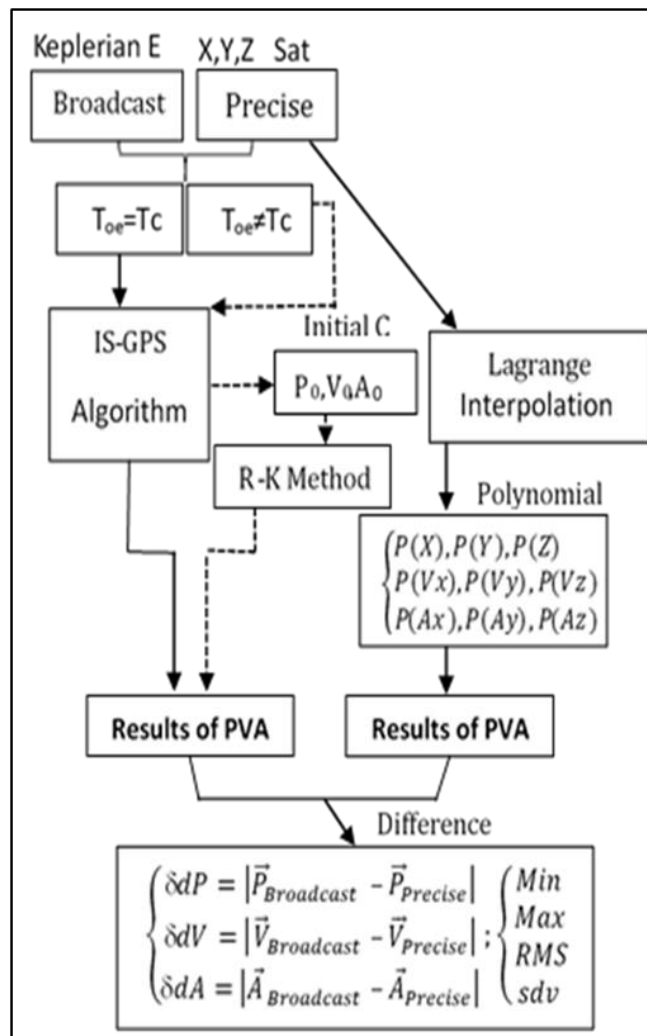


Figure 5. Computational steps of PVA.

During the GPS week number 2244, this process of combined use (IS-GPS Algorithm and the R-K method) is repeated 14 times (twice a day) for the GPS satellite number 9. The differences obtained between the R-K method and the Lagrange interpolation are illustrated in the [Figure 8](#).

The 3D-differences between the broadcast and the precise PVA computation in position varies between 1.38 m and 2.54 m. In velocities the difference varies between 0.14 mm/s and 0.24 mm/s, and in acceleration, the difference varies between 0.003 mm/s² and 1.300 mm/s².

[Figure 9](#) shows the differences every two hours in position (dx, dy, and dz) between the broadcast and precise ephemerides results during the GPS week number 2244 of the satellite GPS number 9.

The differences obtained from the broadcast and precise data seemed to be within a meter or so in position

(dx,dy, dz) and do not exceed 2.4 m in the X, Y, and Z axes; the RMS is 1.66 m and the standard deviation is 0.19 m.

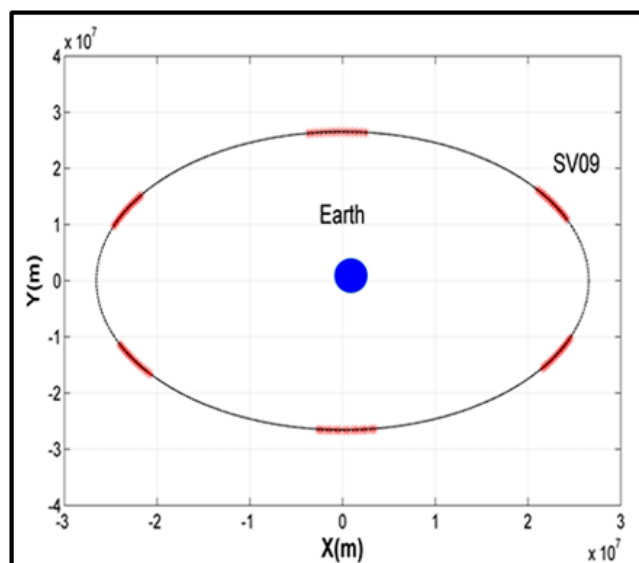


Figure 6. Position of SV 9 in the orbital plane.

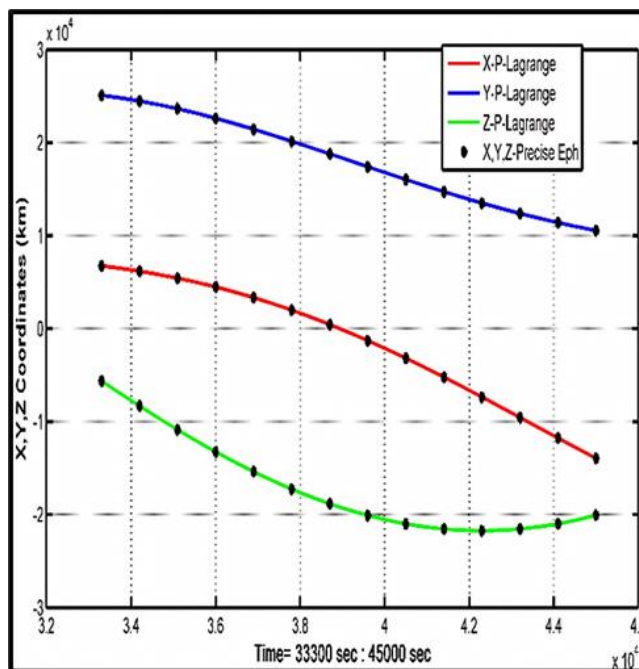


Figure 7. Lagrange polynomial's function $P_m(P)$ of SV 9.

These differences are due to a number of factors, such as:

- The accuracy of each type of ephemeris (broadcast and precise) affects the PVA result.
- The accuracy of the methods used in computation:
 - 1- IS-GPS Algorithm (resolution of the Kepler equation).
 - 2- R-K method (order = 4 and integration step size = 1 sec).
 - 3- Lagrange integration order (order of $P(m) = 13$), [Figure 7](#) and [Equations 30-32](#).
- The difference between the reference of the broadcast ephemeris (Antenna Phase Center) and the reference of the precise ephemeris (Center of Mass). The determination of this offset using ANTEX files (ANTenna Exchange format) reduces these differences [\[13\]](#).

- In Equations 25 and 26, the acceleration of the satellites due to the luni-solar perturbation is assumed to be null. This assumption gives less accurate position, velocity, and acceleration results. In the GLONASS system, these perturbations are transmitted in the broadcast ephemeris files and added as constant values in Equations 25 and 26.

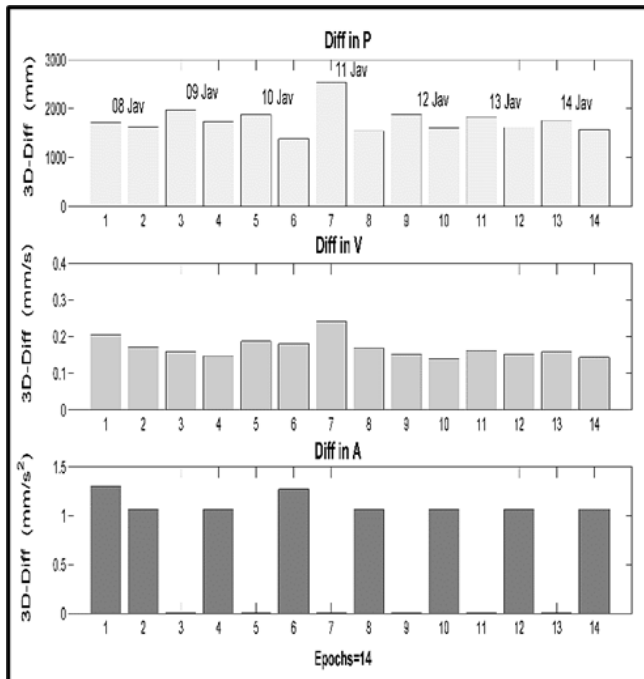


Figure 8. Differences (Broadcast vs. Precise) at 14 epoch (R-K Method and Lagrange interpolation).

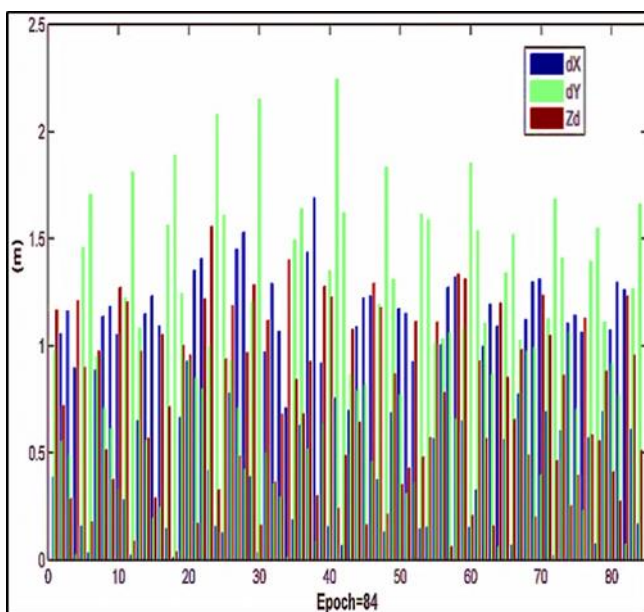


Figure 9. Differences (Broadcast vs. Precise) at 84 epoch (IS-GPS Algorithm, R-K Method and Lagrange interpolation).

6. Conclusion

In GNSS theory, the determination of the receiver position begins with the determination of the satellite position.

This paper presents the IS-GPS Algorithm and the Runge-Kutta integration method for computing the

position, velocity, and acceleration of the GPS satellites using the broadcast ephemerides data. In addition, we compared our results with the Lagrange interpolation method used in the estimation of the GPS satellite vectors P, V, and A using precise ephemeris data.

The velocity and acceleration of satellites are important measures in several GPS applications. In this study, the velocity and acceleration of the GPS satellites are obtained by the derivation of the position equations (IS-GPS Algorithm), the integration of the differential equation of GPS satellite motion by the Runge-Kutta method, and derivation of the Lagrange polynomial.

The introduction of the Runge-Kutta method in the computation of the position, velocity, and acceleration (PVA) of the GPS satellites as an alternative solution requires the determination of initial conditions from the Keplerian elements by the IS-GPS Algorithm.

The difference obtained between the broadcast and the precise PVA computation does not exceed 2.4 m (X, Y, and Z axes) in the position of the GPS satellite number 9 and a few millimeters in velocity and acceleration.

Conflicts of interest

The authors declare no conflicts of interest.

References

- Hofmann-Wellenhof, B., Lichtenegger, H., & Wasle, E. (2007). GNSS—global navigation satellite systems: GPS, GLONASS, Galileo, and more. Springer Science & Business Media.
- IS-GPS (2022). Interface specification document: Navstar GPS Space Segment/Navigation User Segment Interfaces.
- Medjahed, S. A., Niati, A., Kheloufi, N., & Taibi, H. (2021). Implementation of the variation of the luni-solar acceleration into GLONASS orbit calculus. *Geodetski Vestnik*, 65(3), 459-471. <https://doi.org/10.15292/geodetski-vestnik.2021.03.459-471>
- ICD-GLONASS. (2016). Interface control document: General Description of Code, Interface Control Document. Edition 1.0. Moscow.
- El-naggar, A. M. (2012). New method of GPS orbit determination from GCPS network for the purpose of DOP calculations. *Alexandria Engineering Journal*, 51(2), 129-136. <https://doi.org/10.1016/j.aej.2012.06.002>
- Ferrão, P. F. F. N. (2013). Positioning with combined GPS and glonass observations. [Master's Thesis., Técnico Lisboa].
- Roßbach, U. (2001). Positioning and navigation using the Russian satellite system GLONASS. Universität der Bundeswehr München, Studiengang Geodäsie und Geoinformationen.
- GPS.gov. (2023). Interface Control Documents. <https://www.gps.gov/technical/icwg>
- Remondi, B. W. (2004). Computing satellite velocity using the broadcast ephemeris. *GPS solutions*, 8(3), 181-183. <https://doi.org/10.1007/s10291-004-0094-6>

10. Thompson, B. F., Lewis, S. W., Brown, S. A., & Scott, T. M. (2019). Computing GPS satellite velocity and acceleration from the broadcast navigation message. *Navigation*, 66(4), 769-779. <https://doi.org/10.1002/navi.342>
11. Gurtner, W. (2013). The Receiver Independent Exchange Format RINEX, Version 3.02. International GNSS Service (IGS), RINEX Working Group and Radio Technical Commission for Maritime Services. Special Committee 104 (RTCM-SC104)
12. Teunissen, P. J., & Montenbruck, O. (2017). Springer handbook of global navigation satellite systems. <https://doi.org/10.1007/978-3-319-42928-1>
13. Subirana, J. S., Hernandez-Pajares, M., & Zornoza, J. M. J. (2013). GNSS Data Processing: Vol. I [Fundamentals and Algorithms]. ESA Communications.
14. Tusat, E., & Ozyuksel, F. (2018). Comparison of GPS satellite coordinates computed from broadcast and IGS final ephemerides. *International Journal of Engineering and Geosciences*, 3(1), 12-19. <https://doi.org/10.26833/ijeg.337806>
15. Ogaja, C. A. (2013). Appendix 3: Calculation of Satellite Position from Ephemeris Data. *Applied GPS for Engineers and Project Managers*. American Society of Civil Engineers, ASCE Library. <https://ascelibrary.org/doi/book/10.1061/9780784411506#>
16. Montenbruck, O., & Gill, E. K. A. (2014). Models, Methods, and Applications. *Satellite Orbits*, 293-318. Springer.
17. Vallado, D. A., & MacClain, W. D. (2013). *Fundamentals of Astrodynamics and Applications*. Space Technology Library, Microcosm Press.
18. Lin, Y., Guo, H., & Yu, M. (2009). A Comparison for GLONASS Satellite Coordinate Calculation. 2009 International Conference on Information Engineering and Computer Science, 1-4. <https://doi.org/10.1109/ICIECS.2009.5365110>
19. IGS. (2023). International GNSS Service. <https://www.gps.gov/technical/icwg>
20. Hilla, S. (2016). The Extended Standard Product 3 Orbit Format (SP3-c). National Geodetic Survey, National Ocean Service, NOAA, Silver Spring, MD 20910-6233, USA.
21. Wang, J., Li, Y., Zhu, H., & Ma, T. (2018). Interpolation method research and precision analysis of GPS satellite position. *Journal of Systems Science and Information*, 6(3), 277-288. <https://doi.org/10.21078/JSSI-2018-277-12>



© Author(s) 2024. This work is distributed under <https://creativecommons.org/licenses/by-sa/4.0/>



Mapping the structural vulnerability to drought in Morocco

Noureddine Bijaber^{*1}, Atmane Rochdi², Mohammed Yessef³, Houda El Yacoubi²

¹ Royal Centre for Remote Sensing, Rabat, Morocco, nbijaber@yahoo.fr

² Ibn Tofail University, Research Unit of Agro-physiology, Biotechnology and Environment; Laboratory of Natural Resources and Sustainable Development; Kenitra, Morocco, atmane.rochdi@uit.ac.ma, houda.elyacoubi@uit.ac.ma

³ Institut Agronomique et Vétérinaire Hassan II, Rabat, Morocco, y_toufik2006@yahoo.fr

Cite this study: Bijaber, N., Rochdi, A. Yessef, M., & El Yacoubi, H. (2024). Mapping the structural vulnerability to drought in Morocco. *International Journal of Engineering and Geosciences*, 9 (2), 264-280

<https://doi.org/10.26833/ijeg.1404507>

Keywords

Drought
Structural vulnerability
Remote sensing

Research Article

Received: 13.12.2023

Revised: 01.03.2024

Accepted: 24.03.2024

Published: 25.07.2024



Abstract

Because of its recurrence and the durability of its effects, drought in Morocco has become a structural component of the Moroccan climate. It is a real threat to the agricultural sector, which represents nearly 20% of the Moroccan economy. The spatiotemporal variability of this phenomenon makes drought risk management more complex. The current study seeks to map the structural vulnerability to drought in Morocco by using remote sensing techniques to characterize its sensitivity to drought. In this premise, we utilized a weighted combination of soil classes, land cover and socio-economic data with seasonal drought monitoring through a composite index generated monthly over the past twenty years. The generated map shows dominance of areas with high and very high vulnerability risk to drought over respectively 38.5% and 14.4% of the country and this concerns both agricultural and non-agricultural zones. The map also indicates that 36.5% of Morocco presents a medium vulnerability to drought and only 10.6% of the national territory is considered non-vulnerable to drought. This map can be used as a planning tool to support natural resources management and mitigate drought impacts.

1. Introduction

In arid and semi-arid areas, the degradation of natural resources and water scarcity due to recurrent droughts reduce economic and biological productivity and contribute to the ecological deterioration and fragility [1]. Such losses amplify the vulnerability of the agricultural areas to these extreme climate hazards [2].

Due to its arid and semi-arid geographic situation, Morocco faces different climate change induced challenges such as aridity, spatiotemporal scarcity and irregularity of water resources, recurrent droughts, desertification, etc. The climate setting of the country has a considerable impact on agricultural production, which is an important contributor to the national economy and it is strongly dependent on the amount and spatio-temporal distribution of rainfall. During last few years, drought in Morocco resulted in serious losses in agricultural and livestock production and increased the forest fires incidents and the shortage of drinking water storage [3].

Vulnerability may exist because of high exposure to the drought hazard, and it can be either cyclical or structural. The cyclical vulnerability to drought is

defined as the degree of loss in general productivity due to rainfall scarcity in a given limited period of time (month, season and year) [2]. For this type of vulnerability, the impact can be reduced, on one hand, by the first coming rains and on the other hand, by the short-term decisions taken by the government (creation of seasonal jobs in rural areas, mobilization of funds, drought mitigation activities, etc.). The structural vulnerability to drought concerns all the components of the hydrological cycle and all the fields of water use including meteorology, hydrology, agronomy, forestry and socio-economy. This type of vulnerability has a long-term dimension and its assessment can be used as a benchmark in drought mitigation plans by classifying areas according to their level of sensitivity to drought.

It is obvious that the structural and cyclical concepts of vulnerability interact: the first one is described as structural vulnerability to drought because there is a repetitive cyclical vulnerability whose impacts on natural resources are becoming increasingly devastating [2]. In addition, early warning must take into account all the static and dynamic factors that characterize the sensitivity of any ecosystem.

The main purpose of this work is to develop a methodology for mapping structural vulnerability to drought in Morocco. Such a map can be used as a planning tool to support managers and decision-makers in limiting drought impacts and reducing vulnerability before the potential of damage is realized. The first part of this paper presents generalities about vulnerability to drought followed by a detailed description of the methodology adopted for the structural vulnerability mapping (data used, derived parameters, combined indicators and weighting).

2. Generalities on vulnerability to drought

The concept of vulnerability is common to all operational early warning systems. Vulnerability is an overall indicator that measures the capability of a region (or of a group) to resist, cope with and to recover from the impact of a negative event [2]. It takes into account the factors (societal, physical and natural) that contribute to and influence a disaster risk, the probability of occurrence of such event, and the level of exposure to risk of different groups, areas and/or sectors.

Vulnerability is not a measurable feature of a system, such as temperature, precipitation or agricultural production. It is a concept that reflects the complex interaction of several factors that determine a system's sensitivity to the effects of climate change [4]. Vulnerability to drought is the characteristic of an area for which there is a high probability that the drought risk will turn into concrete events such as crop failures, livestock losses, famine, etc. It describes the fragility of the system exposed to an extreme climatic event (drought) and it is related to the intensity and duration of this extreme event.

In the context of drought, there are two main types of vulnerability to take into consideration in monitoring and warning systems. The first one is the seasonal vulnerability, which is based on the modeling of agro-climatic parameters combined with remote sensing data and crop growth modeling for the assessment of the current season based on yield estimates [5,6]. The second type is the structural vulnerability, which refers to the characteristics of a social group or sector in terms of its capacity to anticipate, cope with, and to recover from drought [2].

More specifically, vulnerability to agro-climatic drought can be defined as the "characteristic of an entity (zone or human group) for which there is a high probability that the agro-climatic risk will turn into a concrete event" [7]. The term "*human group*" refers to groups that are not necessarily linked to a specific territory, such as pastoralists or farmers (producers of a specific crop). The term "*concrete event*" refers, for example, to a reduction in the value of the yields which controls the farmers' income [2].

According to the National Drought Mitigation Center [7], the main components of the disaster management cycle are preparedness, mitigation, prediction and early warning activities. Risk management emphasizes these components initiated before drought with the goal of

reducing the impacts associated with subsequent events. For the cycle of drought risk management, the preparedness is the most important phase, and it is the one on which efforts must focus. It includes all the structural decisions and activities to take in case of drought. It concerns the implementation of tools and processes as well as methodologies to develop drought plans and appropriate responses in anticipation to drought occurrence.

Mapping structural vulnerability to drought requires the definition and preparation of relevant and easily accessible indicators and indices representing the entire studied territory [8]. The vulnerability assessment maps contribute to better targeting areas prone to or affected by the disaster. By understanding the causes of vulnerability to drought, managers can design proactive measures to decrease the potential impacts of drought and increase the adaptation capacity of a community [9].

3. Materials and methods

Mapping the structural vulnerability to drought is a complex and challenging task because the phenomenon itself is complex and difficult to assess. Different parameters and factors (physical, social, economic and environmental factors) [10,11] are involved in the study of drought vulnerability and their use may depend on data availability. Despite these limitations and the complexity of the task, we tried to produce a structural vulnerability map for Morocco based on the existing and operational data.

To this purpose, we adopted the methodology of drought vulnerability assessment developed in the Vulnerability Sourcebook, Concept and Guidelines for standardized vulnerability assessments [12]. According to these guidelines, vulnerability is a function of three major drivers, including exposure, sensitivity and adaptive capacity. The combination of exposure and sensitivity determines the potential impact of the vulnerability on people, economic sectors and socio-ecological systems.

3.1. Datasets

Various datasets were gathered and integrated from different sources and with different characteristics by using geographic information systems (GIS) and programming technics. The present study is based on a combination of four groups of datasets, namely: the monthly-generated drought composite index over the last twenty years, the distribution of soil classes, the land cover map and the recent global poverty index resulting from the general population census of Morocco.

3.1.1. Periodic drought index

The Royal Centre for Remote Sensing (CRTS) has recently developed a gridded composite drought indicator (CDI) based on a combination of different parameters derived from various satellite-based earth observation data at the national scale. Row products are periodically downloaded and processed to generate a

monthly basis CDI over Morocco at a 5km resolution (which is the precipitation estimates resolution). This composite index is the result of a study that has been done in the framework of a global project (Land Data Assimilation System, LDAS) financed by the World Bank with the technical support of the American space agency (NASA) and the National Drought Mitigation Centre of the University of Nebraska. The main purpose of the composite approach was to leverage the relevant strengths of each parameter and provide a single index that was representative of different drought severity classes at the national scale [13,14].

The developed CDI tool incorporates information related to four different parameters and indices derived from earth observation data [15]. These parameters are:

- Standardized Precipitation Index (SPI) from satellite-based rainfall data. The Climate Hazards Group InfraRed Precipitation with Station (CHIRPS) represents satellite estimates corrected by integration of rainfall data from weather stations on the ground. These data are available from 1981 to present at 5 km spatial resolution [16]. We used the available CHIRPS archived data set to calculate the standardized precipitation index (SPI) over a two-month period [17,18]. The SPI-2 provides comparison of the precipitation over 2-month specific period with the historical average precipitation of the same 2-month period dating back to 1981.

- Normalized Difference Vegetation Index (NDVI) anomalies. The 10-day maximum-value composite NDVI anomalies generated from MODIS (Moderate Resolution Imaging Spectroradiometer) and VIIRS (Visible Infrared Imager Radiometer Suite) data were periodically downloaded from Famine Early Warning Systems Network (FEWSNET) portal since 2001 [19]. This parameter represents the anomalies of the current vegetation conditions compared to the historical conditions for the same period.

- Land Surface Temperature (LST) based Soil Moisture Proxy anomalies. Two daily satellite-based observations were derived from MODIS Terra sensor: day and night land surface temperature (LST) to calculate a monthly composite diurnal changes in LST. The generated MODIS day-night LST anomalies were used as indicators of soil moisture. Indeed, relative soil moisture can be estimated using LST observations in the thermal infrared region [20]. According to Hain et al., [20] and Wan et al., [21,22], the evolution of LST in the morning hours is strongly dependent on current soil moisture conditions, as wet soil will heat up more slowly and dry soil will heat up more rapidly [20-22].

- Evapotranspiration anomalies (ETA). The ETA gridded data products are open-access and obtained from FEWSNET platform. This parameter is calculated by using the Operational Simplified Surface Energy Balance (SSEBop) model, which is a simplified energy balance method incorporating thermal data from MODIS since 2003 [23].

These four input data sets cover the Moroccan territory with different spatial resolutions (5km for SPI from CHIRPS, 250m for NDVI, 1km for ETA and LST from MODIS). In order to have a uniform spatial resolution for the CDI, all the indices were sampled to a 5km spatial

resolution consisting of 25,589 grid cells in total over Morocco [13].

The CDI is calculated monthly by using the weighted arithmetic aggregation method and by assigning the highest weight to the rainfall-based parameter (40%). Indeed, the 2-month SPI has a strong relationship with drought onset, duration and intensity according to a retrospective comparison between the CDI input parameter maps and real drought episodes from the past (using ground truth data: precipitation measurements and cereal productions). The other three indices (NDVIa, ETA and LST) were considered factors resulting from the impact of rainfall deficit and were equally weighted (20% each). The final CDI map presents four drought intensity classes [24] as described in Table 1.

Table 1. Drought intensity categories.

Drought classes	Class names	CDI Percentiles
D0	No drought	> 20
D1	Moderate	10 to 20
D2	Severe	5 to 10
D3	Extreme	2 to 5
D4	Exceptional	< 2

The composite drought index maps are generated at a monthly time scale with the spatial resolution of 5km since January 2003 during the agricultural seasons (October to April). The analysis of this historical CDI database over the past 20 years has enabled us to study and to assess the severity and duration of the occurred drought events. Areas with the highest drought frequency were the most vulnerable and those with the lowest frequency were less vulnerable [25-27]. The approach of drought frequency analysis was based on the identification of areas where the different drought intensity classes occurred both during the first parts of the growing seasons and also during the most sensitive parts of the growing periods. This represented the first component of the vulnerability, which is 'Exposure'.

3.1.2. Soil data

Soils are threatened by various forms of degradation (erosion, biological and physicochemical degradation, salinization, pollution) that lead to a decrease in soil fertility and productivity [28]. In case of rainfall deficit, water reserves in the superficial layers of the soil become insufficient during the growing season. This "edaphic" drought is the classic drought in agriculture caused by the scarcity and/or bad distribution of rainfall during the agricultural season, and is highly dependent on soil properties (composition, thickness and depth, texture, bio-physicochemical characteristics, etc.).

Soil maps are especially useful when it comes to understanding how different soils may respond to droughts. For example, sandy soils are more prone to drying out quickly and deeply during a drought due to their low water retention capabilities. Meanwhile, clay soils can retain moisture for longer periods and avoid such severe effects from droughts. Gridded information about global soil categories regarding drought sensitivity levels is a fundamental step in the study of structural

vulnerability to drought. Therefore, we used the map published by the International Soil Reference Information Centre (ISRIC) called SoilGrids [29] that provides global information on standard soil properties at different depths (organic carbon, cation exchange capacity, pH, etc.) and on the distribution of soil classes based on the international soil classification systems. The most recent version of SoilGrids is available at 250m spatial resolution [29].

3.1.3. Land cover data

Land cover is an important variable for understanding the vulnerability of an area to drought. It describes the spatial distribution of the main land surface classes (irrigated and non-irrigated crops' cultivated areas, forests, rangelands, water bodies, etc.) and allows their classification based on their sensitivity to drought. For example, areas with grasslands and non-irrigated annual crops will suffer more quickly compared to those with trees and perennial plants that can retain moisture better. It is also important to take into account changes in land use such as irrigated areas or urban development that may increase the fragility of a system during prolonged periods of drought [30].

In the present study, we generated a land cover map at national scale by classifying multi-temporal remotely sensed data sets (Sentinel2 at 10 m resolution). The approach was fully automatic using high-resolution optical image time series acquired between September 2020 and December 2021 (at least two images per month), and classified using an automatic processing chain [31]. Once all the time series tiles were downloaded, the preprocessing phase comprised the following steps:

- (1) Image processing with their validity masks (clouds, cloud shadow, saturation, etc.),
- (2) Temporal gap filing and resampling,
- (3) Reference data preparation and split into training and validation subsets,
- (4) Features extraction from each dataset (NDVI, NDWI and the brightness) and their concatenation to produce a mosaic of the downloaded tiles.

The adopted classification method required the collection of data for training and validation. The advantage of this automatic approach was to rely on existing databases to build the reference data sets needed for supervised classification and the subsequent validation of the results.

The land cover map resulting from Sentinel-2 images classification for the year 2020-2021 had a total accuracy of 85.72% and a Kappa coefficient equal to 0.84. This accuracy level was acceptable to use for the study of the structural vulnerability in Morocco because all the generated classes were merged into four main classes in term of their vulnerability to drought [12,32]. However, since the approach was fully automatic and based on open existing data, the land cover map will be updated at a regular periodicity in the future.

Both soil and land cover data described above present the second component of the vulnerability, which is Sensitivity that determines the degree to which the

ecosystem is affected by the impacts of the first component of vulnerability (Exposure).

3.1.4. Socio-economic data

Structural vulnerability to drought is historically and closely linked to the population poverty, which is a main component of the socio-economic vulnerability. When an area experiences a drought, those living in poverty have little to no access to basic necessities, such as food and water. This part of population is particularly vulnerable to external shocks, including those caused by natural disasters. They have a lower capacity to deal with shocks than non-poor households, due to lower access to savings, borrowing, or social protection [33]. As a result, people living in poverty during periods of drought conditions become particularly vulnerable making them more susceptible to long-term effects such as lowered immunity levels and further health problems.

On the other hand, natural disasters are a key factor for pushing vulnerable households into poverty and keeping households poor. Exposure to natural hazards may reduce incentives to invest and save, since the possibility of losing production and livestock due to a drought, makes these investments less attractive [33]. This vulnerability is more accentuated in rural areas where people are in general engaged in agricultural activities rain dependent.

The impacts of drought across societies, economies and ecosystems are significant and difficult to quantify from an economic perspective [34]. Nowadays, many indices and indicators exist at international level to monitor the human quality of life for each country and describe the socio-economic vulnerability to drought. These vulnerability indices reflect the capacity of a population to anticipate, resist, adapt to and recover from the impact of drought events [12].

In Morocco, the main source of information on socio-economic aspects is the high authority in charge of population planning (Haut-Commissariat au Plan, HCP) that owns all the statistics about the Moroccan population. Among the available indices presenting the degree of social fragility to drought, we selected the global poverty index that incorporated both monetary and multidimensional poverty. This type of poverty described the rate of population with little access to essential services like education, health and living conditions compared to the national poverty line. The available data exist in tabular format resulting from the general population census of Morocco conducted in 2014 [35]. In the present study, we retrieved and spatialized the global poverty index available at communal scale and reclassified it into levels of socio-economic vulnerability. The integration of this parameter into the geodatabase process is detailed below (§3.2.4. Adaptive Capacity).

3.2. Methodology

The approach developed in this study was based on the various parameters and factors described above and it was adopted from the global methodology of drought vulnerability assessment combining the main drivers,

including exposure, sensitivity and adaptive capacity [12]. Figure 1 summarizes the data used and the main steps for structural vulnerability mapping.

The framework presents the selection of indicators

and the weighted combination of parameters to generate the vulnerability classes at national scale [36]. The methods for extracting and combining the different factors for drought vulnerability mapping are described.

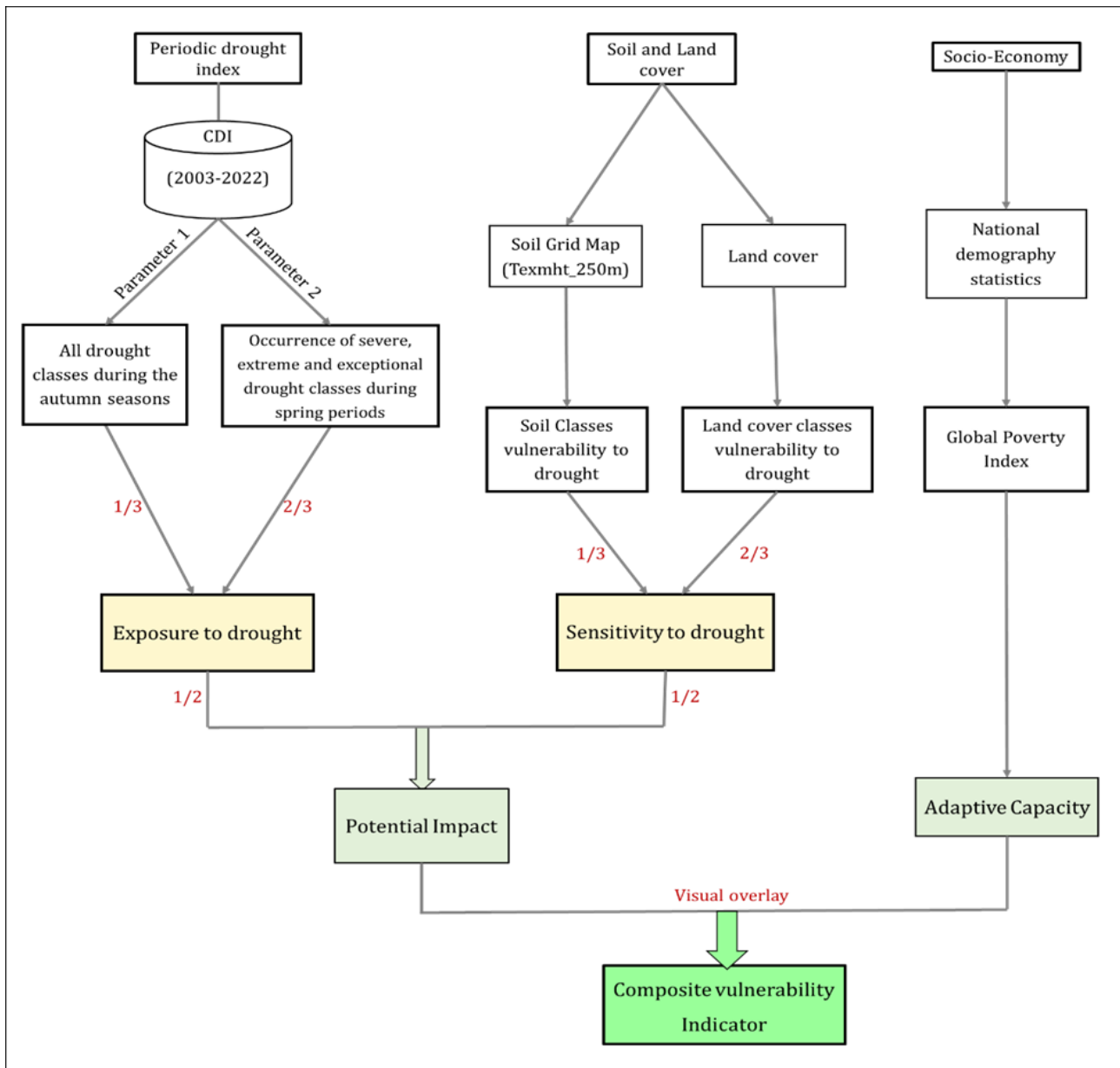


Figure 1. Methodology for mapping the structural vulnerability to drought.

3.2.1. Mapping the exposure to drought

This first component of the vulnerability is related to climate parameters through seasonal drought frequencies. In the periodic CDI composition, the climate parameters are represented by precipitation index (SPI₂), land surface temperature (LST) as well as evapotranspiration. The vegetation index (NDVI_a, weighted 20%) reflects the results of the impact of climate drivers on vegetation status. In Morocco, the agricultural season for cereals is divided in three main periods: the first one concerns soil preparation, seeding and germination from September to December, the second period covers crops development from January to April and the third one is the harvest period from May to

July depending on regions. During the cereal reproductive development periods (spring), there is a strong correlation between the climate parameters and the yields [37].

In the present study, two principal exposure factors were selected from the CDI database generated over the last twenty years [38]. The first one (P1 parameter) is the occurrence of all drought classes recorded in the autumn seasons, and the second parameter (P2) is the occurrence of severe, extreme and exceptional drought classes observed during the spring seasons (January to April of each year).

In other words, the approach consists in calculating for each pixel the number of dry months (moderate, severe, extreme or exceptional drought intensity class)

during the autumn periods to generate the P1 parameter. The autumn periods present the onset of the agricultural seasons in Morocco and the annual productions depend on the amount of precipitation during these parts of the growing seasons. The second step is to calculate, for the same pixel, the number of dry months (only severe, extreme and exceptional drought classes) during the spring periods. The objective of this seasonal separation is to improve the classification accuracy between areas affected by the same drought intensity class. For example, two geographically separate areas belonging to the same drought frequency class according to the first parameter (P1) can be reclassified differently taking into account the presence or not of drought in spring periods (P2 parameter). In Morocco, the level of precipitation (in quantities and geographic repartition) in spring seasons is a critical condition to have a good crop yields mainly for rainfed cereals, which represent the most dominant agricultural areas. For this reason, there is a complementarity between the two parameters P1 and P2, but with no correlation. The high amount of precipitation only in autumn (or in spring) period separately does not necessarily lead to a high productivity at the end of the agricultural season in Morocco.

The procedure consists of preparing separate CDI databases, one for indices calculated from October to December each year since 2003, and the other for drought indices from January to April over the last twenty years. An in-house python model was developed to calculate the number of dry months per pixel and for each parameter (P1 vs P2). Then, this number is converted into drought frequencies ranging from zero (no dry months were recorded) to 100 (the pixel has experienced drought for the whole season and during the last 20 years).

The drought exposure index was then obtained by combining these two parameters P1 and P2 with the corresponding weighting factors. Since the impacts of drought during spring periods are higher than those happening in the beginning of the agricultural seasons in Morocco [37], the P2 parameter received a greater weight and was supposed two times more important than P1. Accordingly, the weights affected to P1 and P2 parameters are respectively 1/3 and 2/3 (Equation 1).

$$\text{Exposure} = 1/3 * P1 + 2/3 * P2 \quad (1)$$

Both parameters P1 and P2 were normalized and aligned the same way: a low (or high) score represented a low (vs high) value in terms of vulnerability [12]. The resulting exposure index values were merged into four drought frequency classes going from the less vulnerable areas (class 1) with a drought frequency less than 30% to the areas with high occurrence of drought (more than 50% for class 4). The resulting map (Figure 2) shows the occurrence of droughts according to the CDI generated from 2003 to 2022.

The map of exposure to drought (Figure 2) illustrates areas that have experienced a higher frequency of

drought events over the past 20 years. The four frequency classes present in this map were evaluated by applying the normalization of categorical indicator values method [12]. The first category (class 1) corresponds to areas for which the frequency of drought is less than 30% (i.e., of the 140 months of CDI data studied, less than 42 months were dry). For classes 2 and 3, the observed drought frequencies are respectively between 30 and 40% (i.e., from 42 to 56 dry months for class 2) and between 40 and 50% (from 56 to 70 dry months out of 140 for class 3). Concerning areas with high level of exposure (class 4), the occurrence of drought exceeded 50%.

The map of exposure to drought shows that class 3 was the most dominant in terms of area (54.7% of the territory) and it concerned all agricultural zones and rangelands. This level of drought exposure (frequency between 40 and 50%) covered the provinces of the Oriental, the North, Saïss, Draa, Souss and the Southeast of the country. The second important class in terms of area was class 2, which occupied 29% of the national territory and corresponded to the non-irrigated agricultural areas and the rangelands of the south and the Oriental.

This map indicates also that the less exposed categories to drought (Class 1: irrigated perimeters and the mountains covered by forests) represented only 2.7% of the territory. However, the highly exposed areas to drought covered more than 13% of the national territory according to the CDI database analysis during the past twenty years and were located in the southern zones and in some provinces of the Oriental region.

3.2.2. Mapping the sensitivity to drought

Sensitivity to drought is approached through the principal characteristics of the system which interact with the exposure factors and that influence the extent of drought impacts. In this study, two main physical and natural factors were identified under sensitivity: soil types and land cover classes.

3.2.2.1. Soil and land cover classes vulnerability

Soil biophysical characteristics are an important factor to consider when studying drought vulnerability. Different types of soils retain different amounts of water and have different nutrient and mineral contents. Soil is an environment that generates and accumulates all the necessary nutrients for faunae and florae (nitrogen, phosphorus, calcium, potassium, iron, etc.), in addition to air and water. The absorption of these elements by vegetation through its root system is strongly dependent on water conditions. Moreover, the impact of a prolonged rainfall deficit varies according to the biophysicochemical characteristics of the soil. Some naturally nutrient-rich soils with higher water holding capacities and appropriate structures and textures are more resistant to drought than other soils with low organic matter content and low water holding capacity.

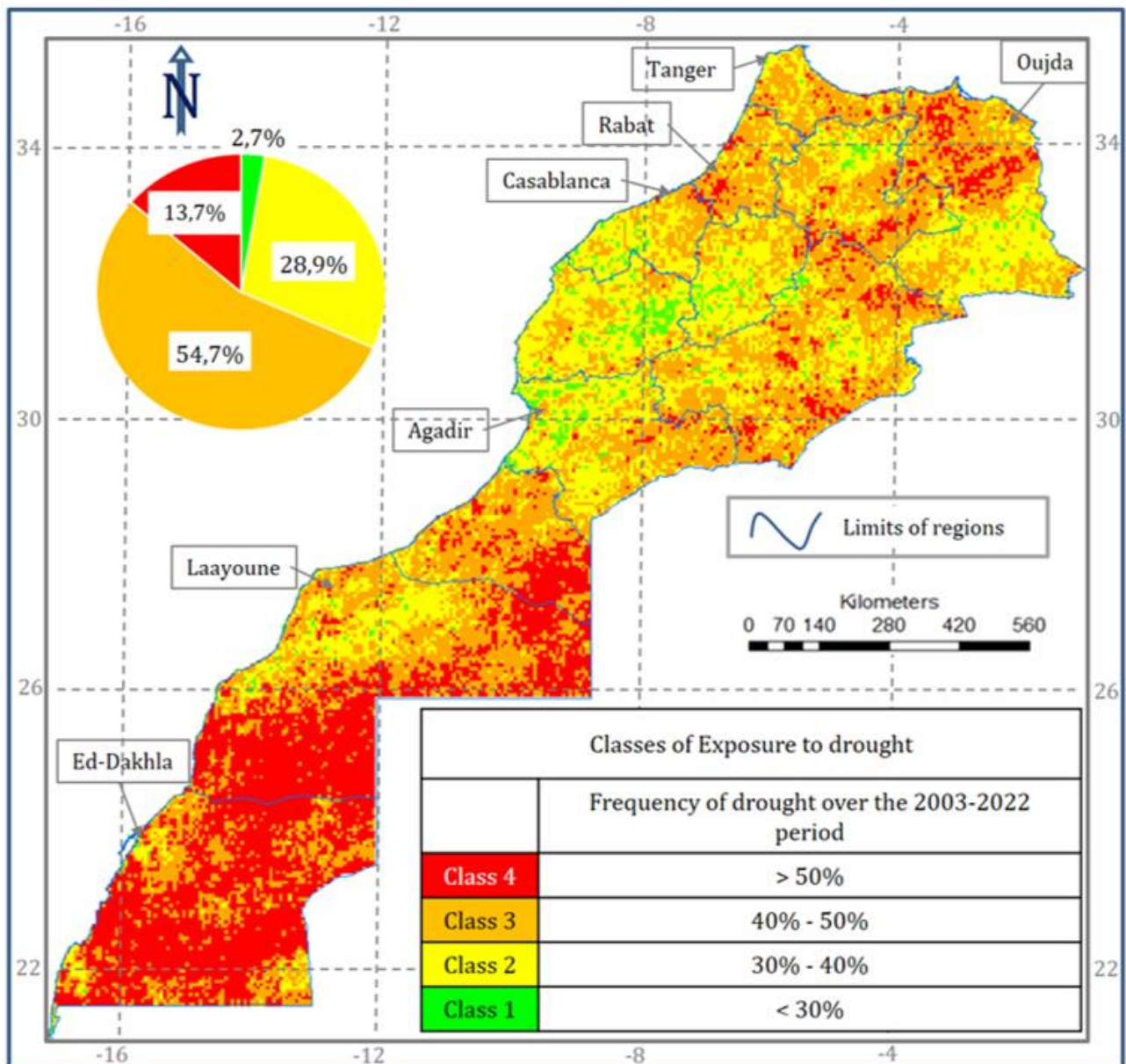


Figure 2. Map of the exposure to drought (2003-2022).

Mapping the soil types at national scale is very important to classify the different soil categories according to their degrees of vulnerability to drought. The map used in this study was a subset from the global map generated by the Soil Reference Information Center (ISRIC), which presents the texture classes of the surface layer (depth of 0.6m) at a spatial resolution of 250m [29]. For each of the main soil classes present in Morocco, the composition in clay, loam and sand was derived from the representation of textural classes according to the triangular diagram of textures of the American Department of Agriculture [39].

In the context of vulnerability to drought, there are strong links between soil characteristics and drought resilience. According to different studies [37,40], soils with dominant sandy composition (sands, loamy sands) present a high vulnerability to drought. These soils are characterized by a high porosity, have a low water retention capacity and are generally poor in organic matter and nutrients. These soil classes cover the south and some eastern zones in Morocco.

Heavier soils like loam and clay loams cover the majority of agricultural and forestry areas in Morocco. The vulnerability to drought of these soil categories is very low because the mixture of clay and loam guarantees a higher water retention capacity and allows aeration of the root zone, which increases crops resistance to rainfall deficit.

Soils having a sandy-clay and sandy-clay-loam texture with variable proportions are moderately vulnerable to drought. This soil class covers the central part of Morocco from the northeast (Oriental provinces) to the southwest (pre-Saharan region and the southern part of the Atlas Mountains).

On the other hand, concerning the land cover classes, the map generated at the national scale by classification includes nine land cover types, namely rainfed cultivated lands, irrigated areas, orchards, greenhouses, forests, rangelands, water bodies, artificial surfaces and bare soils. These land cover units were reclassified into homogeneous groups according to their degree of vulnerability to drought.

Figure 3 presents the synthetic map of the vulnerability to drought in relation to the soil factor (Figure 3a) and the map of land cover vulnerability (Figure 3b).

The map of soil vulnerability results from conversion of soil textures as presented in the initial map (SoilGrid) to their corresponding classes of vulnerability to drought. The resulting map (Figure 3a) shows an increasing degree of vulnerability from the north to the south and from the west to the eastern part of Morocco. Figures indicate that 38.7% of the national territory is composed of clay, clay-loam, loam and sandy clay soils, which present a high fertility and consequently a low vulnerability to drought. This soil vulnerability class is located in the northern and central parts of the country and corresponds to the agricultural and forest areas.

Soils presenting a moderate vulnerability to drought occupy 28.4% of the national territory and extend from

the northeast to the southwest. Composed of a mixture of sand, clay and loam, these soils are covered by rangelands and desert vegetation, which tolerate soils with high proportion of sand. Finally, the southern part of Morocco is completely dominated by sand and loamy sand soils characterized by high vulnerability to drought. These poor soils occupy 32.9% of the national territory and are located in the desert area.

Figure 3b shows the relationship between land cover classes and their vulnerability to drought. In terms of rain dependency, the non-irrigated agricultural areas are highly vulnerable to drought because they typically rely on seasonal rainfall to provide the necessary water for crop production and livestock rearing. This category includes particularly cereal crops, given the importance and the dominance of the areas occupied by this crop in Morocco.

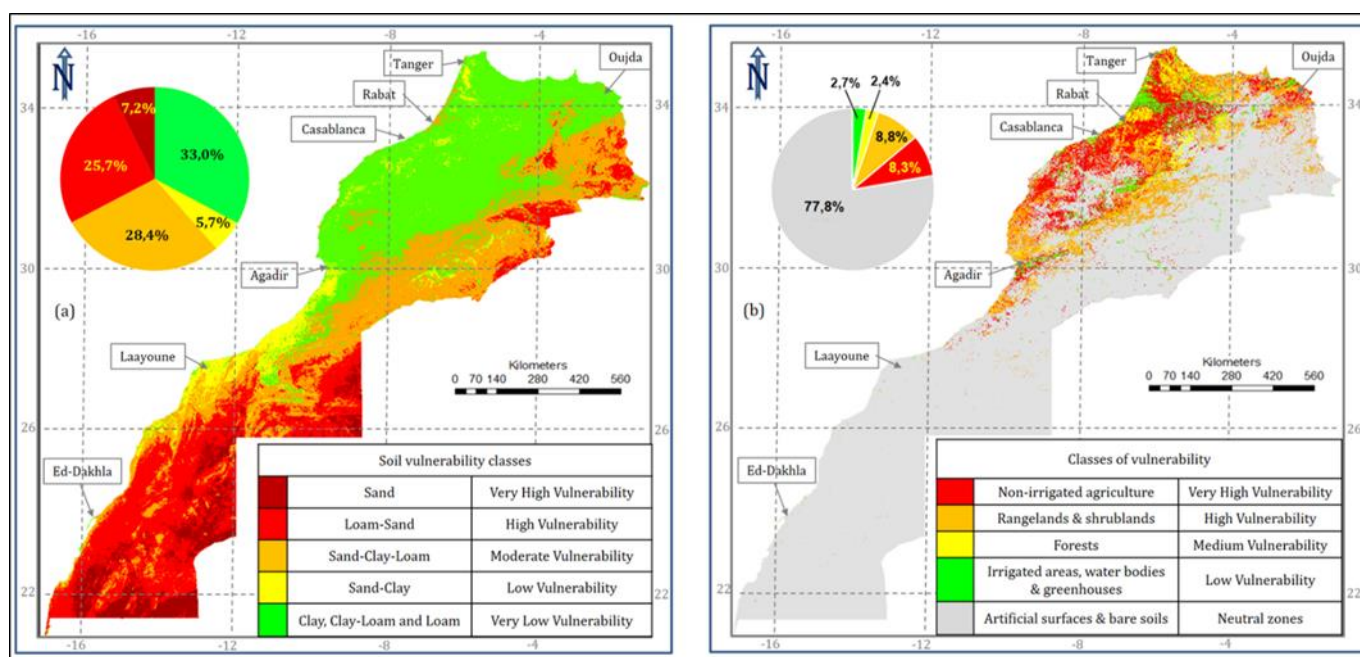


Figure 3. Map of the soil vulnerability (a) and the land cover vulnerability to drought (b).

Like rainfed cultivated areas, rangelands and natural vegetation fields are also sensitive to rainfall deficits and are highly vulnerable to drought. They have a lower degree of vulnerability than rainfed lands, since rangelands are reserved to grazing activities, whereas rainfed agricultural areas allow the generation of nutritional and commercial value-added products that have a direct impact on the population.

Forests are considered moderately vulnerable to drought in short-term because their sensitivity to seasonal precipitation deficit is negatively impacted after a long period due to the resilience of this ecosystem.

On the other hand, land cover classes presenting low vulnerability to drought are namely irrigated zones (including orchards and greenhouses using water from surface and/or groundwater resources) and water bodies (dams, lakes, reservoirs, rivers).

Finally, since the objective of this study is the mapping of agricultural vulnerability to drought, artificial surfaces (urban and rural buildings) and bare

soils are not directly impacted by rainfall deficit due to the limited vegetative resources. For this reason, these land cover types were classified as neutral zones.

3.2.2.2. Sensitivity index

As for the drought exposure index, the sensitivity index results from the weighted combination between soil and land cover vulnerability classes, which are the main factors identified under sensitivity. While soil type tends to be a static parameter and is inherent in the system, land cover might be altered by human activities. Some examples of changes are decreasing of natural vegetation ecosystems (forests, rangelands and some agricultural areas) due to the impact of artificial surfaces development (urban and industrial constructions, mining zones, transportation facilities, etc.), and sometimes due to natural hazards (forest fires, floods, etc.). For this reason, the land cover factor was given a higher weight than soil class's parameter.

Therefore, the weights assigned to soil types and land cover parameters are respectively 1/3 and 2/3. Equation 2 shows how these two factors were aggregated.

$$\text{Sensitivity} = \frac{1}{3} * \text{Soil vulnerability} + \frac{2}{3} * \text{Land cover vulnerability} \quad (2)$$

According to the Vulnerability Sourcebook [12], both parameters soils and land cover were normalized and aligned the same way (a high score represented a high value in terms of vulnerability). The resulting sensitivity index values were merged into four sensitivity classes going from the less sensitive areas (irrigated agriculture on clay-loam soils) to the areas with high sensitivity to drought (rainfed cereals on sandy soils). Figure 4 presents the resulting map of sensitivity to drought.

The map (Figure 4) shows that areas with low sensitivity

to drought are located mainly in the Tangier-Tetouan-Al- Hoceima and Rabat-Sale-Kenitra regions and partially of the Fez-Meknes and Beni-Mellal-Khenifra regions. This category occupied 5% of the national territory and concerned the irrigated zones on favorable soil type and the mountains (Rif and Atlas). Additionally, areas moderately sensitive to drought occupied about 16% of the Moroccan territory and corresponded to the majority of regions covered mainly by rainfed seasonal crops on clay-loam soils. These two first classes merged represent 21% of the national territory and are located in the most fertile agricultural zones.

The map in Figure 4 shows also that 19% of the territory was highly sensitive to drought. This concerns rainfed agricultural areas and rangelands located on sandy clay-loam soils in the eastern, central and southern parts of Morocco.

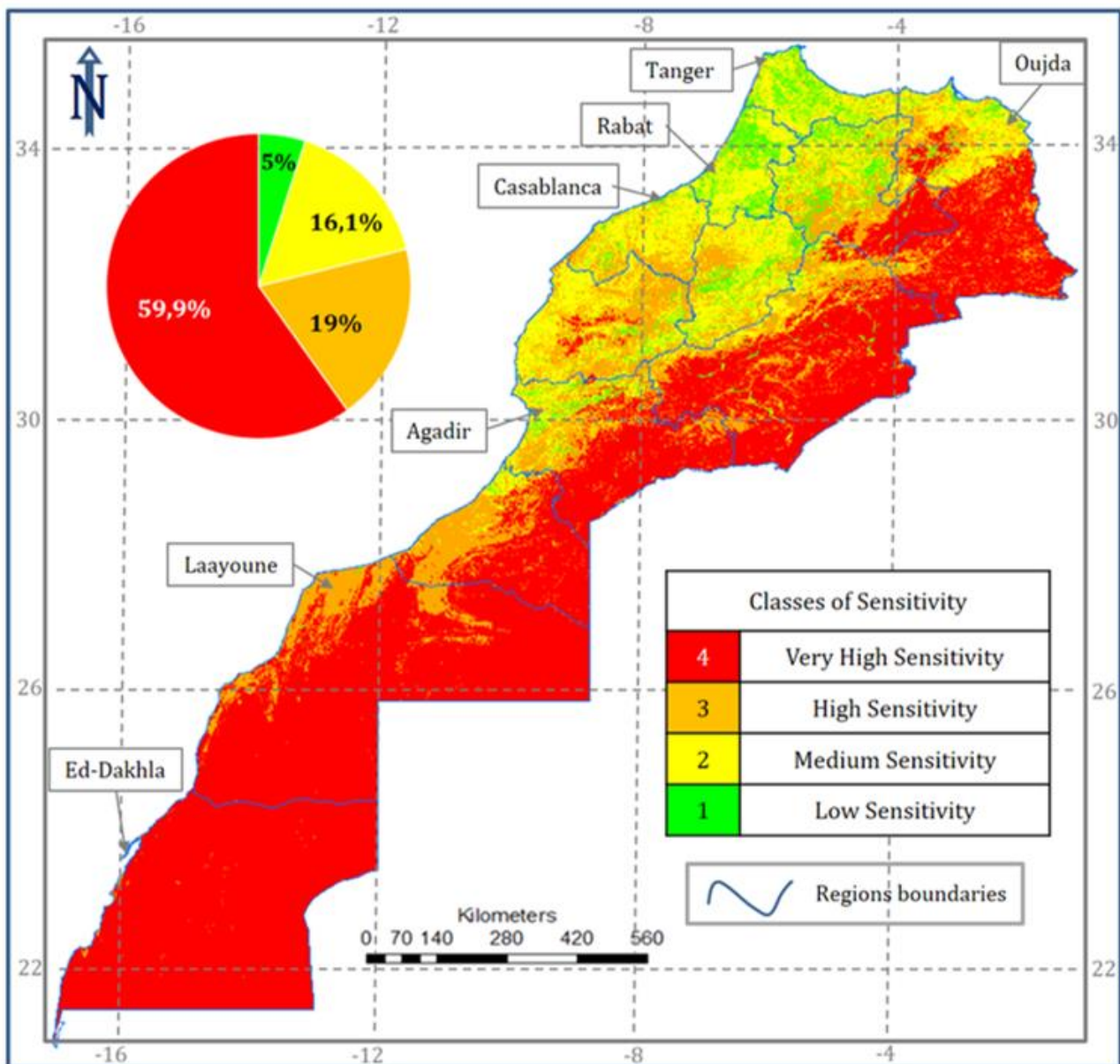


Figure 4. Map of the sensitivity to drought.

Finally, areas presenting a very high sensitivity to drought, stretching from the northeast to the south of

Morocco, covered about 60% of the national territory. This category included all the desert regions and some

provinces of the Souss-Massa, Draa-Tafilalet and Oriental regions. The regions of Fez-Meknes (eastern part) and Marrakech-Safi (Chichaoua province) were also partially concerned by this class of high sensitivity to drought. The geographical distribution of this class reflects the combination of the biophysical nature of these bare sandy-loam soils and the scarcity of rainfall.

3.2.3. Potential impact

In accordance with the Vulnerability Sourcebook [12], exposure (Figure 2) and sensitivity (Figure 4) in combination determine the potential impact of climate change. For example, in the context of drought vulnerability, long period rainfall deficit (exposure) in

combination with non-irrigated crops and sandy soils (sensitivity) will result in loss of yields and income (potential impact). Concerning the weighting approach, we considered each of the two vulnerability components (exposure and sensitivity) as important as the other. For this reason, the two factors were equally weighted (Equation 3).

$$\text{Potential Impact} = 1/2 * \text{Exposure} + 1/2 * \text{Sensitivity} \quad (3)$$

The resulting map of the potential impact of drought in Morocco (Figure 5) illustrates the distribution of four main categories going from areas where the impact of climate change was low to the areas where the potential impact was high.

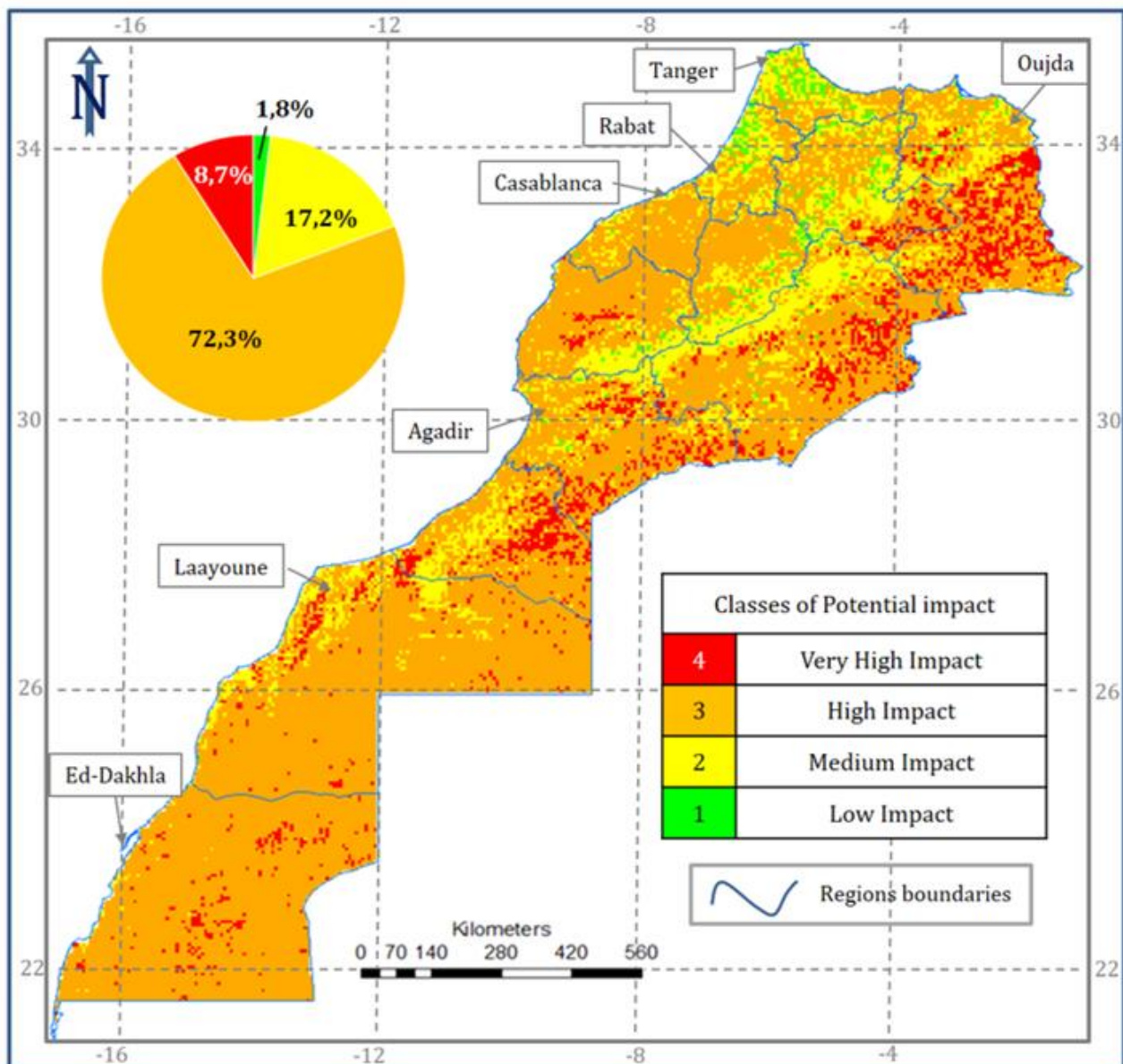


Figure 5. Map of the potential impact.

The map of potential impact shows that less than 2% of the national territory presented low impact of drought on the natural resources. This category is located mainly in the north of the country and corresponds to forest and permanent irrigated areas. The second category (medium potential impact of drought) is located also in

the forest (Rif and Atlas Mountains) and in some irrigated areas. These two classes of potential impact to drought covered 19% of the national territory, and they presented a high resilience to short-term drought due to their biophysical characteristics (rainfall, temperatures, vegetation cover, soil types, topography, etc.).

Areas with high potential impact of drought were dominant (72.3% of the territory) and corresponded to both agricultural zones, rangelands as well as the desert areas in the south of Morocco. For these areas, the impact of drought episodes frequencies combined with inadequate soil texture resulted in a loss of agricultural yields and consequently loss of income.

The last category concerns the rangelands in the Oriental region, Draa and some southern and southeastern provinces where the potential impact of drought was very high. For these zones, vegetation development is strongly dependent on precipitation.

3.2.4 Adaptive capacity

In Morocco, the department in charge of population planning (HCP) has traditionally measured the poverty rate using the monetary approach, which assesses a household's income and expenditure. This monetary approach, initially developed by the World Bank, has reached its limits because poverty is more than just a lack of money. Recent efforts have shifted towards adopting a multidimensional approach that takes into account other indicators such as education, health, housing, and access to basic services [41].

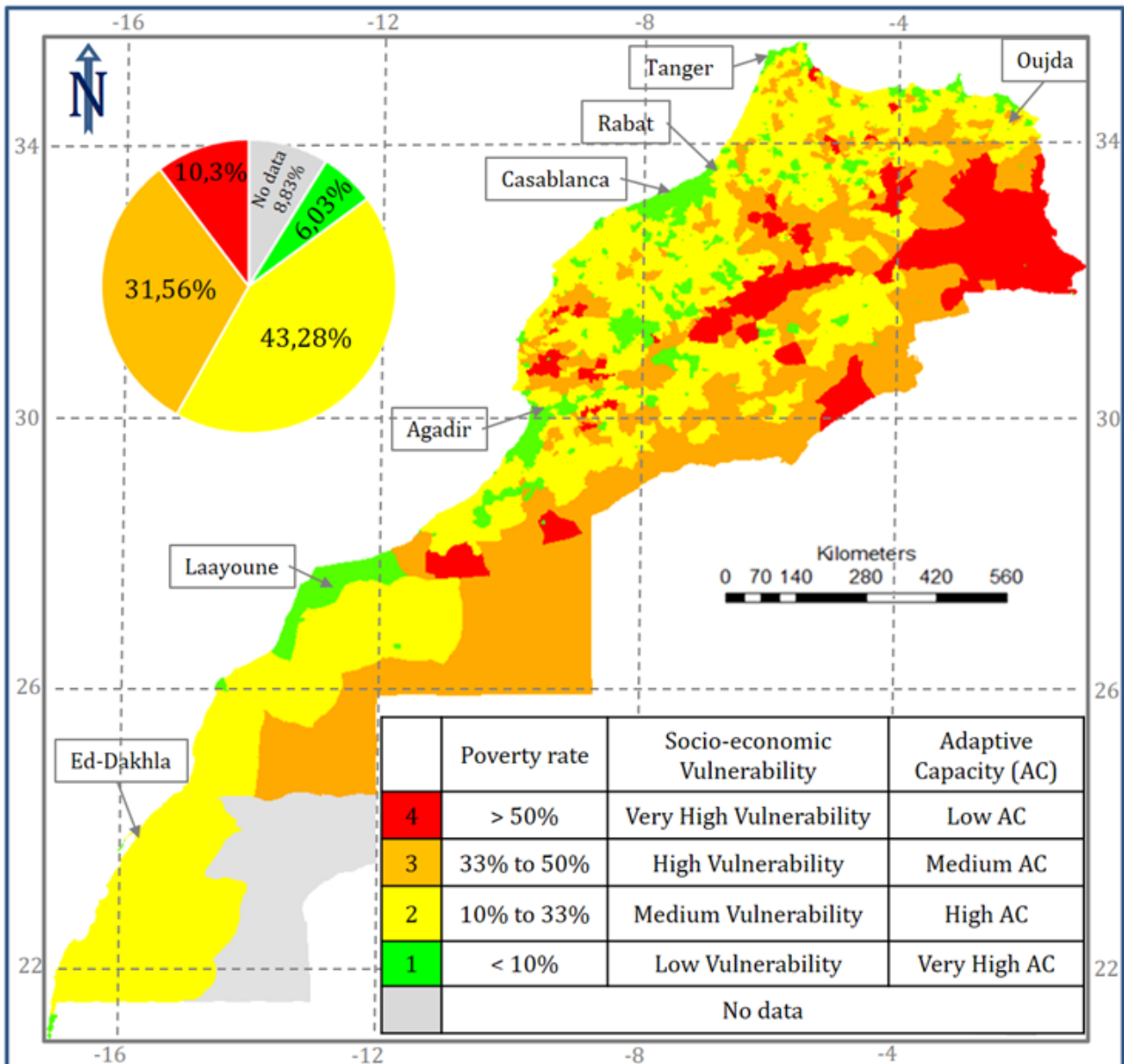


Figure 6. Map of the adaptive capacity to drought.

The methodology adopted by the HCP to calculate and monitor the poverty rate is based on a global approach including both monetary and a multidimensional approach. Since poverty affects people's daily lives and well-being in many ways, this global approach consists of identifying deprivations based on unsatisfied needs in education, health and living conditions (food security,

access to clean water and electricity, housing conditions) from the analysis of the 2014 general population census results. The adopted approach recognizes that poverty affects individuals differently depending on their gender, age group or living in urban vs rural area. A score aggregating the different deprivations is then established by assigning weights to each of the three main categories

(1/3 for education, 1/3 for health and 1/3 for living conditions). This scoring system allows for better understanding of the multifaceted nature of poverty and its underlying causes.

In the present study, we used a global poverty index that was defined by the HCP based on a typology of the general population census results corresponding to the 2004-2014 period. In Morocco, these results are available at the regional, provincial and communal levels in tabular format. The data corresponding to the poverty index at communal scale was retrieved, spatialized and reclassified into levels of socio-economic vulnerability. According to the HCP, a population group is considered multi-dimensionally poor if his deprivation score is above the poverty line, set by convention at 33% [35].

Figure 6 illustrates the distribution of the different socio-economic vulnerability classes at the communal level. To these gridded poverty classes were defined targeted groups of population with different adaptive capacity to drought conditions.

Figure 6 shows that the municipalities and the communes located next to the big cities presented a very low poverty rate and consequently they had a very high adaptive capacity. These 407 communes covered only 6% of the national territory.

The HCP figures indicated also that more than 43% of the national territory (739 communes) was vulnerable to poverty but under the conventional poverty line. This concerned all the areas where agriculture, industry, tourism and artisanal activities contributed in different proportions to the population income. These rural communes with medium vulnerability presented a high capacity of adaptation to reduce drought impacts.

Concerning the communities above the national poverty line, 260 rural communes were considered highly vulnerable to drought and presented a medium adaptive capacity to address climate change impacts. This class of socio-economic vulnerability corresponded to a poverty rate between 33 and 50% and covered about 32% of the national territory.

Finally, the communes with a very high level of vulnerability covered about 10% of the national territory (93 communes) and were located in the provinces of Oriental, Atlas Mountains and other zones in the south. These very high vulnerable communes had a low adaptive capacity to alleviate drought impacts. For example, the rural commune "Oulad Mhammed" in Taourirt province had a poverty rate in 2014 of 90.1% and the rural commune "Tabaroucht" in Azilal province had a poverty rate of 85.6%. This explains the absence of the majority of the living conditions for the population in these two communes. In case of prolonged periods of drought in these vulnerable communities, the impacts would be heavily devastating on natural resources (crop yields and livestock losses, limited access to drinking water, land degradation and consequently desertification).

The contribution of the global poverty index in the study of structural vulnerability to drought is very important in two different ways. On one hand, it allows identifying communities with high adaptive capacity to climate hazards in order to mitigate the potential

impacts, and on the other hand, this parameter highlights areas where drought can have adverse impacts on the poorest populations. In other words, groups in low and medium vulnerability classes (and who have permanent and non-agricultural incomes) are generally more resilient to climate changes. This adaptive capacity reduces the potential impact of climate effects and therefore mitigates vulnerability to drought. On the other hand, poor and highly vulnerable populations are the first to suffer the impacts of drought and constitute a pressure factor that threatens natural resources.

The combination between the potential impact and adaptive capacity maps to generate the synthetic structural drought vulnerability map is presented in the following.

4. Results and discussion

This section of the study consists in generating a composite drought vulnerability index by aggregating the potential impact and adaptive capacity. The gridded representation of this index involves analyzing and mapping the susceptibility of different communities to the impacts of a drought event. This process takes into account all the factors described above namely; climate conditions, soil characteristics, land cover classes and global poverty index.

The methodology adopted to generate this structural vulnerability index was based on an aggregation of the composite indicator of potential impact with adaptive capacity using a visual overlay analysis.

All the indicators used in this study to calculate the potential impact were aligned in the same way. Concerning the adaptive capacity aggregation with the potential impact, it is important to take into account the offsetting between these two components. Indeed, adaptive capacity has a positive influence on vulnerability to drought. It reflects the ability of population to adapt to and recover from drought when it occurs.

According to the vulnerability sourcebook [12], high values for adaptive capacity (rich communities) can offset high drought impact values, and this leads to low vulnerability values in spite of high potential impact. In the same way, areas with high potential impact and low adaptive capacity can be considered as vulnerable areas to drought (hotspots).

Unlike the methodology adopted for the other components of the vulnerability (Exposure, Sensitivity and potential impact) which is based on the weighted arithmetic aggregation, the visual overlay analysis consists in applying GIS functionalities (Map Algebra, Raster calculator) to generate a map where areas corresponding to different combinations between the potential impact and the adaptive capacity components can be highlighted graphically.

The Moroccan adaptive capacity layer includes more than 1500 polygons representing the rural communes and municipalities with values corresponding to the four socio-economic vulnerability classes. Both adaptive capacity and potential impact layers are first standardized per unit area (pixel size) and then combined to generate the resulting vulnerability map.

For each of the potential impact (P.I.) levels, Table 2 shows the proportion of the national territory corresponding to each of the adaptive capacity (A.C.) classes.

By identifying areas more susceptible to drought, planners can prepare mitigation strategies, targeted

responses and resources distribution plans that address the specific needs of the risk. The mapping process could also indicate where additional data collection efforts may be necessary in order to provide assistance before, during or after an actual occurrence.

Table 2. Proportions of the territory for each potential impact and adaptive capacity combination.

Potential Impact (P.I.)	Adaptive Capacity (A.C.)				
	Very high A.C. (%)	High A.C. (%)	Medium A.C. (%)	Low A.C. (%)	A.C. (no data) (%)
Low P.I.	0.15	1.01	0.43	0.24	0
Medium P.I.	1.99	7.41	4.80	2.96	0
High P.I.	3.63	32.59	22.84	5.23	8.01
Very high P.I.	0.27	2.46	3.49	2.10	0.38

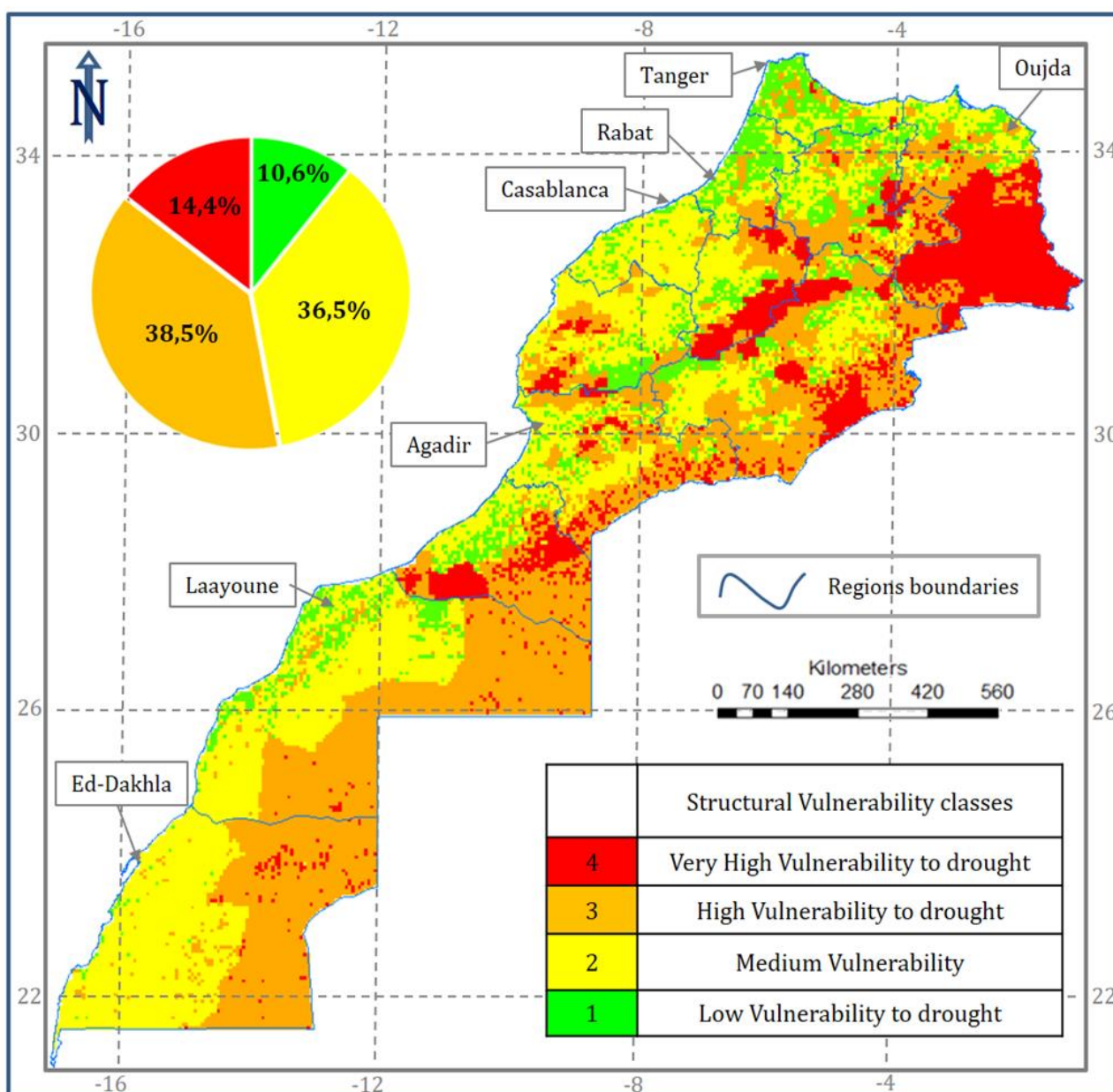


Figure 7. Map of the structural vulnerability to drought in Morocco. Four levels of vulnerability: (1) green: low score, (2) yellow: medium, (3) orange: high and (4) red: very high level of vulnerability to drought.

The different combinations shown in Table 2 were grouped into four main levels of vulnerability to drought. Low vulnerability values correspond to the combination of low to medium potential impact and high to very high adaptive capacity and vice versa, high vulnerability

values result from the union of high to very high impact and low adaptive capacity. Table 2 shows also the intermediate vulnerability levels resulting from the mixture between different intermediate potential impact and adaptive capacity classes. The graphic

representation of these merged classes of the structural vulnerability to drought in Morocco is illustrated in Figure 7.

The geographic distribution of the four vulnerability classes at national scale (Figure 7) shows a slight dominance of areas with high to very high vulnerability to drought. Indeed, these two classes (3 and 4) cover about 53% of the national territory (331.425 km²) and extend from the northeast to the south. With this proportion, it means that a substantial portion of agricultural land is at a risk.

The Oriental provinces and some areas in the Atlas and in the south of the country are very highly vulnerable to drought, representing around 14% of the national territory. In these areas, land cover is dominated by bare soils and rangelands on unfavorable soils (loam-sands and sand-clay-loams), which are reliant upon rainfall. Moreover, these zones are characterized by a very low adaptive capacity, which increase considerably the vulnerability to drought and to climate change in general.

Areas with high vulnerability to drought (class 3) represent about 39% of the national territory and concern almost the totality of the provinces located in the east and southeastern boundary. These regions are characterized by low amount of precipitation and high temperatures coupled with pressures of population growth and poverty. The spatial variation of this level of vulnerability affects desert areas as well as rain-fed agricultural zones.

On the other hand, areas with low to medium vulnerability to drought (classes 1 and 2) represent about 47% of the Moroccan territory (294.700 km²). This concerns the main irrigated areas (Gharb, Loukkos and northwest, Tadla, Doukkala, Al Haouz, Souss-Massa, Ouarzazate, Tafilalet and Moulouya) as well as forests (Rif and Atlas), oasis zones (Draa, Tafilalet) and some coastal zones.

Areas with low vulnerability to drought (class 1) represent only 10.6% of the national territory (66,175 km²) and correspond essentially to irrigated zones where irrigation had become increasingly popular as a means of combating dry spells and helping farmers

control water distribution precisely. Similarly, forest areas are more resistant to drought and can be impacted only after a long period of rainfall deficit.

However, although the favorable components of the vulnerability chain for these zones (high adaptive capacity offsetting the impact of drought), agriculture and livestock remain vulnerable to droughts. In addition, some forests of the Rif and the Atlas Mountains are in a very worrying state of degradation (forest fires, health attacks, overexploitation of wood, etc.), which increases the level of vulnerability of these ecosystems to drought and climate hazards in general.

Locally, the Oriental region is the most affected by the highest drought vulnerability level. Indeed, about 60% of the region is categorized very highly vulnerable to drought and a little more than 20% of the region is highly vulnerable. This part of the region is dominated by rangelands, rainfed agriculture and bare soils. Only 20% of the region is located in low to medium vulnerable areas to drought and this concern the coastal areas, the Moulouya irrigation perimeter and nearby the principal cities (Oujda, Saidia and Nador).

Similarly, the Draa-Tafilalet region is also dominated by areas of high and very high vulnerability to drought, occupying respectively 45.8% and 19% of the regional territory. The western part of the region presents a low to medium vulnerability to drought, and it is mainly covered by oases of Draa-Tafilalet and by the Ouarzazate and Tafilalet irrigated perimeters.

Concerning Beni Mellal-Khenifra, about 59% of the region presents a high to very high vulnerability to drought nearby Khouribga, Khenifra and Azilal provinces. The low (10.2%) to medium (31.2%) vulnerability classes cover the Tadla irrigated perimeter (Beni Mellal and Fquih Ben Saleh provinces).

The eastern part of Fez-Meknes region is dominated by areas categorized high to very high vulnerable to drought, presenting about 48% of its territory (Boulemane province) in the proximity of the Oriental rangelands. The provinces of Fez, Meknes, Ifrane, Sefrou and partly the province of Taounate present a low to medium vulnerability to drought.

Table 3. Proportions of drought vulnerability areas per region.

Regions of Morocco	Levels of vulnerability to drought			
	Low (%)	Medium (%)	High (%)	Very high (%)
Tanger-Tetouan-AlHoceima	47.88	35.02	15.47	1.63
Oriental	7.45	13.16	20.29	59.10
Fes-Meknes	22.48	29.33	37.50	10.68
Rabat-Sale-Kenitra	40.52	39.30	18.65	1.53
Benimellal-Khenifra	10.24	31.20	25.28	33.27
Casablanca-Settat	14.17	81.55	4.28	0
Marrakech-Safi	13.92	54.66	23.11	8.30
Draa-Tafilalet	10.11	25.02	45.83	19.03
Souss-Massa	8.60	34.99	44.49	11.91
Guelmim-Oued-Noun	11.11	21.42	41.11	26.36
LaayouneBoujdour-Sakia-Al-Hamra	8.49	40.20	49.89	1.42
Eddakhla-Oued-Eddahab	0.62	49.94	47.30	2.13

The three regions in the northwest (Tangier-Tetouan-Al-Hoceima, Rabat-Sale-Kenitra and Casablanca -Settat) are characterized by favorable weather conditions,

advantageous soil textures, adequate land covers and a high adaptive capacity. Therefore, these regions present a high proportion of areas with low to medium

vulnerability to drought. The twelve Moroccan regions are listed in Table 3, with the values of relative proportions of each vulnerability to drought level.

The high sensitivity to drought poses significant challenges for the affected regions and the country as a whole. The prolonged areas of drought indicate a widespread and persistent problem that demands immediate attention. One of the consequences of such extensive drought-prone areas is the impact on agriculture, as crop yields are likely to be severely affected. Moreover, water scarcity has become a pressing issue in these drought-prone areas. As rainfall tends to be increasingly insufficient, water sources such as rivers, lakes, and reservoirs dry up or become critically low. This affects not only agricultural irrigation but also it has severe implications for drinking water supply and other industrial needs.

5. Conclusion

Droughts can have severe impacts on natural resources, communities and ecosystems, especially in regions already vulnerable due to poverty and/or limited resources. Vulnerability to drought can vary greatly depending on the adaptive capacity of a community or ecosystem. In areas where adaptive capacity is low, droughts may lead to food shortages, increased poverty rates or even forced migration.

In Morocco, drought has a significant impact on the agricultural productivity because approximately 85% of agricultural areas rely on rainfall, making it highly susceptible to the effects of climate-related risks. Due to its frequent occurrence and long-lasting impact, drought is regarded as a structural component of Morocco's climate.

By evaluating the available data, it is evident that Morocco is globally vulnerable to drought due to various factors such as rainfall deficit, population growth, and overuse of water resources. The country's economy is heavily dependent on agriculture, which in turn depends on rainfall, making it highly susceptible to prolonged dry spells specifically during critical agricultural periods.

This study allowed generating a comprehensive map that highlights which areas of the country are most susceptible to drought and other weather-related disasters. The map of vulnerability to drought is the result from the combination of several biophysical variables including meteorological factors (precipitation, SPI, temperatures and evapotranspiration), remote sensing indices (vegetation index, land surface temperature and multi-temporal high-resolution satellite data to generate land cover maps), soil factor and the population status in terms of the poverty distribution all over the country.

The exposure index, which is one of the main components of the structural vulnerability to drought, allowed us to draw first conclusions about the most vulnerable areas. This index has the advantage that it is applicable for prospective assessments of drought occurrences based mainly on remote sensing data.

By highlighting vulnerable regions, the maps are playing an important role in helping planners and decision-makers take proactive measures to mitigate the

effects of future droughts, develop effective drought response plans and allocate resources where they are most needed. Therefore, the map of structural vulnerability to drought in Morocco constitutes a decision support tool for resource management in case of drought.

Concerning the methodological approach, it is important to highlight the role of spatial observation, which enabled producing indicators that are not only simple to compute but also relevant, accurate and easily accessible. The generated maps provide a comprehensive understanding of drought conditions by considering multiple meteorological variables combined to other biophysical parameters. This composite approach allows capturing the complex interactions between these factors and their impact on agricultural productivity. Moreover, these global indicators involved in the study of vulnerability can be adapted and applied to other similar contexts, making this methodology highly transferable and valuable.

Other indicators can be added to enhance the study of the structural vulnerability to drought. These may include measurements that demonstrate changes in ground and surface water resources, the distribution of livestock, and the identification of drought-resistant crops, etc. By integrating all of these biophysical parameters, a more comprehensive and detailed mapping of structural vulnerability to drought can be achieved. This could serve as a valuable subject for future research.

Acknowledgement

The present study was carried out by the use of various data that made available periodically. The MODIS/LST products were retrieved from the online Data Pool, courtesy of the NASA Land Processes Distributed Active Archive Center (LP DAAC), USGS/Earth Resources Observation and Science Center (EROS), https://lpdaac.usgs.gov/data_access/data_pool. Precipitation estimates (CHIRPS products), anomalies of vegetation indices (NDVIa) and evapotranspiration generated from SSEBop model were monthly downloaded from the USGS FEWS NET Data Portal. Other valuable products (Soil maps, Sentinel_2 images, population poverty in Morocco) were retrieved from different platforms. We would like to extend our sincere gratitude to all the data providers for their cooperation and willingness to process and make all the data open access. Without the availability of this valuable data, this study would not have been feasible with accuracy and reliability of our results.

Author contributions

Noureddine Bijaber: Satellite data collection, Preparation and processing, Methodology and Writing-Original draft preparation. **Atmane Rochdi:** Results validation and Writing-reviewing. **Mohammed Yessef:** Results validation and Writing-reviewing. **Houda El Yacoubi:** Results validation and Writing-reviewing.

Conflicts of interest

The authors declare no conflicts of interest.

References

1. Khorrami, B., & Gündüz, O. (2022). Detection and analysis of drought over Turkey with remote sensing and model-based drought indices. *Geocarto International*, 37(26), 12171-12193. <https://doi.org/10.1080/10106049.2022.2066197>
2. Observatoire du Sahara et du Sahel. (2013). Vers un système d'alerte précoce à la sécheresse au Maghreb. OSS. Collection Synthèse, 4. OSS: Tunis.
3. World Bank. (2022). Country Climate and Development Report: Morocco. Washington, DC: World Bank
4. Fritzsche, K., Schneiderbauer, S., Bubeck, P., Kienberger, S., Buth, M., Zebisch, M., & Kahlenborn, W. (2014). The Vulnerability Sourcebook: Concept and guidelines for standardised vulnerability assessments.
5. Hoque, M., Pradhan, B., Ahmed, N., & Alamri, A. (2021). Drought vulnerability assessment using geospatial techniques in southern Queensland, Australia. *Sensors*, 21(20), 6896. <https://doi.org/10.3390/s21206896>
6. West, H., Quinn, N., & Horswell, M. (2019). Remote sensing for drought monitoring & impact assessment: Progress, past challenges and future opportunities. *Remote Sensing of Environment*, 232, 111291. <https://doi.org/10.1016/j.rse.2019.111291>
7. Wilhite, D. A. (2000). Drought as a natural hazard: Concepts and Definitions. *Drought: A Global Assessment*.
8. Svoboda, M., & Fuchs, B. (2016). Handbook of Drought Indicators and Indices. Integrated Drought Management Programme (IDMP)
9. Iglesias, A., Cancelliere, S., Gabiña, D., López-Francos, A., Moneo, A., & Rossi, G. (2007). Medroplan Drought Management Guidelines and Examples of Application; European Commission. MEDA-Water Programme: Zaragoza, Spain.
10. RICCAR (2017). Training manual on the integrated vulnerability assessment methodology.
11. Szaboova, L. (2023). Climate change, migration and rural adaptation in the Near East and North Africa region. Food and Agriculture Organization of the United Nations.
12. Fritzsche, K., Schneiderbauer, S., Bubeck, P., Kienberger, S., Buth, M., Zebisch, M. & Kahlenborn, W. (2017). The vulnerability sourcebook. Concept and guidelines for standardized vulnerability assessments. Risk Supplement: How to apply the approach with the IPCC AR5 risk concept.
13. Bijaber, N., El Hadani, D., Saidi, M., Svoboda, M. D., Wardlow, B. D., Hain, C. R., ... & Rochdi, A. (2018). Developing a remotely sensed drought monitoring indicator for Morocco. *Geosciences*, 8(2), 55. <https://doi.org/10.3390/geosciences8020055>
14. Fragaszy, S. R., Jedd, T., Wall, N., Knutson, C., Fraj, M. B., Bergaoui, K., ... & McDonnell, R. (2020). Drought monitoring in the Middle East and North Africa (MENA) region: participatory engagement to inform early warning systems. *Bulletin of the American Meteorological Society*, 101(7), E1148-E1173. <https://doi.org/10.1175/BAMS-D-18-0084.1>
15. Svoboda, M. D., Fuchs, B. A., Poulsen, C. C., & Nothwehr, J. R. (2015). The drought risk atlas: enhancing decision support for drought risk management in the United States. *Journal of Hydrology*, 526, 274-286. <https://doi.org/10.1016/j.jhydrol.2015.01.006>
16. Funk, C. C., Peterson, P. J., Landsfeld, M. F., Pedreros, D. H., Verdin, J. P., Rowland, J. D., ... & Verdin, A. P. (2014). A quasi-global precipitation time series for drought monitoring. *US Geological Survey*, 832. <https://dx.doi.org/10.3133/ds832>
17. McKee, T. B., Doesken, N. J., & Kleist, J. (1995). Drought monitoring with multiple time scales. *Proceedings of the Conference on Applied Climatology*.
18. McKee, T. B., Doesken, N. J., & Kleist, J. (1993). The relationship of drought frequency and duration to time scales. *Proceedings of the 8th Conference on Applied Climatology*.
19. Senay, G. B., Velpuri, N. M., Bohms, S., Budde, M., Young, C., Rowland, J., & Verdin, J. P. (2015). Drought monitoring and assessment: remote sensing and modeling approaches for the famine early warning systems network. *Hydro-meteorological Hazards, Risks and Disasters*, 233-262. <https://doi.org/10.1016/B978-0-12-394846-5.00009-6>
20. Hain, C. R., Crow, W. T., Mecikalski, J. R., Anderson, M. C., & Holmes, T. (2011). An intercomparison of available soil moisture estimates from thermal infrared and passive microwave remote sensing and land surface modeling. *Journal of Geophysical Research: Atmospheres*, 116, D15107. <https://doi.org/10.1029/2011JD015633>
21. Wan, Z. (2006). MODIS land surface temperature products users' guide. Institute for Computational Earth System Science, University of California: Santa Barbara, CA, USA, 805, 26.
22. Wan, Z., Zhang, Y., Zhang, Q., & Li, Z. L. (2002). Validation of the land-surface temperature products retrieved from Terra Moderate Resolution Imaging Spectroradiometer data. *Remote Sensing of Environment*, 83(1-2), 163-180. [https://doi.org/10.1016/S0034-4257\(02\)00093-7](https://doi.org/10.1016/S0034-4257(02)00093-7)
23. Senay, G. B., Bohms, S., Singh, R. K., Gowda, P. H., Velpuri, N. M., Alemu, H., & Verdin, J. P. (2013). Operational evapotranspiration mapping using remote sensing and weather datasets: A new parameterization for the SSEB approach. *JAWRA Journal of the American Water Resources Association*, 49(3), 577-591. <https://doi.org/10.1111/jawr.12057>
24. Bijaber N., El Hadani, D., Saidi, M., Svoboda, M. D., Poulsen, C. C., Hain, C. R., Wardlow, B. D., & Yesséf, M. (2017). Suivi mensuel de la sécheresse au Maroc par techniques basées sur l'indice composite. *GéoObservateur n°23*, Rabat, Morocco, 25-37

25. Jia, H., Chen, F., Zhang, J., & Du, E. (2020). Vulnerability analysis to drought based on remote sensing indexes. *International Journal of Environmental Research and Public Health*, 17(20), 7660. <https://doi.org/10.3390/ijerph17207660>
26. Tran, H. T., Campbell, J. B., Tran, T. D., & Tran, H. T. (2017). Monitoring drought vulnerability using multispectral indices observed from sequential remote sensing (Case Study: Tuy Phong, Binh Thuan, Vietnam). *GIScience & Remote Sensing*, 54(2), 167-184. <https://doi.org/10.1080/15481603.2017.1287838>
27. Hanadé Houmma, I., Gadal, S., El Mansouri, L., Garba, M., Gbetkom, P. G., Mamane Barkawi, M. B., & Hadria, R. (2023). A new multivariate agricultural drought composite index based on random forest algorithm and remote sensing data developed for Sahelian agrosystems. *Geomatics, Natural Hazards and Risk*, 14(1), 2223384. <https://doi.org/10.1080/19475705.2023.2223384>
28. Badraoui, M. (2006). *Connaissance et utilisation des ressources en sol au Maroc. Rapport thématique*, 50.
29. Hengl, T., Mendes de Jesus, J., Heuvelink, G. B., Ruiperez Gonzalez, M., Kilibarda, M., Blagotić, A., ... & Kempen, B. (2017). SoilGrids250m: Global gridded soil information based on machine learning. *PLoS One*, 12(2), e0169748. <https://doi.org/10.1371/journal.pone.0169748>
30. Reichhuber, A., Gerber, N., Mirzabae, A., Svoboda, M., López Santos, A., Graw, V., ... & Jia, X. (2019). The land-drought nexus enhancing the role of land-based interventions in drought mitigation and risk management. In *United Nations Convention to Combat Desertification*, Bonn.
31. Inglada, J., Vincent, A., Arias, M., Tardy, B., Morin, D., & Rodes, I. (2017). Operational high resolution land cover map production at the country scale using satellite image time series. *Remote Sensing*, 9(1), 95. <https://doi.org/10.3390/rs9010095>
32. Van Thinh, T., Duong, P. C., Nasahara, K. N., & Tadono, T. (2019). How does land use/land cover map's accuracy depend on number of classification classes?. *Sola*, 15, 28-31. <https://doi.org/10.2151/sola.2019-006>
33. Winsemius, H. C., Jongman, B., Veldkamp, T. I., Hallegatte, S., Bangalore, M., & Ward, P. J. (2018). Disaster risk, climate change, and poverty: assessing the global exposure of poor people to floods and droughts. *Environment and Development Economics*, 23(3), 328-348. <https://doi.org/10.1017/S1355770X17000444>
34. UNDRR (2021). *Global Assessment Report on Disaster Risk Reduction GAR, Special Report on Drought*.
35. Haut-Commissariat au Plan. (2017). *Principaux résultats de la cartographie de la pauvreté multidimensionnelle 2014. Paysage territorial et dynamique*, Rapport.
36. Murthy, C. S., Laxman, B., & Sai, M. S. (2015). Geospatial analysis of agricultural drought vulnerability using a composite index based on exposure, sensitivity and adaptive capacity. *International Journal of Disaster Risk Reduction*, 12, 163-171. <https://doi.org/10.1016/j.ijdrr.2015.01.004>
37. Balaghi, R., Jlibene, M., Tychon, B., & Eerens, H. (2012). *La prédiction agrométéorologique des rendements céréaliers au Maroc*. Institut National de La Recherche Agronomique, Maroc.
38. Bijaber, N., & Rochdi, A. (2019, November). Development of a comprehensive remote sensing technique for drought monitoring in Morocco. In *Conference of the Arabian Journal of Geosciences*, 311-313. https://doi.org/10.1007/978-3-030-72896-0_70
39. de Forges, A. R., Feller, C., Jamagne, M., & Arrouays, D. (2008). Perdus dans le triangle des textures. *Etudes et gestion des Sols*, 15(2), 97-111.
40. Motib, I., Batchi, M., & Fatah, F. (2020). *Conservation Des Ressources Naturelles Pour Une Sécurité Alimentaire Durable Au Maroc*. *European Scientific Journal*, 16, 240-260.
41. Alkire, S., Conconi, A., & Seth, S. (2014). *Multidimensional Poverty Index 2014: Brief methodological note and results*. OPHI briefing, 19.



© Author(s) 2024. This work is distributed under <https://creativecommons.org/licenses/by-sa/4.0/>



An unmanned aerial vehicle based investigation of roof patch suitability for solar panel installation

Nizar Polat ^{*1} , Abdulkadir Memduhoğlu ¹ 

¹ Harran University, Department of Geomatic Engineering, Türkiye, nizarpolat@harran.edu.tr, akadirm@harran.edu.tr

Cite this study: Polat, N., & Memduhoğlu, A. (2024). An unmanned aerial vehicle based investigation of roof patch suitability for solar panel installation. International Journal of Engineering and Geosciences, 9 (2), 281-291

<https://doi.org/10.26833/ijeg.1424400>

Keywords

Solar radiation potential
Unmanned aerial vehicle
GIS
Image processing

Abstract

This study presents a Geographic Information Systems (GIS) and Unmanned Aerial Vehicle (UAV) based approach to determine suitable roof patches of buildings for solar panel installation in Harran University (Şanlıurfa) campus area. Initially, the Solar Radiation Potential (SRP) of the study area was calculated using a UAV-based Digital Surface Model (DSM) in GIS. Then, a correction process was applied to this theoretically calculated SRP by using an adjustment coefficient derived from 5-year measurements of the Solar Power Plant (SPP) located in the region. This coefficient was used to adjust the calculated SRP and compared with the SPP measurements at a concurrent period. The rooftop objects were segmented by textural analysis to determine the suitable panel installation patches on the buildings. Then, the obtained suitable patches are divided into four different classes considering the adjusted total SRP to find panel installation priority. Finally, the calculated electricity potential of the suitable roof patches could meet approximately 65% of the yearly consumption of campus buildings. This paper reveals that in GIS-based SRP studies, it is necessary to detect the rooftop objects to obtain the solar panel installation area more accurately, and a correction should be applied to approximate the theoretically calculated SRP values to the actual values.

Research Article

Received: 23.01.2024
Revised: 12.03.2024
Accepted: 17.03.2024
Published: 25.07.2024



1. Introduction

In today's world, energy usage is perceived as an indicator of technological development and high welfare levels for developed countries. All fundamental and essential aspects of life, such as industry, trade, housing and transportation, depend on energy. However, the primary energy resources of the world such as water and fossil-based fuels, are in continual depletion. This depletion affects human life as well as energy production directly. Moreover, the usage of these primary energy resources causes ecological damages such as drought, air and soil pollution, etc. This has driven many countries to use clean and renewable energy sources such as wind, geothermal and solar [1]. In the past few decades, these alternative renewable energy resources made a rapid change, especially in rural settlements [2]. According to Elliot et al. [3], any kind of renewable energy source provides opportunities for electricity generation at a public service scale, village and farm needs, and off-grid independent energy generation. At this point, some parameters such as energy demand, environmental

conditions and especially power station locations should be considered to establish alternative power systems [4]. In this context, solar energy has the potential to become more popular than other renewable energy sources with its accessibility, economic advantage, and ease of use.

Estimating solar energy is a valuable tool for developing energy strategies, designing facilities and urban planning [5-9]. As it is known the fundamental consideration for solar energy is to detect Solar Radiation Potential (SRP) both spatially and temporally. This potential can obtain either meteorology station measurements (used to estimate the solar radiation through interpolation in the areas) or Geographic Information Systems (GIS) based Digital Surface Model (DSM) approach [10]. A meteorological station based study was performed by Nematollahi and Kim [11]. They calculated the yearly horizontal radiation of 24 meteorology stations for five years to get a feasibility report for new Solar Power Plants (SPP). Meteorology stations may not always be used for several reasons such as inconvenient location, insufficient station number, incompatible technology and missing parameters [12].

Due to the scarcity of meteorology stations, GIS-based studies are more abundant in scientific literature. In these kinds of studies, DSM is an essential input for the SRP calculation based on the hemispherical model. The spatial resolution of the DSM is important and depends on the generation methods. For instance, while a DSM (~1 m) generated with Light Detection and Ranging (LiDAR) data may be sufficient to get the slope and orientation of rooftops in terms of spatial resolution, a Shuttle Radar Topography Mission (SRTM) elevation data (~30 m) could not be used for this purpose. Therefore, high resolution data is required for solar panel installation studies.

The roof of a building is the most suitable patch for solar panel installation. Thus, SRP calculation becomes more complicated due to the requirement for comprehensive knowledge of the geometric and physical conditions of rooftop structures [13]. Generally, in city-scale studies, a LiDAR-based DSM is used to calculate the SRP of the entire city surface. Subsequently, the building footprints and directions are used as constraints to obtain rooftop SRP values [14]. Kucuksari et al. [15] followed a similar procedure and used airborne LiDAR data with GIS in a campus area to calculate SRP using slope, aspect, elevation and insolation as input parameters. Then, to get the long-term net profit of rooftop solar panel installations, electricity potential was examined in consideration of possible costs. Huang et al. [14] proposed a Graphical Processing Unit-based SRP calculation model with LiDAR data using GIS. The suitable roofs were decided according to the yearly average total radiation, slope, and aspect. Verso et al. [16] applied a multi-criteria approach based on GIS and DSM to calculate the SRP. Then several criteria were applied such as building shapes, types, annual solar potential and panel size to detect suitable roofs.

Determining the appropriate roof patches and evaluating their SRP is important for solar panel installation [15]. Depending on the complexity of the urban area, the accuracy and resolution of the spatial data may vary. The high-resolution DSM can be obtained by satellite imagery and laser systems, but it is not efficient in terms of economy, time, and updating. In this context, DSMs with different spatial accuracy and resolution can be produced using Structure-from-Motion (SfM) based Unmanned Aerial Vehicle (UAV) photogrammetry. This approach, which has been used extensively in the last two decades, brings great advantages. It provides cheaper and higher spatial resolution DSM in comparison with LiDAR, especially for local city areas [17].

Compared to conventional manned aerial photogrammetry, UAV photogrammetry has serious advantages in areas such as flight altitude, cost, time, repetitive use, and image processing [18]. It is also suitable for photogrammetric flights. Especially the SfM approach used in the processing of aerial photographs obtained by UAV gives very successful results. This approach is an innovative, user beneficial and low-cost photogrammetric technique, which has been used widely over the last few years [19].

Besides, the possibility of re-use of UAV systems, being automatic, portable, and easy to use in the urban area makes it more advantageous [20]. Thus, UAV-based DSMs can be used in SRP studies for urban areas. In this regard, Shao et al. [21] applied a UAV-based procedure to get high resolution data on roofs. They classified the building types and building roofs (flat, non-flat) to make a better decision for panel installation. Dewanto et al. [22], calculated rooftop SRP from UAV-based DSM and overlaid it on a three-dimensional (3D) model of campus buildings using a web-based GIS environment. Fuentes et al. [23], calculated the SRP of an individual building roof with UAV-based DSM. After solar panel installation, the generated electricity production was compared with the calculated potential for a year.

There are two common gaps in the mentioned SRP studies: (1) the rooftop objects were not considered and (2) the SRP is based on theoretical calculations. Generally, in GIS-based studies, the entire rooftop is considered a potential solar panel installation area. However, this assumption may deviate considerably in the real world, especially in cases of different roof types (flat, non-flat). Moreover, rooftops may be occupied by different objects such as chimneys, air conditioners, ventilation, antennas, or solar water heating panels. In such cases, a detailed analysis of the rooftop is required to calculate accurate SRP. For this analysis, a high-resolution DSM (e.g., pixel < 25 cm) is needed. Thus, rooftop objects can be eliminated and the most suitable areas for solar panel installation can be determined by segmenting roofs in more detail. Although in some studies segmentation is used to detect the roof planes, the rooftop objects on the segmented planes were ignored. Furthermore, SRP calculation performed in hemispherical based GIS software gives approximate results since it does not contain real meteorological factors. This situation causes the calculated SRP to be different from the actual Solar Radiation (SR). While a comparison between generated electricity and GIS-based calculated energy was performed in some studies, no adjustment process mentioned calculated SRP.

The objectives of this study are twofold: first, it attempts to determine the most suitable roof patches for solar panel installation; second, it attempts to adjust the calculated SRP. For this purpose, a textural analysis was performed using high-resolution DSM to detect the rooftop objects. Then, monthly, seasonal and annual coefficients were calculated with the data (for 5 years) obtained from the SPP in the study area and the most suitable coefficient was used to adjust the calculated SRP.

2. Method

The study was held in the Harran University Osmanbey Campus located in Şanlıurfa which is in southeast Turkey (Figure 1). The annual average (last 30 years) of the sunshine duration of the city is over 8.5 h/d [24]. According to the long-term average of SR reported in Global Solar Atlas [25], Şanlıurfa has one of the highest SRP in the country.

The SR of a particular point on the earth depends on the orientation and elevation [26]. Thus, the SRP of that point is mainly calculated according to the hemispherical

viewshed algorithm. A DSM can supply necessary information about the surrounding topography including the obstacle and shadow area of that point [27]. Although DSM is sufficient for SRP calculation, various parameters such as meteorological station data [14], classified satellite images [28] and topographic maps [29] can be used as inputs depending on the purpose of the study. In our case, the building footprints, SPP measurements and UAV based DSM were used as input. The workflow of the study is given in Figure 2.

In the study, a workflow including photogrammetric UAV flight, SfM, textural analysis and GIS based SRP calculation was carried out. There are several important and specific steps within this workflow. First, the high-resolution DSM of the region was produced using SfM-based UAV photogrammetry. Second, textural analysis was performed on high resolution DSM to detect rooftop objects. Third, is the coefficient calculation for the SRP adjustment. Finally, the electricity potential was calculated according to the suitable roof patches and was compared with the actual consumption.

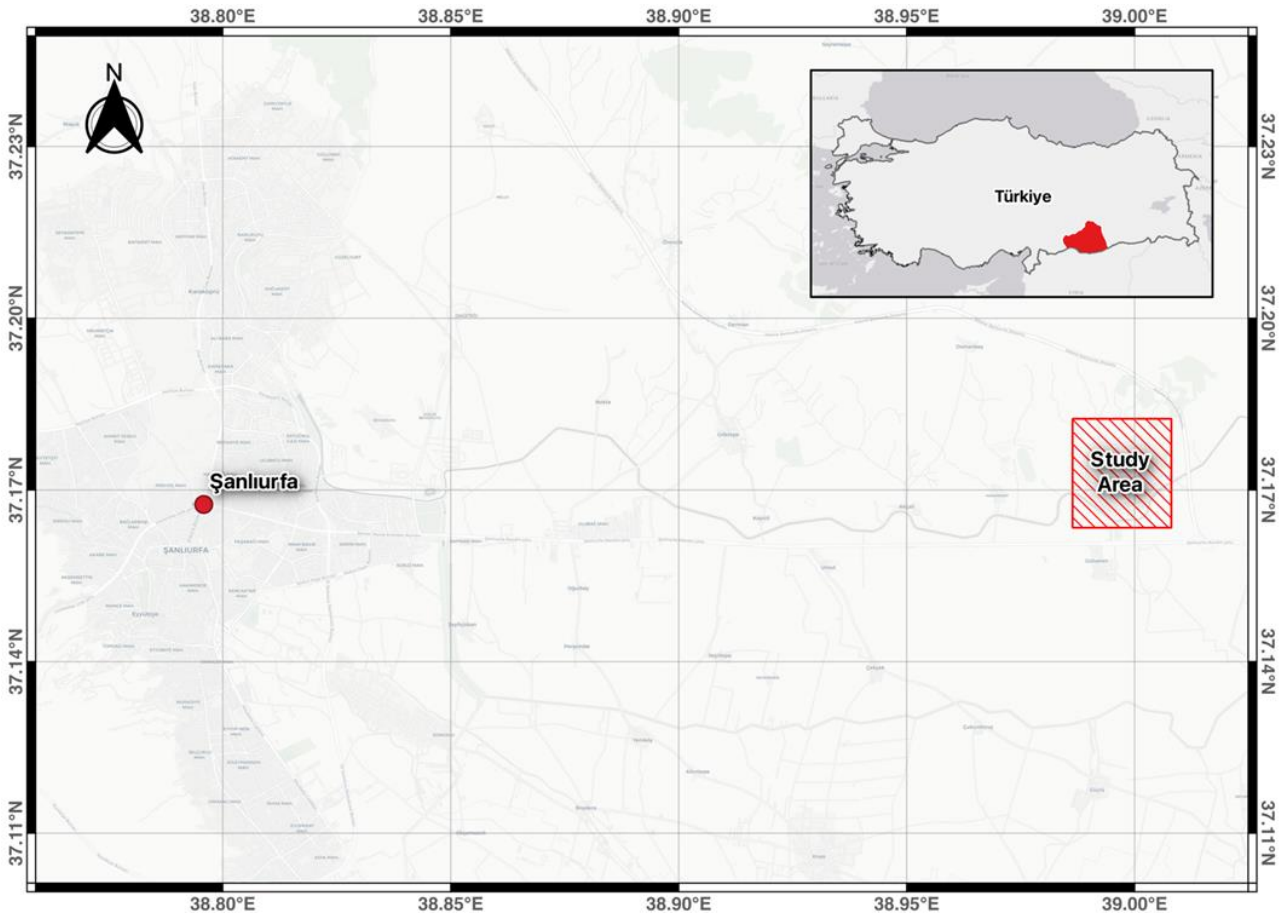


Figure 1. The study area.

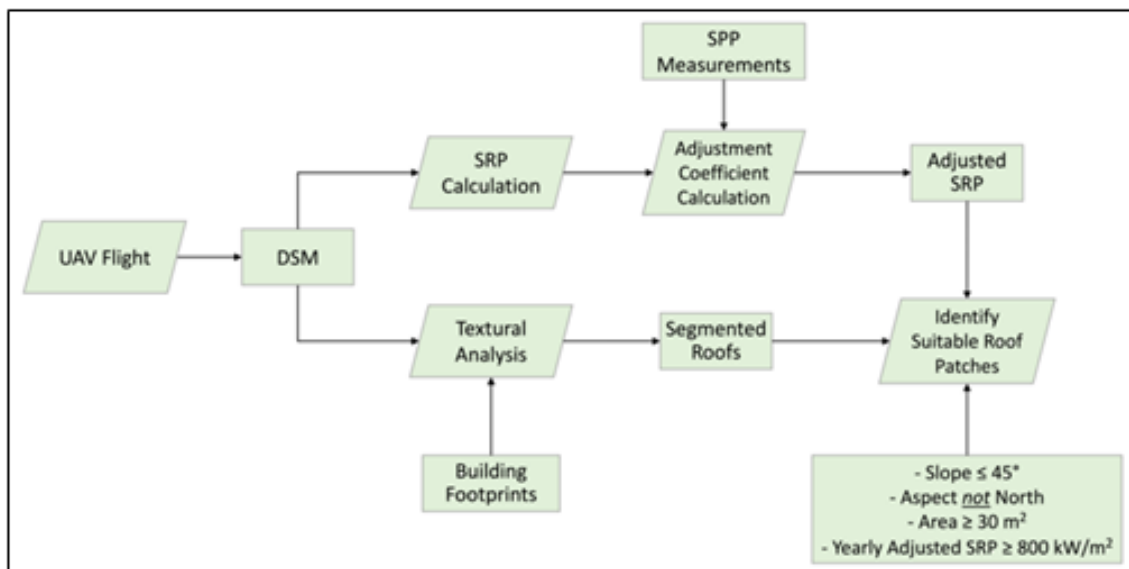


Figure 2. The workflow of the study.

2.1. UAV photogrammetry

There are some differences between SfM and traditional photogrammetry in terms of mathematical and statistical approaches. Traditional photogrammetry looks for solutions by using global consistency, compatibility, the accuracy of measurements and model validity. On the other hand, SfM is an image matching technique that generates a 3D model of an object by automatically aligning positions, camera parameters and 3D geometry of the object with an appropriate overlap rate through a photogrammetric approach [30]. Then, a photogrammetric bundle block adjustment is used to build a local model with all generated 3D points. Today, several SfM-based image processing software can generate high resolution DSM and orthophoto from aerial images captured with UAV platforms [20]. Lucieir et al. [31] managed to generate a 2 cm resolution DSM to get microtopography with Agisoft software. Toprak et al. [18] reached under cm accuracy in a rocky archeological site with the SfM approach. Besides, due to the high spatial resolution data of UAV systems, they can be used in biomass estimation and yield prediction [32], cotton plant height [33] and accurate extraction of buildings in a complex urban area [34].

2.2. Textural analysis

The purpose of texture analysis is to identify flat areas suitable for panel installation. At this point, texture analysis aims to detect objects that disrupt the flatness of a roof section and could obstruct panel installation, such as air conditioning units, antennas, or chimneys.

Images are generally described with color values, brightness and pixel size. On the other hand, texture parameters such as variance, dissimilarity and entropy are rarely used. A pixel of an image can contain color and brightness values. However, the texture becomes meaningful with a set of neighboring pixels. Mathematically, the Gray Level Co-Occurrence Matrix (GLCM) is used to get a two-dimensional histogram of the gray levels of a neighboring pixel pair. In other words, GLCM displays the frequency of pixel pair apparency in an image. GLCM is used to calculate texture parameters which are suggested by Haralick et al. [35]. In this study, the GLCM-based variance parameter was used to detect rooftop object segments. Briefly, variance defines the heterogeneity of pixel neighboring. Equation 1 is used to calculate the variance parameter.

$$Dir_T = \sum S_{Const} * \beta^{m(\theta)} * SunDur_{\theta,\alpha} * SunGap_{\theta,\alpha} * \cos(Anl_{\theta,\alpha}) \quad (3)$$

where:

- θ – with a centroid at a zenith angle.
- α – azimuth angle.
- S_{Const} — The solar flux constant (1367 W/m²) [40].
- β —The atmosphere transmissivity for the shortest path in the zenith direction.
- $m(\theta)$ — The relative optical path length.

$$\sum_{i=0}^{N_g-1} (i - M)^2 P(i) \quad (1)$$

where:

- $P(i)$ denotes pixel probability.
- N_g refers to pixels' gray value.
- M is the mean pixel value obtained from input DSM.

2.3. GIS-based calculation of solar radiation potential

It is a fact that the amount of SR emitted from the sun is different from the amount reaching the earth's surface by passing through the atmosphere. Šúri and Hofierka [36] reported three main elements that affect SR: Earth's position, Earth's topography, and atmospheric conditions. In a GIS-based SRP calculation, above mentioned elements are used as solar parameters, DSM and atmospheric conditions (absorption and dispersion) respectively. DSM is used to determine the maximum possible obstruction angle in consideration of all directions around the geographical location of the study area [27]. The detected angles allow us to get a hemispherical viewshed that consists of both visible and blocked directions in the sky [26]. This sky map is used to calculate the diffuse SR (caused by the scattering of sunlight in the atmosphere) received at a particular location in DSM. Then, the sun map is produced according to the position change of the sun over time (hour, day and month) considering the position of the study area. The sun map is used to estimate the amount of direct SR received by a particular location in DSM [37].

The generated viewshed, sun map, and sky map are used to calculate direct and diffuse SR for every single pixel of DSM in GIS [38]. The whole amount of SRP which is called the global SR ($Global_T$) is derived from the sum of the total direct SR (Dir_T) and total diffuse SR (Dif_T) (Equation 2) [39].

$$Global_T = Dir_T + Dif_T \quad (2)$$

The total direct SR (Dir_T) of a particular location on the earth's surface is the sum of the direct SR from all directions of the sun map (Equation 3) [27].

- $SunDur_{\theta,\alpha}$ — The time duration of the sky map.
- $SunGap_{\theta,\alpha}$ — The gap fraction for the sun map.
- $Anl_{\theta,\alpha}$ — The angle of incidence between the axis normal to the surface and the centroid of the sky sector (tilt angle).

Diffuse radiation (Dif_T) is calculated using Equation (4) [27]:

$$Dif_T = R_{glb} * P_{dif} * Dur * SkyGap_{\theta,\alpha} * Weight_{\theta,\alpha} * \cos(Anagn_{\theta,\alpha}) \quad (4)$$

where:

- θ – with a centroid at a zenith angle.
- α – azimuth angle.
- R_{glb} — The global normal solar radiation.
- P_{dif} — The proportion of global normal radiation flux that is diffused. It is approximately 0.2 for very clear sky conditions and 0.7 for very cloudy sky conditions.
- Dur — The time interval for analysis.
- $SkyGap_{\theta,\alpha}$ — The gap fraction for the sky map.
- $Weight_{\theta,\alpha}$ — The proportion of diffuse radiation originating in each sky sector relative to all directions.
- $Anagn_{\theta,\alpha}$ — The angle of incidence between the intercepting surface and the centroid of the sky sector (tilt angle).

In equations for both diffuse (3) and direct solar radiation (4), the variables θ, α and $Anagn_{\theta,\alpha}$ —which represent the zenith, azimuth, and tilt angles, respectively—are dependent on the Earth's position and vary over time. Latitude plays a significant role in solar geometry, influencing these parameters in relation to the sun's position.

2.4. Estimation of adjustment coefficient

As mentioned in Section 1, GIS-based calculated SRP varies from actual SR. Thus, an adjustment process is needed. For this purpose, monthly average SR data for 6 years were obtained from the SPP located in the study area. 5-years of SR data (2015-2020) were used for the Adjustment Coefficient (AC) estimation and the remaining 1-year (2021) SR data were used for control purposes. The 5-year SR data were grouped into time intervals as monthly, seasonal and yearly and their averages were obtained. Similarly, the calculated SRP data for 2021 were grouped as monthly, seasonal and yearly. The 5-year average of SR values was proportioned to the 2021 calculated SRP values and then monthly, seasonal and annual coefficients were calculated. In the end, 3 different types (monthly, seasonal and annual) of ACs were obtained by using Equation 5.

$$AC_t = \frac{\left(\sum_{i=2015}^{2020} SR_{t_i}\right)/5}{SRP_{2021_t}} \quad (5)$$

where:

- AC is the Adjustment Coefficient.
- t – is the time interval (e.g., January for monthly, Spring for seasonal and year for annual adjustment calculation $t = i$).
- i – is the measured year of the SPP data.
- SR – is the solar radiation value of the corresponding year.
- SRP – is the calculated solar radiation potential from GIS.

By applying these ACs to 2021 calculated SRP, monthly, seasonal and annually corrected SRP values were obtained. The corrected SRP values were compared with 1-year (2021) of measured SR data to determine the most suitable AC. Thus, the GIS-based calculated SRP values are approximate to the real values by using the most suitable AC.

For AC calculation, it is necessary to have a monthly average SR measurement collected from near the region of interest. Since meteorological conditions directly affect the sunshine duration during the day, hourly SR measurements must be obtained for a reliable monthly average SR measurement. In addition, the location of the study area directly affects the SR value. Any significant changes in these parameters will require a recalculation of AC.

2.5. Identifying suitable roof patches

All the roof patches of a building cannot be suitable for solar panel installation due to the above-mentioned rooftop objects. Thus, all roof patches were determined as suggested in Section 2.2. Consequently, rooftop objects were detected, and several parameters were used to identify suitable roof patches.

The first parameter is the minimum installation area. This parameter should be decided according to the solar panel dimensions and orientations to be installed. That means this parameter may vary depending on the project requirements, panel and building type. Although Khanna [41] reported that less than 30 m² of building roof patches may not be suitable for panel installation, Palmer et al. [42] used 8 m² for houses and Huang et al. [14] used 10 m² for urban buildings. We used this value as 30 m² in consideration of large faculty buildings and panel dimensions. The second parameter is the slope. It is not feasible to install panels over a 45-degree slope. So, a lower than 45-degree slope is used as a parameter in this study. The third parameter is the aspect. The study area is located in the northern hemisphere. Therefore, the amount of SRP is inadequate for the north facing roof patches. So, these patches were removed. The last parameter is the minimum amount of the yearly average SRP of the patches. This parameter was used as a yearly minimum of 800 kWh/m².

2.6. Estimation of electricity potential

Spatial variations of solar panel installations on the roof are critical to understanding the SRP [43]. Calculating the electricity potential from SRP depends on the installation scenarios of the panels and the panel properties [44]. In this context, tilt and panel area affect the total number of panels, while efficiency and performance ratio values affect the total electricity potential. For this reason, creating building-based scenarios may give more accurate results. However, this approach is not effective in urban areas with many buildings. Additionally, there is no need for spaces and access roads between the solar panels on a roof, unlike

the solar panels installed in the open area according to an expert opinion from the SPP. Therefore, in our case, it has been assumed that all suitable roof patches are installed with similar solar panels (25% tilt and 1.67 m² panel area) of SPP in the region. Hence, the same panel parameters namely efficiency and performance ratio

values were used for electricity potential calculation. To determine electricity potential Equation 6 was used [13].

In this study, the SR value refers to the adjusted SRP (kWh/m²), the efficiency of the solar panel is 16% and the performance ratio of the solar panel is 88%. The efficiency and performance ratio of the panel were obtained from the manufacturer of the panels.

$$\text{Electricity Potential} = \text{SR value} \times \text{Efficiency} \times \text{Performance Ratio} \quad (6)$$

3. Results and discussion

In the study, ten different photogrammetric flight plans were prepared, and UAV (DJI Mavic 2 Pro) flights were performed to create a high-resolution DSM. For the flight parameters, the elevation was decided as 100 m for 70% overlaps both forward and lateral. 1019 suitable aerial images were captured for the 4.16 km² area. The calculated ground sample distance was 3.7 cm. In the end, the orthophoto and a 25 cm spatial resolution DSM were generated for the study area (Figure 3). All photogrammetric products were generated in Pix4D software.

Before textural analysis, the DSM was masked with building footprints. Then the texture-based variance parameter was generated by using masked DSM and the segments of the rooftop objects were obtained. Sample buildings with original and segmented footprints are given in Figure 4.

As seen in Figure 4, the rooftop objects such as air conditioner parts, antenna, chimney and elevator room were detected successfully. Thus, 147 parts of the original building footprints were segmented into 699 parts. This situation allows us to investigate all segmented roof patches in detail for panel installation.



Figure 3. Orthophoto and DSM of the study area.



Figure 4. Sample buildings with original and segmented footprints.

After the rooftop segmentation, comparison and adjustment were performed between calculated SRP and SPP measurements. To find a suitable AC, three different SR data were used (Table 1). The first one is the calculated SRP of the study area from March 2021 to February 2022. Second is the monthly measurements of the SPP for a continuous period of 5 years from March

2015 to February 2020. This data was used to calculate ACs. The third one is the SPP measurement from March 2021 to February 2022. This data was used to compare adjusted SRP values.

In Table 1, the total of the 1-year SPP measurements (2021-2022) is close to the total of the 5-year SPP measurements (2015-2020). However, the total of the

calculated 1-year SRP (2021-2022) significantly differs from these measurements. Therefore, the 5-year SPP measurements were compared with calculated SRP utilizing monthly, seasonal and annual periods. According to this comparison, three types of ACs were calculated regarding Equation 5 (Table 2).

Table 1. Monthly averages of solar radiation values (kWh/m²).

Month	Calculated SRP (2021-2022)	SPP Meas. (2015-2020)	SPP Meas. (2021-2022)
March	105.13	141.24	123.47
April	139.86	181.14	158.52
May	172.32	211.36	218.13
June	176.11	239.88	219.35
July	178.44	248.62	236.21
August	156.46	219.42	225.46
September	116.07	176.70	208.40
October	79.35	127.97	152.70
November	47.08	85.98	130.99
December	33.96	65.41	72.23
January	43.12	71.49	91.25
February	63.47	92.18	97.96
Total	1311.37	1861.37	1934.66

Table 2. Calculated Acs.

Month	Adjustment Coefficients		
	Monthly	Seasonal	Annual
March	1.343		
April	1.295	1.288	
May	1.227		
June	1.362		
July	1.393	1.386	
August	1.402		
September	1.522		1.502
October	1.613	1.654	
November	1.826		
December	1.926		
January	1.658	1.679	
February	1.452		

The calculated coefficients were used to adjust the SRP values. In order to examine the effects of the coefficients, the calculated and adjusted SRP values for

2021-2022 were compared with SPP measurements for 2021-2022 (Figure 5).

Although there is not a big difference in trend (similar fluctuation) between the SPP measurement (turquoise) and the calculated SRP (blue), there is a considerable difference in quantity. The main reason for this is the lack of meteorological models in GIS-based approach. The theoretical values are approximated to the actual values with the calculated ACs. As seen in Figure 5, the annual adjusted SRP values show the highest deviation from the SPP measurement. Even though the monthly adjusted SRP values were improved, the seasonal adjusted SRP (green) more significantly approached SPP measurement. To express this situation metrically, the averages of monthly differences between all the SRP values and SPP measurements given in Figure 5 were examined (Table 3).

In Table 3, the difference between SPP measurement and seasonal adjusted SRP is the lowest. Therefore, the seasonal coefficient was selected for SRP adjustment. The comparison of averages of yearly total values for calculated SRP, SPP measurement and adjusted SRP values were given in Table 4.

Table 3. The averages of monthly differences (kWh/m²).

Difference Between SPP Meas. (2021-2022)	Calculated SRP	Adjusted SRP		
		Monthly	Seasonal	Annual
	51.94	18.33	17.97	32.60

Table 4. The averages of the yearly total (kWh/m²).

	Calculated SRP	SPP Measurements	Adjusted SRP
2021-2022	1311.37	1934.66	1882.86

According to the averages of yearly total values given in Table 4, the difference between the calculated SRP and the SPP measurement values is approximately 46%. This difference decreases to 3% after the adjustment is applied. In this case, a 43% improvement was achieved by using AC. Thus, the seasonal AC was used to adjust the SRP values of roof patches. The seasonal adjusted total SRP for buildings is given in Figure 6.

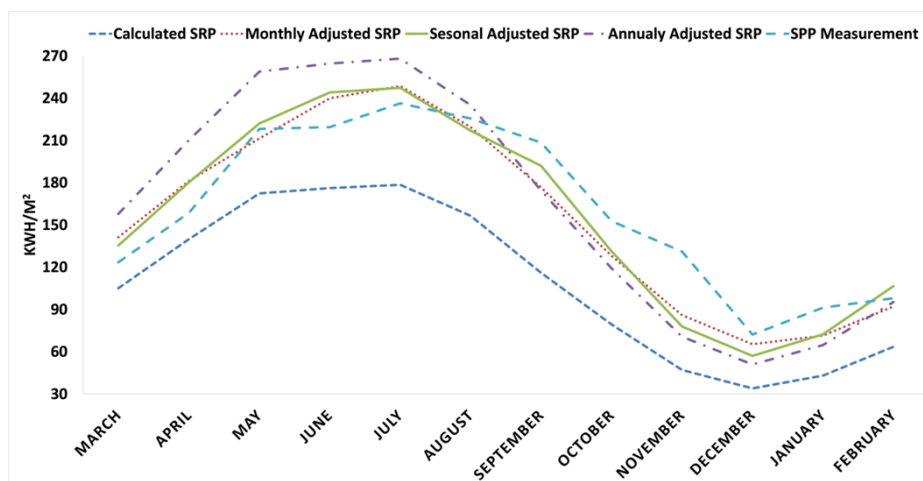


Figure 5. The comparison of monthly solar radiation average values.

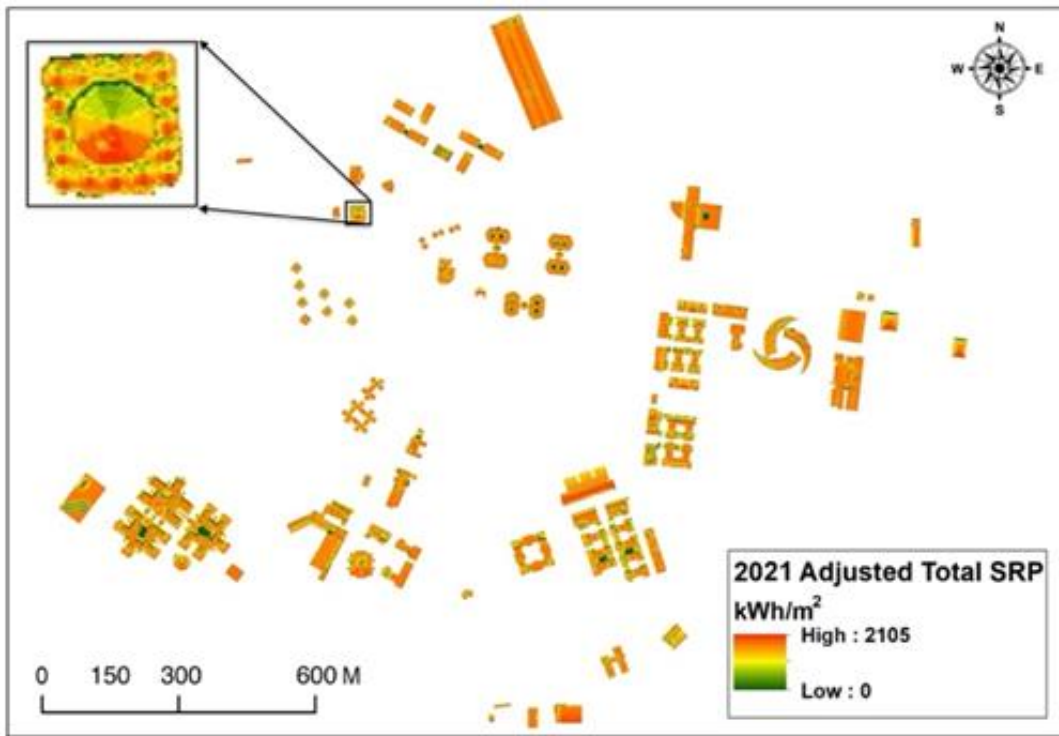


Figure 6. The adjusted total SRP for buildings.

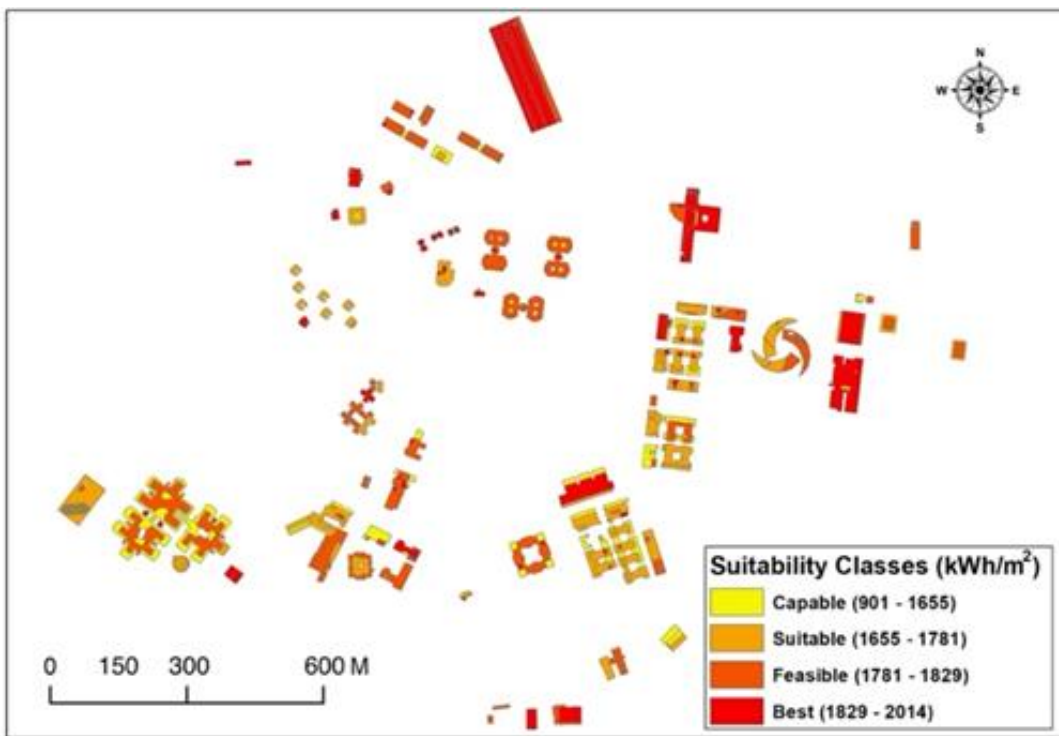


Figure 7. Suitability classes of roof patches for solar panel installation.



Figure 8. Suitability of the sample buildings.

In this study, 262 suitable roof patches were selected from all segmented parts regarding the parameters given in section 2.5. Also, a suitability classification was produced according to adjusted total SRP values to find the priority of the roof patches (Figure 7). Thus, flexibility has been provided in terms of which suitable roof patches should be preferred primarily in solar panel installation projects.

According to the results, the yearly SRP values for suitable patches varied from 901 to 2014 kWh/m² and the average SRP value of the whole suitable roof patches was calculated as 1715 kWh/m². The Capable class has the lowest area (13%) according to the whole suitable area. Similarly, the best class which has the highest SRP values covers 31% of the suitable area. In general, 87% of the suitable areas were highly efficient (yearly over 1655 kWh/m²) for panel installation. A close view of the suitability of the sample buildings is given in Figure 8.

Rooftop segmentation and suitability classification provided detailed information for panel installation. For instance, when Figure 8 was examined, multiple suitability classes can be seen in an individual building due to the segmentation. Thus, it can be easily decided primarily on the installation patch for every building. Additionally, the unsuitable roof patches for solar panel installation were eliminated. It should be noted that the material for the construction of roofs is not investigated in the study. This situation needs to be considered in the installation process.

For further analysis, the adjusted SRP of usable roof patches was converted to the electricity potential. To achieve this, the same installation features of the SPP (25% tilt and 1.67 m² panel area) located in the study area were utilized. According to the panel manufacturer's 16% efficiency and 88% performance ratio values, the yearly theoretical electricity generation potential was calculated as 13 GWh. This calculated amount meets approximately 65% of campus consumption in 2021.

4. Conclusion

Today, traditional energy sources are declining, while energy demand is increasing. This trend is leading people to seek renewable energy sources. As a renewable energy source, solar energy has become more popular due to the wide range of accessibility from all around the world. At this point, the first step to establishing a facility is to determine SRP for the interested area. This process is easier for an open area, but it is complicated for rooftops. In this study, a workflow including photogrammetric UAV flight (DJI Mavic 2 Pro), SfM, image processing and GIS was used to detect both SRP and suitable roof patches for solar panel installation.

In the study, the UAV-based high-resolution DSM and SRP were generated for the study area. Then, three types of ACs were calculated based on long term SPP measurements. These ACs have been applied to the calculated values and compared with the 2021 measurements. Seasonal AC was chosen as it most closely approximates the GIS-based calculated values to the SPP measurements. This AC was used to adjust the SRP values of roof patches. To select suitable areas, the

segmented roof patches and adjusted SRP were examined in consideration of the given installation parameters. Consequently, the selected roof patches were classified to find the priority of panel installation. According to the results, 87% of suitable roof patches were identified as highly efficient (yearly over 1655 kWh/m²) for solar panel installation. For a solid example, the adjusted SRP is converted to the electricity potential and compared with campus electricity consumption for 2021. It is seen that the potential of suitable roof patches corresponds to 65% of the actual electricity consumption for 2021.

It is necessary to visit each roof manually when UAV and GIS are not used to determine suitable areas for panel installation. In these manual visits, suitable areas for installation should be determined by considering the area of the roof, roof objects, and shadow areas. This is time consuming, costly, and labor-intensive when multiple buildings are involved. On the other hand, when UAV is used, roof areas and roof objects are obtained precisely, economically, and quickly, without making any building visits with high resolution orthophoto and DSM of the study area. In addition, the SRP values of the roofs that cannot be obtained by manual building visits can be calculated using GIS. In this way, suitable roof patches for panel installation and their priorities were determined. As a result, the UAV and GIS methods are more practical and effective than the manual method in terms of SRP calculation, data recording, time and personal safety, especially for local areas. Besides, the rooftop segmentation facilitates the detection of suitable areas for solar panel installation. In GIS-based SRP studies, values may deviate from the actual value due to multi-parametric algorithms. At this point, regional ACs may be used to correct the SRP values. In future studies, under which conditions and how much the AC value changes from region to region will be examined.

Acknowledgement

The authors would like to thank Harran University Renewable Energy Research Center (GAPYENEV) and Specialist M. Akif Ilkhan for providing data and their valuable contributions.

Author contributions

Nizar Polat: Conceptualization, Methodology, Software, Field study, Writing-Reviewing and Editing

Abdulkadir Memduhoğlu: Conceptualization, Methodology, Software, Field study, Writing-Reviewing and Editing

Conflicts of interest

The authors declare no conflicts of interest.

References

- Ackermann, T. (2012). Wind power in power systems. John Wiley & Sons.
- Chan, T. F., & Lai, L. L. (2007). An axial-flux permanent-magnet synchronous generator for a

- direct-coupled wind-turbine system. *IEEE Transactions on Energy Conversion*, 22(1), 86-94. <https://doi.org/10.1109/TEC.2006.889546>
3. Elliott, D., Schwartz, M., Scott, G., Haymes, S., Heimiller, D., & George, R. (2003). Wind energy resource atlas of Sri Lanka and the Maldives (No. NREL/TP-500-34518). National Renewable Energy Lab. (NREL), Golden, CO (United States).
 4. Bansal, R. C. (2003). Bibliography on the fuzzy set theory applications in power systems (1994-2001). *IEEE Transactions on Power Systems*, 18 (4) 1291-1299. <https://doi.org/10.1109/TPWRS.2003.818595>
 5. Wang, Z., Bui, Q., Zhang, B., Nawarathna, C. L. K., & Mombeuil, C. (2021). The nexus between renewable energy consumption and human development in BRICS countries: The moderating role of public debt. *Renewable Energy*, 165, 381-390. <https://doi.org/10.1016/j.renene.2020.10.144>
 6. Adjiski, V., Kaplan, G., & Mijalkovski, S. (2023). Assessment of the solar energy potential of rooftops using LiDAR datasets and GIS based approach. *International Journal of Engineering and Geosciences*, 8(2), 188-199. <https://doi.org/10.26833/ijeg.1112274>
 7. Yılmaz, O. S., Gülgen, F., & Ateş, A. M. (2023). Determination of the appropriate zone on dam surface for floating photovoltaic system installation using RS and GIS technologies. *International Journal of Engineering and Geosciences*, 8(1), 63-75. <https://doi.org/10.26833/ijeg.1052556>
 8. Demirgöl, T., Demir, V., & Sevimli, M. F. (2023). Model-Ağacı (M5-tree) yaklaşımı ile HELIOSAT tabanlı güneş radyasyonu tahmini. *Geomatik*, 8(2), 124-135. <https://doi.org/10.29128/geomatik.1137687>
 9. Arca, D., & Çıturoğlu, H. K. (2022). Güneş enerjisi santral (GES) yapım yerlerinin CBS dayalı çok kriterli karar analizi ile belirlenmesi: Karabük Örneği, *Geomatik*, 7(1), 17-25. <https://doi.org/10.29128/geomatik.803200>
 10. Choi, Y., Suh, J., & Kim, S. M. (2019). GIS-based solar radiation mapping, site evaluation, and potential assessment: A review. *Applied Sciences*, 9(9), 1960. <https://doi.org/10.3390/app9091960>
 11. Nematollahi, O., & Kim, K. C. (2017). A feasibility study of solar energy in South Korea. *Renewable and Sustainable Energy Reviews*, 77, 566-579. <https://doi.org/10.1016/j.rser.2017.03.132>
 12. Martín, A. M., Domínguez, J., & Amador, J. (2015). Applying LIDAR datasets and GIS based model to evaluate solar potential over roofs: a review. *Aims Energy*, 3(3), 326-343. <https://doi.org/10.3934/energy.2015.3.326>
 13. Yalcin, M., Dereli, M. A., & Ugur, M. A. (2019). Modeling of solar energy potential with geographical information system and remote sensing integration: A case study for Bergama, Turkey. *International Symposium on Applied Geoinformatics (ISAG-2019)*, 136-164.
 14. Huang, Y., Chen, Z., Wu, B., Chen, L., Mao, W., Zhao, F., ... & Yu, B. (2015). Estimating roof solar energy potential in the downtown area using a GPU-accelerated solar radiation model and airborne LiDAR data. *Remote Sensing*, 7(12), 17212-17233. <https://doi.org/10.3390/rs71215877>
 15. Kucuksari, S., Khaleghi, A. M., Hamidi, M., Zhang, Y., Szidarovszky, F., Bayraktan, G., & Son, Y. J. (2014). An Integrated GIS, optimization and simulation framework for optimal PV size and location in campus area environments. *Applied Energy*, 113, 1601-1613. <https://doi.org/10.1016/j.apenergy.2013.09.002>
 16. Verso, A., Martin, A., Amador, J., & Dominguez, J. (2015). GIS-based method to evaluate the photovoltaic potential in the urban environments: The particular case of Miraflores de la Sierra. *Solar Energy*, 117, 236-245. <https://doi.org/10.1016/j.solener.2015.04.018>
 17. Polat, N., & Uysal, M. (2018). An experimental analysis of digital elevation models generated with Lidar Data and UAV photogrammetry. *Journal of the Indian Society of Remote Sensing*, 46(7), 1135-1142. <https://doi.org/10.1007/s12524-018-0760-8>
 18. Toprak, A. S., Polat, N., & Uysal, M. (2019). 3D modeling of lion tombstones with UAV photogrammetry: a case study in ancient Phrygia (Turkey). *Archaeological and Anthropological Sciences*, 11(5), 1973-1976. <https://doi.org/10.1007/s12520-018-0649-z>
 19. Uysal, M., Toprak, A. S., & Polat, N. (2015). DEM generation with UAV Photogrammetry and accuracy analysis in Sahitler hill. *Measurement*, 73, 539-543. <https://doi.org/10.1016/j.measurement.2015.06.010>
 20. Polat, N., & Uysal, M. (2017). DTM generation with UAV based photogrammetric point cloud. *The International Archives of the Photogrammetry, Remote Sensing and Spatial Information Sciences*, 42, 77-79. <https://doi.org/10.5194/isprs-archives-XLII-4-W6-77-2017>
 21. Shao, H., Song, P., Mu, B., Tian, G., Chen, Q., He, R., & Kim, G. (2021). Assessing city-scale green roof development potential using Unmanned Aerial Vehicle (UAV) imagery. *Urban Forestry & Urban Greening*, 57, 126954. <https://doi.org/10.1016/j.ufug.2020.126954>
 22. Dewanto, B. G., Novitasari, D., Tan, Y. C., Puruhito, D. D., Fikriyadi, Z. A., & Aliyah, F. (2020). Application of web 3D GIS to display urban model and solar energy analysis using the unmanned aerial vehicle (UAV) data (Case study: National Cheng Kung university buildings). *IOP Conference Series: Earth and Environmental Science*, 520(1), 012017. <https://doi.org/10.1088/1755-1315/520/1/012017>
 23. Fuentes, J. E., Moya, F. D., & Montoya, O. D. (2020). Method for estimating solar energy potential based on photogrammetry from unmanned aerial vehicles. *Electronics*, 9(12), 2144. <https://doi.org/10.3390/electronics9122144>
 24. Turkish State Meteorological Service (2021). Turkish State Meteorological Service. <https://mgm.gov.tr/kurumici/turkiye-guneslenme-suresi.aspx>

25. Global Solar Atlas (2021). Global Solar Atlas. <https://globalsolaratlas.info/map?c=37.68382,36.112061,6>.
26. Rich, P., Dubayah, R., Hetrick, W., & Saving, S. (1994). Using viewshed models to calculate intercepted solar radiation: applications in ecology. American Society for Photogrammetry and Remote Sensing Technical Papers. American Society of Photogrammetry and Remote Sensing, 524-529.
27. Fu, P., & Rich, P. M. (2002). A geometric solar radiation model with applications in agriculture and forestry. Computers and Electronics in Agriculture, 37(1-3), 25-35. [https://doi.org/10.1016/S0168-1699\(02\)00115-1](https://doi.org/10.1016/S0168-1699(02)00115-1)
28. Kircali, Ş., & Selim, S. (2021). Site suitability analysis for solar farms using the geographic information system and multi-criteria decision analysis: the case of Antalya, Turkey. Clean Technologies and Environmental Policy, 23, 1233-1250. <https://doi.org/10.1007/s10098-020-02018-3>
29. Nelson, J. R., & Grubestic, T. H. (2020). The use of LiDAR versus unmanned aerial systems (UAS) to assess rooftop solar energy potential. Sustainable Cities and Society, 61, 102353. <https://doi.org/10.1016/j.scs.2020.102353>
30. Snavely, N., Seitz, S. M., & Szeliski, R. (2008). Modeling the world from internet photo collections. International Journal of Computer Vision, 80, 189-210. <https://doi.org/10.1007/s11263-007-0107-3>
31. Lucieer, A., Turner, D., King, D. H., & Robinson, S. A. (2014). Using an Unmanned Aerial Vehicle (UAV) to capture micro-topography of Antarctic moss beds. International Journal of Applied Earth Observation and Geoinformation, 27, 53-62. <https://doi.org/10.1016/j.jag.2013.05.011>
32. Li, B., Xu, X., Zhang, L., Han, J., Bian, C., Li, G., ... & Jin, L. (2020). Above-ground biomass estimation and yield prediction in potato by using UAV-based RGB and hyperspectral imaging. ISPRS Journal of Photogrammetry and Remote Sensing, 162, 161-172. <https://doi.org/10.1016/j.isprsjprs.2020.02.013>
33. Yang, H., Hu, X., Zhao, J., & Hu, Y. (2021). Feature extraction of cotton plant height based on DSM difference method. International Journal of Precision Agricultural Aviation, 4(1), 59-69. <https://doi.org/10.33440/j.ijpaa.20210401.151>
34. Boonpook, W., Tan, Y., & Xu, B. (2021). Deep learning-based multi-feature semantic segmentation in building extraction from images of UAV photogrammetry. International Journal of Remote Sensing, 42(1), 1-19. <https://doi.org/10.1080/01431161.2020.1788742>
35. Haralick, R. M., Shanmugam, K., & Dinstein, I. H. (1973). Textural features for image classification. IEEE Transactions on Systems, Man, and Cybernetics, (6), 610-621. <https://doi.org/10.1109/TSMC.1973.4309314>
36. Šúri, M., & Hofierka, J. (2004). A new GIS-based solar radiation model and its application to photovoltaic assessments. Transactions in GIS, 8(2), 175-190. <https://doi.org/10.1111/j.1467-9671.2004.00174.x>
37. ESRI (2021). Modeling solar radiation. <https://pro.arcgis.com/en/pro-app/latest/tool-reference/spatial-analyst/modeling-solar-radiation.htm>
38. ESRI (2021). How solar radiation is calculated. <https://pro.arcgis.com/en/pro-app/latest/tool-reference/spatial-analyst/how-solar-radiation-is-calculated.htm>
39. Fu, P. (2000). A geometric solar radiation model with applications in landscape ecology. [Doctoral dissertation, University of Kansas].
40. Fröhlich, C., & Brusa, R. W. (1981). Physikalisch-meteorologisches observatorium, world radiation center, davos, switzerland. Sol Physics, 74, 16-19.
41. Khanna, D. (2020). Estimate solar power potential. In: Learn ArcGIS. <https://learn.arcgis.com/en/projects/estimate-solar-power-potential/#>
42. Palmer, D., Koumpli, E., Cole, I., Gottschalg, R., & Betts, T. (2018). A GIS-based method for identification of wide area rooftop suitability for minimum size PV systems using LiDAR data and photogrammetry. Energies, 11(12), 3506. <https://doi.org/10.3390/en11123506>
43. Yang, Y., Campana, P. E., Stridh, B., & Yan, J. (2020). Potential analysis of roof-mounted solar photovoltaics in Sweden. Applied Energy, 279, 115786. <https://doi.org/10.1016/j.apenergy.2020.115786>
44. Zhong, Q., & Tong, D. (2020). Spatial layout optimization for solar photovoltaic (PV) panel installation. Renewable Energy, 150, 1-11. <https://doi.org/10.1016/j.renene.2019.12.099>



© Author(s) 2024. This work is distributed under <https://creativecommons.org/licenses/by-sa/4.0/>



Registration of interferometric DEM by deep artificial neural networks using GPS control points coordinates as network target

Ahmed Serwa^{*1}, Abdul Baser Qasimi², Vahid Isazade³

¹ Helwan University, Department of Civil Engineering, Cairo, Egypt, ahmed_serwa@yahoo.com

² Samangan University, Department of Geography, Samangan, Afghanistan, qasimi.abdul.a@smgu.edu.af

³ Kharazmi University, Department of Geographical Sciences, Tehran, Iran, vahidisazade75@gmail.com

Cite this study:

Serwa, A., Qasimi, A. B., & Isazade, V. (2024). Registration of interferometric DEM by deep artificial neural networks using GPS control points coordinates as network target. *International Journal of Engineering and Geosciences*, 9 (2), 292-301

<https://doi.org/10.26833/ijeg.1467293>

Keywords

Remote sensing
DEM
Registration
Distortion

Abstract

The interferometric Shuttle Radar Topography Mission (SRTM) satellite's digital elevation model (DEM) is an important tool for studying topographic features on a medium-spacing scale. Data were collected and processed using the satellite's orbital and navigation parameters with selected global GPS stations for verification. Distortion may be expressed by surveying measurements, such as position, distance, area, and shape. This study focuses on this distortion and proposes a new registration method to reduce its effect. Because of generality, the purpose shapes were excluded from this study. The proposed registration method depends on precise GPS control points that act as the ground truth for describing the considered surveying measurements. The processing was carried out using deep artificial neural networks (DANN) to produce a new registered DEM. A comparison was made between the original DEM and the new one, focusing on the selected surveying measurements. Another comparison was made between the GPS coordinates and SRTM polynomials to determine the potential of the proposed system. Some statistical investigations were applied to determine the level of significance of the distortion in each surveying measurement. The study shows that the distortion is highly significant; therefore, the proposed registration method is recommended to fix the distortion. An important finding is the enhancement in local coordinates scope.

Research Article

Received: 09.04.2024
Revised: 05.05.2024
Accepted: 06.05.2024
Published: 25.07.2024



1. Introduction

Remote sensing is a technology used to reduce costs and time by adopting automation [1]. The Radar Shuttle Radar Topography Mission (SRTM) collects interferometric radar data to produce near-global topographic products [2]. SRTM data are the main source of global topographic data, which depend on orbital navigation parameters to compute the space coordinates of the ground surface in addition to predefined ground control points (GCPs) for verification. The accuracy of the SRTM data varies from place to place, owing to the difference between the system reference properties and the proposed local reference properties. The accuracy of the SRTM DEM has been thoroughly investigated all over the world in many countries [3]. Many trials have been conducted to achieve the best performance of the SRTM DEM for use in engineering applications, for example, not for exclusion of the following research works. Su and Guo

[4] developed a practical way to correct the SRTM DEM in vegetated areas based on light detection and ranging (LiDAR) data. A similar investigation was conducted by Su et al. [5] but optical satellite images were added as a source for validation. Ochoa et al. [6] developed a methodology for the correction of digital elevation models for plain topography based on ground control points using a traditional methodology. Zhou et al. [7] investigated an adaptive terrain-dependent methodology for SRTM DEM correction for hard topography based on the M-estimator. Julzarika, Harintaka and Kartika [8] fused multiple DEM data sources, including SRTM DEM, to reach the optimum representation of vegetation areas. The use of artificial intelligence (AI) in remote sensing is an important modern aspect [9]. Deep artificial neural networks (DANN) provide good results in the processing and optimization of remote sensing data [10]. In addition to the previous literature, some research handle DEM from

different point of view, such as: Altunel [11] who studied the effect of DEM resolution on topographic wetness index. Bildirici and Abbak [12] studied the accuracy of SRTM DEM in comparison to local data within Turkey. Çubukçu et. al., [13] studied digital elevation modeling using artificial neural networks from the side of deterministic and geostatistical interpolation methods. Yakar [14] who studied Digital elevation model generation using robotic total station. Yalçın [15] studied DEM and GIS-based assessment of structural elements in the collision zone with a case study. Yılmaz and Erdogan [16] studied Designing high resolution countrywide DEM for Turkey. Yakar [17] investigated the effect of the grid resolution on the description of the surface. While Sarıturk [18] study on object detection and classification are among the most popular topics in Photogrammetry and Remote Sensing studies. Yakar et. al., [19] studied the performance of photogrammetric and terrestrial laser scanning methods in volume computing of excavation and filling sites. non-invasive, and inexpensive data collection technique [20] Yılmaz studied on examination the role of erosion of the surrounding soil by using Digital Elevation Model (DEM) [21].

This study attempts to find a practical approach to refine and register the SRTM DEM to the global reference to produce a corrected local one. To accomplish this research objective, one must understand the source of the SRTM DEM error. The error sources may vary in effect and value; therefore, we mention only the most effective and sensible sources according to the common literature. "conclusion" and they should be written in 10 font size, justify, bold and capital letters.

2. SRTM DEM error sources

SRTM DEM error sources can be abstracted to the baseline roll, phase, beam differential, timing, and position of the platform [2]. Figure 1 shows the SERTM error sources in abstracted form. The errors in interferometric measurements can be divided into two types: static and dynamic (time-varying) errors. The static errors were constant over the data collection period.

Because of their behavior, they can be calibrated using GCPs. Dynamic errors result from the motion of the interferometric mast and changes in the beam steering. Owing to their nature, dynamic errors can be partially waged by dynamic calibration and mosaicking. The SRTM error sources can be explained as follows. Baseline Roll Errors: These errors are caused by a lack of knowledge of the baseline roll angle, which induces a cross-track slope error in the proposed topography;

therefore, its magnitude is equal to the roll error. Phase Errors: These errors are caused by both thermal or differential speckle noise and systematic phase changes owing to antenna pattern mismatches of the instrument electronics. Beam Differential Errors: Systematic phase differences between the SRTM beams induce height differences at beam overlaps. This difference can be time dynamic because the beam steering angles vary according to the topography to maintain the swath constant. Timing and Position Errors: These are caused by uncompensated delays in the system or errors in the estimated baseline position, resulting in geolocation errors. These errors were treated using targets with known positions that can be identified in the radar image or topography. Figure 2 shows the SRTM Measurement Geometry used to emphasize the nature and behavior of the interferometric data acquisition system.

To clarify the source of errors in SRTM data, one needs to understand the geometry of the interferometric measurement and attitude and orbit determination avionics (AODA). The main measurement vectors are B, the vector of the interferometric baseline; P, the vector from the origin of the WGS84-fixed origin to the phase center of the inboard antenna; V, the platform velocity vector; PG, the vector from the WGS84-fixed origin to the GPS antenna in the outboard frame; G, the vector from the outboard origin to the GPS antenna; Po, the vector from the outboard origin to the outboard phase center GPS antenna; A, the vector from the inboard origin to the outboard origin; and Pi, the vector from the inboard origin to the phase center of the inboard. The interferometric baseline B and the position of the inboard antenna phase center P can be determined by Equation 1-2.

$$B = A - P_i + P_o \tag{1}$$

$$P = P_G - (G + A - P_i) \tag{2}$$

Where:

A: the vector measured from the origin of the inboard system to the origin of the outboard system.

P_i: the vector measured from the origin of the inboard system to the phase center of the inboard antenna.

P_o: the vector measured from the origin of the outboard system to the phase center of the outboard antenna.

P_G: the vector measured from the Earth-fixed frame to a GPS receiver in the outboard antenna.

G: the vector measured from the origin of the outboard system to the GPS receiver.

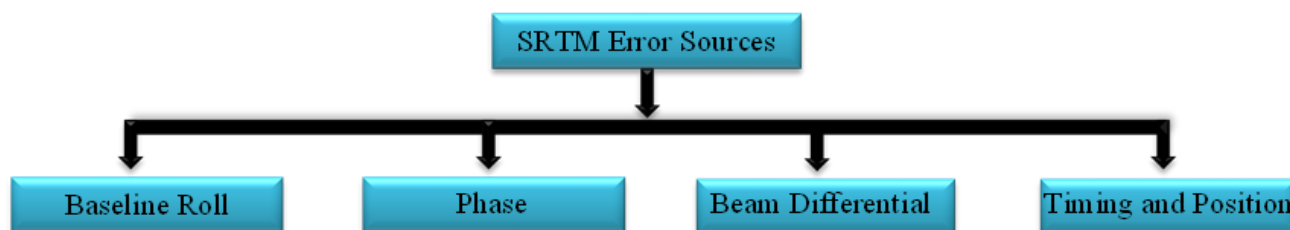


Figure 1. SRTM error sources.

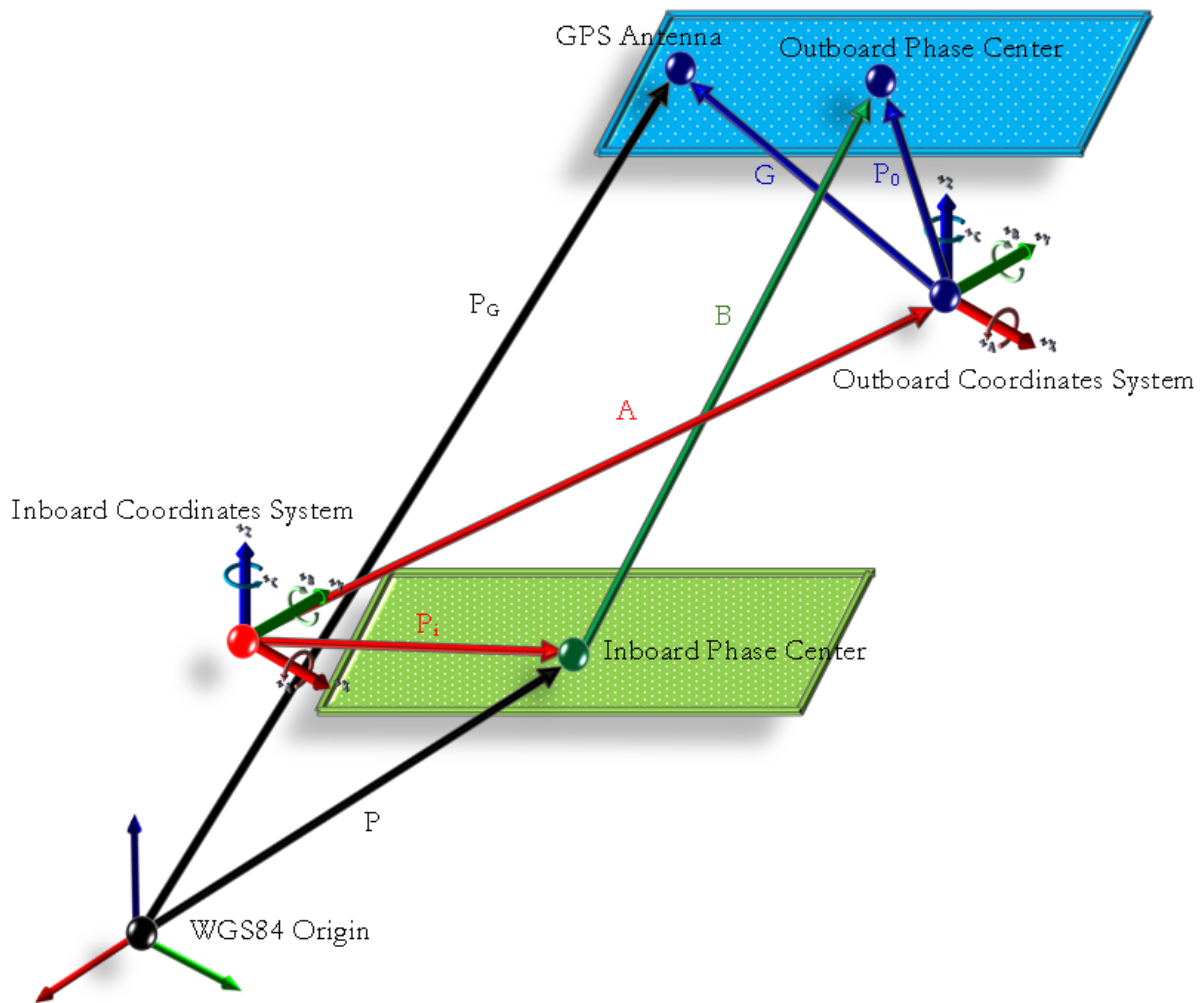


Figure 2. SRTM measurement geometry.

The error propagation of the interferometry can be deduced from the two Equations (1 and 2). Each error source has its own behavior and effect on the overall accuracy of the final DEM. Therefore, each error source had its own correction formulation. This study proposes an agglomerative methodology to express all error sources and their correction by applying a DANN in its supervised form. SRTM DEM correction can be carried out using many approaches, according to the literature. The most common general approach is mentioned in the previous section.

3. Method

This research is a trial to achieve a better representation of the SRTM DEM by applying registration using DANN. The methodology depends on using well-defined ground control points (GCPs) as a target for the DANN. While the SRTM DEM points are the input to the DANN, optimization can be carried out to achieve an output near the target GCPs. A selected group of points was chosen in both the SRTM DEM and the output DEM to verify the registration performance. Software is used to perform the tasks necessary to achieve the research objective. ENVI (by L3HARRIS) and DANND0, which were developed by Serwa in [22, 23] are

used to apply the necessary tasks in the developed system. A detailed description of the developed system is presented in the next section.

3.1. System overview

Figure 3 shows a systematic diagram of the proposed system. The system starts with the input of both the original SRTM DEM and a group of well-defined GPS points (GCPs) in the ENVI environment. Then, ENVI is used to perform the primitive task of determining the coordinates of the GCPs in the original SRTM DEM. At this stage, the GCPs have two coordinate values: the first belongs to the original SRTM DEM reference, while the second belongs to the GPS reference. Theoretically, both systems have the same reference in datum and projection (WGS 84), but practically, they are not the same because of the difference in conditions and data acquisition methodology. SRTM DEM depends on multiple sources such as KGPS distributed in large areas in addition to GEO-SAR and Ocean GCPs stations. The user depends directly on GPS in engineering applications. DANND0 software was then used to apply the DANN algorithm developed and refined by Serwa [10]. The result of this stage is the DANN SRTM DEM coordinates, which should be compared with the GPS reference

coordinates to adopt the accuracy assessment. To stand on a heavy base, other coordinates were obtained using the SRTM polynomials (first order) by assigning GPS

coordinates as a destination (target) and SRTM DEM coordinates as the source (input). Therefore, a tri-tier comparison was adopted.

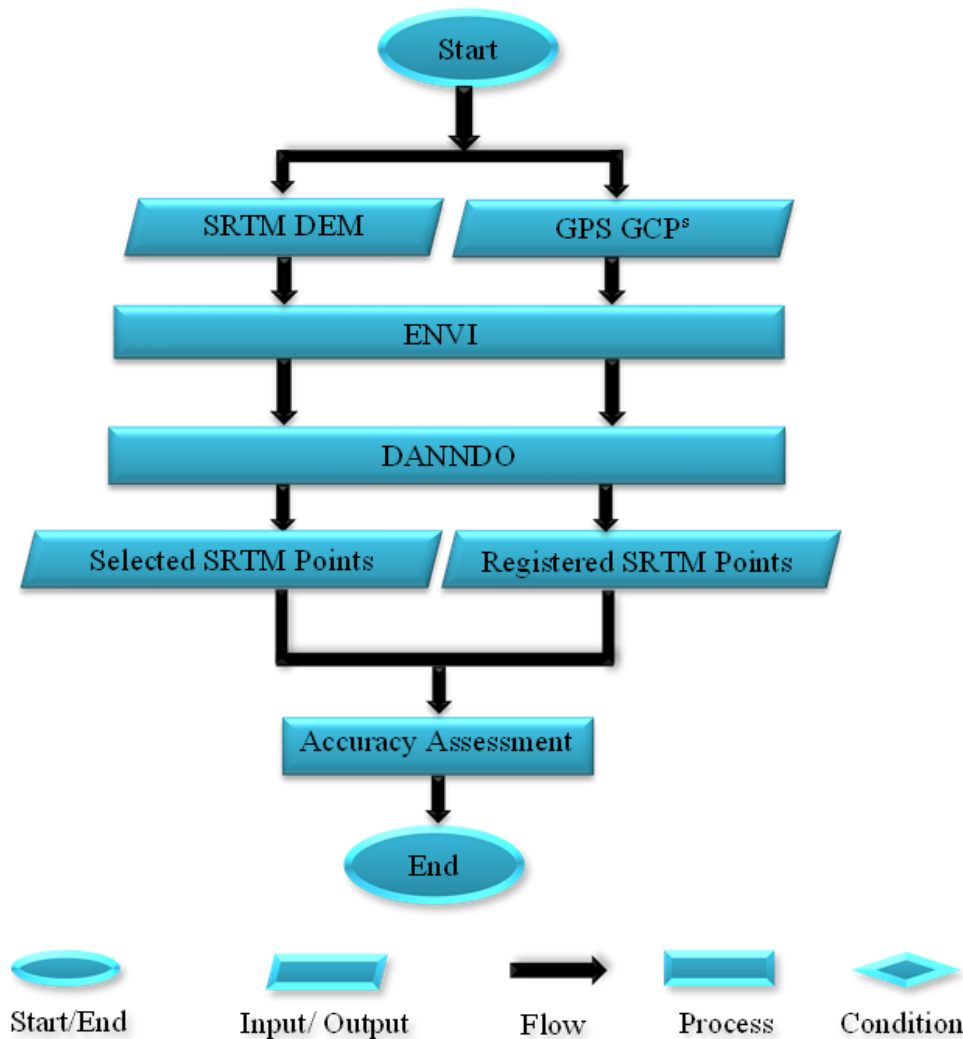


Figure 3. Systematic diagram of the research work.

3.2. Research data

The study area is part of the Aswan government in southern Egypt. SRTM DEM data of the research area were selected as the main data. Figure 4 shows the research area with the SRTM coverage. Four SRTM parts were required to cover the study area, so a mosaic was created. Eleven GCPs were selected for the study area, as shown in Figure 5. Ten virtual lines were used from each point to verify the linear accuracy of the registration process.

It is known that all requirements to obtain high measuring accuracy are taken such GCPs position selection, suitable measuring time 3–5 h, clear weather, etc. The selection of the GDOP in the GPS unit settings is necessary to obtain good accuracy even if there are more satellites.

Post-processing was performed to guarantee high accuracy. The distribution of GCPs is uniform and well defined. The measured coordinates of the 11 GCPs on the SRTM DEM model are tabulated in Table 1.

Each of the two GCPs is connected to form a virtual line, so we have fifty-five virtual lines (10+9+8+7+6+5+4+3+2+1). The tested fifty-five lines (L1 to L55) are tabulated as the first and second points in Table 2. The 1st refers to the starting point of the line and 2nd refers to the end point of the line. All the fifty-five lines were required to examine the distortion of the SRTM DEM as relative positioning. The coordinates of the 11 points were used to examine the distortion as absolute positioning. Both coordinates and lines were used to measure the performance level of the developed registration method. The values (coordinates and lengths) obtained from the GPS RTK devices were compared to the corresponding values obtained from the SRTM DEM (before and after registration). The values obtained from the GPS RTK were considered as the reference for this study. One must note that the tested lines varied in length to guarantee the generality of the study. The lines are used to express the relative accuracy of the selected GCPs and to examine the possible distortion of the registration process that may happen.



Figure 4. Study area with SRTM coverage.

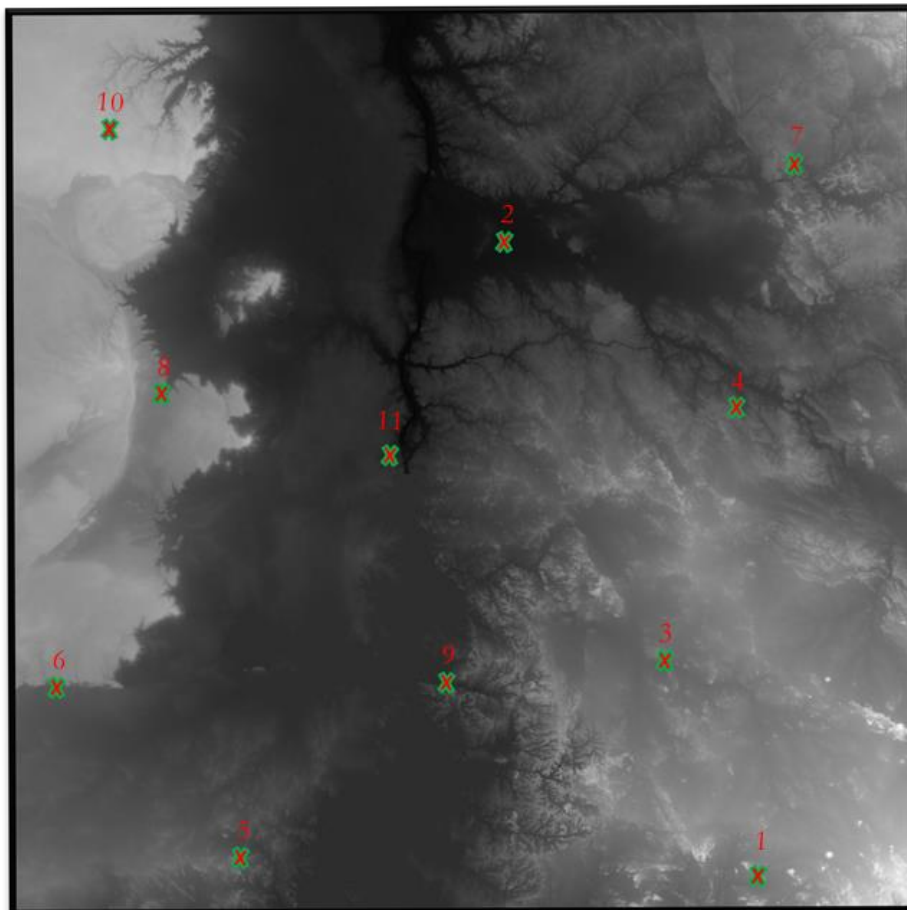


Figure 5. Distribution of GCPs in the study area.

Table 1. Coordinates of the GPS RTK coordinates of GCPs.

Pt #	X(m)	Y(m)	Z(m)
1	4894706.557	3225058.685	2506843.692
2	4873970.238	3179726.309	2602051.813
3	4889028.873	3203812.701	2544410.157
4	4876272.598	3184869.959	2591490.078
5	4932975.348	3167873.758	2504372.125
6	4936967.961	3139491.269	2531845.863
7	4844461.177	3174284.116	2662790.544
8	4924124.074	3118209.851	2582091.044
9	4923969.782	3149010.829	2544998.351
10	4892962.537	3124899.017	2632605.538
11	4896745.246	3164032.431	2578557.316

Table 2. List of the tested 55 lines.

Start End											
	1	2	3	4	5	6	7	8	9	10	11
1	NA	L1	L2	L3	L4	L5	L6	L7	L8	L9	L10
2	NA	NA	L11	L12	L13	L14	L15	L16	L17	L18	L19
3	NA	NA	NA	L20	L21	L22	L23	L24	L25	L26	L27
4	NA	NA	NA	NA	L28	L29	L30	L31	L32	L33	L34
5	NA	NA	NA	NA	NA	L35	L36	L37	L38	L39	L40
6	NA	NA	NA	NA	NA	NA	L41	L42	L43	L44	L45
7	NA	NA	NA	NA	NA	NA	NA	L46	L47	L48	L49
8	NA	NA	NA	NA	NA	NA	NA	NA	L50	L51	L52
9	NA	NA	NA	NA	NA	NA	NA	NA	NA	L53	L54
10	NA	NA	NA	NA	NA	NA	NA	NA	NA	NA	L55
11	NA	NA	NA	NA	NA	NA	NA	NA	NA	NA	NA

3.3 DANN algorithm

In this study, DANN is adopted in the architecture of a multilayer perceptron (MLP), which is famous for such applications, and the algorithm of back propagation neural networks (BPNN) is adopted. The final presented algorithm is known as the DANN. The DANND software package of DANND is used to apply the required algorithms. One must be stabilized to declare any debate concerning the optimization process. The architecture of the DANN consists of an input layer (q) which represents the inputs, hidden layers (t, k, etc.) that represent the processing points of the input data and responsible for delivering the final processing to the output layer, and an output layer (m) which is responsible for producing the final network output, as indicated in Figure 6. In first (learning stage), the input vector Xq is the raw SRTM DEM point. The output vector Om is the corresponding computed value of the network. The structure of the DANN was selected after many trials to achieve a stable structure.

The DANN with BPNN was described by Serwa and Saleh [1].

The process of deep BPNN for remote sensing classification problems can be explained in the following steps:

- Step 1: Input SRTM DEM coordinates.
- Step 2: Input GPS coordinates for the selected GCPs.
- Step 3: setting up training and testing data sets.

Step 4: Input SRTM DEM data vector to the input unit in the input layer.

Step 5: Get the output value of each neuron in the input layer.

Step 6: Get the input value for each neuron in the first hidden layer.

Step 7: Get the output value for each neuron in the first hidden layer.

Step 8: Get the input value for each neuron in the next hidden layer.

Step 9: Get the output value for each neuron in the current hidden layer.

Step 10: Repeat step 8 and Step 9 for all hidden layers.

Step 11: Get the input value for each neuron in the output layer (the final output).

Step 12: Get the network error value using.

Step 13: Investigate if the error limit is exceeded or all pixels is entered go to step 22 otherwise continue.

Step 14: Get the error value in the output unit using.

Step 15: Update the weights between the output layer and the final hidden layer.

Step 16: Get the error in the hidden unit.

Step 17: Update the weights between the last hidden layer and the previous one.

Step 18: Repeat Step 16 and 17 for all intermediate hidden layers.

Step 19: Compute the error value in the first hidden layer neuron.

- Step 20: Update the weights between the input layer and the first hidden layer.
- Step 21: Go to step 4.
- Step 22: Store the final weights.
- Step 23: Apply steps 4 to 11 for all SRTM DEM data except training dataset.

Detailed information regarding the DANN algorithm is available in Serwa [10]. Figure 7 shows the main interface of DANND0 SW, which was used to apply the DANN with the BPNN algorithm. The tested network structure was 3,7,8 and 3 for the input, hidden, and output layers, respectively.

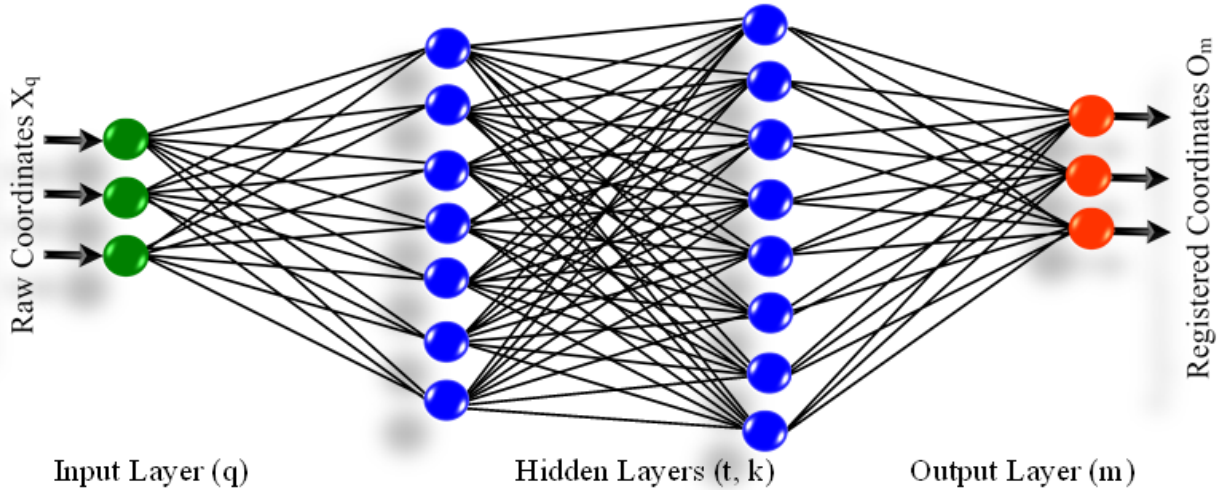


Figure 6. DANN architecture -input layer (q), hidden layers (t and k) and output layer (m).

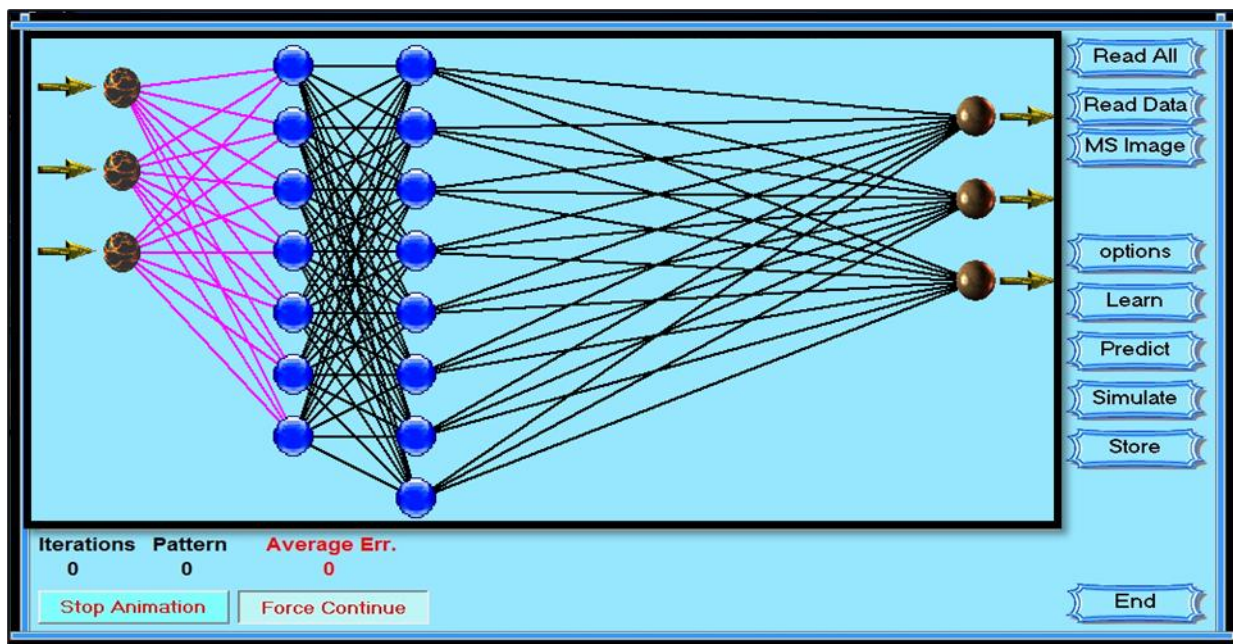


Figure 7. DANND0 SW interface.

4. Results

After the DANN is stabilized, it can be used to obtain the final output of the SRTM DEM coordinates. Table 3 shows the final errors in both DANN and SRTM DEM polynomials (1st order). While Table 4 lists the coordinates of the GCPs obtained from the GPS RTK Trimble device with the corresponding DANN SRTM DEM coordinates in addition to the SRTM DEM polynomials (1st order). GCPs have high precision (*.###) and it reaches mms. The coordinates of the GCPs were obtained by following the necessary requirements for using the GPS RTK device.

The SRTM DEM coordinates of the selected GCPs were obtained by registration using the DANN on DANND0 SW. The SRTM DEM polynomials was obtained by calculation using the solver in Excel. The SRTM DEM coordinates are the inputs for the DANN algorithm, whereas the GPS RTK coordinates are the target for the network output.

The results are summarized in Tables 4 and 5, for the X direction, $\sigma_x= 21.990m$ with an average absolute error of 16.631m. For the Y direction, $\sigma_y= 18.168m$ with an average absolute error of 14.129m. For the Z direction, $\sigma_z= 28.707m$ with an average absolute error of 21.662m. For R, the space vector $\sigma_R= 40.469m$ with an average absolute error of 34.217m.

Table 3. Coordinates of DANN SRTM DEM and SRTM DEM polynomials.

Point #	Errors in DANN Coordinates			Errors in Polynomials Coordinates		
	X(m)	Y(m)	Z(m)	X(m)	Y(m)	Z(m)
1	-46.302	-38.720	-8.997	-13.306	-32.120	11.511
2	-22.533	-3.023	2.251	-9.457	5.508	-10.419
3	8.767	-10.372	-67.198	35.043	-3.938	-58.323
4	-5.360	-11.895	22.904	9.907	-3.557	13.893
5	-3.475	-19.319	-63.205	48.841	-28.197	-17.804
6	-54.784	4.291	-60.991	-3.243	-8.099	-18.807
7	-2.109	-27.894	34.791	-9.58	-11.753	-9.088
8	-23.515	-8.025	-27.431	16.611	-18.664	-3.912
9	-52.207	-10.607	-19.145	-8.486	-18.567	11.982
10	-6.420	24.096	-40.972	13.15	22.655	-47.83
11	-42.056	1.470	28.011	-15.315	2.3696	34.720

Table 4. Coordinates of the GCPs in both GPS RTK, DANN SRTM DEM and SRTM DEM polynomials.

Point #	GPS RTK			DANN SRTM DEM			SRTM DEM Polynomials		
	X(m)	Y(m)	Z(m)	X(m)	Y(m)	Z(m)	X(m)	Y(m)	Z(m)
1	4894706.557	3225058.685	2506843.692	4894719.864	3225090.806	2506832.181	4894752.86	3225097.405	2506852.689
2	4873970.238	3179726.309	2602051.813	4873979.695	3179720.801	2602062.232	4873992.771	3179729.332	2602049.561
3	4889028.873	3203812.701	2544410.157	4888993.83	3203816.64	2544468.48	4889020.105	3203823.073	2544477.356
4	4876272.598	3184869.959	2591490.078	4876262.691	3184873.516	2591476.185	4876277.958	3184881.855	2591467.173
5	4932975.348	3167873.758	2504372.125	4932926.507	3167901.956	2504389.93	4932978.824	3167893.077	2504435.331
6	4936967.961	3139491.269	2531845.863	4936971.205	3139499.368	2531864.671	4937022.745	3139486.977	2531906.854
7	4844461.177	3174284.116	2662790.544	4844470.757	3174295.869	2662799.632	4844463.287	3174312.01	2662755.753
8	4924124.074	3118209.851	2582091.044	4924107.463	3118228.515	2582094.956	4924147.589	3118217.877	2582118.475
9	4923969.782	3149010.829	2544998.351	4923978.268	3149029.396	2544986.369	4924021.989	3149021.436	2545017.497
10	4892962.537	3124899.017	2632605.538	4892949.387	3124876.362	2632653.368	4892968.958	3124874.92	2632646.51
11	4896745.246	3164032.431	2578557.316	4896760.561	3164030.061	2578522.595	4896787.302	3164030.96	2578529.304

Table 5. Results summary.

	σ_x (m)	dX Avg(m)	σ_y (m)	dY Avg(m)	σ_z (m)	dZ Avg(m)	σ_R (m)	dR Avg(m)
DANN SRTM DEM	21.990	16.631	18.168	14.129	28.707	21.662	40.469	34.217
SRTM DEM Polynomials	32.959	24.321	19.201	14.519	41.992	34.172	56.731	51.259

X, Y, Z, and R express the absolute positioning of the space coordinates. The results for the lengths (relative positioning) for all 55 lines are $\sigma_L = 37.263m$ with an average absolute error of 30.032m. For the SRTM polynomials, $\sigma_x=22.763m$ (not better than DANN) with average absolute error =24.321m, $\sigma_y=19.201m$ (worse than DANN) with average absolute error= 14.519m, $\sigma_z=41.992m$ (better than DANN) with average absolute error=34.172m, and $\sigma_R=56.731m$ (worse than DANN) with average absolute error=51.259m. A 2nd order polynomials is applied but it gives a worst result. To determine the potential of the DANN registration methodology, a statistical test of hypothesis was conducted. The performance of the DANN registration can be measured in many ways. The most significant method was to test the hypothesis. Assuming a 95% level of confidence, the first hypothesis is that there is no significant difference between the true (reference) GPS RTK measurements and the resulting DANN-registered measurements, which indicates success. The alternative is that there is a significant difference between them, which indicates failure of the DANN registration process. The testing sample is 11 in the case of X, Y, Z, and R (absolute position) < 30, so that the degree of freedom for is 10 for both hypotheses. Using a 95% level of significance, a critical value of $\pm 2\sigma$ can be obtained as the acceptance limit for all measurements. It is obvious that all average absolute error values for all measurements are less than 2σ or even less than σ (68% level of significance). Therefore, we must accept the hypothesis

that there is no significant difference between GPS RTK measurements and DANN-registered measurements. The alternative hypothesis must be rejected, and registration using DANN is reliable. Figure 8 shows the final registered SRTM DEM with GCPs.

5. Conclusion

The results show that using DANN is feasible due to the enhancement in accuracy compared with the classical napping polynomials. Referring to the research objective, it can be concluded that using the DANN registration methodology is the most effective. The reason behind the effectiveness is obtaining a good (small) acceptable distortion in both absolute positioning (X, Y, Z, and R) and relative positioning (lengths). It should be noted that there is no need to compare the research results with any other registration method because of the dependence on high-accuracy GPS-RTK GCPs. In other words, the ground reference is very accurate, and the DANN registration results show no significant difference. Although the DANN algorithm is very sensitive to the initial network weights, it provides good results in this research because of the use of a high-accuracy network target (GPS RTK GCPs). Accordingly, it is recommended to use the DANN registration methodology with high-accuracy GPS-RTK GCPs. When using a first-order polynomials to register the SRTM DEM, it is obvious that it is not better at all because most errors in all directions are higher than DANN method. Even applying 2nd order polynomials, it is

not better than DANN. One important note concerning the limitations of this study is that it can be considered as a local system for a certain part of the earth's surface. The reason is the errors and distortions that are dependent

on the size of the area may increase. The behavior in such a case cannot be predicted.

For future recommendations, one should consider using deep learning algorithms (e.g. convolution neural networks, deep belief neural networks etc.).

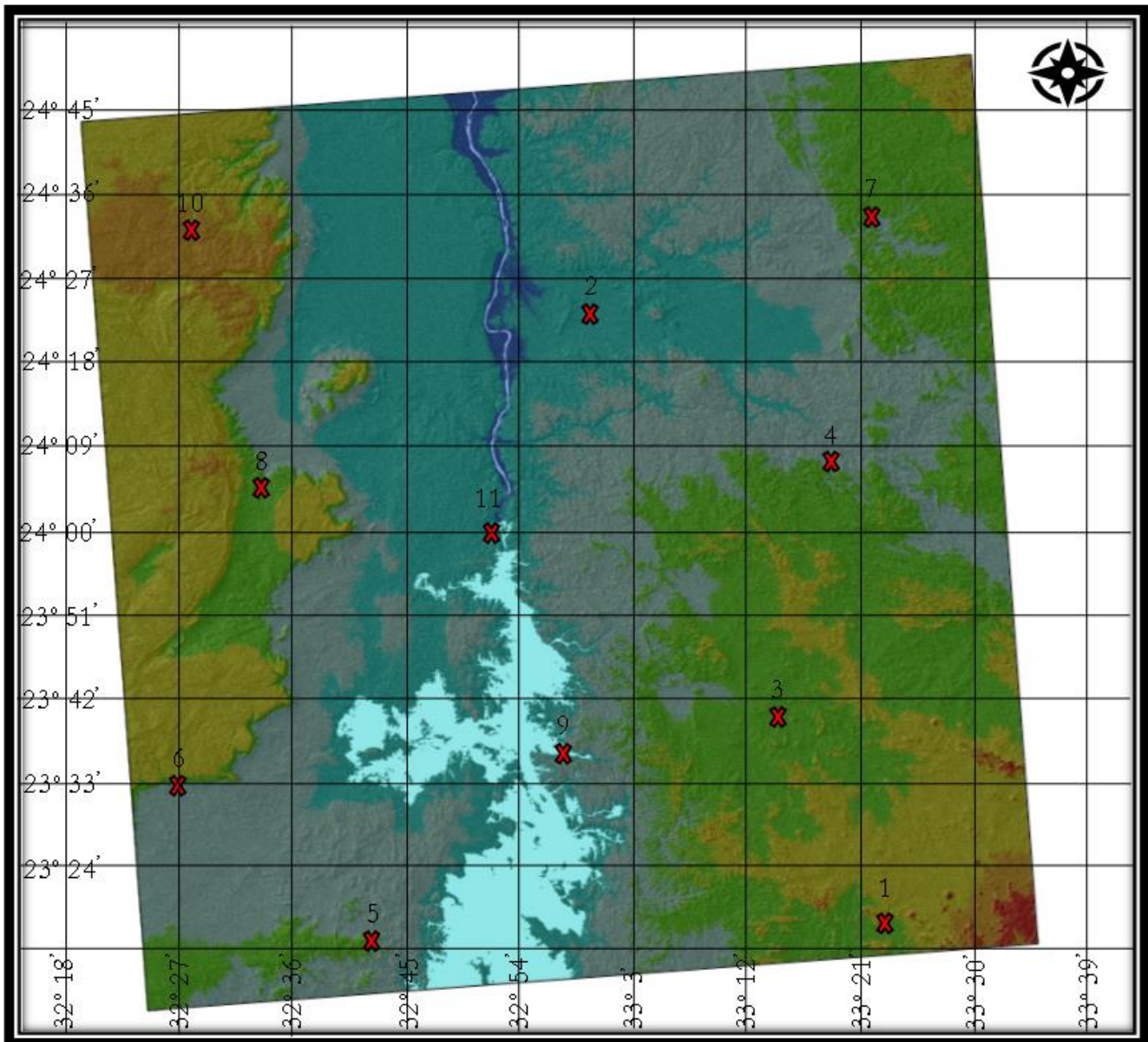


Figure 8. The final registered DEM with GCPs shown.

Author contributions

Ahmed Serwa: Conceptualization, Methodology, Software, Field study and Writing-Original draft preparation

Abdul Baser Qasimi: Data curation, Writing-Original draft preparation, Software, Validation.

Vahid Isazade: Visualization, Investigation, Writing-Reviewing and Editing.

Conflicts of interest

The authors declare no conflicts of interest.

References

1. Serwa, A., & Saleh, M. (2021). New semi-automatic 3D registration method for terrestrial laser scanning data of bridge structures based on artificial neural networks. *The Egyptian Journal of Remote Sensing and Space Science*, 24(3), 787-798. <https://doi.org/10.1016/j.ejrs.2021.06.003>
2. Rodriguez, E., Morris, C. S., Belz, J. E., Chapin, E. C., Martin, J. M., Daffer, W., & Hensley, S. (2005). An assessment of the SRTM topographic products.
3. Chen, C., Yang, S., & Li, Y. (2020). Accuracy assessment and correction of SRTM DEM using ICESat/GLAS data under data coregistration. *Remote Sensing*, 12(20), 3435. <https://doi.org/10.3390/rs12203435>

4. Su, Y., & Guo, Q. (2014). A practical method for SRTM DEM correction over vegetated mountain areas. *ISPRS Journal of Photogrammetry and Remote Sensing*, 87, 216-228. <https://doi.org/10.1016/j.isprsjprs.2013.11.009>
5. Su, Y., Guo, Q., Ma, Q., & Li, W. (2015). SRTM DEM correction in vegetated mountain areas through the integration of spaceborne LiDAR, airborne LiDAR, and optical imagery. *Remote Sensing*, 7(9), 11202-11225. <https://doi.org/10.3390/rs70911202>
6. Ochoa, C. G., Vives, L., Zimmermann, E., Masson, I., Fajardo, L., & Scioli, C. (2019). Analysis and correction of digital elevation models for plain areas. *Photogrammetric Engineering & Remote Sensing*, 85(3), 209-219. <https://doi.org/10.14358/PERS.85.3.209>
7. Zhou, C., Zhang, G., Yang, Z., Ao, M., Liu, Z., & Zhu, J. (2020). An adaptive terrain-dependent method for SRTM DEM correction over mountainous areas. *IEEE Access*, 8, 130878-130887. <https://doi.org/10.1109/ACCESS.2020.3009851>
8. Julzarika, A., Harintaka, H., & Kartika, T. (2021). Vegetation Height Estimation using Satellite Remote Sensing in Peat Land of Central Kalimantan. *Journal of Environmental Analysis and Progress*, 6(1), 24-34. <https://doi.org/10.24221/jeap.6.1.2021.3001.024-034>
9. Serwa, A., & El-Semary, H. H. (2020). Semi-automatic general approach to achieve the practical number of clusters for classification of remote sensing MS satellite images. *Spatial Information Research*, 28(2), 203-213. <https://doi.org/10.1007/s41324-019-00283-z>
10. Serwa, A. (2022). Development of soft computational simulator for optimized deep artificial neural networks for geomatics applications: remote sensing classification as an application. *Geodesy and Cartography*, 48(4), 224-232. <https://doi.org/10.3846/gac.2022.15642>
11. Altunel, A. O. (2023). The effect of DEM resolution on topographic wetness index calculation and visualization: An insight to the hidden danger unraveled in Bozkurt in August, 2021. *International Journal of Engineering and Geosciences*, 8(2), 165-172. <https://doi.org/10.26833/ijeg.1110560>
12. Bildirici, İ. Ö., & Abbak, R. A. (2020). Türkiye ve çevresinde SRTM sayısal yükseklik modelinin doğruluğu. *Geomatik*, 5(1), 1-9. <https://doi.org/10.29128/geomatik.551071>
13. Çubukçu, E. A., Demir, V., & Sevimli, M. F. (2022). Digital elevation modeling using artificial neural networks, deterministic and geostatistical interpolation methods. *Turkish Journal of Engineering*, 6(3), 199-205. <https://doi.org/10.31127/tuje.889570>
14. Yakar, M. (2009). Digital elevation model generation by robotic total station instrument. *Experimental Techniques*, 33(2), 52-59. <https://doi.org/10.1111/j.1747-1567.2008.00375.x>
15. Yalçın, C. (2022). DEM and GIS-based assessment of structural elements in the collision zone: Çağlayançerit, Kahramanmaraş (Türkiye). *Advanced Remote Sensing*, 2(2), 66-73.
16. Yılmaz, A., & Erdoğan, M. (2018). Designing high resolution countrywide DEM for Turkey. *International Journal of Engineering and Geosciences*, 3(3), 98-107. <https://doi.org/10.26833/ijeg.384822>
17. Yakar, M., Yılmaz, H. M., & Yurt, K. (2010). The effect of grid resolution in defining terrain surface. *Experimental Techniques*, 34, 23-29. <https://doi.org/10.1111/j.1747-1567.2009.00553.x>
18. Saritürk, B., Bayram, B., Duran, Z., & Seker, D. Z. (2020). Feature extraction from satellite images using segnet and fully convolutional networks (FCN). *International Journal of Engineering and Geosciences*, 5(3), 138-143. <https://doi.org/10.26833/ijeg.645426>
19. Yakar, M., Yılmaz, H. M., & Mutluoglu, O. (2014). Performance of photogrammetric and terrestrial laser scanning methods in volume computing of excavation and filling areas. *Arabian Journal for Science and Engineering*, 39, 387-394. <https://doi.org/10.1007/s13369-013-0853-1>
20. Browning Jr, D. C. (2024). Close-range photogrammetry for analysis of rock relief details: An investigation of symbols purported to be Jewish Menorahs in Rough Cilicia. *Mersin Photogrammetry Journal*, 6(1), 39-51. <https://doi.org/10.53093/mephoj.1434605>
21. Yılmaz, H. M., Yakar, M., Mutluoglu, O., Kavurmaci, M. M., & Yurt, K. (2012). Monitoring of soil erosion in Cappadocia region (Selime-Aksaray Turkey). *Environmental Earth Sciences*, 66, 75-81. <https://doi.org/10.1007/s12665-011-1208-4>
22. Serwa, A. (2017). Optimizing activation function in deep artificial neural networks approach for landcover fuzzy pixel-based classification. *International Journal of Remote Sensing Applications*, 7, 1-10. <https://doi.org/10.14355/ijrsa.2017.07.001>
23. Ismail, S. A., Serwa, A., Abood, A., Fayed, B., Ismail, S. A., & Hashem, A. M. (2019). A Study of the Use of Deep Artificial Neural Network in the Optimization of the Production of Antifungal Exochitinase Compared with the Response Surface Methodology. *Jordan Journal of Biological Sciences*, 12(5), 543-551.





Comparative analysis of non-invasive measurement methods for optimizing architectural documentation

Serhan Tuncer^{*1} , Uğur Avdan² 

¹ Eskişehir Technical University, Department of Architecture, Türkiye, stuncer@eskisehir.edu.tr

² Eskişehir Technical University, Institute of Earth and Space Sciences, Türkiye, uavdan@eskisehir.edu.tr

Cite this study:

Tuncer, S., & Avdan, U. (2024). Comparative analysis of non-invasive measurement methods for optimizing architectural documentation. *International Journal of Engineering and Geosciences*, 9 (2), 302-313

<https://doi.org/10.26833/ijeg.1424881>

Keywords

Terrestrial laser scanners
UAV
Photogrammetry
Architectural documentation
Non-invasive survey methods

Abstract

Architectural documentation not only plays a critical role in the conservation of historical structures, but also enables their detailed comprehension of the structure. This study aims to assess the most effective methods for drawing and modeling architectural structures and present their advantages and disadvantages. Measurements play a significant role in this context, and today's technology offers the potential to accelerate this process and enhance accuracy. However, the application of these technologies can impose additional burdens such as elevated expenses, the requisite for specialized personnel, and the management of substantial data volumes. Therefore, determining the appropriate measurement method in line with the quality of architectural documentation is essential. For this study, the Mosque of Kurşunlu Complex in Eskişehir was selected for its historical and topographical attributes which enabled all methods to be examined. The data produced via terrestrial laser scanning, aerial photogrammetry and terrestrial photogrammetry methods were examined in terms of the production of drawings and models for different analysis methods such as structure, daylight and building acoustics, as well as survey drawings required for the architectural documentation processes of the building. The study concluded that no single method could produce holistic data on its own, and the best results for comprehensive documentation were achieved by integrating terrestrial laser scanning and aerial photogrammetry. Furthermore, for products that do not require comprehensive data, photogrammetric methods were more efficient.

Research Article

Received: 24.01.2024
Revised: 20.02.2024
Accepted: 25.02.2024
Published: 26.07.2024



1. Introduction

Historically, structures have not only provided functional spaces but have also been expressions of humanity's engineering and aesthetic capabilities. The long-term and effective use of these structures requires maintenance, repair, enhancement, and restoration. Consequently, the need for drawings of the structure is essential, serving as guides that enables us to understand and manage the building. However, in some cases, two-dimensional architectural drawings do not suffice. For example, when analyzing building physics such as statics, lighting, sound, ventilation, heating, etc., in a digital environment, three-dimensional models are also required. Also the use of 3D drawings is of great importance for both academic studies and applied conservation studies. They play a crucial role in restoration planning, improving stakeholders'

understanding and contributing to the archiving and reconstruction of cultural heritage [1, 2]. The measurement process is crucial in achieving the precision required for the drawing or model production to meet specific needs. Comprehensive architectural documentation, for instance, can prevent the building from performing its original function throughout the documentation process, or, if the building is a cultural heritage, it may not be accessible for visitors during this process. To prevent such situations documentation should be executed with minimal intervention. Therefore, it is essential to keep the process short and minimize contact with the structure to obtain accurate data.

Non-invasive technology methods contribute significantly to architectural measurement in terms of speed and precision [3]. However, these methods can pose disadvantages in some cases due to their high cost,

the need for skilled personnel, and large data sizes [4]. Furthermore, in architectural documentation, the location of the building, surrounding structures or objects, architectural features of the building, current functionality, and even ornamental details directly impact the choice of documentation method. Consequently, it is important to determine a method that is suitable for all these conditions before starting an architectural documentation project. This study attempts to determine the most effective non-invasive methods offered by technology for different types of drawings and solid model productions required by various methods of analysis.

2. Method

2.1. Measurement methods

Recent advancements in technology have facilitated the effective utilization of digital measurement methods in the documentation of cultural heritages [5]. These developments have brought significant progress in terms of precision and accuracy, strengthening efforts in the conservation of historical and cultural heritage. These methods, which basically detect three-dimensional depth using light, are divided into active and passive methods throughout literature. Active methods, which generate their own energy, include techniques such as lidar, radar, tomography, and holography. Passive methods that rely on measuring light without an independent energy source include photogrammetry, shape from focus, and microscopy. These methods are diverse in their application depending on the characteristics of the object to be documented [6].

Both active and passive methods are effectively used in the documentation processes of cultural heritage assets, each with its own set of advantages and disadvantages. Therefore, these methods have been integrated to capitalize on their respective strengths. In architectural documentation, the most preferred methods are laser scanning and photogrammetric techniques, which are also evaluated in this study.

Utilized since the early 1980s, terrestrial laser scanning technologies offer the advantage of rapidly

generating large volumes of data. However, they have a limited capacity to produce precise data from the upper surfaces of tall structures and sharp corners, as well as limitations in documenting the visible light range. Consequently, additional photogrammetric measurements may be required for color data acquisition [7].

Photogrammetric methods offer solutions that are much more affordable. They can provide better results in terms of documentation of texture and colors, but require expertise in the stages of data production and processing [8]. Besides, the data production density and sensitivity are lower than laser scanning [7].

2.2. Study area

To compare the measurement methods, the Mosque of Kurşunlu Complex, a 16th century structure located in the historic district of Odunpazarı in Eskişehir, Türkiye, was selected. This structure was chosen because it presents different levels of challenges for measurements to be carried out with the aforementioned methods. The building is still in use as a mosque, and it is located in a historical area, therefore having a constant flow of visitors. This directly affects the day and time range of the measurements. The mosque is also located within a courtyard of a complex with trees of different heights and buildings with different functions. These elements were also effective in the selection of the tools to be used for the measurement. The topography of the building, its architectural details, its single entrance and ornamental details were all factors in determining the suitable measurement method. With this ensemble of distinctive features, the Kurşunlu Complex Mosque was ideal for testing different measurement methods (Figure 1).

The application of non-invasive measurement methods such as optical measurement, aerial photogrammetry, and terrestrial photogrammetry were used to investigate the most effective method for producing drawings and models of the building that are required as input by different analysis methods. The work plan for this process and the software used are presented in Figure 2.



Figure 1. Aerial view of the Kurşunlu Complex [9].

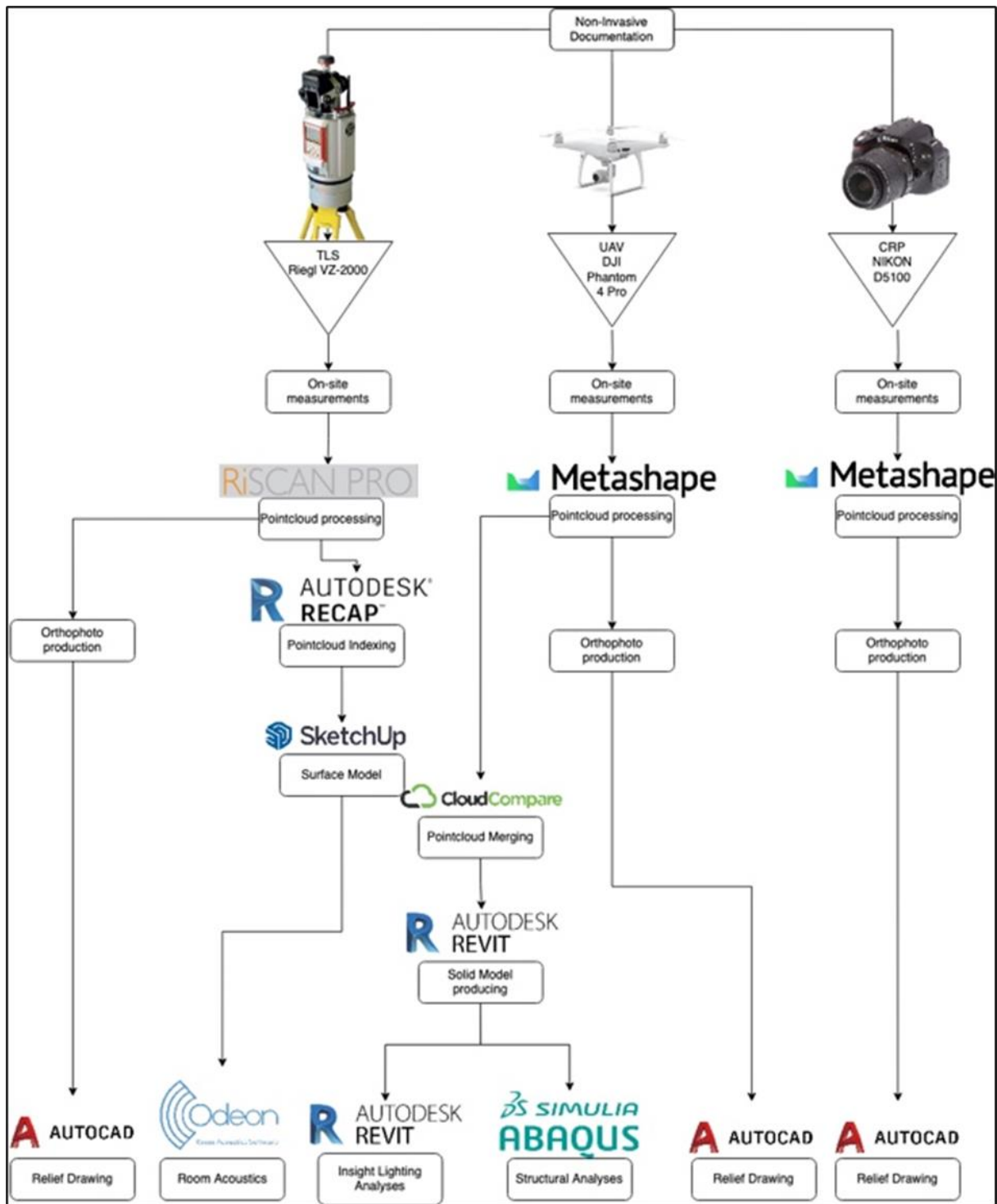


Figure 2. Software used in the study and the workflow.

3. Data collection

3.1. Terrestrial laser scanner

Terrestrial laser scanners can process a large amount of data in a very short time. Modern versions are easily portable and operate without a separate computer, thanks to integrated operating systems [10]. However, these scanners are expensive and require trained personnel to operate [11].

The scanning of Kurşunlu Mosque was conducted using a Riegl VZ-2000 model 3D terrestrial laser scanner. This laser scanner operates based on the principle of time-of-flight. Under the normal light and reflection

conditions, it exhibits a sensitivity of 5 mm at 50 meters and can measure within the range of 1 to 2000 meters. The emitted laser beam from the scanner falls within the near-infrared spectrum, with a wavelength ranging from 0.7 μm to 1.3 μm . The scanner has the capability to rotate along a 100° vertical axis and a 360° horizontal axis. The angular resolution of the device can be increased up to 0.001°, and it has the capacity to acquire 400,000 point data per second [12]. The exterior facades and interior volume of the structure were scanned from a total of 20 stations, each with a 0.040° angular resolution. The Kurşunlu Complex site's dense tree coverage and surrounding buildings effect the positioning of the scanning stations around the mosque. For the exterior

facades, scanning was conducted from 11 different stations. However, as there was no platform which provided a comprehensive view of the dome surface, sufficient data from the superstructure could not be captured. To produce comprehensive data, it is essential to integrate measurements from both the interior and exterior of the structure. The laser scanner's software, Riscan Pro, allows for the integration of point clouds without the use of reflectors. To achieve this, a sufficient amount of common identifiable surfaces between positions is required. The presence of only one door in the mosque inhibits the positioning of a sufficient common surface between the last externally scanned position and the first internally scanned position. To address this issue, 10 reflectors with a 5 cm diameter were strategically placed in the last external and first internal positions to connect the two groups of point clouds. As for the interior volume of the structure, scanning was conducted from 6 different stations, resulting in 9 scans in total. The aspect ratio of the structure and the height of the dome prevent the entire dome from being captured from a single perspective. Therefore, to gather data of the upper structure, three stations were set up with a vertical angle of 45°. The entire measurement process was completed in 45 minutes, and an average of 7.5 million points were collected from each position, resulting in a total of 222,448,595 points measured.

3.2. Photogrammetric documentation

The photogrammetry method is the process of taking photographs with standard cameras and subjecting them to various corrections to transform them into map-like, measurable images. Photogrammetry is classified based on the location where the image is taken, evaluation methods, or application area. In these methods, essentially, high overlap sequential photographs are taken, allowing for the generation of 3D models and orthophotos. The calibration values of the cameras are of great importance, as well as ensuring that the consecutive photographs taken have at least a 60% overlap ratio [13]. In this study, Kurşunlu Mosque was measured using both aerial photogrammetry and terrestrial photogrammetric methods.

3.2.1. Aerial photogrammetry

Unmanned aerial vehicles (UAVs) are able to perform both pre-planned automated flights and user-controlled flights. Pre-planning variables such as flight altitude, flight path, image overlap ratio, and the number of captured photographs, facilitate faster and more precise acquisition of data. However, conducting automated flights, especially within dense urban environments, is not always feasible due to varying heights and surrounding structures. Manual flight control also requires skilled personnel. UAVs enable the rapid imaging of extensive areas and are more cost-effective compared to terrestrial laser scanners [14].

The planning for the documentation process using the UAV began with the DJI Phantom Professional 3 model. It

can be controlled remotely or programmed for various flight modes [15]. As Kurşunlu Complex is a densely populated area and one of the most visited regions in Eskişehir, flight time and day were meticulously determined to minimize any potential hazards. The flight took place around 09:15, after ensuring that a group of visiting students had left the area. To prevent pilot-related errors, the automated flight followed a predetermined route. The circular flight mode, which captures photographs with the object of interest at the center, was selected. To avoid accidents, the flight altitude of the vehicle was set at 35 meters; 3 meters above the minaret, which is the tallest structure in the complex.

The flight plan was uploaded to the UAV, and the flight was initiated. However, due to an oversight in planning the starting point location, the UAV crashed into the minaret between the "home point" and the "starting point", causing damage to the UAV, with its debris scattering across the complex. Thanks to the accurate determination of the flight day and time, no living beings were harmed. Nevertheless, the documentation could not be carried out.

A second flight was conducted using the DJI Phantom 4 Professional model UAV [16]. As in the first attempt, the most suitable day and time for the complex were chosen for the flight. The flight for the exterior of the mosque was completed at 10:08 AM. However, it was not possible to collect data from the interior of the structure using the UAV. Although the UAV was able to enter the building through its single door, its movement was obstructed by the chandelier, preventing comprehensive photographing. Additionally, the camera mounted underneath the UAV can only move vertically up to 45 degrees; rendering it impossible to gather data from the interior's upper structure.

3.2.2. Terrestrial photogrammetry

The number of equipment available for terrestrial photogrammetry studies is increasing. Photogrammetry software can produce map-like, measurable data not only from SLR cameras but also from mobile phone cameras [17]. To obtain these data, it is important not only to be able to identify the calibration values of the equipment used but also to capture photographs with the correct overlap ratio. Therefore, this measurement method can be described as the most cost-effective.

In the study, a Nikon D5100 camera was used with a Nikkor 18-300 mm lens. With a camera resolution of 16MP, 80 high-overlap images were obtained from inside the structure and 140 images from outside.

4. Data modelling

Data collected from the field was processed using different software programs based on the method used. Data generated with the terrestrial laser scanner were georeferenced, merged, and processed into a comprehensive point cloud using its proprietary software, "Riscan Pro". The aerial and ground-based

photographs were photogrammetrically processed using "Agisoft Metashape" software.

4.1. Terrestrial laser scanner

Point clouds generated with the terrestrial laser scanner were processed individually for each position.

The point clouds were colorized using undistorted images captured by the scanner's camera, and objects around the mosque, as well as reflection noises, were all removed. When the interior and exterior scanning positions were connected, a comprehensive point cloud consisting of a total of 116,821,366 points was generated (Figure 3).

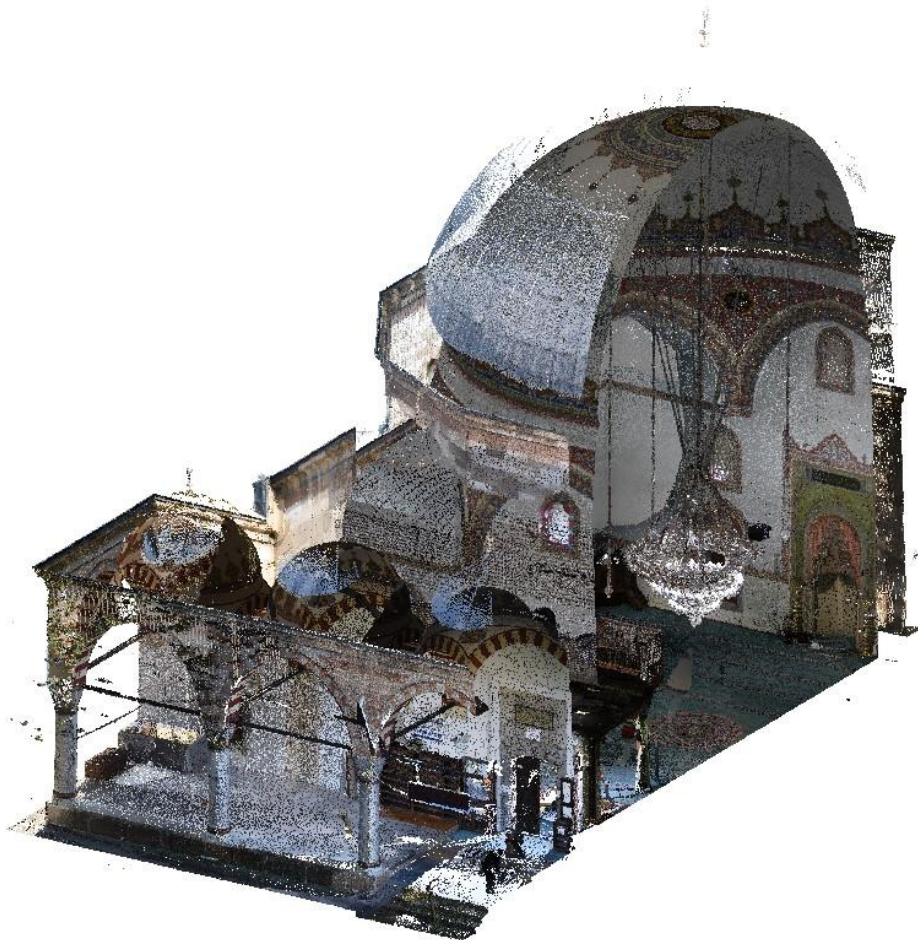


Figure 3. A cross section of point clouds generated with the terrestrial laser scanner.

4.2. Aerial photogrammetry

After the data obtained by the unmanned aerial vehicle (UAV) was subjected to photogrammetric processing, a point cloud consisting of a total of 21,023,345 points was produced in the final product. Due to the obstruction of the surrounding structures and tall trees, sufficient images could not be produced from the entrance section and southern facade of the building. In Figure 4, large gaps are seen in these sections where data was insufficient in the point cloud.

4.3. Terrestrial photogrammetry

In documentation with a camera, objects around the building also prevented the entire facade being photographed from every point and from the same distance to the building. This caused the overlap rates

between consecutive frames to decrease and prevented the production of a comprehensive point cloud.

Inside the building, 80 frames of photos were processed with different depth filtering settings offered by the software in an attempt to produce a dense point cloud that could be used as a base. In this process, the data was first processed with the aggressive depth filter and a point cloud of 5,232,512 points was produced, but there was too much noise to allow the reading of the model. Subsequently, low-quality photos were deleted, and light and contrast adjustments were made on the remaining 63 images. In the newly created point cloud, the noise decreased, but it was evident that no points were produced on white surfaces. To produce points in these areas as well, the depth filter was lowered by one step and the photos were reprocessed with the moderate filter. It was concluded that the noise in the final product was caused by the inability to detect depth in the white surfaces (Figure 5).



Figure 4. The point clouds generated with the data obtained from UAV.

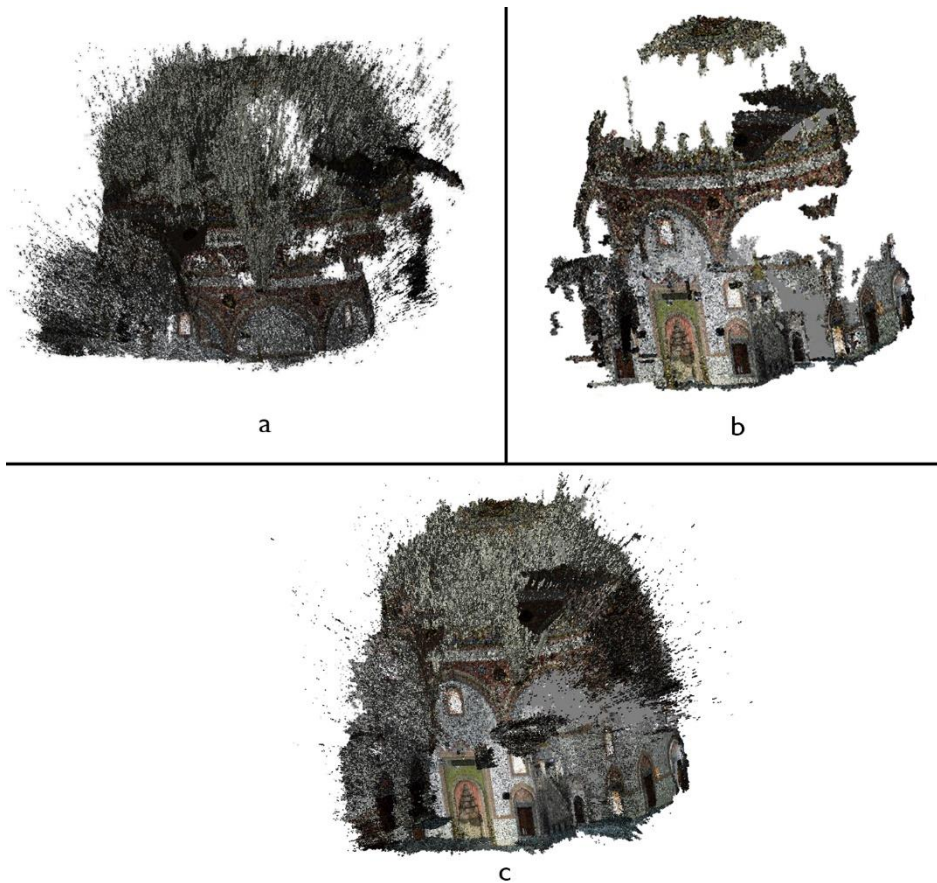


Figure 5. Point clouds are generated from camera images with different depth filter settings. a. processed with aggressive filtering using all photos, b. processed with aggressive filtering using best photos, c. processed with moderate filtering using best photos.

5. Results

5.1. Measurement sensitivity

For comparison, measurements of identical spaces were conducted both on the output obtained as well as conventional measurements. The diagonal measurements of the ground and the measurements of

the west facade, which are common to all three methods, were taken as references in the comprehensive models produced. These measurements were compared with those made with a steel tape measure on site. When the results in [Table 1](#) are examined, it is evident that the measurements made with non-invasive methods have sufficient accuracy for architectural drawing and modeling.

Table 1. Comparative measurements carried out on the western facade of the building.

	In-situ measurements (cm)	TLS (cm)	AP (cm)	TP (cm)
a. Left window jamb, short side	166	166,3	166	166
b. Left window jamb, long side	183	183,4	182,8	182,6
c. Right window jamb diagonal	212	212,8	212,5	211,9
d. Length of the Facade	1445	1444	1445	1444
e. Height of the facade	771	772,4	772,8	772,2
f. Diagonal measurements of the interior floor	2070	2074	-	-

5.2. Evaluation of outputs according to different analyses

As previously mentioned, drawings and models of architectural structures are needed for different reasons and the structure of outputs to be produced also varies as a result. Therefore, in addition to the drawing base for architectural surveying, solid models were also generated from the collected data for acoustic, structural, and daylight analyses; each requiring specific levels of detail.

It is important to note that no single method alone can generate a comprehensive model. While terrestrial laser scanning provided detailed data of the building's facades and interiors, it produced very few data points from the roof level. Conversely, the unmanned aerial vehicle generated detailed data from the roof level but was limited in capturing data from within the structure. The documentation work carried out with the camera also did not yield a cohesive result for model generation. Therefore, integrating measurement results obtained through different methods is required for comprehensive modeling. Integration was performed using "CloudCompare," an open-source software that effectively processes point clouds. With this software, common points in the existing point clouds were manually marked, allowing the alignment of two-point cloud data sets from the same area, resulting in a comprehensive dataset.

5.2.1. Drawing bases for architectural surveys

Architectural survey drawings are cross-sections and elevations that encompass all the details of a structure. Therefore, architectural survey drawings include plans of different levels as well as facade drawings [18]. Facade drawings require a greater level of information to visualize architectural details on surfaces. Orthophotos are photogrammetric outputs that provide both measurable and photographic information of these details. An orthophoto is a photograph or a set of photographs in which geometric and perspective distortions caused by differences in height, tilt, and curvature are corrected, resulting in a fixed scale image [19, 20]. It is possible to obtain orthophoto outputs with all the methods used in the study. However, data could not be generated from every point of the building using these methods. Therefore, only the west facade, which serves as a common surface for data generation, was used in orthophoto production.

Orthophoto production from terrestrial laser scanning data was performed using the orthophoto extension of the "Riscan Pro" software. For this process, the software requires models created by the

triangulation method from positions that view the area where orthophotos will be produced. After these models are created, the 'undistortion' process, which corrects lens-induced distortions, is applied. Then, the orthophoto of the relevant area can be produced. Although the general details of the facade can be read, the low resolution due to the production of the orthophoto negatively affects its use as a base (Figure 6).

The steps for orthophoto production from data obtained with the camera and the UAV are identical. A 3D model was produced from the dense point clouds created in the "Agisoft Metashape" software. Then, the orthophoto of the west facade was produced using the software's orthomosaic tool. In both methods, the details of the structure can be easily read in the orthophotos. The UAV-sourced orthophoto has the advantage of including information regarding the upper structure, enabling the creation of a complete image which includes the drum area. Data could not be produced from the upper levels in the orthophoto sourced from the camera, as in the terrestrial laser scanner; but the visual quality of the produced orthophoto is higher than that of both methods (Figure 7).

When the generated orthophotos are evaluated as a base for architectural survey drawings, significant differences can be observed, especially in terms of material degradation details. In Figure 8, details of stone degradation, located near the left window on the second floor of the structure, are presented from the produced orthophotos. Although the degradation is discernible in all three methods, only the orthophoto produced with terrestrial photogrammetry provides a drawable level of detail. Many other deteriorations on the facade are also depicted in detail in the drawing based on this orthophoto.

With the floor plans, the only effective method capable of documenting both the interior and exterior of the structure was terrestrial laser scanning. They are therefore the only effective method for plan drawings which include wall thickness. However, the limited data generated for the roof structure hinders the production of the roof plan and sections. For this reason, integrated data was used. The generated point clouds were indexed in "Autodesk ReCap" software. This allows data containing a large number of points to be seamlessly used as a base in Autodesk Software Corporation's other software programs. The indexed point clouds were opened in "Autodesk AutoCAD" software, sections of desired thicknesses from different elevations were taken, and floor plans were created. Since it was possible to create vertical sections in the desired axis of the structure, elevation sections could also be quickly generated.



Figure 6. The orthophoto of the west facade produced from TLS data.



Figure 7. Orthophotos of the west façade. a. produced from UAV and b. produced from TF.

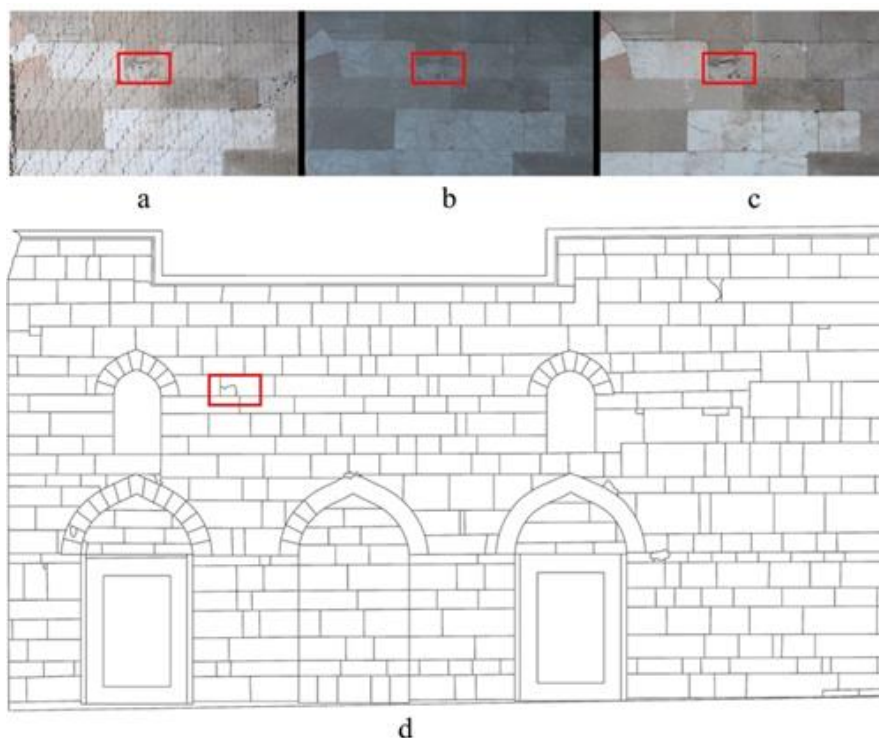


Figure 8. Details of the deterioration near the second-floor left window of the building. a. produced by laser scanning, b. produced by UAV, c. produced by terrestrial photogrammetry method and d. survey drawing produced from terrestrial photogrammetric sourced orthophoto.

There are notable differences between plan drawings produced with the collected data and those used in publications. In publications related to the structure, the transition element to the dome is described as a squinch but drawn as semi domes in the plans. A squinch is a transitional element placed at the corners of a square-plan structure, transforming it into an octagonal shape and providing a more favorable surface for the dome to rest on [21]. A squinch consists of two arches at right angles to each other, which both ensure the load transfer of the system. In a semi-dome, which is essentially a

continuous arch form, load transfer occurs through all surfaces. In other words, these two architectural elements function entirely differently from each other, and it is crucial for them to be accurately represented in architectural drawings. Slicing the comprehensive point cloud parallel to the ground at 10 cm intervals reveals how the squinch should be represented in plan drawings. Figure 9 shows sections taken from the point cloud following the plan used in publications and the plan drawn on top of this section.

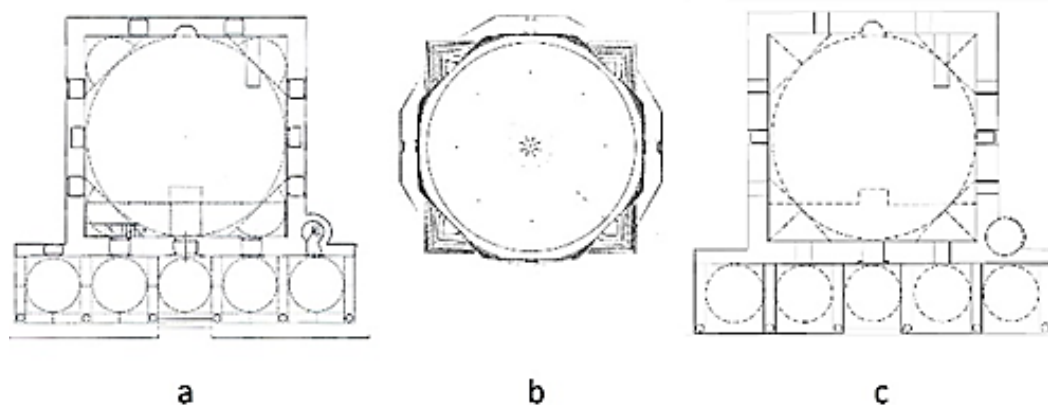


Figure 9. Plan drawings a. Drawing from publications [22], b. Horizontal sections from point cloud c. Plan drawing with the help of sections.

5.2.2. Solid model production for different analyses

To analyze structural elements in the computer environment, digital solid models are required. However, each analysis requires model production in different forms and details. Some require precise measurements of details such as wall thicknesses and arch spans, while others require simpler models. This directly influences the choice of measurement methods. Choosing the right measurement methods for accurate analyses directly impacts the time and cost of projects. The data produced from the measurement methods in this study were utilized to create models for acoustic, structural, and daylight analyses. Ultimately, the study aimed to determine the documentation methods required for model production at different levels.

Indoor daylight analyses were carried out with “Autodesk Revit” software. Since “Revit” is an Autodesk product, it can easily use the point clouds indexed in the “Recap” software as a base. In daylight analysis, it is crucial for window positions to be accurate in the models, for models to be sealed with no openings other than the windows, and for wall thicknesses to be included. Therefore, the models must be comprehensive and solid. With the indexed point cloud used as a base in the software, solid model generation was easily achieved, and daylight analysis was successfully conducted.

“Abaqus CAE” software was used as a reference for structural analyses. In these, all structural elements are drawn separately, and each element's materials and properties are be individually processed. With the help of

“Revit,” even the most complex geometric structures, such as the main dome and squinches, were seamlessly created and transferred to “Abaqus CAE” software.

The “Odeon” software was used for the acoustic analysis. In such analyses, it is preferable to use models that are as simple as possible, composed of surfaces, with no gaps [23]. In this case, modeling only the inner surfaces of the structure in a shell-like form was sufficient. Terrestrial laser scanning provides these conditions per se. However, modeling the complex geometric structures of masonry architecture for the software poses some challenges. Particularly, models must not have gaps at points where circular elements like domes, half-domes, and squinches meet the angled body walls. Although solid models in different formats can be imported to “Odeon” software, a plug-in has been produced for “SketchUp.” For this reason, the model for acoustic analysis was produced in “SketchUp” software. The model was transferred to “Odeon” and tested using a validation tool, confirming the absence of any gaps.

6. Discussion and conclusions

The most prominent result in this study is the significant differences between conventional methods and non-invasive technology methods. With conventional methods, it is necessary to conduct field work during daylight hours, transfer measurement results to paper overnight, and make corrections on-site the next day [24]. This could mean spending at least two days in the field. Even with terrestrial laser scanning, which requires the longest time spent on site, both

interior and exterior measurements of the structure were completed in a total of 1 hour and 40 minutes. For facade surveys, the photography process for photogrammetric production was completed in just a few minutes.

For conventional methods, three people usually need to be positioned on different parts of the field. While two people fix the measuring instrument, one person performs the readings [24]. In this study, all measurements were carried out by a single person.

The drawing error in the published floorplans of the structure emphasizes the importance of incorporating non-invasive technology methods into measurement processes. The fact that the dome transition element, a squinch, is represented as a semi-dome in plan drawings, have directly affected scientific studies to date. Documentation methods involved in the process should also be valued for preventing human errors.

In conclusion, no documentation method alone can collect enough data to produce a comprehensive model. Unless the terrestrial laser scanner is elevated from the ground, it cannot collect data from the outside the building or the superstructure. Although Kurşunlu Mosque is located on a quite hilly topography, there is no elevation allowing for this measurement. In addition, this mosque is relatively small in scale compared to other Ottoman structures of the period. Therefore, the terrestrial laser scanner alone is not sufficient for comprehensive documentation of monumental structures. With unmanned aerial vehicles, terrain

conditions caused serious problems. Surrounding buildings and natural obstacles prevented the complete documentation of the mosque. Nevertheless, sensitive data production for modeling was provided from the outer wall and the superstructure. In data processing, a loss of precision was observed, especially in the corners of the building. With the terrestrial photogrammetric methods, it was not possible to evaluate the data obtained from inside the building. The large number of single-colored and prolonged surfaces within the building caused problems in creating the final outputs. To conclude, it is not quite possible to use a single method for a comprehensive documentation of a monumental architectural structure. Therefore, it is important to determine the methods to be used based on the characteristics of the structure and the type of desired final product before starting documentation studies.

Terrestrial laser scanning has come closest to producing comprehensive data. However, it was less successful in orthophoto production compared to other methods. The quality of the produced orthophoto is so low that it is not possible to draw on it. The inability to read details on the facade and the gaps in some places affected the quality and production speed of the result drawing. In the terrestrial laser scanner software, there is a long data processing time for orthophoto production. Considering the cost, it falls behind other methods, especially in orthophoto production.



Figure 10. Comparison of methods according to the outputs and relevant suggestions.

For data generation and processing, UAV and camera documentation have the same photogrammetric foundations [25-27]. Therefore, the same software and data processing methods have been used for both. However, the resulting orthophotos show differences. Among the three products, documentation conducted with a camera produced orthophotos are most suitable for reading facade details and for drawing on. However, some distortions have been observed in the orthophoto from documentation with a camera, especially towards the north side of the facade. The absence of distortions in the southern part indicates the necessity of taking photographs perpendicular to the surface. Large trees in the northern corner of the facade obstructed the capturing of images directly facing this area. Uncontrolled adjustment of the overlap ratio in the images and a limited number of photos resulted in empty spaces and distortions in the produced orthophoto. In the production of a facade survey base, terrestrial photogrammetry is the most efficient method in terms of time and cost. However, achieving sufficient accuracy and precision requires expertise in fieldwork.

The orthophoto produced from data obtained through UAV is clear and legible, allowing for easy drawing. The method's high overlap ratio in the photos and its ability to capture more data from the upper corners have reduced distortion. In the initial documentation, an accident led to the destruction of the UAV, but the chosen flight time ensured no significant damage was caused. This incident demonstrates that uncontrolled UAV use in large and densely populated cities carries critical risks.

Upon evaluating all these data, despite its disadvantages in terms of cost, speed, and the need for expertise, it is apparent that utilizing UAVs is the most effective method for facade survey due to the accuracy of the resulting output.

Methods that can be preferred depending on the nature of the analysis have been presented with strengths and weaknesses. In Figure 10, positive and negative aspects of each method are listed according to the desired output, and recommended methods are specified separately.

Acknowledgement

This paper was extracted from an MSc thesis entitled "Comparison of Advanced Technology Methods in the Creation of Architectural Models," conducted by Serhan Tuncer at Eskisehir Technical University under the supervision of Prof. Dr. Uğur Avdan.

Author contributions

Serhan Tuncer: Conceptualization, Methodology, Data Collection, Analysis, Investigation, Writing - Original Draft, Writing - Review & Editing

Uğur Avdan: Supervision, Validation, Writing - Review & Editing

Conflicts of interest

The authors declare no conflicts of interest.

References

- Özendi, M. (2022). Kültür varlıklarının yersel lazer tarama yöntemi ile dijital dokümantasyonu: Zonguldak Uzun Mehmet Anıtı örneği. *Geomatik*, 7(2), 139-148. <https://doi.org/10.29128/geomatik.917528>
- Uslu, A., & Uysal, M. (2017). Arkeolojik eserlerin fotogrametri yöntemi ile 3 boyutlu modellenmesi: Demeter Heykeli örneği. *Geomatik*, 2(2), 60-65. <https://doi.org/10.29128/geomatik.319279>
- Sarıtaş, B., Aydar, U., & Karademir, B. (2023). The Use of Terrestrial Laser Scanning Technology in the Documentation of Cultural Heritage: The Case of Bezmialem Valide Sultan Fountain. *Advanced LiDAR*, 3(2), 62-69.
- Köse, S., & Us, H. (2023). Application of Terrestrial Laser Scanning (TLS) Technology for Documentation of Cultural Heritage Buildings and Structures: A Case Study Sarı İsmail Sultan Tomb. *Advanced LiDAR*, 3(1), 35-40.
- Doğan, Y., & Yakar, M. (2018). GIS and three-dimensional modeling for cultural heritages. *International Journal of Engineering and Geosciences*, 3(2), 50-55. <https://doi.org/10.26833/ijeg.378257>
- Pavlidis, G., & Royo, S. (2017). 3D Depth Scanning. *Digital Techniques for Documenting and Preserving Cultural Heritage: Arc Humanities Press*, 195-198.
- Bertellini, B., Gottardi, C., & Vernier, P. (2020). 3D survey techniques for the conservation and the enhancement of a Venetian historical architecture. *Applied Geomatics*, 12, 53-68. <https://doi.org/10.1007/s12518-019-00267-6>
- Guery, J., Hess, M., & Mathys, A. (2017). Photogrammetry. *Digital Techniques for Documenting and Preserving Cultural Heritage: Arc Humanities*, 229-235.
- www.kulturportali.gov.tr
- Yaman, A., & Yılmaz, H. M. (2017). The effect of object surface colors on terrestrial laser scanners. *International Journal of Engineering and Geosciences*, 2(2), 68-74. <https://doi.org/10.26833/ijeg.296835>
- Reznicek, J., & Pavelka, K. (2008). New low-cost 3d scanning techniques for cultural heritage documentation. *The International Archives of the Photogrammetry, Remote Sensing and Spatial Information Sciences*, 37, 5298-5301.
- Riegl, M. (2015). *General Description and Data Interfaces*. Horn: Riegl Laser Measurement Systems.
- Hanke, K., & Grussenmeyer, P. (2002). *Architectural Photogrammetry: Basic Theory, Procedures, Tools*. ISPRS Commission, 5.
- Jo, Y. H., & Hong, S. (2019). Three-dimensional digital documentation of cultural heritage site based on the convergence of terrestrial laser scanning and unmanned aerial vehicle photogrammetry. *ISPRS International Journal of Geo-Information*, 8(2), 53. <https://doi.org/10.3390/ijgi8020053>
- DJI, M. (2016). *DJI Phantom 3 User Manual*: DJI.
- DJI, M. (2016). *DJI Phantom 4 User Manual*: DJI.

17. Asadpour, A. (2021). Documenting historic tileworks using smartphone-based photogrammetry. *Mersin Photogrammetry Journal*, 3(1), 15-20. <https://doi.org/10.53093/mephoj.899432>
18. Pellegri, G. (2015). Survey and drawing representation of architecture and environment: different teaching approach for architects and engineers. *Procedia-Social and Behavioral Sciences*, 174, 4090-4095. <https://doi.org/10.1016/j.sbspro.2015.01.1159>
19. Özbalmumcu, M. (2007). Fotogrametrik yöntemle ortofoto harita üretiminin temel esasları, ortofotonun yararları ve kullanım alanları. TUFUAB IX. Teknik Sempozyumu, İstanbul.
20. Xiang, H., & Tian, L. (2011). Method for automatic georeferencing aerial remote sensing (RS) images from an unmanned aerial vehicle (UAV) platform. *Biosystems Engineering*, 108(2), 104-113. <https://doi.org/10.1016/j.biosystemseng.2010.11.003>
21. Harris, C. M. (2006). *Dictionary of Architecture and Construction*. New York: McGraw-Hill Book Company
22. İnce, K. (2011). *Eskişehir Kurşunlu Külliyesi*. Ankara: Bilgin Kültür Sanat.
23. Christensen, C. L., & Koutsouris, G. (2013). *ODEON Room Acoustics Software*. Denmark: Scion DTU
24. Ahunbay, Z. (2016). *Tarihi Çevre Koruma ve Restorasyon*. İstanbul: YEM Yayın.
25. Doğan, Y. (2019). 3D Modelling of Bridges by UAV Photogrammetry Method. *Mersin Photogrammetry Journal*, 1(1), 7-11.
26. Aktan, N., Çolak, A., & Yılmaz, H. M. (2022). Production of orthophoto by UAV data: Yaprakhisar example. *Advanced UAV*, 2(1), 17-23.
27. Karataş, L., Alptekin, A., Karabacak, A., Yakar, M. (2022). Detection and documentation of stone material deterioration in historical masonry buildings using UAV photogrammetry: A case study of Mersin Sarisih Inn. *Mersin Photogrammetry Journal*, 4(2), 53-61. <https://doi.org/10.53093/mephoj.1198605>



© Author(s) 2024. This work is distributed under <https://creativecommons.org/licenses/by-sa/4.0/>